Mechanisms and Machine Science

Abdelbadia Chaker
Claudio Villegas Ulloa
Houssem Saafi *Editors*

Emerging Fields in Mechanism and Machine Science

Proceedings of IFToMM EFIMMS 2026

IFToMM

Springer

Mechanisms and Machine Science 205

Series Editors

IFToMM, *Fredericton, Canada*
Marco Ceccarelli, *Department of Industrial Engineering, University of Rome Tor Vergata, Roma, Italy*

Advisory Editors

Juan Carlos Jauregui Correa, *Universidad Autonoma de Queretaro, Queretaro, Mexico*
Gokhan Kiper, *Izmir Institute of Technology, Urla, Türkiye*
Chin-Hsing Kuo, *University of Wollongong, Wollongong, NSW, Australia*
Matteo Russo, *Dept. Of Industrial Engineering, University of Rome Tor Vergata, Rome, Italy*
Yukio Takeda, *Tokyo Institute of Technology, Tokyo, Japan*
Mónica Urízar, *University of the Basque Country UPV/EHU, Bilbao, Spain*

This book series establishes a well-defined forum for monographs, edited Books, and proceedings on mechanical engineering with particular emphasis on MMS (Mechanism and Machine Science). The final goal is the publication of research that shows the development of mechanical engineering and particularly MMS in all technical aspects, even in very recent assessments. Published works share an approach by which technical details and formulation are discussed, and discuss modern formalisms with the aim to circulate research and technical achievements for use in professional, research, academic, and teaching activities.

This technical approach is an essential characteristic of the series. By discussing technical details and formulations in terms of modern formalisms, the possibility is created not only to show technical developments but also to explain achievements for technical teaching and research activity today and for the future.

The book series is intended to collect technical views on developments of the broad field of MMS in a unique frame that can be seen in its totality as an Encyclopaedia of MMS but with the additional purpose of archiving and teaching MMS achievements. Therefore, the book series will be of use not only for researchers and teachers in Mechanical Engineering but also for professionals and students for their formation and future work.

The series is promoted under the auspices of International Federation for the Promotion of Mechanism and Machine Science (IFToMM).

Prospective authors and editors can contact Mr. Pierpaolo Riva (publishing editor, Springer) at: pierpaolo.riva@springer.com

Indexed by SCOPUS and Google Scholar.

Abdelbadia Chaker · Claudio Villegas Ulloa · Houssem Saafi
Editors

Emerging Fields in Mechanism and Machine Science

Proceedings of IFToMM EFIMMS 2026

Springer

Editors
Abdelbadia Chaker
CNRS – University of Poitiers – ENSMA
Institut PPRIME
Poitiers, France

Claudio Villegas Ulloa
Dept. of Mechanical Engineering (DIMec)
Universidad del Bio-Bio
Concepcion, Region del Bio-Bio, Chile

Houssem Saafi
University of Sousse
National Engineering School of Sousse
Sousse, Tunisia

ISSN 2211-0984 ISSN 2211-0992 (electronic)
Mechanisms and Machine Science
ISBN 978-3-032-22269-5 ISBN 978-3-032-22270-1 (eBook)
https://doi.org/10.1007/978-3-032-22270-1

© The Editor(s) (if applicable) and The Author(s), under exclusive license
to Springer Nature Switzerland AG 2026

This work is subject to copyright. All rights are solely and exclusively licensed by the Publisher, whether the whole or part of the material is concerned, specifically the rights of translation, reprinting, reuse of illustrations, recitation, broadcasting, reproduction on microfilms or in any other physical way, and transmission or information storage and retrieval, electronic adaptation, computer software, or by similar or dissimilar methodology now known or hereafter developed.
The use of general descriptive names, registered names, trademarks, service marks, etc. in this publication does not imply, even in the absence of a specific statement, that such names are exempt from the relevant protective laws and regulations and therefore free for general use.
The publisher, the authors and the editors are safe to assume that the advice and information in this book are believed to be true and accurate at the date of publication. Neither the publisher nor the authors or the editors give a warranty, expressed or implied, with respect to the material contained herein or for any errors or omissions that may have been made. The publisher remains neutral with regard to jurisdictional claims in published maps and institutional affiliations.

This Springer imprint is published by the registered company Springer Nature Switzerland AG
The registered company address is: Gewerbestrasse 11, 6330 Cham, Switzerland

If disposing of this product, please recycle the paper.

Preface

The International Federation for the Promotion of Mechanism and Machine Science (IFToMM) is one of the largest global scientific communities dedicated to the advancement of mechanism and machine science and its applications. Since its establishment in 1969, IFToMM has been committed and successful to uniting individuals from diverse nationalities and academic systems to move forward scientific and technological knowledge in all areas related to mechanism and machine science, fostering strong international collaboration.

The IFToMM Young Faculty Group, as one of the four IFToMM Cross-Disciplinary groups (CDGs), is a collective of early-career academics working to further this mission. By bringing together young professors and lecturers from around the world, the group seeks to explore how mechanism and machine science can contribute to solving future academic and technological challenges.

The Second Edition of the IFToMM International Symposium on Emerging Fields in Mechanism and Machine Science (EFI^{MMS} 2026) comes after a successful first edition in 2023 and is jointly supported by the Cross Disciplinary Groups "IFToMM Women's Group" (WG) and "IFToMM Graduate Student Group" (GGG) for a stronger global reach. It is organized collaboratively by the University of Sousse in Tunisia and the University of Poitiers in France and held from 15 to 17 April 2026 in Monastir, Tunisia. The joint symposium aims at bringing together young researchers and students from the whole spectrum of disciplines covered by IFToMM, offering a focused and engaging environment for participants to present and publish their work, explore collaborative opportunities, and discuss emerging trends and challenges in the field, and also inviting experienced researchers for interaction with the next generations.

A collection of 46 papers that were selected based on a peer-review process, with authors from Europe, Africa, South America, Asia, covers a wide range of highly modern interdisciplinary research topics such as: 1) Mechanism theory and kinematics, 2) parallel robots, 3) Bio-inspired and compliant systems, 4) Vibration and materials and 5) Simulation, advanced and IA-based control. The conference additionally hosted a hands-on workshop on the Mechanism Developer (MechDev) software, a kinematics tool used for the design and analysis of planar linkages, geared linkages, and cam mechanisms.

We wish to express our gratitude to the authors, reviewers, Mechanism and Machine Theory Journal, Award Committee and Scientific Committee for their valuable contribution to ensure the scientific quality of the EFI^{MMS} 2026. Finally, we would like to thank IFToMM organization for their support to the success of the conference.

Abdelbadia Chaker
Claudio Villegas
Houssem Saafi

Organization

Honorary Chair

Lotfi Romdhane	American University of Sharjah, UAE

General Co-Chairs

Houssem Saâfi	University of Sousse, Tunisia
Abdelbadia Chaker	University of Poitiers, France
Claudio Villegas	University of Bio-Bio, Chile

Scientific Committee

Zaven Khanamiryan	National Polytechnic University of Armenia, Armenia
Qizhi Meng	Tsinghua University, China
Shanmukha Sundaram	GMR Institute of Technology, India
Giovanni Mottola	University of Messina, Italy
Sajjad Keshtkar	Tokyo Metropolitan University, Japan
Maria Contreras Calderón	Tecnológico de Monterrey / UTEQ, Mexico
Omar Mendoza	Swedish University of Agricultural Sciences, Mexico
Daniel Lavayen	Pontifical Catholic University of Peru, Peru
Michał Olinski	Wrocław University of Science and Technology, Poland
Filipe Marques	University of Minho, Portugal
Pau Català	Polytechnic University of Catalonia (UPC), Spain
Raul Gismeros	Carlos III University of Madrid, Spain
Fernando Viadero	University in Spain, Spain
Onur Denizhan	Batman University, Türkiye
Mertcan Koçak	University in Türkiye, Türkiye
Surendra Kumar Saini	University of Namibia, Namibia

Organizing Committee

Abdelfattah Mlika	University of Sousse, Tunisia
Louis Guigon	University of Duisburg-Essen, Germany
Ajmi Houidi	University of Sousse, Tunisia
Houssein Lamine	University of Sousse, Tunisia
Refka Ajili	University of Sousse, Tunisia
Imen Doudech	University of Poitiers, France

Contents

Mechanism theory and kinematics

On the Design of an Overconstrained Vaccine Administration Robot Manipulator: Kinematic Synthesis and Optimization 3
Mertcan Koçak, Tuğrul Uslu, Alperen Arıcı, Mustafa Volkan Yazıcı, and Erkin Gezgin

Design Optimization of Redundant Spherical Parallel Manipulator with an Unlimited Self-Rotation 16
Chaima Lahdiri, Houssem Saafi, and Abdelfattah Mlika

Kinematic Analysis of a Spherical Parallel Mechanism with 3-Degree of Redundancy 25
Terence Essomba

Structural Synthesis of Platform Type Manipulators via Connection-Based Adjacency Matrix: Preliminary Automated Topology Sketching 35
Tuğrul Uslu, Mustafa Volkan Yazıcı, Mertcan Koçak, and Erkin Gezgin

A Study of a Remote Center of Motion Mechanism as a Laparoscopic Training Tool Holder 47
Imen Doudech, Abdelbadia Chaker, Ajmi Houidi, Abdelfattah Mlika, and Med Amine Laribi

Workspace and Energetic Performance Analysis of a 2-DOF Planar Parallel Manipulator 56
Lorenzo Scalera, Renato Vidoni, and Alessandro Gasparetto

Mechanism Design and Inverse Kinematics of a 5-DOF Hybrid (Parallel–Serial) Manipulator 66
Alexey Novikov, Pavel Laryushkin, and Alexey Fomin

A Novel One-Degree-of-Freedom Deployable Unit Consisting of Four Parallelogram Linkages 76
Qizhi Meng and Andrés Kecskeméthy

A Bio-Inspired Tendon-Driven Morphing Hydrofoil: Design, Modeling, and Variable Stiffness Characterization 87
Xin Wang, Bai Chen, Jie Ling, Tianwei Zhang, and Yayi Shen

Design and Kinematic Geometric Analysis of a Reconfigurable Bricard Mechanism with Rolling Joints 97
Tianye Xu, Huanxiao Li, Long Li, and Shengnan Lyu

Experimental Test of a Wave Energy Converter with a Bioinspired Negative Stiffness Mechanism 107
Camila Alarcón-Gómez, Claudio Villegas-Ulloa, Fabian Pierart-Vásquez, Diego Carrasco-Valenzuela, and Roberto Delgado-Orias

Development of a Two-Degree-of-Freedom Model of Forearm for Pronation-Supination Motion 116
Mehmet Öksüz and Behzat Bahadir Kentel

A New Perspective on Number Synthesis: Introduction and Application of Topological Requirements for Kinematic Chain Filtering 126
Gustavo Valdatti Souza, Estevan Hideki Murai, Andrea Piga Carboni, and Daniel Martins

Friction Torque and Energy Loss Prediction of Single Degree-of-Freedom Mechanisms Considering the Effects of Variable Inertia 137
P. Català, J. M. Veciana, and L. Jordi

Dimensioning Human Operated Balanced Manipulators for Material (Un)Loading Operations 145
İlkim Zahide Bozdemir, Ünal Dana, Erkin Gezgin, and Levent Çetin

Robotics and control

Travel Path and Trajectory Planning for Robot-Assisted Multidirectional Additive Manufacturing 159
Mark Witte, Ziyun Yang, Mathias Hüsing, and Burkhard Corves

An Autonomous Obstacle-Avoiding Rolling Robot Based on a Parallel Mechanism 171
Xinrui Tao, Jiayao Ma, and Yan Chen

Actuation Along a Single Linear Axis: The Dynamics of the Single-Rail Tripteron 183
Paolo Boscariol and Iacopo Tamellin

Numerical Analysis of a Variable-Stiffness Actuator Intended for Exoskeleton Use 193
John E. Bermeo, Eduardo Castillo-Castañeda, Abdelbadiâ Chaker, and Med Amine Laribi

Capability Mapping of a Tendon-Driven Continuum Robot Using Task-Space Sampling and PSO-Based IK 207
Mohammad Jabari, Carmen Visconte, Giuseppe Quaglia, Abdelbadia Chaker, and Med Amine Laribi

About the Design and Development of the Omnidirectional Electric Powered Wheelchair MoviWE.Q 215
Luigi Tagliavini, Andrea Botta, Giovanni Colucci, Lorenzo Baglieri, Simone Duretto, Francesco Amodio, Lorenzo Toccaceli, and Giuseppe Quaglia

Underactuated Gravity-Assisted Cable Robot for Microphone Transportation 225
Mykhailo Riabtsev, Med Amine Laribi, and Victor Petuya

AI-Augmented Adaptive Control of Lower-Limb Exoskeletons Considering Human Parametric Variations 236
Zaven Khanamiryan and Azatuhi Ulikyan

Gait Trajectory Planning for Biped Robots via LIPM and LPM Models 247
Refka Ajili, Badreddine Kribi, and Ajmi Houidi

Automated GPU Code Generation for Rigid-Body Simulations Using SYMKIN Symbolic Optimizer 256
Louis Guigon, Benjamin Boudon, Youcef Mezouar, Chedli Bouzgarrou, and Andrés Kecskeméthy

Motion Simulation for the Anatomical Reconstruction of Facial Muscles and Skulls with a Spherical 3D Printer 264
Lucian-Mihai Micle, Elida Tulcan, Carmen Sticlaru, Alexandru Oarcea, and Erwin-Christian Lovasz

Latency and Safety Assessment of Low-Cost Distance Sensor Integration into ROS2 for Human–Robot Collaboration 274
Sophie Charlotte Keunecke, Marcel Ochsendorf, Mathias Hüsing, and Burkhard Corves

Optimization of PID-Controlled Semi-active Suspensions Using Metaheuristic Algorithms for Improved Railway Vehicle Passenger Comfort 285
Helmi Mahmoudi and Ajmi Houidi

LQR Trajectory Tracking Control for Connected and Automated Vehicles in Unsignalized Intersections 295
Fernando Viadero-Monasterio, Miguel Meléndez-Useros, Nianhua Zhang, Beatriz López Boada, and María Jesús López Boada

Experimental Evaluation of Position-Based Visual Servoing Using AprilTag for Mobile Robot Docking 305
Houssein Lamine, Hassen Makki, and Lotfi Romdhane

Vibration and Materials

Hybrid Actuator and Sensor Fault Diagnosis for Active Steering Systems 315
Miguel Meléndez-Useros, Fernando Viadero-Monasterio, María Jesús López Boada, and Beatriz López Boada

Anisotropic Polyurethane Foams: Evolution of Mechanical Properties Under Cyclic Compression 326
Dorra Ben Abdeljelil, Sami Chatti, and Raja Ouled Ahmed Ben Ali

Experimental Study of the Axial Crushing Mechanics of Yoshimura Tubes 335
Daniel Lavayen, Johan Barrueta, Ludwing Gonzales, Jesus Monge, Mario Quispe, Erick Requena, and Estefania Hermoza

Evaluation of Equivalent Residual Stress Under Variable Loads for Fatigue Crack Propagation 345
Brahim Bouaziz, Maher Eltaief, and Chokri Bouraoui

Numerical Study of the Effects of Thickness and Bracing on Lute Acoustics ... 353
Atef Dhokkar, Mohamed Ali Rezgui, and Ali Trabelsi

Estimation of Remaining Useful Life in Bearings Using Fusion of Machine Vision Features and Vibration Analysis 368
Tania Elizabeth Sandoval-Valencia, Jose Emiliano Lopez-Ramirez, Eric Leonardo Huerta-Manzanilla, Gerardo Hurtado-Hurtado, and Juan Carlos Jauregui-Correa

Application of Support Vector Machines and Principal Component Analysis for Wheel Wear Progression Diagnosis in a Scaled Railway Vehicle 378
Gerardo Hurtado-Hurtado, Tania Elizabeth Sandoval Valencia, Luis Morales-Velázquez, and Juan Carlos Jáuregui Correa

Residual Vibration Suppression for Arbitrary Move Times Using a Novel Fourier-Based Profile Tuning 388
Mehmet Erkan Kütük and Sadettin Kapucu

Development and Validation of a Load Equivalence Framework for Predicting Crack Growth in Al 2024-T3 Aluminum Alloy 398
Brahim Bouaziz, Maher Eltaief, and Chokri Bouraoui

Finite Element Analysis of a Novel Active Ankle-Foot Prosthesis for Improved Load Distribution 407
Akhmejanov Sayat, Zhetenbayev Nursultan, Sultan Aidos, Bigaliyeva Zhanar, Shylmyrza Ussen, Nurgizat Yerkebulan, and Sergazin Gani

Anomaly Detection in Scale Model Trains Using LSTM Neural Networks 419
Jose Emiliano Lopez-Ramirez, Tania Elizabeth Sandoval-Valencia, Hannia Rangel-Escobar, Eric Leonardo Huerta-Manzanilla, J. E. Basaldúa-Sánchez, and Juan Carlos Jauregui-Correa

A Review of Additively Manufactured Polymer and Steel Gears - Tribology and Modeling 431
Mahmood M. Mustafa, Mustafa A. Ali, Rania W. Abdula, Omar D. Mohammed, and Haitham M. Wadullah

Education and history of mechanisms

Implementing a Student-Centered Teaching Strategy in a Theory of Machines and Mechanisms Course 443
Paulo Flores

A Seven-Step Procedure to Model and Simulate Dynamics of Machines and Mechanisms 454
Paulo Flores

MECAPUCP: Interactive Teaching Tool for Mechanism Kinematics 464
Alonso Velis, Mirko Flores, Tamie Tokuda, Daniel Lavayen, Estefania Hermoza, Enrique Carrillo, and Jorge Rodríguez

The Italian Initiative for MMS Early Career Researchers: Lessons Learned and Historical Development 476
Giovanni Mottola, Matteo Russo, and Edoardo Ida

Author Index 487

Mechanism theory and kinematics

On the Design of an Overconstrained Vaccine Administration Robot Manipulator: Kinematic Synthesis and Optimization

Mertcan Koçak(✉), Tuğrul Uslu, Alperen Arıcı, Mustafa Volkan Yazıcı, and Erkin Gezgin

İzmir Katip Çelebi University, İzmir 35620, Türkiye
mertcan.kocak@ikcu.edu.tr

Abstract. Vaccination remains one of the most effective public-health interventions for preventing diseases worldwide, that requires scalable delivery solutions. While robotic implementation in vaccine administration remains unusual, cost-effectiveness must be an essential condition for widespread adoption; otherwise, such automation lacks practical application. Currently, healthcare robotics mainly rely on high degree-of-freedom complex manipulators, which often introduce excessive kinematic solutions with high cost. Consequently, low-cost, target-specific systems utilizing reduced mobility rather than general-purpose complexity are critically needed to execute automated vaccination widely available and accessible. In this study, a compact overconstrained robot manipulator is developed through effective structural and kinematic synthesis methodology, followed by dimensional optimization with defined design constraints to ensure manufacturable and effective design. The resultant kinematic structure ensures the entire vaccination cycle, allowing autonomous syringe waste management procedures. Aligning with safety goals, a custom end-effector was designed to achieve a "no-touch" disposal capability, where the unit was prototyped and its operational feasibility for the disposal was validated.

Keywords: Vaccine Administration · Kinematic Synthesis · Overconstrained · Medical Robotics

1 Introduction

Vaccination remains one of the most effective public-health interventions and continues to be essential for disease prevention worldwide [1]. Routine childhood immunization programs proceed protection against many vaccine-preventable diseases and global coverage remains high for core antigens. In 2024, while global efforts maintained a DTP3 coverage of 85%, a critical inequality remains in healthcare delivery. Approximately 14.3 million children who are classified as "zero-dose" were entirely missed by immunization programs, highlighting the urgent need for more scalable and accessible vaccination solutions [2]. At the same time, the COVID-19 pandemic demonstrated the

© The Author(s), under exclusive license to Springer Nature Switzerland AG 2026
A. Chaker et al. (Eds.): EFIMMS 2026, MMS 205, pp. 3–15, 2026.
https://doi.org/10.1007/978-3-032-22270-1_1

need for extremely rapid, large-scale vaccination campaigns, with billions of doses managed worldwide, with ongoing COVID vaccination efforts tracked by global datasets [3]. These realities create continuous pressure on systems that must inject vaccines safely, quickly and at scale [4].

There are several motivations for introducing automation into vaccine injection, primarily driven by the limitations of manual administration. The quality and success of manual injections depends on the operator with variability, which can lead to events such as Shoulder Injury Related to Vaccine Administration (SIRVA) due to incorrect needle depth or placement [5, 6]. Automated vaccination systems may address these challenges by offering standardized injection techniques with precise control over angle, depth, and dosage. Furthermore, similar to the efficiency gains observed in intelligent blood collection robot [7], autonomous vaccinators hold the promise of improving dosage and reducing the physical and cognitive workload on healthcare workers during mass vaccine campaigns as well as enabling more reproducible data capture and traceability. These can improve reliability and quality of service delivery in both routine and surge-capacity settings. At the same time, for automated solutions to be practical in the contexts where they are most needed, cost-effectiveness and compactness are critical design constraints. Recent studies emphasize that scalability and rapid deployment capabilities are essential for effective pandemic response [8]. Furthermore, broader surveys of healthcare robotics indicate that solutions remaining excessively expensive or technically complex face significant barriers to widespread clinical adoption and sustainability [9].

Despite this potential, in the literature fully automated or robotic vaccine administration is rare. Reviews of robotics during the COVID-19 crisis indicate that while applications for logistics, disinfection and telepresence were widely adopted, systems capable of direct physical patient interaction, such as clinical autonomous interventions, remained limited and largely experimental [10]. In the work of Ampadu et al. [11], they described a software module implemented on a humanoid Pepper robot designed to detect the bare shoulder, identify the injection spot and perform the procedure in less than 60 s with an 80% success rate. Similarly, as an industrial application, the Cobi platform has been introduced by Cobionix and is stated by the manufacturer to be the world's first autonomous robot capable of performing intramuscular injections with 6 degree-of-freedom (DOF) [12]. Alongside, the World Health Organization's (WHO) Immunization Agenda 2030 (IA2030) actively promotes such innovation to improve health security, universal health coverage, and equity [13]. However, bridging the gap between these global motivations and the current experimental state of robotic interventions requires severe academic and translational work.

While high DOF universal manipulators are technically capable of performing a wide set of clinical tasks, their cost, complexity and safety validation requirements make them less suitable for mass-deployable vaccination stations. Although the motion of injection occurs in spatial direction, the task requirements can be reduced to a lower DOF kinematic within the targeted direction. In this study, this is achieved by proposing a methodology with scientific background to build a low-DOF and low-cost robotic manipulator for vaccine injection. The methodology is developed with kinematic synthesis and an optimized structural design that overcomes the task's geometric redundancies, where

three DOF overconstrained macro-positioning injection motion is completed by maintaining the specific injection direction constant during injection phase. To complete this, a custom end-effector is designed and prototyped to execute the micro-positioning required for the injection process. Critically, this unit integrates a passive release mechanism to enable "no-touch" syringe disposal, leading to fully automated vaccination cycles. The work is positioned as an early stage academic contribution in terms of methodology toward safe, scalable automated vaccination with the objective of creating a mechanism that is manufacturable, affordable and capable of reproducible intramuscular injection in standard clinical environments.

2 Kinematic Synthesis and Optimization

2.1 Design Constraints

The fundamental design constraints are derived from the standard clinical protocols for intramuscular vaccine administration. Complications related with injection can be decreased if the right point is accurately projected. The four standard sites for intramuscular administration are the deltoid (arm), gluteus maximus (upper outer buttock), vastus lateralis (thigh), and gluteus medius (lateral hip) [14]. For this study, the deltoid muscle is selected as the main injection site due to its ease of access for convenience and sufficient muscle. The injection spot is in the middle of the deltoid muscle about three fingers across the deltoid muscle and below the acromion process (2.5 cm to 5 cm) [15]. According to nursing guidelines, the needle must be inserted at a 90° with respect to the skin surface to ensure the vaccine is injected deep into the muscle fascia rather than the subcutaneous tissue (see Fig. 1) [14, 16]. To be applicable for a wide range of adult anthropometrics, the linear carrier that displaces needle at injection phase must support a needle depth of up to 38 mm (1.5 in.), which is the recommended maximum needle length for men and women over 90 kg, while allowing for adjustable depth settings for patients with lower body mass index [14, 16].

In order to reduce injection-related pain and avoid mechanical complications, it is vital to ensure patient stability and muscle relaxation. The deltoid muscle must be passive and relaxed throughout the procedure, according to clinical nursing standards [17]. The system design includes a dedicated arm support fixture to accomplish this standardization without depending on active patient compliance. This support unit is designed to maintain the patient's arm in a passive abduction of approximately 20°, a position that minimizes isometric contraction in the deltoid fibers and maximizes the contact of the acromion process for land-mark identification [17, 18]. In order to achieve a 90° injection relative to the skin surface, the orientation of the robot's end-effector becomes a critical design parameter. Given the custom arm-support fixture, this requires the injection axis to be maintained at approximately 70° with respect to the global vertical direction, which serves as a key design constraint (see Fig. 1).

In addition to the injection path, the system requires a multifunctional workspace to handle the complete vaccination cycle, including the loading of the syringe and the disposal of medical waste. In order to move the end-effector between the loading station, the injection zone and the disposal unit, the mechanism must have suitable planar

motion capabilities. To align with safety and sustainability goals, the design must integrate an automated release mechanism that throw outs the used syringe directly into a sharps container immediately after the procedure. In order to follow WHO guidelines for preventing needle-stick injuries and guaranteeing safe waste management in automated healthcare settings, this "no-touch" disposal strategy is crucial (see Fig. 1) [19].

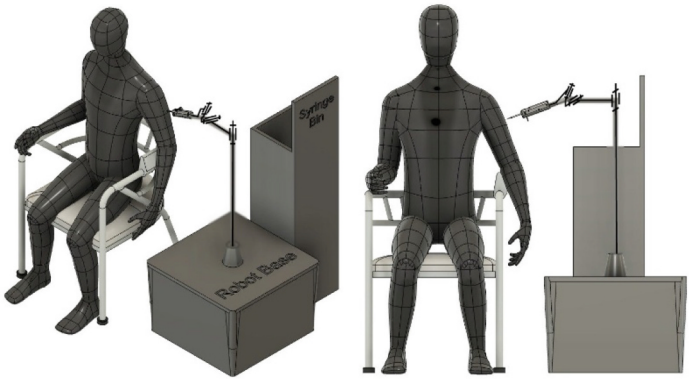

Fig. 1. Patient, concept robot, disposal unit (Human Dummy Model [20], Chair Model [21]).

While these tasks could theoretically be executed by a generic multi DOF robotic manipulator equipped with a medical gripper, such an approach does not have the efficiency of task oriented, thus become in conflict with the design motivations of compactness, cost-effectiveness and portability. High-DOF serial manipulators utilize spatial workspaces, deploying them for tasks that are essentially defined by repetitive trajectory tracking introduces excessive kinematic mobility. This structural over-design increases control complexity and manufacturing costs, as the task involves following a deterministic path rather than navigating free environments. Thus, in order to execute administration as efficient as possible by following task-specific approach, underactuation becomes a critical constraint for a robot manipulator. This necessitates both structural and kinematic synthesis approach to identify a kinematic chain that provides the required planar motion and linear stiffness within a minimal spatial path, offering a sustainable alternative to generalized robotic arms.

2.2 Structural Synthesis

Utilizing the outcomes of the design constraints, detailed information about both the number of required joints and their configurations are presented by considering motion phases as; syringe reloading, injection, syringe disposal. The minimum degree of freedom of the structure is decided as three which can move the end-effector on a straight line that is not parallel to any base coordinate frame axis in the task space. During the injection phase, as given in the design constraints, the main objective is to move the end-effector linearly through waypoints specified with injection direction. However, in other tasks, pure linear motion is not required. Thus, forming the structure by using

translation capable joints would result in loss of dexterity in overall motion to guarantee the accuracy of the linear motion only during the injection. To avoid this limitation, structure is decided to be formed by revolute joints that are configured in such a way that the resulting structure is non-planar (see Fig. 2a).

Another reason for this revolute-joint configuration is the ability to shape the mechanism into a compact planar form when viewed from above in the ground-parallel projection. This planar configuration enables efficient execution of tasks such as syringe loading and disposal (see Fig. 2b). Achieving given compact form requires the second active joint, located on the middle, to be set and held at a specific angle, which is $\theta_2 = 0°$ or $\theta_2 = 180°$, aligning the first and last joints with each other as well as the global vertical axis. Thanks to this reconfigurable compact form state, the mechanism can have suitable planar motion capabilities parallel to the ground, allowing loading and disposal operations to be performed efficiently.

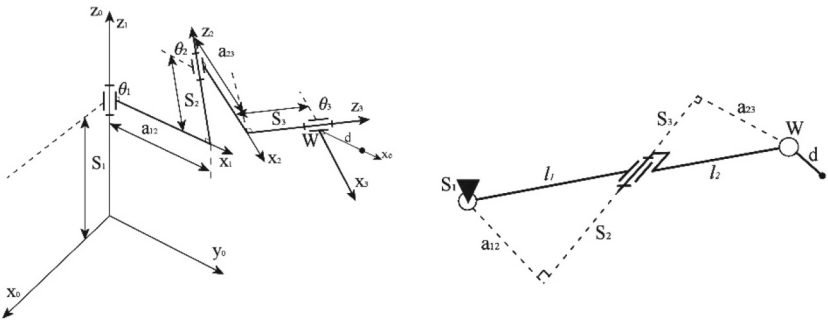

Fig. 2. (a) Kinematic representation of most general form RRR with D-H parameters; (b) Compact form as planar configuration.

Once kinematic structure of the manipulator was decided in order to follow desired end-effector motion constraints, construction parameters of the manipulator should be calculated via kinematic synthesis procedures due to overconstrained nature of the structure.

2.3 Kinematic Synthesis

Task with an overconstrained spatial task is defined as advancing a needle along a prescribed direction vector **d** with sufficient accuracy for intramuscular vaccination. Although the motion of injection process appears naturally spatial, the task requirements can be reduced to a lower DOF kinematic within the targeted direction. Specifically, once the injection site is properly positioned with respect to the manipulator, the main requirement becomes generating a translational motion along a predetermined orientation. The rotational deviations around vector **d** allows the utilization of a reduced DOF architecture without compromising task feasibility.

The manipulator is synthesized such that its end-effector can be oriented to align with the desired vector **d**, while the final DOF provides the necessary linear advancement

during needle insertion. Because rotation around **d** does not influence the injection outcome, the solution space admits an under-actuated mode that can be exploited to simplify the mechanism and reduce cost, weight and overall system complexity.

To formulate the kinematic synthesis procedure mathematically, it is necessary to express the end-point position of the structurally synthesized robot. For this purpose, the Denavit-Hartenberg (D-H) parameter table was constructed, and the pose of point ${}^{0}P_{w}$, given in Fig. 2a, was represented using the D-H parameters as summarized in Table 1.

Table 1. Denavit-Hartenberg table for serial manipulator.

#	a	α	s	θ
1	0	0	s_1	θ_1
2	a_{12}	-π/2	s_2	θ_2
3	a_{23}	π/2	s_3	θ_3

The total transformation expression from the origin to frame on point W (${}_{3}{}^{0}T$) can be given as in Eq. 1.

$$
{}_{3}{}^{0}T = \begin{bmatrix}
\mathrm{c}\theta_1\mathrm{c}\theta_2\mathrm{c}\theta_3 - \mathrm{s}\theta_1\mathrm{s}\theta_3 & -\mathrm{c}\theta_1\mathrm{c}\theta_2\mathrm{s}\theta_3 - \mathrm{s}\theta_1\mathrm{c}\theta_3 & \mathrm{c}\theta_1\mathrm{s}\theta_2 & a_{23}\mathrm{c}\theta_1\mathrm{c}\theta_2 + s_3\mathrm{c}\theta_1\mathrm{s}\theta_2 + a_{12}\mathrm{c}\theta_1 - s_2\mathrm{s}\theta_1 \\
\mathrm{s}\theta_1\mathrm{c}\theta_2\mathrm{c}\theta_3 + \mathrm{c}\theta_1\mathrm{s}\theta_3 & -\mathrm{s}\theta_1\mathrm{c}\theta_2\mathrm{s}\theta_3 + \mathrm{c}\theta_1\mathrm{c}\theta_3 & \mathrm{s}\theta_1\mathrm{s}\theta_2 & a_{23}\mathrm{s}\theta_1\mathrm{c}\theta_2 + s_3\mathrm{s}\theta_1\mathrm{s}\theta_2 + a_{12}\mathrm{s}\theta_1 + s_2\mathrm{c}\theta_1 \\
-\mathrm{s}\theta_2\mathrm{c}\theta_3 & \mathrm{s}\theta_2\mathrm{s}\theta_3 & \mathrm{c}\theta_2 & -a_{23}\mathrm{s}\theta_2 + s_3\mathrm{c}\theta_2 + s_1 \\
0 & 0 & 0 & 1
\end{bmatrix} \tag{1}
$$

The needle to be placed after the point W must be translated according to a specific orientation during injection. To achieve this, the relationship here must be clearly stated. Tool distance from ${}^{0}P_{w}$ to ${}^{0}P_{E}$ (needle tip) becomes the length of vector **d,** and the orientation of the end-effector will be the unit vector of **d** ($\hat{\mathrm{d}} = \hat{d}_{x0} + \hat{d}_{y0} + \hat{d}_{z0}$), that is defined with respect to origin frame. Here, the vector **d** is expressed with the vector form in Eq. 2.

$$
{}^{0}P_{E} = {}^{0}P_{w} + \boldsymbol{d} \tag{2}
$$

The position expression of ${}^{0}P_{E}$ can be extracted from the matrix given in Eq. 1. In this case, ${}^{0}P_{E}$ can be expressed as in Eq. 3 by combining it with the vector **d**.

$$
{}^{0}P_{E} = \begin{bmatrix}
|d|\hat{d}_{x0} + a_{23}\mathrm{c}\theta_1\mathrm{c}\theta_2 + s_3\mathrm{c}\theta_1\mathrm{s}\theta_2 + a_{12}\mathrm{c}\theta_1 - s_2\mathrm{s}\theta_1 \\
|d|\hat{d}_{y0} + a_{23}\mathrm{s}\theta_1\mathrm{c}\theta_2 + s_3\mathrm{s}\theta_1\mathrm{s}\theta_2 + a_{12}\mathrm{s}\theta_1 + s_2\mathrm{c}\theta_1 \\
|d|\hat{d}_{z0} - a_{23}\mathrm{s}\theta_2 + s_3\mathrm{c}\theta_2 + s_1
\end{bmatrix} = \begin{bmatrix} X_E \\ Y_E \\ Z_E \end{bmatrix} \tag{3}
$$

During the motion, the frame at point W is allowed rotate around the unit vector (in the direction of vector **d**). The formulation of rotation matrix around a unit vector $\hat{m}$ with angle ψ is given in Eq. 4.

$$
R_{(\hat{m})} = \begin{bmatrix}
c\psi + m_x^2(1-c\psi) & m_x m_y(1-c\psi) - m_z s\psi & m_x m_z(1-c\psi) + m_y s\psi \\
m_x m_y(1-c\psi) + m_z s\psi & c\psi + m_y^2(1-c\psi) & m_y m_z(1-c\psi) - m_x s\psi \\
m_x m_z(1-c\psi) - m_y s\psi & m_y m_z(1-c\psi) + m_x s\psi & c\psi + m_z^2(1-c\psi)
\end{bmatrix} \tag{4}
$$

The rotation matrix ${}_3{}^0R$ that was extracted from ${}_3{}^0T$ in Eq. 1 should be equal to rotation matrix $R_{(\hat{m})}$ given in Eq. 4. By using this equality, the inverse task is utilized and required input angles can be revealed as in Eq. 5.

$$\theta_2 = atan2\left(\sqrt{R_{(\hat{m})}(1,3)^2 + R_{(\hat{m})}(2,3)^2}, R_{(\hat{m})}(3,3)\right)$$

$$\theta_1 = atan2\left(R_{(\hat{m})}(2,3)/s\theta_{2'} R_{(\hat{m})}(1,3)/s\theta_2\right)$$

$$\theta_3 = atan2\left(R_{(\hat{m})}(3,2)/s\theta_{2'}{}^{R_{(\hat{m})}(3,1)}/s\theta_2\right) \tag{5}$$

By grouping the unknowns and construction parameters, the kinematic synthesis methodology is built with the least square approximation by revealing pseudo-inverse algorithm. Here as in Eq. 6, n number of design points are chosen with the index of i.

$$\underbrace{\begin{bmatrix} \hat{d}_{x0} & c\theta_1^i c\theta_2^i & c\theta_1^i s\theta_2^i & c\theta_1^i & -s\theta_1^i & 0 \\ \hat{d}_{y0} & s\theta_1^i c\theta_2^i & s\theta_1^i s\theta_2^i & s\theta_1^i & c\theta_1^i & 0 \\ \hat{d}_{z0} & -s\theta_2^i & c\theta_2^i & 0 & 0 & 1 \\ \hat{d}_{x0} & c\theta_1^{i+1} c\theta_2^{i+1} & c\theta_1^{i+1} s\theta_2^{i+1} & c\theta_1^{i+1} & -s\theta_1^{i+1} & 0 \\ \hat{d}_{y0} & s\theta_1^{i+1} c\theta_2^{i+1} & s\theta_1^{i+1} s\theta_2^{i+1} & s\theta_1^{i+1} & c\theta_1^{i+1} & 0 \\ \hat{d}_{z0} & -s\theta_2^{i+1} & c\theta_2^{i+1} & 0 & 0 & 1 \\ \vdots & \vdots & \vdots & \vdots & \vdots & \vdots \end{bmatrix}}_{\mathbf{A}\ 3nx6} \underbrace{\begin{bmatrix} d \\ a_{23} \\ s_3 \\ a_{12} \\ s_2 \\ s_1 \end{bmatrix}}_{\mathbf{x}\ 6x1} = \underbrace{\begin{bmatrix} X_E^i \\ Y_E^i \\ Z_E^i \\ X_E^{i+1} \\ Y_E^{i+1} \\ Z_E^{i+1} \\ \vdots \end{bmatrix}}_{\mathbf{B}\ 3nx1} \tag{6}$$

The known variables with the given orientation information as in vector **d** (components of $\hat{d}_{x0}$, $\hat{d}_{y0}$ and $\hat{d}_{z0}$) and n number of design points as position and poses, least square approximation is utilized by using the following pseudo-inverse algorithm given in Eq. 7.

$$\mathbf{x} = \left(\mathbf{A}^T\mathbf{A}\right)^{-1}\mathbf{A}^T\mathbf{B} \tag{7}$$

2.4 Optimization and Results

To execute kinematic synthesis procedure, several parameters must be defined by the designer. These parameters are used to generate the design points, which specify the position and orientation of the end-effector for each of these points in the task. The parameters required to define these design points include:

- 3D coordinates point of starting position (X_E^i, Y_E^i, Z_E^i; $i = 0$) that defines the initial contact point of needle before injection,
- End-effector orientation that defines the injection orientation in terms of Euler angles in *ZYZ* convention (***ZYZ* Euler angle convention is chosen because it provides direct mapping to the joint angles of the robot**),
- Path length from initial contact point of needle to final contact in the direction of specified orientation,

- Initial and final axis-angle rotations along the path.

By utilizing these parameters, an array of design points defining the task of the robot can be created. Axis-angle rotations are linearly interpolated across the design points and then converted to Euler angles in *ZYZ* convention. The design points are then evenly spaced along the path, with each design point assigned to a specific position and orientation. Considering design constraints of the task, some of these parameters can be given, while others are selected as optimization parameters.

Optimization Parameters. The base position of the robot is measured from a sitting vaccination pose for an adult. The needle contact point on skin is set as $\boldsymbol{Z_E^0} = 1060$ mm above the floor. The *y*-coordinate is fixed at $\boldsymbol{Y_E^0} = 300$ mm, representing the lateral distance from the robot base to the needle entry point. The *x*-coordinate of the needle tip point ($\boldsymbol{X_E^0}$) is therefore the first optimization parameter. As mentioned in design constraints, due to the placed fixture to fix the orientation of the patient's arm ($20°$), the orientation of the needle path should be orthogonal to the skin surface at the point of injection. Note that during the kinematic synthesis, in order to define end-effector orientation design points fixed orientation of the arm should also be considered.

In order to express end-effector injection orientation in *ZYZ* Euler convention, two of the non-successive *Z* rotations are assumed as $40°$ and $20°$, respectively. Then, to reach target desired orientation to ensure orthogonal injection, *Y* rotation is calculated ($Z = 40°$, $Y = 21.34°$, $Z = 20°$). These values are utilized as initial reference for design point orientations. These values are utilized as initial reference for design point orientations. Note that these values represent the fixed orientation between 3rd and the end-effector frame e, thus being construction parameters. The path length was set to *45* mm so that desired maximum depth of the vaccination should be in the range. To balance accuracy and computational cost, design point positions were spaced at *0.2* mm intervals along this path. The initial and final axis-angle rotations along the path were defined as the second and third optimization parameters ($\boldsymbol{\psi_i}$,$\boldsymbol{\psi_f}$), respectively. Each design point orientations along the axis are distributed homogenously within this interval.

For the optimization task, SciPy scientific computing library was used. Multiple initial guesses of optimization parameters were provided, and the task were executed with L-BFGS-B [22] implementation in SciPy library. The cost function for the optimization task is designed to be position root mean square (RMS) error of the design points. The optimization process is terminated when the RMS error had reached sub-millimeter accuracy. The optimization task yielded the construction parameters in Table 2 with an RMS error of *0.7553* mm.

Table 2. Preliminary numerical results of construction parameters.

d[mm]	a_{23}[mm]	s_3[mm]	a_{12}[mm]	s_2[mm]	s_1[mm]	X_E^0 [mm]	Y_E^0 [mm]
299.15	*−13.06*	*−5.02*	*188.32*	*−6.16*	*1151.87*	*−34.96*	*300.00*

Error along each axis provided in the Fig. 3, and norm of the error vectors are presented in Fig. 4 to illustrate peak error values.

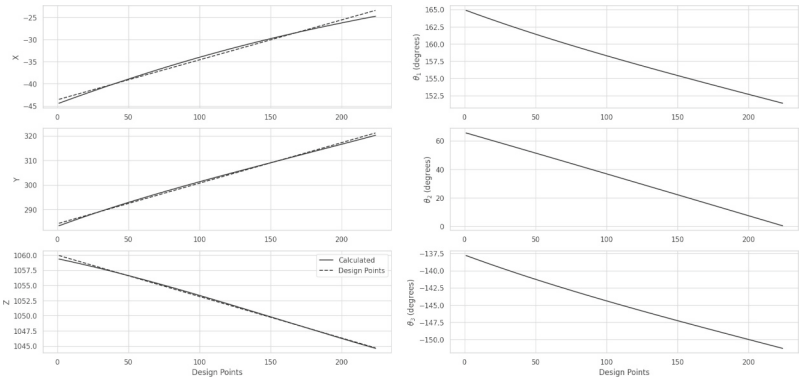

Fig. 3. (a) Travel along design points; (b) Corresponding motor angles.

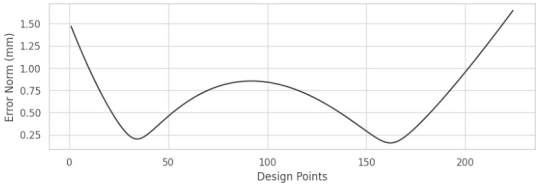

Fig. 4. Norm of error vector along design points.

As seen in Fig. 4, peak errors were observed with preliminary results at the beginning and the end of the travel, thus an optimization procedure after this step is decided to be beneficial.

Post Optimization Design. The robot's d parameter can be adjusted without affecting the kinematics by offsetting the robot base position. This offset compensates for the difference between the original and new d values along the euler angles utilized for generation of the design points. Based on the end effector design, the d parameter was resized to *280* mm. As shown in Fig. 4, peak errors occur at the beginning and the end of the travel. Consequently, the first 10 design points (*2* mm) and the last 25 design points (*5* mm) were removed from the path. The robot base was then offset along the negative end-effector orientation to compensate for *2* mm of travel removed from the start of the path. With these considerations, the final parameters were refined and given in Table 3.

Table 3. Preliminary numerical results of construction parameters after post optimization.

d[mm]	a_{23}[mm]	s_3[mm]	a_{12}[mm]	s_2[mm]	s_1[mm]	X_E^0 [mm]	Y_E^0 [mm]
280.00	*−13.06*	*−5.02*	*188.32*	*−6.16*	*1146.00*	*−42.69*	*285.86*

Travel and error graphs are provided in Figs. 5 and 6. Along the new shortened path RMS position error was calculated as *0.6087* mm. Comparison of Figs. 4 and 6 showcases the error refinement after post optimization. The workspace of the resultant manipulator is also shown in Fig. 7 to illustrate the reachable regions.

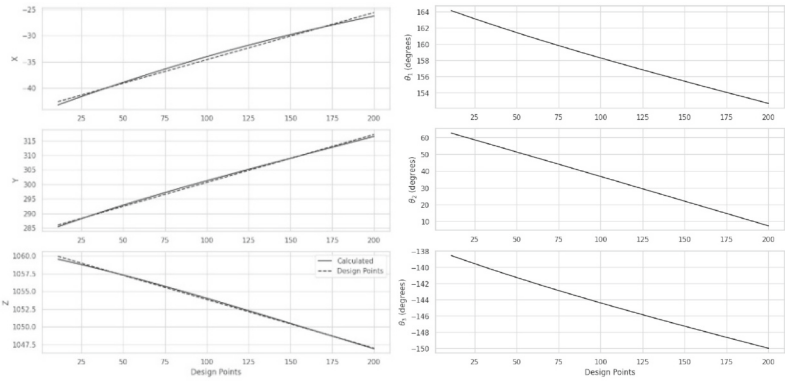

Fig. 5. (a) Travel along design points after post optimization; (b) Corresponding motor angles after post optimization.

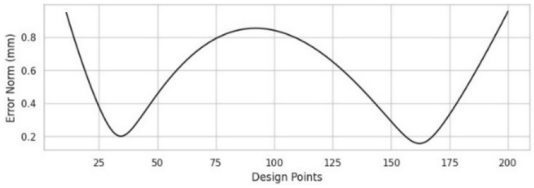

Fig. 6. Norm of error vector along design points after post optimization.

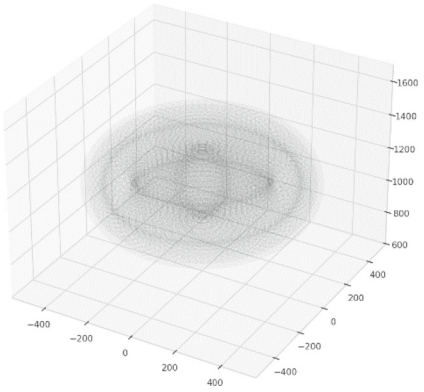

Fig. 7. Workspace of the resultant manipulator.

3 End Effector Design and Prototyping

To achieve the "no-touch" disposal, a custom end effector design is realized that can be separated from the used syringe with the help of a passive latch. The primary objective was to achieve safe syringe disposal without adding the weight and complexity of an extra electronic actuator. To solve this, a passive release mechanism based on a slider-crank linkage was designed. This mechanism allows the robot to detach and drop the syringe simply by pressing a mechanical latch against a rigid surface (e.g., a waste bin wall), utilizing contact force rather than software-controlled actuation.

3.1 Mechanical Design

The mechanical structure was constrained by the dimensions of standard 0.3 ml Pre-Filled Syringes (PFS). These syringes are critical in clinical settings for delivering precise low-volume doses, such as in pediatric immunizations, where dose accuracy is paramount [23]. The end-effector structure rigidly houses the syringe barrel to ensure stability. For the injection process, a linear actuator with a *20* mm stroke was integrated to drive the plunger with precise control. The passive disposal system remains locked during injection and is triggered only when the external latch is compressed against a surface, mechanically releasing the syringe downwards (see Fig. 8).

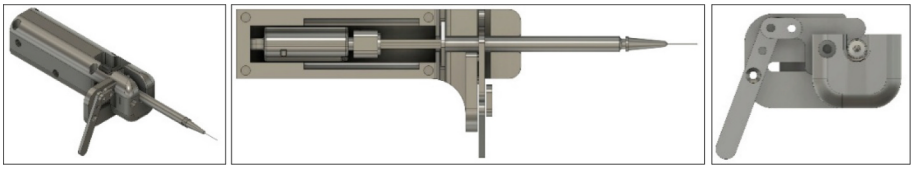

Fig. 8. 3D End-effector model design including syringe.

3.2 Prototyping

Prototype of the end effector was manufactured by using rapid prototyping in order to validate its expected working principle. Once the sub components were assembled, manually executed functional tests confirmed the preliminary design's feasibility. Linear actuator effectiveness is verified successfully by the completion of proper injection stroke, ensuring the complete expulsion of the vaccine fluid. Additionally, proposed passive release system, which utilizes a simple single degree of freedom slider-crank mechanism, and a spring-loaded latch for disposal operation is able to efficiently detach the syringe upon wall contact, thus enabling "no-touch" waste management strategy (see Fig. 9).

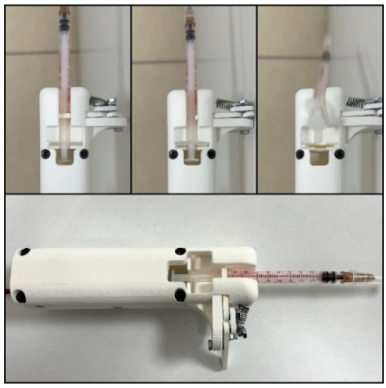

Fig. 9. End-effector prototype working with “no-touch” disposal mechanism.

4 Conclusion

In this work, an effective kinematic synthesis methodology is proposed followed with an optimization procedure for a task-specific, overconstrained low-cost robot manipulator to be utilized as an intramuscular vaccine administration. Together with the given design constraints, numerical procedure is executed and post optimization successfully refined the kinematic synthesis results. The resulting structure successfully fulfills the kinematic motion path in required spatial direction during motion of deltoid injections. Furthermore, the integration of a passive arm fixture promotes standardized muscle relaxation. To achieve passive “no-touch” syringe disposal, a custom end-effector mechanism is proposed, modeled manufactured and validated. Collectively, these contributions establish a framework for scalable, manufacturable and economically practical automated vaccination stations.

Future work of this study will include overall manufacturing of the robot manipulator based on the results presented in kinematic synthesis and post-optimization sections. Additionally, the development of precise control algorithms and kinematic hardware verification studies will be conducted on a life-like mockup model to prove the system’s motion characteristic performance under real-world conditions. Research is planned to be extended to the mechanical integration of the automated syringe loading module, aiming to realize the compact system form. The ultimate objective of the later phase is to verify the complete autonomous vaccination cycle, including loading, injection and disposal together and fully functional prototype.

Acknowledgements. This work was initiated with the course given by Prof. Levent Çetin. The authors would like to express their deepest gratitude to Prof. Levent Çetin.

References

1. Andre, F.E., et al.: Vaccination greatly reduces disease, disability, death and inequity worldwide. Bull. World Health Organ. **86**, 140–146 (2008)

2. WHO (World Health Organization) Immunization Coverage Fact Sheet.: https://www.who.int/news-room/fact-sheets/detail/immunization-coverage Last accessed 27 Nov 2025
3. Mathieu, E., et al.: A global database of COVID-19 vaccinations. Nat. Hum. Behav. **5**(7), 947–953 (2021)
4. Wouters, O.J., et al.: Challenges in ensuring global access to COVID-19 vaccines: production, affordability, allocation, and deployment. Lancet. **397**(10278), 1023–1034 (2021)
5. Bancsi, A., Houle, S.K., Grindrod, K.A.: Shoulder injury related to vaccine administration and other injection site events. Can. Fam. Physician. **65**(1), 40–42 (2019)
6. Nakajima, Y., et al.: Establishing a new appropriate intramuscular injection site in the deltoid muscle. Hum. Vaccin. Immunother. **13**(9), 2123–2129 (2017)
7. Wang, Y., et al.: Intelligent blood collection robot: key technologies, clinical applications, and future challenges. Front. Bioeng. Biotechnol. **13**, 1587114 (2025)
8. Tavakoli, M., Carriere, J., Torabi, A.: Robotics, smart wearable technologies, and autonomous intelligent systems for healthcare during the COVID-19 pandemic: an analysis of the state of the art and future vision. Adv. Intell. Syst. **2**(7), 2000071 (2020)
9. Kyrarini, M., et al.: A survey of robots in healthcare. Technologies. **9**(1), 8 (2021)
10. Gao, A., et al.: Progress in robotics for combating infectious diseases. Science. Robotics. **6**(52), eabf1462 (2021)
11. Ampadu, K.O., Rokohl, F., Mahmood, S., Reichenbach, M., Huebner, M.: InjectMeAI—software module of an autonomous injection humanoid. Sensors. **22**(14), 5315 (2022)
12. Cobonix (Waterloo Startup Performs First Ever Robotic Intramuscular Injection).: https://uwaterloo.ca/news/media/waterloo-startup-performs-first-ever-robotic-intramuscular Last accessed 27 Nov 2025
13. WHO (World Health Organization) Immunization Agenda.: A Global Strategy to Leave No One Behind, https://www.who.int/teams/immunization-vaccines-and-biologicals/strategies/ia2030 2030 Last accessed 27 Nov 2025
14. Nicoll, L.H., Hesby, A.: Intramuscular injection: an integrative research review and guideline for evidence-based practice. Appl. Nurs. Res. **15**(3), 149–162 (2002)
15. Anita McCutcheon, J., Rees Doyle, G.: Clinical procedures for safer patient care. BCcampus. (2015)
16. Depar, U. S.: Vaccine Administration: Intramuscular (IM) Injection Adults 19 years of age and older
17. Potter, P.A., Perry, A.G., Stockert, P.A., Hall, A., Ostendorf, W.R.: Fundamentals of Nursing-e-Book: Fundamentals of Nursing-e-Book. Elsevier Health Sciences (2025)
18. Neumann, D.A.: Kinesiology of the Musculoskeletal System-e-Book: Kinesiology of the Musculoskeletal System-e-Book. Elsevier Health Sciences (2016)
19. Chartier, Y. (ed.): Safe Management of Wastes from Health-Care Activities. World Health Organization (2014)
20. GrabCad Human_Dummy by Alex Alex.: https://grabcad.com/library/human_dummy-1 Last accessed 01 Dec 2025
21. GrabCad Chair by Umesh Joseph.: https://grabcad.com/library/chair-1025 Last accessed 01 Dec 2025
22. Byrd, R.H., Lu, P., Nocedal, J., Zhu, C.: A limited memory algorithm for bound constrained optimization. SIAM J. Sci. Comput. **16**(5), 1190–1208 (1995)
23. Makwana, S., Basu, B., Makasana, Y., Dharamsi, A.: Prefilled syringes: an innovation in parenteral packaging. Int. J. Pharm. Investig. **1**(4), 200 (2011)

Design Optimization of Redundant Spherical Parallel Manipulator with an Unlimited Self-Rotation

Chaima Lahdiri(✉), Houssem Saafi, and Abdelfattah Mlika

Mechanical Laboratory of Sousse, University of Sousse, Sousse, Tunisia
chaima.lahdiri@eniso.u-sousse.tn

Abstract. This paper deals with the optimization of a redundant spherical parallel manipulator (RSPM). The manipulator consists of two spherical five-bar mechanisms connected through a common end-effector, providing three degrees of freedom and offering unlimited self-rotation capability. To enhance its performance, the geometric parameters are optimized using a hybrid DE–Jaya method. The objective of this optimization is to reduce the geometric parameters while improving the manipulator's dexterity.

Keywords: RSPM · unlimited self-rotation capability · hybrid DE-Jaya

1 Introduction

Spherical parallel manipulators (SPMs) are a class of parallel robots characterized by a closed-loop architecture with concurrent joint axes, making them particularly suitable for applications requiring high stiffness, accuracy, and dynamic performance, such as haptic devices. Recent developments include the generatively optimized compact 3-DoF SPM, which employs four identical kinematic chains connecting the base to the moving platform, incorporates compact actuators, and is designed to maximize both manipulability and workspace efficiency [1], and a cable-driven coaxial spherical parallel mechanism for ultrasound scans, which enables precise remote operation and haptic feedback in medical applications [2]. In addition, a parallel haptic device using an electrorheological fluid has been proposed for minimally invasive surgery, capable of accurately reproducing torque and force through real-time control of the viscosity of the fluid [3]. Another example is the 3-RRR SPM with coaxial input axes, offering unlimited rotation [4]. Despite these advances, spherical parallel manipulators continue to present significant challenges, such as the presence of parallel singularities, restricted for self-rotation capability, and limited workspace [5]. Various solutions have been proposed, including geometric optimization [6] and redundancy [7, 8], with Saafi et al. [9, 10] successfully eliminating singularities in a redundant SPM. To address these challenges, we need to optimize geometric parameters in order to improve the dexterity of manipulators, extend their self-rotation capabilities, and improve their precision, particularly in medical applications.

© The Author(s), under exclusive license to Springer Nature Switzerland AG 2026
A. Chaker et al. (Eds.): EFIMMS 2026, MMS 205, pp. 16–24, 2026.
https://doi.org/10.1007/978-3-032-22270-1_2

The Jaya algorithm, first proposed by Rao [11], has attracted considerable interest as an effective method for optimization due to its simplicity and parameter-free structure. It has been successfully applied in various mechanical and robotic design problems. For instance, Migallon et al. [12] proposed parallel improvements of the Jaya algorithm and demonstrated its effectiveness in optimizing engineering systems, achieving faster convergence and better solution quality compared to classical evolutionary methods. Differential Evolution (DE), known for its robustness and simplicity, has also shown strong performance in solving complex engineering problems, as reviewed by Ahmad et al. [13]. Building on the strengths of both algorithms, hybrid strategies such as the DE–Jaya method [14] have emerged to combine the global exploration capability of DE with the rapid convergence of Jaya. Nguyen-Van et al. [15] applied a DE–Jaya hybrid algorithm to the dimensional synthesis of a four-bar mechanism and showed that the hybrid approach offers superior global search ability and yields more accurate optimal solutions than either DE or Jaya alone. Collectively, these studies highlight the growing effectiveness of both standalone Jaya and hybrid DE–Jaya optimization methods in addressing challenging engineering design problems.

In this work, the kinematics of a redundant spherical parallel manipulator is presented. An optimization procedure is then developed using a hybrid method that combines the Jaya algorithm with Differential Evolution. In the proposed strategy, the mutation step is performed using Jaya, while the crossover operator is adopted from Differential Evolution. This design allows the hybrid optimizer to exploit the complementary strengths of both methods: Jaya provides strong exploitation by systematically guiding solutions toward the best candidate and away from the worst, whereas Differential Evolution enhances exploration through its crossover mechanism, which preserves population diversity and enables effective global search. As a result, the hybrid approach achieves a balanced trade-off between exploration and exploitation, improving convergence reliability.

This paper is organized as follows: Sect. 2 introduces the kinematics of the redundant spherical parallel manipulator. Section 3 presents the optimization procedure. Finally, Sect. 4 concludes the paper.

2 The Redundant Spherical Parallel Manipulator Structure

The Redundant Spherical Parallel Manipulator (RSPM) is a spherical parallel mechanism that provides three rotational degrees of freedom, consisting of two tilt rotations and one complete self-rotation. Its structure is formed by two spherical five-bar mechanisms connected through a moving platform. Each five-bar mechanism includes four links and five revolute joints. The revolute joints attached to the base are actuated, whereas the remaining joints are passive. Since the system uses four actuators for only three degrees of freedom, the RSPM is considered a redundant architecture.

The two spherical five-bar mechanisms have different geometric parameters. For each mechanism, the geometry of its links is defined by the angles between their consecutive revolute joint axes. The first five-bar mechanism is characterized by the angles α_1 and β_1, while the second five-bar mechanism has its own angles α_2 and β_2.

The orientation of the $\mathbf{Z_{1k}}$ axes relative to the global Z-axis is defined by the angle δ, while the pose of the mobile platform is described using the ZXZ Euler angles (ψ, θ, ϕ). The size of the mobile platform is specified by the parameter 2γ (Fig. 1).

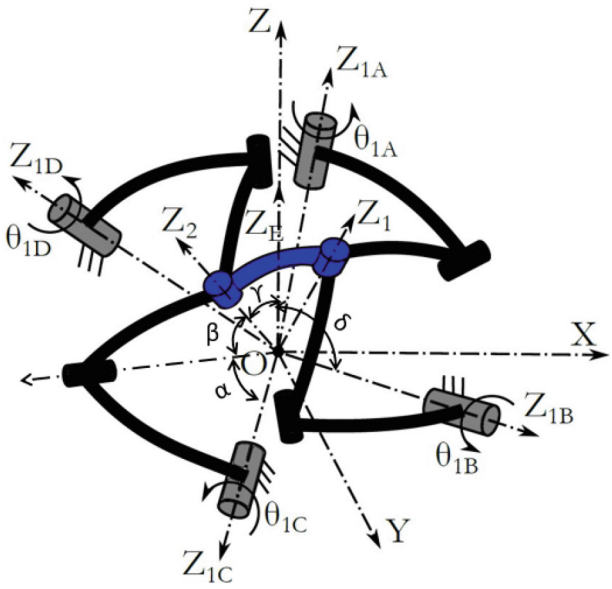

Fig. 1. The redundant spherical parallel manipulator kinematic

The kinematic modeling and analysis of the proposed RSPM have been previously reported in [16]. In that work, the complete kinematic formulation was derived, including the identification of the actuated and passive joints and the computation of the Jacobian matrix.

The dexterity analysis, evaluated using the Jacobian condition number, reveals that the manipulator exhibits relatively low dexterity over significant portions of the workspace, with values approaching 0.26. These results highlight the limitations of the initial geometric design and motivate the optimization process proposed in this paper, which aims to enhance the dexterity distribution while preserving the unlimited self-rotation capability.

3 Optimization Used Hybrid DE Jaya Method

3.1 Principe of Hybrid DE Jaya Method

The hybrid DE-JAYA algorithm is an approach that combines the JAYA algorithm with differential evolution (DE) in order to improve both convergence and exploration capabilities in optimization problems. The fundamental principle of JAYA is to adaptively move each solution closer to the best individual in the population while moving it away

from the worst, without requiring complex parameters. The integration of DE introduces differential crossover, which favors population diversity and reduces the risk of premature convergence to local minimums.

The main steps of the Hybrid DE-JAYA algorithm, along with the corresponding equations, are presented below:

1. Initialization: Generate an initial population is presented in Eq. (1)

$$\mathbf{Y_i^0} = \mathrm{Lb} + \mathrm{rand} \bullet (\mathrm{Ub} - \mathrm{Lb}), \text{ for } \mathrm{i} = 1 \ldots \mathrm{Np} \tag{1}$$

where Np is the population size and Ub and Lb is the upper and lower parameters

2. Identification of Extremes:

As shown in Eq. (2), the best and worst individuals in the population are identified by evaluating the objective function across all candidates:

$$\begin{cases} \mathbf{Y_{best}^G} = \min\limits_{\mathrm{i}} \left(\mathbf{F_i^G}\right) \\ \mathbf{Y_{worst}^G} = \max\limits_{\mathrm{i}} \left(\mathbf{F_i^G}\right) \end{cases} \tag{2}$$

Where F is the objective function

3. JAYA Mutation

Equation 3 defines the mutated vector for each individual i = 1…Np and each variable j = 1…Nvar (variable number):

$$\mathbf{Z_{i,j}^G} = \mathbf{Y_{i,j}^G} + \mathrm{r1} \times \left(\mathbf{Y_{best,j}^G} - \mathbf{Y_{i,j}^G}\right) - \mathrm{r2} \times \left(\mathbf{Y_{worst,j}^G} - \mathbf{Y_{i,j}^G}\right) \tag{3}$$

4. Differential Evolution Crossover:

The crossover operation in Differential Evolution is defined by Eq. (4), where the trial vector $\mathbf{T_{i,j}^G}$ is constructed from donor and target vectors depending on the crossover probability Cr and a randomly chosen index randj.

$$\mathbf{T_{i,j}^G} = \begin{cases} \mathbf{Z_{i,j}^G} & \text{if rand} < \mathrm{Cr} \text{ or } \mathrm{j} = \mathrm{randj} \\ \mathbf{Y_{i,j}^G} & \text{else} \end{cases} \tag{4}$$

Where Cr is the crossover rate where Cr ∈ [0.1,1]

5. Selection

The selection mechanism is defined by Eq. (5). If the trial vector gives a better objective function value than the target vector, it replaces the current individual in the next generation; otherwise, the target vector is retained.

$$\mathbf{Y_I^{G+1}} = \begin{cases} \boldsymbol{T_i^G} & \text{if } \mathrm{F_{trial,i}^G} < \mathrm{F_i^G} \\ \boldsymbol{Y_i^G} & \text{else} \end{cases} \tag{5}$$

3.2 Optimization of RSPM

The objective of the optimization is to minimize the geometric parameters of the mechanism while ensuring satisfactory kinematic performance(dexterity) and complete coverage of a prescribed workspace. The target workspace is defined as a conical region with a 26° apex angle, representing the admissible inclination range of the end-effector. To simplify the optimization process, only the boundary of this workspace is considered, represented by 20 discrete points Pj , as illustrated in Fig. 2.

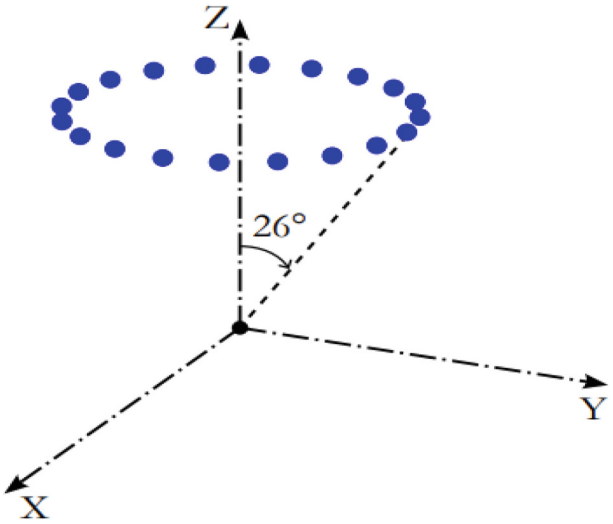

Fig. 2. The Prescribed Workspace Boundaries in Cartesian Space.

This optimization was applied to the RSPM, where the parameter of the first five-bar is defined by α1 and, β1 while the second five-bar mechanism is represented by α2 and, β2. T The objective function is defined as the sum of the squares of the geometric parameters and is formulated as follows:

$$\underset{\mathbf{X}}{\text{minimize}} \quad F(\mathbf{X}) = \sum_{i}^{6} Xi^2 \tag{6}$$

Where $\mathbf{X} = \left[\, \alpha 1 \ \beta 1 \ \alpha 2 \ \beta 2 \ \gamma \ \delta \,\right]$

To enhance the dexterity, we will impose constraint on the optimization process, related to the condition number such that:

$$CD(\mathbf{X}, Pj) : k(\mathbf{J}) \leq Kmax \ , \text{for } j = 1 \ldots 10 \tag{7}$$

Where Kmax is the maximum acceptable value for the condition number, which is set to 25 [17] during the optimization process.

In addition, workspace inclusion constraints are imposed to guarantee that all target orientations remain inside the workspace. These constraints are expressed as:

$$\mathrm{CDj}\ (\mathbf{X}, \psi, \theta, \varphi) : \frac{C_j^2}{A_j^2 + B_j^2} \leq 1 \text{ for } j = 1, 2, 3, 4 \tag{8}$$

where Aj, Bj, and Cj are geometric coefficients defining the admissible workspace region for each kinematic chain.

The design variables are bounded by lower and upper limits: $x_{inf} \leq xi \leq x_{sup}$

The boundary values x_{inf} and x_{sup} are defined in Table 1.

Table 1. The lower and upper bounds of the geometric parameters of the system.

	α1(°)	β1(°)	α2(°)	β2(°)	γ(°)	δ(°)
x_{inf}	50	50	50	50	20	50
x_{sup}	80	80	80	80	30	70

Several studies have shown that large crossover rate (CR) values typically ranging from 0.7 to 1, enhance population diversity and exploration capability, particularly in highly nonlinear optimization problems such as robotic geometric design [18, 19].

In this study, the optimization of the RSPM for different CR values yields the corresponding vectors of optimal design parameters, as summarized in Table 2.

Table 2. Optimal parameters.

Cr	α1 (°)	β1 (°)	α2 (°)	β2 (°)	γ (°)	δ (°)	Min dexterity	Max dexterity
0.7	67.4	61	67	64	28.5	61	0.146	0.547
0.8	64.7	61.9	65	61.4	27.8	61.5	0.174	0.531
0.9	64	64.5	68	67	28.5	67	0.247	0.547

As shown in Table 2, increasing the CR generally leads to improved dexterity performance. In particular, the minimum dexterity index increases significantly from 0.146 for CR = 0.7 to 0.247 for CR = 0.9, indicating a more uniform and robust kinematic performance throughout the prescribe workspace. Although the maximum dexterity remains relatively stable, with values close to 0.55 for both CR = 0.7 and CR = 0.9, the configuration corresponding to CR = 0.9 provides the best compromise between minimum and maximum dexterity.

A good distributed dexterity of the optimized manipulator is shown in Fig. 3 for different values of the self-rotation angle. The results obtained demonstrate reasonable dexterity in the prescribed workspace, with values ranging from approximately 0.25 to a maximum of approximately 0.55. Moreover, the optimized configurations allow

the mechanism to achieve an unlimited self-rotation throughout the defined workspace (Fig. 4).

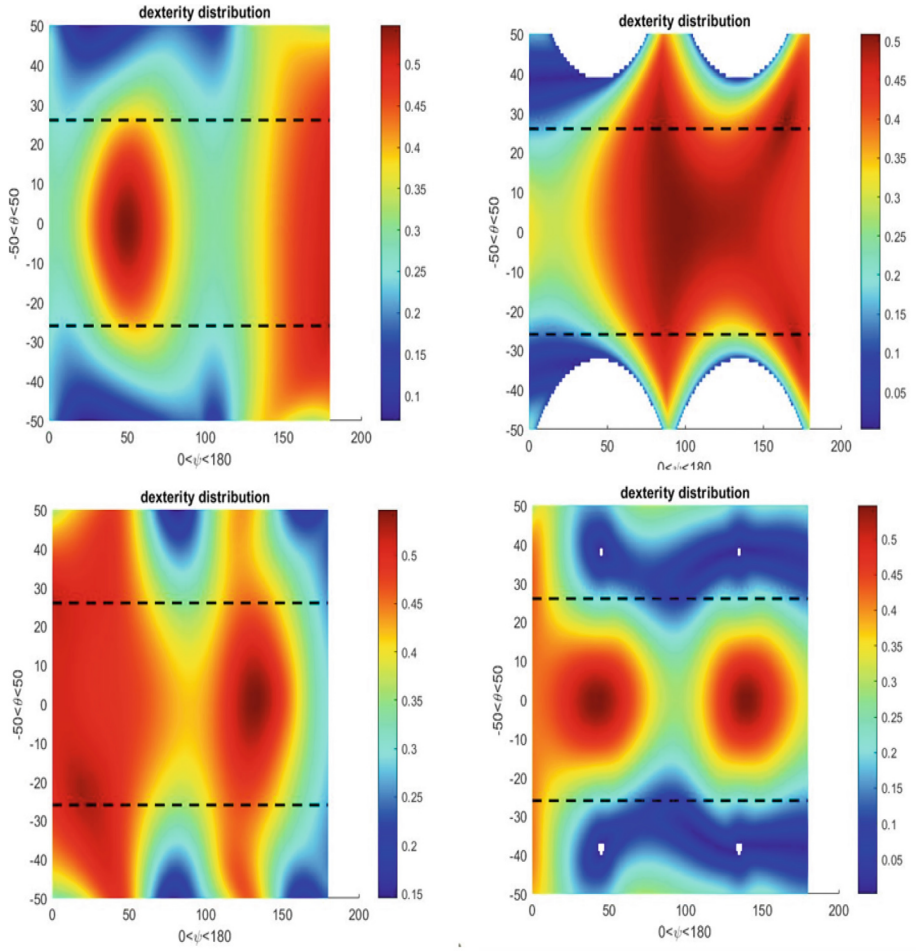

Fig. 3. Dexterity distribution of the RSPM resulting from the optimization for $\phi = 0\,°, 90\,°, 180\,°, 270\,°$).

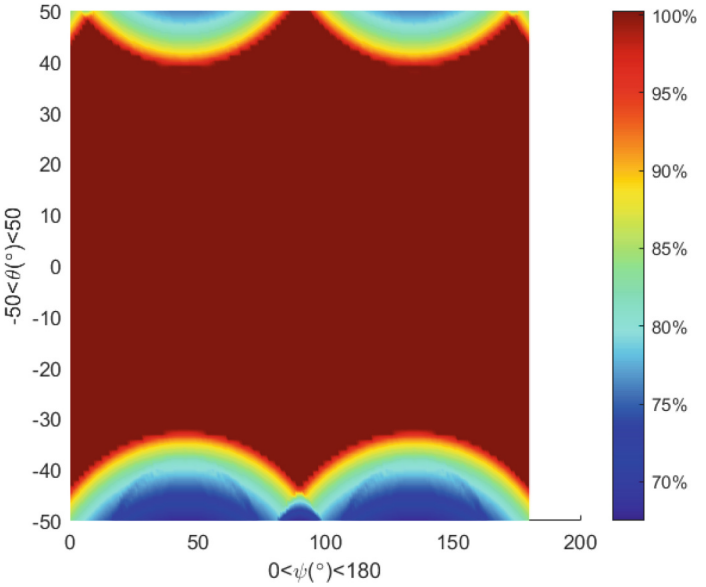

Fig. 4. Self-rotation distribution of the RSPM resulting from the optimization.

4 Conclusion

In this paper, a redundant spherical parallel manipulator was optimized using a hybrid evolutionary method that combines the JAYA algorithm with Differential Evolution. The proposed hybrid optimizer benefits from the exploitation capability of JAYA and the exploration strength of DE, making it particularly suitable for the highly nonlinear geometric behavior of spherical parallel manipulators. An optimization procedure was performed on the manipulator architecture, aiming to maximize its dexterity while minimizing geometric parameters. The hybrid JAYA–DE method successfully improved the dexterity of the mechanism, achieving a maximum value of 0.55 within the prescribe workspace. Throughout the optimization process, the manipulator preserved its unlimited self-rotation capability.

References

1. Walia, K., Navaraj, W., Breedon, P.: Generatively optimised compact 3-DoF spherical parallel manipulator with tightly integrated actuators. Front. Mech. Eng. **11**, 1629405 (2025)
2. Seraj, M., Kamrava, M.H., Tiseo, C.: Parametric design of a cable-driven coaxial spherical parallel mechanism for ultrasound scans. arXiv preprint arXiv: 2512.06995. (2025)
3. Han, Y.M., Choi, S.B., Oh, J.S.: Tracking controls of torque and force of 4-degree-of-freedom haptic master featuring smart electrorheological fluid. J. Intell. Mater. Syst. Struct. **27**(7), 915–924 (2016)
4. Tursynbek, I., Shintemirov, A.: Infinite rotational motion generation and analysis of a spherical parallel manipulator with coaxial input axes. Mechatronics. **78**, 102625 (2021)

5. Khoshnoodi, H., Rahmani Hanzaki, A., Talebi, H.A.: Kinematics, singularity study and optimization of an innovative spherical parallel manipulator with large workspace. J. Intell. Robot. Syst. **92**, 309–321 (2018)
6. Pulloquinga, J.L., et al.: A type II singularity avoidance algorithm for parallel manipulators using output twist screws. Mech. Mach. Theory. **183**, 105282 (2023)
7. Valero, F., et al.: Reconfiguration of a parallel kinematic manipulator with 2T2R motions for avoiding singularities through minimizing actuator forces. Mechatronics. **69**, 102382 (2020)
8. Shen, C., et al.: Kinematics analysis and singularity avoidance of a parallel mechanism with kinematic redundancy. Chinese J. Mech. Eng. **35**(1), 113 (2022)
9. Saafi, H., Laribi, M.A., Zeghloul, S.: Forward kinematic model improvement of a spherical parallel manipulator using an extra sensor. Mech. Mach. Theory. **91**, 102–119 (2015)
10. Saafi, H., Laribi, M.A., Zeghloul, S.: Redundantly actuated 3-RRR spherical parallel manipulator used as a haptic device: improving dexterity and eliminating singularity. Robotica. **33**(5), 1113–1130 (2015)
11. Rao, R.: Jaya: a simple and new optimization algorithm for solving constrained and unconstrained optimization problems. Int. J. Ind. Eng. Comput. **7**(1), 19–34 (2016)
12. Migallón, H., Jimeno-Morenilla, A., Sanchez-Romero, J.-L.: Parallel improvements of the Jaya optimization algorithm. Appl. Sci. **8**(5), 819 (2018)
13. Ahmad, M.F., et al.: Differential evolution: a recent review based on state-of-the-art works. Alex. Eng. J. **61**(5), 3831–3872 (2022)
14. Mlaouhi, I., Najeh Ben Guedria, Bouraoui, C.: An efficient hybrid differential evolution–Jaya algorithm for enhancing vibration behaviour in automotive turbocharger systems. Eng. Optim. **56**(9), 1493–1515 (2024)
15. Nguyen-Van, S.Y., et al.: A new study on optimization of four-bar mechanisms based on a hybrid-combined differential evolution and Jaya algorithm. Symmetry. **14**(2), 381 (2022)
16. Lahdiri, C., Saafi, H., Mlika, A.: Working mode study of a new spherical parallel manipulator with an unlimited self rotation capability. In: IFToMM International Conference on Mechanisms, Transmissions and Applications, pp. 171–179. Springer, Cham (2023)
17. Lahdiri, C., et al.: Optimal design of a new redundant spherical parallel manipulator with an unlimited self-rotation capability. Robotica. **43**(1), 300–315 (2025)
18. Li, M., Qiao, L.: A review and comparative study of differential evolution algorithms in solving inverse kinematics of mobile manipulator. Symmetry. **15**(5), 1080 (2023)
19. Gamperle, R.: Parameter study for differential evolution. Proc. WSEAS NNA-FSFS-EC. **2002**, 293 (2002)

Kinematic Analysis of a Spherical Parallel Mechanism with 3-Degree of Redundancy

Terence Essomba(✉)

National Central University, Taoyuan City 32001, Taiwan
tessomba@cc.ncu.edu.tw

Abstract. Remote Center of Motion mechanisms are known to rotate their end effector around a point. Spherical Parallel Mechanisms, which use spherical linkages in parallel, have a good kinematic performance close to the workspace center. But the large number of links and joints tends to compromise their behavior as their end effector moves away from it and approaches other parts like their base or other links. Reconfiguration features allow a mechanism to change its configuration for the same end effector position. In the present study, pantographic linkages are used to re-orient the SPM base as reconfiguration method. A preliminary analysis of its kinematic and velocity models is conducted. The reconfiguration joint variables are then determined in order to optimize the kinematic performance of the mechanism. After completing the inverse kinematic model, the reconfigurable mechanism is evaluated and compared to its non-reconfigurable counterpart.

Keywords: Spherical Parallel Mechanism · Reconfigurable Mechanism · Remote Center of Motion · Kinematic Performance

1 Introduction

Mechanisms with Remote Center of Motion (RCM) have attracted a considerable attention as they are highly suitable with many surgical applications. Indeed, these applications often require rotating an instrument around a fixed point which is the Center of Rotation (CoR). RCM mechanism refers to a mechanical architecture that generates this kinematics without the need of synchronizing its input joints. In other words, randomly operating any joint of the mechanism will systematically rotate the end effector around the CoR. These mechanisms can be classified in several categories regarding their architecture: isocenter [1], circular tracking arc [2], pantograph [3], etc.

One popular method to generate an RCM is to rely on spherical architectures. Their links have a spherical shape and their revolute joint axes all intersect at the CoR. This type of architecture can be mounted as serial mechanisms [4]. In order to combine the advantages of both parallel mechanisms and spherical mechanisms, Spherical Parallel Mechanism (SPM) can be obtained by mounting two or three spherical linkages in parallel [5]. However, the major disadvantage of parallel architectures results from the larger number of linkages which causes reduced workspace. Another issue comes from the additional Jacobian matrices which create new singularities.

© The Author(s), under exclusive license to Springer Nature Switzerland AG 2026
A. Chaker et al. (Eds.): EFIMMS 2026, MMS 205, pp. 25–34, 2026.
https://doi.org/10.1007/978-3-032-22270-1_3

A solution for countering these weaknesses consist in integrating reconfigurable features into parallel mechanisms. As the mechanism is capable of changing its configuration for a given end effector position, its characteristic can be controlled to either avoid undesirable encounters (collisions, singularities) or to improve performances [6].

Several instances of reconfigurable parallel mechanisms can be found in the literature [7–11]. But cases of reconfigurable SPM remain rare. A 3-RRR SPM with reconfigurable base has been proposed for craniotomy. Three synchronized pantographic linkages were used to reposition the mechanism base [12]. It was then demonstrated that the reconfiguration allowed maintaining a better kinematic performance while conducting craniotomy trajectories.

In the present study, an improved version of the mechanism and a more advanced analysis is conducted. First, the three pantographic linkages are now controlled independently for enhanced adaptability. Second, the reconfigurable variables (which are now tripled in number) are treated real input variables in the velocity model. And finally, the values of these variables are now determined analytically, instead of relying on numerical method. The next section will present the new mechanism and its reconfiguration method. The inverse kinematic and velocity models will be derived in Sect. 3. The best reconfiguration regarding a specific requirement will be determined in Sect. 4. The improved performances of the reconfigurable mechanism are shown in Sect. 5.

2 Mechanical Architecture

The 3-RRR SPM is a parallel mechanism connecting its base and end effector via three legs. Each leg is a serial spherical linkage composed of a proximal and a distal link. The proximal link connects with the base by the active rotational joint. The distal link connects with the proximal link and end effector via passive revolute joints. On each leg labelled as k = A, B or C, the active revolute joint is designated by its axis noted $\mathbf{z_{k1}}$. The passive joint axis between the proximal and distal link is noted $\mathbf{z_{k2}}$ and the one belonging to the end effector is noted $\mathbf{z_{k3}}$. The link dimensions are given using the angle between their adjacent joint axes. To facilitate the study, the proximal and distal link dimension is measure by the angle α and the end effector by the angle β.

Classically, the base of the 3-RRR classical SPM (cSPM) is formed by the active joint axes $\mathbf{z_{k1}}$, which are fixed. The new reconfigurable SPM (rSPM) can modify the geometry of its base by re-orienting its active joint axes $\mathbf{z_{k1}}$. As the axes $\mathbf{z_{k1}}$ rotate, they shall remain directed to the mechanism CoR to maintain the RCM feature. As shown in Fig. 1, the mechanical concept uses pantographic linkage for rotating the active joint axes around the CoR. The pantographic linkages CoR are aligned with the mechanism. Each leg of the new SPM is therefore described as a PaRRR architecture. For a given orientation of the mechanism end effector, the active pantographic joint (Pa-joint) is used to reconfigure the mechanism base and its variable is noted μ_k for the leg k. It is measured between the origin reference frame $\mathbf{z_0}$ and the active joint axis $\mathbf{z_{k1}}$. The active revolute joint (R-joint) is actuated to control the end effector orientation, noted θ_k. The end effector is located by its central axis $\mathbf{z_E}$ and its orientation is obtained through the angular coordinates ψ, θ and ϕ. Using intrinsic rotations, the associated rotation matrix

is calculated as follows:

$$\mathbf{R_E} = \mathbf{R}(\mathbf{z}, \psi) \bullet \mathbf{R}(\mathbf{x}, \theta) \bullet \mathbf{R}(\mathbf{z}, \phi) \tag{1}$$

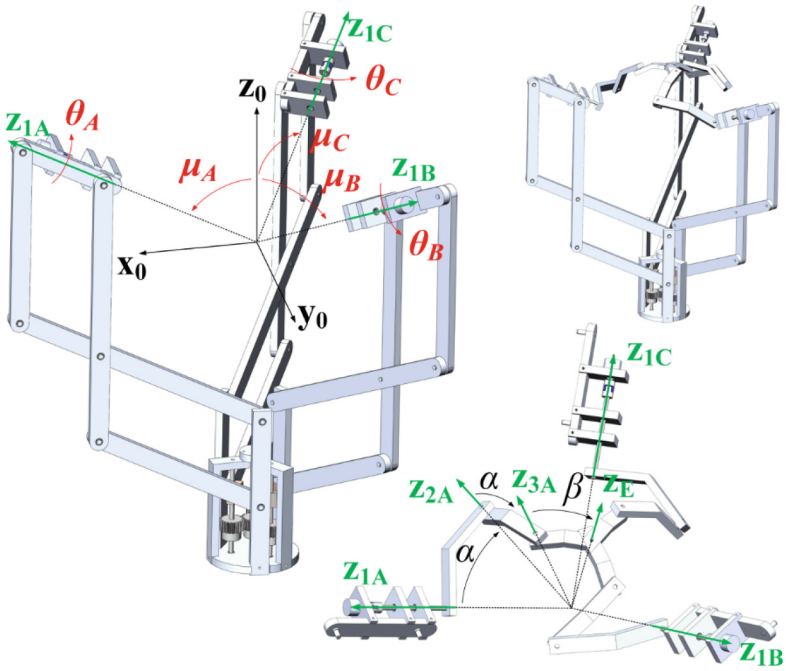

Fig. 1. Architecture of the 3-PaRRR Spherical Parallel Mechanism

3 Kinematic Analysis

3.1 Inverse Kinematic Model

The IKM allows calculating the input joint variables μ_k and θ_k for a given orientation (ψ, θ, ϕ) of the mechanism end effector. As a parallel architecture, a constraint equation setting the condition of kinematic closure shall involve both abovementioned variables. Classically, the constraint equation for this type of SPM is written as:

$$\mathbf{z_{k2}} \bullet \mathbf{z_{k3}} = \cos\alpha \tag{2}$$

Vectors $\mathbf{z_{k2}}$ are obtained using a series of intrinsic rotations involving the Pa-joints the R-joints and the proximal link angle. Their coordinates are calculated as follows:

$$\begin{cases} \mathbf{z_{A2}} = \mathbf{R}(\mathbf{y}, \mu_A) \bullet \mathbf{R}(\mathbf{z}, \theta_A) \bullet \mathbf{R}(\mathbf{y}, \alpha) \bullet \mathbf{z_0} \\ \mathbf{z_{B2}} = \mathbf{R}(\mathbf{z}, 2\pi/3) \bullet \mathbf{R}(\mathbf{y}, \mu_B) \bullet \mathbf{R}(\mathbf{z}, \theta_B) \bullet \mathbf{R}(\mathbf{y}, \alpha) \bullet \mathbf{z_0} \\ \mathbf{z_{c2}} = \mathbf{R}(\mathbf{z}, -2\pi/3) \bullet \mathbf{R}(\mathbf{y}, \mu_C) \bullet \mathbf{R}(\mathbf{z}, \theta_C) \bullet \mathbf{R}(\mathbf{y}, \alpha) \bullet \mathbf{z_0} \end{cases} \tag{3}$$

Vectors $\mathbf{z_{k3}}$ are found using the intrinsic rotations of the mechanism end effector and its dimension as follows:

$$\begin{cases} \mathbf{z_{A3}} = \mathbf{R_E} \bullet \mathbf{R}(\mathbf{y}, \beta) \bullet \mathbf{z_0} \\ \mathbf{z_{B3}} = \mathbf{R_E} \bullet \mathbf{R}(\mathbf{z}, 2\pi/3) \bullet \mathbf{R}(\mathbf{y}, \beta) \bullet \mathbf{z_0} \\ \mathbf{z_{C3}} = \mathbf{R_E} \bullet \mathbf{R}(\mathbf{z}, -2\pi/3) \bullet \mathbf{R}(\mathbf{y}, \beta) \bullet \mathbf{z_0} \end{cases} \tag{4}$$

Substituting Eq. (2) with Eq. (3) and (4), leads to the following expression:

$$A_k \cos\theta_k + B_k \sin\theta_k = C_k \tag{5}$$

Where A_k, B_k and C_k are function of the mechanism variables and parameters. The R-joint variables can be isolated and calculated by solving Eq. (5). Their expression is written as:

$$\theta_k = \text{ATAN2}(B_k, A_k) \pm \cos^{-1}\left(\frac{C_k}{\sqrt{A_k^2 + B_k^2}}\right) \tag{6}$$

However, the Pa-joint variables μ_k are still unknown at this point. For a given orientation (ψ, θ, ϕ) of the end effector, there is a range values for μ_k where Eq. (6) is solvable and θ_k can be found. Therefore, unique values of μ_k shall be found based on a specific condition.

3.2 Velocity Model

The velocity model of the mechanism is obtained through simple differential kinematics. The constraint equation Eq. (2) is differentiated with the time as follows:

$$\dot{\mathbf{z}}_{\mathbf{k2}} \bullet \mathbf{z_{k3}} = -\mathbf{z_{k2}} \bullet \dot{\mathbf{z}}_{\mathbf{k3}} \tag{7}$$

The derivate of vector $\mathbf{z_{k3}}$ is expressed with the angular velocity of the end effector noted $\boldsymbol{\omega}$. Vectors $\mathbf{z_{k2}}$ are written as a combination of angular velocities $\dot{\mu}_k$ and $\dot{\theta}_k$ around axes $\mathbf{u_k}$ and $\mathbf{z_{k1}}$ respectively. This yields the following velocity model:

$$\left(\dot{\mu}_{\mathbf{k}}\mathbf{u_k} + \dot{\theta}_{\mathbf{k}}\mathbf{z_{k1}}\right) \times \mathbf{z_{k2}} \bullet \mathbf{z_{k3}} = \mathbf{z_{k2}} \times \mathbf{z_{k3}} \bullet \boldsymbol{\omega} \tag{8}$$

Where $\begin{cases} \mathbf{u_A} = \mathbf{y_0} \\ \mathbf{u_B} = \mathbf{R}(\mathbf{z}, 2\pi/3) \bullet \mathbf{y_0} \\ \mathbf{u_c} = \mathbf{R}(\mathbf{z}, -2\pi/3) \bullet \mathbf{y_0} \end{cases}$

When applied to the three legs of the rSPM, it can be written in a matrix form as:

$$\begin{bmatrix} \mathbf{J}_{\boldsymbol{\mu}} & \mathbf{J}_{\boldsymbol{\theta}} \end{bmatrix} \begin{bmatrix} \dot{\boldsymbol{\mu}} \\ \dot{\boldsymbol{\theta}} \end{bmatrix} = \mathbf{J}_{\boldsymbol{\omega}} \bullet \boldsymbol{\omega} \tag{9}$$

Where $\mathbf{J_\mu} =$ diag $(\mathbf{u_k} \times \mathbf{z_{k2}} \bullet \mathbf{z_{k3}})$, $\mathbf{J_\theta} =$ diag $(\mathbf{z_{k1}} \times \mathbf{z_{k2}} \bullet \mathbf{z_{k3}})$

And $\mathbf{J}_{\boldsymbol{\omega}} = \begin{bmatrix} (\mathbf{z_{A2}} \times \mathbf{z_{A3}})^{\mathbf{T}} \\ (\mathbf{z_{B2}} \times \mathbf{z_{B3}})^{\mathbf{T}} \\ (\mathbf{z_{C2}} \times \mathbf{z_{C3}})^{\mathbf{T}} \end{bmatrix}$

The matrix form of the velocity model reveals the existence of two serial Jacobian matrices ($\mathbf{J_\mu}$ and $\mathbf{J_\theta}$) and one parallel Jacobian matrix ($\mathbf{J_\omega}$). Two of these matrices ($\mathbf{J_\theta}$ and $\mathbf{J_\omega}$) are identical with those of the classical 3-RRR SPM. The new matrix $\mathbf{J_\mu}$ is associated with reconfiguration of the mechanism base.

4 Reconfiguration Model

4.1 Formulation of the Reconfiguration Condition

Through its reconfiguration ability, it is possible for the mechanism to modify its configuration for a given position of the end effector to improve its characteristics. In the present study, it is chosen to reconfigure the mechanism to optimize its kinematic performance. The kinematic performance of the rSPM is dependent on the three Jacobian matrices. Their respective geometrical interpretation is facilitated by the vectorial form of their terms. The kinematic performance given by matrix $\mathbf{J_\theta}$ depends on the placement of vectors $\mathbf{z_{k1}}$, $\mathbf{z_{k2}}$ and $\mathbf{z_{k3}}$. Based on the kinematics of the mechanism, vectors $\mathbf{z_{k3}}$ is directly positioned by the end effector coordinates and $\mathbf{z_{k2}}$ by the R-joint variables. Vectors $\mathbf{z_{k1}}$ are directly positioned by the Pa-joint variables. Therefore, a geometrical condition between the vectors $\mathbf{z_{k1}}$, $\mathbf{z_{k2}}$ and $\mathbf{z_{k3}}$ shall lead to specific values for variables μ_k. The kinematic performance generated by a Jacobian matrix can be calculated as the determinant of that matrix, which is known as the manipulability. Based on Eq. (9), the manipulability of matrix $\mathbf{J_\theta}$ is calculated as follows:

$$\det \mathbf{J_\mu} = \prod_{k=A}^{C} (\mathbf{z_{k1}} \times \mathbf{z_{k2}}) \bullet \mathbf{z_{k3}} \tag{10}$$

The manipulability from matrix $\mathbf{J_\theta}$ is as high as possible when the term $(\mathbf{z_{k1}} \times \mathbf{z_{k2}}) \bullet \mathbf{z_{k3}}$ has the maximum value for all legs. This brings the mechanism legs in a particular configuration illustrated in Fig. 2. The mechanism joint axes for one leg are projected on a straight plane. The cross product of $\mathbf{z_{k1}}$ and $\mathbf{z_{k2}}$ is noted $\mathbf{z_{k12}}$. Therefore, there is a right angle between $\mathbf{z_{k1}}$ and $\mathbf{z_{k12}}$ and between $\mathbf{z_{k2}}$ and $\mathbf{z_{k12}}$. The angles between $\mathbf{z_{k1}}$ and $\mathbf{z_{k3}}$ and between $\mathbf{z_{k3}}$ and $\mathbf{z_{k12}}$ are respectively noted γ and ε.

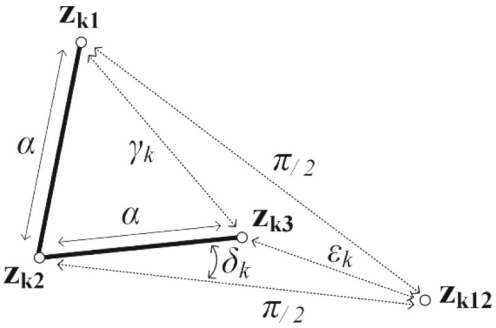

Fig. 2. Mechanism leg configuration projected on a straight plane.

By observing the resulting geometry, the diagonal terms d_k of $\mathbf{J_\theta}$ can be written as:

$$d_k = \sin\alpha \cos\varepsilon_k \tag{11}$$

On the other hand, spherical trigonometry involving angles ε_k and δ_k yields:

$$d_k = \sin^2\alpha \cos\delta_k \tag{12}$$

The value of d_k is maximum when $\delta_k = 0$. This result is substituted in another spherical trigonometry equation linking angle α and γ_k, leading to the following condition:

$$\cos \gamma_k = \cos^2 \alpha \tag{13}$$

Finally, the constraint equation that ensure the highest possible kinematic performance from matrix $\mathbf{J_0}$ for all legs is written as:

$$\mathbf{z_{k1}} \bullet \mathbf{z_{k3}} = \cos^2 \alpha \tag{14}$$

This means that for a given position of the end effector given by $\mathbf{z_{k3}}$, the reconfiguration joint variables μ_k should be adjusted to place the proximal joint $\mathbf{z_{k1}}$ so that the condition in Eq. (14) is respected.

4.2 Final Inverse Kinematic Model

Solving the mechanism IKM required finding the R-joint variables θ_k for a given orientation of the end effector. Finding θ_k on the other end, requires finding the Pa-joint variables for the maximum kinematic performance given by $\mathbf{J_0}$. As discussed in Sect. 4.1, the constraint Eq. (14) ensure that condition.

The coordinates of axes $\mathbf{z_{k3}}$ are given by Eq. (4) and those of axes $\mathbf{z_{k1}}$ by:

$$\begin{cases} \mathbf{z_{A1}} = \mathbf{R}(\mathbf{y}, \mu_A) \bullet \mathbf{z_0} \\ \mathbf{z_{B1}} = \mathbf{R}(\mathbf{z}, 2\pi/3) \bullet \mathbf{R}(\mathbf{y}, \mu_B) \bullet \mathbf{z_0} \\ \mathbf{z_{c1}} = \mathbf{R}(\mathbf{z}, -2\pi/3) \bullet \mathbf{R}(\mathbf{y}, \mu_C) \bullet \mathbf{z_0} \end{cases} \tag{15}$$

Expanding Eq. (14) with Eq. (4) and (15) leads to the following expression:

$$D_k \cos \mu_k + E_k \sin \mu_k = F_k \tag{16}$$

Where D_k, E_k and F_k are function of the mechanism Pa-joint variables and parameters. The Pa-joint variables are then isolated and calculated as follows:

$$\mu_k = \text{ATAN2}(E_k, D_k) \pm \cos^{-1}\left(\frac{F_k}{\sqrt{D_k^2 + E_k^2}}\right) \tag{17}$$

For a given orientation of the end effector, the Pa-joint variables must be determined first using Eq. (17). Then, their values can be used in Eq. (6) to calculate the R-joint variables. At this point, the velocity model can be calculated as shown in Sect. 3.2.

5 Performance of the Mechanism

The rSPM is compared to its classical version in order to evaluate the contribution of the reconfiguration in terms of kinematic performance. The cSPM has a trihedral base that rigidly positions its R-joint axes $\mathbf{z_{k1}}$. The resulting angle between $\mathbf{z_{k1}}$ and $\mathbf{z_0}$ is 0.9553 rad or around 57.74°.

The dexterity is calculated as a Jacobian matrix condition number. This index is then inverted to obtain a value ranging from 0 (singularity) to 1 (isotropy). Over a defined workspace, the dexterity is calculated for all Jacobian matrices, which include:

– The serial and parallel matrices $\mathbf{J_\theta}$ and $\mathbf{J_\omega}$ for both mechanisms
– The total matrix $\mathbf{J} = \mathbf{J_\omega^{-1}} \bullet [\mathbf{J_\mu}\ \mathbf{J_\theta}]$ for the rSPM
– The total matrix $\mathbf{J} = \mathbf{J_\omega^{-1}} \bullet \mathbf{J_\theta}$ for the cSPM.

For each point of the defined workspace, the IKM is first solved to verify its reachability for both mechanisms. An orientation is considered as reachable by rSPM only if an optimum reconfiguration conditioned by Eq. (14) is achievable. When both mechanisms can reach an orientation, the local dexterity of all matrices is calculated for comparison. The workspace covers the angles ψ and ϕ from 0 to 360° with 10° resolution and angle θ from 0 to 60° with a 5° resolution. Both mechanisms link dimension were set to $\alpha = 35°$ and $\beta = 25°$.

The simulation revealed that around 28% of the defined workspace is reachable by both the cSPM and rSPM at the same time. The resulting dexterity is displayed in Figs. 3, 4, and 5.

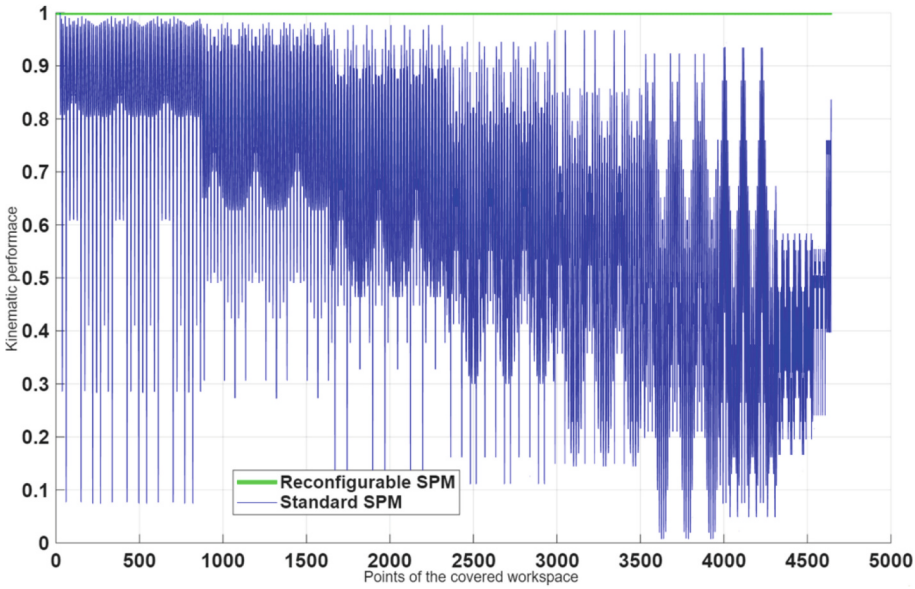

Fig. 3. Evolution of the serial dexterity over the workspace.

The detailed comparison results between the two mechanisms are listed in Table 1. When comparing the dexterity of matrix $\mathbf{J_\theta}$, the reconfigurable mechanism always returns the maximum value and is 0.363 superior to the classical SPM in average. The difference can reach 0.992, which suggest that while the classical SPM is approaching one of its singularities, the reconfigurable SPM still returns the maximum value for this matrix. For the parallel and total Jacobian matrices, the reconfigurable SPM returns a higher value on 61.5% and 64.9% of the covered workspace respectively. In average, the dexterity of the reconfigurable mechanism is superior to that of the classical one.

The results presented above show the reconfiguration feature allow better kinematic performance for the new rSPM as compared with its classical version. The method for

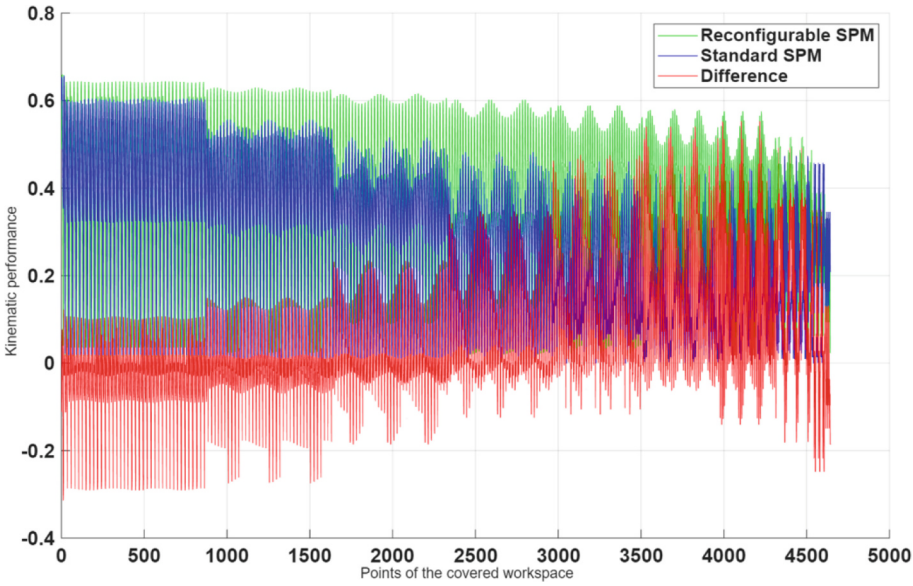

Fig. 4. Evolution of the parallel dexterity over the workspace.

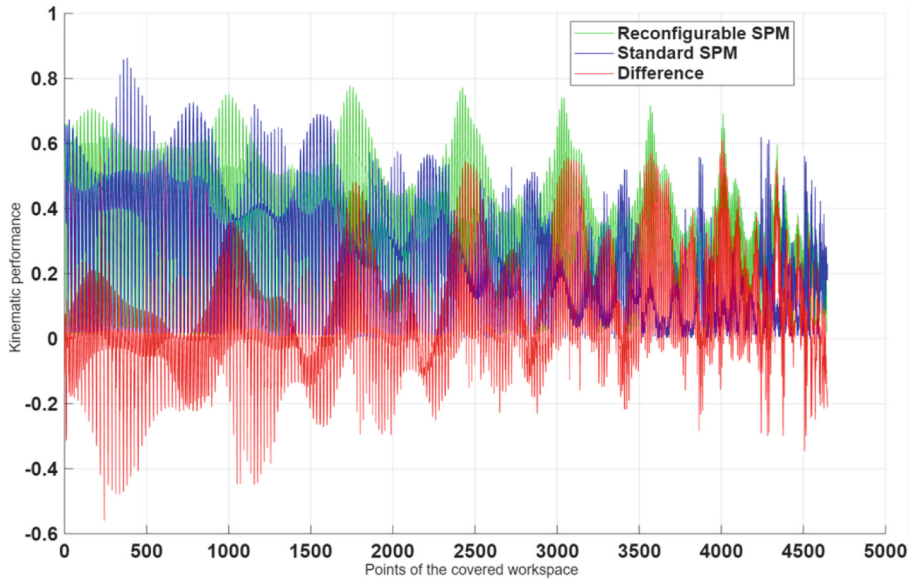

Fig. 5. Evolution of the total dexterity over the workspace.

determining the reconfigurable variables allows generating a constant isotropy from the serial Jacobian matrix. Optimizing the dexterity from that matrix does not significantly compromise the other matrices as the total dexterity remains higher most of the time.

Table 1. Kinematic performance of the 3-PaRRR rSPM and comparison with the 3-RRR cSPM.

Matrices	Kinematic performance			Absolute difference			Superiority rate
	Min	Average	Max	Min	Average	Max	
$\mathbf{J_\mu}$	0	0.549	1	N/A	N/A	N/A	N/A
$\mathbf{J_\theta}$	1	1	1	0	0.363	0.992	99.7%
$\mathbf{J_\omega}$	0.004	0.355	0.659	−0.313	0.067	0.553	61.5%
$\mathbf{J}$	0.003	0.330	0.778	−0.559	0.071	0.613	64.9%

The present study however, does not consider other aspects such as collisions which may reduce the accessible workspace for both mechanisms at different level. Also, the reachability of an orientation is validated only for an optimum reconfiguration of the rSPM. In reality, the rSPM should be able to extend its workspace by sacrificing some dexterity using a non-optimum reconfiguration. The formulation derived in Sect. 4.1 could be revised in this regard.

6 Conclusion

The classical 3-RRR SPM has been modified into a new reconfigurable 3-PaRRR SPM. The use of pantographic linkages to re-orient its base while maintaining a unique CoR and therefore keeping an RCM mechanism. The inverse kinematic model and velocity model are derived as a preliminary analysis considering that the reconfiguration joint variables are known. To determine the reconfiguration, a criterion is selected based on the kinematic performance of the mechanism. From the velocity model, the serial Jacobian matrix is more directly affected by the reconfiguration joints. Therefore, a constraint equation is found to find the reconfiguration joints that optimize the abovementioned matrix. The inverse kinematic model is then refined to solve for the reconfiguration joints first and the active rotational joints. A series of simulation are then carried out to compare the kinematic performance with that of the classical SPM in identical conditions. It revealed that the serial Jacobian matrix systematically returns an isotropy value. Also, the overall kinematic performance of the reconfigurable SPM is superior to the classical one most of the time, showing the contribution of the reconfiguration features.

Acknowledgments. This study was funded by National Science and Technology Council of Taiwan under grant number: NSTC 114-2221-E-008-040-MY3.

Disclosure of Interests The authors have no competing interests to declare that are relevant to the content of this article.

References

1. Ghodoussi, M., Butner, S.E., Wang, Y.: Robotic Surgery - the transatlantic case. In: Proceedings of IEEE International Conference on Robotics and Automation, vol. 2, pp. 1882–1888. IEEE, Washington DC, USA (2002)

2. Zhou, Z., et al.: Design and validation of an MRI conditional surgical robot for neurosurgery with remote center-of-motion. Trans. Can. Soc. Mech. Eng. **49**(3), 543–555 (2025)
3. Lin, R., Guo, W., Cheng, S.S.: Type synthesis of 2R1T remote center of motion parallel mechanisms with a passive limb for minimally invasive surgical robot. Mech. Mach. Theory. **172**, 104766 (2022)
4. Guo, W., Li, R., Cao, C., Gao, Y.: Kinematics, dynamics, and control system of a new 5-degree-of-freedom hybrid robot manipulator. Adv. Mech. Eng. **8**(11), 1687814016680309 (2016)
5. McAleenan, A., Jian, Y., Jin, Y., Sun, D., Moore, J.: Design and control system development of a new 3R1T parallel robot for minimally invasive surgery. In: Laribi, M.A., Carbone, G., Pisla, D., Zeghloul, S. (eds.) New Trends in Medical and Service Robotics. MESROB 2025. Mechanisms and Machine Science, vol. 186, pp. 448–457. Springer, Cham (2025)
6. Luces, M., Mills, J.K., Benhabib, B.: A review of redundant parallel kinematic mechanisms. J. Intell. Robot. Syst. **86**(2), 175–198 (2017)
7. Zhang, X., Zhang, X.: A comparative study of planar 3-RRR and 4-RRR mechanisms with joint clearances. Robot. Comput. Integr. Manuf. **40**, 24–33 (2016)
8. Azulay, H., Mahmoodi, M., Zhao, R., Mills, J.K., Benhabib, B.: Comparative analysis of a new 3-PPRS parallel kinematic mechanism. Robot. Comput. Integr. Manuf. **30**, 369–378 (2014)
9. Gan, D., Dai, J.S., Sanevirane, L.: Reconfigurability and unified kinematics modeling of a 3rTPS metamorphic parallel mechanism with perpendicular constraint screws. Robot. Comput. Integr. Manuf. **29**, 131–128 (2013)
10. Huang, G., Guo, S., Zhang, D., Qu, H., Tang, H.: Kinematic analysis and multi-objective optimization of a new reconfigurable parallel mechanism with high stiffness. Robotica. **36**(2), 187–203 (2018)
11. Kang, X., Dai, J.S.: Relevance and transferability for parallel mechanisms with reconfigurable platforms. J. Mech. Robot. **11**(3), 031012 (2019)
12. Essomba, T., Hsu, Y., Sandoval Arevalo, J.S., Laribi, M.A., Zeghloul, S.: Kinematic optimization of a reconfigurable spherical parallel mechanism for robotic-assisted craniotomy. ASME J. Mech. Robot. **11**(6), 060905 (2019)

Structural Synthesis of Platform Type Manipulators via Connection-Based Adjacency Matrix: Preliminary Automated Topology Sketching

Tuğrul Uslu(✉), Mustafa Volkan Yazıcı, Mertcan Koçak, and Erkin Gezgin

İzmir Katip Çelebi University, İzmir 35620, Türkiye
tugrul.uslu@ikcu.edu.tr

Abstract. The structural synthesis of platform-type manipulators is a critical phase in the design of mechanisms aiming specific tasks. Previous work based on Connection-based Adjacency Matrix (CAM) introduced to mathematical definitions to structures in order to automate the generation of unique coarse topologies, however the results were only numerical with absence of graphical output. This study presents the visualization algorithm by introducing a preliminary automated topology sketching methodology integrated with the CAM framework. In order to generate graphical representations of coarse topologies, the proposed algorithm interprets the connectivity data of the adjacency matrix that distinguishes between ground, platforms, hinges, and branches with the nature of CAM. The procedure is validated through case studies covering Alizade's direct and Gezgin's inverse structural synthesis approaches as well as manually given CAMs. By providing a direct visual translation of the mathematical synthesis results, the proposed tool enables designers to efficiently navigate through extensive solution spaces and identify appropriate topologies for further dimensional design.

Keywords: Auto-sketching · Structural Synthesis · Connection-based Adjacency Matrix · Platform-type Manipulators

1 Introduction

Recent developments in mechanism science shows that one of the most popular research topics in this field is the elimination of human error possibilities in manual calculations in structural design studies and the topology generation studies. Generation of the methods to describe the topologies in mathematical form become an effective way to use computer power in calculations. Therefore, most of the studies in this topic focused on the generation of the kinematic chains by using algorithms. In this regard, researchers focused on the ways to describe the topologies in mathematical form and the distinguishing isomorphism in these methods. These methods can be listed as path and cycle enumeration [1, 2], canonical form method [3, 4], permutation method [5, 6], permutation groups [7, 8], path matrix method [9], characteristic polynomial [10, 11], link

© The Author(s), under exclusive license to Springer Nature Switzerland AG 2026
A. Chaker et al. (Eds.): EFIMMS 2026, MMS 205, pp. 35–46, 2026.
https://doi.org/10.1007/978-3-032-22270-1_4

or joint distance method [12, 13], Hamming number method [14, 15], standard code method [16], eigenvalues and eigenvector method [17, 18], artificial neural network [19, 20], link or joint adjacency [21] and the connection-based adjacency matrix method [22]. Thanks to these studies representations of the topologies mathematically have paved the way for sketching of the topologies.

The design of planar linkage mechanisms has increasingly shifted toward automated, algorithmic methods to remove the burden of manual enumeration and sketching of topologies. Sun et al. [23] exemplified this trend by proposing a graphical joint–joint adjacency matrix representation, which encodes the connectivity of multiple-joint linkages in a mathematical form. Such graph-based encodings enable systematic generation and analysis of mechanism structures. Early studies in this field developed various sketching algorithms. Mauskar and Krishnamurty [24] introduced a loop-configuration approach to automatically generate mechanism sketches, effectively enumerating possible closure loops in a topology. Olson et al. [25] provided a systematic type-synthesis procedure, surveying and unifying previous synthesis methods in a comprehensive literature review. Chieng and Hoeltzel [26] applied a combinatorial algorithm for sketching planar kinematic chains and even epicyclic gear trains, demonstrating automatic construction of complex mechanisms.

These studies paved the way for recent studies and expanded the scope and performance of the results. Belfiore and Pennestri [27] focused on automatic sketching of planar kinematic chains, ensuring that generated linkages satisfy geometric and kinematic constraints. Chiu and Yan [28] extended these techniques to generalized kinematic chains, proposing an algorithm that can sketch arbitrarily configured chains. Pucheta et al. [29] tackled the problem of sketching non-fractionated kinematic chains (chains without fixed repeating patterns), automating generation of such linkage sketches. Bedi and Sanyal [30] also contributed a loop-based algorithm tailored for planar mechanisms, optimizing loop selection to create valid sketches. These methods demonstrate that by encoding topology mathematically, one can systematically enumerate and sketch viable linkage structures. Also, Morlin et al. [31, 32] focused on the Matroid theory that abstracts kinematic constraints as independence structures, enabling the systematic detection of rigid subchains through circuit analysis. This framework addresses the limitations of graph-based methods regarding structural degeneracy and provides a formal basis for resolving inconsistencies in mechanism enumeration.

Beyond topology enumeration, researchers have addressed how to layout and visualize these generated chains effectively. Yang et al. [33] investigated optimal layouts of the underlying topological graphs to make automatic sketches clearer and more informative. In a follow-up, Yang et al. [34] proposed a novel sketching method for planar chains that emphasizes both mechanical correctness and aesthetic layout. These approaches ensure that automatically generated mechanism diagrams are both functionally accurate and visually comprehensible.

In parallel with algorithmic methods, modern approaches leverage data-driven and creative techniques. Lin et al. [35] explored creative synthesis of topologies, using algorithms to discover novel linkage designs. Deshpande and Purwar applied machine learning to structural synthesis: they trained models to design defect-free four-bar linkages [36] and used deep generative models for broader linkage creativity [37]. Fogelson et al.

[38] introduced GCP-HOLO, which generates high-order linkage graphs to aid in path synthesis tasks. The importance of data in these approaches is highlighted by Nurizada et al. [39], who compiled a large dataset of single-DOF planar linkages and their coupler curves for machine learning–driven synthesis. Other recent developments include multidisciplinary modular synthesis frameworks [40], contrastive learning of joint design–performance representations [41], and tools that convert hand-drawn linkage sketches into precise digital models [42]. Collectively, these studies chart a shift toward automated, data-driven, and interdisciplinary methods for generating and sketching planar kinematic chains.

In this study, the lack of visualization tools for Alizade's direct [43] and Gezgin's inverse [44] structural synthesis methodologies are addressed. While the authors previously initiated a methodology to automate these procedures using a connection-based adjacency matrix [22], a matrix without visualization is often insufficient for verifying design requirements. This paper summarizes the process involving the adjacency matrix and demonstrates how to generate visualizations, either from the matrix alone or through the complete synthesis methodology. The main goal is to provide designers with the flexibility to evaluate thousands of generated results depending on the design requirements, which is totally inefficient to draw and visualize all of the results manually. Through the proposed software methodology, all configurations without multiple nodes can be visualized easily and effectively, enabling the designer to select the most appropriate topology for further design and development. The proposed automated topology sketching method for the structural synthesis of parallel robot manipulators outputs coarse manipulator topologies. To achieve a complete kinematic structure of a parallel manipulator in a desired subspace and degrees of freedom (DoF), joint distribution phase as presented by Yazici et al. [45] must be executed. It should be noted that joint axes directions should also be aligned considering selected subspace constraints.

2 Connection-Based Adjacency Matrix

One of the fundamental prerequisites for establishing the kinematic structure of any platform-type manipulator, depending on the specific design constraints and a defined task, is to synthesize a manipulator structural group with zero mobility. In this context, the structural synthesis method proposed by Alizade [43] provides a flexible design process that accounted for the various subspaces and connectivity structures of platform-type manipulators. This method was fundamentally based on the proposed universal mobility formula in Eq. 1.

$$M = \sum f_i - \lambda\left(j_p - B - c\right) \tag{1}$$

In this formula, M is the mobility of the manipulator, $\sum f_i$ is the total degree of freedom of all joints on manipulator, λ is the space or sub-space, j_p is the number of total pairing elements on platforms, B is the total number of mobile platforms and c is the number of connections between platforms.

Utilizing Eq. 1, two distinct procedures could be implemented for the structural design of platform-type manipulators. In the authors' previous work [22], these procedures were mentioned as Alizade's direct [43] and Gezgin's inverse [44] methods, and details regarding the processes and differences were provided. When the specifics of both methods are considered, the process leading to the common point could be summarized. In the direct method, once the required number (B) and type of platforms (j_p) are determined, all possible topological configurations can be generated. Conversely, in the inverse method, the desired number of legs (c_l) was specified taking into account the actuators to be grounded, alongside the number of platforms (B). All topological configurations suitable for this condition were derived; subsequently, the total number of connections (c) required to form structural groups was determined, and joint-based design was performed. In the phase where both methods proceeded together, a significant number of topologies could appear depending on the given conditions, execution manual work nearly impossible. Addressing this fact, the mathematical foundation of the method was established in the previous study [22]. Similar to examples in the literature, a matrix-based structure was constructed; however, a connection-based adjacency matrix (CAM) was formulated by considering the connection variations (branch type or hinge type) in Alizade's equation on structural groups. Furthermore, a topology generation algorithm following the stated direct and inverse structural synthesis methods was presented. By eliminating isomorphisms or special cases that might occur during generation, the creation of unique topologies was ensured.

The CAM served as the fundamental framework for characterizing the topology of any manipulator. By quantifying the topological structure, this matrix representation simplified its translation into a computational environment and its subsequent processing as data. This approach enabled the development of an algorithm capable of automatically generating coarse manipulator topologies, a task previously performed manually using Alizade's method. The transition to automated generation proved important in minimizing designer effort and potential errors, particularly when dealing with large sets of possible topologies. In this context, the general structure of the connection-based adjacency matrix is outlined in Table 1.

Table 1. General structure of Connection-based Adjacency Matrix (CAM).

#	P_0		P_1		P_2		…	Pn	
	h	b	h	b	h	b		h	b
Ground (P_0)	0	0	h_{01}	b_{01}	h_{02}	b_{02}	…	h_{0n}	b_{0n}
Platform 1 (P_1)	h_{10}	b_{10}	0	0	h_{12}	b_{12}	…	h_{1n}	b_{1n}
Platform 2 (P_2)	h_{20}	b_{20}	h_{21}	b_{21}	0	0	…	h_{2n}	b_{2n}
…	…	…	…	…	…	…	…	…	…
Platform n (P_n)	h_{n0}	b_{n0}	h_{n1}	b_{n1}	h_{n2}	b_{n2}	…	0	0

The CAM was defined as an array consisting of *n* rows and *2n* columns, where each entry denoted the number of connections between two platforms. In this matrix, the ground and each platform of the topology are represented by a single row and a pair of columns. The reason behind using two columns to each entity is the necessity to explicitly distinguish between hinge-type (*h-hinge*) and branch-type (*b-branch*) connections. The ground was consistently labelled as the first row and the initial two columns of the matrix. Due to the basic structure of the adjacency matrix, the values of elements h_{ij} and b_{ij} were identical to h_{ji} and b_{ji}, respectively. Furthermore, matrix elements located at the intersection of rows and columns representing the same platform were set to zero. Since a non-zero value in these positions would imply a self-connecting platform, which is a condition considered topologically meaningless for the mechanism, these values were permanently fixed at zero.

In a case study related with structural synthesis methodology including CAM, methodology is exemplified with its basics [46]. *By applying approach in authors' design, constraint parameters are listed as in* Table 2.

Table 2. Case study requirements.

Subspace (λ)	3
Manipulator mobility (M)	3
Manipulator's number of platform numbers (B)	3
Platform types	3, 3, 5 ($j_p = 11$)
Possible number of connections (c) [22]	2, 3, 4

By applying the connection-based adjacency matrix approach to the design of a mobile platform robot, comprising two triangular and one pentagonal platform with constraint parameters listed in Table 2, a total of 46 distinct topological configurations were identified. Specifically, for connection numbers (c) of 2, 3, and 4, the analysis yielded 7, 18, and 21 configurations, respectively. Among 46 distinct topologies, two results are given as examples to reveal a better representation (Table 3).

Despite their mathematical formulation, these matrices are challenging for designers to interpret without visual aids. Since manual visualization of the extensive results is not feasible, and a limitation previously identified as a topic for future work in [46], a new visualization methodology is introduced. This approach enables the designer to evaluate the mechanisms generated by the CAM and select the most suitable one. Accordingly, the remainder of this paper describes the sketching method.

Table 3. Manually drawn topology representation with corresponding CAM structure groups ($M = 0$) as examples.

Example topologies fulfills given requirements; manually drawn	Corresponding CAM	$\sum f_i$

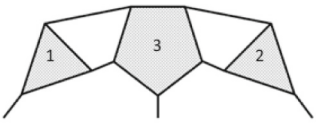

#	P_0		P_1		P_2		P_3	
	h	b	h	b	h	b	h	b
P_0	0	0	0	1	0	1	0	1
P_1	0	1	0	0	0	0	0	2
P_2	0	1	0	0	0	0	0	2
P_3	0	1	0	2	0	2	0	0

12

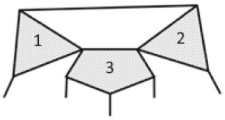

#	P_0		P_1		P_2		P_3	
	h	b	h	b	h	b	h	b
P_0	0	0	0	1	0	1	0	3
P_1	0	1	0	0	0	1	1	0
P_2	0	1	0	1	0	0	1	0
P_3	0	3	1	0	1	0	0	0

15

3 Sketching Method

For automatically sketching the topologies, a physics-based layout method is utilized. The method treats the connections points of the platforms as a system of interconnected particles connected via virtual springs, which are iteratively simulated to obtain a final arrangement that serves as a visual aid for the sketched CAM matrix. The sketching algorithm takes a CAM, which describes connections between platforms and connection types, as an input. Each platform described in the CAM is visualized as an n-sided polygon where n is the number of connections of the platform. To present each platform in a 2D plane, all vertices of the platform polygons are given a globally unique index number.

The physics simulation is initialized by positioning centroid point of the platform re placed equally spaced along a circle with radius proportional to the total number of mobile platforms. Connection points belonging to each platform are then placed with a small random jitter around platforms' centroid. The physics simulation is performed with each vertices point connected with virtual springs based on connections in the CAM matrix and the platform the vertices belong to. The system evolves over a fixed number of iterations t using a constant time step dt. At each iteration, a net force is computed for every vertices based on the following components. Note that every vertice is assumed to have one unit mass.

Branch Springs. Connections between vertices of different platforms connected via a branch are assigned a spring with rest length l_b and a spring constant of k_b.

Hinge Springs. Connections between vertices of different platforms connected via a hinge are assigned a spring with rest length of *0* and a spring constant of k_h.

Platform Internal Springs. Vertices belonging to the same platform are connected by internal springs to form a polygon. These springs have a rest length of l_i and a spring constant of k_i.

Repulsive Forces. A repulsive force between all non-connected vertice pairs is applied to reduce overlap. This force is inversely proportional to the square of the distance between non-connecting vertice pairs and is only applied within a cutoff radius r_c. Another repulsive force between overlapping platforms is also applied to push them apart for visual clarity. This repulsion is proportional to the amount of overlap and is applied to each vertice of overlapping platforms.

The net force on each vertice is numerically integrated using Hooke's law to update its velocity and position. A damping factor v_d is applied to simulate friction to ensure that the system settles. Forces applied to vertices are linearly reduced proportional to simulation time to encourage stability in output. Following refinement steps are also applied.

Convexity Interpolation. In every iteration, vertices of each platform are linearly interpolated onto a regular n-sided polygon (n depending on degree of each platform) with a weight of α_{lerp}, preventing platforms from collapsing or forming concave shapes.

Branch Crossings Elimination. A branch crossing detection and resolution step is periodically (i.e. for every *100* iterations to reduce computational costs.) executed. This step checks for segment intersections between all branch connection pairs. If a crossing is detected between two branch connections, the connection vertice indices of one branch are swapped with the other to re-route the connection in order to resolve the crossing.

Proposed auto-sketching methodology can be seen in action in Fig. 1. Notice that at iteration 100, branch crossing elimination step swaps vertice indices of crossing branches to solve the crossing.

4 Case Study and Results

The sketching method described is performed for various CAM inputs with simulation parameters given in Table 4. In Fig. 2, resulting topology sketches can be seen for Alizade's direct structure synthesis methodology for 3 triangular platforms. In Fig. 3, results sketched from Gezgin's inverse structural synthesis are given for $B = 2$ and $c_{leg} = 3$. In Table 5, the same CAM are given but instead of hand drawn, topologies resulting from the CAM are drawn with the described sketching method.

For each CAM input, the result of the sketching method is converted into PNG or SVG formatted image files by using Matplotlib library. Depending on the simulation parameters, computing power, size and connections of CAM, output drawing of the sketching method takes at most few seconds and most of the time less than a second.

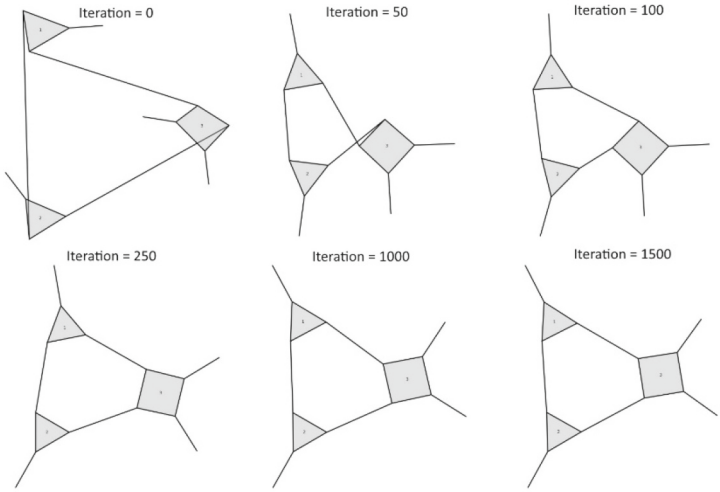

Fig. 1. Refinements in the auto-sketching of a target topology through iterations (numbers show the iteration step)

Table 4. Parameters used in auto-sketching topologies in the study

t (total iterations)	*dt (unit time)*	l_b *(unit length)*	k_b *(force/unit length)*	k_h *(force/unit length)*	l_i *(unit length)*	k_i *(force/unit length)*	r_c *(unit length)*	v_d *(ratio)*	α_{lerp} *(ratio)*
1500	*0.2*	*3.5*	*1*	*15*	*2*	*1.25*	*6*	*0.85*	*0.25*

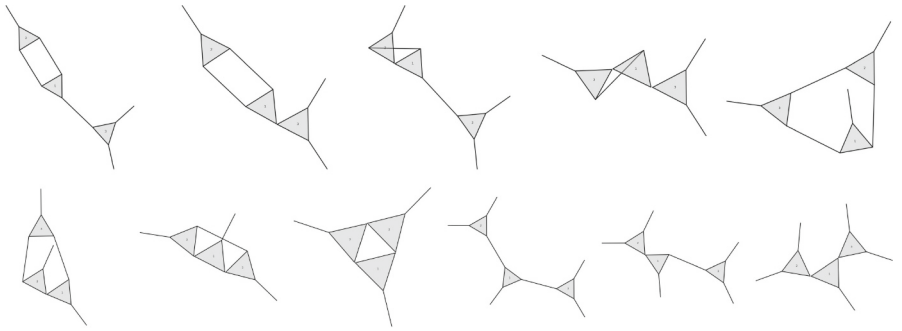

Fig. 2. Every possible topology without multiple nodes formed by 3 triangular platforms drawn by preliminary automatic sketching methodology.

It can be seen that while sketching methodology is promising in accurately drawing topologies from CAM, visual clarity is lacking. In instances where more than 2 branches cross each other, the current branch crossing elimination method is unable to solve the crossings.

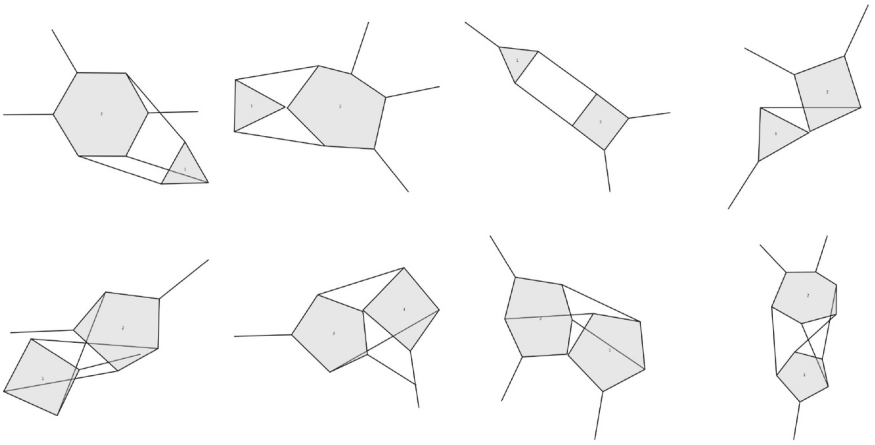

Fig. 3. Every possible 3 legged 2 platforms topology without multiple nodes drawn by preliminary automatic sketching methodology.

Table 5. Auto-sketched topology representation with corresponding CAM as examples.

Example topologies fulfills given requirements drawn by sketching method; auto-sketched	Corresponding CAM	$\sum f_i$

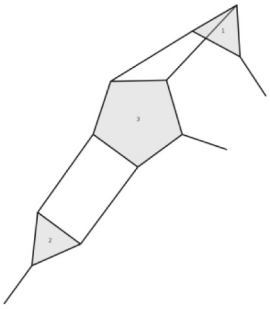

#	P_0		P_1		P_2		P_3	
	h	b	h	b	h	b	h	b
P_0	0	0	0	1	0	1	0	1
P_1	0	1	0	0	0	0	0	2
P_2	0	1	0	0	0	0	0	2
P_3	0	1	0	2	0	2	0	0

12

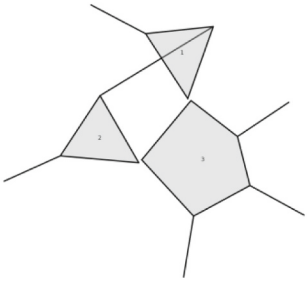

#	P_0		P_1		P_2		P_3	
	h	b	h	b	h	b	h	b
P_0	0	0	0	1	0	1	0	3
P_1	0	1	0	0	0	1	1	0
P_2	0	1	0	1	0	0	1	0
P_3	0	3	1	0	1	0	0	0

15

5 Conclusion

Utilized together and/or integrated with custom designer software, automatic topology sketching can be a useful tool for visualization and verification of structural design. This study presents an accurate topology drawing methodology with room for improvement in visual clarity. Although the same simulation parameters are used for every input CAM, dynamic selection of simulation parameters depending on the CAM input given might produce clearer results and might hasten output by skipping unnecessary calculations. It should be noted that the output of the proposed auto-sketching methodology only creates coarse manipulator topologies in order to carry on the design of any parallel manipulator joint distribution step on the extracted topologies should be performed and joint axes should be aligned with respect to desired mobility and subspace constraints.

Future work of this study will improve upon refinement steps to improve visual clarity. A custom graphical user interface will be developed to aid designers in topology selection, analysis and visualization.

References

1. Sozanski, T.: Enumeration of weak isomorphism classes of signed graphs. J. Graph Theory. **4**(2), 127–144 (1980)
2. Harary, F., Palmer, E.M., Robinson, R.W., Schwenk, A.J.: Enumeration of graphs with signed points and lines. J. Graph Theory. **1**(4), 295–308 (1977)
3. Babai, L., Luks, E.M.: Canonical labelling of graphs. In: Proceedings of the Fifteenth Annual ACM Symposium on Theory of Computing, pp. 171–183 (1983)
4. Hou, A., Zhong, Q., Chen, Y., Hao, Z.: A practical graph isomorphism algorithm with vertex canonical labeling. J. Comput. **9**(10), 2467–2474 (2014)
5. Stueckle, S.: On natural isomorphisms of cycle permutation graphs. Graphs Combinatorics. **4**(1), 75–85 (1988)
6. Colbourn, C.J.: On testing isomorphism of permutation graphs. Networks. **11**(1), 13–21 (1981)
7. Luks, E.M.: Parallel algorithms for permutation groups and graph isomorphism. In: 27th Annual Symposium on Foundations of Computer Science SFCS1986, pp. 292–302. IEEE (1986)
8. Babai, L.: Graph isomorphism in quasipolynomial time. In: Proceedings of the forty-eighth annual ACM Symposium on Theory of Computing, pp. 684–697 (2016)
9. Mustafa, J., Hasan, A., Khan, R.A.: An application of modified path matrix approach for detection of isomorphism among epicyclic gear trains. J. Inst. Eng. India Ser. C. **101**, 463–472 (2020)
10. Mowshowitz, A.: The characteristic polynomial of a graph. J. Comb. Theory Ser. B. **12**(2), 177–193 (1972)
11. Reddy, I.R., Reddy, C.V.K., Rao, Y.V.D., Shekar, A.C.: Comparison of tests for isomorphism in planetary gear trains. IOP Conf. Ser.: Mater. Sci. Eng. **981**(4), 042023. IOP Publishing (2020)
12. Yadav, J.N., Pratap, C.R., Agrawal, V.P.: Detection of isomorphism among kinematic chains using the distance concept. J. Mech. Des. **117**(4) (1995)
13. Sarkar, S.C., Khare, A.K.: Detecting the effect of uncertainty and isomorphism in 10 bar kinematic chains using all possible paths for motion transmission. Mech. Mach. Theory. **39**(8), 893–900 (2004)

14. Sun, W., Kong, J., Sun, L.: The improved hamming number method to detect isomorphism for kinematic chain with multiple joints. J. Adv. Mech. Des. Syst. Manuf. **11**(5), JAMDSM0061-JAMDSM0061 (2017)
15. Rao, A.C.: Hamming number technique — I. Further applications. Mech. Mach. Theory. **32**(4), 477–488 (1997)
16. Shin, J.K., Krishnamurty, S.: Development of a standard code for colored graphs and its application to kinematic chains. J. Mech. Des. **116**(1), 189–196 (1994)
17. He, P.R., Zhang, W.J., Li, Q.: Eigenvalue and eigenvector information of graphs and their validity in detection of graph isomorphism. In: International Design Engineering Technical Conferences and Computers and Information in Engineering Conference, vol. 36533, pp. 421–428. American Society of Mechanical Engineers (2002)
18. Cao, D., Yuan, H.: Graphs characterized by the second eigenvalue. J. Graph Theory. **17**(3), 325–331 (1993)
19. Kong, F.G., Li, Q., Zhang, W.J.: An artificial neural network approach to mechanism kinematic chain isomorphism identification. Mech. Mach. Theory. **34**(2), 271–283 (1999)
20. Bouritsas, G., Frasca, F., Zafeiriou, S., Bronstein, M.M.: Improving graph neural network expressivity via subgraph isomorphism counting. IEEE Trans. Pattern Anal. Mach. Intell. **45**(1), 657–668 (2022)
21. Dargar, A., Khan, R.A., Hasan, A.: Application of link adjacency values to detect isomorphism among kinematic chains. Int. J. Mech. Mater. Des. **6**, 157–162 (2010)
22. Volkan Yazıcı, M., Koçak, M., Uslu, T., Gezgin, E.: Structural synthesis of platform type manipulators via connection-based adjacency matrix: topology generation. J. Mech. Des. **147**(1), 013302 (2025)
23. Sun, W., Kong, J., Sun, L.: A novel graphical joint-joint adjacent matrix method for the automatic sketching of kinematic chains with multiple joints. Mech. Mach. Theory. **150**, 103847 (2020)
24. Mauskar, S., Krishnamurty, S.: A loop configuration approach to automatic sketching of mechanisms. Mech. Mach. Theory. **31**(4), 423–437 (1996)
25. Olson, D.G., Erdman, A.G., Riley, D.R.: A systematic procedure for type synthesis of mechanisms with literature review literaturbe-sprechung. Mech. Mach. Theory. **20**(4), 285–295 (1995)
26. Chieng, W.H., Hoeltzel, D.A.: A combinatorial approach for the automatic sketching of planar kinematic chains and epicyclic gear trains. (1990)
27. Belfiore, N.P., Pennestri, E.: Automatic sketching of planar kinematic chains. Mech. Mach. Theory. **29**(1), 177–193 (1994)
28. Chiu, Y.T., Yan, H.S.: An algorithm for the automatic sketching of generalized kinematic chains. In: 14th IFToMM World Congress, pp. 25–30, Taipei, Taiwan (2015)
29. Pucheta, M.A., Ulrich, N.E., Cardona, A.: Automated sketching of non-fractionated kinematic chains. Mech. Mach. Theory. **68**, 67–82 (2013)
30. Bedi, G.S., Sanyal, S.: Loop based algorithm for automatic sketching of planar kinematic chains. In: Proceedings of the 1st International and 16th National Conference on Machines and Mechanisms, pp. 452–456 (2013)
31. Morlin, F.V.: Detection of Rigid Subchains in Kinematic Chains by Means of Matroid Theory. (2021)
32. Morlin, F.V., Carboni, A.P., Martins, D.: Synthesis of Assur groups via group and matroid theory. Mech. Mach. Theory. **184**, 105279 (2023)
33. Yang, W., Ding, H., He, Y., Wu, M.: Studying the optimal layout of topological graphs to facilitate the automatic sketching of kinematic chains. J. Mech. Des. **139**(8), 082301 (2017)
34. Yang, W., Ding, H., Kecskeméthy, A.: A new method for the automatic sketching of planar kinematic chains. Mech. Mach. Theory. **121**, 755–768 (2018)

35. Lin, J., Ning, J., Goldfeder, J., Lipson, H.: Creative synthesis of kinematic mechanisms. ArXiv: 2510.03308. (2025)
36. Deshpande, S., Purwar, A.: A machine learning approach to kinematic synthesis of defect-free planar four-bar linkages. J. Comput. Inf. Sci. Eng. **19**(2), 021004 (2019)
37. Fogelson, M., Tucker, C.S., Cagan, J.: GCP-HOLO: generating high-order linkage graphs for path synthesis. J. Mech. Des. **145**(11), 112203 (2023)
38. Deshpande, S., Purwar, A.: Computational creativity via assisted variational synthesis of mechanisms using deep generative models. J. Mech. Des. **141**(12), 122002 (2019)
39. Nurizada, A., Dhaipule, R., Lyu, Z., Purwar, A.: A dataset of 3m single-dof planar 4-, 6-, and 8-bar linkage mechanisms with open and closed coupler curves for machine learning-driven path synthesis. J. Mech. Des. **147**(4), 041702 (2025)
40. Shahmansouri, N., Cheong, H., Tessier, A., Butscher, A.: Multidisciplinary modular approach to kinematic mechanism synthesis. ECCOMAS Congress Proceedings. (2024)
41. Nobari, A., Srivastava, A., Gutfreund, D., Ahmed, F.: Link: Learning joint representations of design and performance spaces through contrastive learning for mechanism synthesis. arXiv preprint arXiv: 2405.20592. (2024)
42. Nurizada, A., Purwar, A.: Transforming hand-drawn sketches of linkage mechanisms into their digital representation. J. Comput. Inf. Sci. Eng. **24**(1), 011010 (2024)
43. Alizade, R., Bayram, Ç.: Structural synthesis of parallel manipulators. Mech. Mach. Theory. **39**(8), 857–870 (2004)
44. Gezgin, E.: Structural synthesis of parallel manipulators based on a different approach. Dokuz Eylül Üniv. Mühendis. Fak. Fen Mühendis. Derg. **21**(61), 225–234 (2019)
45. Yazıcı, M.V., Koçak, M., Uslu, T., Gezgin, E.: Methodological joint distribution for platform type manipulator topologies. In: IFToMM Symposium on Mechanism Design for Robotics MEDER2024, pp. 33–42. Springer, Timişoara, Romania, Cham (2024)
46. Yazıcı, M.V., Koçak, M., Uslu, T., Gezgin, E.: Platform tipi manipülatörlerin yapısal sentezinde bağlantı temelli komşuluk dizeyinin bir vaka çalışması üzerinde uygulanması. In: 22. Ulusal Makina Teorisi Sempozyumu (22nd National Symposium of Theory of Machines) UMTS2025, pp. 183–190, Ankara, Türkiye (2025)

A Study of a Remote Center of Motion Mechanism as a Laparoscopic Training Tool Holder

Imen Doudech[1,2], Abdelbadia Chaker[1,2(✉)], Ajmi Houidi[2], Abdelfattah Mlika[2], and Med Amine Laribi[1]

[1] Department GMSC, Pprime Institute CNRS, University of Poitiers, Poitiers UPR, 3346, France
{imen.doudech,abdelbadia.chaker,
med.amine.laribi}@univ-poitiers.fr
[2] Mechanical Laboratory of Sousse (LMS), University of Sousse, Sousse, Tunisia
ajmi.houidi@issatso.rnu.tn, abdelfattah.mlika@eniso.u-sousse.tn

Abstract. Training in laparoscopic surgery is mandatory and extends over a long period of time. Physical simulators, commonly known as box trainers, have become standard tools for surgical training; however, they generally lack integrated measurement systems that enable objective validation of skill acquisition. As a result, performance assessment often remains qualitative and highly dependent on expert observation, which limits the standardization and reproducibility of the certification process. This paper presents a miniaturized surgical tool holder designed for integration into physical simulators to enable quantitative performance assessment. The proposed system is based on a parallel mechanism with a Remote Center of Motion (RCM-PM). The methodology includes the kinematic and static analysis of the mechanism, with the formulation of both direct and inverse kinematic models. Static balancing of the mechanism is investigated as a passive gravity compensation strategy to counteract the torques induced by the weight of the structure and to minimize the required actuation torque, allowing the use of smaller actuators. The required counterweights are computed using the developed analytical models and validated through comparative simulations using a CAD-based dynamic solver. The results demonstrate a strong correlation between the analytical calculations and the dynamic simulations. Moreover, the proposed passive balancing strategy reduces the required holding torque by more than 70%, effectively neutralizing gravitational effects and ensuring transparent operation for the trainee.

Keywords: RCM Parallel Mechanism · Laparoscopic Training · laparoscopic surgery · Static Balancing

1 Introduction

Minimally invasive surgery (MIS) has become a clinical standard due to its proven benefits for patients such as trauma reducing, pain reducing and short recovery [1]. However, it poses considerable technical challenges for surgeons, who must manipulate

© The Author(s), under exclusive license to Springer Nature Switzerland AG 2026
A. Chaker et al. (Eds.): EFIMMS 2026, MMS 205, pp. 47–55, 2026.
https://doi.org/10.1007/978-3-032-22270-1_5

long instruments to a reverse fulcrum effect at the incision point while coordinating through camera feedback on a 2D screen.

Rigorous surgical training is a key phase for surgeons to master MIS skills. Traditionally, it relies on a learning model based on practice on anatomical models, cadavers, or observing surgical procedures alongside senior surgeon [1]. While this process provides valuable practical experience, it lacks objectivity in validating acquired skills.

Different types of simulators address the challenges of surgical training, each offering a distinct training strategy. The most advanced are virtual reality simulators, which provide immersive and interactive environments for practicing complex procedures and building both confidence and technical proficiency [2]. However, their high cost and limited force feedback capabilities can limit their accessibility.

On the other hand, box trainers are highly affordable and widely accessible [3]. They allow residents to develop essential skills, such as precision and hand-eye coordination [4], using real instruments that offer authentic tactile feedback. These trainers can also be augmented with sensors to monitor training sessions and provide objective performance evaluations [5, 6].

To meet this need, we propose the integration of a robotic mechanism within the trainer box with a Remote Center of Motion (RCM), as it reproduces the pivoting constraints of the fixed incision point.

In this work, we present an RCM parallel mechanism designed to track a standard laparoscopic instrument and enable quantitative assessment of the learner's movements with a perspective of integrating an active assistance for a better technique appropriation. The paper is organized as follows: Sect. 2 details the workspace definition required for laparoscopic tasks. Section 3 introduces mechanical architecture and kinematic models. In Sect. 4, the static balancing strategy is presented. Section 5 is dedicated to the simulation results of the static balancing analysis and the numerical comparison of the analytical model with SolidWorks Motion simulation.

2 Laparoscopic Task Analysis

The movement of a laparoscopic instrument is constrained by the small incision point, which acts as a fixed mechanical pivot. This point defines the instrument's range of motion, which has four (3R + T) degrees of freedom DOF) as presented in Fig. 1(a).

Among these degrees of freedom (DOF), the two pivotal rotations (R1) and (R2) that are the principal ones for navigation within the surgical workspace, self-rotation (R3) and translation (T) along the instrument's main axis, for insertion and withdraw.

To guide our workspace design, we relied on existing studies. A key reference shows that an apex angle cone of 26° is adequate for MIS tasks [5, 7, 8]. Whilst this value was retained as our minimum target, the approach is to assure that the mechanism itself never becomes a limiting factor during training. In fact, while the precise surgical movements of an expert are performed within a restricted working cone, scenarios for novices often involve wider and less controlled movements.

For this reason, a wide workspace, defined by an angular excursion of $\pm 60°$ in both rotation around the X and Y axes, was chosen. This workspace, derived from the kinematic analysis model, is presented in Fig. 1(b). This extended range ensures that the user's movements are never constrained by mechanical limitations.

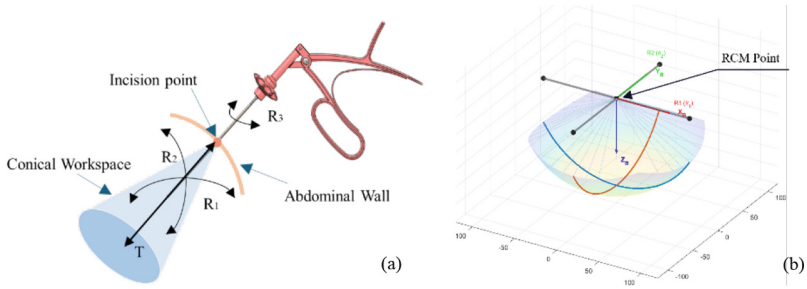

Fig. 1. (a) The 4 DoF of a laparoscopic instrument. (b) Mechanism working space based on the kinematic model

3 Mechanical Architecture and Kinematics

The suggested two-degrees-of-freedom mechanism features two arc shaped links arranged orthogonally one to the other, connected to the base via revolute joints. Each arc carries a single slider that can move along its circular guide (via a prismatic joint). The two sliders are connected by a revolute joint whose axis intersect on *O*, the sphere's center (RCM) [9], forming the moving platform of the parallel manipulator on which the laparoscopic instrument is mounted (Fig. 2).

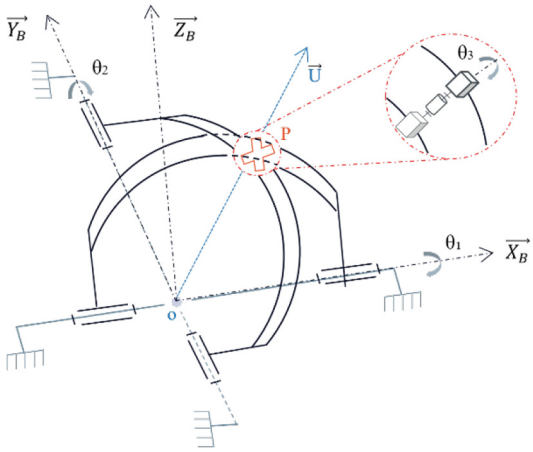

Fig. 2. Kinematic diagram of the proposed mechanism

As illustrated in the kinematic diagram Fig. 3, the first arc generates the rotation θ_1 around the $\overrightarrow{X_B}$ axis, the second arc generates the rotation θ_2 around the $\overrightarrow{Y_B}$ axis, and the revolute joint between the two sliders, shown in the enlarged detail, allows a passive self-rotation θ_3. The intersection of the planes of these two arcs defines a unique direction vector **U**, which coincides with the axis of the surgical instrument. This kinematic structure adapts to the pivoting constraint of the surgical instrument through the abdominal incision.

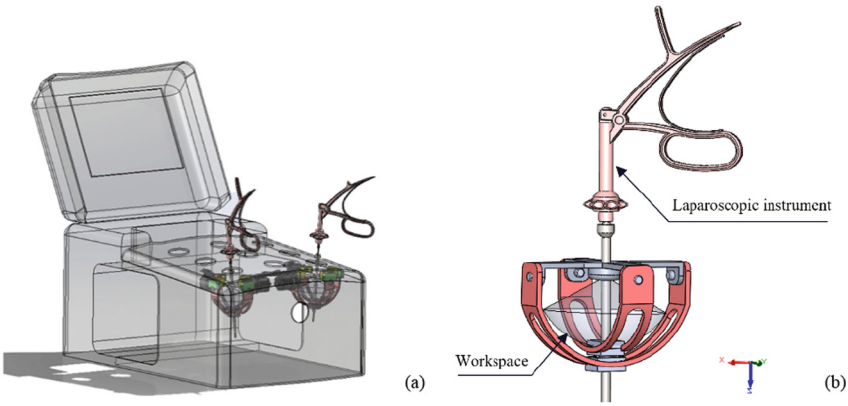

Fig. 3. (a) Conceptual integration of the proposed mechanism into a box trainer (b) the CAD prototype with its associated workspace

This resulting architecture creates a compact mechanical structure capable of reproducing laparoscopic motions suitable for integration into a box trainer. Figure 3 shows (a) the CAD model of a commercial box trainer where two RCM-PM mechanisms are integrated and (b) the CAD prototype with its associated workspace of ±60° in both rotation X and Y axes.

The kinematic model determines the link between the two actives joints (θ_1, θ_2) and the orientation of the instrument, represented by its unit direction vector $\mathbf{U} = \left[u_x; u_y; u_z\right]^T_{R_B}$ where R_B is the base reference frame of the mechanism, as shown in Fig. 3. The model is based on the fundamental geometric constraint of the architecture: the axis of the instrument **U** must belong to both circular arc planes at the same time.

This translates into the following system of equations, where **U** is orthogonal to the normal of each arc plane:

$$u_y \cdot \cos(\theta_1) + u_z \cdot \sin(\theta_1) = 0 \tag{1}$$

$$u_x \cdot \cos(\theta_2) - u_z \cdot \sin(\theta_2) = 0 \tag{2}$$

$$u_x{}^2 + u_y{}^2 + u_z{}^2 = 1 \tag{3}$$

Solving the system of Eqs. (1, 2, 3) allows us to express the orientation of the instrument **U** as a function of the entry joint angles (θ_1, θ_2). The direct kinematic model (DKM) of the mechanism, which relates the joint angles (θ_1, θ_2) to the Cartesian position P = (X, Y, Z) of the instrument tip in the base frame, is given by:

$$X(\theta_1, \theta_2) = \frac{\mathrm{R} \cdot \cos(\theta_1) \sin(\theta_2)}{\mathrm{S}(\theta_1, \theta_2)} \tag{4}$$

$$Y(\theta_1, \theta_2) = \frac{-\mathrm{R} \cdot \cos(\theta_2) \sin(\theta_1)}{\mathrm{S}(\theta_1, \theta_2)} \tag{5}$$

$$Z(\theta_1, \theta_2) = \frac{\mathrm{R} \cdot \cos(\theta_2) \cos(\theta_1)}{\mathrm{S}(\theta_1, \theta_2)} \tag{6}$$

With: $\mathrm{S}(\theta_1, \theta_2) = \sqrt{\cos^2(\theta_1) + \sin^2(\theta_1) \cos^2(\theta_2)}$

On the other hand, the Inverse Kinematic Model calculates the joint angles (θ_1, θ_2) to get the instrument orientation **U**, obtained simply as:

$$\theta_1 = \operatorname{atan} 2(-\mathrm{Y}, \mathrm{Z}) \tag{7}$$

$$\theta_2 = \operatorname{atan} 2(\mathrm{X}, \mathrm{Z}) \tag{8}$$

Deriving the Direct Kinematic Model gives the Jacobian matrix J. This matrix relates the articular velocities $\dot{\theta}$ to the angular velocity of the instrument and will be used in the next section for static analysis.

$$\mathbf{J}_p(\theta_1, \theta_2) = \frac{R}{S^3} \begin{bmatrix} -\mathrm{s}(\theta_1) s(\theta_2) \mathrm{c}^2(\theta_2) & \mathrm{c}(\theta_1) c(\theta_2) \\ -\mathrm{c}(\theta_1) c(\theta_2) & \mathrm{s}(\theta_1) s(\theta_2) c^2(\theta_1) \\ -\mathrm{s}(\theta_1) c^3(\theta_2) & -\mathrm{s}(\theta_2) c^3(\theta_1) \end{bmatrix} \tag{9}$$

With: c = cos et s = sin

4 Static Balancing Analysis

The moving parts of the mechanism, the rotating arcs and the sliding instrumented platform, are subject to gravity. This induces variable torques on the joints depending on the robot's configuration (θ_1, θ_2). Without balancing, the mechanism would tend to "fall" towards its equilibrium position under its own weight, requiring constant motor torque to maintain a position.

The objective of static balancing is to cancel out these gravitational effects, ensuring that the mechanism can be placed in any configuration and remain motionless, based on weight compensation.

4.1 Mathematical Modeling

To achieve this, a passive counterweight compensation method was implemented. The analysis considers the mechanism structure including the sliding platform. Although the platform creates a kinematic coupling between the axes, a mass distribution strategy was adopted to decouple the compensation design.

The static model considers gravity as the only external force. The total gravitational torque τ_{gi} exerted on each joint i (i = 1, 2) is the sum of the torque generated by the arc and the contribution of the platform, given by:

$$\tau_{gi}(\theta i) = \left(m_{arc,i} \cdot l_{arc,i} + m_{plat} \cdot R_c\right) g \cdot \sin(\theta_i) \tag{10}$$

Where: τ_{gi}: gravitational torque on joint i [N. mm]

$m_{\text{arc},\,i}$: Mass of arc i [kg]
$l_{\text{arc},\,i}$: Distance between the rotation axis and the center of mass of arc i [mm].
m_{plat}: Total mass of the instrumented platform [kg].
R_c: Radial distance to the platform's center of mass [mm].
g: Gravitational acceleration [m/s^2].

To compensate, a counterweight m_{cp} is added on a lever d_{cp}, generating an opposing torque:

$$\tau_{ci}(\theta_i) = -m_{cp,i} \cdot g \cdot d_{cp} \cdot \sin(\theta_i) \tag{11}$$

The optimal counterweight mass is calculated considering the maximum torque configuration $\pm 60°$. This ensures stability even in configurations where a single axis bears the full gravitational load of the platform (formed by the two sliders). By setting $\tau_{gi} + \tau_{ci} = 0$, we obtain the sizing equation:

$$m_{cp,i} = \frac{m_{arc,i} \cdot l_{arc,i} + m_{plat} \cdot R_c}{d_{cp}} \tag{12}$$

Where: $m_{arc,\,i} \cdot l_{arc,\,i}$: The static moment of the arc structure.

$m_{plat} \cdot R_c$: The static moment of the entire instrumented platform.
d_{cp}: The chosen lever arm for the counterweight.

4.2 Parameter Identification

The model was parameterized using the physical properties of the prototype extracted from the CAD software (SolidWorks). The mechanism components were modeled in AISI 1020 steel, and the resulting geometric, and counterweight parameters are summarized in Table 1.

Table 1. Physical Parameters and Counterweight Sizing

Parameter	Symbol	Value (Unit)	Description
Gravitational Acc.	g	9.81(m/s^2)	Standard gravity
Lever arm distance	d_{cp}	10(mm)	Counterweight lever length
Platform total mass	m_{plat}	22.8(g)	Total mass of the sliding
Platform radius	R_c	44(mm)	Effective radial distance
Arc1 mass	$m_{arc,\,1}$	42.8(g)	Mass of outer arc
Arc1 CoM distance	$l_{arc,\,1}$	23.26(mm)	Axis-to-CoM distance (arc 1)
Arc2 mass	$m_{arc,\,2}$	36.4(g)	Mass of inner arc
Arc2 CoM distance	$l_{arc,\,2}$	18.92(mm)	Axis-to-CoM distance (arc 2)
Resulting CW1	$m_{cp,\,1}$	2 x 99.98(g)	Required counterweight mass (2 sides)
Resulting CW2	$m_{cp,\,2}$	2 x 84.59(g)	Required counterweight mass (2 sides)

5 Simulation and Results

5.1 Simulation Setup and Input Trajectory

To validate the analytical model and evaluate the proposed balancing strategy, a comparative study was conducted. The same input trajectory $\theta(t)$ was applied to both the analytical model (MATLAB) and the simulation (SolidWorks Motion). The mechanism was subjected to a composite trajectory designed to cover the relevant workspace $\pm 60°$. The simulation lasts 10 s and is divided into three phases, as shown in Fig. 4.

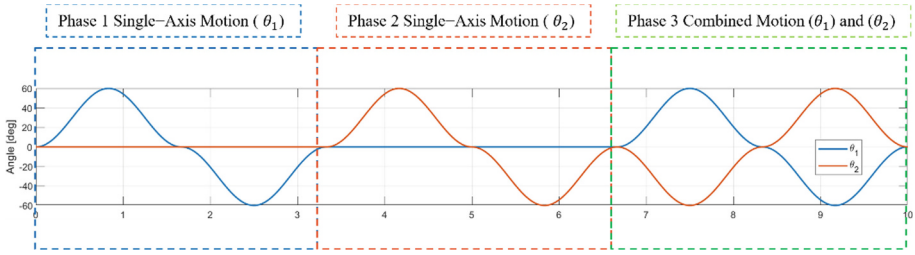

Fig. 4. Reference joint trajectories $\theta_1(t)$ and $\theta_2(t)$ applied to both analytical and CAD models.

Phase 1 ($0 < t < 3.3s$): Single-Axis Motion (θ_1). The outer axis (θ_1) performs a sinusoidal oscillation of amplitude $\pm 60°$, while the inner axis (θ_2) remains locked at 0°. This phase isolates the behavior of the first actuator carrying the full load.

Phase 2 ($3.3 < t < 6.6s$): Single-Axis Motion (θ_2). The outer axis is locked at 0°, and the inner axis (θ_2) oscillates with an amplitude of $\pm 60°$. This validates the behavior of the second axis independently.

Phase 3 ($6.6 < t < 10s$): Combined Motion. Both axes θ_1 *and* θ_2 move simultaneously with phase-shifted sinusoidal trajectories. This phase tests the system under loading conditions where kinematic coupling is induced by the platform.

5.2 Results and Discussion

The balancing strategy was first evaluated using the analytical model and then validated by a multibody simulation in SolidWorks Motion. Figure 5 shows the required motor torques for both axes over the three motion phases, comparing the uncompensated analytical model, the compensated model, and the CAD validation.

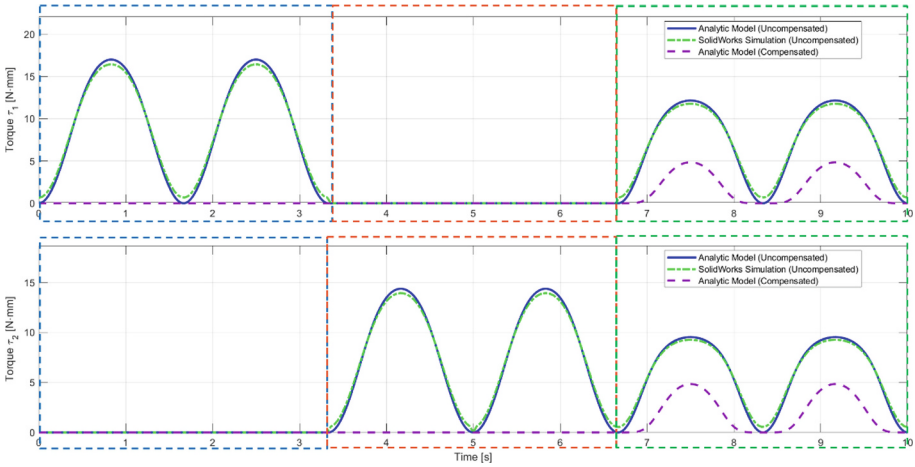

Fig. 5. Torque analysis of the RCM-PM mechanism with and without compensation

- Analytical Model Without Compensation (Solid Blue Lines): The motors must overcome gravitational torques, reaching peaks of 16.98 N·mm (Axis 1) and 14.37 N·mm (Axis 2).
- Analytical Model With Compensation (Dashed Purple Lines): The residual torque drops to zero during single-axis motions (Phases 1 and 2). This confirms that sizing the counterweights based on the total platform mass cancels the load when one axis supports the mechanism. During simultaneous motion (Phase 3), a small residual torque remains (peak <5 N·mm) due to the geometric coupling of the platform.
- SolidWorks Simulation (Dash-dot Green Lines): The uncompensated CAD simulation results show good correlation with the analytical results. The peak torque values 16.5 N·mm (Axis 1) and 14 N·mm (Axis 2) and the signals closely match the analytical model without compensation (Solid Blue Lines) with an error under 0.5 N·mm. This validates the quasi-static assumption used for the design.

The minor spikes observed at direction changes are due to inertial effects ($J\ddot{\theta}$), which are interpreted by the software solver but are negligible compared to gravity at these operating speeds and slight geometric CoM offsets captured by the CAD solver, which remain negligible compared to the gravitational loads.

6 Conclusion

This paper presented the design and analysis of a Remote Center of Motion Parallel Mechanism intended for laparoscopic training assessment. Based on the motion constraints of laparoscopic instruments, a workspace specification was defined. The proposed architecture consists of two orthogonal circular arcs, ensuring a fixed RCM. A kinematic model with its Jacobian was derived to describe the instrument tip orientation around a fixed RCM at the trocar.

A static analysis was conducted to quantify the gravitational torques induced by the structure and the sliding instrumented platform. To improve manipulability, a passive balancing strategy using counterweights was proposed. Analytical results demonstrated that sizing the counterweights based on the total platform mass neutralizes the load during single axis motions and reduces it during coupled motions.

A dynamic multibody simulation (SolidWorks Motion) was employed to validate these predictions. The simulation showed a strong correlation with the analytical model, confirming the accuracy of the quasi-static approach. The results prove that the proposed compensation strategy reduces the required holding torque by over 70%, rendering the mechanism nearly weightless for the operator.

Future work will focus on the physical manufacturing of the prototype and the integration of the surgical instrument. Subsequent steps will involve experimental validation using motion capture during real training exercises to evaluate how the mechanism can support both guidance and objective assessment of laparoscopic skills.

References

1. Brian, R., Davis, G., Park, K.M., Alseidi, A.: Evolution of laparoscopic education and the laparoscopic learning curve: a review of the literature. Laparosc. Surg. **6**, 1–11 (2022)
2. Shahrezaei, A., Sohani, M., Taherkhani, S., Zarghami, S.Y.: The impact of surgical simulation and training technologies on general surgery education. BMC Med. Educ. **24**(1), 1297 (2024)
3. Tee, C.L., Grieve, D.A.: Development and validation of an inexpensive home-made laparoscopic trainer for surgical training. J. Surg. Simul. **7**(1), 92–97 (2020)
4. Topalli, D., Cagiltay, N.E.: Eye-hand coordination patterns of intermediate and novice surgeons in a simulation-based endoscopic surgery training environment. J. Eye Mov. Res. **11**(6), 1–14 (2018)
5. Bouzid, S., Chaker, A., Arsicault, M., Bennour, S., Laribi, M.A.: Design of a compact motion tracking device with a remote center of motion dedicated to laparoscopic surgery. In: Mechanisms and Machine Science, vol. 124, pp. 42–51. Springer (2023)
6. Bouzid, S., et al.: A novel integrated motion tracking device for objective laparoscopic training assessment: development and validation. J. Med Devices. **20**(1), 011001 (2026)
7. Chaker, A., Mlika, A., Laribi, M.A., Romdhane, L., Zeghloul, S.: Synthesis of spherical parallel manipulator for dexterous medical task. Front. Mech. Eng. **7**(2), 150–162 (2012)
8. Laribi, M.A., Riviere, T., Arsicault, M., Zeghloul, S.: A design of slave surgical robot based on motion capture. In: 2012 IEEE International Conference on Robotics and Biomimetics (ROBIO), pp. 600–605. IEEE (2012)
9. Uslu, T., Guzin, D., Gezgin, E.: Integration of surgical navigation to a spherical parallel manipulator utilized for robotic brain biopsy. In: 34th Florida Conference on Recent Advances in Robotics FCRAR 2021, pp. 13–14 (2021)

Workspace and Energetic Performance Analysis of a 2-DOF Planar Parallel Manipulator

Lorenzo Scalera(✉), Renato Vidoni, and Alessandro Gasparetto

University of Udine, Udine, Italy
lorenzo.scalera@uniud.it

Abstract. Achieving sustainability and energy efficiency in mechatronic and robotic systems represents one of the current challenges in modern industrial and manufacturing processes. In this context, the kinematic configuration of a manipulator, together with the analysis of the task location, can play a significant role in minimizing the overall energy consumption. This paper presents the workspace and energetic analysis of a planar parallel manipulator with two degrees of freedom, corresponding to two actuated prismatic joints. The kinematic and dynamic models of the considered mechanical system are derived and the influence of the relative position and orientation of the two linear axis is carried out. The results of extensive numerical simulations demonstrate the effectiveness of the proposed approach and its capability of reducing the mechanical energy consumed by the manipulator in a pick-and-place operation.

Keywords: dynamic modelling · energy efficiency · parallel manipulator · robotics · workspace analysis

1 Introduction

Nowadays, the fight against climate changes and the increase of energy costs have pursued the research towards more sustainable and efficient industrial manufacturing processes. The need for sustainable development of industry and responsible consumption and production have also been highlighted by the Sustainable Development Goals of the 2030 Agenda of the United Nations [1].

In the field of mechatronics and robotics, several approaches for energy efficiency have been proposed in the recent years. These approaches leverage structural parameters (e.g., the robot structure, the links geometry, the adoption of elastic elements placed in parallel or in series to the main actuators, the introduction of generative drives), trajectory parameters (e.g., the coefficients that define the motion law), as well as the optimal task placement in the robot workspace. Strategies that combine one or more of these approaches have also been developed. For example, in [2] the authors present an approach to minimize the energy consumption in a Delta-2 parallel robot by adopting both springs for storing potential energy and capacitors for recovery braking energy. In [3], a task-dependent energetic analysis is presented and applied to a planar robot with

© The Author(s), under exclusive license to Springer Nature Switzerland AG 2026
A. Chaker et al. (Eds.): EFIMMS 2026, MMS 205, pp. 56–65, 2026.
https://doi.org/10.1007/978-3-032-22270-1_6

three degrees of freedom (DOFs). An analysis of the effects of the task placement inside the workspace on the energetic performance of a parallel manipulator with 4 DOFs is shown in [4]. Furthermore, in [5] an optimization approach is described for the optimal placement of a pick-and-place task in the workspace of the same robot. Regarding the task-related energetic performance of robotic manipulators, local and trajectory-based indexes are proposed in [6] leveraging the concept of inertia ellipsoid.

Furthermore, in [7] a strategy combining diverse optimization variables (i.e., trajectory parameters, geometrical design parameters, and the position and orientation of the task in the robot workspace) is illustrated and validated on a verified model of a Delta parallel robot with 3 DOFs. In [8], the kinematic synthesis and mechanism design of a six-bar jumping leg for elastic energy storage is reported. A recent example regarding the workspace analysis can be found in [9], where the authors present the size optimization of a planar 3-DOF redundantly actuated parallel mechanism. More recently, in [10] a comparison of planar parallel manipulators for pick-and-place tasks based on workspace and energetic analysis is described. Furthermore, the dynamic modelling, parameter identification and trajectory planning methodology for a high-speed parallel mechanism is presented in [11].

In this paper, we present the workspace and energetic analysis of a parallel planar manipulator with 2 DOFs. The degrees of freedom of the considered mechanism correspond to two actuated prismatic joints. Differently from previous works, the influence of the relative position and orientation of the axis of the two prismatic joints on the workspace size and shape of the manipulator, as well on its energy consumption, is here considered. The kinematic and dynamic models of the mechanical system are derived and the results of extensive numerical tests demonstrate the feasibility of the proposed approach and its capability of reducing the energy consumption up to 90.19% in a pick-and-place operation.

The paper is organized as follows: Sect. 2 describes the kinematic and dynamic models of the considered manipulator with 2 DOFs. The simulation test bed is illustrated in Sect. 3. Section 4 presents the numerical results, including the workspace analysis in Sect. 4.1 and the energetic analysis in Sect. 4.2. Finally, the paper is concluded in Sect. 5.

2 2-DOF Planar Parallel Manipulator

The considered 2-DOF parallel manipulator is shown in Fig. 1. It consists of a planar mechanism where points A and B, as well as the axis ABF and EDH are fixed to the ground. The free coordinates q_1 and q_2 define the length of segments AB and ED, respectively. The motion of the end-effector (point L) is constrained by the two parallelogram structures.

To evaluate the performance of the manipulator in terms of workspace and energy consumption, the position, velocity, and acceleration analysis are derived. Furthermore, to compute the forces $\boldsymbol{F}$ needed to steer the parallel mechanism along the trajectory $(\boldsymbol{q}, \dot{\boldsymbol{q}}, \ddot{\boldsymbol{q}})$, the dynamics of the system is evaluated as:

$$\boldsymbol{F} = \boldsymbol{M}(\boldsymbol{q})\ddot{\boldsymbol{q}} + \boldsymbol{C}(\boldsymbol{q}, \dot{\boldsymbol{q}})\dot{\boldsymbol{q}} + \boldsymbol{g}(\boldsymbol{q}) + \boldsymbol{f}_s + \boldsymbol{F}_v\dot{\boldsymbol{q}} \tag{1}$$

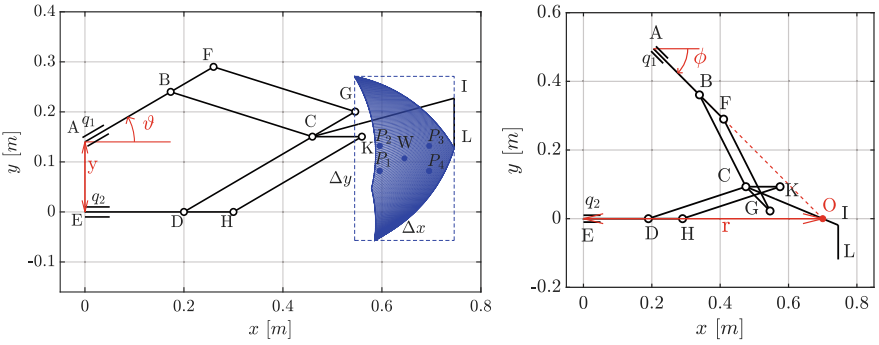

(a) Case A. (b) Case B.

Fig. 1. Considered planar manipulator, parameters used to define the position and orientation of its linear axis (in red), and points of the pick-and-place task.

Table 1. Geometrical and dynamical parameters of the considered manipulator.

AB	q_1	m_{AB}	0.32 kg	$q_{1,min} = q_{2,min}$	0.00 m
ED	q_2	m_{ED}	0.32 kg	$q_{1,max} = q_{2,max}$	0.200 m
$BC = CD$	0.30 m	$m_{BC} = m_{CD}$	0.32 kg	g	9.81 m/s^2
$FG = HK$	0.30 m	$m_{FG} = m_{HK}$	0.32 kg	f_s	2.40 N
$BF = DH$	0.10 m	$m_{BF} = m_{DH}$	0.11 kg	f_v	0.24 Ns/m
$CG = CK$	0.10 m	$m_{CG} = m_{CK}$	0.11 kg	m_{ee}	2 kg
CI	0.30 m	m_{CI}	0.32 kg	S	$4 \cdot 10^{-4}$ m^2
IL	0.10 m	m_{IL}	0.11 kg	ρ	2700 kg/m^3

where $\boldsymbol{M}(\boldsymbol{q})$ is the mass matrix, $\boldsymbol{C}(\boldsymbol{q}, \dot{\boldsymbol{q}})$ includes the Coriolis and centrifugal terms, whereas the vector $\boldsymbol{g}(\boldsymbol{q})$ accounts for the gravitational force. Friction effects are described as in [7] by the static friction force $\boldsymbol{f_s} = f_s \tanh(\dot{\boldsymbol{q}})$, and the viscous friction force $\boldsymbol{F_v} = \text{diag}[f_v\ f_v]$. However, alternative friction formulations can be adopted, as in [12].

The mechanical energy E consumed by the parallel manipulator during a prescribed trajectory is obtained by integrating the mechanical power P (computed from the absolute values of joint velocities $\dot{\boldsymbol{q}}$ and joint forces $\boldsymbol{F}$) provided by the two actuators of the prismatic joints over the total time T:

$$E = \int_0^T \sum_{i=1}^{2} P_i \, dt = \int_0^T \sum_{i=1}^{2} |\dot{q}_i||F_i| \, dt \tag{2}$$

In this work, we assume the links of the mechanism to be rigid. The revolute and prismatic joints are modeled as ideal and without clearance. Furthermore, no uncertainties in the kinematic and dynamic parameters are considered.

3 Simulation Test Bed

The kinematic and dynamic models of the considered 2-DOF planar manipulator presented in Sect. 2 are implemented in Matlab R2025b, using a computer running Windows 11 Pro with an Intel Core i7-8565U CPU @ 1.80 GHz and 16.0 GB of RAM. The geometrical and dynamical parameters used in the numerical simulations are reported in Table 1. The nomenclature of the links of the manipulator and their corresponding mass values m follows the one reported in Fig. 1. $q_{i,min}$ and $q_{i,max}$ represent the lower and upper position limits of the free coordinates q_i, with $i = 1, 2$. Moreover, g is the gravitational acceleration, f_s and f_v represent the static and viscous friction coefficients, respectively, whereas m_{ee} is the end-effector mass. Finally, S represents the cross-section area of the links, and ρ is the density of the links, which are assumed to be made of aluminum.

In this work, two different test cases are considered:

- **Case A**: The influence of the distance y (i.e., the vertical coordinate y_A of point A) between the origin of the two actuated parallel axis, and the angle ϑ of axis AB with respect to the horizontal plane is analyzed. The parameters y and ϑ are shown in Fig. 1a .
- **Case B**: We consider that the two actuated axes may initially be superimposed, and that one rotates by an angle ϕ with respect to the other about a rotation center located at a horizontal distance r from point D. The influence of parameters ϕ and r, shown in Fig. 1b , on the worskpace area and energy consumption of the manipulator is considered in this case.

In both cases, the actuated prismatic joint ED is fixed and horizontal. Furthermore, the last segment IL of the mechanism is kept vertical by adjusting the angle $C\hat{I}L$ according to ϑ in case A, or ϕ in case B. In the numerical tests, the parameter y is varied from 0.05 to 0.40 m, ϑ from $-60°$ to $60°$, r from 0.20 to 0.80 m, and ϕ from $-10°$ to $-45°$. For both the workspace and the energetic analysis, the range of all parameters, as well as the position range of the free coordinates, is discretized into 100 equally spaced points. In the numerical tests, the configurations of the mechanism affected by singularity issues are automatically discarded in both the considered test cases.

For the workspace analysis, the free coordinates are varied throughout their entire range, and the position of the end-effector obtained through forward kinematics is recorded. To compute the area of the workspace, the *alphaShape* Matlab function is adopted, which creates a bounding area that envelops a set of 2D points. In preliminary tests, the *alpha* parameter of the *alphaShape* function was manually tuned to a value equal to 0.01 to tighten the fit around the points in the workspace and create a non-convex region. This non-convex region closely follows the actual distribution of data points, capturing concavities and indentations of the manipulator workspace. In order to better study the influence of the considered parameters on the manipulator workspace, the Δx and Δy dimensions of the rectangle inscribing the workspace are also computed.

For the energetic analysis, we consider a pick-and-place task defined by four way points in the Cartesian space of the manipulator (Fig. 1a). For each com-

bination of parameters, the task is placed at the center point (W_x, W_y) of the rectangle inscribing the workspace. The coordinates of the four points defining the pick-and-place task are then computed as: $P_1 = (W_x - d_x/2, W_y - d_y/2)$, $P_2 = (W_x - d_x/2, W_y + d_y/2)$, $P_3 = (W_x + d_x/2, W_y + d_y/2)$, and $P_4 = (W_x + d_x/2, W_y - d_y/2)$, where d_x=0.10 m and d_y=0.05m. The trajectory of the planar manipulator is planned in the joint space as a rest-to-rest motion between each couple of consecutive way points using a fifth-degree polynomial motion law. Each segmant has a duration equal to h=0.20 s, and the trajectory is discretized at 1 kHz. For each numerical test, a round-trip pick and place is considered: six point-to-point trajectory segments are planned with a total time equal to T=1.2 s.

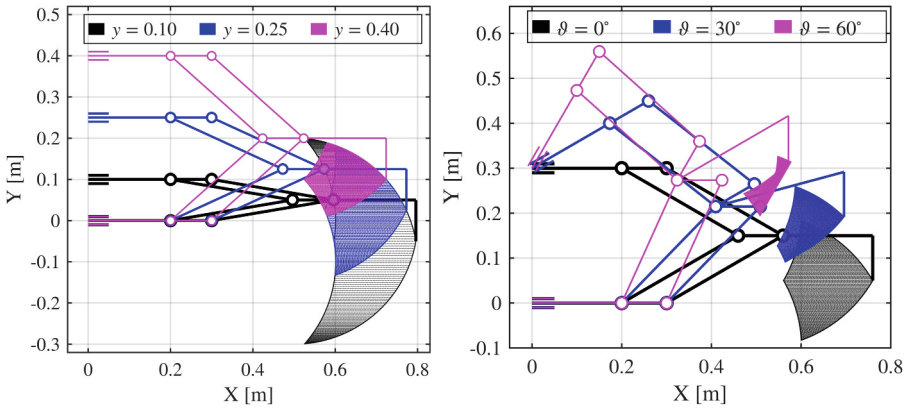

(a) Influence of y. (b) Influence of ϑ.

Fig. 2. Workspace analysis in case A.

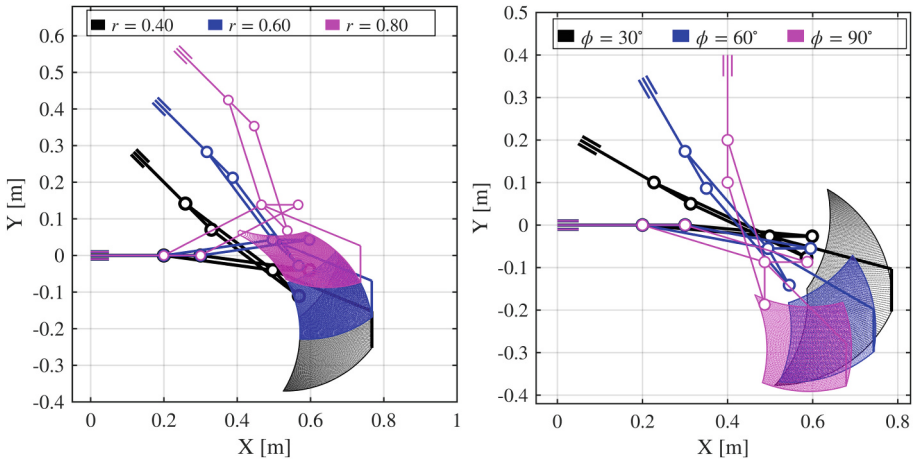

(a) Influence of r. (b) Influence of ϕ.

Fig. 3. Workspace analysis in case B.

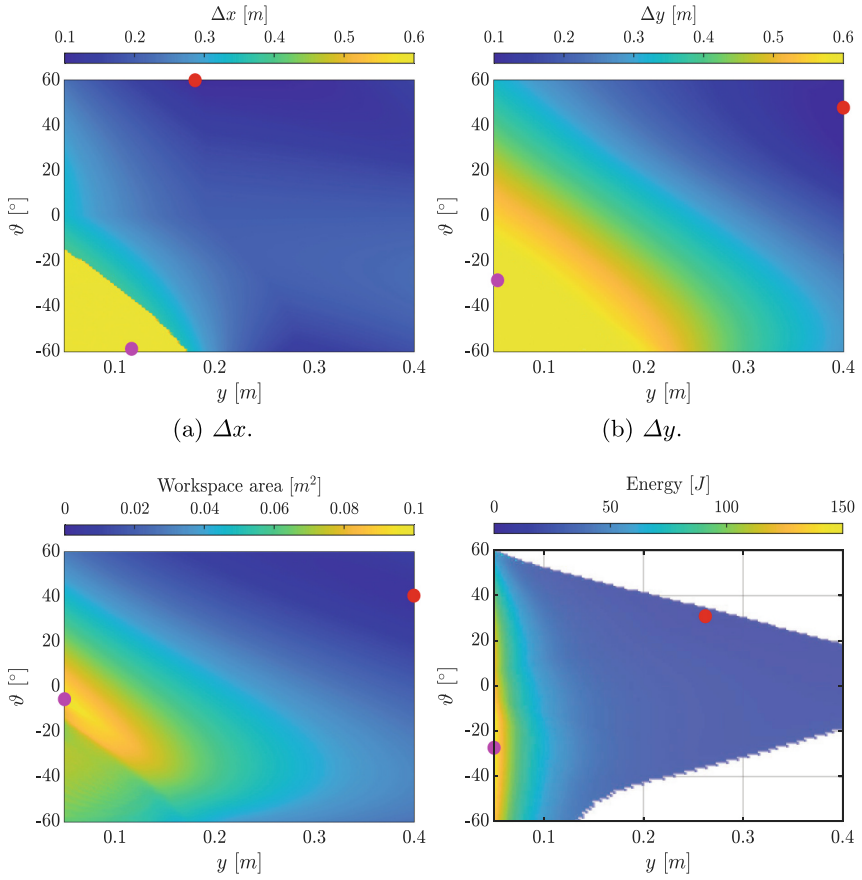

(a) Δx. (b) Δy.

(c) Workspace area. (d) Mechanical energy.

Fig. 4. Numerical results of case A. Maximum values are highlighted in magenta, and minimum values in red.

4 Numerical Results

In this section, the numerical results related to cases A and B are presented. In Sect. 4.1 the results of the workspace analysis are illustrated, whereas the results of the energetic analysis are shown in Sect. 4.2.

4.1 Workspace Analysis

Figure 2 shows selected examples of workspace analysis in case A. Figure 2a reports the kinematic configuration of the manipulator and its corresponding workspace for different values of parameter y, whereas the influence of ϑ on the configuration of the manipulator and its workspace is shown in Fig. 2b . Furthermore, the maps of the dimensions of the workspace Δx, Δy, and workspace

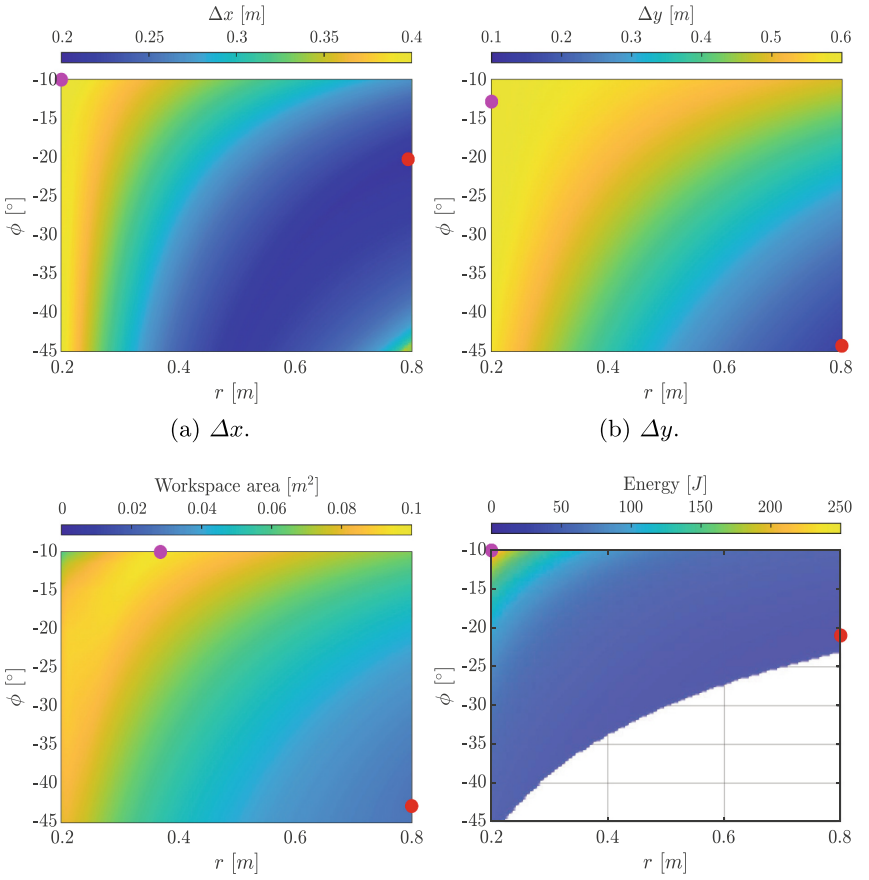

(a) Δx. (b) Δy.

(c) Workspace area. (d) Mechanical energy.

Fig. 5. Numerical results of case B. Maximum values are highlighted in magenta, and minimum values in red.

area as function of y and ϑ for case A are illustrated in Fig. 4a , 4b , and 4c , respectively.

Examples of workspace dimensions and shapes for case B are shown in Fig. 3. More in detail, Fig. 3a illustrates the effect of varying parameter r on the workspace area, whereas the influence of ϕ can be appreciated in Fig. 3b . The color maps of workspace dimensions Δx, Δy and area with respect to r and ϕ are reported in Fig. 5a, 5b, and 5c.

Table 2 reports the numerical results of the workspace analysis: the minimum and maximum values of the workspace area for cases A and B, and the corresponding parameters. As it can be seen from the table, in case A the maximum workspace area is equal to $A_{max} = 0.097\,\mathrm{m}^2$. This value of maximum workspace area represents an improvement of 3133.33% with respect to the case on min-

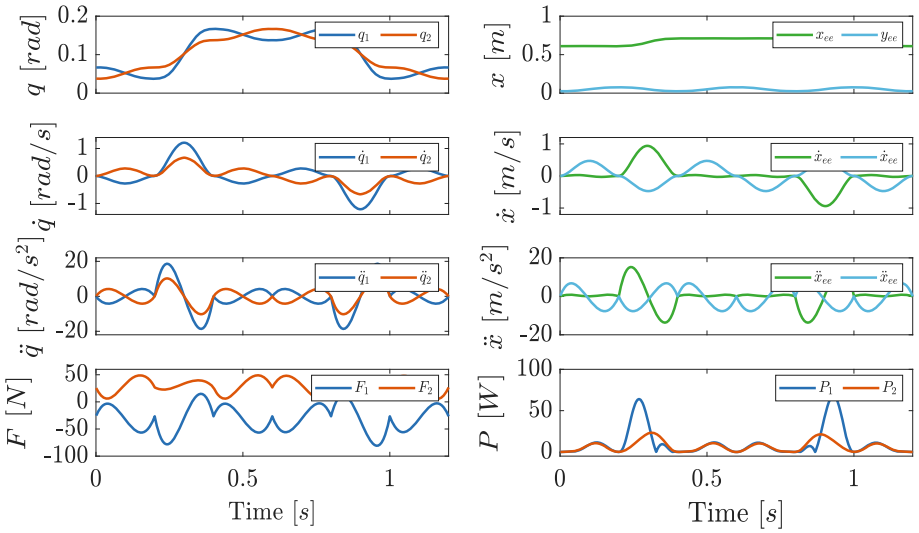

Fig. 6. Example of pick-and-place trajectory for y=0.300 m and $\vartheta = 0°$: kinematic variables in the joint and in the Cartesian space, joint forces and powers.

Table 2. Numerical results: minimum and maximum values of the workspace area in cases A and B, and corresponding parameters.

Case		Workspace area $[m^2]$	Parameters	
A	A_{max}	0.097	y=0.050 m	$\vartheta = -5.45°$
	A_{min}	0.003	y=0.400 m	$\vartheta = 40.61°$
B	A_{max}	0.095	r=0.370 m	$\phi = -10°$
	A_{min}	0.027	r=0.800 m	$\phi = -42.88°$

imum area ($A_{min} = 0.003\,\mathrm{m}^2$). Regarding case B, the maximum area is equal to $A_{max} = 0.095\,\mathrm{m}^2$, and corresponds to a percentage improvement of 251.85% with respect to the worst case ($A_{min} = 0.027\,\mathrm{m}^2$). These results highlight that a proper design of the relative position and orientation of the linear axis of the considered parallel manipulator can lead to a considerable improvement of the kinematic performance of the system.

4.2 Energetic Analysis

Figure 4d shows the results of the energetic analysis for case A, where each point of the map represents the mechanical energy consumed by the manipulator for completing a round-trip pick-and-place task placed at the center of the robot workspace, where the kinematic configuration of the mechanism is defined by parameters y and ϑ. The energy map is computed only for the combinations of parameters (y, ϑ) for which all four way points of the pick-and-place opera-

Table 3. Numerical results: minimum and maximum values of the mechanical energy for cases A and B, and corresponding parameters.

Case		Mechanical energy $[J]$	Parameters	
A	E_{max}	148.61	y=0.050 m	$\vartheta = -27.27°$
	E_{min}	16.14	y=0.262 m	$\vartheta = 30.91°$
B	E_{max}	231.40	r=0.200 m	$\phi = -10°$
	E_{min}	22.70	r=0.800 m	$\phi = -20.96°$

tion fall inside the robot workspace and allow the manipulator to complete the task in compliance with all the geometrical constraints of the planar robot. The corresponding energy map for case B is shown in Fig. 5d, where each point represents the energy expenditure of the mechanism, when the relative position of the linear axis is designed using a pair of parameters (r, ϕ).

Figure 6 reports an example of pick-and-place trajectory in the joint space and in the Cartesian space, together with the graphs of forces and powers at robot joints for the case with y=0.300 m and $\vartheta = 0°$.

The values of minimum and maximum energy consumption for cases A and B and the corresponding parameters can be found in Table 3. In case A, the minimum energy consumption ($E_{min} = 16.14\ J$) represents a percentage reduction equal to 89.14% with respect to the case of maximum energy ($E_{max} = 148.61\ J$). In case B, the energy consumption for the same pick-and-place task spans from the worst case with $E_{max} = 231.40\ J$ to the optimal case with $E_{min} = 22.70\ J$, which corresponds to a percentage reduction equal to 90.19%. However, the energy-optimal solutions might slightly change if the task is off-center with respect to the workspace or if d_x and d_y vary. The results of this energetic analysis demonstrate the performance of the proposed approach and its capability of considerably reducing the energy consumed by the parallel manipulator with a proper choice of the design parameters.

5 Conclusions

In this paper, the workspace and energetic analysis of a 2-DOF planar parallel manipulator has been presented. By properly designing the relative positions of its actuated linear axis, the combination of parameters that allow to obtain the largest workspace area and the minimum energy consumption for a pick-and-place operation, placed at the center of the rectangle inscribing the workspace, have been found. The results of extensive numerical tests have shown the feasibility of the proposed approach and its capability in increasing the size of the workspace, as well as reducing the energy consumption of the manipulator. Future works will include the validation of the proposed approach, and the optimization of the lengths of the robot links to further improve its performance in terms of workspace dimensions and energy efficiency.

Acknowledgements. The authors thank Mr. Simone Balloch for his help in developing the first analysis of the robotic system.

References

1. United Nations, Sustainable Development Goals (2015). https://www.un.org/sustainabledevelopment/
2. Carabin, G., Palomba, I., Wehrle, E., Vidoni, R.: Energy expenditure minimization for a Delta-2 robot through a mixed approach. In: European Congress on Computational Methods in Applied Sciences and Engineering (ECCOMAS 2019), pp. 383–390. Springer (2019)
3. Boscariol, P., Scalera, L., Gasparetto, A.: Task-Dependent energetic analysis of a 3 D.O.F. industrial manipulator. In: Berns, K., Görges, D. (eds) Advances in Service and Industrial Robotics. RAAD 2019. Advances in Intelligent Systems and Computing. vol. 980, pp. 162–169. Springer, Cham. (2019)
4. Scalera, L., Boscariol, P., Carabin, G., Vidoni, R., Gasparetto, A.: Enhancing energy efficiency of a 4-DOF parallel robot through task-related analysis. Machines **8**(1), 10 (2020)
5. Scalera, L., Boscariol, P., Carabin, G., Vidoni, R., Gasparetto, A.: Optimal task placement for energy minimization in a parallel manipulator. In: Lovasz, EC., Maniu, I., Doroftei, I., Ivanescu, M., Gruescu, CM. (eds) New Advances in Mechanisms, Mechanical Transmissions and Robotics . MTM & Robotics 2020. Mechanisms and Machine Science. vol. 88, pp. 12–22. Springer, Cham. (2020)
6. Vidussi, F., Boscariol, P., Scalera, L., Gasparetto, A.: Local and trajectory-based indexes for task-related energetic performance optimization of robotic manipulators. J. Mech. Robot. **13**(2), 021018 (2021)
7. Fabris, G., Scalera, L., Gasparetto, A.: Dynamic modelling and energy-efficiency optimization in a 3-DOF parallel robot. Int. J. Adv. Manuf. Tech. **132**(5), 2677–2699 (2024)
8. Du, Q., et al.: Kinematic synthesis and mechanism design of a six-bar jumping leg for elastic energy storage and release based on dead points. Mech. Mach. Theory **202**, 105777 (2024)
9. Zhang, J., et al.: Workspace analysis and size optimization of planar 3-DOF redundantly actuated parallel mechanism. J. Mech. Sci. Technol. **38**(2), 957–967 (2024)
10. Nezzi, C., Gufler, V., Berger, A., Vidoni, R.: Energy expenditure comparison of planar robotic manipulators for pick-and-place operations. In: International Workshop IFToMM for Sustainable Development Goals, pp. 634–643. Springer (2025)
11. Liang, D., Jian, Y., Song, Y., Wang, Z., Liu, J.: Dynamic modelling, parameter identification and multi-performance integrated trajectory planning methodology for a new high-speed parallel mechanism. Mech. Mach. Theory **218**, 106285 (2025)
12. Fabris, G., Scalera, L., Boscariol, P., Gasparetto, A.: Experimental analysis and comparison of friction models applied to the UR5e robot. In: Lovasz, EC., Ceccarelli, M., Ciupe, V. (eds) Mechanism Design for Robotics. MEDER 2024. Mechanisms and Machine Science. vol. 166 MMS, pp. 125–133. Springer, Cham. (2024)

Mechanism Design and Inverse Kinematics of a 5-DOF Hybrid (Parallel–Serial) Manipulator

Alexey Novikov[1], Pavel Laryushkin[1,2], and Alexey Fomin[1(✉)]

[1] Mechanical Engineering Research Institute of the Russian Academy of Sciences (IMASH RAN), Moscow 101000, Russia
alexey-nvkz@mail.ru

[2] Bauman Moscow State Technical University (BMSTU), Moscow 105005, Russia

Abstract. The proposed study discusses mechanism design and inverse kinematics of a novel 5-DOF parallel–serial manipulator. The parallel part of the manipulator is a 4-DOF mechanism with 2T2R motion pattern, equipped with four RRR kinematic chains and extendable platform. The fifth DOF realizes additional prismatic motion. Therefore, the proposed manipulator allows to reproduce five independent movements—three translations and two rotations (3T2R motion pattern). The inverse kinematics solution provides the relationships between the coordinates of the end-effector and five driving movements (generalized coordinates). The proposed algorithm for inverse kinematics is demonstrated by numerical example simulated in MATLAB. The example discusses spiral trajectory of the end-effector for which driving coordinates are calculated.

Keywords: 5-DOF manipulator · hybrid (parallel–serial) manipulator · 3T2R motion pattern · inverse kinematics · MATLAB simulation

1 Introduction

Diverse areas of human activity require the use of high-tech devices developed on the basis of various mechanisms. Many processes require high speed and precision positioning of the output link, as well as increased maneuverability and structural rigidity. In such cases, parallel mechanisms have proven their efficiency. They typically have a multiple-link design, due to the operation of several independently driven kinematic chains. To reduce the complexity of the kinematic chains, it is preferable to use the simplest and most reliable joints. Therefore, 1-DOF (degree of freedom) rotational joints can be used in the mechanism chains, which can form the simplest linkages – planar dyads (RRR, where R denotes a rotational joint).

Depending on the application of parallel mechanisms with planar dyads, their output link may have from one to six DOF, however mechanisms with three, four, and five DOF are most often used in various technological processes. 2-DOF mechanisms are applied less frequently. Study [1] presents one of such mechanisms that has 2R motion pattern. It

© The Author(s), under exclusive license to Springer Nature Switzerland AG 2026
A. Chaker et al. (Eds.): EFIMMS 2026, MMS 205, pp. 66–75, 2026.
https://doi.org/10.1007/978-3-032-22270-1_7

is used as an orientation system for a satellite communication antenna. Paper [2] shows a number of 2-DOF mechanisms with 2 T motion pattern.

In addition to the number of DOF, the scope of application of a given mechanism is also determined by the type of motion pattern. Therefore, there are number of studies devoted to the type synthesis of mechanisms with a specific number of DOF and a given motion pattern. Mechanisms with planar dyad kinematic chains are often encountered in such studies. For example, papers [3–8] discuss type synthesis of mechanisms with 3 T, 3R, and 2R1T motion patterns. Authors of papers [9–13] develop mechanisms with 3T1R and 3R1T motion patterns. Papers [14, 15] demonstrate synthesized mechanisms with 3T2R and 3R2T motion patterns. Study [16] discusses a 6-DOF mechanism for teleoperated robotic cervical spine surgery.

However, parallel mechanisms are not free from drawbacks. The main of them are relatively small workspace and the presence of singularities in which the output link can lose DOF or become uncontrollable. Therefore, there are currently a growing number of scientific papers, which investigate hybrid mechanisms and manipulators. Depending on the type of a hybrid mechanism, it may include only parallel kinematic chains, i.e., be a parallel-parallel mechanism [17, 18], or parallel and serial kinematic chains, i.e. be a parallel-serial or a serial-parallel mechanism [18–27].

Increasing demands on the functional capabilities of mechanisms and expansion of their application areas make it more practical to use hybrid mechanisms in various technological processes. A hybrid structure allows to eliminate many disadvantages of parallel mechanisms. Hybrid mechanisms can be used as devices for moving surgical or diagnostic instruments relative to the patient [25, 28], for post-traumatic rehabilitation operations [22], as devices for gripping, carrying, or packaging various objects [24], as devices for performing assembly operations [29], etc.

Considering the above-formulated motivation for using hybrid mechanisms in technology, this study discusses a novel 5-DOF hybrid (parallel–serial) manipulator, which includes advantages of parallel systems as well as serial ones. Moreover, the discussed manipulator includes RRR kinematic chains, which make its design simpler.

2 Manipulator Design

In this section, we consider the design of a novel 5-DOF manipulator. Figure 1 shows its kinematic scheme and the computer-aided design (CAD) model. The manipulator includes fixed link 1, driving levers 2 with actuators 2′, driven levers 3, rods 4, links 5 and 6 forming an extendable platform, screw 7 with actuator 7′, guides 6′ rigidly mounted on link 6 and carriage 8 with elements 8′, and output link 9.

The manipulator consists of parallel and serial parts. The parallel part has 2T2R motion pattern, while the serial part has 1 T motion pattern. Thus, the overall motion pattern of the manipulator is 3T2R. In this case, $\underline{\text{R}}$RR dyads (underscore means that the joint is actuated) are used as chains connecting the platform to the fixed link, where the first joint from the fixed link is the actuated one.

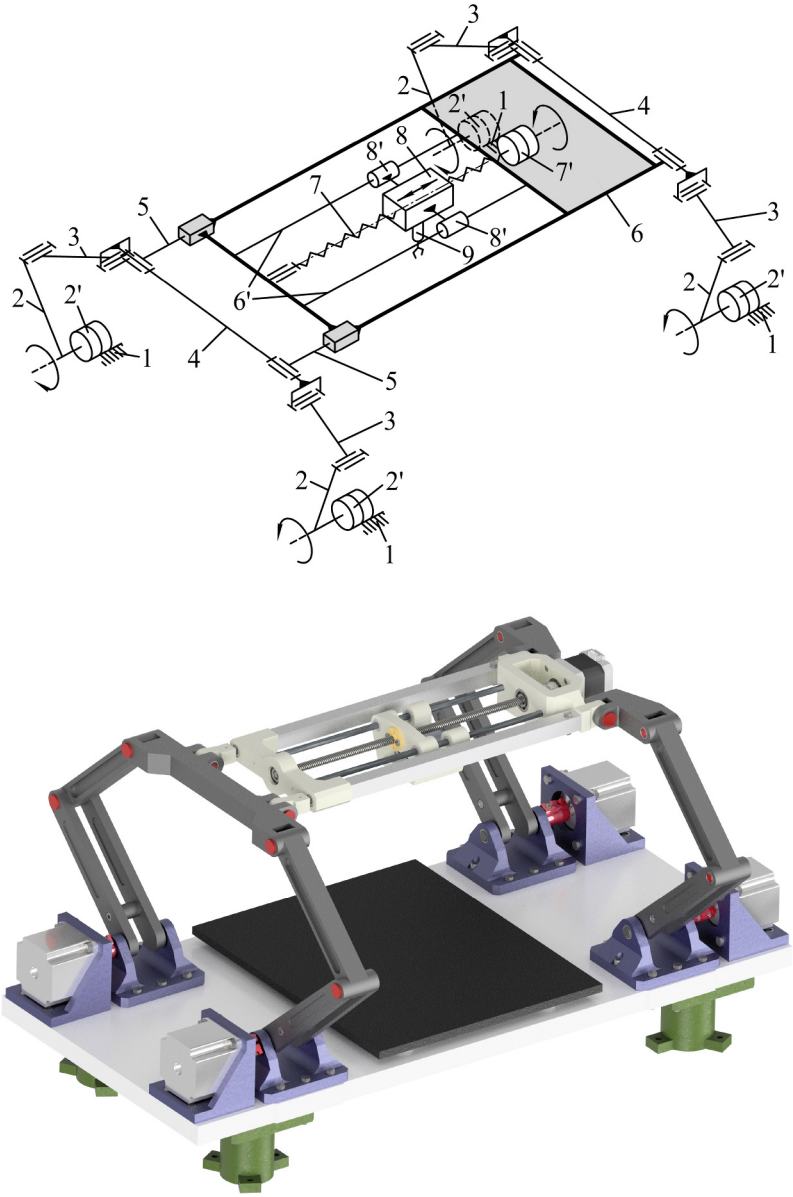

Fig. 1. Mechanism design of a 5-DOF hybrid (parallel–serial) manipulator: kinematic scheme (upper picture) and CAD model (lower picture).

The advantage of the proposed manipulator is not only in providing five DOF of the output link, but also it allows for significant displacement of the output link along the platform's longitudinal dimension. Therefore, its application may be related to mechanical engineering for processing elongated machine parts or to medicine for spinal surgeries.

Furthermore, the manipulator provides significant vertical platform displacements using RRR chains. One should also note that the manipulator decouples the movements of the parallel and serial parts, which is very convenient to control this system. Although the manipulator has five DOF, a sixth degree (rotation of output link 9 around its own axis) can be added by independently actuating output link 9. In the next section, we will discuss the inverse kinematics of the proposed manipulator.

3 Inverse Kinematics

The proposed algorithm of the inverse kinematics uniformly allows to study 5-DOF variation as well as 6-DOF one. The 6-DOF design differs only by the independent rotational DOF, which completely correspond to the rotation in its drive.

We assume that the position of the end-effector, i.e. coordinates x, y, and z of point E, and the orientation of platform $C_1C_2C_3C_4$ (angles φ_x and φ_y) are known. Therefore, the objective of the inverse kinematics is to find corresponding values of input angles θ_1, θ_2, θ_3, θ_4 and carriage position s.

One can see that coordinate x depends only on s and φ_y. Denoting the position of points A_3, A_4, B_3, B_4, C_3, and C_4 along the Ox axis as $x_3 = x_4$ (i.e. $x_3 = x_4 = x_{A3} = x_{A4} = x_{B3} = x_{B4} = x_{C3} = x_{C4}$), we can write:

$$x = x_3 + s\cos\varphi_y - l_{DE}\sin\varphi_y, \tag{1}$$

where l_{DE} is the length of the end-effector.

Constraint Eq. (1) can be rewritten to obtain a closed-form solution for s:

$$s = \frac{1}{\cos\varphi_y}\left(x - x_3 + l_{DE}\sin\varphi_y\right). \tag{2}$$

Let us now consider the front view of the manipulator presented in Fig. 2 in the plane of kinematic chains RRR.

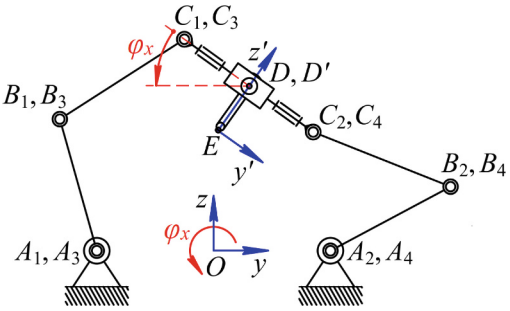

Fig. 2. Front view of the discussed manipulator (when $\varphi_y = 0$).

Practically, we have a planar 4-RRR manipulator [30] with variable height, which depends on the value of φ_y and position of point E that depends on the same angle and length s (Fig. 3).

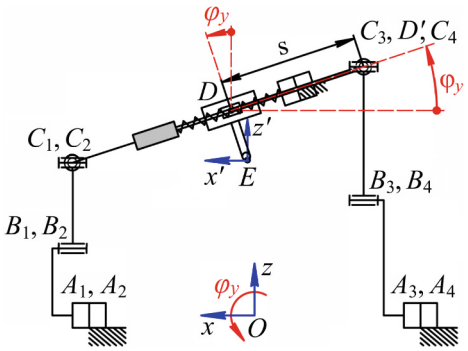

Fig. 3. Side view of the discussed manipulator (when $\varphi_x = 0$).

One can see that the platform of the discussed manipulator has rectangular shape. This, however, is just one possible case. Segments C_1C_2 and C_3C_4 are always parallel, and by the design, they cannot move sideways with respect to each other. In other words, the platform could possibly be a trapezoid with C_1C_2 and C_3C_4 being its bases. However, as there is no possibility for the relative sideways motions of the side bases, the rectangular shape appears to be the most convenient and natural design choice.

Let $x_1 = x_2$ (i.e. $x_1 = x_2 = x_{A1} = x_{A2} = x_{B1} = x_{B2} = x_{C1} = x_{C2}$) be the x-coordinate of points A_1, A_2, B_1, B_2, C_1, and C_2. Then the lengths of the projections of segments C_1C_3 and C_2C_4 onto plane Oyz will have the following form:

$$l_{C1C3}^{Oyz} = l_{C2C4}^{Oyz} = (x_1 - x_3)\tan\varphi_y. \tag{3}$$

The length of the projection of segment ED' onto plane Oyz can be represented as the sum of the projections of segments ED and DD' onto the same plane Oyz and determined by the formula:

$$l_{DE}^{Oyz} + l_{DD'}^{Oyz} = l_{DE}\cos\varphi_y + s \cdot \sin\varphi_y. \tag{4}$$

The z'-coordinates of points C_1, C_2, C_3, and C_4 in the platform reference frame $Ey'z'$ can be written as follows:

$$\begin{gathered} z'_{C1} = z'_{C2} = s \cdot \sin\varphi_y + l_{DE}\cos\varphi_y - (x_1 - x_3)\tan\varphi_y, \\ z'_{C3} = z'_{C4} = s \cdot \sin\varphi_y + l_{DE}\cos\varphi_y. \end{gathered} \tag{5}$$

The y'-coordinate of the discussed points are known from the design of the manipulator. The coordinates of C_1, C_2, C_3, and C_4 in the $Oxyz$ reference frame can be obtained by rotating and translating the vector containing the coordinates in $Ey'z'$ frame:

$$\begin{pmatrix} y_{Ci} \\ z_{Ci} \end{pmatrix} = \mathbf{R}\begin{pmatrix} y'_{Ci} \\ z'_{Ci} \end{pmatrix} + \begin{pmatrix} y \\ z \end{pmatrix}, \tag{6}$$

where rotation matrix $\mathbf{R}$ is defined as follows:

$$\mathbf{R} = \begin{pmatrix} \cos\varphi_x & -\sin\varphi_x \\ \sin\varphi_x & \cos\varphi_x \end{pmatrix}.$$

Now, the remaining part of the inverse kinematics is rather straightforward. First, we define coordinates of points B_1, B_2, B_3, and B_4:

$$y_{Bi} = y_{Ai} + l_{ABi}\cos\theta_i, z_{Bi} = z_{Ai} + l_{ABi}\sin\theta_i. \tag{7}$$

On the other hand, the length of B_iC_i can be expressed in terms of the corresponding coordinates of B_i and C_i:

$$l_{BCi}^2 = (y_{Ci} - y_{Bi})^2 + (z_{Ci} - z_{Bi})^2. \tag{8}$$

Substituting (5), (6), and (7) into (8) for each i-th leg, four constraint equations containing θ_i can be obtained. The inverse kinematics then becomes solved by finding the values of θ_i from each of these equations which can be done in a closed-form.

4 Numerical Example

It's important to note that the links in the contours of the opposite planar kinematic chains should have different lengths to avoid their coincidence in the vertical plane. With a symmetrical arrangement of these contours and with identical link lengths, the moving platform will acquire an uncontrolled DOF, because the mechanism will be in a singular configuration.

Let us now consider a numerical example of the inverse kinematics for the manipulator with the following dimensions (in m): $x_1 = x_2 = 0.5$; $x_3 = x_4 = -0.5$; $y'_{C1} = y'_{C3} = -0.25$; $y'_{C2} = y'_{C4} = 0.25$; $y_{A1} = y_{A3} = -0.4$; $y_{A2} = y_{A4} = 0.4$; $z_{A1} = z_{A2} = z_{A3} = z_{A4} = 0$; $l_{C1C2} = l_{C3C4} = 0.5$; $l_{A1B1} = l_{A2B2} = 0.5$; $l_{A3B3} = l_{A4B4} = 0.75$; $l_{BiCi} = 0.5$; $l_{DE} = 0.15$.

In this example we will simulate the conical spiral trajectory which can be described by the following equations:

$$x = c\gamma\cos\gamma, y = c\gamma\sin\gamma, \tag{9}$$

where $c = 0.05$ is the coefficient that governs the rate of growth of the spiral radius. The spiral has four full turns, and coordinate z changes linearly from 0.6 to 0.3 m. At any point of the spiral the end-effector is always pointing to the origin of the reference frame (point O). Visualization of the trajectory along with the manipulator itself is shown in Fig. 4.

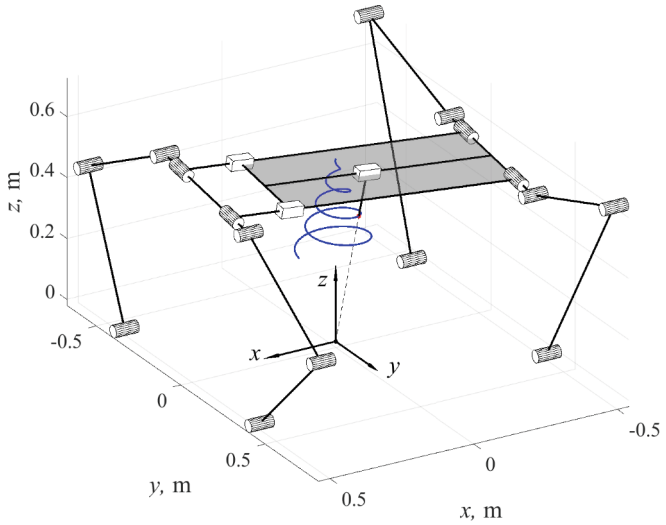

Fig. 4. The motion trajectory of the manipulator's end-effector for solving the inverse kinematics.

Thus, during the simulation we change the value of γ from 0° to 4 × 360° with an increment of 1°. Figure 5 shows the diagrams of the end-effector coordinates and Fig. 6 shows the diagrams of the driving joint coordinates.

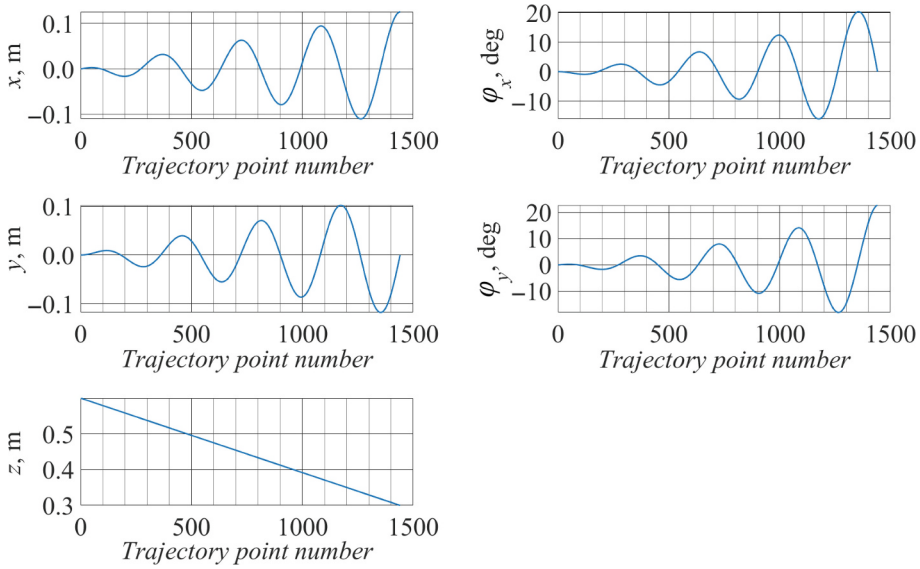

Fig. 5. Coordinates of the end-effector along the simulated spiral trajectory.

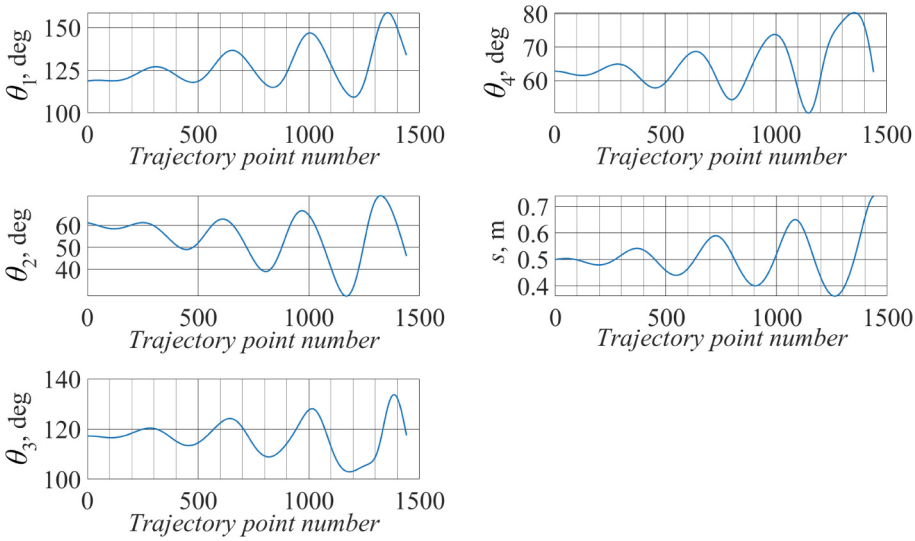

Fig. 6. Driving joint coordinates along the simulated spiral trajectory.

5 Conclusions

The study demonstrated mechanism design and performed inverse kinematic analysis of a novel 3T2R hybrid (parallel-serial) manipulator with five DOF, where the parallel part provides four DOF and 2T2R motion pattern and the serial part adds additional DOF and 1 T motion pattern. In the inverse kinematic analysis, we computed the displacements in the actuators based on the five given coordinates of the end-effector. During the analysis we investigated the motion of the end-effector along spiral trajectory. The numerical example simulated in MATLAB package realized the developed analytical algorithm. The techniques proposed in this article can be applied to other hybrid manipulators with parallel-serial architectures. The future works will use the inverse kinematics algorithm to construct the workspace, perform velocity analysis, and analyze singularities.

Acknowledgments. This study was funded by Russian Science Foundation grant No 25-19-00929, https://rscf.ru/en/project/25-19-00929/.

References

1. Song, Y., Qi, Y., Dong, G., Sun, T.: Type synthesis of 2-DoF rotational parallel mechanisms actuating the inter-satellite link antenna. Chin. J. Aeronaut. **29**(6), 1795–1805 (2016). https://doi.org/10.1016/j.cja.2016.05.005
2. Yaşır, A., van der Wijk, V., Herder, J.: Kinematic synthesis of fully decoupled planar parallel mechanisms by using multiple pantograph geometries. In: Okada, M. (ed.) Advances in Mechanism and Machine Science. IFToMM WC 2023. Mechanisms and Machine Science, vol. 147, pp. 1–10. Springer, Cham (2023). https://doi.org/10.1007/978-3-031-45705-0_78

3. Gogu, G.: Structural synthesis of fully-isotropic translational parallel robots via theory of linear transformations. Eur. J. Mech. A Solids. **23**(6), 1021–1039 (2004). https://doi.org/10.1016/j.euromechsol.2004.08.006
4. Kong, X., Gosselin, C.M.: Type synthesis of 3-DOF translational parallel manipulators based on screw theory. ASME J. Mech. Des. **126**(1), 83–92 (2004). https://doi.org/10.1115/1.1637662
5. Kong, X., Gosselin, C.M.: Type synthesis of 3-DOF spherical parallel manipulators based on screw theory. ASME J. Mech. Des. **126**(1), 101–108 (2004). https://doi.org/10.1115/1.1637655
6. Xie, F., Liu, X.-J., Li, T.: Type synthesis and typical application of 1T2R-type parallel robotic mechanisms. Math. Probl. Eng. **2013**, 206181 (2013). https://doi.org/10.1155/2013/206181
7. Xu, Y., Zhang, D., Yao, J., Zhao, Y.: Type synthesis of the 2R1T parallel mechanism with two continuous rotational axes and study on the principle of its motion decoupling. Mech. Mach. Theory. **108**, 27–40 (2017). https://doi.org/10.1016/j.mechmachtheory.2016.09.007
8. Gosselin, C.M., Vollmer, F., Cote, G., Wu, Y.: Synthesis and design of reactionless three-degree-of-freedom parallel mechanisms. IEEE Trans. Robot. Autom. **20**(2), 191–199 (2004). https://doi.org/10.1109/TRA.2004.824696
9. Kong, X., Gosselin, C.M.: Type synthesis of 3T1R 4-DOF parallel manipulators based on screw theory. IEEE Trans. Robot. Autom. **20**(2), 181–190 (2004). https://doi.org/10.1109/TRA.2003.820853
10. Li, Q., Huang, Z.: Type synthesis of 4-DOF parallel manipulators. In: Proceedings of the 2003 IEEE International Conference on Robotics and Automation, Taipei, Taiwan, pp. 755–760 (2003). https://doi.org/10.1109/ROBOT.2003.1241684
11. Gogu, G.: Structural synthesis of fully-isotropic parallel robots with Schönflies motions via theory of linear transformations and evolutionary morphology. Eur. J. Mech. A Solids. **26**(2), 242–269 (2007). https://doi.org/10.1016/j.euromechsol.2006.06.001
12. Li, Q., Herve, J.M.: Parallel mechanisms with bifurcation of Schoenflies motion. IEEE Trans. Robot. **25**(1), 158–164 (2009). https://doi.org/10.1109/TRO.2008.2008737
13. Guo, S., Fang, Y., Qu, H.: Type synthesis of 4-DOF nonoverconstrained parallel mechanisms based on screw theory. Robotica. **30**(1), 31–37 (2012). https://doi.org/10.1017/S0263574711000439
14. Piccin, O., Bayle, B., Maurin, B., de Mathelin, M.: Kinematic modeling of a 5-DOF parallel mechanism for semi-spherical workspace. Mech. Mach. Theory. **44**(8), 1485–1496 (2009). https://doi.org/10.1016/j.mechmachtheory.2008.11.012
15. Fang, Y., Tsai, L.-W.: Structure synthesis of a class of 4-DoF and 5-DoF parallel manipulators with identical limb structures. Int. J. Robot. Res. **21**(9), 799–810 (2002). https://doi.org/10.1177/027836490202100931 4
16. Koszulinski, A., Sandoval, J., Arsicault, M., Laribi, M.A.: Development of a 6-degrees-of-freedom hybrid interface intended for teleoperated robotic cervical spine surgery. J. Mech. Robot. **17**(2), 021007 (2025). https://doi.org/10.1115/1.4065917
17. Pan, Y., Gao, F., Du, H.: Fault tolerance criteria and walking capability analysis of a novel parallel-parallel hexapod break walking robot. Robotica. **34**(3), 619–633 (2016). https://doi.org/10.1017/S0263574714001738
18. Zhou, H., Qin, Y., Chen, H., Ge, S., Cao, Y.: Structural synthesis of five-degree-of-freedom hybrid kinematics mechanism. J. Eng. Des. **27**(4–6), 390–412 (2016). https://doi.org/10.1080/09544828.2016.1150968
19. Saafi, H., Laribi, M.A., Zeghloul, S.: Optimal torque distribution for a redundant 3-RRR spherical parallel manipulator used as a haptic medical device. Robot. Auton. Syst. **89**, 40–50 (2017). https://doi.org/10.1016/j.robot.2016.12.005

20. Antonov, A., Fomin, A., Glazunov, V., Kiselev, S., Carbone, G.: Inverse and forward kinematics and workspace analysis of a novel 5-DOF (3T2R) parallel–serial (hybrid) manipulator. Int. J. Adv. Robot. Syst. **18**(2) (2021). https://doi.org/10.1177/1729881421992963
21. Pisla, D., Plitea, N., Gherman, B.G., Vaida, C., Pisla, A., Suciu, M.: Kinematics and design of a 5-DOF parallel robot used in minimally invasive surgery. In: Lenarčič, J., Stanišić, M. (eds.) Advances in Robot Kinematics: Motion in Man and Machine, pp. 1–12. Springer, Dordrecht (2010). https://doi.org/10.1007/978-90-481-9262-5_11
22. Reinaldo, C., Phu, S.N., Essomba, T., Nurahmi, L.: Kinematic comparisons of hybrid mechanisms for bone surgery: 3-PRP-3-RPS and 3-RPS-3-PRP. Machines. **10**(11), 979 (2022). https://doi.org/10.3390/machines10110979
23. Zhou, M., et al.: Towards robotic-assisted subretinal injection: a hybrid parallel–serial robot system design and preliminary evaluation. IEEE Trans. Ind. Electron. **67**(8), 6617–6628 (2020). https://doi.org/10.1109/TIE.2019.2937041
24. Elsamanty, M., et al.: Workspace analysis and path planning of a novel robot configuration with a 9-DOF serial-parallel hybrid manipulator (SPHM). Appl. Sci. **13**(4), 2088 (2023). https://doi.org/10.3390/app13042088
25. Diao, Y., Yao, L., Chen, Z., Zang, J., Luo, H.: Configuration and kinematic analysis of a novel hybrid surgical robot with a ball joint. In: Proceedings of the 2009 International Workshop on Intelligent Systems and Applications, Wuhan, China, pp. 1–4 (2009). https://doi.org/10.1109/IWISA.2009.5072790
26. Lin, G., Huang, P., Wang, M., Xu, Y., Zhang, R., Zhu, L.: An inverse kinematics solution for a series-parallel hybrid banana-harvesting robot based on deep reinforcement learning. Agronomy. **12**(9), 2157 (2022). https://doi.org/10.3390/agronomy12092157
27. Rahul, K., Raheman, H., Paradkar, V.: Design of a 4 DOF parallel robot arm and the firmware implementation on embedded system to transplant pot seedlings. Artif. Intell. Agric. **4**, 172–183 (2020). https://doi.org/10.1016/j.aiia.2020.09.003
28. Joubair, A., Zhao, L.F., Bigras, P., Bonev, I.: Absolute accuracy analysis and improvement of a hybrid 6-DOF medical robot. Ind. Robot. **42**(1), 44–53 (2015). https://doi.org/10.1108/IR-09-2014-0396
29. Yan, Z., Wang, Y., Liu, H., Xiao, J., Huang, T.: An improved data-driven calibration method with high efficiency for a 6-DOF hybrid robot. Machines. **11**(1), 31 (2023). https://doi.org/10.3390/machines11010031
30. Petelin, D., Fomin, A., Laryushkin, P., Fomina, O., Carbone, G., Ceccarelli, M.: Design, kinematics and workspace analysis of a novel 4-DOF kinematically redundant planar parallel grasping manipulator. Machines. **11**(3), 319 (2023). https://doi.org/10.3390/machines11030319

A Novel One-Degree-of-Freedom Deployable Unit Consisting of Four Parallelogram Linkages

Qizhi Meng(✉) and Andrés Kecskeméthy

Chair for Mechanics and Robotics, Faculty of Engineering, University of Duisburg-Essen, Duisburg 47057, Germany
mqz15@tsinghua.org.cn

Abstract. This paper proposes a novel one-degree-of-freedom (1-DOF) deployable unit consisting of four parallelogram linkages. The unit is constructed by combining two 2Pa-3R (Pa: parallelogram linkage, R: revolute joint) deployable mechanisms and removing their 3R linkages. The kinematic properties of the resulting unit mechanism in the initially assembled configuration are analyzed in a global coordinate frame. It is shown that the angles between the normal vectors of the four shared nodes between parallelogram linkages remain constant, which implies that each node possesses a radial reciprocating motion capability. Furthermore, the mobility of the mechanism is investigated to examine the global preservation of kinematic properties. The analysis demonstrates that the proposed deployable unit is a single-DOF mechanism. This mobility characteristic does not violate the initial assembly conditions, so several desirable properties are maintained throughout the motion: the four shared nodes perform reciprocating motions with respect to a fixed point in space, and each pair of opposite shared nodes exhibits only 1-DOF relative translation along their connecting line. These important properties provide a solid basis for applying the proposed unit in a wider range of deployable structures and functional modules.

Keywords: Deployable Unit · Parallelogram Linkage · Mechanism Design · Kinematic Analysis · 1-DOF Property · Radially Reciprocating Motion

1 Introduction

Deployable mechanisms are widely used in large space trusses, morphing civil structures, and programmable mechanical metamaterials. At the system level, many of these deployable structures are obtained by periodic assembly of basic deployable units. The kinematic and dynamic behaviors, as well as the packaging efficiency of the entire structure, are therefore strongly influenced by the unit design. In space engineering, unit-based deployable booms, antenna backup structures, and solar array supports enable stowing large functional apertures within a limited launch volume and controlled deployment in orbit [1, 2]. At smaller scales, unit cell concepts are used in mechanical metamaterials, where arrays of kinematic cells provide programmable shape changes and tunable mechanical responses [3, 4]. As a result, the synthesis of deployable units with excellent deployable performance and robust motion has become an important topic in mechanism and machine science.

© The Author(s), under exclusive license to Springer Nature Switzerland AG 2026
A. Chaker et al. (Eds.): EFIMMS 2026, MMS 205, pp. 76–86, 2026.
https://doi.org/10.1007/978-3-032-22270-1_8

Previous studies in deployable mechanisms have established several families of unit mechanisms that can be combined into larger deployable structures. Planar and spatial scissor-like elements, such as translational, polar, and angulated units, give simple bar-and-joint cells with clear geometric rules that are convenient for scaling [5, 6]. Hoberman-type angulated elements and their extensions have been applied to radially expanding domes and spherical mechanisms with large expansion ratios [7]. Another well-known family is based on overconstrained spatial linkages such as the Bennett mechanism. Networks of Bennett linkages can approximate cylindrical surfaces and have been used as deployable backbones for reflector antennas and other curved structures [8, 9]. These unit mechanisms have enabled many successful applications to deployable reflectors, cylindrical antennas, and adaptive roofs. At the same time, the three-dimensional joint layouts and mixed joint types in some of these units can increase manufacturing complexity and make modular integration more difficult.

In recent years, there has been increasing interest in deployable cellular mechanisms and modular units tailored to aerospace truss structures. Rigid-link basic units with good composability and deployment performance have been proposed, which can be assembled into regular polygonal prisms and ring-truss deployable mechanisms [10]. To improve reliability in the space environment, constant-height deployable mechanisms composed only of revolute joints have been introduced and used to construct deployable ring trusses for satellite mesh reflector antennas [11]. Deployable cellular structures based on pyramid and prism units have also been developed for large supporting trusses, along with modular assembly strategies featuring central and planar symmetry [12]. Furthermore, a type synthesis and structure screening approach for deployable cellular mechanisms has been proposed to guide the design and selection of unit topologies with favorable motion-force interaction performance [13]. These studies show that unit-level design is important not only for geometric deployability but also for motion and force transmission in large modular deployable systems.

Motivated by these developments, this paper proposes a novel 1-DOF deployable unit consisting of four parallelogram linkages. The resulting structure uses only revolute joints and has a symmetric motion pattern, which is attractive for truss- and cell-based deployable assemblies. The rest of the paper is organized as follows. Section 2 describes the construction of the proposed unit and its relation to the underlying 2Pa-3R mechanisms. Section 3 presents the global kinematic model based on a proximal variant of the Denavit-Hartenberg convention. Section 4 analyzes the properties in the initially assembled configuration. Section 5 studies the mobility over the workspace, with emphasis on the global preservation of geometric relationships between node planes. Section 6 provides kinematic simulations while Sect. 7 concludes the paper.

2 Construction of the Deployable Unit

In our previous work [10, 13], deployable mechanisms with 2Pa and 4R backbones have been proposed. These deployable mechanisms exhibit excellent deployment performance and modular expandability. Taking the 2Pa-3R mechanism as an example, as shown in Fig. 1, it is a closed-loop mechanism composed of two kinematic linkages, 2Pa and 3R, and contains 11 revolute joints in total. The four revolute joints located in

plane *HIML* form one planar parallelogram linkage, and the four revolute joints located in plane *IJNM* form the other planar parallelogram linkage. The three revolute joints located in plane *HJNL* constitute a planar 3R linkage. The top view of the 2Pa-3R mechanism is an isosceles triangle with vertex 2δ lying in plane *IHJ*. As shown in Fig. 1(b), the overall envelope of the 2Pa-3R mechanism is confined within a triangular prism bounded laterally by the planes *HIML*, *IJNM*, and *HJNL*. It should be emphasized that the closed-loop mechanism is symmetric with respect to the vertical plane *KIMP*, with points *K* and *P* being the midpoints of *HJ* and *LN*, respectively.

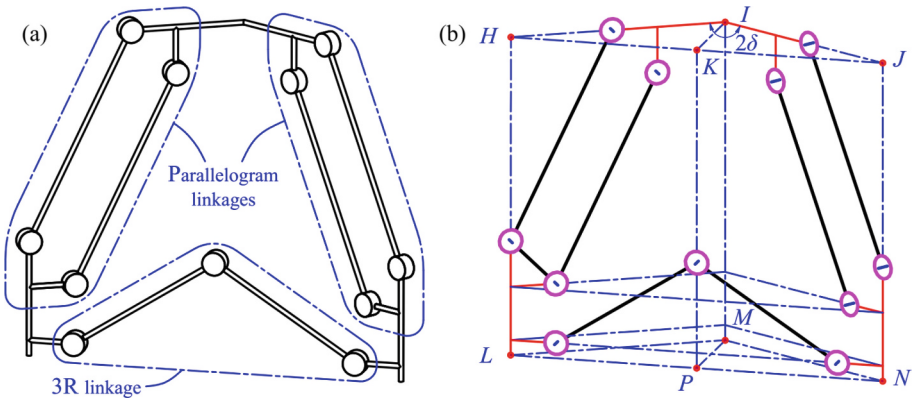

Fig. 1. The 2Pa-3R deployable mechanism: (a) 3D CAD model, (b) kinematic diagram.

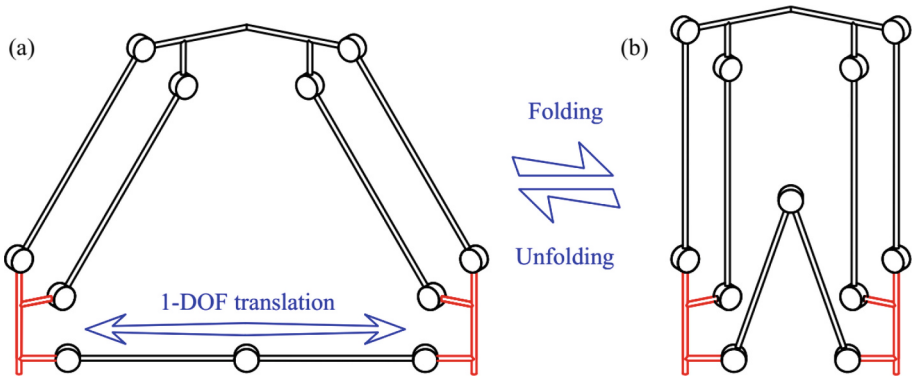

Fig. 2. 1-DOF translation property: (a) deployed configuration, (b) folded configuration.

In the previous work [10], it has been demonstrated that the 2Pa-3R deployable mechanism exhibits a 1-DOF property and possesses excellent deployment/stowage performance. Taking the lower left and right nodes as references, as illustrated in Fig. 2, the motion of the 2Pa-3R deployable mechanism can be characterized as a 1-DOF

translation along the line connecting these two nodes. Figure 2(a) and (b) show the deployed configuration and the folded configuration of the mechanism, respectively.

The construction of the deployable unit based on the 2Pa-3R deployable mechanism is described as follows. The procedure consists of three steps. First, two identical 2Pa-3R deployable mechanisms are arranged symmetrically with respect to the base triangle plane *LMN* shown in Fig. 1(b), one above and one below the base plane. Second, the two 2Pa-3R mechanisms are rotated by a certain angle about the line *LN* so that their corresponding edges *LH* are no longer collinear, thereby forming the intermediate 2-[2Pa-3R] mechanism shown in Fig. 3(a). Finally, the two 3R linkages in the 2Pa-3R mechanisms are removed, resulting in a deployable unit composed of four parallelogram linkages. As shown in Fig. 3(b), owing to this structural feature, this unit is hereafter referred to as the 4Pa (Pa: parallelogram linkages) deployable unit.

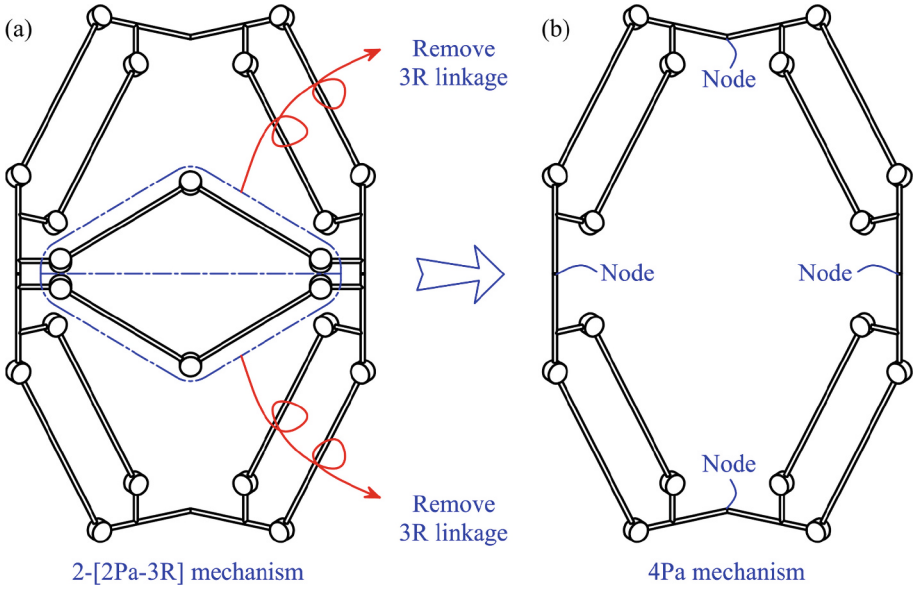

Fig. 3. Construction of the deployable unit consisting of four parallelogram linkages by integrating two 2Pa-3R mechanisms and then removing two 3R linkages: (a) the intermediate 2-[2Pa-3R] mechanism, (b) the constructed 4Pa deployable unit with four shared nodes.

It is readily observed that the constructed 4Pa deployable unit exhibits a high degree of symmetry, possessing both a vertical and a horizontal plane of symmetry. If, during the construction process, the two adopted 2Pa-3R mechanisms are not identical, the resulting 4Pa deployable unit will retain only a single plane of symmetry, which coincides with that of the original 2Pa-3R mechanisms, namely the vertical plane *KIMP* shown in Fig. 1(b). In the following, the analysis is carried out for the 4Pa deployable unit with two planes of symmetry.

3 Structural Equations of the Deployable Unit

To formulate the structural equations and develop the kinematic model, the 4Pa deployable unit is regarded as a closed-loop mechanism composed of two 2Pa limbs, namely a left 2Pa limb and a right 2Pa limb. The coordinate frames are assigned according to the proximal Denavit-Hartenberg (DH) convention, as illustrated in Fig. 4. The $\boldsymbol{Z}_i$ or $\boldsymbol{Z}'_i$-axes are aligned with the axes of the revolute joints, the $\boldsymbol{X}_i$ or $\boldsymbol{X}'_i$-axes are chosen along the common perpendiculars between $\boldsymbol{Z}_i$ and $\boldsymbol{Z}_{i+1}$ (or between $\boldsymbol{Z}'_i$ and $\boldsymbol{Z}'_{i+1}$), and the $\boldsymbol{Y}_i$ or $\boldsymbol{Y}'_i$-axes are determined by the right-hand rule.

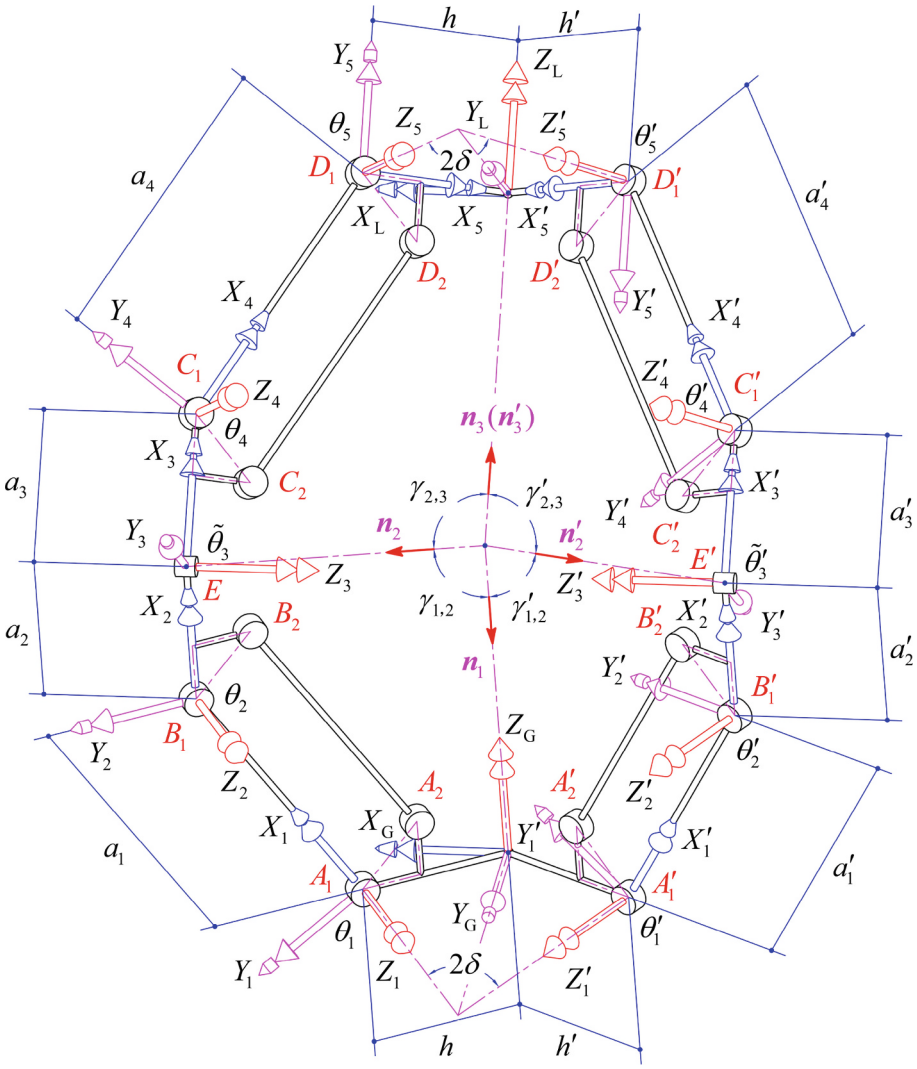

Fig. 4. Coordinate system definition and geometric parameters of the 4Pa deployable unit.

The origin of the global coordinate frame is located at point I of the lower 2Pa-3R mechanism, as shown in Fig. 1(b). The $\boldsymbol{X}_{\mathrm{G}}\boldsymbol{Y}_{\mathrm{G}}$-plane lies in the plane containing the axes of joints A_1 and A_1', and $\boldsymbol{Y}_{\mathrm{G}}$ is chosen as the bisector of angle $\angle A_1IA_1'$. The origin of the local coordinate frame is located at point I of the upper 2Pa-3R mechanism, also indicated in Fig. 1(b). The $\boldsymbol{X}_{\mathrm{L}}\boldsymbol{Y}_{\mathrm{L}}$-plane lies in the plane containing the axes of joints D_1 and D_1', and $\boldsymbol{Y}_{\mathrm{L}}$ is chosen as the bisector of angle $\angle D_1ID_1'$.

It should be noted that, for modeling convenience, the revolute joints associated with axes $\boldsymbol{Z}_3$ and $\boldsymbol{Z}_3'$ are introduced as virtual joints. They correspond to the relative rotations imposed in the construction of the 4Pa deployable unit. Once the construction is completed, the associated joint variables $\tilde{\theta}_3$ and $\tilde{\theta}_3'$ become fixed parameters and do not change during the motion of the mechanism.

Define $\boldsymbol{Z}_i(\theta;\ d)$ as the homogeneous transformation representing a rotation of angle θ about the $\boldsymbol{Z}_i$-axis, followed by a translation of distance d along the same axis. Its matrix form is given by

$$\boldsymbol{Z}_i(\theta;\ d) = \begin{bmatrix} \cos\theta & -\sin\theta & 0 & 0 \\ \sin\theta & \cos\theta & 0 & 0 \\ 0 & 0 & 1 & d \\ 0 & 0 & 0 & 1 \end{bmatrix} \tag{1}$$

Similarly, define $\boldsymbol{X}_i(\alpha;\ a)$ as the homogeneous transformation representing a rotation of angle α about the $\boldsymbol{X}_i$-axis, followed by a translation of distance a along the $\boldsymbol{X}_i$-axis. The corresponding matrix can be written as

$$\boldsymbol{X}_i(\alpha;\ a) = \begin{bmatrix} 1 & 0 & 0 & a \\ 0 & \cos\alpha & -\sin\alpha & 0 \\ 0 & \sin\alpha & \cos\alpha & 0 \\ 0 & 0 & 0 & 1 \end{bmatrix} \tag{2}$$

Accordingly, for 2Pa limb 1, the homogeneous transformation from frame G to frame L can be expressed as

$${}^{\mathrm{G}}\boldsymbol{T}_{\mathrm{L}} = {}^{\mathrm{G}}\boldsymbol{T}_0\,{}^0\boldsymbol{A}_1\,{}^1\boldsymbol{A}_2\,{}^2\boldsymbol{A}_3\,{}^3\boldsymbol{A}_4\,{}^4\boldsymbol{A}_5\,{}^5\boldsymbol{T}_{\mathrm{L}} \tag{3}$$

where

$$\begin{cases} {}^{\mathrm{G}}\boldsymbol{T}_0 = \boldsymbol{Z}_{\mathrm{G}}(\delta;\ 0) \\ {}^0\boldsymbol{A}_1 = \boldsymbol{X}_0(-\pi/2;\ h)\boldsymbol{Z}_1(-\theta_1;\ 0) \\ {}^1\boldsymbol{A}_2 = \boldsymbol{X}_1(0;\ a_1)\boldsymbol{Z}_2(-\theta_2;\ 0) \\ {}^2\boldsymbol{A}_3 = \boldsymbol{X}_2(\pi/2-\delta;\ a_2)\boldsymbol{Z}_3(-\tilde{\theta}_3;\ 0) \\ {}^3\boldsymbol{A}_4 = \boldsymbol{X}_3(-(\pi/2-\delta);\ a_3)\boldsymbol{Z}_4(-\theta_4;\ 0) \\ {}^4\boldsymbol{T}_5 = \boldsymbol{X}_4(0;\ a_4)\boldsymbol{Z}_5(-\theta_5;\ 0) \\ {}^5\boldsymbol{T}_{\mathrm{L}} = \boldsymbol{X}_5(-\pi/2;\ h)\boldsymbol{Z}_{\mathrm{L}}(\pi-\delta;\ 0) \end{cases} \tag{4}$$

In the same manner, for 2Pa limb 2, we have

$${}^{\mathrm{G}}\boldsymbol{T}_{\mathrm{L}} = {}^{\mathrm{G}}\boldsymbol{T}'_0\,{}^0\boldsymbol{A}'_1\,{}^1\boldsymbol{A}'_2\,{}^2\boldsymbol{A}'_3\,{}^3\boldsymbol{A}'_4\,{}^4\boldsymbol{A}'_5\,{}^5\boldsymbol{T}'_{\mathrm{L}} \tag{5}$$

where

$$\begin{cases} {}^{\mathrm{G}}\boldsymbol{T}'_0 = \boldsymbol{Z}'_{\mathrm{G}}\big(\pi - \delta;\, 0\big) \\ {}^{0}\boldsymbol{A}'_1 = \boldsymbol{X}'_0\big(\pi/2;\, h'_1\big)\boldsymbol{Z}'_1\big(\theta'_1;\, 0\big) \\ {}^{1}\boldsymbol{A}'_2 = \boldsymbol{X}'_1\big(0;\, a'_1\big)\boldsymbol{Z}'_2\big(\theta'_2;\, 0\big) \\ {}^{2}\boldsymbol{A}'_3 = \boldsymbol{X}'_2\big(-(\pi/2 - \delta);\, 0\big)\boldsymbol{Z}'_3\big(\tilde{\theta}'_3;\, 0\big) \\ {}^{3}\boldsymbol{A}'_4 = \boldsymbol{X}'_3\big(\pi/2 - \delta;\, a'_3\big)\boldsymbol{Z}'_4\big(\theta'_4;\, 0\big) \\ {}^{4}\boldsymbol{T}'_5 = \boldsymbol{X}'_4\big(0;\, a'_4\big)\boldsymbol{Z}'_5\big(\theta'_5;\, 0\big) \\ {}^{5}\boldsymbol{T}'_{\mathrm{L}} = \boldsymbol{X}'_5\big(\pi/2;\, h'\big)\boldsymbol{Z}'_{\mathrm{L}}\big(\delta;\, 0\big) \end{cases} \tag{6}$$

Therefore, the loop-closure condition of the 4Pa deployable unit can be written as

$${}^{\mathrm{G}}\boldsymbol{T}_0{}^{0}\boldsymbol{A}_1{}^{1}\boldsymbol{A}_2{}^{2}\boldsymbol{A}_3{}^{3}\boldsymbol{A}_4{}^{4}\boldsymbol{A}_5{}^{5}\boldsymbol{T}_{\mathrm{L}} = {}^{\mathrm{G}}\boldsymbol{T}'_0{}^{0}\boldsymbol{A}'_1{}^{1}\boldsymbol{A}'_2{}^{2}\boldsymbol{A}'_3{}^{3}\boldsymbol{A}'_4{}^{4}\boldsymbol{A}'_5{}^{5}\boldsymbol{T}'_{\mathrm{L}} \tag{7}$$

4 Kinematic Properties in Initially Assembled Configuration

Under the initially assembled configuration, the unit mechanism is symmetric with respect to both the left-right and upper-lower halves. Hence the following relations hold: $\tilde{\theta}_3 = \tilde{\theta}'_3, \theta_1 = \theta'_1 = \theta_5 = \theta'_5 = \theta, \theta_2 = \theta'_2 = \theta_4 = \theta'_4 = \pi/2 - \theta$.

We next examine the normal vectors of the four node planes. For 2Pa limb 1, the four relevant normal vectors are

$$\begin{cases} \boldsymbol{n}_1 = \begin{bmatrix} 0 & 0 & -1 \end{bmatrix}^{\mathrm{T}} \\ \begin{bmatrix} \boldsymbol{n}_3^{\mathrm{T}} & 0 \end{bmatrix}^{\mathrm{T}} = {}^{\mathrm{G}}\boldsymbol{T}_0{}^{0}\boldsymbol{A}_1{}^{1}\boldsymbol{A}_2{}^{2}\boldsymbol{A}_3{}^{3}\boldsymbol{A}_4{}^{4}\boldsymbol{A}_5{}^{5}\boldsymbol{T}_{\mathrm{L}}\begin{bmatrix} z_{\mathrm{L}}^{\mathrm{T}} & 0 \end{bmatrix}^{\mathrm{T}}, z_{\mathrm{L}}^{\mathrm{T}} = \begin{bmatrix} 0 & 0 & 1 \end{bmatrix}^{\mathrm{T}} \\ \begin{bmatrix} \big(z_2^{\mathrm{G}}\big)^{\mathrm{T}} & 0 \end{bmatrix}^{\mathrm{T}} = {}^{\mathrm{G}}\boldsymbol{T}_0{}^{0}\boldsymbol{A}_1{}^{1}\boldsymbol{A}_2\begin{bmatrix} z_2^{\mathrm{T}} & 0 \end{bmatrix}^{\mathrm{T}}, z_2^{\mathrm{T}} = \begin{bmatrix} 0 & 0 & 1 \end{bmatrix}^{\mathrm{T}} \\ \begin{bmatrix} \big(z_4^{\mathrm{G}}\big)^{\mathrm{T}} & 0 \end{bmatrix}^{\mathrm{T}} = {}^{\mathrm{G}}\boldsymbol{T}_0{}^{0}\boldsymbol{A}_1{}^{1}\boldsymbol{A}_2{}^{2}\boldsymbol{A}_3{}^{3}\boldsymbol{A}_4\begin{bmatrix} z_4^{\mathrm{T}} & 0 \end{bmatrix}^{\mathrm{T}}, z_4^{\mathrm{T}} = \begin{bmatrix} 0 & 0 & 1 \end{bmatrix}^{\mathrm{T}} \end{cases} . \tag{8}$$

Defining $\boldsymbol{n}_2 = z_2^{\mathrm{G}} \times z_4^{\mathrm{G}}$, we have

$$\boldsymbol{n}_2 = \cos\delta\big[\cos\delta\sin\tilde{\theta}_3 \;\; \sin\delta\sin\tilde{\theta}_3 \;\; \sin\delta\big(1 - \cos\tilde{\theta}_3\big)\big]^{\mathrm{T}} \tag{9}$$

We then consider the corresponding normal vectors for 2Pa limb 2. The three relevant normal vectors are

$$\begin{cases} \begin{bmatrix} \boldsymbol{n}'^{\mathrm{T}}_3 & 0 \end{bmatrix}^{\mathrm{T}} = {}^{\mathrm{G}}\boldsymbol{T}'_0{}^{0}\boldsymbol{A}'_1{}^{1}\boldsymbol{A}'_2{}^{2}\boldsymbol{A}'_3{}^{3}\boldsymbol{A}'_4{}^{4}\boldsymbol{A}'_5{}^{5}\boldsymbol{T}'_{\mathrm{L}}\begin{bmatrix} z_{\mathrm{L}}^{\mathrm{T}} & 0 \end{bmatrix}^{\mathrm{T}}, z_{\mathrm{L}}^{\mathrm{T}} = \begin{bmatrix} 0 & 0 & 1 \end{bmatrix}^{\mathrm{T}} \\ \begin{bmatrix} \big(z'^{\mathrm{G}}_2\big)^{\mathrm{T}} & 0 \end{bmatrix}^{\mathrm{T}} = {}^{\mathrm{G}}\boldsymbol{T}'_0{}^{0}\boldsymbol{A}'_1{}^{1}\boldsymbol{A}'_2\begin{bmatrix} z'^{\mathrm{T}}_2 & 0 \end{bmatrix}^{\mathrm{T}}, z'^{\mathrm{T}}_2 = \begin{bmatrix} 0 & 0 & 1 \end{bmatrix}^{\mathrm{T}} \\ \begin{bmatrix} \big(z'^{\mathrm{G}}_4\big)^{\mathrm{T}} & 0 \end{bmatrix}^{\mathrm{T}} = {}^{\mathrm{G}}\boldsymbol{T}'_0{}^{0}\boldsymbol{A}'_1{}^{1}\boldsymbol{A}'_2{}^{2}\boldsymbol{A}'_3{}^{3}\boldsymbol{A}'_4\begin{bmatrix} z'^{\mathrm{T}}_4 & 0 \end{bmatrix}^{\mathrm{T}}, z'^{\mathrm{T}}_4 = \begin{bmatrix} 0 & 0 & 1 \end{bmatrix}^{\mathrm{T}} \end{cases} \tag{10}$$

Defining $\boldsymbol{n}'_2 = -z'^{\mathrm{G}}_2 \times z'^{\mathrm{G}}_4$, we have

$$\boldsymbol{n}'_2 = \cos\delta\big[-\cos\delta\sin\tilde{\theta}'_3 \;\; \sin\delta\sin\tilde{\theta}'_3 \;\; \sin\delta\big(1 - \cos\tilde{\theta}'_3\big)\big]^{\mathrm{T}} \tag{11}$$

Combining Eqs. (8), (9), (10) and (11) it follows that, in the initially assembled configuration,

$$\boldsymbol{n}_2^{\mathrm{T}}\boldsymbol{n}_1 = \boldsymbol{n}_2^{\mathrm{T}}\boldsymbol{n}_3 = \boldsymbol{n'}_2^{\mathrm{T}}\boldsymbol{n}_1 = \boldsymbol{n'}_2^{\mathrm{T}}\boldsymbol{n}'_3 \equiv \sin\delta\cos\delta\left(\cos\tilde{\theta}'_3 - 1\right) \tag{12}$$

which depends only on the structural parameters. Consequently, the angles between adjacent normal vectors satisfy

$$\gamma_{1,2} = \gamma_{2,3} = \gamma'_{1,2} = \gamma'_{2,3} \tag{13}$$

The above results describe the kinematic properties of the unit in the initially assembled configuration. In the next section, these properties will be examined over the entire workspace in order to determine whether they are preserved globally, which requires a mobility analysis of the mechanism.

5 Global Invariance of Kinematic Properties

Since limbs 1 and 2 are each composed of two parallelogram linkages, it is known from Ref. [10] that a planar parallelogram is a 1-DOF mechanism and that the velocity of the short coupler link is perpendicular to both the revolute-joint axes and the long links. In 2Pa limb 1, the velocity direction of the parallelogram $A_1B_1B_2A_2$ is along the $\boldsymbol{Y}_1$-axis, and the velocity direction of the parallelogram $C_1D_1D_2C_2$ is along the $\boldsymbol{Y}_4$-axis. Hence, the direction of the constraint force is along $\boldsymbol{Y}_1^G \times \boldsymbol{Y}_4^G$, where

$$\begin{cases} \left[\left(\boldsymbol{Y}_1^{\mathrm{G}}\right)^{\mathrm{T}}\ 0\right]^{\mathrm{T}} = {}^{\mathrm{G}}\boldsymbol{T}_0{}^0\boldsymbol{A}_1\left[\boldsymbol{Y}_1^{\mathrm{T}}\ 0\right]^{\mathrm{T}}, \boldsymbol{Y}_1^{\mathrm{T}} = \left[0\ 0\ 1\right]^{\mathrm{T}} \\ \left[\left(\boldsymbol{Y}_4^{\mathrm{G}}\right)^{\mathrm{T}}\ 0\right]^{\mathrm{T}} = {}^{\mathrm{G}}\boldsymbol{T}_0{}^0\boldsymbol{A}_1{}^1\boldsymbol{A}_2{}^2\boldsymbol{A}_3{}^3\boldsymbol{A}_4\left[\boldsymbol{Y}_4^{\mathrm{T}}\ 0\right]^{\mathrm{T}}, \boldsymbol{Y}_4^{\mathrm{T}} = \left[0\ 0\ 1\right]^{\mathrm{T}} \end{cases} \tag{14}$$

In 2Pa limb 2, the velocity direction of the parallelogram $A'_1B'_1B'_2A'_2$ is along the $\boldsymbol{Y}'_1$-axis, and that of the parallelogram $C'_1D'_1D'_2C'_2$ is along the $\boldsymbol{Y}'_4$-axis. Thus, the direction of the constraint force is along $\boldsymbol{Y}'^{\mathrm{G}}_1 \times \boldsymbol{Y}'^{\mathrm{G}}_4$, where

$$\begin{cases} \left[\left(\boldsymbol{Y}'^{\mathrm{G}}_1\right)^{\mathrm{T}}\ 0\right]^{\mathrm{T}} = {}^{\mathrm{G}}\boldsymbol{T}'_0{}^0\boldsymbol{A}'_1\left[\boldsymbol{Y}'^{\mathrm{T}}_1\ 0\right]^{\mathrm{T}}, \boldsymbol{Y}'^{\mathrm{T}}_1 = \left[0\ 0\ 1\right]^{\mathrm{T}} \\ \left[\left(\boldsymbol{Y}'^{\mathrm{G}}_4\right)^{\mathrm{T}}\ 0\right]^{\mathrm{T}} = {}^{\mathrm{G}}\boldsymbol{T}'_0{}^0\boldsymbol{A}'_1{}^1\boldsymbol{A}'_2{}^2\boldsymbol{A}'_3{}^3\boldsymbol{A}'_4\left[\boldsymbol{Y}'^{\mathrm{T}}_4\ 0\right]^{\mathrm{T}}, \boldsymbol{Y}'^{\mathrm{T}}_4 = \left[0\ 0\ 1\right]^{\mathrm{T}} \end{cases} \tag{15}$$

The velocity direction of the end connection between limbs 1 and 2 is therefore $\boldsymbol{V} = \left(\boldsymbol{Y}_1^{\mathrm{G}} \times \boldsymbol{Y}_4^{\mathrm{G}}\right) \times \left(\boldsymbol{Y}'^{\mathrm{G}}_1 \times \boldsymbol{Y}'^{\mathrm{G}}_4\right)$, which is calculated as

$$\boldsymbol{V} = kp\left[0\ -\sin\tilde{\xi}\ \cos\tilde{\xi}\right]^{\mathrm{T}} \tag{16}$$

where

$$\tilde{\xi} = \tilde{\theta}_3/2 \tag{17}$$

$$k = 2\cos\delta\sin\theta\left(\sin^2\delta\sin^2\theta\sin\tilde{\theta}_3 + 2\sin\delta\sin\theta\cos\theta\cos\tilde{\theta}_3 - \sin\tilde{\theta}_3\cos^2\theta\right) \quad (18)$$

$$p = 2\left(\sin\delta\sin\theta\sin\tilde{\xi} + \cos\theta\cos\tilde{\xi}\right) \quad (19)$$

We next derive the position of the origin of the local frame L with respect to the global frame G. Its homogeneous representation is

$$\left[\left(\boldsymbol{O}_{\mathrm{L}}^{\mathrm{G}}\right)^{\mathrm{T}}\ 1\right]^{\mathrm{T}} = {}^{\mathrm{G}}\boldsymbol{T}'_0{}^0\boldsymbol{A}'_1{}^1\boldsymbol{A}'_2{}^2\boldsymbol{A}'_3{}^3\boldsymbol{A}'_4\left[\boldsymbol{O}_{\mathrm{L}}\ 1\right]^{\mathrm{T}}, \boldsymbol{O}_{\mathrm{L}} = \left[0\ 0\ 0\right]^{\mathrm{T}}, \quad (20)$$

from which we obtain

$$\boldsymbol{O}_{\mathrm{L}}^{\mathrm{G}} = q\left[0\ -\sin\tilde{\xi}\ \cos\tilde{\xi}\right]^{\mathrm{T}} \quad (21)$$

where

$$q = -2\left(a_1\sin\delta\cos\theta\sin\tilde{\xi} - a_1\sin\theta\cos\tilde{\xi} - b_1\cos\tilde{\xi} + h\sin\delta\sin\tilde{\xi}\right) \quad (22)$$

Comparing Eqs. (16) and (21) it is seen that the end-effector has 1-DOF with respect to the base frame, as long as the coefficients k, p, and q do not vanish. This mobility corresponds to a one-dimensional translational motion, and the velocity direction is along $\boldsymbol{O}_L^G$. Hence, the mobility of the mechanism does not alter the initially assembled configuration, i.e., Eq. (13) remains valid in its workspace. The proposed deployable unit therefore possesses a radial reciprocating motion capability. Figure 5 provides a visual demonstration of its motion capability.

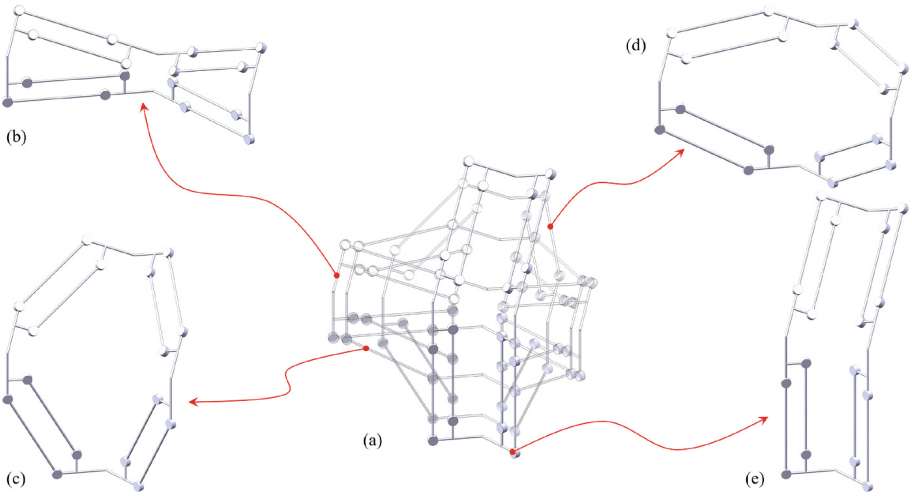

Fig. 5. Configurations of the CAD models in SolidWorks of the 4Pa deployable unit: (a) Combinatorial model, (b) $\theta = 0°$, (c) $\theta = 30°$, (d) $\theta = 60°$, and (e) $\theta = 90°$.

6 Kinematic Simulations of the 4Pa Deployable Unit

To validate the established structural equations and the kinematic model, kinematic simulations of the 4Pa deployable mechanism are carried out in MATLAB R2021a. The geometric parameters used in the simulations are listed in Table 1. Configurations of the 4Pa deployable unit with $\theta = 0°$, $30°$, $60°$, and $90°$ are shown in Fig. 6, where the out-loop joints are plotted only to display clearly. It can be observed that the configurations exhibit the motion characteristics predicted by the preceding analysis.

Table 1. Geometric parameters and their values of the 4Pa deployable unit.

Geometric Parameters	Notations	Values	Unit
$A_1B_1 = C_1D_1 = A_1'B_1' = C_1'D_1'$	$a_1 = a_4 = a_1' = a_4'$	30	mm
$B_1E = C_1E = B_1'E' = C_1'E'$	$a_2 = a_3 = a_2' = a_3'$	8	mm
$O_GA_1 = O_GA_1' = O_LD_1 = O_LD_1'$	$h = h'$	5	mm
$\angle(\boldsymbol{X}_2, \boldsymbol{X}_3) = \angle(\boldsymbol{X}_2', \boldsymbol{X}_3')$	$\tilde{\theta}_3 = \tilde{\theta}_3'$	30	°
$\angle(\boldsymbol{Y}_G, \boldsymbol{Z}_1) = \angle(\boldsymbol{Y}_G', \boldsymbol{Z}_1')$	δ	30	°

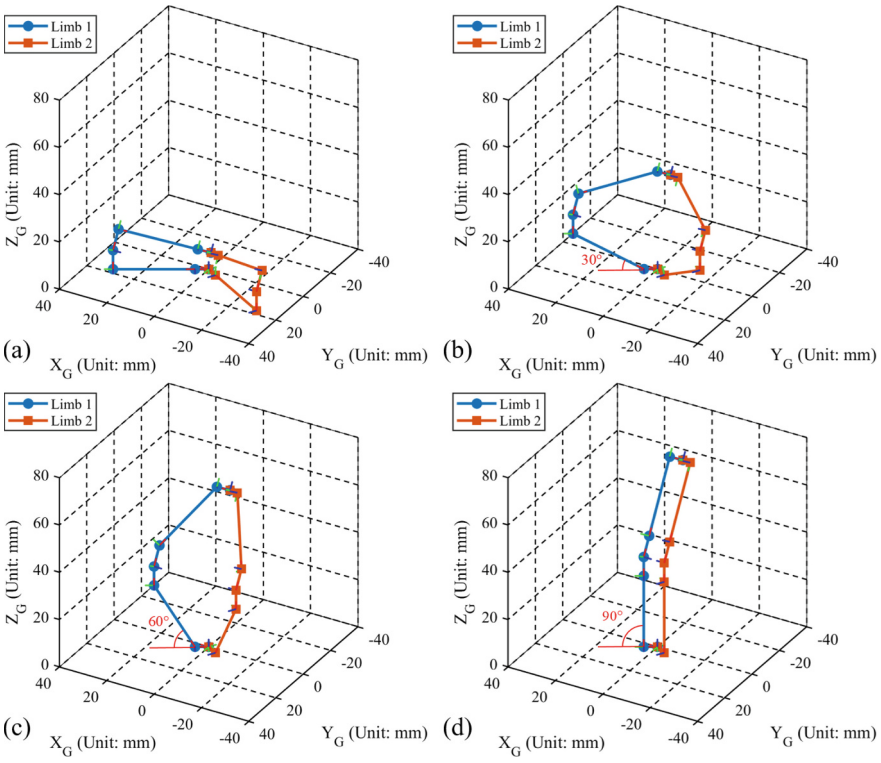

Fig. 6. Configurations of the 4Pa deployable unit under conditions of $\theta_1 = \theta_1' = \theta_5 = \theta_5' = \theta$ and $\theta_2 = \theta_2' = \theta_4 = \theta_4' = \pi/2 - \theta$ (a) $\theta = 0°$, (b) $\theta = 30°$, (c) $\theta = 60°$, and (d) $\theta = 90°$.

7 Conclusions

This paper presented a novel 1-DOF deployable unit consisting of four parallelogram linkages, obtained by combining two 2Pa-3R deployable mechanisms and removing their 3R linkages. Using a global-frame kinematic model, it was shown that in the initially assembled configuration, the angles between the normal vectors of the four node planes remain constant, indicating a radial reciprocating motion of the nodes with respect to a fixed point. A mobility analysis confirmed that the mechanism has a single DOF. These properties provide a promising basis for using the proposed 4Pa deployable unit as a building block in deployable trusses and functional modules.

Acknowledgments. The first author, Qizhi Meng, acknowledges the support by a Fellowship from the Alexander von Humboldt (AvH) Foundation of Germany. We acknowledge support by the Open Access Publication Fund of the University of Duisburg-Essen.

References

1. Wang, B., Zhu, J., Zhong, S., Liang, W., Guan, C.: Space deployable mechanics: a review of structures and smart driving. Mater. Des. **237**, 112557 (2024)
2. Sauder, J., Gebara, C., Reddy, N.H., García-Mora, C.J.: A framework for small satellite deployable structures and how to deploy them reliably. Commun. Eng. **3**, 72 (2024)
3. Meng, Z., Liu, M., Yan, H., Genin, G.M., Chen, C.Q.: Deployable mechanical metamaterials with multistep programmable transformation. Sci. Adv. **8**(23), eabn5460 (2022)
4. Silverberg, J.L., et al.: Using origami design principles to fold reprogrammable mechanical metamaterials. Science. **345**, 647–650 (2014)
5. Roovers, K., De Temmerman, N.: Deployable scissor grids consisting of translational units. Int. J. Solids Struct. **121**, 45–61 (2017)
6. Liao, Y., Krishnan, S.: Deployable scissor structures: classification of modifications and applications. Autom. Constr. **165**, 105547 (2024)
7. Cai, J., Xu, Y., Feng, J.: Kinematic analysis of Hoberman's linkages with the screw theory. Mech. Mach. Theory. **63**, 28–34 (2013)
8. Lu, S., Zlatanov, D., Ding, X.: Approximation of cylindrical surfaces with deployable Bennett networks. J. Mech. Robot. **9**(2), 021001 (2017)
9. Chen, Y., You, Z.: Mobile assemblies based on the Bennett linkage. Proc. R. Soc. A: Math. Phys. Eng. Sci. **461**, 1229–1245 (2005)
10. Meng, Q., Liu, X.-J., Xie, F.: Structure design and kinematic analysis of a class of ring truss deployable mechanisms for satellite antennas based on novel basic units. Mech. Mach. Theory. **174**, 104881 (2022)
11. Meng, Q., Tang, R., Liu, X.-J.: Novel constant-height deployable mechanisms with only revolute joints and constructed deployable ring trusses for satellite mesh reflector antennas. Mech. Mach. Theory. **200**, 105718 (2024)
12. Meng, Q., Jiang, M., Ceccarelli, M.: Deployable cellular structures of pyramids and prisms for construction of large-scale deployable supporting trusses. Mech. Mach. Theory. **209**, 106001 (2025)
13. Meng, Q., Ceccarelli, M.: Type synthesis and structure screening of deployable cellular mechanisms based on the graphical method and motion-force interaction performance. Mech. Mach. Theory. **205**, 105893 (2025)

A Bio-Inspired Tendon-Driven Morphing Hydrofoil: Design, Modeling, and Variable Stiffness Characterization

Xin Wang[1], Bai Chen[1], Jie Ling[1], Tianwei Zhang[2,3], and Yayi Shen[1,4](✉)

[1] College of Mechanical and Electrical Engineering, Nanjing University of Aeronautics and Astronautics, Nanjing, China
yayi.shen@nuaa.edu.cn
[2] The Shenzhen Institute of Artificial Intelligence and Robotics for Society, Shenzhen, China
[3] The Chinese University of Hong Kong - Shenzhen, Shenzhen, China
[4] National Key Laboratory of Helicopter Aeromechanics, Nanjing, China

Abstract. Bio-inspired flapping propulsion offers remarkable hydrodynamic efficiency; however, replicating the complex active hydro-elastic behaviors of biological swimmers, such as penguins, remains a significant robotic challenge. Existing rigid or passively flexible foils often fail to exploit the full potential of real-time stiffness modulation. To address this, this paper presents a novel bio-inspired morphing hydrofoil featuring a tendon-driven articulated structure that mimics the penguin's carpal joint. We establish a comprehensive theoretical framework coupling multi-body kinematics with continuum stiffness analysis to guide the design. A specialized core-to-skin multi-material fabrication process is developed, integrating a rigid transmission system within a gradient-stiffness silicone body. Experimental characterization validates the mechanism's ability to actively decouple structural stiffness from geometric configuration, achieving a tunable stiffness range. Furthermore, preliminary unsteady hydrodynamic simulations demonstrate that the active morphing mode generates superior thrust profiles compared to fixed-stiffness baselines. This work provides a compact and robust solution for next-generation variable-stiffness underwater propulsion.

Keywords: Bio-inspired Robotics · Underwater Propulsion · Flapping Foil · Variable Stiffness · Morphing Mechanism · Tendon-driven

1 Introduction

Underwater propulsion constitutes a cornerstone technology for diverse maritime applications, ranging from deep-sea exploration and environmental monitoring to infrastructure inspection and defense operations, primarily executed

This work was partially supported by the National Natural Science Foundation of China (Grant No. 62503223) and the Fundamental Research Funds for the Central Universities (Grant No.NG2025001).

© The Author(s), under exclusive license to Springer Nature Switzerland AG 2026
A. Chaker et al. (Eds.): EFIMMS 2026, MMS 205, pp. 87–96, 2026.
https://doi.org/10.1007/978-3-032-22270-1_9

by Autonomous Underwater Vehicles (AUVs) and Remotely Operated Vehicles (ROVs) [7]. For decades, these platforms have predominantly relied on conventional screw propellers. While effective for steady-state cruising, rotary thrusters exhibit inherent limitations regarding low-speed maneuverability and generate significant acoustic signatures, which can interfere with sensitive scientific instrumentation and compromise stealth capabilities [14].

In contrast, bio-inspired flapping foil propulsion, emulating the locomotion of highly efficient swimmers such as manta rays, sea turtles, penguins, and cetaceans, presents a transformative alternative [3,4,13,16]. This paradigm offers superior agility, reduced noise emission, and minimized wake turbulence. Crucially, the hydrodynamic efficiency of biological swimmers stems not merely from rigid oscillations, but from complex hydroelastic behaviors—specifically, the active bending and twisting deformations that optimize flow interaction throughout the stroke cycle [8]. The intricate undulatory kinematics of a penguin's wing or the flexible deformation of a fish tail enable these creatures to achieve unparalleled propulsive efficiency [5,9], serving as the fundamental inspiration for next-generation underwater propulsion systems [4].

Despite the potential of bio-mimetic propulsion, significant challenges remain in replicating these biological capabilities. Existing research has largely focused on rigid foils executing combined heaving and pitching motions [1], or foils exhibiting passive flexibility that deform solely under hydrodynamic loading. While recent advancements in rigid-flexible-soft coupled designs have demonstrated remarkable efficacy in achieving structural compactness and minimizing dimensional coupling for kinematic modeling [17], a distinct research gap persists. Although morphing wings are well-established in the literature concerning rajiform swimmers like manta rays [2,11], the systematic analysis of active flexibility and its integration into the rigid-limb flapping mechanisms of sea turtles and penguins has received limited attention [12].

A critical barrier to advancing this field lies in integrating large-amplitude active deformation with real-time stiffness control within a compact form factor [15]. Current attempts utilizing homogeneous soft materials or composite structures often suffer from a lack of deep bio-mimetic morphological fidelity, failing to fully exploit the potential of active flow control [6,10]. Furthermore, existing active morphing solutions frequently rely on complex actuation architectures that compromise system durability and complicate waterproofing. Consequently, there is a pressing need for a robust, simplified design capable of achieving targeted kinematics under large deformations, supported by an experimental framework to validate its hydrodynamic advantages.

Addressing these challenges, this paper presents the design and realization of a bio-inspired flexible flapping foil driven by an active tendon mechanism. Drawing upon the anatomical observations of penguin wings, the proposed system employs a lightweight cable-driven transmission combined with a strategic distribution of rigid and compliant materials to replicate the dynamic stiffness modulation and active bending characteristics of biological flippers. A dedicated two-degree-of-freedom (2-DOF) experimental platform was constructed to evaluate the prototype, providing empirical validation of the performance enhance-

ments yielded by the active bending design. This work offers a compact and effective solution for active variable-stiffness propulsion, laying a solid foundation for the future implementation of real-time control strategies and model-based optimization in bio-mimetic AUVs.

2 Theoretical Framework

This section outlines the mathematical principles guiding the bio-mimetic design. We establish a linkage-based kinematic model to map the articulated structure, a stiffness formulation to justify the tendon-driven modulation, and an unsteady hydrodynamic model to predict propulsive forces.

2.1 Kinematic Modeling of the Articulated Foil

To replicate the penguin's wing morphology, the foil is modeled as a two-segment articulated linkage. We define a body-fixed coordinate system where the x-axis aligns with the swimming direction and the y-axis with the span. The motion comprises a primary flapping rotation $\phi(t)$ around the x-axis, a feathering rotation $\theta(t)$ around the y-axis, and an active bending deflection $\gamma(t)$ at the discrete joint located at spanwise distance L_0.

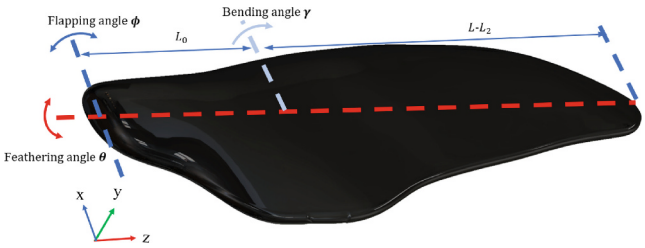

Fig. 1. Kinematic and structural configuration of the articulated foil.

The spatial trajectory of the wingtip (y_{tip}, z_{tip}) in the transverse plane is derived by summing the vectors of the rigid proximal segment (length L_0) and the flexible distal segment (length $L - L_0$):

$$y_{tip}(t) = L_0 \cos(\phi(t)) + (L - L_0)\cos(\phi(t) + \gamma(t)) \quad (1)$$

$$z_{tip}(t) = L_0 \sin(\phi(t)) + (L - L_0)\sin(\phi(t) + \gamma(t)) \quad (2)$$

where $\phi(t) = \phi_0 \sin(2\pi f t)$ and $\gamma(t) = \gamma_0 \sin(2\pi f t + \psi)$. This kinematic model directly informs the mechanical design, mandating a rigid proximal structure for power transmission and a compliant distal joint for shape modulation.

2.2 Stiffness Modulation Mechanism

The stiffness modulation is achieved through the antagonistic tension of the tendons. As the tension T increases, the tendons exert a compressive preload on the flexible silicone-filled joints. This preload increases the restoring force required for transverse displacement, effectively increasing the bending stiffness of the joint without altering its rest shape.

The effective stiffness tensor $\mathbb{C}_{eff}$ can be decomposed into a passive material component and an active geometric component:

$$\mathbb{C}_{eff} = \mathbb{C}_{pas} + \mathbb{C}_{act}(\alpha_c) \approx \mathbb{C}_{mat} + \frac{T(\alpha_c)}{A_0}(\mathbf{n} \otimes \mathbf{n}) \tag{3}$$

where $T(\alpha_c)$ is the tension. Here, $\mathbb{C}_{pas}$ represents the constant elasticity of the polymer materials. The term $\mathbb{C}_{act}$ is the controllable stiffness induced by the tendon tension $T(\alpha_c)$, where α_c is the control input. This relationship theoretically validates that by regulating the antagonistic tension, the foil can actively shift between a "rigid" state for power transmission and a "flexible" state for efficient flow interaction. This model is intended to be predictive; by regulating the tendon tension, the potential energy landscape of the structure is modified, allowing for real-time impedance control during different phases of the flapping cycle.

2.3 Unsteady Hydrodynamics

The propulsive forces are derived based on the potential flow theory for unsteady airfoils (Theodorsen's and Garrick's models [1]). The total normal force per unit span $F_n(s,t)$ is the sum of added mass and circulatory contributions:

$$F_n(s,t) = \underbrace{-\frac{\pi}{4}\rho c^2 \left(a_n(s,t)\right)}_{\text{Added Mass}} + \underbrace{2\pi\rho c V_{eff} Q(s,t) C(k)}_{\text{Circulatory}} \tag{4}$$

Equation 4 accounts for both the non-circulatory added mass force and the circulatory lift force. The downwash $Q(s,t)$ is specifically modified to include the relative velocity induced by the active bending rate $\dot{\gamma}$, representing the hydrodynamic coupling between shape deformation and flow interaction (Fig. 2).

3 System Design

To empirically validate the theoretical framework established in Sect. 2, a robotic experimental platform was developed. The design process was driven by stringent functional requirements, including a high thrust-to-weight ratio for potential autonomous vehicle integration, reliable waterproofing for submerged operation, and a target operational frequency range of 0.5–2.0 Hz to match biological prototypes. The final mechanical system integrates a rigid aluminum test rig with a bio-inspired morphing foil, ensuring structural integrity under cyclic hydrodynamic loading while maintaining a compact form factor to minimize parasitic drag.

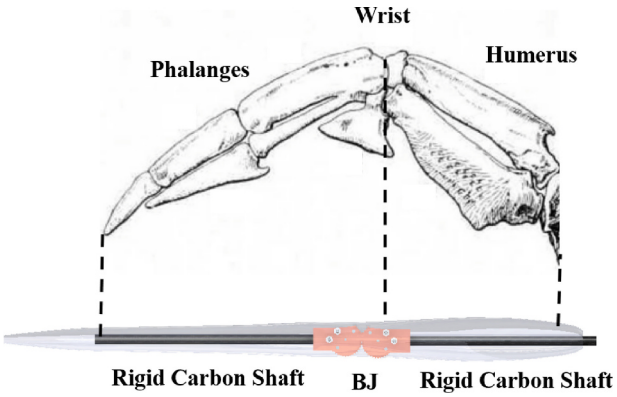

Fig. 2. Bio-mimetic morphological mapping. The robotic design abstracts the complex skeletal structure of a penguin's flipper into a simplified articulated linkage. The biological carpal joint (wrist), responsible for curvature control, is mapped to the tendon-driven bending joint, while the humerus and phalanges correspond to the rigid proximal shaft and the compliant distal segment, respectively.

3.1 Bio-mimetic Morphological Mapping

The design of the robotic foil draws morphological inspiration from the functional anatomy of the penguin wing, which is renowned for its propulsive efficiency. Unlike rigid airfoils, a penguin's wing possesses a complex skeletal structure capable of varying stiffness and curvature during the stroke cycle.

As depicted in Fig. 1, our design abstracts this biological complexity into a two-segment articulated structure. The primary structural innovation lies in the discrete bending joint, mimicking the carpal joint (wrist) of the penguin. This joint enables active span-wise curvature control, a key factor in optimizing hydrodynamic performance. To validate the rationality of this design, a kinematic mapping analysis was conducted. The relationship between the tendon actuation and the resulting bending angle demonstrates a consistent, near-linear response, confirming that the mechanism can effectively replicate the large-deformation kinematics of the biological prototype with high fidelity.

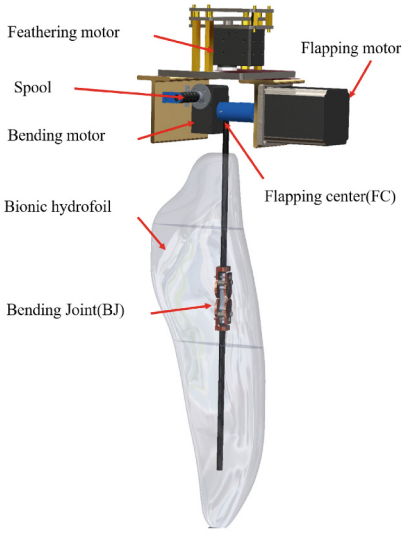

(a) System configuration showing test rig and foil assembly

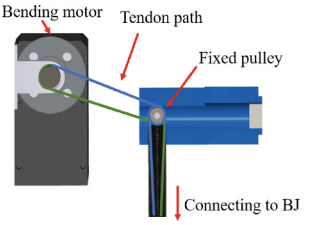

(b) Tendon routing path and spool mechanism

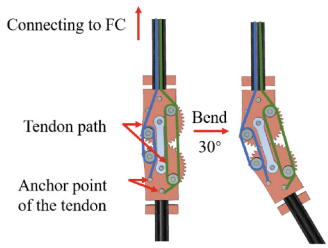

(c) Bending joint mechanism: Straight vs. 30° deflection

Fig. 3. Detailed mechanical design of the robotic hydrofoil. (a) Overall assembly illustrating the placement of flapping, feathering, and bending motors; (b) Close-up of the tendon routing system decoupling bending from flapping; (c) Working principle of the antagonistic tendon-driven bending joint.

3.2 Mechanical Configuration and Actuation

The experimental apparatus features a drive system to decouple multi-degree-of-freedom motions. The primary flapping is driven by a high-torque 57-stepper motor via a crank-rocker mechanism, converting rotation to reciprocal oscillations (Fig. 3a). To address coupling between flapping and tendon tension, tendons are routed from the foil root through a hollow carbon fiber shaft. Fixed pulleys at the flapping center redirect tendons vertically to an overhead motor, maintaining constant path length during flapping and decoupling bending actuation, with minor stiffness loss. Tendons are secured to the bending motor's spool with set screws for tension adjustment. A third motor atop the assembly drives feathering by rotating the foil. The bending joint employs a compact, constant-length tendon drive with two antagonistic tendons for bending and restoration, minimizing volume. It achieves 30° maximum deflection, deforming the distal segment (45%–100%of the wing length) to modulate stiffness. Antagonistic tension ensures torque application under hydrodynamic load. The joint is under 12 mm thick—thinner than a Gentoo penguin's wing—preserving a streamlined profile. A gear interface ensures efficient force and angle transmission.

4 Fabrication and Prototyping

To realize the bio-inspired variable stiffness characteristics, a specialized multi-material fabrication process was developed. The foil was manufactured using a vacuum casting technique with variable silicone concentrations to achieve a specific stiffness gradient along the span.

The fabrication process follows a rigorous "stiffness-mapping" approach. First, a theoretical stiffness gradient was designed to mimic the internal structure of a penguin wing. From the root to the tip, the material distribution is defined as follows: (1) 0%–21.2% span uses pure PLA for rigid connection; (2) 21.3%–29.6% span comprises a PLA shell filled with silicone; (3) 29.7%–39.2% span (the bending joint area) utilizes a pure silicone membrane for maximum flexibility; (4) 39.3%–50.4% span reverts to a PLA shell filled with silicone; and (5) 50.5%–100% span employs PLA-CF (Carbon Fiber reinforced PLA) for distal rigidity. This gradient design preliminarily realizes the passive stiffness variation required during underwater flapping.

The manufacturing procedure comprises three key steps (Fig. 4). First, internal tendons are pre-threaded through the hollow carbon fiber shaft and bending joint. Second, multi-stage casting is conducted from tip to root using a modular mold, injecting 4035 Mold silicone into each cavity with vacuum degassing to eliminate bubbles. After a 24-hour cure, the prototype is de-molded along designed parting lines, yielding a monolithic, flexible morphing foil with embedded sensing and actuation elements that achieves complex bio-mimetic mechanics without costly industrial equipment.

The distribution of materials follows a gradient strategy. The "PLA-filled-with-silicone" structure (Regions II and IV) consists of 3D-printed hollow PLA lattices which are subsequently injected with liquid silicone under vacuum. This hybrid architecture prevents buckling of the skin while maintaining flexibility.

The design of the robotic foil draws morphological inspiration from the functional anatomy of the penguin wing, which is renowned for its propulsive efficiency. Unlike rigid airfoils, a penguin's wing possesses a complex skeletal structure capable of varying stiffness and curvature during the stroke cycle.

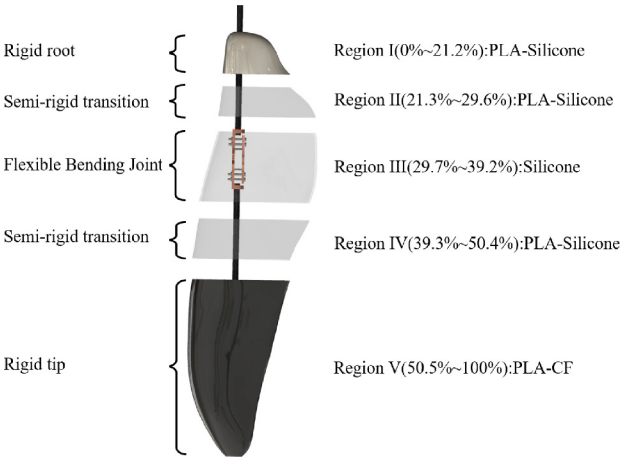

Fig. 4. Exploded view of the multi-material stiffness gradient. The foil comprises five regions: semi-rigid PLA-silicone transitions (Regions I, II, IV), a flexible pure silicone bending joint (Region III), and a rigid PLA-CF tip (Region V).

5 Conclusion and Future Work

This paper presented the systematic design, theoretical modeling, and fabrication of a bio-inspired morphing hydrofoil. Drawing morphological inspiration from the penguin wing, we realized a tendon-driven articulated structure capable of active spanwise bending and stiffness modulation. A key contribution of this work is the development of a core-to-skin multi-material fabrication process, which successfully integrates a rigid transmission system within a vacuum-cast gradient silicone body, resolving the conflict between structural integrity and morphological compliance.

The study validates the bio-mimetic approach. Analyses confirm that the antagonistic tendon drive decouples geometric curvature from effective structural stiffness, enabling tunable mechanical impedance. Coupling this active stiffness with flapping kinematics yields smoother, higher-magnitude thrust than conventional designs, establishing a foundation for variable-stiffness underwater propulsion.

Future work will close the control loop by integrating embedded strain sensors for adaptive, real-time tension regulation in response to flow. Comprehensive water-tank PIV experiments will also visualize wake topology to elucidate the flow-control mechanisms.

References

1. Bai, F., Wang, Z., Wang, X., Ren, P., Liu, Y., Xue, G.: Numerical investigation and swimming performance evaluation on self-propelled hydrodynamics of hybrid-driven biomimetic robotic fish. J. Ocean Eng. Sci. S2468013325000737 (2025). https://doi.org/10.1016/j.joes.2025.10.002
2. Bao, T., et al.: Effects of motion parameters on the propulsion characteristics of flexible pectoral fins in bio-manta robots. Ocean Eng. **309**, 118377 (2024). https://doi.org/10.1016/j.oceaneng.2024.118377
3. Fish, F.E., Schreiber, C.M., Moored, K.W., Liu, G., Dong, H., Bart-Smith, H.: Hydrodynamic performance of aquatic flapping: efficiency of underwater flight in the manta. Aerospace **3**(3) (2016). https://doi.org/10.3390/aerospace3030020, https://www.mdpi.com/2226-4310/3/3/20
4. van der Geest, N., Garcia, L., Borret, F., Nates, R., Gonzalez, A.: Soft-robotic green sea turtle (Chelonia mydas) developed to replace animal experimentation provides new insight into their propulsive strategies **13**(1), (1198). https://doi.org/10.1038/s41598-023-37904-5
5. van der Geest, N., Garcia, L., Nates, R., Borrett, F.: New insights into sea turtle propulsion and their cost of transport point to a potential new generation of high-efficient underwater drones for ocean exploration. J. Marine Sci. Eng. **11**(10) (2023). https://doi.org/10.3390/jmse11101944, https://www.mdpi.com/2077-1312/11/10/1944
6. Giordano, A., et al.: A soft robotic morphing wing for unmanned underwater vehicles. Adv. Intell. Syst. **6**(6), 2300702 (2024). https://doi.org/10.1002/aisy.202300702
7. Griffiths, G., Edwards, I.: AUVs: designing and operating next generation vehicles. In: Elsevier Oceanography Series, vol. 69, pp. 229–236. Elsevier (2003). https://doi.org/10.1016/S0422-9894(03)80038-7
8. Harada, N., Oura, T., Maeda, M., Shen, Y., Kikuchi, D.M., Tanaka, H.: Kinematics and hydrodynamics analyses of swimming penguins: wing bending improves propulsion performance. J. Exper. Bio. **224**(21), jeb242140 (2021). https://doi.org/10.1242/jeb.242140
9. Harada, N., Tanaka, H.: Kinematic and hydrodynamic analyses of turning manoeuvres in penguins: body banking and wing upstroke generate centripetal force. J. Exper. Bio. **225**(24), jeb244124 (2022). https://doi.org/10.1242/jeb.244124
10. James, C.R., et al.: A novel aquatic propulsor inspired by mobuliform swimming. In: OCEANS 2022, Hampton Roads, pp. 1–10. IEEE, Hampton Roads, VA, USA (2022). https://doi.org/10.1109/OCEANS47191.2022.9977324
11. meng Liu, Q., et al.: Unified scheme design and control optimization of flapping wing for next-generation manta ray robot. Ocean Eng. **309**, 118487 (2024). https://doi.org/10.1016/j.oceaneng.2024.118487
12. Shen, Y., Ding, Z., Wang, X., Mao, Z., Huang, Z., Chen, B.: Biomimetic hydrofoil propulsion: harnessing the propulsive capabilities of sea turtles and penguins for robotics. Biomimetics **10**(5) (2025). https://doi.org/10.3390/biomimetics10050272
13. Shen, Y., Harada, N., Katagiri, S., Tanaka, H.: Biomimetic realization of a robotic penguin wing: design and thrust characteristics. IEEE/ASME Trans. Mechatron. **26**(5), 2350–2361 (2021). https://doi.org/10.1109/TMECH.2020.3038224
14. Vasilescu, I., Detweiler, C., Doniec, M.: AMOUR V: a hovering energy efficient underwater robot capable of dynamic payloads. The Int. J. Robot. Res. **29**(5), 547–570 (2010). https://doi.org/10.1177/0278364909358275

15. Wang, X., Zhao, J., Pei, X., Wang, T., Hou, T., Yang, X.: Bioinspiration review of aquatic unmanned aerial vehicle (AquaUAV). Biomimetic Intell. Robot. **4**(2), 100154 (2024). https://doi.org/10.1016/j.birob.2024.100154
16. Xia, D., Lei, M., Gai, Q., Xu, Z., Zou, T.: Development of a robotic dolphin capable of underwater horizontal and surface vertical movement. Ocean Eng. **342**, 122965 (2025). https://doi.org/10.1016/j.oceaneng.2025.122965
17. Zhou, P., Yao, J., Zhang, S., Wei, C., Zhang, H., Qi, S.: A bioinspired fishbone continuum robot with rigid-flexible-soft coupling structure. Bioinspiration Bio. **17**(6), 066012 (2022). https://doi.org/10.1088/1748-3190/ac8c10

Design and Kinematic Geometric Analysis of a Reconfigurable Bricard Mechanism with Rolling Joints

Tianye Xu, Huanxiao Li, Long Li, and Shengnan Lyu(✉)

Beihang University, Beijing 100191, China
shengnan_lyu@buaa.edu.cn

Abstract. This paper presents a reconfigurable Bricard mechanism with rolling joints capable of achieving multiple distinct motion modes. The mechanism combines four revolute joints and two rolling joints, each equipped with synchronous cables and tape springs to drive motion and provide self locking at kinematic bifurcations for kinematic reconfiguration. The instantaneous screw axis (ISA) of the rolling joints is analyzed, and an equivalent Bricard mechanism representing the system is derived. The mechanism's kinematic reconfiguration, including plane-symmetric Bricard motion and arc-translation motion, is characterized using screw system geometry. Finally, a 3D printed prototype is used to validate the predicted multimodal motions of the reconfigurable mechanism.

Keywords: Reconfigurable mechanism · Bricard mechanism · Rolling joint · Kinematic geometry

1 Introduction

Bricard mechanisms, first introduced by Raoul Bricard in 1897 [2], are a classical class of over-constrained closed-loop linkages that exhibit continuous mobility despite violating the Grubler-Kutzbach (G-K) equation for determining degrees of freedom [9,11]. These mechanisms are of fundamental importance in mechanism science due to their ability to move while maintaining constant link lengths and joint constraints. The established families of Bricard mechanisms include Type I (line symmetric) [7], Type II (plane-symmetric) [18], and Type III [12,14].

A notable subclass is the plane-symmetric Bricard linkage [13,19], which exhibits reflectional symmetry with respect to a central plane. This symmetry simplifies geometric modeling and enables the synthesis of spatial motions through modular repetition. Recent studies have extended the use of Bricard units to deployable structures [16], reconfigurable mechanisms [4], and adaptive robotic systems [17].

This research has been supported by the Natural Science Foundation of China under Grants 52192632 and 52222501.

© The Author(s), under exclusive license to Springer Nature Switzerland AG 2026
A. Chaker et al. (Eds.): EFIMMS 2026, MMS 205, pp. 97–106, 2026.
https://doi.org/10.1007/978-3-032-22270-1_10

From a theoretical perspective, Bricard mechanisms serve as canonical models for studying abnormal mobility, motion bifurcation, and kinematic geometry in over-constrained systems. These properties make them attractive for constructing mechanisms with complex kinematic and static behavior, such as reconfigurable or adaptive mechanisms, particularly in applications requiring non-standard motion patterns.

The analysis of kinematic reconfiguration in Bricard mechanisms has attracted significant attention. Chen and You [6] analyzed the kinematic bifurcation of a two fold symmetrical Bricard 6R mechanism. Yao studied the kinematics of general plane-symmetric Bricard mechanisms [19], and Chen proposed a flexible plane-symmetric Bricard mechanism [5]. Feng investigated the kinematics of general plane-symmetric Bricard linkages and their bifurcation variations [8]. Due to the intricate over-constrained nature of these mechanisms, algebraic approaches to kinematic reconfiguration are often complex and non-intuitive. Geometric methods, particularly those based on screw system theory, provide an effective and intuitive framework for mechanism synthesis and kinematic analysis.

Building on these insights, this paper presents a reconfigurable Bricard mechanism with integrated rolling joints and develops a geometric method to analyze its kinematic reconfiguration. The main contributions of this work are as follows:

1. A reconfigurable Bricard mechanism with rolling joints is proposed, capable of performing plane-symmetric Bricard motion and arc-translation motion through kinematic reconfiguration.
2. ISA of the rolling joints is analyzed, leading to the derivation of an equivalent Bricard mechanism that represents the reconfigurable system.
3. Kinematics of the mechanism is characterized using a geometric approach based on screw systems, providing an intuitive representation of the kinematic reconfiguration. The multimodal motions are further validated through a mechanism prototype.

The remainder of this paper is organized as follows. Section 2 introduces the design and motion modes of the reconfigurable Bricard mechanism with rolling joints. Section 3 analyzes the kinematic reconfiguration of the mechanism using geometric methods. Section 4 evaluates the multimodal performance of the mechanism through a prototype. Finally, Sect. 5 concludes the paper.

2 Design

2.1 Multimodal Motion Modes

As shown in Fig. 1, the reconfigurable Bricard mechanism consists of six joints (16). Joints 1, 3, 4, and 6 are revolute pairs, while Joints 2 and 5 are rolling joints. The mechanism is actuated by two tape springs embedded in the rolling joints. In the initial folded configuration, the tape springs are fully bent. As they recover elastically, the mechanism gradually deploys and follows a plane-symmetric Bricard motion. This motion continues until the mechanism reaches

a kinematic bifurcation, where Links 123 become collinear and Links 456 also become collinear. At this configuration, the tape springs return to their undeformed state and provide a self-locking stiffness that holds Joints 2 and 5 in place. Once these joints are locked, the coupler of the mechanism transitions to an arc-translation motion. This family of poses forms a circular translational submanifold of $SE(2)$ [15].

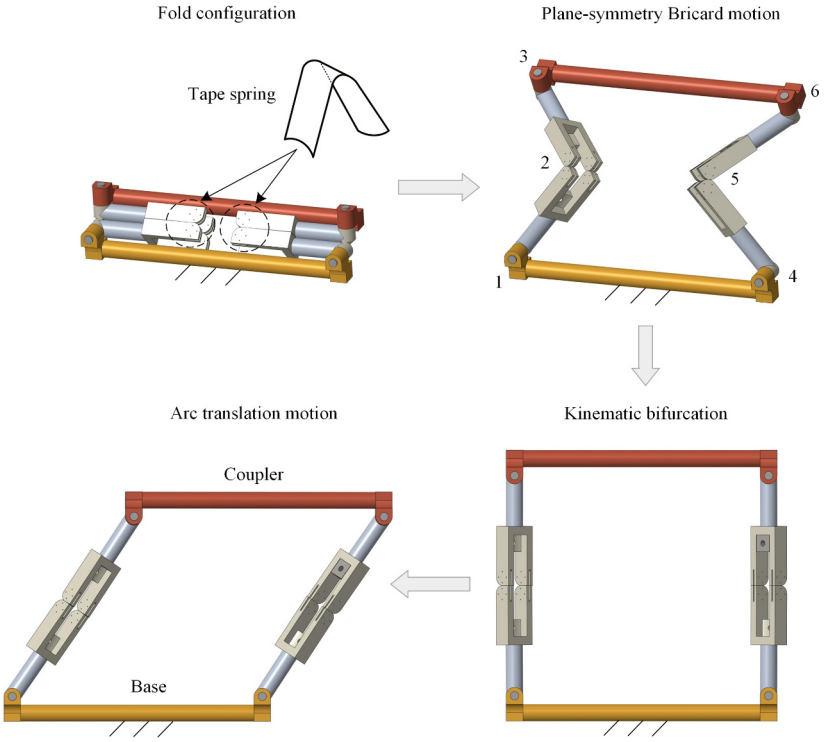

Fig. 1. Multimodal motion modes of the Bricard mechanism.

2.2 The Rolling Joint

As shown in Fig. 2(a), the rolling joint incorporates a pair of rolling-contact cylindrical surfaces, a set of cables, and a tape spring. In Fig. 2(b), circumferential grooves are machined on the inner surfaces of the cylinders, and crossing cables are routed through these grooves. During motion, the cables alternately wind around the grooves of the two cylinders, ensuring consistent surface contact and enabling pure rolling.

The torqueangle behavior of the tape spring is shown in Fig. 2(c). In the fully folded configuration, the rotation angle reaches $\varphi = 180°$, and the restoring torque drives the mechanism to unfold. When the mechanism reaches the

bifurcation configuration, the rotation angle decreases to $\varphi = 0°$, at which point the tape spring provides sufficient stiffness to hold both rolling joints in place and allow the mechanism to transition to the next motion mode.

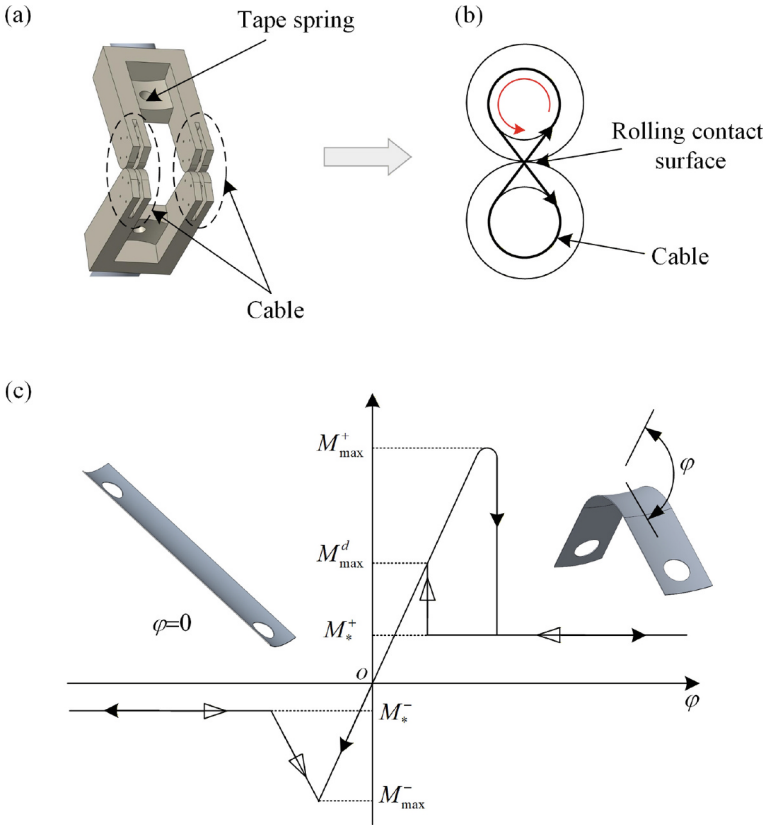

Fig. 2. The rolling joint. (a) Joint design. (b) Cable transmission. (c) Torque–angle curve of the tape spring.

3 Kinematic Analysis

3.1 The Equipped Bricard Mechanism

As shown in Fig. 3(a), for Rolling Joints 2 and 5, pure rolling ensures that ISA of the relative motion passes through the instantaneous contact point between the two cylinders and remains parallel to their axes. The joint twists are denoted as $\boldsymbol{S}_1\boldsymbol{S}_6$, with their corresponding axes $\boldsymbol{L}_1\boldsymbol{L}_6$ and unit direction vectors $\boldsymbol{l}_1\boldsymbol{l}_6$. The

mechanism satisfies the following geometric constraints:

$$\begin{cases} \boldsymbol{l}_1 \parallel \boldsymbol{l}_4, \quad \boldsymbol{l}_3 \parallel \boldsymbol{l}_6 \\ \angle(\boldsymbol{l}_1, \boldsymbol{l}_2) = \angle(\boldsymbol{l}_5, \boldsymbol{l}_6) = \alpha \\ \angle(\boldsymbol{l}_2, \boldsymbol{l}_3) = \angle(\boldsymbol{l}_4, \boldsymbol{l}_5) = -\alpha \\ l_{14} = l_{36} \\ l_{12} = l_{23} = l_{45} = l_{56} \end{cases} \tag{1}$$

where l_{ij} denotes the distance between axes $\boldsymbol{L}_i$ and $\boldsymbol{L}_j$.

From (1), the mechanism composed of four revolute pairs and two rolling joints is kinematically equivalent to a plane-symmetric Bricard mechanism, as shown in Fig. 3(b). When Joints 2 and 5 roll, the contact points shift and the equivalent link lengths l_{12}, l_{23}, l_{45}, and l_{56} vary during motion. Even so, the constraints in (1) remain satisfied throughout the motion. Therefore, the mechanism can be represented equivalently by a 6R Bricard mechanism with variable link lengths.

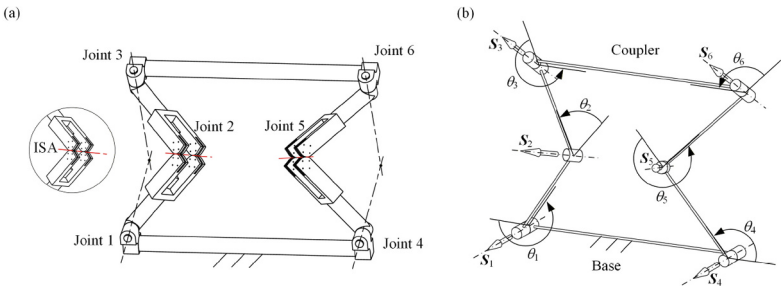

Fig. 3. Equivalent Bricard mechanism of the rolling-joint system. (a) ISA of the rolling joint. (b) Equivalent Bricard mechanism.

3.2 Geometric Analysis for Kinematic Reconfiguration

For the proposed reconfigurable Bricard mechanism with rolling joints, as shown in Fig. 3(a), the instantaneous screw axis (ISA) of each rolling joint varies continuously over the motion range. This variation makes it difficult to construct analytical models in standard forms, such as the product-of-exponentials formulation [3]. Even for the equivalent Bricard mechanism shown in Fig. 3(b), the joint equations reported in the literature [16] contain highly nonlinear trigonometric expressions. These equations are difficult to solve, and their solution sets often do not clearly represent or distinguish the different motion modes of the mechanism.

To address these limitations, this study analyzes kinematic reconfiguration by exploiting the geometric properties of the screw system associated with the

mechanism, rather than relying on analytical formulations. This geometric approach provides a more direct and intuitive interpretation of the distinct kinematic characteristics and motion transitions.

First, the kinematic geometry of a single 3R subchain, either 1–2–3 or 4–5–6, is considered. Each subchain connects the coupler to the base, as shown in Fig. 3(b). The twist subspace spanned by $\boldsymbol{S}_1$, $\boldsymbol{S}_2$, and $\boldsymbol{S}_3$ corresponds to two different screw-system types in Hunt's classification [10], depending on the intermediate joint angle θ_2.

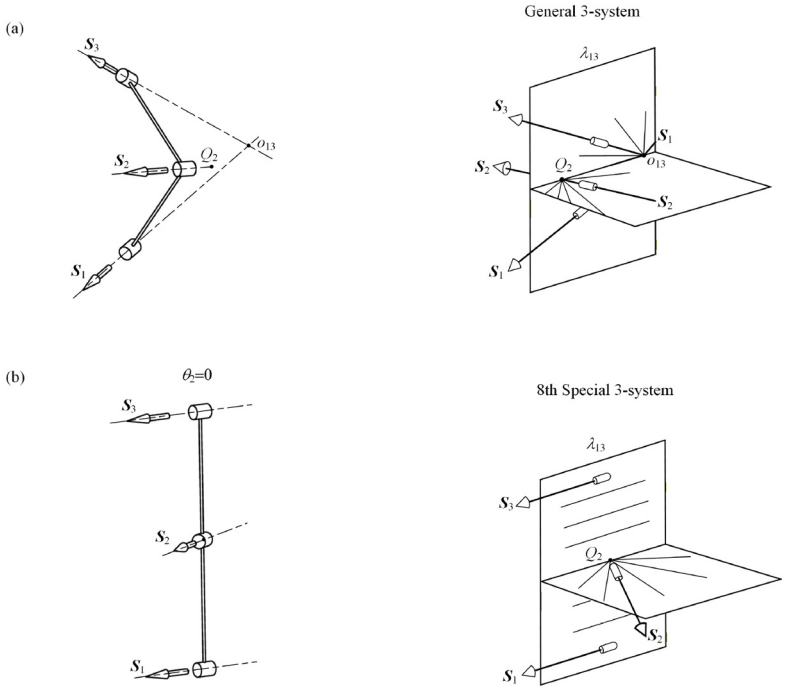

Fig. 4. Kinematic geometry of the 3R subchain. (a) Screw system in the plane-symmetric Bricard motion. (b) Screw system in the arc-translation motion.

As shown in Fig. 4(a), when $\theta_2 \neq 0$ and $\theta_2 \neq \pi$, the axes $\boldsymbol{L}_1$ and $\boldsymbol{L}_3$ intersect at a point o_{13}. The axis $\boldsymbol{L}_2$ intersects the plane λ_{13} spanned by $\boldsymbol{L}_1$ and $\boldsymbol{L}_3$ at a point Q_2 that differs from o_{13}. The resulting twist subspace is a general 3-system with middle principal pitch zero. Its zero-pitch screws form a regulus of a degenerate hyperboloid [10]. This regulus consists of two planar pencils of lines in two intersecting planes, with their centers on the intersection line. One pencil is centered at o_{13} in λ_{13}, and the other is centered at Q_2, with its plane defined by $\boldsymbol{L}_2$ and o_{13}. The nonzero principal pitches depend on the angle between the two planes and the distance between the centers. For the subchain 4–5–6, the corresponding points are o_{46} and Q_5.

As shown in Fig. 4(b), when $\theta_2 = 0$, the twist subspace becomes an 8th Special screw system with special pitch zero. The zero-pitch screws form a regulus of a degenerate hyperbolic paraboloid. This regulus consists of two planar pencils of lines, one parallel and one concurrent, in two planes that intersect at a right angle along a common generator [10]. In this case, $\boldsymbol{L}_1$ and $\boldsymbol{L}_3$ are parallel, and $\boldsymbol{L}_2$ intersects the plane λ_{13} at the system center.

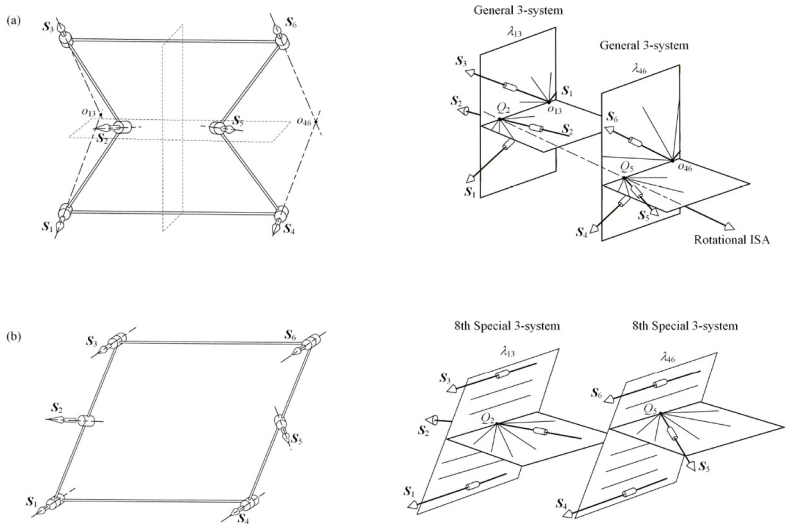

Fig. 5. Kinematic geometry of the mechanism in different motions. (a) Screw system in the plane-symmetric Bricard motion. (b) Screw system in the arc-translation motion.

In the configuration shown in Fig. 5(a), the two 3R subchains 1–2–3 and 4–5–6 form a mirror pair. The instantaneous motion of the coupler with respect to the base is given by the intersection of the two general 3-systems associated with the subchains. The only admissible common screw is the line Q_2Q_5, which produces the plane-symmetric Bricard motion [1]. When $\theta_2 = \theta_5 = 0$ and $\theta_1 = \pi/2$, the twist spaces of both subchains become 8th Special 3-systems. In this configuration, the mechanism reaches a kinematic bifurcation, and the tape springs constrain θ_2 and θ_5. This constraint enables a transition to the next motion mode.

When the tape springs enforce $\theta_2 = \theta_5 = 0$, the instantaneous motion of the coupler with respect to the base is determined by the intersection of the two 8th Special 3-systems of the subchains. As shown in Fig. 5(b), the only possible intersection is the common line of the planes λ_{13} and λ_{46}, which lies at infinity. This indicates that the instantaneous screw is a pure translation. The direction of translation is normal to both planes λ_{13} and λ_{46}, generating the circular translational submanifold of $SE(2)$ [15].

4 Prototype Test

A mechanism prototype was fabricated to validate the design and demonstrate the multimodal motions of the reconfigurable Bricard mechanism. All components were produced by 3D printing. Revolute joints were assembled by inserting axis pins into matching holes. Rolling joints were built from printed cylinders with circumferential grooves and a nylon cord to synchronize rotation and prevent slippage. Thin-walled cylindrical shells served as elastic components, storing elastic energy during bending and providing passive actuation.

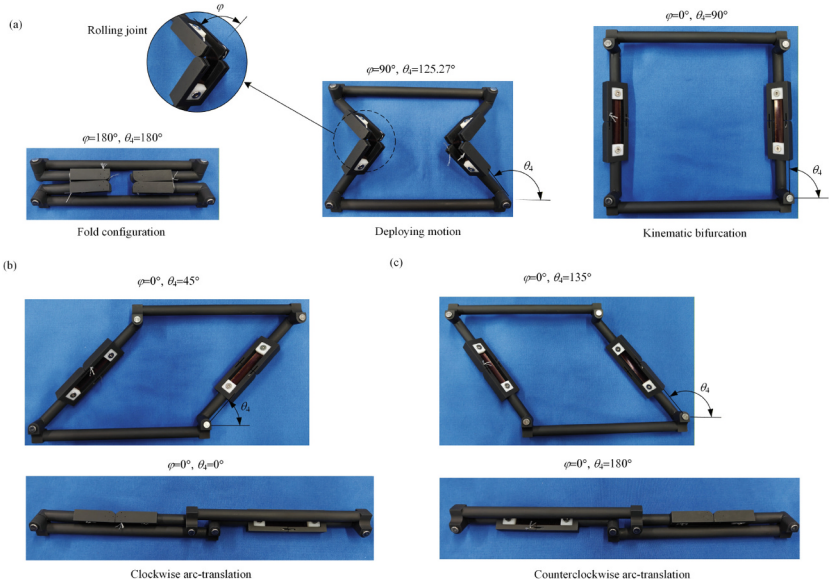

Fig. 6. Mechanism prototype. (a) Plane-symmetric Bricard motion. (b) clockwise arc-translation motion. (c) anticlockwise arc-translation motion.

As shown in Fig. 6(a), when the tape spring bending angle is $\varphi = 180°$, the mechanism is in a folded configuration with $\theta_4 = 180°$. Driven by the bending potential energy of the tape spring, the mechanism evolves along the plane-symmetric Bricard motion. As φ decreases, θ_4 decreases accordingly, and the mechanism reaches a kinematic bifurcation. At this motion, the structure changes from a bundled folded state to a rectangular shape, with $\varphi = 0°$ and $\theta_4 = 90°$.

At the kinematic bifurcation, the mechanism admits two arc-translation motions, as shown in Fig. 6(b). A clockwise rotation of θ_4 from 90° produces a clockwise arc translation of the upper platform, while a counterclockwise rotation, as shown in Fig. 6(c), produces a counterclockwise arc translation. In both cases, the tape spring remains straight ($\varphi = 0$), and its self-locking stiffness

maintains structural stability. Consequently, the output platform achieves a total arc-translation range of 180°.

5 Conclusion

This paper proposes a novel reconfigurable Bricard mechanism incorporating rolling joints. The combination of rolling joints and synchronous cables ensures no-slip rolling motion, while tape springs provide self-locking at kinematic bifurcation points to enable reliable kinematic reconfiguration. The mechanism supports both plane-symmetric Bricard motion and arc-translation. An ISA analysis of the rolling joints yields an equivalent kinematic representation. A geometric analysis based on screw systems further clarifies the kinematic reconfiguration of the mechanism. Experiments on a 3D-printed prototype validate the predicted multimodal motions.

Compared with existing Bricard mechanisms, the proposed design offers clear practical advantages. Rolling contact joints reduce friction and wear, thereby improving motion efficiency, enhancing durability, and reducing maintenance requirements. The integrated tape-spring-driven structure enables passive actuation without complex transmission components, resulting in a compact and mechanically simple design. In addition, the inherent self-locking stiffness of the tape springs ensures stable motion, which is particularly beneficial for shape-holding tasks.

These features make the proposed mechanism particularly suitable for applications requiring smooth reconfiguration, high reliability, and energy efficiency. Potential applications include deployable and reconfigurable robotic structures, adaptive mechanisms for aerospace and space-deployable systems, and morphing architectural or mechanical components where low friction, compact actuation, and stable multimodal motion are critical.

References

1. Baker, J.E.: An analysis of the Bricard linkages. Mech. Mach. Theory **15**(4), 267–286 (1980)
2. Bricard, R.: Mémoire sur la théorie de l'octaèdre articulé. Journal de Mathématiques pures et appliquées **3**, 113–148 (1897)
3. Brockett, R.W.: Robotic manipulators and the product of exponentials formula. In: Mathematical Theory of Networks and Systems: Proceedings of the MTNS-83 International Symposium Beer Sheva, Israel, June 20–24, 1983, pp. 120–129. Springer (2005)
4. Chai, X., Dai, J.S.: Three novel symmetric Waldron-Bricard metamorphic and reconfigurable mechanisms and their isomerization. J. Mech. Robot. **11**(5), 051011 (2019)
5. Chen, G., et al.: A study on the flexible Bricard mechanisms with plane-symmetric structure. Mech. Mach. Theory **188**, 105404 (2023)
6. Chen, Y., You, Z.: Two-fold symmetrical 6r foldable frame and its bifurcations. Int. J. Solids Struct. **46**(25), 4504–4514 (2009)

7. Chen, Y., You, Z., Tarnai, T.: Threefold-symmetric Bricard linkages for deployable structures. Int. J. Solids Struct. **42**(8), 2287–2301 (2005)
8. Feng, H., Chen, Y., Dai, J.S., Gogu, G.: Kinematic study of the general plane-symmetric Bricard linkage and its bifurcation variations. Mech. Mach. Theory **116**, 89–104 (2017)
9. Grübler, M.: Allgemeine Eigenschaften der zwangläufigen ebenen kinematischen Ketten. L. Simion (1884)
10. Hunt, K.H.: Kinematic geometry of mechanisms. Oxford University Press (1978)
11. Kutzbach, K.: Einzelfragen aus dem gebiet der maschinenteile. Zeitschrift der Verein Deutscher Ingenieur **77**(1), 168 (1933)
12. Lu, S., Zlatanov, D., Ding, X., Zoppi, M., Guest, S.D.: A network of type III Bricard linkages. J. Mech. Robot. **11**(1), 011013 (2018)
13. Lyu, S., Yao, P., Xiao, H., Zhang, W., Ding, X.: Approximating cylinders with bundle-folding plane-symmetric Bricard linkages. Int. J. Mech. Sci. **221**, 107231 (2022)
14. Lyu, S., et al.: Bundle folding type III Bricard linkages. Mech. Mach. Theory **144**, 103663 (2020)
15. Meng, J., Liu, G., Li, Z.: A geometric theory for analysis and synthesis of sub-6 DoF parallel manipulators. IEEE Trans. Rob. **23**(4), 625–649 (2007)
16. Qi, X., Huang, H., Miao, Z., Li, B., Deng, Z.: Design and mobility analysis of large deployable mechanisms based on plane-symmetric Bricard linkage. J. Mech. Des. **139**(2), 022302 (2017)
17. Shang, H., Wei, D., Kang, R., Chen, Y.: A deployable robot based on the Bricard linkage. In: Mechanism and Machine Science: Proceedings of ASIAN MMS 2016 and CCMMS 2016, pp. 737–747. Springer (2017)
18. Viquerat, A., Hutt, T., Guest, S.: A plane symmetric 6R foldable ring. Mech. Mach. Theory **63**, 73–88 (2013)
19. Yao, S., et al.: On the kinematics of general plane-symmetric Bricard mechanisms. Mech. Mach. Theory **190**, 105433 (2023)

Experimental Test of a Wave Energy Converter with a Bioinspired Negative Stiffness Mechanism

Camila Alarcón-Gómez, Claudio Villegas-Ulloa(✉), Fabian Pierart-Vásquez, Diego Carrasco-Valenzuela, and Roberto Delgado-Orias

Department of Mechanical Engineering, School of Engineering, Universidad del Bio-Bio, Avenue Collao 1202, Concepción, Chile
cvillegas@ubiobio.cl

Abstract. Harnessing wave energy offers a promising avenue for diversifying the energy matrix and mitigating climate change, given its high global power density. However, the commercial viability of Wave Energy Converters (WECs) remains limited by low conversion efficiency, primarily due to challenges in maintaining resonance across variable ocean wave spectra. This study presents the experimental evaluation of a floating column point absorber WEC incorporating a bio-inspired Negative Stiffness Mechanism (NSM), designed to tune the natural frequency to incident wave frequencies by counteracting hydrostatic stiffness. The NSM employs pre-compressed springs in a geometric linkage, with spring positions (1 to 5, from mechanism centre outwards) varying the moment arm and pre-compression to achieve tunable negative stiffness, modelled via linearised Lagrange equations and the Principle of Virtual Work. Wave tank tests (0.7–1.6 Hz) revealed that the optimal Position 3 configuration doubled heave oscillation amplitude to 5.14 mm at 0.87 Hz, versus 2.46 mm without springs, broadening the resonant bandwidth and enhancing power take-off potential.

Keywords: Wave Energy Converter (WEC) · Negative Stiffness Mechanism (NSM) · Dynamic Frequency Tuning · Resonant Frequency · Hydrostatic Stiffness · Power Take-Off (PTO) · Point Absorber (PA) · Non-linear System · Effective Stiffness · Heave Motion

1 Introduction

The global energy landscape is undergoing a necessary and rapid transition away from carbon-intensive sources to meet climate change mitigation targets. The implementation of sustainable energy solutions is not merely an environmental preference but an economic and societal imperative [1,2]. Within this context, ocean energy, particularly wave energy, represents one of the most promising yet underexploited high-density renewable resources. Wave energy exhibits a higher power density and a more predictable, consistent generation profile, unlike

© The Author(s), under exclusive license to Springer Nature Switzerland AG 2026
A. Chaker et al. (Eds.): EFIMMS 2026, MMS 205, pp. 107–115, 2026.
https://doi.org/10.1007/978-3-032-22270-1_11

wind and solar power, which are intermittent and highly dependent on daily weather cycles. This is particularly true in exposed coastal and offshore locations. Consequently, wave energy is strategically positioned to provide grid stability and act as a reliable baseload component in future energy systems.

Despite this immense potential, the wave energy sector remains at a lower Technology Readiness Level (TRL) compared to mature industries such as wind and solar. This stagnation is largely attributed to two primary, interconnected technical challenges: device survival in extreme storm conditions and the achievement of high energy conversion efficiency in normal sea states. This paper focuses specifically on the latter, examining advanced concepts to maximise energy capture.

Wave Energy Converters (WECs), particularly the widely studied Point Absorber (PA) type, operate on the principle of harnessing the heave motion induced by incident waves. According to linear wave theory, the maximum energy absorption occurs when the WEC oscillates at resonance, where the natural frequency of the device (ω_n) matches the excitation frequency of the incoming waves (ω) [3]. Under this condition, the oscillation amplitude is maximised, leading to a peak power transfer to the Power Take-Off (PTO) system.

The dynamic behaviour of a WEC in heave can be described as a mass-spring-damper system, where the effective mass incorporates the device's physical mass and its added mass due to hydrodynamic interactions [4]. the system's stiffness is dictated by the summation of the hydrostatic stiffness (buoyancy restoring force), the mooring stiffness, and the stiffness of any PTO or structural components. Thus, the natural frequency is linked to such parameters.

The fundamental challenge for conventional PA WECs stems from the highly variable nature of the ocean environment. The spectrum of wave periods encountered at a deployment site is wide. However, conventional WECs, especially those with large waterplane areas, possess a high hydrostatic in relation to the resonance zone for the incidents waves. This inherent high stiffness often results in a fixed natural frequency (ω_n) that is significantly higher than the frequency of the most energetic waves (ω), causing the device to operate in an off-resonance condition for a majority of its operational life [5].

Furthermore, ancillary systems, such as the mooring lines, contribute additional stiffness to the system, particularly in deeper water or under tension. The effect of the dynamic axial stiffness of elastic moorings on the WEC's performance cannot be ignored, as it directly impacts the overall effective stiffness [6].

In summary, the high and relatively inflexible system stiffness is the primary physical constraint preventing conventional PAs from achieving continuous, high-efficiency energy capture across the varying ocean spectrum. Therefore, to unlock the commercial viability of wave energy, there is an urgent engineering requirement for advanced control and mechanical systems capable of dynamic frequency tuning [5]. A promising technical solution involves manipulating the effective stiffness of the system to actively or passively control the natural frequency. Modern research has increasingly focused on incorporating non-linear

elements into the WEC structure or PTO system to achieve this tuning [7]. One of the most effective non-linear components for this application is the Negative Stiffness Mechanism (NSM).

The Negative Stiffness Mechanism (NSM) employed herein functions by introducing a passive elastic element comprising pre-compressed springs arranged in a geometric linkage that generates a counteracting force opposing the primary stiffness components, effectively reducing the overall system stiffness [8]. This bio-inspired mechanical arrangement exploits geometric nonlinearities—typically through inclined or buckling spring configurations—to provide a controlled negative stiffness zone within a specific displacement range, enabling the tunability of the resonant frequency of the Wave Energy Converter (WEC). Such mechanisms, as detailed in [8], achieve resonance frequency adaptation by balancing hydrostatic restoring forces with tunable negative stiffness, thereby improving energy capture efficiency across variable wave conditions (Fig. 1).

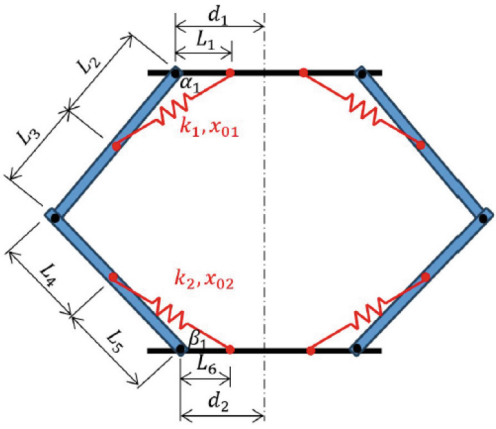

Fig. 1. Diagram of the bioinspired mechanism. Note: These results are based on [9].

2 Methodology

This research employs an experimental approach. The study is founded on the development of a governing dynamic model, its computational simulation, and a parametric evaluation of the NSM design variables to achieve system optimisation.

2.1 Theoretical Model and Principles

The WEC is conceptualised as a PA-type device moving in the heave degree of freedom [4], coupled with a PTO system. To achieve dynamic tuning, a Negative

Stiffness Mechanism (NSM) is integrated. The NSM is bio-inspired by structural principles observed in nature, where a controlled stiffness variation facilitates high amplitude motion with minimal external effort.

Instrumentation and Model Formulation: The dynamic behaviour of the WEC, treated as a single body oscillating in the heave degree of freedom (y), is governed by the second-order Lagrange equation. This formulation allows the integration of conservative forces (potential energy V, kinetic energy T) and non-conservative forces (wave excitation, radiation damping, and the PTO force F_{PTO}).

$$\frac{d}{dt}\left(\frac{\partial L}{\partial \dot{y}}\right) - \frac{\partial L}{\partial y} = F_{\text{Non-Conservative}} \tag{1}$$

Where: L = T - V

The resulting differential equation of motion in the time domain, incorporating hydrodynamic forces. The final, linearised equation of motion in the frequency domain, used for calculating the complex amplitude of motion ($Y(\omega)$) and the extracted power, is:

$$[-\omega^2(m + A(\omega)) + i\omega(B(\omega) + B_{PTO}) + K_{eff}]Y(\omega) = F_{ex}(\omega) \tag{2}$$

where $A(\omega)$ and $B(\omega)$ are the frequency-dependent added mass and radiation damping coefficients, respectively. Numerical simulation of the system dynamics is performed using specialised computational fluid dynamics (CFD) and time-domain tools (e.g., **ANSYS® Aqwa**™).

For modal analysis and linear frequency-domain study, the non-linear equation is linearised via Taylor expansion about static equilibrium ($y = 0$), yielding

$$F_{\text{Restore}}(t) \approx K_{\text{eff}} \cdot y(t) \tag{3}$$

where $K_{\text{eff}} = K_{\text{hydrostatic}} + K_{\text{mooring}} + K_{\text{NSM}}$. The design objective is to select $K_{\text{NSM}} < 0$ such that K_{eff} is sufficiently reduced, thereby tuning the WEC natural frequency $\omega_n = \sqrt{K_{\text{eff}}/m_{\text{eff}}}$ to prevalent lower wave frequencies.

2.2 Experimental Procedure

Beyond the theoretical framework, specific numerical results are presented that demonstrate the effectiveness of the Negative Stiffness Mechanism (NSM) in dynamically adjusting the natural frequency (f_n) of the WEC. The experiments were conducted in the wave tank facility at the Universidad del Bío-Bío and consisted of systematically varying the stiffness configuration by measuring the resulting heave oscillation amplitude (A) across an excitation frequency (f) range from **0.7** Hz to **1.6** Hz.

The experimental matrix employed two main configurations: a No-Spring (NS) configuration for establishing the linear baseline, and five discrete Spring-Assisted (SA) configurations, labelled Positions 1 to 5, correspond to varying spring attachment points, with position 1 being $L_1 = 100mm$ and position 5

being $L_1 = 35mm$, effectively modifying the spring moment arm to achieve different levels of precompression and the resulting effective stiffness. As shown in Fig. 2a, The springless mechanism remains in a state of equilibrium due to the buoyancy of the buoy. In other hand, in Fig. 2b, the positions are numbered starting from the centre of the mechanism (position 1) towards the ends (position 5).

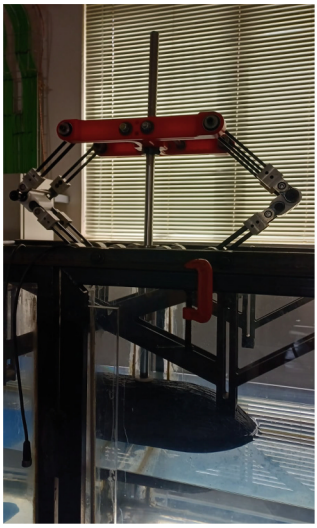

(a) No-Spring configuration.

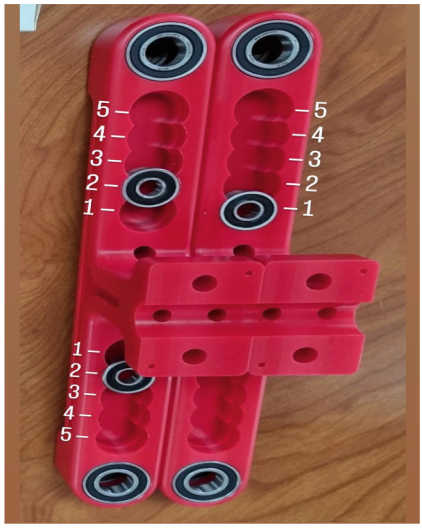

(b) Spring positions, from the centre to the ends.

Fig. 2. The two main configurations employed.

To ensure the robustness and reliability of the data, the entire set of measurements, covering all spring positions, was repeated across the entire predefined wave excitation frequency range.

Following the physical testing phase, the raw time-series data captured from the sensors were processed and analysed using bespoke numerical scripts developed in `MATLAB`. This programming stage was crucial for two primary analytical functions: firstly, converting the initial electrical voltage signals into calibrated physical heave displacement amplitudes (in mm); and secondly, employing peak-finding and filtering algorithms to calculate the steady-state maximum amplitude for every unique combination of spring position and excitation frequency. These processed datasets were then used to construct the final frequency response curves, which enabled the precise identification of the system's dynamic performance and its optimal resonant tuning for maximum energy capture.

3 Results and Discussion

The main objective of the NSM is to counteract hydrostatic stiffness, thereby shifting f_n from a state of intrinsically high stiffness (high f_n) towards lower frequencies, where the typical waves that produce energy are found (low f_n).

The graph 'Frequency vs Displacement' illustrates the response curve of the system for the various stiffness configurations of the mechanism. The configuration exhibiting the highest effective stiffness is **Position 3** (68 mm), which shifts the natural resonant frequency (ω_n) to **0.87** Hz, where a maximum recorded displacement of 5.14 mm is observed. The primary objective for such systems, such as a Wave Energy Converter (WEC), is precisely to tune the system's ω_n to the predominant wave frequencies (ω_{wave}) in order to maximise the oscillation amplitude and, consequently, the power take-off. It is noteworthy that the spring-assisted configurations (Positions 1, 2, 3, 4, and 5) generally achieve a greater maximum amplitude than the no-spring case (maximum of 2.46 mm), underscoring the effectiveness of the variable stiffness system in enhancing the WEC's performance across a broader operational frequency band (Fig. 3).

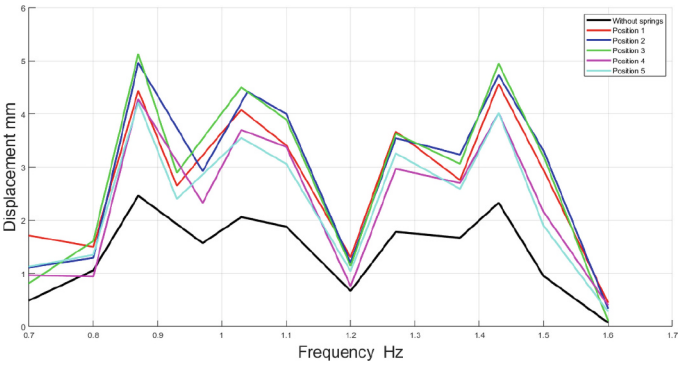

Fig. 3. Displacement Response Curve for the WEC Across Five Distinct Stiffness Configurations (Positions 1–5). The figure illustrates the significant augmentation of the Wave Energy Converter's (WEC's) dynamic response and heave oscillation amplitude at the inherent natural frequency, achieved by tuning the Negative Stiffness Mechanism (NSM).

The analysis of the maximum displacement amplitude of the Wave Energy Converter (WEC) as a function of the excitation frequency (F_{ex}) is paramount for assessing the converter's efficiency. The displacement, Disp (mm), is calculated from the measured voltage amplitude, A (V), using the calibration factor derived from the sensor's sensitivity:

$$\text{Disp} = \frac{a \cdot A}{b} \tag{4}$$

Table 1. Maximum Displacement Amplitudes and Corresponding Resonant Frequencies for each Stiffness Configuration.

Configuration	Max.Disp. mm	1°Peak Hz	2°Peak mm	Hz
No-Spring (NS)	2.46	0.88	2.32	1.43
Position 1 (SA)	4.44	0.88	4.56	1.44
Position 2 (SA)	4.96	0.88	4.73	1.44
Position 3 (SA)	5.14	0.88	4.94	1.44
Position 4 (SA)	4.27	0.88	4.02	1.44
Position 5 (SA)	4.22	0.88	4.02	1.44

where $a = 200$ mm distance from the sensor to the buoy and $b = 10.13$ V, yielding a conversion factor of approximately 19.74 mm/V (Table 1).

The experimental data confirms that the No-Spring (NS) configuration serves as the system's performance baseline, exhibiting a linear natural frequency (ω_n) at 0.87 Hz with a modest maximum heave displacement of **2.46** mm, which rapidly decays at higher excitation frequencies. In marked contrast, all Spring-Assisted (SA) configurations, leveraging the **Negative Stiffness Mechanism (NSM)** to reduce effective stiffness, achieved significantly amplified resonant motion, with Position 3 attaining the absolute maximum of **5.14** mm at 0.87 Hz. A defining characteristic of the non-linear SA operation is the observation of **dual displacement peaks**—one near the inherent 0.87 Hz resonance and a secondary peak around 1.43 Hz—effectively broadening the WEC's high-response bandwidth. This dual-peak behaviour, particularly well-defined in the optimally tuned Positions 1, 2, and 3, validates the NSM strategy as effective for maximising power capture through extended resonance synchronisation.

Specifically, the Position 3 configuration achieved the optimal alignment, yielding the maximum measured heave oscillation amplitude of **5.14** mm precisely at 0.87 Hz, a result that directly maximises velocity and, hence, Power Take-Off (PTO) performance since $P \propto \dot{Y}^2 B_{\mathrm{PTO}}$. This demonstrable effectiveness in stiffness manipulation directly addresses the fundamental efficiency limitations of fixed-stiffness wave energy converters and is directly analogous to technologies employed by industry leaders (e.g., Corpower Ocean's 'WaveSpring Phase Control'), confirming that variation of the position of the springs modifies the response of the WEC..

4 Conclusions

This study has presented the empirical validation of a bio-inspired Negative Stiffness Mechanism (NSM) integrated into a Point Absorber Wave Energy Converter (WEC). The primary engineering challenge of fixed, intrinsically high hydrostatic stiffness, which limits WEC efficiency by restricting operation to off-resonance conditions, has been effectively addressed through the strategic introduction of non-linear negative stiffness.

The results validate the central hypothesis of dynamic frequency tuning for this mechanism. The NSM proved capable of enhancing the WEC's response in resonant frequency ω_n through simple mechanical configuration adjustments. This mechanism also enhanced the response of a broadband frequency, showing that the use of NSM can be useful at resonant frequency as well as at nearby frequencies. Specifically, position 3 configuration demonstrated optimal tuning, achieving the highest measured heave oscillation amplitude (**5.14** mm) at the target resonance frequency of 0.87 Hz. Given that the power extracted by the Power Take-Off (PTO) system is directly proportional to the square of the oscillation velocity ($P \propto \dot{Y}^2 B_{\mathrm{PTO}}$), this amplitude maximisation translates into a maximisation of the system's energy capture potential within the critical operational band. However, the position of the amplitude peaks did not change in general, showing no evidence of change in the resonant frequencies. This could be because of two effects. First, the effective mass could change in proportion to the change of stiffness, which should be evaluated in future work. Second, the peak amplitude could correspond to resonance of the water flume. A CFD model can be realized to verify this last assumption.

Future research should concentrate on developing active or semi-active control strategies to dynamically adjust the NSM configuration in real-time, thereby ensuring continuous resonance and maximising annual energy production across variable sea states.

References

1. Agency, I.I.E.: World energy outlook 2023. Technical report (2023). https://www.iea.org/terms
2. Olabi, A.G., Abdelkareem, M.A.: Renewable energy and climate change. Renew. Sustain. Energy Rev. **158**, 112111 (2022). https://doi.org/10.1016/J.RSER.2022.112111
3. Falnes, J.: On non-causal impulse response functions related to propagating water waves. Appl. Ocean Res. **17**, 379–389 (1995). https://doi.org/10.1016/S0141-1187(96)00007-7
4. Yu, Z., Falnes, J.: State-space modelling of a vertical cylinder in heave. Appl. Ocean Res. **17**, 265–275 (1995). https://doi.org/10.1016/0141-1187(96)00002-8
5. Ringwood, J.V., Zhan, S., Faedo, N.: Empowering wave energy with control technology: possibilities and pitfalls. Annu. Rev. Control. **55**, 18–44 (2023). https://doi.org/10.1016/j.arcontrol.2023.04.004

6. Depalo, F., et al.: Effects of dynamic axial stiffness of elastic moorings for a wave energy converter. Ocean Eng. **251** (2022). https://doi.org/10.1016/j.oceaneng.2022.111132
7. Ju, K., Xu, S., Zhang, H., Jin, S.: A study on a novel multi-body floating-point absorber with a nonlinear power take-off system and its hydrodynamic performance. Sci. Total Environ. (2025). https://doi.org/10.1016/j.scitotenv.2025.161032
8. Pu, H., et al.: Bio-inspired quasi-zero stiffness vibration isolator with quasilinear negative stiffness in full stroke. J. Sound Vib. **574** 118240. https://doi.org/10.1016/J.JSV.2024.118240
9. Villegas, C., Carrasco, D., Pierart, F.: Nonlinear-stiffness mechanism inspired in nature for wave energy conversion: a quick performance evaluation of its linear-stiffness zone (2024). https://doi.org/10.17185/duepublico/82701

Development of a Two-Degree-of-Freedom Model of Forearm for Pronation-Supination Motion

Mehmet Öksüz(✉) and Behzat Bahadir Kentel

TED University, Ankara 06420, Turkey
{mehmet.oksuz,behzat.kentel}@tedu.edu.tr

Abstract. This study presents the development of a novel biomechanical model for forearm pronation–supination (PS) motion that introduces a two-degree-of-freedom mechanism. The model includes a moving rotational axis (MRA) to represent the PS axis of the forearm. Furthermore, whereas some previous models allow only translational motion of the ulna, the new design integrates an additional revolute joint at the elbow, combined with a prismatic joint, to capture anatomically relevant rotational behavior of the ulna.

Compared with previous approaches, which incorporate four segments (elbow, wrist, ulna, and radius) but do not account for the distal inclination of the moving rotational axis, the current mechanism introduces this inclination through a variable slope of the proximal revolute-prismatic joint pair. Similar to anatomically grounded three-segment structure, the proposed model also employs three segments, offering a balance of biomechanical realism and kinematic simplicity.

The resulting mechanism is compared with previous models and demonstrates similar PS behavior while providing a more anatomically complete representation of ulnar motion. This work contributes a novel and efficient modeling strategy for studying forearm kinematics in biomechanical and rehabilitation applications.

Keywords: Biomechanics · Forearm Kinematic Model · Pronation-Supination (PS) · Moving Rotational Axis (MRA)

1 Introduction

Forearm pronation and supination—rotations that turn the hand palm up (supination) or palm down (pronation)—are essential for everyday tasks such as grasping, manipulating objects, and self-care. These motions arise from the coordinated articulation of the ulna and radius with the distal and proximal radioulnar joints, while the humerus provides proximal support through the elbow. The proximal radioulnar joint enables the radial head to rotate around the ulna, stabilized by the annular ligament, whereas the distal radioulnar joint permits the radius to cross over the ulna to complete PS. Figure 1 shows the positions of the ulna and radius during PS, highlighting their orientations and overall forearm configuration [1, 2].

© The Author(s), under exclusive license to Springer Nature Switzerland AG 2026
A. Chaker et al. (Eds.): EFIMMS 2026, MMS 205, pp. 116–125, 2026.
https://doi.org/10.1007/978-3-032-22270-1_12

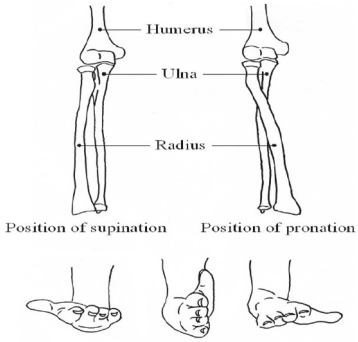

Fig. 1. Forearm bones (humerus, ulna and radius) in supination and pronation positions [2].

In vivo biomechanical studies and imaging-based investigations have deepened our understanding of how the bones and soft tissues move dynamically during forearm rotation. For instance, studies using 3D imaging and registration techniques have documented how the radius rotates relative to the ulna, and how the instantaneous axis of rotation shifts during motion, suggesting that PS involves more than a simple fixed-axis pivot [3]. Other investigations, including those combining motion analysis and finite element or musculoskeletal modeling, have quantified how muscular forces vary across different elbow flexion angles and PS positions, showing that pronation efficiency and torque generation depend strongly on bone geometry and joint posture [4, 5]. These findings emphasize that realistic modeling of forearm motion should account for both translation and rotation of the bones, not only for kinematics, but also for accurate simulation of functional movement.

Kinematic and biomechanical models of forearm PS have evolved over decades. Early biomechanical descriptions treated the forearm as a simple pivot, with the radius rotating about a fixed ulnar shaft and a single rotational axis [6]. However, such classical approaches failed to capture complex phenomena, including the “evasive” ulna motion observed in imaging studies. To address these limitations, Weinberg et al. introduced a refined kinematic model that simulated ulna motion and bone angulations during PS [7]. Subsequent subject-specific computational models based on CT or MRI enabled more realistic simulations across the full PS range while incorporating anatomical variability [8, 9]. Despite these developments, achieving a balance between anatomical fidelity, accurate bone kinematics (including ulna–radius rotation and translation), and computational tractability remains challenging.

Considering two different recent mechanisms, Weinberg et al. modeled the forearm using four links with two degrees of freedom. In the model shown in Fig. 1a, an additional wrist link is included besides the radius, ulna, and humerus. This model does not provide a direct angle for pronation–supination (PS) rotation [10]. However, in the model presented in Fig. 2a, the PS rotation angle is directly defined by the rotation of the MRA. This model provides three links that represent the radius, ulna and humerus. Furthermore, ulnar translation is taken into account, while ulnar rotation is neglected [11].

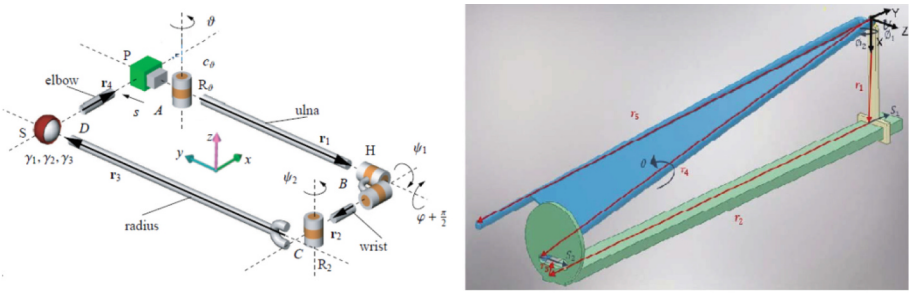

(a) (b)

Fig. 2. Previous models which are proposed by Weinberg [10] and Araz [11].

In this study, a new model for forearm PS motion is presented. The design is developed by considering the models of Araz and Weinberg. The modifications include simplifying the distal joint configuration by removing the "sphere-in-slot" joint and adding an extra revolute joint at the elbow, combined with a prismatic joint. This configuration allows anatomically realistic ulnar rotation while maintaining a three-segment forearm structure. By designing a slope angle for the proximal revolute-prismatic joint pair to capture the natural inclination of the forearm's PS rotational axis, the model aims to achieve a balance between anatomical accuracy and kinematic simplicity. The motion behavior of the proposed model is compared with the previous mechanisms, and the results show that it provides a more representative description of forearm bone motion, thereby supporting further developments in biomechanical modeling, rehabilitation devices, and sports applications.

2 Development of a Novel Forearm Model

In this study, the analysis provides the PS motion of the forearm, the ulnar angular position, and the spatial position of the MRA. The shoulder complex and upper arm are assumed to remain fixed in their neutral anatomical configuration. Figure 3 illustrates the proposed mechanism that represents a two-degree-of-freedom forearm model consisting of three interconnected segments and three mechanical joints. In this formulation, the PS angle and the ulnar rotational angle serve as the independent degrees of freedom defining the system's kinematic behavior. Consequently, the spatial position of the MRA is determined as a dependent variable.

The proposed mechanism is composed of three primary segments. Link 1 corresponds to the proximal coupling between the ulna and radius at the elbow. Link 2 represents the ulna itself, while link 3 denotes the radius segment, which integrates both the radial bone and the MRA. At the proximal end of the ulna, a combined prismatic–revolute joint is implemented, enabling axial translation and angular displacement of the ulna, denoted as s and θ_u, respectively. Furthermore, the prismatic-revolute joint can be set to a prescribed angle γ using an adjustable joint.

The radioulnar articulation is modeled using a spherical joint at the proximal radioulnar joint (PRUJ) and a spherical joint at the distal radioulnar joint (DRUJ). The segment

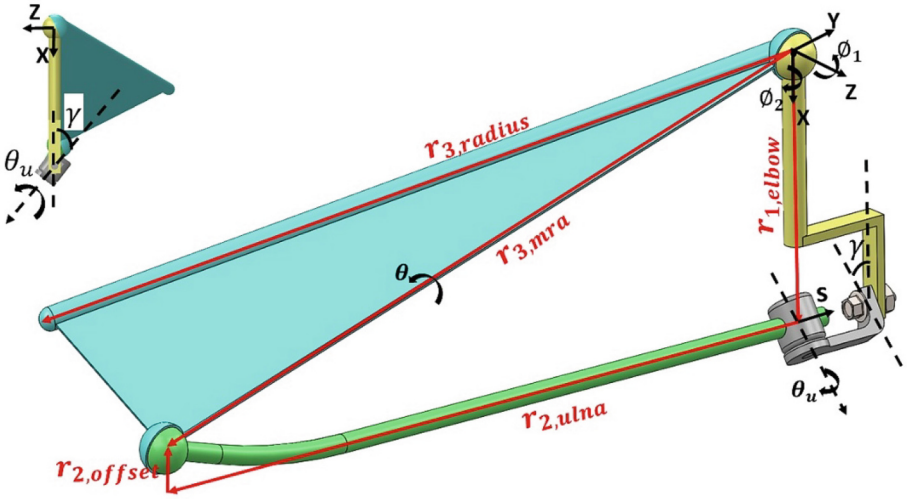

Fig. 3. Proposed forearm model with back-side view.

connecting these two joints defines the position and orientation of the MRA together with the radius bone. The angles ϕ_1 and ϕ_2 describe the orientation of the MRA relative to the radius coordinate frame —specifically, its inclination with respect to the z and x axes, respectively— while the PS angle θ corresponds to rotation of the MRA about its own axis. The rotations of MRA at the distal end are expressed by $_1$ and $_2$, respectively. At the DRUJ, the angular displacement of the ulna θ_u governs the distal shifting of the MRA distal end. Prior anatomical investigations have reported a coupled relationship between PS motion and the trajectory of MRA at distal radioulnar joint [12, 13]. For this reason, the proposed model is formulated so that ulnar rotation and PS motion occur in a coordinated manner.

The model parameters are expressed as vectors defined with respect to the reference coordinate frame attached to the proximal radius head. In this formulation, the ulna and the radius are represented by the vectors $\mathbf{r_{2,ulna}}$ and $\mathbf{r_{3,radius}}$, respectively. The proximal coupling between the two bones at the elbow is denoted by the fixed vector $\mathbf{r_{1,elbow}}$, whose direction extends from the proximal radius head (PRH) toward the proximal ulna head (PUH). Prior anatomical and imaging studies have demonstrated that the rotational axis does not pass directly through the center of the distal ulna head (DUH) [12–14]. Therefore, at the distal end of the ulna, a distance $\mathbf{r_{2,offset}}$ is defined between the center of the DUH and the distal end of the MRA. The MRA itself is represented by the vector $\mathbf{r_{3,mra}}$, extending from the PRH to the DUH. Finally, the position of the distal radius head (DRH) is specified by the vector $\mathbf{r_{3,radius}}$.

The proposed kinematic framework is intended as a generic representation of the forearm. Consequently, link dimensions are derived from 50th-percentile anthropometric data reported in established generic forearm models, as summarized in Table 1 [10]. This parameterization enables the model to reflect the characteristic motion behavior of an average adult forearm.

Table 1. Forearm Model Parameters

Parameters	Vectors	Magnitudes (mm)
Ulnar Height	$\mathbf{r_{1,elbow}}$	25
Ulnar Length	$\mathbf{r_{2,ulna}}$	269
Offset	$\mathbf{r_{2,offset}}$	0.2
MRA Length	$\mathbf{r_{3,mra}}$	270
Radius Length	$\mathbf{r_{3,radius}}$	269

Previous investigations have demonstrated that the position of the MRA changes continuously as PS motion occurs [13, 15, 16]. Accordingly, in the present model, each instantaneous MRA location corresponds directly to the associated PS angle and the concurrent ulnar rotation.

Moreover, studies involving multiple participants have shown that the MRA follows subject-specific trajectories in such a way that the distal end of the axis moves on an (almost) inclined line at the distal radioulnar joint (DRUJ) for most individuals [17]. To obtain this inclined line at DRUJ, the model configuration is adjusted. For this purpose, the prismatic-revolute joint at the proximal end of the ulna is allowed to rotate about an adjustable joint. The deviation from the vertical is assigned as angle γ (Fig. 3). This angle may be set for each subject since angle γ is a subject-specific parameter.

3 Kinematic Analysis of Forearm Motion

3.1 Inverse Kinematics

As outlined in the model development section, the PS angle θ and the ulnar rotational angle θ_u, which governs the instantaneous position of the MRA, are designated as the degrees of freedom of the mechanism. These quantities serve as the prescribed input variables for the proposed model. Once the angular state of the ulna has been specified, the remaining joint variables can be determined through inverse kinematic analysis. To establish the relationships among these joint variables, a vector loop-closure formulation is constructed, as expressed in Eq. (1).

$$\mathbf{T}\left[x, r_{1,elbow}\right] \cdot \mathbf{T}\left[y, s\right] \cdot \mathbf{R}\left[y, -\gamma\right] \cdot \mathbf{R}[x, \theta_u] \cdot \mathbf{T}\left[y, -r_{2,ulna}\right] \cdot \mathbf{T}\left[x, -r_{2,offset}\right] \quad (1)$$

$$\mathbf{R}[z, \phi_1] \cdot \mathbf{R}[x, \phi_2] \cdot \mathbf{T}\left[y, -r_{3,mra}\right] \cdot \mathbf{R}[x, \psi_2] \cdot \mathbf{R}[z, \psi_1]$$

The operator '$\cdot$' denotes products of two consecutive transformations, while **T** and **R** represent pure translation and pure rotation transformation matrices, respectively.

Using Eq. (1), all transformation matrices of the mechanism are derived. In the inverse kinematic analysis, the position vectors on both sides of the equation are set equal, allowing the joint variables ϕ_2, s, and ϕ_1 to be determined, as presented in Eqs. (2), (3) and (4), respectively.

$$\phi_2 = \text{atan2}\left(r_{2,\text{ulna}}\cos\gamma\sin\theta_u + r_{2,\text{offset}}\sin\gamma, \sqrt{\left(r_{3,\text{mra}}{}^2 - \left(r_{2,\text{ulna}}\cos\gamma\sin\theta_u + r_{2,\text{offset}}\sin\gamma\right)^2\right)}\right) \quad (2)$$

$$s = r_{2,\text{ulna}}\cos\theta_u - \sqrt{\left(r_{3,\text{mra}}{}^2\cos^2\phi_2 - \left(r_{1,\text{elbow}} - r_{2,\text{offset}}\cos\gamma + r_{2,\text{ulna}}\sin\gamma\sin\theta_u\right)^2\right)} \quad (3)$$

$$\phi_1 = \text{atan2}\left(r_{1,\text{elbow}} - r_{2,\text{offset}}\cos\gamma + r_{2,\text{ulna}}\sin\gamma\sin\theta_u, r_{2,\text{ulna}}\cos\theta_u - s\right) \quad (4)$$

As previously discussed, the distal end of the MRA is considered to move on an inclined line with a slope γ. This angle γ can be adjusted for subject-specific applications. By incorporating motion data from individual subjects, the value of the angle γ can be estimated to accurately reproduce subject-specific forearm kinematics.

By using inverse kinematics, $_1$ and $_2$ are found as mirror rotations of ϕ_1 and ϕ_2 at the distal side, respectively. The magnitudes are found to be equal, but the directions are opposite.

3.2 Forward Kinematics

Forward kinematics is employed to determine the orientation of the radius segment throughout PS motion. Initially, the joint variables are determined through an inverse kinematic analysis based on the ulnar rotational angle θ_u. This allows the orientation of the MRA relative to the fixed humeroradial reference frame to be defined during PS motion. Subsequently, forward kinematic analysis is used to calculate the rotation of the radius vector $\mathbf{r_{3,radius}}$ about the MRA vector $\mathbf{r_{3,mra}}$ using the Rodrigues rotation formula. The resulting position of the DRH is tracked during the PS motion. Since the hand is anatomically connected to the radius [10], this analysis provides insight into how the radius and hand move with respect to the humeroradial reference frame as they rotate around the MRA with the PS angle θ.

4 Results

Based on the subject-specific MRA trajectories reported in a previous study [17], the total displacement range of the MRA at the distal end is approximated as 10 mm. To achieve this displacement within the proposed model, the limits of the ulnar rotational angle θ_u is set between $-1.065°$ and $1.065°$. For the simulations, both degrees of freedom are varied simultaneously in a coordinated manner. PS angle θ is varied linearly from $-90°$ to $90°$ over the full PS motion whereas the ulnar rotational angle θ_u is incremented in its working range, accordingly.

The dynamic behavior of the rotational axis, together with the joints and bones responsible for generating PS motion, plays a critical role in accurately characterizing forearm kinematics. Therefore, in the previous section, kinematic formulations were developed with a specific focus on three key components: the orientation of the MRA, the axial displacement of the ulna, and the location of the distal radius head. In the present section, the results of these mentioned analyses are presented under separate subsections.

4.1 The Axial Displacement of the Ulna

During PS motion, the configuration of the elbow joint also changes. The axial translation of the ulna at the humeroulnar articulation is therefore examined, and the corresponding displacement variable s is presented in Fig. 4.

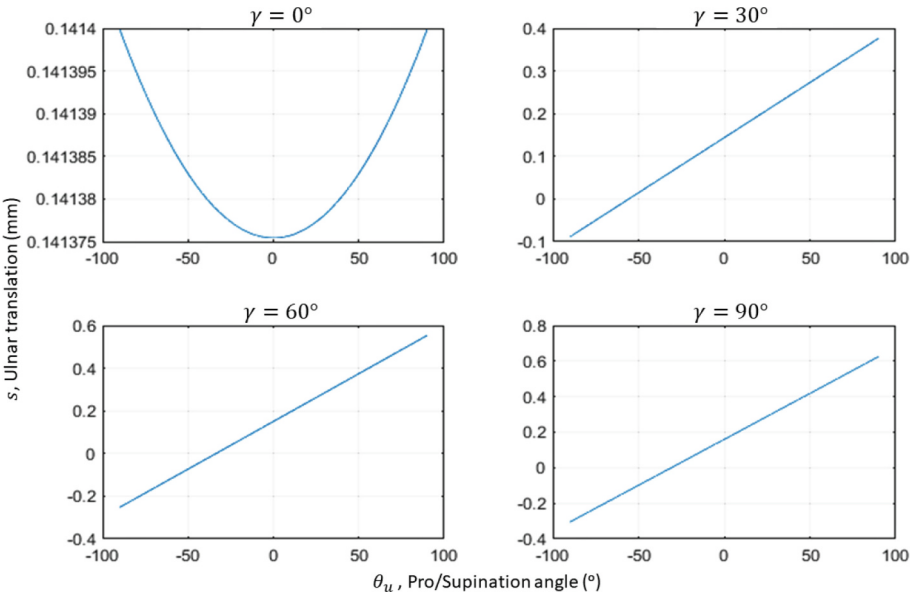

Fig. 4. Ulnar translation at humeroulnar joint as a function of the PS angle with various slope of revolute-prismatic pair γ.

When γ is set to 0°, the translational movement of the ulna remains nearly constant at approximately 0.141 mm. According to Araz's design, ulnar translation has a range between 0.142 mm to 0.188 mm [11]. However, as the slope of the humeroulnar joint γ increases toward 90°, axial displacement spans a wider interval, ranging from −0.3 mm to 0.625 mm. From an anatomical standpoint, the ulna is known to exhibit prismatic translation [12–14], which indicates that γ cannot realistically equal 0°. As a result of constant prismatic ulnar translation, the present model represents more realistic. This raises an important question: Does the joint slope at the humeroulnar interface give rise to the observed ulnar translation, or does the inherent sliding motion of the ulna necessitate the presence of such a joint slope? This issue will be addressed in a future work. Moreover, as expected, an increase in γ leads to a clear expansion in the allowable range of prismatic translation of the ulna.

4.2 The Orientation of the MRA

As detailed in the kinematic analysis section, the joint variables characterize the position of the MRA vector relative to the fixed humeroradial coordinate system, which is defined

at the proximal end of the radius. Throughout the PS motion, the geometric relationships at the elbow joint also undergo changes, and the corresponding angular variations at the humeroradial articulation are examined.

In this representation, the Euler angles ϕ_1 and ϕ_2 specify the orientation of the MRA vector, whereas the third Euler angle corresponds to the rotation associated with PS around the MRA axis. When γ is equal to 0°, ϕ_1 remains nearly constant at approximately 5.271°, because the distal point of the MRA translates along a direction nearly parallel to the z-axis. This calculated angle is consistent with Araz's kinematic analysis, as his model also defines a 5.263° orientation of the MRA about the z-axis [11]. Conversely, ϕ_2 exhibits a linear relationship with PS angle, spanning a range of about 2.12° as expected. As γ increases, the variation in ϕ_1 becomes more pronounced, while the range of ϕ_2 diminishes. When γ reaches 90°, ϕ_2 approaches a constant value near 0°, reflecting the fact that the distal end of the MRA predominantly translates parallel to the x-axis under this configuration.

4.3 The Location of the Distal Radius Head

The orientation of the MRA and the axial position of the ulna were determined through the inverse kinematic analysis presented in the previous section. Once the MRA orientation is known, the pose of the radius can subsequently be computed using forward kinematics. Figure 5 illustrates the rotation of the radius vector $\mathbf{r}_{3,radius}$ about the MRA vector as it changes throughout the full PS cycle. During this motion, the trajectory of the distal radius head is also examined to characterize its spatial behavior.

The prismatic–revolute joint pair represents the proximal radioulnar joint. This joint pair is inclined by an angle γ. This inclination reproduces the linear translation observed at the distal end of the MRA from an anatomical perspective. Accordingly, the orientation of the radius at its distal point was evaluated for γ values of 0°, 30°, 60°, and 90°. When

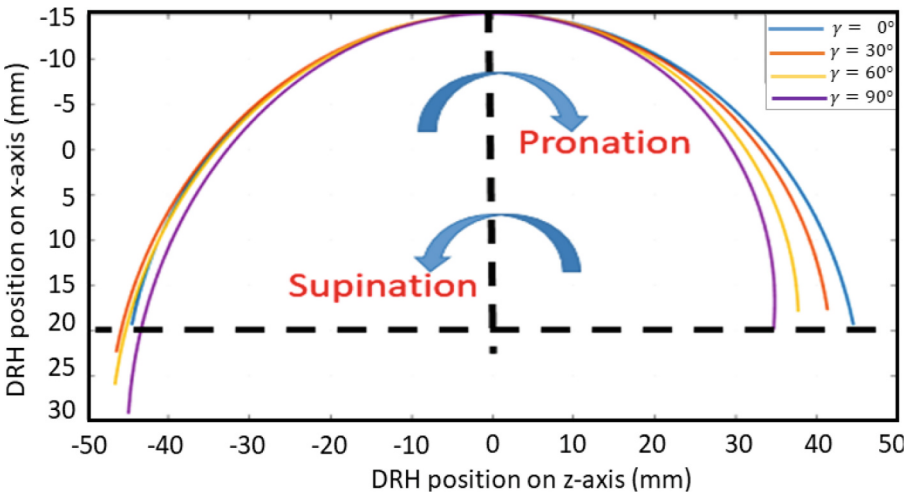

Fig. 5. The location of the distal radius head with various slope of revolute-prismatic pair γ.

$\gamma = 0°$, the radial head exhibited a fully symmetric behavior. In contrast, for higher γ angles, the distal end of the radial head displayed an asymmetric motion pattern, as expected.

5 Discussion and Conclusion

This study introduced a simplified yet anatomically informed kinematic mechanism for representing forearm PS motion. By revising the distal articulation and integrating a revolute–prismatic joint pair at the proximal ulna, the model provides a more realistic depiction of ulnar rotation and the MRA behavior compared with previous models in the literature. These modifications allow the mechanism to maintain low computational complexity while improving anatomical coherence.

The results show that the model can reproduce the main features of forearm rotation, such as the axial translation of the ulna and the changing orientation of the MRA. The slope angle γ is an important factor that influences these behaviors; higher values create displacement patterns that match in-vivo observations more closely. The forward kinematic analysis also showed that the mechanism avoids unrealistic hand abduction and produces wrist paths that agree with anatomical expectations. Overall, these findings indicate that the proposed structure accurately represents the essential spatial relationships between the ulna, radius, and hand.

Compared with existing models in the literature, the present approach offers a balanced alternative between overly simplified fixed-axis representations and computationally demanding musculoskeletal models. Its ability to mimic MRA shifting, direct PS angle representation and asymmetric distal radius motion suggests strong utility for applications in rehabilitation engineering, ergonomic assessment, and upper-limb device design.

Future work will focus on validating the model against experimental measurements, incorporating subject-specific anatomical data, and integrating soft-tissue constraints to further enhance biomechanical accuracy. Despite these limitations, the findings indicate that the proposed mechanism provides a promising foundation for efficient and anatomically meaningful simulation of forearm PS motion.

References

1. Kenhub Homepage. https://www.kenhub.com/en/library/anatomy/pronation-and-supination. Last accessed 27 Nov 2025
2. Moriwaki, Y., et al.: Development of forearm models based on human musculoskeletal system. J. Biomed. Sci. Eng. **4**(1), 1–12 (2009)
3. Taylor, C., et al.: In vivo 3D kinematic analysis of the distal radioulnar joint during pronation-supination. J. Biomech. **49**(10), 2178–2186 (2016)
4. Kuczynski, K., et al.: Muscle force contribution to forearm rotation torque: cadaveric study. Clin. Biomech. **18**(9), 731–738 (2003)
5. Crisco, J.J., et al.: Helical axis analysis of the forearm in vivo. J. Biomech. **41**(7), 1620–1629 (2008)
6. Hall, S.J.: Textbook of Human Kinetics, 3rd edn. Human Kinetics, Champaign (2002)

7. Weinberg, A.M., et al.: A new kinematic model of pro- and supination of the human forearm. J. Biomech. **33**(5), 567–575 (2000)
8. Kawano, F., Fukui, Y., Sugimura, K.: Construction of 3D skeletal model for pronation and supination of the forearm. In: Proceeding of the 2008 SAE World Congress, pp. 1–12. SAE International, Detroit (2008)
9. O'Driscoll, S.W., et al.: 3D modeling of forearm pronation and supination using CT-based methods. Clin. Orthop. Relat. Res. **466**(3), 616–624 (2008)
10. Kecskemethy, A., Weinberg, A.: An improved elasto-kinematic model of the human forearm for biofidelic medical diagnosis. Multibody Dyn. **12**(1), 1–21 (2005)
11. Araz, M., Kentel, B.: Preliminary design of a novel kinematic forearm model for pro/supination motion. In: Proceedings of the IEEE Conference (2020)
12. Duck, T.R., King, G.J., Johnson, J.A.: Screw displacement axes of the forearm pro-supination. In: 47th Annual Meeting, Orthopaedic Research Society, California (2001)
13. Tay, S.C., et al.: A method for in-vivo kinematic analysis of the forearm. J. Biomech. **41**(1), 56–62 (2008)
14. Matsuki, K.O., et al.: In vivo 3D kinematics of normal forearms: analysis of dynamic forearm rotation. Clin. Biomech. **25**(10), 979–983 (2010)
15. Nakamura, T., Yabe, Y., Horiuchi, Y., Yamazaki, N.: In vivo motion analysis of forearm rotation utilizing magnetic resonance imaging. Clin. Biomech. **14**(5), 315–320 (1999)
16. Veeger, D.H.E.J., Yu, B.: Orientation of axes in the elbow and forearm for biomechanical modeling. In: Proceedings of the Fifteenth Southern Biomedical Engineering Conference (1996)
17. Tay, S.C., Riet, R.V., Kazunari, T., Amrami, K.K., An, K.-N., Berger, R.A.: In-vivo kinematic analysis of forearm rotation using helical axis analysis. Clin. Biomech. **25**(7), 655–659 (2010)

A New Perspective on Number Synthesis: Introduction and Application of Topological Requirements for Kinematic Chain Filtering

Gustavo Valdatti Souza(✉), Estevan Hideki Murai, Andrea Piga Carboni, and Daniel Martins

UFSC, Laboratory of Applied Robotics - LAR, Federal University of Santa Catarina, Florianopolis, SC, Brazil

gustavo.valdatti@ufsc.br

Abstract. Mechanism development has traditionally relied on designers' experience and intuition, creating subjective processes. While systematic methodologies following Hartenberg and Denavit's three-stage approach provide structured frameworks for mechanism synthesis through kinematic chain enumeration and evaluation, contemporary methods lack systematic classification of practical mechanical characteristics. This absence constrains computational filtering development, maintaining designer-dependent processes with considerable subjectivity. This study presents a novel methodology for automating kinematic chain filtering in number synthesis through topological requirements that enable systematic observation and quantification of characteristics in state-of-the-art mechanisms via graph analysis. The methodology comprises nine stages introducing topological requirements categorized into degree requirements (DR), subchain requirements (SR), and relationship requirements (RR). The C-paths concept for classifying kinematic pairs and subchain classification into isolated and shared categories are introduced. Computational algorithms filter chains based on these requirements, validated through three case studies: vehicle rear suspension, finger exoskeletons, and excavator articulated arms. Results demonstrate substantial candidate reduction while preserving viable solutions: rear suspension from 35 to 6 graphs, exoskeleton from 6,856 to 117 chains, and excavator from 83,547 to 1,235 solutions. The approach eliminates human error and enables systematic evaluation with enhanced precision and efficiency, establishing a more structured, objective, and computationally efficient design process for mechanism synthesis.

Keywords: Mechanism synthesis · Topological requirements · Kinematic chains · Graph theory · Number synthesis

1 Introduction

The development of mechanisms begins with identifying specific needs and selecting potential solutions to meet identified requirements. Historically, mecha-

Supported by organization FINEP and CNPq.

© The Author(s), under exclusive license to Springer Nature Switzerland AG 2026
A. Chaker et al. (Eds.): EFIMMS 2026, MMS 205, pp. 126–136, 2026.
https://doi.org/10.1007/978-3-032-22270-1_13

nism development relied heavily on designers' experience and intuition, creating dependencies that limited systematic innovation. To overcome these limitations, structured methodologies for mechanism synthesis have evolved, offering systematic approaches to creating viable mechanisms through synthesis processes [1]. Mechanism synthesis, as established by Hartenberg and Denavit [2], comprises three fundamental stages: number synthesis, type synthesis, and dimensional synthesis. Number synthesis, the most critical stage according to Mruthyunjaya [3], determines the structural configuration of candidate kinematic chains. However, existing methodologies face significant challenges in efficiently filtering large sets of enumerated chains while maintaining practical relevance. Current approaches to mechanism synthesis suffer from several critical limitations. First, the absence of systematic frameworks for classifying observable practical requirements increases dependence on individual designer expertise. Second, the lack of standardized criteria impedes implementation of automated methods for kinematic chain filtering [4]. Third, evaluation of generated chains becomes susceptible to errors due to insufficient structured guidance toward critical characteristics. These limitations result in resource-intensive processes that are both costly and error-prone, particularly when analyzing extensive mechanism sets. The complexity and magnitude of chain sets often render manual analysis impractical, highlighting the need for computational automation in the synthesis process. This work, building upon the foundation established in [5] with minor modifications, introduces a comprehensive methodology that addresses these challenges through systematic introduction of topological requirements, enabling computational filtering of kinematic chains while maintaining practical engineering relevance.

2 Related Work

Several authors have expanded on Hartenberg and Denavit's [2] work. Yan [6] proposed a six-step methodology focusing on generalization of similar existing mechanisms. While providing a streamlined process through "twin" mechanisms analysis, this approach lacks explicit consideration of crucial structural characteristics such as circuit numbers and workspace requirements. Tsai [7] introduced a systematic methodology using graph theory, combinatorial analysis, and computational algorithms. This approach converts functional requirements into structural characteristics for systematic mechanism enumeration. However, its complexity poses implementation challenges, particularly in kinematic chain filtering due to insufficient systematic specification of filtering requirements. Murai [8] developed an eleven-step methodology incorporating preliminary steps for customer requirements analysis and state-of-the-art research. This approach introduces three requirement blocks: enumeration and two selection phases based on structural and practical characteristics. While more structured than previous methodologies, it lacks rigorous delineation and categorization of practical mechanical characteristics. Ding, Yang, and Kecskeméthy [9] proposed a seven-step methodology beginning with customer requirements analysis and utilizing pre-developed databases for chain enumeration. This approach categorizes

requirements into structural characteristics, functional requirements, and other design constraints. However, it fails to define characteristics in an organized and replicable manner. Despite these advances, existing methodologies lack systematic frameworks for classifying practical requirements observable in mechanisms, limiting automated filtering implementation and maintaining dependence on designer expertise.

3 Proposed Methodology

3.1 Methodological Framework

The proposed methodology consists of nine structured stages, addressing gaps identified in existing approaches through systematic integration of topological requirements. The methodology enhances traditional synthesis processes by introducing computational filtering tools that reduce subjectivity while maintaining practical relevance. The nine stages include: (1) Customer requirements identification, (2) Technological research and discussion, (3) Requirements definition, (4) Number synthesis, (5) Evaluation of viable kinematic chains, (6) Type synthesis, (7) Dimensional synthesis, (8) Prototype fabrication, and (9) Documentation and manufacturing. Specifically, this work concentrates on Stage (5), Evaluation of viable kinematic chains, where the topological requirements serve as the main filtering criteria. This targeted application represents the core innovation, differentiating this methodology from previous approaches by enabling a precise, objective, and computational mechanism selection process.

3.2 Topological Requirements Classification

The key innovation of this methodology is the introduction of topological requirements as a distinct filtering category. Unlike traditional structural requirements (mobility, circuits) used for enumeration, topological requirements capture local characteristics observable in successful mechanisms. They translate practical engineering insights—such as specific link configurations or connection arrangements—into mathematically tractable filtering criteria. These requirements are organized into three hierarchical categories, summarized in Table 1.

Degree Requirements (DR) focus on individual link characteristics. Since the degree of a link (number of connected joints) directly correlates with its functional role, these requirements filter chains based on the necessary complexity of reference, end-effector, or intermediate links.

Subchain Requirements (SR) address higher-order structures formed by sequences of connected links. We classify these into two types: *Isolated subchains* (or C-paths), which are autonomous units consisting exclusively of binary links in series; and *Shared subchains*, which maintain connections with multiple mechanism branches to distribute loads or define complex kinematic relationships. Specific SR definitions allow the identification of subsystems like linear actuators or transmission lines (see Fig. 1).

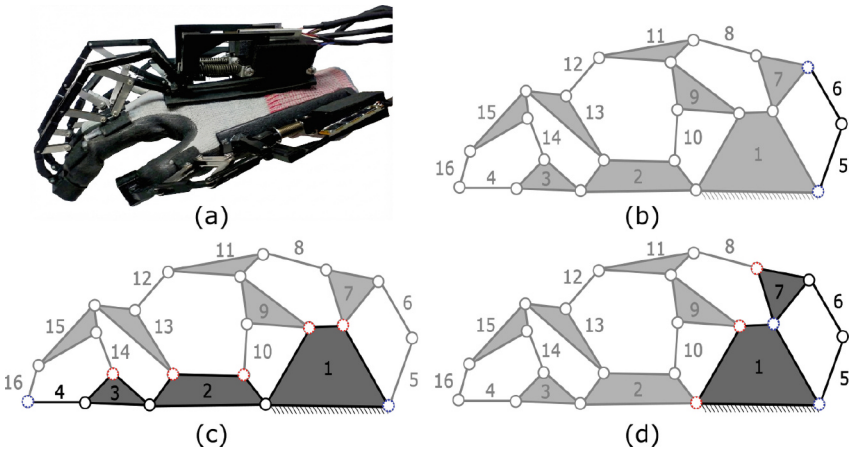

Fig. 1. Subchain requirements (SR) applied in an exoskeleton, adapted from [10] - (a) Original mechanism, (b) SRI, (c) SRSS and (d) SRSP.

Relation Requirements (RR) define mandatory connectivity patterns. These requirements ensure the proper integration of the previously specified elements, establishing rules for how the base, end-effector, and subchains must connect to one another to ensure functional feasibility.

Table 1. Summary of the proposed Topological Requirements for kinematic chain filtering.

Category	Code	Requirement Description
Degree Requirements (DR)	DRR	Reference link type specification
	DRE*i*	End-effector link type(s) specification
	DRI*i*	Intermediate link types specification
Subchain Requirements (SR)	SRI*i*	Isolated serial subchain (C-paths)
	SRSS*i*	Shared serial subchain specifications
	SRSP*i*	Shared parallel subchain specifications
Relation Requirements (RR)	RRR*i*	Base-to-structure connections
	RRE*i*	End-effector-to-structure connections
	RRS*i*	Inter-subchain connections
	RRG*i*	General connectivity specifications

Note: The index 'i' indicates that multiple requirements of this type may exist.

3.3 C-Paths Concept

A complementary innovation introduces C-paths, defining subchains consisting exclusively of binary links arranged in series within larger kinematic structures. The parameter C represents the total number of kinematic pairs connecting binary link series, including boundary connections. This nomenclature correlates with connectivity parameters and aligns with graph theory representations. Figure 2 shows the realization of a 3-path.

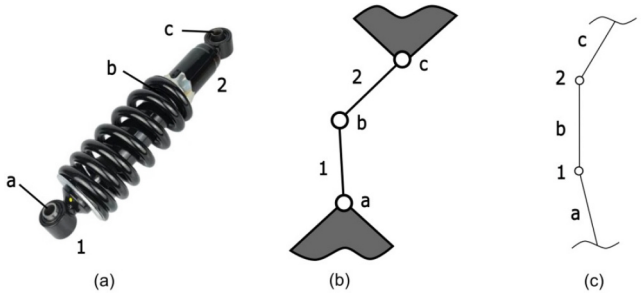

Fig. 2. Realization of a 3path Realization of a 3-path: (a) Real shock absorber, (b) Structural representation, (c) Graph representation.

4 Case Studies and Results

4.1 Overview of Applications

Three case studies in [5] validate the proposed methodology across different engineering contexts, demonstrating versatility and effectiveness in reducing candidate chain numbers while maintaining practical relevance.

4.2 Rear Suspension Mechanism for Two-Wheeled Vehicles

Requirements Definition. The rear suspension case study establishes structural requirements based on existing systems while exploring new design alternatives. To push performance boundaries and circumvent patent restrictions, more complex parameters were adopted: mobility $M = 2$, circuits $\nu = 3$, and planar workspace $\lambda = 3$. Topological requirements reflect practical suspension system characteristics:

- **DRR:** Reference link must be ternary, enhancing adjustable characteristics and providing more direct subcircuit-damping relationships
- **SRI:** Two 3-path subchains representing linear actuators
- **RRR:** Reference link must connect to both actuators

Results and Analysis. The atlas compilation revealed 35 distinct non-degenerate graphs for the specified structural requirements. Systematic algorithmic verification reduced this set through progressive filtering:

1. **Degree Requirements Filtering:** DRR application reduced chains to 32
2. **Subchain Requirements Filtering:** SRI application identified 11 graphs with two 3-paths
3. **Relation Requirements Filtering:** RRR application yielded 6 final mechanisms with ternary links connected to two 3-paths

The methodology successfully reduced the initial set by 83%, demonstrating effective filtering while maintaining viable candidates. Each resulting mechanism satisfies all topological requirements, providing design alternatives that meet suspension system specifications. Figure 3 shows the graphs and structural representations of the six remaining kinematic chains.

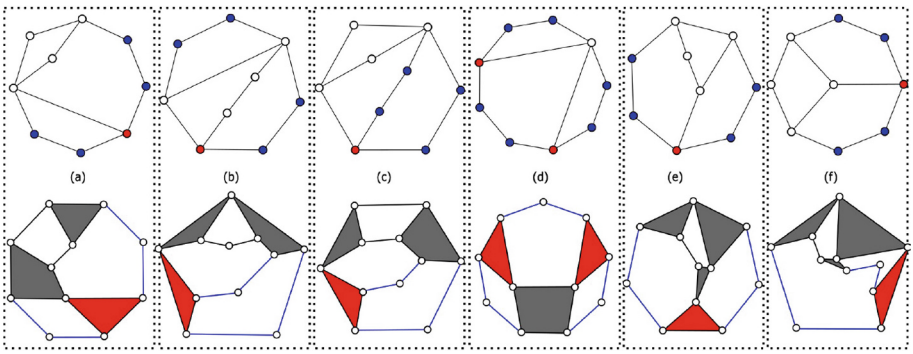

Fig. 3. Results after applying the topological requirement filters

Functional Representation. One mechanism (Fig. 3 (e)) was arbitrarily selected for detailed functional representation, illustrating practical implementation of the synthesis results. The representation demonstrates how topological requirements translate into mechanically feasible configurations suitable for two-wheeled vehicle applications (Fig. 4).

4.3 Additional Case Studies Summary

The results of the other two case studies are briefly presented in this section. However, a comprehensive analysis of these cases will be reported in future publications.

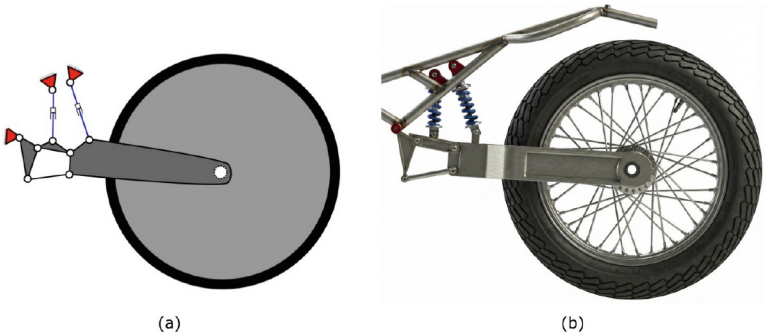

Fig. 4. (a) Functional representation of one possible candidate, (b) Rendering of the mechanism.

Hand Exoskeleton for Fingers 2-5. The exoskeleton case study addressed rehabilitation mechanisms for fingers 2–5, utilizing structural requirements $M = 1$, $\nu = 5$, $\lambda = 3$. Complex topological requirements captured anatomical movement patterns and actuation system characteristics. The methodology reduced 6.856 initial chains to 117 viable candidates, demonstrating effectiveness in handling large-scale synthesis problems.

Excavator Articulated Arm Mechanism. The excavator case study represented the most challenging scenario, addressing $M = 3$, $\nu = 5$, $\lambda = 3$ requirements for hydraulic excavation systems. The methodology processed 83.547 initial chains, reducing them to 1.235 viable solutions while maintaining practical relevance for construction and mining applications (Table 2).

Table 2. Kinematic chain filtering results for the three case studies.

Case Study	Initial No.	Final No.	Reduction (%)
Rear Suspension	35	6	83%
Finger Exoskeleton	6.856	117	98%
Excavator Arm	83.547	1.235	99%

5 Discussion

5.1 Methodology Effectiveness

The proposed methodology demonstrates significant advantages over existing approaches across multiple dimensions. The systematic reduction of candidate chains (83% for suspension, 98% for exoskeleton, 99% for excavator) illustrates

effective filtering while preserving practical solutions. Computational automation eliminates human error risks and enables evaluation of extensive kinematic chain sets, addressing scalability challenges in traditional synthesis approaches. The structured categorization of topological requirements provides replicable criteria for diverse mechanism types.

5.2 Innovation Impact

The introduction of topological requirements fundamentally bridges the gap between theoretical graph representation and practical mechanism characteristics. Established graph-based synthesis methods, such as those by Tsai [7], Yan [6], Murai [8], and Ding [9], have primarily focused on the systematic *enumeration* of kinematic chains based on global structural parameters. While these methodologies occasionally incorporate local constraints—such as limiting link degrees for specific tasks—these are often applied in an intuitive, ad-hoc manner tailored to a specific case study rather than through a generalized formalism. The key novelty of the proposed methodology lies in shifting the focus from enumeration to *filtering* by establishing a **structured framework for local topological requirements** through the defined categories (DR, SR, and RR). By formalizing what was previously treated intuitively, this advancement enables automated filtering based on directly observable mechanism features, significantly reducing dependence on designer expertise while ensuring functional feasibility. Furthermore, the integrated C-paths concept provides systematic subchain classification, offering new perspectives for mechanism analysis and synthesis by enhancing the understanding of connectivity patterns and their relationship to functional performance.

5.3 Practical Applications

Case study results demonstrate the methodology's applicability across diverse engineering contexts, from transportation systems to rehabilitation devices and construction equipment. The systematic approach facilitates exploration of innovative solutions while ensuring practical feasibility. The computational implementation enables integration into existing design workflows, supporting both academic research and industrial applications. The methodology's structured nature makes it suitable for educational purposes and knowledge transfer.

5.4 Computational Scalability and Efficiency

A critical challenge in mechanism synthesis is the combinatorial explosion of kinematic chains. The proposed methodology addresses scalability through a hierarchical filtering strategy implemented using primarily the SageMath graph library. While general subgraph isomorphism algorithms are computationally intensive (often NP-complete), our approach reduces complexity by decomposing the problem into three optimized layers:

1. **Partition-Based Filtering ($O(1)$ per group):** The first stage leverages the link assortment (partition) of the kinematic chains. Since the graphs are stored as graph6 lists within files named according to their partition (encoding the degree sequence, i.e., the number of vertices of degree 2, 3, and so on), the algorithm can instantly accept or reject entire groups of graphs without evaluating the individual chains contained within that partition. This eliminates the vast majority of non-viable candidates by discarding partitions that lack the sufficient number of specific link types defined by the degree and subchain requirements at virtually zero computational cost. This efficiency is achieved by leveraging the pre-computed organization of the database.
2. **Heuristic Subchain Identification (Polynomial Time):** Instead of applying a generic subgraph isomorphism algorithm to identify topological features related to subchain requirements, the methodology employs a directed neighbor-search algorithm. For specific shared serial and parallel subchain requirements (SRSS and SRSP), the algorithm identifies candidate start vertices and iteratively verifies neighbors that match the sequence, explicitly preventing backtracking. In the case of shared parallel subchain requirements (SRSP), it additionally verifies whether the initial and final links are connected, representing a closed loop. For isolated subchains (SRI/C-paths), the algorithm detects boundary vertices (links with degree > 2 connected to a binary link) and traverses the binary chain to determine its length. This reduces the problem to a local path-tracing operation, which is polynomial and highly efficient given the limited length of practical kinematic subchains.
3. **Relation Verification via Cached Indices ($O(1)$ per check):** The efficiency of the final stage relies on data caching. During the subchain identification process, the unique identifiers (IDs) of key elements—such as the base link (DRR), end-effector (DRE), and subchain connection points—are stored. Consequently, checking Relation Requirements (RR) does not require graph traversal; the algorithm simply queries the adjacency matrix to verify if the pre-identified IDs are connected.

This hierarchical approach ensures that computationally expensive operations are only performed on a pre-filtered subset of candidates. In the excavator case study, this strategy allowed the efficient processing of 83.547 initial chains, demonstrating the method's scalability for high-complexity mechanism synthesis.

6 Conclusions

This work presents a novel methodology for mechanism synthesis that significantly advances the field through systematic introduction of topological requirements. The key contributions include:

1. **Systematic Classification:** Introduction of degree, subchain, and relation requirements providing structured filtering criteria

2. **Computational Automation:** Development of algorithms enabling automated chain filtering based on topological characteristics
3. **Practical Validation:** Demonstration of effectiveness across three diverse engineering applications
4. **Innovation Framework:** Establishment of systematic approach reducing subjectivity while maintaining practical relevance

The methodology successfully addresses critical limitations in existing synthesis approaches by providing objective, replicable criteria for kinematic chain evaluation. The substantial reduction in candidate chains (83–99% across case studies) while maintaining viable solutions demonstrates the approach's effectiveness and efficiency. Future work includes expanding algorithmic capabilities, developing graphical interfaces for broader application, and integrating additional mechanism theory concepts such as symmetry evaluation and actuated control degrees. The methodology's structured nature provides a foundation for continuous enhancement and adaptation to emerging mechanism design challenges.

Acknowledgment. This study was financed by the Financiadora de Estudos e Projetos (FINEP), project number 0378/23, and Conselho Nacional de Desenvolvimento Científico e Tecnológico (CNPq), process number 141047/2025-9 and 312980/2025-6. The authors acknowledge the Laboratory of Applied Robotics (LAR) at the Federal University of Santa Catarina (UFSC) for providing infrastructure and technical support.

References

1. Silva, S.d.S., Souza, G.V., Exel, G.P., Rincon, L.M., Martins, D.: Development of a new functional and discrete finger prosthesis. In: 27th ABCM International Congress of Mechanical Engineering, Florianópolis-SC, Brazil (2023)
2. Hartenberg, R.S., Denavit, J.: Kinematic Synthesis of Linkages. McGraw-Hill, New York (1964)
3. Mruthyunjaya, T.S.: Kinematic structure of mechanisms revisited. Mech. Mach. Theory **38**(4), 279–320 (2003)
4. Ding, J., Li, X., Ding, H., Yang, W.: Computer aided synthesis method for the configuration of the mechanical arm of face-shovel hydraulic excavator based on contracted graph and open loop kinematic chains. Mech. Mach. Theory **197**, 105627 (2024)
5. Souza, G.V.: A new methodology for evaluating kinematic chains in number synthesis through topological requirements. M.S. thesis, Universidade Federal de Santa Catarina, Florianópolis, Brazil (2025)
6. Yan, H.S.: Creative design of mechanical devices. Springer, Singapore (1999)
7. Tsai, L.: Mechanism Design: Enumeration of Kinematic Structures According to Function. CRC Press (2000)
8. Murai, E.H.: Number synthesis methods for mechanism design: an alternative approach. Ph.D. thesis, Universidade Federal de Santa Catarina (2019)

9. Ding, H., Yang, W., Kecskeméthy, A.: Automatic Structural Synthesis and Creative Design of Mechanisms. Springer, Singapore (2022)
10. Jo, I., Bae, J.: Design and control of a wearable and force-controllable hand exoskeleton system. Mechatronics **41**, 90–101 (2017)

Friction Torque and Energy Loss Prediction of Single Degree-of-Freedom Mechanisms Considering the Effects of Variable Inertia

P. Català[1(✉)], J. M. Veciana[2], and L. Jordi[2]

[1] Department of Mechanical Engineering, Universitat Politècnica de Catalunya, EPSEM, Avenue de les Bases de Manresa 61-73, 08242 Manresa, Spain
pau.catala@upc.edu

[2] Department of Mechanical Engineering, Universitat Politècnica de Catalunya, ETSEIB, Avenue Diagonal 647, 08028 Barcelona, Spain
{joaquim.maria.veciana,lluisa.jordi}@upc.edu

Abstract. Single Degree-of-Freedom (SDOF) mechanisms are used in huge range of applications. An affordable, simple and purely mechanic experimental method to evaluate their energy efficiency (e.g. energy loss due to friction), is the free-deceleration method. The studies that claim to apply this experimental method to SDOF systems, always consider the inertia of the entire system as a constant value. The novelty of this study is to model the effects of considering a variable inertia when applying the free-deceleration method to evaluate energy loss due to friction. The problem formulation is based in the work-energy theorem to obtain the equation of motion for a SDOF mechanism; in this case, a slider-crank mechanism. A test stand is presented to derive experimental values of the instantaneous total friction torque, the mean total friction torque per cycle and the energy loss per cycle.

Keywords: Friction Torque Measurement · Energy Loss Measurement · Free-Deceleration Method · Variable Inertia · Single Degree-of-Freedom Mechanisms

1 Introduction

The evaluation of frictional and mechanical losses that impact energy efficiency in transmissions, mechanisms and machines is gaining relevance when choosing between feasible solutions. Some examples of studies comparing energy efficiency for well-known Single Degree-of-Freedom (SDOF) linkage mechanisms without experimental validation are found in [1, 2], focused in clean energy applications and legged robotics, respectively.

An experimental technique used to evaluate the energy efficiency due to frictional or mechanical losses for SDOF mechanisms is the free-deceleration method, also known as run-down method or coast-down method. The method consists in accelerating the system until a steady-state with a mean constant input velocity, cutting sharply the

© The Author(s), under exclusive license to Springer Nature Switzerland AG 2026
A. Chaker et al. (Eds.): EFIMMS 2026, MMS 205, pp. 137–144, 2026.
https://doi.org/10.1007/978-3-032-22270-1_14

input power and then recording the transient period until the standstill of the system. The frictional or mechanical losses are obtained by analysing the recorded deceleration profile. The free-deceleration method theoretical fundamentals are in the work-energy theorem; it is claimed as a straight-forward, purely mechanic and cheap experimental method, requiring a single sensor capable of recording velocities.

Experimental studies that obtain frictional losses for SDOF systems using the free-deceleration method, always assume the inertia of the entire system to be constant. Examples of these experimental studies include the evaluation of friction loss in a shaft supported by two high-speed bearings [3], a single tapered roller bearing under big radial loads mounted in a shaft supported by other two bearings [4], a reactive wheel actuator used in a spacecraft application [5], the bearings mounted on the hub of a wheelchair [6], and the comparison of energy loss between a slider-crank mechanism and an eccentric cam mechanism [7].

This study presents a novel expansion of the free-deceleration method to SDOF systems characterized by variable inertia. An experimental test stand, which employs a slider-crank mechanism as a SDOF system, is presented.

2 Problem Formulation

The experimental test stand consists of a slider-crank mechanism acting against a compression spring (Fig. 1a), a flywheel with a 90-toothed disc (encoder), a clutch and a DC motor (Fig. 1b). The schematic representation of the slider-crank mechanism is shown in Fig. 1c. The experimental angular velocity $\dot{\varphi}_1$ is derived using an opto-encoder sensor (Fig. 1d) that gives a square signal which allows the measurement of the time interval between consecutive teeth. The signal analyser is set to a 500 kHz sampling rate. The geometric and dynamic parameters for the slider-crank mechanism are presented in Table 1.

Table 1. Geometric and dynamic parameters.

Parameters and values			
$l_1 = 25$ mm	$l_{OG_1} = 0.06$ mm	$m_1 = 17.2$ kg	$I_{G_1} = 0.0775$ kgm^2
$l_2 = 85$ mm	$m_2 = 0.114$ kg	$I_{G_2} = 1.28 \cdot 10^{-4}$ kgm^2	$m_3 = 1.3$ kg
$k_s = 1.23$ N/mm	$F_{pre} = 25.83$ N		

According to Fig. 1c, the system's mobility is described by the generalized coordinates $\mathrm{q} = \{\varphi_1, \varphi_2, y\}^{\mathrm{T}}$ and generalized velocities $\dot{\mathrm{q}} = \{\dot{\varphi}_1, \dot{\varphi}_2, \dot{y}\}^{\mathrm{T}}$. The independent coordinate is considered to be φ_1. By applying the closed loop method, two constraint equations can be found and after differentiation, the expressions of the generalized velocities are obtained.

$$\dot{\varphi}_2 = \frac{l_1 \cos\varphi_1}{\sqrt{l_2^2 - (l_1 \sin\varphi_1)^2}}\dot{\varphi}_1 \tag{1}$$

$$\dot{y} = \left(l_1 \sin\varphi_1 - \frac{l_1^2 \sin\varphi_1 \cos\varphi_1}{\sqrt{l_2^2 - (l_1 \sin\varphi_1)^2}} \right) \dot{\varphi}_1 \tag{2}$$

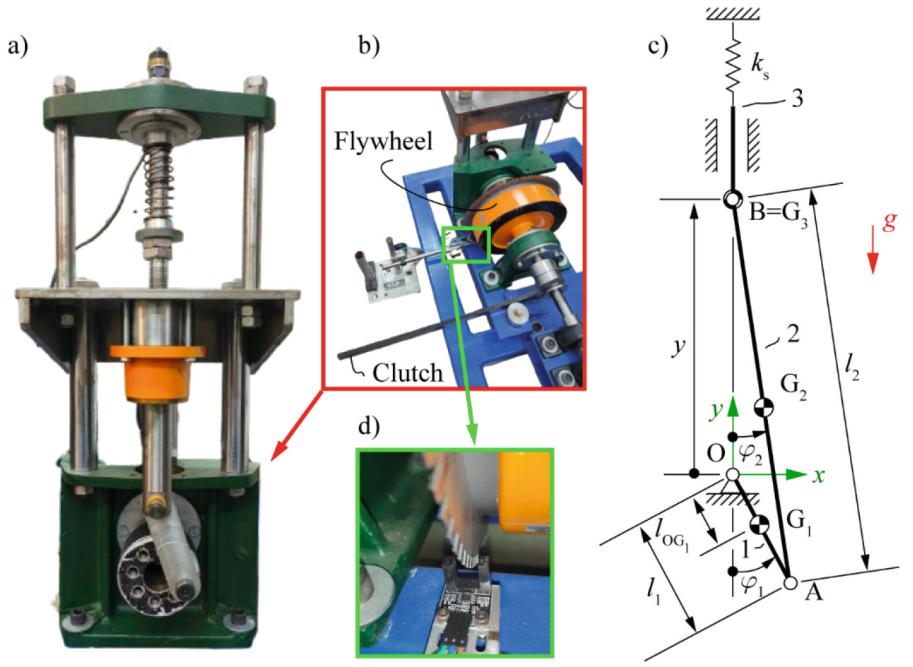

Fig. 1. a) The slider-crank mechanism (front); b) Flywheel and clutch (back); c) Schematic representation; d) opto-encoder and the 90-toothed disc attached to the flywheel.

The work-energy theorem, applied between two mechanical states (1 and 2), establishes that the variation in the system's kinetic energy (ΔE_k) is equal to the total work done by internal and external forces (W). The work done by conservative forces (the compression spring force and the gravitational force) is expressed as the negative variation of the potential energy, $W_{cons} = -\Delta E_p$. The work done by non-conservative forces corresponds to energy loss due to friction, expressed as W_{loss}. Thus, the variation of the mechanical energy of the system yields $\Delta E_m = \Delta E_k + \Delta E_p$, and the work-energy theorem can be written as Eq. (3)

$$\Delta E_m]_1^2 = \sum W_{loss}]_1^2 \tag{3}$$

For the slider-crank mechanism mounted on the test stand, which is positioned on a vertical plane, the free-deceleration transient period begins once the clutch is activated. During this period, the equation of motion is expressed with Eq. (4), which is obtained by differentiating the work-energy theorem with respect to time. In Eq. (4),

$I_{\mathrm{red}}(\varphi_1)$ represents the variable inertia of the entire system and $T_{\mathrm{red}}(\varphi_1, \dot{\varphi}_1)$ is the resultant torque of the overall system of forces reduced to the coordinate φ_1. During the free-deceleration period, $T_{\mathrm{red}}(\varphi_1, \dot{\varphi}_1)$ represents only the total friction torque of the overall SDOF mechanism because the DC motor does not act on the system.

$$I_{\mathrm{red}}(\varphi_1)\ddot{\varphi}_1 + \frac{1}{2}\frac{\mathrm{d}I_{\mathrm{red}}(\varphi_1)}{\mathrm{d}\varphi_1}\dot{\varphi}_1^2 + \frac{\mathrm{d}E_{\mathrm{p}}}{\mathrm{d}\varphi_1} + T_{\mathrm{red}}(\varphi_1, \dot{\varphi}_1) = 0 \tag{4}$$

The terms in Eq. (4) are obtained with Eqs. (5), (6) and (7), respectively

$$I_{\mathrm{red}}(\varphi_1) = m_1 l_{\mathrm{OG_1}}^2 + I_{\mathrm{G_1}} + m_2\left(\frac{l_1^2}{4}\cos^2\varphi_1 + l_1^2\sin^2\varphi_1 - \frac{l_1^3\sin^2\varphi_1\cos\varphi_1}{\sqrt{l_2^2-(l_1\sin\varphi_1)^2}} + \frac{l_1^4\sin^2\varphi_1\cos^2\varphi_1}{4\left(l_2^2-(l_1\sin\varphi_1)^2\right)}\right) + I_{\mathrm{G_2}}\frac{l_1^2\cos^2\varphi_1}{l_2^2-(l_1\sin\varphi_1)^2} + m_3\left(l_1^2\sin^2\varphi_1 - \frac{l_1^4\sin^2\varphi_1\cos^2\varphi_1}{l_2^2-(l_1\sin\varphi_1)^2}\right) \tag{5}$$

$$\mathrm{d}I_{\mathrm{red}\,\varphi_1}(\varphi_1)/\mathrm{d}\varphi_1 = m_2\left(\frac{\frac{3}{4}l_1^2\sin(2\varphi_1) + \frac{l_1^3\sin\varphi_1\left(l_1^2\sin^2\varphi_1+3l_2^2\sin^2\varphi_1-2l_1^2\sin^4\varphi_1-2l_2^2\right)}{\left(l_2^2-(l_1\sin\varphi_1)^2\right)^{3/2}} + \frac{l_1^4\cos\varphi_1\sin\varphi_1\left(l_1^2\sin^4\varphi_1-2l_2^2\sin^2\varphi_1+l_2^2\right)}{2\left(l_2^2-(l_1\sin\varphi_1)^2\right)^2}\right) + I_{\mathrm{G_2}}\frac{2l_1^2\cos\varphi_1\sin\varphi_1\left(l_1^2-l_2^2\right)}{\left(l_2^2-(l_1\sin\varphi_1)^2\right)^2} - m_3\left(\frac{l_1^2l_2^2\sin(2\varphi_1)\left(l_1^2-l_2^2\right)}{\left(l_1^2\cos^2\varphi_1-l_1^2+l_2^2\right)^2}\right) \tag{6}$$

$$\mathrm{d}E_{\mathrm{p}}/\mathrm{d}\varphi_1 = m_1 g l_{\mathrm{OG_1}}\sin\varphi_1 + (m_2+m_3)gl_1\sin\varphi_1 - \left(\frac{m_2}{2}+m_3\right)g\frac{l_1^2\sin\varphi_1\cos\varphi_1}{\sqrt{l_2^2-(l_1\sin\varphi_1)^2}} + \left(F_{\mathrm{pre}} + k_{\mathrm{s}}\left(-l_1\cos\varphi_1 + \sqrt{l_2^2-(l_1\sin\varphi_1)^2} - (l_2-l_1)\right)\right)\left(l_1\sin\varphi_1 - \frac{l_1^2\sin\varphi_1\cos\varphi_1}{\sqrt{l_2^2-(l_1\sin\varphi_1)^2}}\right) \tag{7}$$

The values of $I_{\mathrm{red}}(\varphi_1)$, $\mathrm{d}I_{\mathrm{red}}(\varphi_1)/\mathrm{d}\varphi_1$ and $\mathrm{d}E_{\mathrm{p}}/\mathrm{d}\varphi_1$ are presented in Fig. 2. These variable values are calculated for an entire cycle of the slider-crank mechanism using the parameters from Table 1 in Eqs. (5), (6) and (7).

A sensitivity analysis is performed for each geometric and dynamic parameter listed in Table 1, excluding the compression spring parameters. The sensitivity analysis evaluates the values of $I_{\mathrm{red}}(\varphi_1)$, $\mathrm{d}I_{\mathrm{red}}(\varphi_1)/\mathrm{d}\varphi_1$ and $\mathrm{d}E_{\mathrm{p}}/\mathrm{d}\varphi_1$, considering a 5% increase in each individual parameter. The results are presented in Table 2. For $I_{\mathrm{red}}(\varphi_1)$, the sensitivity is calculated using Eq. (8) as the mean percentage difference, while for $\mathrm{d}I_{\mathrm{red}}(\varphi_1)/\mathrm{d}\varphi_1$ and $\mathrm{d}E_{\mathrm{p}}/\mathrm{d}\varphi_1$, the analysis is conducted by adapting Eq. (8).

$$\bar{s}_{I\mathrm{red}} = \frac{I_{\mathrm{red}\,5\%}(\varphi_1) - I_{\mathrm{red}}(\varphi_1)}{I_{\mathrm{red}}(\varphi_1)} \cdot 100\% \tag{8}$$

According to Table 2, for this particular SDOF slider-crank mechanism: $I_{\mathrm{red}}(\varphi_1)$ is significantly sensitive to the moment of inertia of the rod-flywheel link ($I_{\mathrm{G_1}}$); $\mathrm{d}I_{\mathrm{red}}(\varphi_1)/\mathrm{d}\varphi_1$ is highly sensitive to the length of the crank (l_1) and significantly sensitive to the mass of the slider (m_3); $\mathrm{d}E_{\mathrm{p}}/\mathrm{d}\varphi_1$ is significantly sensitive to the length of the crank (l_1).

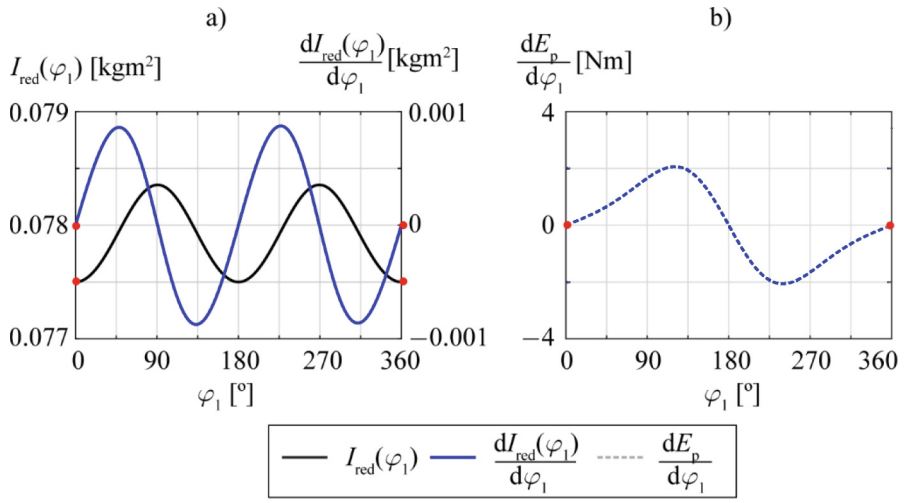

Fig. 2. For an entire cycle of the slider-crank mechanism: a) $I_{red}(\varphi_1)$ and $dI_{red}(\varphi_1)/d\varphi_1$; b) $dE_p/d\varphi_1$.

Table 2. Results of the sensitivity analysis for $I_{red}(\varphi_1)$, $dI_{red}(\varphi_1)/d\varphi_1$ and $dE_p/d\varphi_1$.

	$\Delta l_1 = 26.3$ mm	$\Delta l_{OG_1} = 0.061$ mm	$\Delta m_1 = 18.0$ kg	$\Delta I_{G_1} = 0.0814$ kgm^2
$\bar{s}_{Ired}$	0.06%	0%	0%	5%
$\bar{s}_{dIred/d\varphi_1}$	10.3%	0%	0%	0%
$\bar{s}_{dEp/d\varphi_1}$	6%	0.03%	0.04%	0%
	$\Delta l_2 = 89.3$ mm	$\Delta m_2 = 0.120$ kg	$\Delta I_{G_2} = 1.34 \cdot 10^{-4}$ kgm^2	$\Delta m_3 = 1.37$ kg
$\bar{s}_{Ired}$	0%	0%	0%	0.03%
$\bar{s}_{dIred/d\varphi_1}$	0%	0.33%	0%	4.67%
$\bar{s}_{dEp/d\varphi_1}$	0.4%	0.1%	0%	1.02%

3 Experimental Results

The free-deceleration method was carried out starting from a steady-state with a mean constant input velocity $\dot{\varphi}_1 = 54.3$ rad/s. The temporal evolution of $\dot{\varphi}_1$ is depicted in Fig. 3a; the clutch disconnected the mechanism from the DC motor at $t = 5.5$ s. In Fig. 3b, it is depicted the angular acceleration $\ddot{\varphi}_1$ conveniently filtered to remove the high frequency noise from $t = 8$ s to $t = 14$ s (the clear region in Fig. 3a). This time interval is selected to be far from the clutch activation –a perturbation distinct from the free-deceleration transient period– as well as from the first rebound of the closure spring.

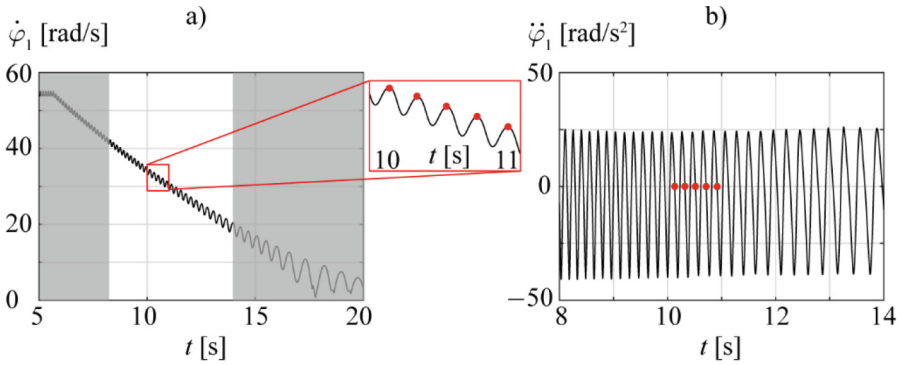

Fig. 3. a) Experimental angular velocity; b) Experimental angular acceleration.

The friction torque T_{red} is obtained by evaluating Eq. (4) with the experimental values. The contribution of each term of Eq. (4) to T_{red} is shown in Fig. 4, being $T_{\text{red }1} = I_{\text{red}}(\varphi_1)\ddot{\varphi}_1$, $T_{\text{red }2} = 1/2 \cdot \frac{\text{dI}}{\text{red}}(\varphi_1)/\text{d}\varphi_1 \cdot \ddot{\varphi}_1^2$ and $T_{\text{red }3} = \text{d}E_{\text{p}}/\text{d}\varphi_1$. Comparing $T_{\text{red }1}$ and $T_{\text{red }2}$, it can be observed the contribution of the inertia derivative term ($T_{\text{red }2}$) compared to the acceleration term ($T_{\text{red }1}$) for the SDOF mechanism mounted on the test stand. In Figs. 2, 3 and 4 configurations where $\varphi_1 = n \cdot 360^{\circ}$ (with $n = 0,\ 1,\ 2\ldots$) are highlighted with red dots within the interval t= 10 s to t= 11 s; in these configurations, $T_{\text{red }1} \neq 0$ (Fig. 4a), $T_{\text{red }2} = 0$ (Fig. 4b) and $T_{\text{red }3} = 0$ (Fig. 4b), according to values shown in Fig. 2 or Eqs. (5), (6) and (7), respectively.

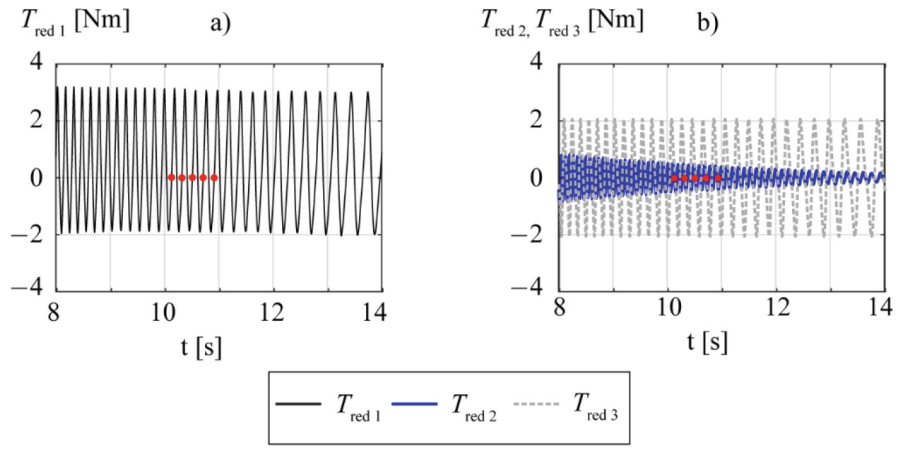

Fig. 4. Contribution of each term of the equation of motion to the friction torque during the free-deceleration a) Acceleration term; b) Inertia derivative and potential energy derivative terms.

Finally, the conveniently filtered (to avoid noise signals) total friction torque T_{red} versus time is depicted in Fig. 5a, and the mean friction torque per cycle $T_{\text{red mean}}$ versus the mean angular velocity per cycle $\dot{\varphi}_{1\text{ mean}}$, is depicted in Fig. 5b. Analogously, the red dots indicate these described previous configurations of the slider-crank mechanism

within the interval $t = 10$ s to $t = 11$ s. Within the interval from $t = 8$ s to $t = 14$ s, 28 entire cycles are completed; from $t = 10$ s to $t = 11$ s, 5 entire cycles are completed as can be seen in Figs. 2, 3, 4 and 5. From the 1st first to the 28th entire cycle, the mean experimental angular velocity per cycle $\dot{\varphi}_{1\ \text{mean}}$ falls from 41.9 rad/s to 19.7 rad/s (−53 %) and $T_{\text{red mean}}$ falls from 0.353 Nm to 0.282 Nm (−20 %). This trend of reducing the total friction torque, while decreasing the angular velocity, is explained because the existing experimental total friction torque, presents a certain behaviour that can be modelled via viscous friction model.

It should be noted that the experimental results for T_{red}, when applying the free-deceleration method and accounting for variable inertia, are highly sensitive to the synchronization between the encoder's rising edges and the precise identification of a specific mechanism configuration. In this study, this particular configuration corresponds to $\varphi_1 = n \cdot 360^{\circ}$ (with $n = 0,\ 1,\ 2\ldots$), which is a minimum dead point configuration for coordinate y (Fig. 1c), highlighted with red dots in Figs. 2, 3, 4 and 5 (only from $t = 10$ s to $t = 11$ s). For this reason, it is advantageous to work with averaged $T_{\text{red mean}}$ per cycle (Fig. 5b).

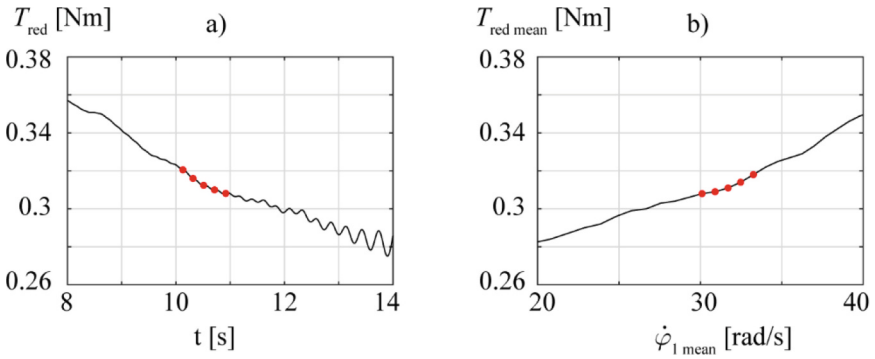

Fig. 5. a) Total friction torque versus time; b) Mean total friction torque per cycle versus mean angular experimental velocity per cycle.

The energy loss E_{loss} for complete cycles, previously named W_{loss} in Eq. (3), is obtained with Eq. (9), predicting an energy loss per cycle that goes from 2.2 J for the 1st cycle to 1.8 J for the 28th cycle, which means a reduction of −20 %. During the 28 cycles, the total amount of accumulated energy loss due to friction for this slider-crank mechanism is equal to 55.7 J.

$$E_{\text{loss}} = \oint T_{\text{red}} \mathrm{d}\varphi_1 \tag{9}$$

4 Conclusions

This study shows how to calculate experimentally energy efficiency for a slider-crank mechanism, specifically considering the effect of variable inertia as shown in Fig. 4. A sensitivity analysis has been carried out and presented in Table 2. For this particular

mechanism: i) the inertia derivative term is highly sensitive to the length of the crank (l_1), considering that in Eq. (6), l_1 appears several times raised to a positive integer power; ii) the inertia is significantly sensitive to the moment of inertia of the crank-flywheel link (I_{G_1}).

The free-deceleration method eliminates the need for expensive sensors, such as force/torque transducers, which are the most widely established method to evaluate energy efficiency for SDOF transmissions or mechanisms [8, 9]. This study is aligned with other studies that claims as a novelty the proposal of more affordable experimental methods to force/torque transducer, as it is the case of [10], for a roller chain transmission. By employing a cost-effective opto-encoder to record the input angular velocity, it is derived the total friction torque, the mean friction torque per cycle and the energy loss per cycle. Nevertheless, this method requirements are: i) an accurate quantification of the inertia of each link, that a priori can be easily achieved by means of a CAD model that takes in consideration material properties and all the components; ii) the precise synchronization between the encoder's rising edges with a particular mechanism configuration.

References

1. Yang, H.S., Zhu, H.Q., Xiao, X.Z.: Comparison of the dynamic characteristics and performance of beta-type Stirling engines operating with different driving mechanisms. Energy. **275**, 127535 (2023)
2. Komoda, K., Wagatsuma, H.: Energy-efficacy comparisons and multibody dynamics analyses of legged robots with different closed-loop mechanisms. Multibody Syst. Dyn. **40**(2), 123–153 (2017)
3. Tian, S., Chen, X., Chen, T., He, Y.: Experimental study on frictional loss of high-speed bearings based on free-deceleration and energy-balance methods. Ind. Lubr. Tribol. **71**(4), 509–514 (2019)
4. Cai, G., Hou, Y., Wang, X., Sun, S., Zhang, Y., Wang, N.: A measurement method for friction torque between rollers and raceways of tapered roller bearings under radial heavy load conditions. Tribol. Int. **200**, 110071 (2024)
5. Muthuganapathy, P., Chaturvedi, S.K., Gargama, H., Sasikumar, P.: Friction torque prediction of precision ball bearing unit for reaction wheel actuators for spacecraft applications. Int. J. Syst. Assur. Eng. Manag., 1–14 (2025)
6. Bascou, J., Sauret, C., Lavaste, F., Pillet, H.: Is bearing resistance negligible during wheelchair locomotion? Design and validation of a testing device. Acta Bioeng. Biomech. **19**(3), 165–176 (2017)
7. Català, P., Veciana, J.M., Jordi, L.: Energy loss comparison between kinematically equivalent mechanisms: slider-crank and eccentric cam. Mech. Based Des. Struct. Mach. **52**(11), 9435–9457 (2024)
8. Pabiszczak, S., Kowal, M.: Efficiency of the eccentric rolling transmission. Mech. Mach. Theory. **169**, 104655 (2022)
9. Wang, X., Wang, H., Li, L., Hao, L.: An improved transmission efficiency prediction method for nonlinear characteristics of the cycloid reducer. Proc. Inst. Mech. Eng. C J. Mech. Eng. Sci. **238**(20), 10266–10284 (2024)
10. Wragge-Morley, R., Yon, J., Lock, R., Alexander, B., Burgess, S.: A novel pendulum test for measuring roller chain efficiency. Meas. Sci. Technol. **29**(7), 075008 (2018)

Dimensioning Human Operated Balanced Manipulators for Material (Un)Loading Operations

İlkim Zahide Bozdemir[1], Ünal Dana[2(✉)], Erkin Gezgin[2], and Levent Çetin[2]

[1] Graduate School of Natural and Applied Sciences, Department of Robotics Engineering, Izmir Katip Çelebi University, Izmir, Turkey
[2] Department of Mechatronics Engineering, Izmir Katip Çelebi University, Izmir, Turkey
unal.dana@gmail.com

Abstract. In industrial applications, particularly in assembly and material handling processes that require human-machine collaboration, balanced manipulators play a critical role. The primary objective of these systems is to compensate for the gravitational force of a load, imparting a sensation of "weightlessness" to the operator, thereby enhancing both positioning and ergonomics simultaneously. In industrial production, operator support systems are typically either pneumatic balanced manipulators or fully automated robots. These systems possess disadvantages such as the requirement for compressed air, energy inefficiency, and maintenance costs. This study aims to present a method of dimensioning to select the necessary electrical actuator for the balanced manipulators. The proposed methodology follows a sequential optimization approach: first, structural synthesis derives the link lengths and kinematic architecture directly from the required workspace volume; second, kinematic analysis validates the reachable boundaries against the task requirements; and third, dynamic analysis utilizes a static equilibrium model to determine the optimal counterweight mass, thereby minimizing the load on the actuator. Finally, a motion simulation identifies the peak force requirements. The results validate the method by successfully dimensioning a system capable of handling a 1000 N payload using an 8 kN electrical linear actuator.

Keywords: Operator support systems · Balanced Manipulators · Mechanical Design

1 Introduction

Hand operated balanced manipulators are serial manipulators that an operator can easily guide by applying physical force, which automatically maintain a fixed position or motion when released. The hand operated balanced manipulators are often used as operator support systems. These operator support systems are primarily used for loading and translation purposes in production, assembly, and packaging centers to assist operators. Therefore, their structure is designed to support this purpose. For this reason, some hand operated serial manipulators utilize a balancing mechanism and are referred to as balanced manipulators [1].

© The Author(s), under exclusive license to Springer Nature Switzerland AG 2026
A. Chaker et al. (Eds.): EFIMMS 2026, MMS 205, pp. 145–156, 2026.
https://doi.org/10.1007/978-3-032-22270-1_15

Balanced mechanisms consist of a load, a fulcrum, and a counterweight. Balanced manipulators are using the same concept, except they have a more complex structure; in order to understand these complex structures, analyzing the balanced mechanisms and their components is necessary. A counterweight is a systematically calculated mass used to balance a mechanism. Its primary function is to "neutralize the overturning moment (tipping moment) caused by the load and control the system's center of gravity (center of gravity) [2]. A subset of these manipulators is based on a pantograph structure, which is a parallelogram mechanism. The mechanism possesses kinematic linearity between inputs and outputs. It is also proven that the two rectilinear input motions which exist in a pantograph structure are not coupled, and therefore are suitable for being used as generalized coordinates in control Devices possessing such a mechanism and designed to balance the force of gravity are classified as "Balanced Manipulators" [3]. Generally, these robotic systems are composed of two main components: a fixed base (column) and an end-effector. To enable operators to use these serial manipulators directly, a robot-human interface can be incorporated on the end-effector, which allows the operator to guide the load with precision.

Balanced manipulators are used in any application that combines human expertise, eye and hand coordination, and flexibility, with robotic stability and precision, such as assembly, installation, lifting, transporting, positioning, and more [4]. The creation and industrial application of manual balanced manipulators (HOBM) began in 1964 when Robert A. Olsen suggested a new, original balanced assembly. This invention was the basis for the development of the manual balanced manipulator by Reizou Matsumoto in 1975, which is the prototype of the modern HOBM [5].

In Fig. 1a and b, some of the balanced manipulators used as operator support systems are shown. There are similarities and differences between these types of balanced manipulators. The structure of the two are same until the end effector. The most noticeable difference between them is their end effector structure, the counterweight, and the actuator supporting the counterweight. Another difference between them is the length of the links on the manipulator. The main source of these differences is simply the requirements of the work done. The work done by these manipulators can be put into two main subjects, which are translation and loading. Translation requirement of the work affects the difference in some of the link lengths and the structure of the end effector, the loading affects some specific link lengths, the weight of the counterweight, and the selected actuators. These specifications are important when deciding the design procedure [6].

1.1 Problem Definition

Dimensioning robotic manipulators is the process of selecting optimal robot size and capacity for a desired application. This process requires optimizing the robot's performance, accuracy, durability, and cost to meet both its current operations and operational capabilities. Incorrect sizing can lead to lost productivity, quality issues, high costs, and even system failures.

In this paper, a dimensioning method specially configured to design an HOBM structure (Fig. 2) fit for the loading and translation required is proposed, and that method is

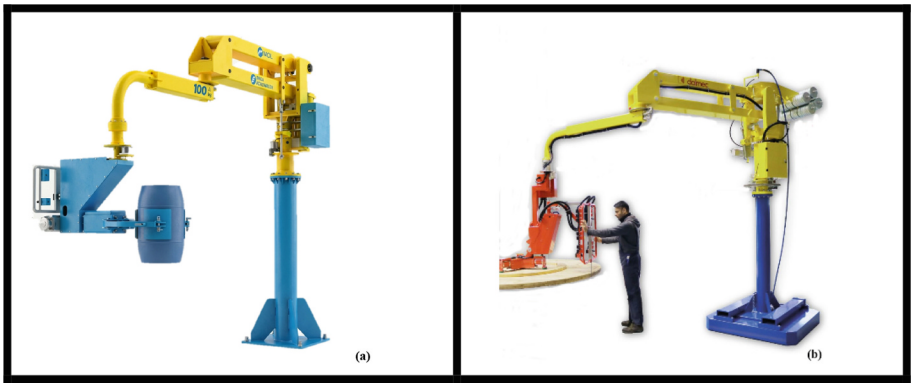

Fig. 1. (a) PM Drumful [8], (b) DALMEC Maxipartner [7]

used to design an innovative HOBM structure. The proposed system utilizes a combination of an electrical linear actuator and a counterweight mechanism to balance the gravitational force, instead of employing pneumatic cylinders. While standard design procedures are generally applicable, the unique characteristics of this balanced architecture introduce specific design steps that significantly increase the complexity of the dimensioning process. Therefore, a specialized approach is necessary to accurately determine the system parameters and select the appropriate electrical actuator.

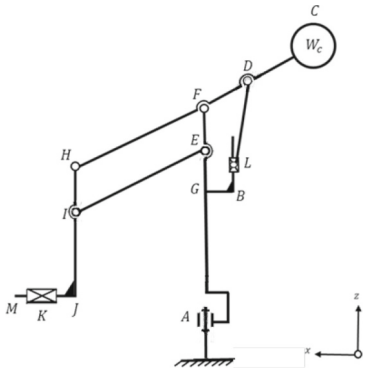

Fig. 2. The main structure of the proposed HOBM.

2 Design Procedure

The standard procedure for dimensioning should be, respectively, structural synthesis, kinematic analysis, and dynamic analysis. In structural synthesis, the number of links, the number of joints, and the number of degrees of freedom are determined. The determination of the general structure depends on the designer's knowledge about literature and

the purpose of the design. When the structure is ready, the kinematic analysis showing the relationship between actuation and the output position in terms of link lengths and actuation can be done. In dimensioning problems, usually, the work required is specified, and the needed output positions are given by this required work. In this case, the inverse kinematic analysis will give the required possible link lengths depending on the required workspace. When the link lengths are decided through the design procedures, dynamic analysis is needed to calculate the torque and forces on each joint in terms of link mass, link lengths, output position, output velocity, and output acceleration of the manipulator. The required work should define the variables like load, output position, velocity, and acceleration, but other parameters, such as link mass and inertia, are dependent on an actual design rather than a structural synthesis because the link mass and inertia are related to other subjects, such as material strength and mechanical design. In order to find an approximate value just for dimensioning better, designers can make assumptions about possible mass and inertia, or complete the mechanical design and calculate approximate torque and forces on each joint. This step is crucial in order to select necessary actuators and reconsider the link lengths and structure, since the objective is an optimal design.

In the following sections, the required design procedure for HOBM is presented step by step.

2.1 Structural Synthesis

The structural synthesis is the foundational and initial phase of the design process. This step is where the skeleton of the manipulator is defined. In our case, the structural synthesis is already suggested in Fig. 2. This suggested structure defines the joint types and link connections, but the problem for dimensioning remains because the link lengths are not suggested. To determine the optimal link lengths, defining the workspace parameters and establishing their relationship with the mechanism's geometry through kinematic analysis is important. While this is valid for most link lengths, this does not mean some of them can't be initially defined and limited. In the structural synthesis step, knowledge of the manipulator's main functions and constraints from its definition helps to determine the link lengths.

The main structure given in Fig. 3 is envisioned considering the necessary movements of the end point of the balanced manipulator. Each joint of the HOBM causes or allows a set of movements at the end effector. The summation of the possible locations when linked together generates a three-dimensional space called the workspace. This workspace should contain the necessary work environment, which affects the structure of the manipulator. Therefore, the knowledge of the required work done is necessary for dimensioning.

2.2 Kinematic Analysis

Kinematic analysis describes the motion related to the geometrical constraints; part of the design procedure only considers the geometrical relations. Initially, the required workspace of the end effector was found; this required workspace must be possible via the manipulator's motion. In order to prove that this workspace is achieved, a kinematic

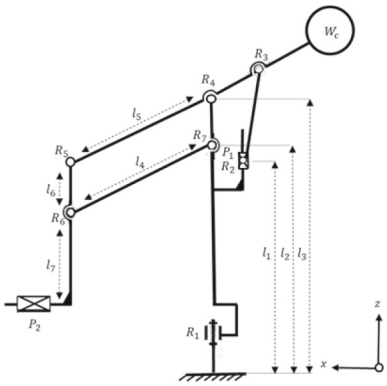

Fig. 3. HOBM structure with joints and links defined.

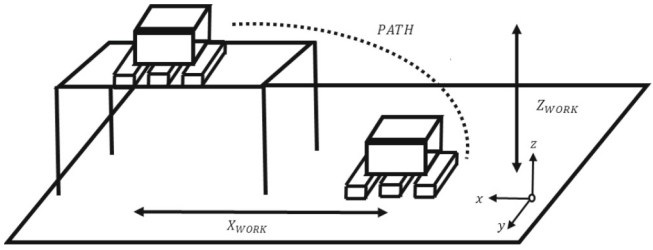

Fig. 4. Parameters of loading and translation in the workspace.

analysis is necessary. The kinematic analysis solution for every possible joint position will give the achieved workspace. Since the kinematic analysis is dependent on the link lengths, and the achieved workspace is dependent on the kinematic analysis, the relationship between the link lengths and the required workspace will be found.

The achieved workspace calculated by the kinematic analysis is the reachable workspace. The reachable workspace is the absolute boundary of the manipulator's reach. This workspace is found by the kinematic analysis solution and describes the manipulator's total range and does not concern the degrees of freedom of the end effector. The degrees of freedom inside the workspace can change at singularities, and if a specific orientation is desired for the task. This decrease in degrees of freedom is unwanted if all of the DOF are required for the task. The region where the end effector reaches with arbitrary orientations is called the dexterous workspace. The dexterous workspace could also affect the dimensioning processes.

2.3 Dynamical Analysis

The dynamical analysis is the study of the forces and torques required to move the manipulator. In this study, dynamical analysis is required only to solve dimensioning problems and to calculate the required force and torque on the linear actuator (P_1); thus, first, the link length l_8 is determined using a simple static equilibrium. In this equilibrium,

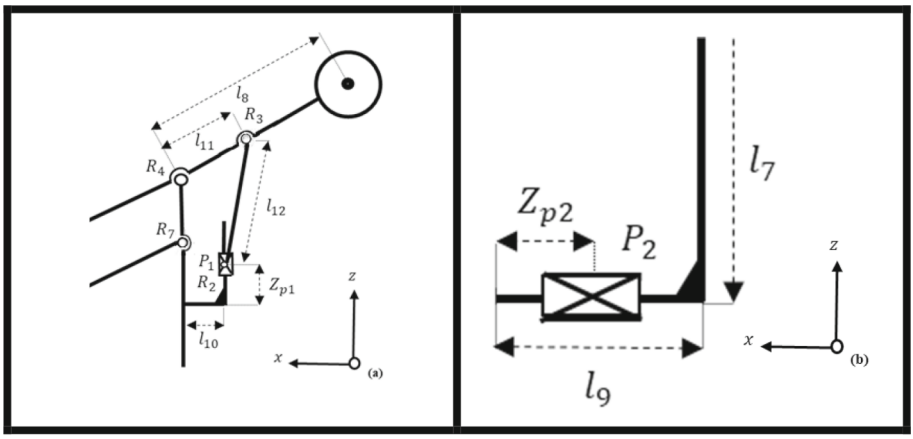

Fig. 5. Prismatic joint on balanced manipulator (a), Prismatic joint on end effector (b).

the manipulator base structure (Fig. 3) and balanced manipulator structure (Fig. 5a) are used to calculate the required counterweight given the compensation percentage, force on the R_6 joint, and angle between l_1 and l_4. When the compensation percentage of the counterweight gets closer to %100, the force requirement of the linear actuator decreases. This static equilibrium is necessary to find the link lengths and start the mechanical design processes.

The mechanical design is essential in order to get the link mass and inertia to start the dynamical analysis. The mechanical design of links directly affects the torque requirements on joints. Generally, the links in manipulators on big structures consist of square box beams; therefore, for dimensioning purposes, the most suitable square box beam should be chosen, considering the maximum deflections.

Designing a mechanical structure using a 3D CAD and a dynamic analysis simulation program is a fast and reliable way to perform a dynamic analysis. In the simulation, every dimensional parameter and the mechanical properties of the manipulator will be simulated. In the simulation, when the load is carried to the desired position with desired velocities, the forces and torques acting on each joint will be calculated by the computer. This way, the complex inverse kinematics and Jacobian calculations won't be needed.

3 Results and Discussion

3.1 Structural Synthesis

The main structure given in Figs. 2 and 3 is determined using the preliminary knowledge about HOBM and configured to make a simpler dynamical analysis. This configuration makes the calculation of load on the linear actuator simpler. The following scenario is given to define the required workspace to start the functional design procedure regarding the structural design parameters for structural synthesis given under the Sect. 3.2.

In an assembly center, a workpiece on top of a pallet needs to be put onto a table picked up from the ground (Fig. 4). The workpiece's location is assumed inside the

manipulator's reachable workspace; this assumption is made to not be concerned about the manipulator's distance to the workpiece, therefore only concern remaining is the required translations. The required translation in three dimensions is given as X_{Work}, $Y_{Work,}$ and Z_{Work}; the weight of the workpiece is given as W_{work}.

When the parameters X_{Work}, $Y_{Work,}$ and Z_{Work} are used to create a volume called workspace. This volume should fit inside the reachable workspace. Thus, inside this space, the end effector of the manipulator can reach any point, meaning it can also take any path inside the workspace (Fig. 6).

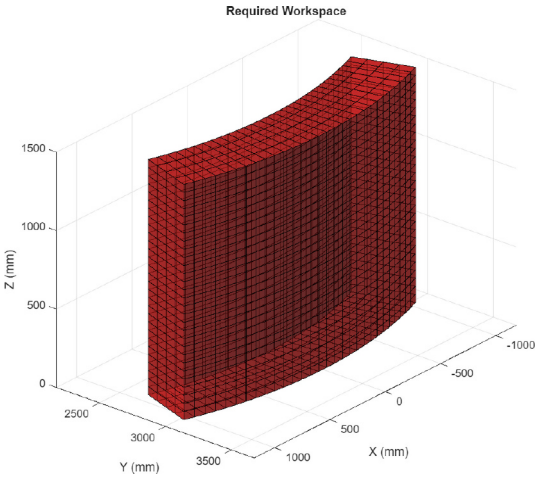

Fig. 6. Required Workspace of HOBM

3.2 Kinematic Analysis

The structural dimensions of the HOBM are defined by specific lengths that define its geometry and range of motion as indicated in Figs. 2, 3 and 5. In particular, the fixed vertical base is established by l_1, the height from the ground to the actuator mount (point B), l_2, the height to the lower body pivot (point E), and l_3, the height to the main upper pivot (point F). Installed on this base, the manipulator utilizes a parallelogram mechanism to maintain a constant load orientation; it consists of the lower arm l_4 (segment EI) and the upper arm l_5 (segment FH), which have equal length and are vertically separated at the end by the coupler link l_6. The reach and interaction point for the operator are specified by the end-effector's vertical length l_7 and horizontal length $l_{9,}$ while the system's balance and actuation are determined by l_8, the lever arm connecting to the counterweight l_{11} (segment FC), the link connecting the linear actuator to point D, l_{12} and l_{10}, the horizontal offset for the linear actuator.

In Table 1, the effect of the workspace parameters on HOBM dimensions and reachable workspace is given. The affected dimensions can be associated with the following equations.

$$Z_{Work} = l_2 + l_5 \cos(\theta_7) - l_7 \tag{1}$$

Table 1. Workspace parameter effects on HOBM dimensions.

Workspace Parameters	Type	Affected by Dimensions
Z_{Work}	Vertical Height	$l_1, l_2, l_5, l_7, l_{10}, l_{11}, l_{12}$
Y_{Work}	Radial Depth	l_5, l_9
X_{Work}	Rotational Reach	θ_1, l_5, l_9

$$\theta_{7min} = \arccos((l_2\text{-}l_7)/l_5) \tag{2}$$

In Eq. (1), the effect of dimensional parameters l_2, l_5, l_7, and θ_7 on vertical height is given. θ_7 is the angle between l_1 and l_5; this angle is limited because of the available workspace on the Z axis (Z_{Work} minimum is zero). Therefore, in Eq. (2), the minimum value for θ_7 is determined by setting Z_{Work} as zero in Eq. (1). θ_7 is dependent on the dimensional parameters l_1, l_{12}, l_{11}, and l_{10}; thus, their dimensions are connected.

$$Y_{Work} = l_{9max}\text{-}l_{9min} \tag{3}$$

In Eq. (3), it is stated that the stroke on P_2 is the only variable that affects the translation on the Y axis, but also, there is an unreachable space on Y direction caused by dimensions l_5 and l_{9min}.

$$X_{Work} = \cos(\theta_1)(l_5 \sin(\theta_7) + l_9) \tag{4}$$

In Eq. (4), X_{Work} is described using the angle of joint 1 (θ_1) and the projection of links on the Y axis. When joint 1 rotates, the cosine component of the projection of links in the Y axis is the translation in the X axis, and the sine component is the translation in the Y axis. Although the translation on the fixed axis Y is not independent from the translation on the X axis when only actuated by joint 1.

Using these equations, it is possible to determine the dimensions required to generate the reachable workspace that will contain the required workspace in Fig. 7.

Validation of the workspace required is done by placing it inside the reachable workspace and checking if it fits inside, since the manipulator's placement location can be anywhere (Fig. 8).

3.3 Dynamic Analysis

Now that the dimensional parameters depending on the workspace are defined. The dimensional parameters that should be decided according to the dynamical analysis remain. In order to continue this step, a mechanical design is necessary. The mechanical design step is crucial to determine the link weights, link inertias, counterweight, and some of the remaining link lengths.

In the mechanical design process, the choice of link material is determined by analyzing the most loaded element of the structure. In this case, the most loaded element is the link between H and C points (Fig. 2). A rectangular box beam size should be selected

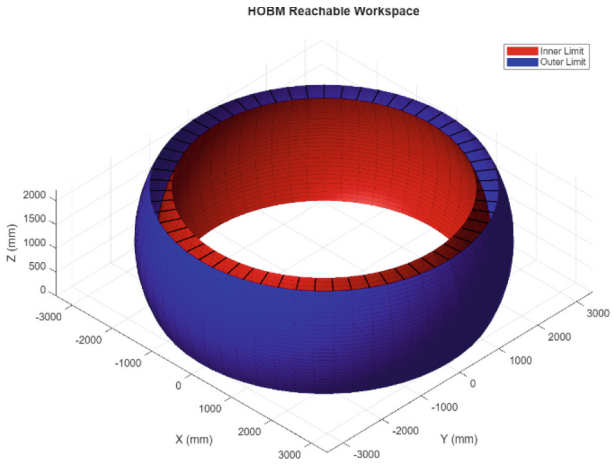

Fig. 7. Reachable Workspace of HOBM

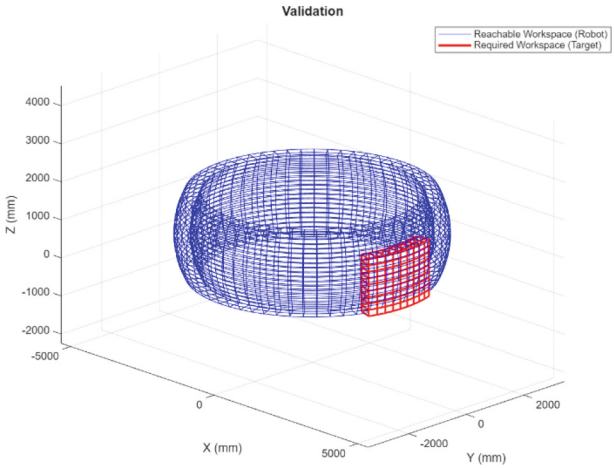

Fig. 8. Validation of Workspace

for that link, together with the counterweight and some of the dimensional parameters such as l_8. The length between point F and C is 1_8, and the length between point F and D is l_{11} (Fig. 5a). The approximate load on the link through point H to point C is shown in Fig. 9, considering the forces acting on the HC beam are vertical (at z axis) to simplify the equation for an initial design procedure. This method will result in an approximate counterweight because the most dominant forces are vertical.

In order to make the counterweight less than the weight of the workpiece, l_8 must be smaller than l_5. This ensures that the center of mass of the HC beam must be between points H and F. The lengths l_{11} (FD) and l_5 (HF) are defined in the kinematic analysis, and the W_{Work} is 1000 N. Now the only remaining unknowns are l_8, counterweight W_{cz}, and linear actuator force F_{P1z}. If the forces on Fig. 9 are considered to be in static equilibrium

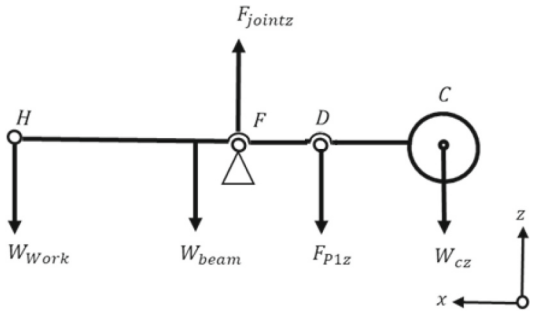

Fig. 9. Forces on rectangular box beam HC

when F_{P1z} is zero, then the smallest linear actuation would break this equilibrium, and movement would occur. This is exactly the use of counterweight, so with Eq. (5), the parameters are decided in order to make the compensation percentage closer to %100. In the following equation, since the beam's size is unknown, it is not used. This would make the compensation percentage smaller than %100, but later on, when the beam size is selected, counterweights can be added to lessen that error.

$$W_{Work} l_5 = W_{cz} l_8 \tag{5}$$

When the l_8 and W_{cz} are selected for a preliminary design, the beam size can be selected by choosing a small-sized beam and strengthening the beam until the calculation of deflection at the points C and H are on acceptable levels. The maximum deflection (δ) at the end point of the beam is obtained by dividing the product of the applied force (X) and the cube of the beam length (L) by three times the bending stiffness (EI), which represents the beam's material stiffness (E) and cross-sectional shape resistance area moment (I). The formula used for deflection at the free end of the beam is as follows.

$$\delta = \frac{XL^3}{3EI} \tag{6}$$

Table 2. Structural parameters of the designed HOBM.

Parameter	Value (mm)	Parameter	Value (mm)	Parameter	Value (deg, kg)
l_1	1992	l_8	600	θ_7	52.3°–127.7°
l_2	2240	l_9	500–1000	M_1	156.142
l_3	2350	l_{10}	206	M_2	2.240
l_4	1700	l_{11}	300	M_3	1.852
l_5	1700	l_{12}	380	M_4	40.088
l_6	110	Z_{p1}	0–320	M_5	35.883
l_7	1200	Z_{p2}	0–500	M_6	52.779

Initial mechanical design is completed using the dimensional parameters in Table 2 and the mechanical design defines the mass distribution such that M_1 corresponds to the segment between A-F, M_2 to G-L, M_3 to L-D, M_4 to H-C, M_5 to I-E, and M_6 to H-M. In order to select an electrical linear actuator, a motion analysis is simulated. In the simulation, the linear actuator follows the motion profile in Fig. 10, and the required force on the electrical linear actuator to generate that movement is given in Fig. 11.

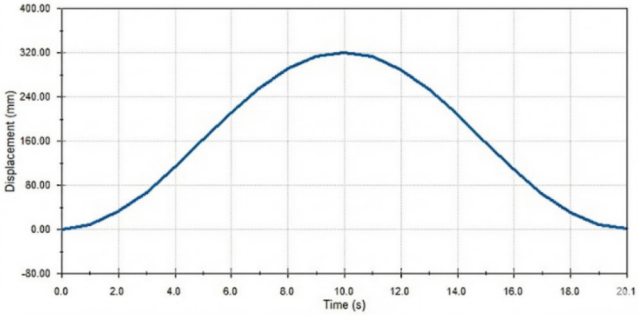

Fig. 10. The stroke of the linear actuator against time

In the motion simulation shown in Fig. 11, the required force on the linear actuator initiates at 6.18 kN and exhibits a proportional increase relative to the stroke. The initial static equilibrium calculation in Eq. (5) suggested a counterweight (W_c) of 2833 N; however, this theoretical value resulted in slight errors as it neglected the mechanism's total structural weight and inertial components. To address these discrepancies the counterweight was tuned to 3400 N in the simulation environment.

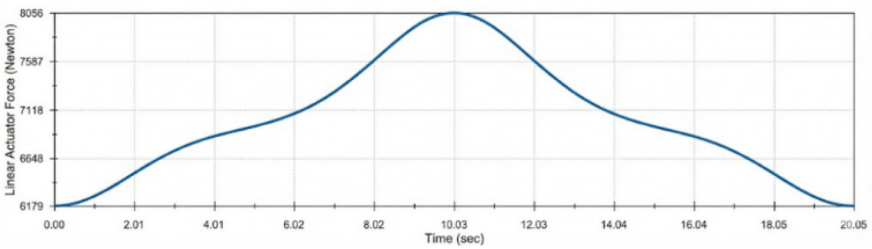

Fig. 11. The required force on the electrical linear actuator against time

4 Conclusion

This study successfully applied a dimensioning methodology to derive the HOBM structure defined in Table 2 directly from the required workspace parameters. The results confirmed that an 8 kN electrical linear actuator with a 320 mm stroke is sufficient to

drive the derived system with a 1000 N payload. This demonstrates that the method can effectively determine the structural dimensions, counterweight, and actuator capacity for this type of manipulators.

References

1. Arakelian, V.: The History of the Creation and Development of Hand Operated Balanced Manipulators. Department GMA, INSA-Rennes, 20 Avenue des Buttes de Coësmes CS 14315
2. Eckenstein, N., Yim, M.: Modular Advantage and Kinematic Decoupling in Gravity Compensated Robotic Systems. Department of Mechanical Engineering, University of Pennsylvania, Philadelphia, PA 19104
3. Yang, D. C. H., Line, Y. Y.: Dept. of Mechanical, Aerospace and Nuclear Engineering, University of California, Los Angeles, CA 90024, U.S.A
4. Matsumoto, R.: Load handling equipment. US Patent 3 883 105, 13 May 1975
5. Olsen, R.: A balanced assembly. US Patent 3 134 340, 26 May 1964
6. Rout, B.K., Mittal, R.K.: Optimal Design of Manipulator Parameter Using Evolutionary Optimization. Tech. Robotica. **28**(03), 381–395 (2010)
7. DALMEC Homepage. https://www.dalmec.com/en/manipulators/maxipartner/. Last accessed 26 Nov 2025
8. PM Homepage. https://pmmanipulators.com/tr/Products-Detail-tr/drumful/31. Last accessed 26 Nov 2025

Robotics and control

Travel Path and Trajectory Planning for Robot-Assisted Multidirectional Additive Manufacturing

Mark Witte(✉), Ziyun Yang, Mathias Hüsing, and Burkhard Corves

RWTH Aachen University, Aachen, Germany
{witte,yangz,huesing,corves}@igmr.rwth-aachen.de
https://www.igmr.rwth-aachen.de

Abstract. In Robot-Assisted Multidirectional Additive Manufacturing (RAM-AM), the travel paths (non-printing transitions) between separate printing segments are rarely planned explicitly. This often results in discontinuities, inefficient connections, and severe collision risks, particularly in moving-bed configurations where the entire part moves relative to the nozzle. We propose a decoupled planning pipeline that first computes a safe, smooth geometric path in the platform frame and subsequently generates an executable joint-space trajectory under kinematic limits. The geometric planning utilizes an A* search on an OctoMap-based voxel grid with an asymmetric layered cost map to actively steer the end-effector away from the printed structure. This raw path is smoothed using sparse B-splines, and orientations are optimized by blending Spherical Linear Interpolation (Slerp) with Artificial Potential Fields (APF) to maximize clearance. For trajectory generation, we resolve kinematic redundancy by sampling pose tolerances and selecting a globally consistent joint sequence via second-order Dynamic Programming (DP), explicitly penalizing joint jerks and singularities. Validated on a 6-DoF KUKA KR6 R900 sixx, the method is demonstrated in scenarios involving complex obstacles like holes. Results show that our approach guarantees safe obstacle avoidance where standard baselines fail, yields significantly smoother motions, and that exploiting the redundant rotation about the extrusion axis drastically reduces the inverse kinematics search effort.

Keywords: Robot-Assisted Multidirectional Additive Manufacturing · Inter-Segment Travel Path Planning · OctoMap-based A* · Second-Order Dynamic Programming · Trajectory Optimization

Part of the research presented was funded by the DFG as part of the FunkDAF research project. Project Number 513808244.

© The Author(s), under exclusive license to Springer Nature Switzerland AG 2026
A. Chaker et al. (Eds.): EFIMMS 2026, MMS 205, pp. 159–170, 2026.
https://doi.org/10.1007/978-3-032-22270-1_16

1 Introduction

Additive manufacturing (AM) offers high design freedom and efficient material utilization, with fused deposition modeling (FDM) among the most widely adopted processes due to its low cost and simplicity [14,19]. However, conventional layer-wise FDM exhibits anisotropic mechanical behavior and struggles with overhangs, motivating multi-directional printing strategies on platforms with additional degrees of freedom [14]. Robot-assisted multi-axis systems have thus emerged to realize multi-directional deposition and support reduction [5,12,15,20].

In Robot-Assisted Multidirectional AM (RAM-AM), segmentation and slicing algorithms typically generate detailed intra-segment print paths but do not explicitly plan the *travel paths* (non-printing moves) between adjacent segments. As a result, transitions often suffer from spatial discontinuities, inefficient connections, and collision risks when executed on real hardware. Since realistic parts are decomposed into hundreds of segments, inter-segment planning is a frequent operation that must remain computationally efficient while strictly honoring obstacle avoidance and the robot's kinematic constraints. This motivates an approach that plans safe, smooth, and executable inter-segment travel paths, regardless of the specific kinematic configuration.

We address this gap with a decoupled pipeline. First, a safe and smooth geometric path is computed in the platform-fixed frame by combining a guided A* search with smoothing and orientation assignment. Second, an executable joint-space trajectory is generated by sampling and selecting a globally consistent joint sequence via dynamic programming. The method is validated on a 6-DoF industrial arm.

The main contributions of this work are:

(i) An asymmetric layered cost map for A*-based geometric path planning on an OctoMap representation, ensuring safe obstacle clearance [7].
(ii) An orientation assignment strategy combining an artificial potential field (APF) with Slerp interpolation for smooth, safety-aware motions [10].
(iii) A joint-space trajectory optimizer using pose tolerance sampling, IK sampling, and second-order dynamic programming to ensure motion smoothness under kinematic limits [3,16].
(iv) Experimental validation in three scenarios (standard, cylindrical, gate-shaped obstacle), demonstrating improved clearance, avoidance of unsafe hole traversal, and smoother paths.

The paper is organized as follows. Section 2 reviews related work on multi-axis AM, path planning, and trajectory planning. Section 3 details the proposed methodology and the specific hardware setup. Section 4 presents experimental results. Section 5 discusses implications and limitations, and Sect. 6 outlines future work.

2 Related Work

Motion planning for robotic AM is a critical factor for process quality and is typically decoupled into geometric path planning and kinematic trajectory generation. Recent studies emphasize that optimized path planning significantly influences the geometric accuracy of thin-walled structures and overall print success [4].

Regarding geometric planning, sampling-based algorithms (RRT*, PRM) are standard for high-DoF robots due to their scalability [2,9]. However, in manufacturing contexts, their stochastic nature is a significant drawback, leading to non-repeatable and jagged paths that require extensive post-processing. Artificial Potential Fields (APF) offer fast, reactive avoidance but are prone to local minima in complex topologies [10].

Conversely, graph-search methods (Dijkstra, A*) on discretized voxel grids provide deterministic, resolution-optimal solutions [17,18]. While emerging data-driven approaches explore reinforcement learning on graphs to handle diverse geometries [8], deterministic graph-search remains superior for ensuring hard safety constraints in industrial setups. Since AM environments are inherently volumetric and efficiently represented by OctoMaps [7], A* is particularly suitable. This is supported by recent work from Osmanović et al. [13], who demonstrated in 2025 that integrating OctoMap-based collision detection within the ROS MoveIt! framework significantly enhances safety and collision avoidance efficiency in dynamic robotic environments.

Trajectory generation transforms the geometric path into joint commands, necessitating the resolution of kinematic redundancy, specifically the rotation around the extrusion axis in 6-DoF setups. While classical approaches optimize execution time [1,16] or jerk [11] for fixed joint configurations, selecting the optimal sequence from the redundant solution space is non-trivial. Local optimization often leads to singularities or joint-limit violations. Global optimization techniques via Dynamic Programming (DP) can effectively resolve this redundancy by evaluating costs over the entire sequence [16], ensuring smooth and executable motion.

3 Methodology

We adopt a decoupled pipeline, illustrated in Fig. 1, that splits the problem into geometric planning and kinematic trajectory generation.

The physical hardware consists of a 6-DoF robot that manipulates a printing platform relative to a fixed extruder. Direct planning in the world coordinate system $\{W\}$ would require updating the obstacle map (of the printed part) with every robot movement. To avoid this complexity, we reverse the kinematic chain for the first stage and treat the problem as a movable nozzle configuration within the static platform coordinate system $\{P\}$. This allows us to model the printed part as a static obstacle map. Once a safe path is found in $\{P\}$, it is transformed back to the world coordinate frame $\{W\}$ to generate executable joint commands for the actual robot with a movable bed.

The implementation leverages ROS2 for modularity and MoveIt for kinematics and collision tooling [3]. Intermediate data are exchanged via JSON (paths) and CSV (trajectories) to keep each stage efficient.

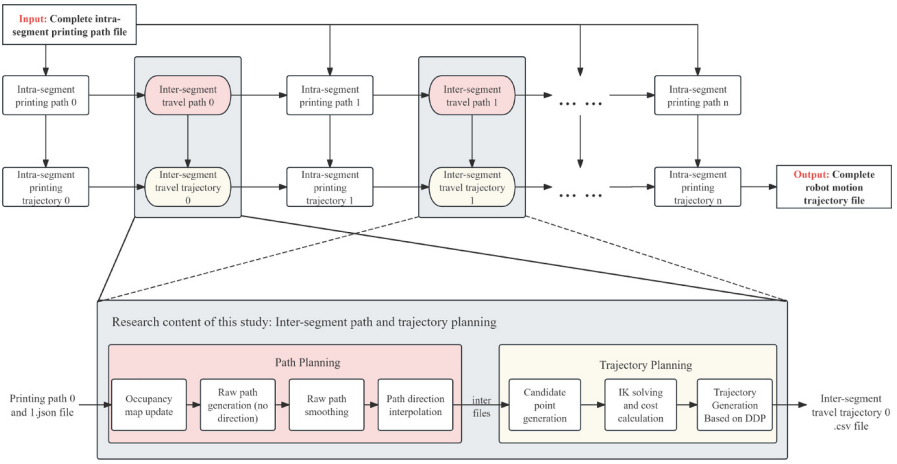

Fig. 1. Overview of the framework. The Geometric Path Planning (left) operates in the simplified platform frame $\{P\}$, while Trajectory Planning (right) transforms the result to the world frame $\{W\}$ to solve for robot kinematics.

3.1 Geometric Path Planning in the Platform Frame

To accelerate search, obstacles (e.g.: previously printed segments) are voxelized into an OctoMap at 3 mm resolution [7]. Safe start and goal points are created by a small lift along the local z-axis to ensure the path leaves obstacle voxels before global search.

First, we run A* on the voxel grid using the evaluation function $f(n) = g(n) + h(n)$. The heuristic $h(n)$ combines the Euclidean distance $d(n, \text{goal})$ with an asymmetric, layered cost map $C(l)$ derived from a BFS distance transform:

$$h(n) = d\big(n, \text{goal}\big) + \lambda_1 \, C(l), \qquad d\big(n, \text{goal}\big) = \big\|\mathbf{x}_n - \mathbf{x}_{\text{goal}}\big\|_2. \tag{1}$$

Let $l \in \mathbb{N}$ be the distance-in-layers to the nearest obstacle. The layered penalty $C(l)$ is defined piecewise to steer the path away from obstacles (high C_{in}) without excessive deviation (low C_{min}):

$$C(l) = \begin{cases} C_{\text{def}}, & l = 0, \\ C_{\text{in}} - \dfrac{C_{\text{in}} - C_{\text{min}}}{L_{\text{mid}}}\, l, & 1 \le l \le L_{\text{mid}}, \\ C_{\text{out}} + \dfrac{C_{\text{min}} - C_{\text{out}}}{L_{\text{max}} - L_{\text{mid}}}\,(l - L_{\text{mid}}), & L_{\text{mid}} < l \le L_{\text{max}}, \\ C_{\text{def}}, & l > L_{\text{max}}. \end{cases} \tag{2}$$

Here, L_{mid} defines the inflection point of the penalty curve. A lazy evaluation computes voxel costs only upon expansion to speed up search.

Next, the raw voxel path is smoothed using sparse cubic B-splines and resampled at uniform arc length (e.g.: 1 mm) to mitigate staircase effects while preserving the encoded obstacle clearances [6]. The curve is defined as:

$$\mathbf{P}(u) = \sum_i N_{i,3}(u)\,\mathbf{P}_i, \qquad u \in [0,1], \tag{3}$$

using downsampled control points $\mathbf{P}_i$ (e.g.: every third waypoint).

Finally, we assign orientations. The extrusion axis (local z-axis) is determined by blending spherical linear interpolation (Slerp) with an artificial potential field (APF) [10]. The safety-aware direction $\mathbf{Z}_{\text{opt}}(t)$ at path parameter t is:

$$\mathbf{Z}_{\text{opt}}(t) = w_{\text{interp}}(t)\,\mathbf{Z}_{\text{interp}}(t) + \big(1 - w_{\text{interp}}(t)\big)\,\mathbf{F}_{\text{repel}}(t), \tag{4}$$

where $\mathbf{Z}_{\text{interp}}(t) = \text{Slerp}(\mathbf{Z}_{\text{start}}, \mathbf{Z}_{\text{end}}, t)$. The composite repulsion force $\mathbf{F}_{\text{repel}}(t)$ combines obstacle repulsion $\mathbf{F}_{\text{obs}}$ and a platform-normal preference $\mathbf{F}_{\text{plat}}$:

$$\mathbf{F}_{\text{repel}}(t) = \omega_1\,\mathbf{F}_{\text{obs}}(t) + \omega_2\,\mathbf{F}_{\text{plat}}, \qquad \mathbf{F}_{\text{plat}} = (1,0,0)^\top, \tag{5}$$

$$\mathbf{F}_{\text{obs}}(t) = \sum_j \eta\,\frac{\mathbf{P}(t) - \mathbf{Q}_j}{\big\|\mathbf{P}(t) - \mathbf{Q}_j\big\|_2^3 + \epsilon}. \tag{6}$$

Here, $\mathbf{Q}_j$ denotes the position of the j-th obstacle voxel, η is a gain constant, and ϵ prevents division by zero. A bell-shaped weight $w_{\text{interp}}(t)$ reduces APF influence near endpoints to preserve continuity.

3.2 Joint-Space Trajectory Generation in the World Frame

This section introduces a sampling-and-DP strategy to select optimal joint transitions. First, the planned path is transformed from the platform frame $\{P\}$ to the world frame $\{W\}$ to represent the actual platform motion relative to the fixed nozzle ${}^{W}T_N$:

$${}^{W}T_P(s) = {}^{W}T_N\,\big({}^{P}T_N(s)\big)^{-1}, \quad \text{where} \quad \begin{pmatrix} R & t \\ 0 & 1 \end{pmatrix}^{-1} = \begin{pmatrix} R^\top & -R^\top t \\ 0 & 1 \end{pmatrix}. \tag{7}$$

For each waypoint on this path, we sample 24 pose candidates (6 positions, 4 orientations) within small tolerances to exploit kinematic redundancy. Multiple inverse kinematics (IK) solutions $\mathbf{q}$ per candidate are computed. These candidates are evaluated using four costs:

$$C_{\Delta q} = \omega_{\Delta q}\,\big\|\mathbf{q}_k - \mathbf{q}_{k-1}\big\|_W^2, \qquad \text{(Displacement)} \tag{8}$$

$$C_a = \omega_a\,\big\|\mathbf{q}_k - 2\mathbf{q}_{k-1} + \mathbf{q}_{k-2}\big\|_W^2, \qquad \text{(Acceleration)} \tag{9}$$

$$C_l = \omega_l \sum_m \left(\frac{1}{q_{\max,m} - q_m + \epsilon} + \frac{1}{q_m - q_{\min,m} + \epsilon}\right), \qquad \text{(Joint Limits)} \tag{10}$$

$$C_s = \frac{\omega_s}{\det\big(J^\top J\big) + \epsilon}, \qquad \text{(Singularity)} \tag{11}$$

using a weighted norm $\|\mathbf{x}\|_W^2 = \mathbf{x}^\top W \mathbf{x}$ and the manipulator Jacobian J.

A globally consistent joint sequence is selected via second-order dynamic programming (DP) on state pairs $(u, v) \to (v, w)$ to account for the acceleration cost [16]:

$$\begin{aligned} \mathrm{DP}_{k+1}[v, w] = C_{\mathrm{node}}\big(\mathbf{q}_{k+1}^w\big) + \min_{u \in L_{k-1}} \Big\{ \mathrm{DP}_k[u, v] + C_{\mathrm{edge}}\big(\mathbf{q}_k^v, \mathbf{q}_{k+1}^w\big) \\ + C_a\big(\mathbf{q}_{k-1}^u, \mathbf{q}_k^v, \mathbf{q}_{k+1}^w\big) \Big\}, \end{aligned} \tag{12}$$

where $C_{\mathrm{node}} = C_l + C_s$ and $C_{\mathrm{edge}} = C_{\Delta q}$. The resulting sequence is time-parameterized to generate the final trajectory.

4 Results

4.1 Experimental Setup and Metrics

For evaluation inter-segment planning between Layer 0 and Layer 1 of the Stanford Bunny model, a standard benchmark in computer graphics and AM research is used. The slicing data and intra-segment paths are based on the multi-axis decomposition method by Dai et al. [5]. Already deposited material is voxelized into an OctoMap as obstacles. Planning and visualization are performed in ROS2, and trajectories are executed on a KUKA KR6 R900 sixx industrial arm. Three scenarios are considered, as shown in Fig. 2: (i) a standard transition, (ii) an added cylindrical obstacle, and (iii) a gate-shaped structure to test the planner's behavior at openings (cf. Sect. 3).

To evaluate performance, we report planning time, path length (L_{total}), bending energy (E_{bend}), average obstacle distance ($\overline{D}_{\mathrm{obs}}$), and smoothness metrics. Let the discrete path samples be $\{\mathbf{P}_i\}_{i=1}^N$. The metrics are defined as:

$$L_{\mathrm{total}} = \sum_{i=1}^{N-1} \big\|\mathbf{P}_{i+1} - \mathbf{P}_i\big\|_2, \tag{13}$$

$$E_{\mathrm{bend}} = \sum_{i=2}^{N-1} k_i^2 \, \big\|\mathbf{P}_{i+1} - \mathbf{P}_{i-1}\big\|_2, \tag{14}$$

$$\overline{D}_{\mathrm{obs}} = \frac{1}{N} \sum_{i=1}^{N} \min_{j \in \mathrm{Obs}} \big\|\mathbf{P}_i - \mathbf{Q}_j\big\|_2, \tag{15}$$

$$K_{\max} = \max_{2 \le i \le N-1} \theta_i, \quad \theta_i = \measuredangle\big(\mathbf{P}_i - \mathbf{P}_{i-1},\ \mathbf{P}_{i+1} - \mathbf{P}_i\big), \tag{16}$$

$$\overline{\theta} = \frac{1}{N-2} \sum_{i=2}^{N-1} \theta_i, \quad \overline{a} = \frac{1}{N-2} \sum_{i=2}^{N-1} \big\| \ (\mathbf{P}_{i+1} - \mathbf{P}_i) - (\mathbf{P}_i - \mathbf{P}_{i-1}) \ \big\|_2. \tag{17}$$

Here, θ_i represents the discrete turning angle between path segments, k_i denotes the local curvature at point $\mathbf{P}_i$, and Obs is the set of all obstacle voxel centers $\mathbf{Q}_j$.

4.2 Geometric Path Planning Results

This section evaluates the geometric path generation (A* vs. Cost Map) and its subsequent refinement (Smoothing and Orientation), with visual results for the planning scenarios shown in Fig. 2.

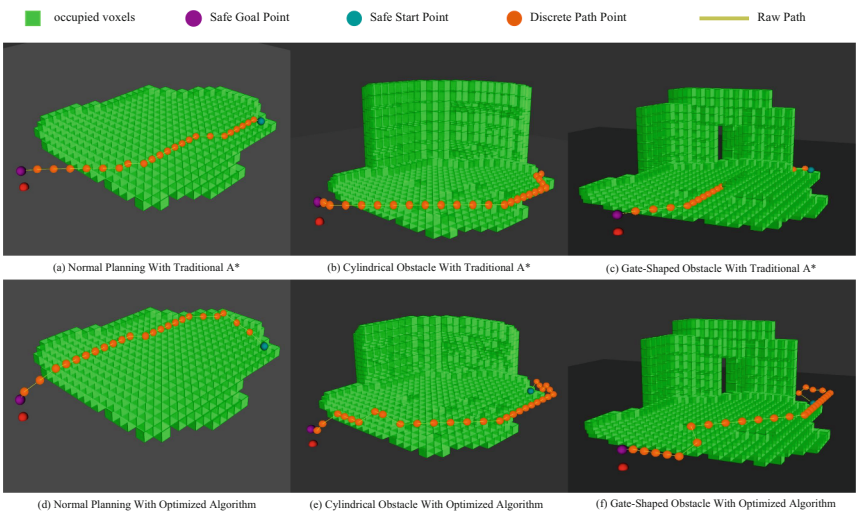

Fig. 2. Comparison of baseline A* (top row) and the proposed method (bottom row) on three obstacle types: (a,d) standard, (b,e) cylindrical, and (c,f) gate-shaped.

Path Planning: Baseline A* Vs. Asymmetric Cost Map. The asymmetric layered cost map (cf. Sect. 3) consistently increases safety margins ($\overline{D}_{\text{obs}}$) compared to a baseline A* implementation. As quantified in Table 1, the obstacle clearance is more than doubled in all scenarios. Crucially, in the gate scenario (Fig. 2f), the cost inflation steers the path safely around the opening, whereas the baseline A* (Fig. 2c) finds the shortest path through the hole. While geometrically valid for a point, traversing the hole is kinematically unsafe for the actual print head assembly. The proposed method correctly identifies the safer outer path, albeit at the cost of increased planning time (from 17 ms to 170 ms) due to the larger search space and heuristic calculation. However, this runtime remains well within the limits for offline planning.

Path Smoothing and Orientation Assignment. The raw paths from the optimized A* search exhibit higher bending energy due to the discrete voxel grid. We apply sparse cubic B-splines to smooth the path before orientation assignment. As detailed in Table 2, this method drastically reduces bending energy

Table 1. Performance comparison of Baseline A* vs. Cost Map A* (Ours).

Scenario	Algorithm	Time (ms)	L_{total} (m)	$\overline{D}_{obs}$ (m)
Standard	Baseline A*	16	0.0799	0.0063
	Cost Map A* (Ours)	54	0.0893	**0.0136**
Cylinder	Baseline A*	39	0.0924	0.0075
	Cost Map A* (Ours)	257	0.1052	**0.0108**
Gate	Baseline A*	17	0.0800	0.0056
	Cost Map A* (Ours)	170	0.1080	**0.0122**

(E_{bend}) and the acceleration proxy ($\overline{a}$) across all scenarios, effectively removing the jaggedness of the raw A* output. Following smoothing, orientation is assigned. Pure Slerp between endpoint orientations can align the extrusion axis too close to obstacles in complex geometries (cylinder, gate). Blending Slerp with our APF visibly increases mid-path safety margins while preserving smooth endpoint continuity.

Table 2. Path smoothing metrics per scenario showing the impact of Sparse B-Spline optimization.

Scenario	Path Type	E_{bend} (-)	$K_{\max}$ (°)	L_{total} (m)	$\overline{\theta}$ (rad)	$\overline{a}$ (m)
Standard	Raw Path	361.77	130.00	0.0893	0.2576	1.10e-3
	Sparse B-Spline	**95.07**	79.55	0.0905	0.0551	6.51e-5
Cylinder	Raw Path	695.22	215.72	0.1139	0.3414	1.49e-3
	Sparse B-Spline	**97.23**	65.87	0.1088	0.0478	5.57e-5
Gate	Raw Path	803.31	234.16	0.1080	0.3236	1.42e-3
	Sparse B-Spline	**229.62**	163.50	0.1011	0.0736	7.59e-5

4.3 Joint-Space Trajectory Generation Results

This section evaluates the generation of the final, executable robot trajectory.

Trajectory Planning and Optimization. For each waypoint, 24 pose candidates (position/orientation tolerances) are generated. Multiple IK solutions are computed and scored by the four joint-space costs. The globally consistent sequence is selected via second-order dynamic programming (cf. Eq. 12). The resulting platform trajectories are collision-free. Joint profiles across all six axes are continuous with reduced jumps and smoothed accelerations under representative weights (e.g.: $\omega_{\Delta q} = 4.0$, $\omega_a = 2.0$, $\omega_l = 0.2$, $\omega_s = 0.3$).

Influence of Redundant Rotational Degrees of Freedom. A key finding during trajectory generation relates to the redundant rotation around the extrusion axis (local z). Rotating the local x/y axes before back-transformation (cf. Sect. 3) leaves the geometric path unchanged but moves the platform relative to the nozzle, which significantly changes the IK difficulty for the given hardware layout. In experimental comparisons, a 180° rotation reduced the required IK search window from 150° (Path 1) to only 30° (Path 3). This indicates that exploiting this redundancy significantly improves IK solvability and overall trajectory smoothness.

4.4 Summary of Findings

The decoupled pipeline systematically increases safety (larger obstacle clearances, avoidance of hole traversal), yields markedly better path quality after smoothing (lower maximum curvature and bending energy), and produces robust, smooth joint trajectories via second-order DP. All steps operate at offline-feasible runtimes. Furthermore, exploiting redundant rotations about the extrusion axis was shown to be a critical factor for reducing IK search effort and improving trajectory elegance on the given system kinematics.

5 Discussion

The proposed decoupled pipeline effectively balances safety, smoothness, and offline feasibility for inter-segment travel in robot-assisted multidirectional FDM. By decomposing the problem into platform-frame geometric planning and world-frame trajectory generation, we significantly reduce search complexity and leverage robust voxel-based heuristics. However, this approach introduces characteristic trade-offs concerning safety guarantees and parameter sensitivity.

5.1 Indirect Safety via Layered Cost Maps Vs. Explicit Guarantees

The asymmetric, layered cost map reliably steers the end-effector away from obstacles and discourages risky shortcuts, such as traversing openings, even though the nozzle is abstracted as a point mass (Sect. 3). However, this safety is *implicit*. As observed in the gate scenario, if the cost map's inflation width is small relative to the hole size, internal passages may remain cost-competitive with safer outer bypasses. The empirical rule derived in Sect. 4, setting the inflation width to at least one-third of the maximum feature width, proved robust across our experiments. Nevertheless, to convert this probabilistic safety into a hard guarantee, future iterations should incorporate explicit collision checks with the full nozzle and fixture geometry, either as a lazy check during A* expansion or as a validation step post-smoothing.

5.2 Generalization and Empirical Parameterization

The pipeline's performance currently relies on the empirical parameterization of its core components, affecting three key stages: (1) The A* heuristic (λ_1) and cost map configuration (C_{in}, $L_{\max}$) define the aggressiveness of obstacle avoidance. (2) The APF weights (ω_1, ω_2) and the blending function balance smoothness against clearance during orientation assignment. (3) The DP weights ($\omega_{\Delta q}, \omega_a, \omega_l, \omega_s$) govern the trade-off between trajectory smoothness and kinematic safety. While the chosen parameters proved effective for the tested geometries, they are specific to the robot's workspace and the part scale. To generalize the pipeline to different kinematic chains or part families, systematic tuning methods, such as grid search or Bayesian optimization, would be advisable to automate parameter selection.

5.3 Utilization of Redundant Rotational Degrees of Freedom

A critical insight from this work is the utility of the redundant rotation about the extrusion axis (local z). Rotating the local x/y axes prior to the back-transformation (Sect. 3) leaves the geometric deposition path unchanged but significantly alters the robot's configuration in the world frame. As demonstrated in Sect. 4, a simply static rotation of 180° reduced the required IK search window from 150° to 30°, indicating a much "healthier" kinematic region. This suggests that this redundant DoF should not be fixed arbitrarily but treated as an effective optimization variable in pre-processing to enhance IK solvability and motion smoothness.

6 Conclusion and Future Work

This work presented a decoupled motion planning pipeline for non-printing travel moves in robot-assisted multidirectional additive manufacturing. By separating the problem into platform-frame geometric planning and world-frame trajectory generation, we achieved a robust balance between computational efficiency and motion quality. The experimental validation on a 6-DoF industrial robot demonstrated that the asymmetric layered cost map significantly improves safety margins and successfully prevents risky hole traversals compared to standard path planning. Furthermore, second-order dynamic programming effectively resolves kinematic redundancy, resulting in smooth, jerk-limited joint trajectories. Crucially, exploiting the redundant rotation about the extrusion axis proved to be a decisive factor for solving inverse kinematics in complex workspace areas.

Future work will focus on transitioning from implicit safety to hard guarantees by integrating explicit collision checks, such as Signed Distance Fields, directly into the search loop. Additionally, we aim to replace empirical parameter tuning with automated optimization methods to facilitate rapid adaptation to different kinematic structures.

References

1. Bobrow, J.E., Dubowsky, S., Gibson, J.S.: Time-optimal control of robotic manipulators along specified paths. Int. J. Robot. Res. **4**(3), 3–17 (1985). https://doi.org/10.1177/027836498500400301
2. Chen, G., Luo, N., Liu, D., et al.: Path planning for manipulators based on an improved probabilistic roadmap method. Robot. Comput.-Integr. Manuf. **72**, 102196 (2021)
3. Coleman, D., Sucan, I., Chitta, S., et al.: Reducing the barrier to entry of complex robotic software: a moveit! case study. arXiv preprint arXiv:1404.3785 (2014)
4. Csekei, M., Sido, J., Niznan, P., Ruzarovsky, R.: Optimization of parameters in robotic additive manufacturing of thin-walled tubes: experimental analysis and path planning. MM Sci. J. 6972–6980 (2025). https://doi.org/10.17973/MMSJ.2025_03_2024002
5. Dai, C., Wang, C.C.L., Wu, C., Lefebvre, S., Fang, G., Liu, Y.J.: Support-free volume printing by multi-axis motion. ACM Trans. Graph. **37**(4), 1–14 (2018). https://doi.org/10.1145/3197517.3201342
6. Gasparetto, A., Boscariol, P., Lanzutti, A., et al.: Path planning and trajectory planning algorithms: a general overview. In: Carbone, G., Gomez-Bravo, F. (eds.) Motion and Operation Planning of Robotic Systems. Mechanisms and Machine Science, LNCS, vol. 29, pp. 3–27 . Springer, Cham (2015). https://doi.org/10.1007/978-3-319-14705-5_1
7. Hornung, A., Wurm, K.M., Bennewitz, M., et al.: Octomap: an efficient probabilistic 3d mapping framework based on octrees. Auton. Robot. **34**(3), 189–206 (2013). https://doi.org/10.1007/s10514-012-9321-0
8. Huang, Y., Guo, Y., Su, R., Han, X., et al.: Learning based toolpath planner on diverse graphs for 3d printing. ACM Trans. Graph. **43**(4) (2024). https://doi.org/10.1145/3687933
9. Karaman, S., Frazzoli, E.: Sampling-based algorithms for optimal motion planning. Int. J. Robot. Res. **30**(7), 846–894 (2011)
10. Khatib, O.: Real-time obstacle avoidance for manipulators and mobile robots. In: Proceedings of the IEEE International Conference on Robotics and Automation, pp. 500–505 (1985). https://doi.org/10.1109/ROBOT.1985.1087247
11. Kyriakopoulos, K.J., Saridis, G.N.: Minimum jerk path generation. In: Proceedings of the IEEE International Conference on Robotics and Automation, pp. 364–369 (1998)
12. Larochelle, P.M., Ishak, I.: A robot arm based additive manufacturing system. In: Proceedings of CCToMM Mechanisms, Machines, and Mechatronics (M3) Symposium (2019)
13. Osmanović, A., et al.: Affordable collision detection for a 3d-printed robotic arm. Technical Gazette **32**(6), 2066–2072 (2025). https://doi.org/10.17559/TV-20250320002497
14. Shahrubudin, N., Lee, T.C., Ramlan, R.: An overview on 3D printing technology: technological, materials, and applications. Procedia Manuf. **35**, 1286–1296 (2019). https://doi.org/10.1016/j.promfg.2019.06.089
15. Shen, H., Diao, H., Yue, S., et al.: Fused deposition modeling five-axis additive manufacturing: machine design, fundamental printing methods and critical process characteristics. Rapid Prototyp. J. **24**(3), 548–561 (2018). https://doi.org/10.1108/RPJ-05-2017-0096

16. Shin, K.G., McKay, N.D.: A dynamic programming approach to trajectory planning of robotic manipulators. IEEE Trans. Autom. Control **31**(6), 491–500 (1986)
17. Wang, Y.F., Cao, X.H., Guo, X.: Warehouse agv path planning method based on improved a* algorithm and system short-term state prediction. Computer Integrated Manufacturing Systems (2022). online First
18. Wei, K., Gao, Y., Zhang, W., et al.: A modified dijkstra's algorithm for solving the problem of finding the maximum load path. In: 2019 IEEE 2nd International Conference on Information and Computer Technologies (ICICT), pp. 10–13 (2019)
19. Wong, K.V., Hernandez, A.: A review of additive manufacturing. Int. Sch. Res. Not. **2012**, Article ID 208760, 10 (2012). https://doi.org/10.5402/2012/208760
20. Wu, C., Dai, G., Fang, Y.J., Liu, C.C.L.: General support-effective decomposition for multi-directional 3-D printing. IEEE Trans. Autom. Sci. Eng. **17**(2), 599–610 (2020). https://doi.org/10.1109/TASE.2019.2938219

An Autonomous Obstacle-Avoiding Rolling Robot Based on a Parallel Mechanism

Xinrui Tao(✉), Jiayao Ma, and Yan Chen

Tianjin University, Tianjin 300350, China
{1024201067,yan_chen}@tju.edu.cn

Abstract. Rolling robots offer efficient locomotion and terrain adaptability, making them ideal candidates for environmental exploration and search-and-rescue missions. However, enabling these robots to autonomously navigate complex environments typically requires sophisticated sensory networks and centralized control architectures, which increase structural complexity and energy consumption. Here, we present a rolling robot based on mechanical intelligence that achieves autonomous obstacle avoidance through structural responsiveness alone, eliminating the need for electronic sensors or processors. Our design leverages a spatial parallel mechanism coupled with a continuously driven pendulum. Upon encountering an obstacle, the pendulum spontaneously shifts from a forward to a backward bias, reversing the driving torque and inducing a passive diameter contraction on one side of the robot. This geometric asymmetry triggers a deterministic "backward-turn-forward" maneuver, allowing the robot to steer away from the obstruction. We derive the kinematic constraints to optimize the radius contraction ratio and establish a dynamic model to predict the steering trajectory. Experimental validation demonstrates that the lightweight prototype can autonomously navigate a maze with 90° turns using only a single actuator. This work illustrates how mechanical intelligence derived from intrinsic structural dynamics can replace complex control loops, providing a robust, energy-efficient approach for designing autonomous machines in unstructured environments.

Keywords: Rolling robot · Parallel mechanism · Obstacle avoidance · Mechanical intelligence

1 Introduction

Rolling robots are characterized by their considerable locomotion speed and excellent terrain adaptability, capabilities that enable them to effectively traverse small obstacles or gaps [1]. Prominent examples include pendulum-driven spherical robots [2–5], cylindrical robots that achieve rolling by altering their profile shapes [6–8], and polygonal robots that roll by shifting their centers of mass via airbags or other actuators [9, 10]. However, when confronted with larger, impassable obstacles, rolling robots must rely on steering capabilities to circumvent them. Common steering strategies include pendulum translation, where the internal pendulum is actively translated along the rotational

© The Author(s), under exclusive license to Springer Nature Switzerland AG 2026
A. Chaker et al. (Eds.): EFIMMS 2026, MMS 205, pp. 171–182, 2026.
https://doi.org/10.1007/978-3-032-22270-1_17

axis to laterally shift the center of mass [2–4]; multi-rotor control, which utilizes reaction torques generated by regulating the speeds of multiple internal flywheels [11]; and shape morphing, which differentially pressurizes internal chambers to induce asymmetric deformation [12]. Consequently, realizing these functions demands specific actuation systems—linear rails, multiple motors, or pneumatic valves—which significantly increases design complexity by requiring additional structures and sophisticated control algorithms.

A novel category of mechanically intelligent robots has emerged that replaces centralized controllers with structural responsiveness, utilizing physical interaction to autonomously adapt their trajectories. Specifically, these robots achieve autonomous adaptation by employing embedded bistable mechanisms to trigger reflexive motion reversal [13], harnessing implicit body-environment coupling to alter limb synchronization for steering [14], and utilizing contact-driven energy landscape modulation to passively reprogram motion sequences [15]. Leveraging this design philosophy, we present an autonomous obstacle-avoiding rolling robot based on a parallel mechanism composed of six identical linkages consisting of four revolute joints and one cylindrical joint (4R1C). The robot exploits the spontaneous state transition of a driven pendulum to passively alter its geometry upon collision, thereby automatically converting straight forward motion into a steering maneuver. To clearly illustrate the distinct advantages of this study, Table 1 summarizes the key differences between existing research and our proposed approach. Section 2 details the mechanical design and theoretical analysis, using kinematics to optimize the contraction ratio and dynamics to predict trajectories. Section 3 reports on the prototype fabrication and experimental validations. Section 4 summarizes the conclusions.

Table 1. Comparison of existing research and the proposed obstacle-avoiding rolling robot.

Robot	Number of sensors	Number of actuators
Spherical Robot (ARIES) [4]	Multiple (IMU/Lidar)	2 (Motors)
Tensegrity Robot [10]	Multiple (Encoders)	24–48 (Motors)
Soft Cylindrical Robot [12]	Multiple (IMU)	6 (Pumps)
This work	0 (None)	1 (Single Motor)

2 Mechanical Design and Theoretical Analysis

2.1 Design and Working Principle of the Rolling Robot

The robot features an asymmetric structural configuration constructed from four distinct components: the variable-diameter ring, the variable-diameter mechanism, the pendulum section, and the anti-topple ring (as shown in Fig. 1a). These components are assembled around a central drive shaft. On one side, the variable-diameter mechanism is rigidly fixed to the shaft to transmit torque, supporting the flexible variable-diameter ring. On the other side, the anti-topple ring connects to the drive shaft via a cylindrical joint,

permitting relative rotation and axial sliding to accommodate deformation. Unilateral contraction of the variable-diameter mechanism allows the robot to toggle between a cylindrical straight rolling state and a conical turning state (Fig. 1b). Centered between these two sections is the pendulum section, which integrates the geared motor, battery, and wireless switch, functioning as the primary driving unit to power the robot.

The autonomous obstacle avoidance capability arises from the interaction between the pendulum's spontaneous dynamics and the mechanism's structural deformability. The operation sequence is described as follows:

i. Unimpeded Locomotion: During normal operation, the motor maintains the pendulum in a forward-biased position. This generates a driving torque that keeps the variable-diameter mechanism fully expanded, resulting in a cylindrical geometry for straight-line motion.
ii. Collision and Reversal: When the robot is blocked by an obstacle, the internal pendulum rotates past its top point into a backward-biased position due to gravity, thereby reversing the direction of the driving torque (Fig. 1b, Step 1).
iii. Contraction and Steering: Governed by the kinematics, this reverse torque forces the variable-diameter ring to contract. The resulting radius discrepancy transforms the robot into a conical rolling geometry, executing a curved backward turn away from the obstruction (Fig. 1b, Step 2).
iv. Restoration: Upon passing the bottom point, the pendulum reverts to a forward bias, re-expanding the mechanism (Fig. 1b, Step 3) and enabling the robot to resume straight forward motion (Fig. 1b, Step 4).

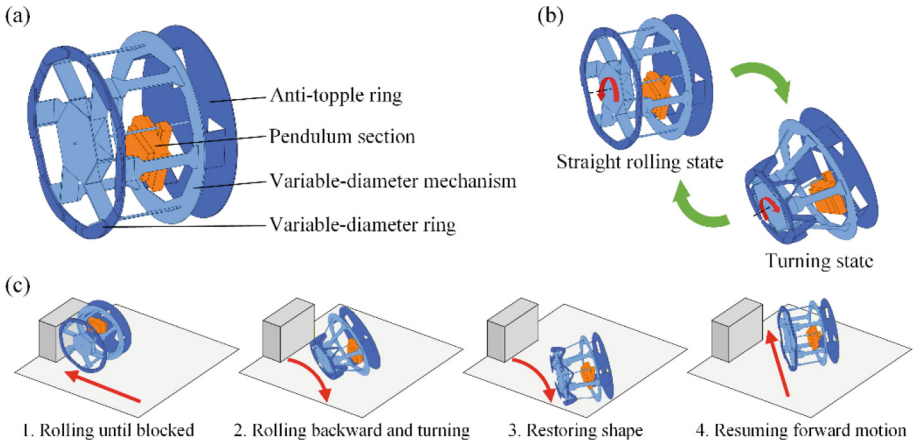

Fig. 1. Design and working principle of the rolling robot. (a) Schematic diagram and components of the rolling robot. (b) Straight rolling state and turning state of the rolling robot. (c) Sequential demonstration of the obstacle avoidance maneuver.

2.2 Analysis of the Variable-Diameter Mechanism

In this section, a kinematic analysis is performed to investigate the deformation characteristics of the variable-diameter mechanism, with the primary objective of establishing the relationship between geometric parameters and the variable radius. This analysis serves as the basis for optimizing the link length ratio to maximize the mechanism's contraction capability.

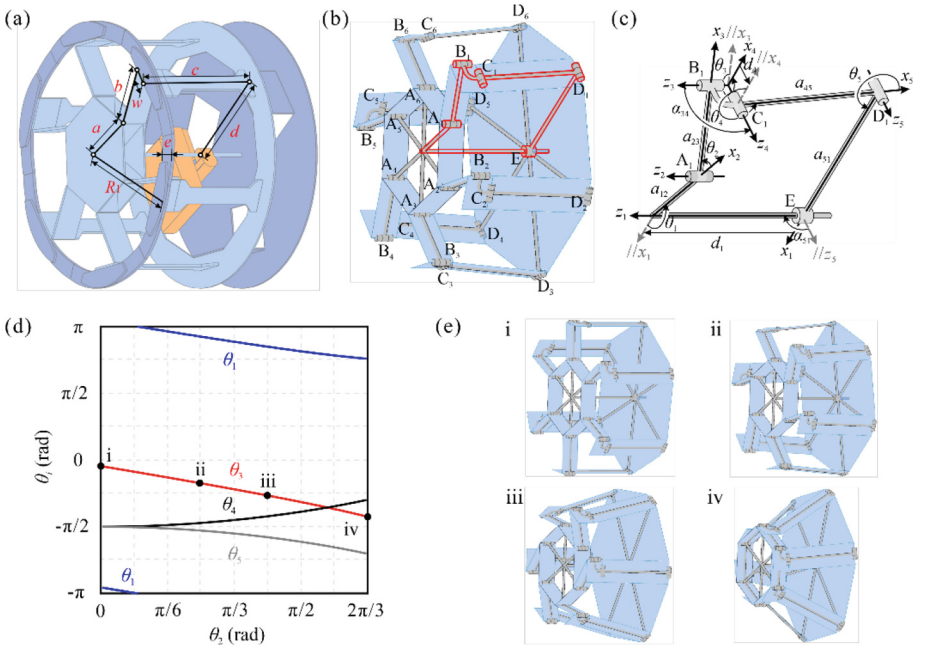

Fig. 2. Kinematic model and analysis of the variable-diameter mechanism. (a) Geometric parameters of the variable-diameter mechanism. (b) Schematic of the overall spatial parallel mechanism composed of six radially arranged kinematic chains. (c) Kinematic diagram of the extracted single-loop mechanism with defined geometric parameters. (d) Kinematic curves of θ_1 and θ_3-θ_5 versus θ_2. (e) Motion sequences of the mechanism corresponding to states i-iv.

The geometric parameters of the variable-diameter mechanism and the variable-diameter ring are illustrated in Fig. 2a, where a and b denote the lengths of the two connecting links extending from the central drive shaft to the variable-diameter ring. c represents the length of the link connecting the variable-diameter ring to the constant-radius side of the variable-diameter mechanism, while d defines the radial distance from the central drive shaft to the connection point. w corresponds to the positional offset distance between the two links connecting the variable-diameter ring. Furthermore, the ring's width is defined as e, and its radius is denoted as R_1. As illustrated in Fig. 2b, the variable-diameter mechanism is designed as a spatial parallel mechanism composed of six identical kinematic chains arranged symmetrically around the central drive shaft. This specific 4R1C spatial parallel configuration was selected for its superior stiffness

and stability over serial linkages. Furthermore, its single degree of freedom (1-DOF) ensures deterministic, synchronized radial contraction using only one input. Crucially, this kinematic response effectively couples with the pendulum's reverse torque to trigger the passive 'backward-turn' maneuver without additional actuators. Consequently, for a single kinematic chain, a spatial closed-loop model can be extracted. A coordinate system is established using the Denavit-Hartenberg method [16], wherein z_i lies along the rotation axis of joint i; x_i points along the common normal from $z_{i\text{-}1}$ to z_i; $a_{i(i+1)}$ represents the normal distance between z_i and z_{i+1}; $\alpha_{i(i+1)}$ denotes the rotation angle from z_i to z_{i+1} about axis x_i; d_i is the normal distance between x_i and x_{i+1}; and θ_i is the rotation angle between x_i and x_{i+1} about the z_i axis. The kinematic schematic of the 4R1C mechanism is illustrated in Fig. 2c, where

$$a_{12} = a,\ \ a_{23} = b,\ \ a_{34} = 0,\ \ a_{45} = c,\ \ a_{51} = d$$

$$d_2 = d_3 = d_5 = 0, d_4 = w \tag{1}$$

$$\alpha_{12} = \alpha_{23} = \alpha_{45} = 0,\ \ \alpha_{34} = \alpha_{51} = \frac{\pi}{2}$$

By applying the closure equation, the kinematic equations governing the mechanism are derived directly. With θ_2 designated as the independent input variable, the angle θ_1 is implicitly determined through the geometric constraint in the axial direction, expressed as

$$a\sin\theta_1 + b\sin(\theta_1 + \theta_2) = -w \tag{2}$$

Upon solving for θ_1, the angles of the remaining joints θ_3 to θ_5 are subsequently calculated:

$$\theta_5 = -\arccos\left(-\frac{d + a\cos\theta_1 + b\cos(\theta_1 + \theta_2)}{c}\right) \tag{3}$$

$$\theta_3 = \pi - \theta_1 - \theta_2 \tag{4}$$

$$\theta_4 = \pi - \theta_5 \tag{5}$$

Considering the requirements for the pendulum's workspace and the ease of fabrication, we selected the following design parameters as $a + b = 35$ mm, $c = 30$ mm, and $w = 5$ mm. To establish a baseline for the kinematic analysis, we assume a length ratio of $k = a/(a + b) = 0.5$. Furthermore, to ensure that the diameters on both sides of the robot are identical when the variable-diameter mechanism is fully expanded, d is determined by $d = \sqrt{(a+b)^2 - w^2} = 34.64$ mm.

The kinematic curves of θ_1 and θ_3– θ_5 versus θ_2 are shown in Fig. 2c. The unique solution for all dependent variables verifies that the extracted mechanism has one degree of freedom. Furthermore, since the overall parallel mechanism is composed of six identical chains arranged with central symmetry, the motion of all chains is synchronized. Consequently, the entire parallel mechanism possesses a single degree of freedom.

Figure 2d illustrates the motion sequences of the mechanism. The results indicate that as θ_2 increases, the mechanism exhibits a clear trend of contraction on one side, which aligns well with our design requirements.

Combined with the kinematic analysis, the effect of the length ratio k on R_1 is evaluated to optimize the contraction ratio. The width of the variable-diameter ring is fixed at $e = 5$ mm to ensure ease of fabrication and structural integrity. Thus, the maximum radius of the ring corresponds to $R_{1\max} = a + b + e = 40$ mm. Then, it follows from the geometric relationships that

$$R_1 = a\cos\theta_1 + \sqrt{b^2 - (e + a\sin\theta_1)^2} \tag{6}$$

And the radius contraction ratio η corresponding to R_1 is given by:

$$\eta = \frac{R_{1\,\max} - R_1}{R_{1\,\max}} \times 100\% \tag{7}$$

Furthermore, to intuitively characterize the impact of the drive shaft's rotation on the mechanism's contraction, we define the "initial state" as the configuration where the two links connecting the drive shaft and the variable-diameter ring are collinear. As the drive shaft rotates from this position, inducing contraction, its angle relative to the initial state is denoted as θ. From the geometric constraints, the relationship between the joint angle θ_1 and the input θ is given by:

$$\theta = \pi + \arcsin\left(\frac{w}{a+b}\right) - \theta_1 \tag{8}$$

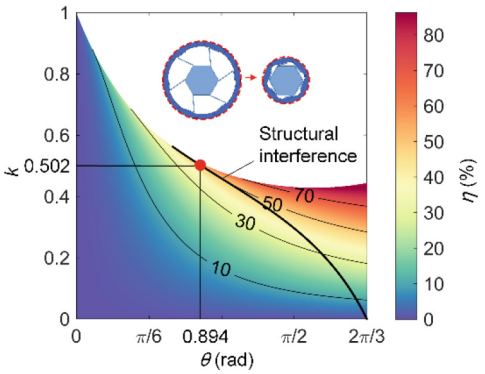

Fig. 3. Geometric parameter analysis for maximum radius contraction ratio.

Using Eqs. (6) and (8), a numerical sweep was performed to evaluate the joint influence of the link length ratio k and the input angle θ on the contraction ratio. As visualized in the contour plot of Fig. 3, the contraction ratio η exhibits a positive correlation with the input angle θ, indicating that a larger rotation drives the mechanism into a more compact configuration. In contrast, the influence of the length ratio k follows a non-monotonic

trend, peaking when the link lengths are nearly symmetrical. However, the reachable workspace is physically bounded by the relative joint angle θ_2. To prevent structural interference between the connecting links, θ_2 is constrained to not exceed $2\pi/3$ rad. This geometric constraint imposes an upper limit on the achievable input angle θ. When this boundary condition is incorporated, the contraction ratio reaches a constrained maximum of 50.54% at $k = 0.502$ and $\theta = 0.894$ rad.

2.3 Analysis of the Obstacle-Avoidance Maneuver

Following the kinematic optimization, we proceed to a dynamic analysis to investigate the robot's behavior during the critical "backward-turn-forward" maneuver triggered by obstacle interaction. The purpose of this analysis is to model the coupling between the internal pendulum's motion, the mechanism's deformation, and the robot's resulting rolling path. By establishing a dynamic model based on the geometric asymmetry induced by contraction, we aim to predict the robot's trajectory theoretically. To establish a tractable dynamic model, we simplify the pendulum section as a lumped mass point and treat the variable-diameter mechanism as a rigid body with equivalent mass and inertia. Furthermore, the analysis assumes motion on a flat horizontal plane with Coulomb friction, while neglecting air resistance.

The motion is governed by the geometric asymmetry between the variable-diameter ring (radius R_1, deformed state) and the constant-radius side of the variable-diameter mechanism (radius R_2). As shown in Fig. 4, this difference creates a tilt angle β and determines the rolling radius R:

$$R = R_1 + \frac{R_2 - R_1}{d_1} l_x \tag{9}$$

where d_1 is the vertical distance between rings, and l_x is the axial distance from the pendulum to the variable-diameter ring.

To predict the trajectory, we analyze three coupled sections: the pendulum, the robot body, and the variable-diameter mechanism. First, applying the Newton-Euler equations to the pendulum (Plane A in Fig. 4) rotating about O_1, the moment balance yields:

$$M_{O1} + F_{IAx} l \cos\gamma + F_{IAy} l \sin\gamma + M_{IA} - m_1 g l \sin\beta \cos\gamma = 0 \tag{10}$$

where M_{O1} is the resistance torque, γ is the pendulum angle ($\gamma = \theta + \varphi + \omega t$), F_{IAx} / F_{IAy} and M_{IA} represent the inertial forces and moment of the pendulum mass center A, respectively. This equation establishes the relationship between the motor drive and the pendulum's motion.

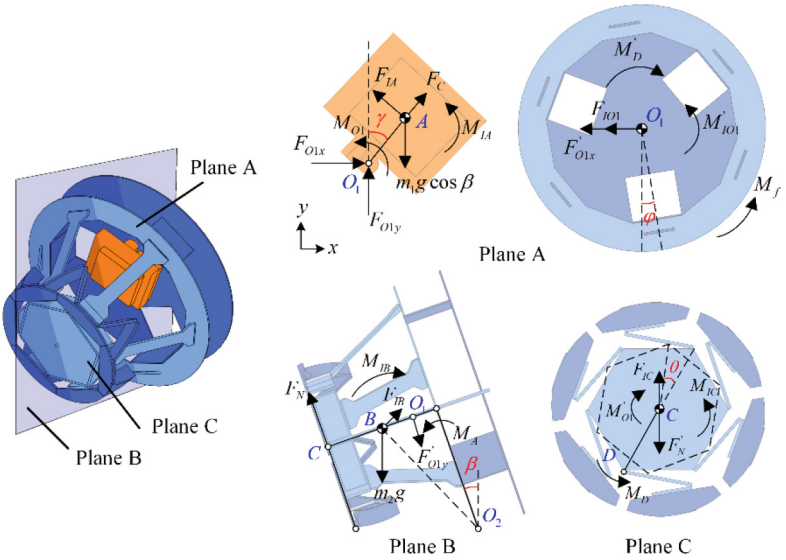

Fig. 4. Dynamics of the obstacle avoidance maneuver analyzed through three distinct planes.

The forces generated by the pendulum are transmitted to the drive shaft, inducing the robot to tilt and turn. Analyzing the cross-section perpendicular to the ground (Plane B in Fig. 4), the equilibrium of moments about the pivot point O_2 is expressed as

$$F_N d_1 + F_{IB}\sqrt{\left(\frac{d_1}{2}\right)^2 + R_2^2} + M_{IB} - m_2 g\left(\frac{d_1}{2}\cos\beta + R_2 \sin\beta\right) - F_{O1y}(d_1 - l_x) - M_A = 0 \tag{11}$$

where F_N is the support force from mechanism deformation, M_A is the driving moment, and F_{IB} / M_{IB} denote the inertial effects of the robot body. This equation captures how the pendulum's position governs the robot's tilt stability.

Finally, considering the rolling motion (Plane C in Fig. 4), the driving torque must overcome the rolling resistance M_f and the total inertia. The overall motion equation is given by:

$$M_D - F_{Ox}R - F_{IO1}R - M_{IO1} - M_f = 0 \tag{12}$$

where M_D denotes the restoring moment generated by the bending of the flexure hinges, and F_{IO1} / M_{IO1} are the inertial terms at the shaft. To accurately quantify the restoring moment M_D, the flexure hinges are modeled as equivalent torsional springs. The equivalent rotational stiffness k_h of a single flexure hinge is derived as $k_h = \frac{Ew_h t_h^3}{12l_h(1-\nu^2)}$, where E and ν denote the Young's modulus and Poisson's ratio of the hinge, respectively. w_h, t_h, and l_h represent the width, thickness, and effective length of the hinge. Consequently, the total restoring moment M_D is the summation of the elastic moments generated by all deforming hinges within the parallel mechanism, expressed as a function of the mechanism's joint angles.

Solving these coupled differential equations (Eqs. (9, 10, 11 and 12)) in MATLAB yields the theoretical trajectory. Figure 5 presents the theoretical trajectory, originating from the position where the robot is blocked. The first segment of the path clearly shows a curved backward motion, verifying that the torque reversal successfully induces a differential diameter, compelling the robot to steer like a rolling cone. Subsequently, the trajectory exhibits a sharp inflection point followed by a straight line along a new vector. This transition signifies the pendulum's return to a forward-biased position, where the mechanism re-expands to a cylinder to resume straight rolling. The resulting V-shaped path mathematically validates that the proposed mechanism can autonomously generate the necessary steering geometry to bypass obstacles.

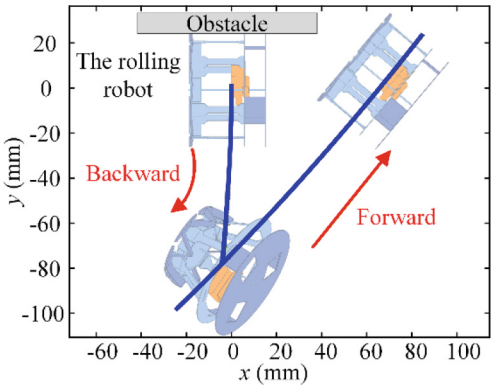

Fig. 5. Theoretical trajectories during the obstacle avoidance maneuver.

3 Fabrication and Experiments

We employed a simplified fabrication approach for the robot, primarily utilizing polyethylene terephthalate (PET) and polyimide (PI) films due to their lightweight properties and ease of processing. Specifically, the variable-diameter mechanism and the variable-diameter ring consist of a three-layer sandwich structure, comprising a 0.1-mm-thick PI film sandwiched between two 0.5-mm-thick PET layers. At the hinge locations, the PET layers are removed, leaving only the PI film to function as flexure hinges. The anti-topple ring is fabricated from single-layer PET sheets. All fabricated components are assembled using adhesive and bolts. A metal shaft with a diameter of 1 mm traverses the center of the variable-diameter mechanism and the anti-topple ring; the shaft is rigidly fixed to the variable-diameter mechanism, whereas it forms a cylindrical joint with the anti-topple ring, allowing for relative rotation and sliding. Components such as the geared motor and lithium battery are mounted onto the metal shaft, serving as a self-driven pendulum. The resulting robot features an overall diameter of 80 mm, a width of 53 mm, and a total weight of 21.3 g. Figure 6a illustrates the fabricated robot.

To validate the robot's capabilities, we first tested its fundamental obstacle avoidance maneuver on a horizontal surface. As shown in the snapshots in Fig. 6c, the robot successfully executed the "backward-turn-forward" action sequence upon interacting with

a block. The trajectory of the robot's geometric center was recorded and superimposed onto the theoretical model (Fig. 6b). The experimental data (red dots) align reasonably well with the theoretical trajectory (blue curve), both exhibiting a characteristic V-shaped path that confirms the deterministic nature of the steering mechanism. Following this verification, a custom maze was constructed to evaluate the robot's performance in a complex environment (Fig. 6d). The maze layout consists of a 300 mm straight section followed by sections of 350 mm, 300 mm, and 150 mm, connected by 90° clockwise turns, and finally a 90° counter-clockwise turn to the exit. The robot initiated locomotion at a forward speed of approximately 5.7 body diameters/s. Upon colliding with the first wall (t = 1.2 s), the obstruction triggered the backward steering maneuver, causing the robot to traverse laterally along the wall at roughly 0.59 body widths/s. By repeating this autonomous strategy, the robot successfully navigated all corners and reached the exit in 21 s.

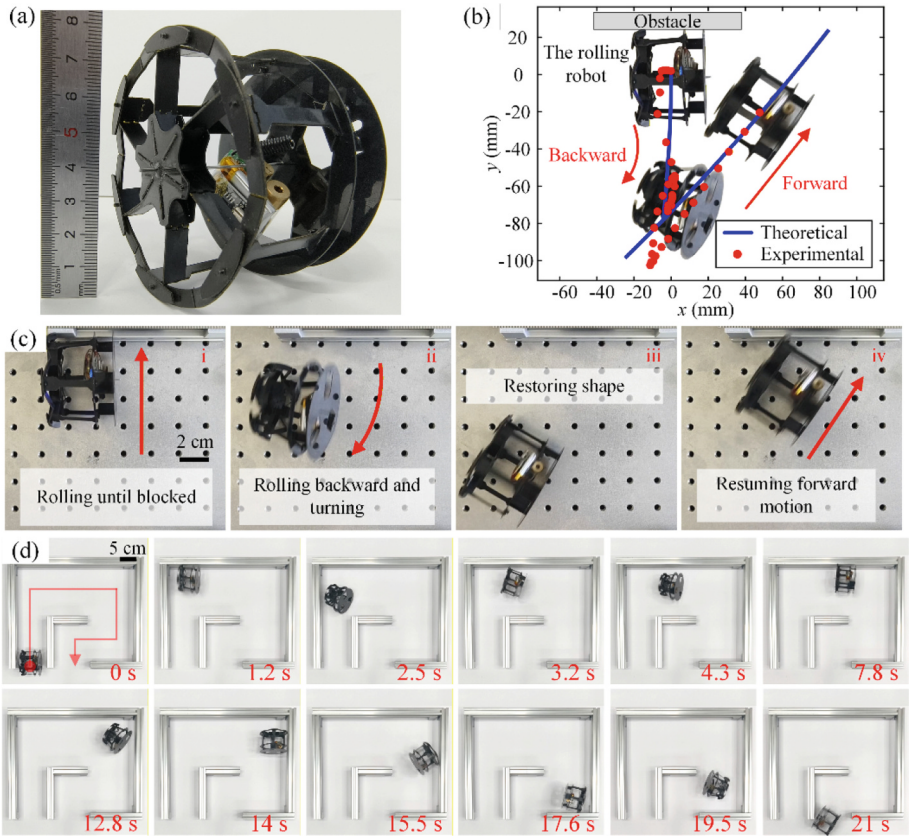

Fig. 6. Experimental validation of the rolling robot. (a) The fabricated prototype. (b) Comparison between the theoretically predicted trajectory and the experimentally recorded position of the robot's center. (c) Snapshots of the obstacle avoidance maneuver: (i) approaching the obstacle; (ii) executing a backward turn; (iii) shape restoration; (iv) resuming forward motion. (d) Time-lapse sequence of the robot autonomously navigating a maze with multiple 90° turns.

4 Conclusion

This work presents a novel approach to autonomous mobility by embedding mechanical intelligence into a rolling robot based on a parallel mechanism. Unlike traditional robots, the robot uses a variable-diameter mechanism coupled with a pendulum drive to respond to obstacles by physically performing a backward-turn-forward maneuver, eliminating the need for electronic sensors. Following kinematic optimization for maximum contraction and dynamic analysis for trajectory prediction, a lightweight (21.3 g) prototype was fabricated using laser-cut PET and polyimide films. Experimental validation in a maze environment showed rapid navigation (21 s) with autonomous 90° cornering. This research underscores the potential of mechanical intelligence, demonstrating that intrinsic structural adaptation can effectively replace complex control loops, offering a robust, energy-efficient solution for unstructured exploration.

However, it is worth noting that the current theoretical trajectory is derived based on simplified equivalent models for the flexure hinges and ideal dynamic assumptions, which have not been rigorously validated in this study. These modeling simplifications inevitably introduce discrepancies between the theoretical predictions and the actual experimental results. Future work will focus on refining the dynamic model to minimize these deviations.

References

1. Armour, R.H., Vincent, J.F.: Rolling in nature and robotics: a review. J. Bionic Eng. **3**(4), 195–208 (2006)
2. Qiang, Z., Zengbo, L., Yao, C.: A back-stepping based trajectory tracking controller for a non-chained nonholonomic spherical robot. Chin. J. Aeronaut. **21**(5), 472–480 (2008)
3. Cai, Y., Zhan, Q., Xi, X.: Path tracking control of a spherical mobile robot. Mech. Mach. Theory. **51**, 58–73 (2012)
4. Belzile, B., St-Onge, D.: ARIES: cylindrical pendulum actuated explorer sphere. IEEE/ASME Trans. Mechatron. **27**(4), 2142–2150 (2022)
5. Diouf, A., Belzile, B., Saad, M., St-Onge, D.: Spherical rolling robots—design, modeling, and control: a systematic literature review. Robot. Auton. Syst. **175**, 104657 (2024)
6. Li, W.B., Zhang, W.M., Zou, H.X., Peng, Z.K., Meng, G.: A fast rolling soft robot driven by dielectric elastomer. IEEE/ASME Trans. Mechatron. **23**(4), 1630–1640 (2018)
7. Masuda, Y., Ishikawa, M.: Development of a deformation-driven rolling robot with a soft outer shell. In: 2017 IEEE International Conference on Advanced Intelligent Mechatronics (AIM), pp. 1651–1656. IEEE (2017)
8. Li, W.B. et al.: Electrically activated soft robots: speed up by rolling. Soft Rob. **8**(5), 611–624 (2021)
9. Chen, H.Y. et al.: RUBIC: an untethered soft robot with discrete path following. Front. Rob. AI. **6**, 52 (2019)
10. Kim, K., Agogino, A.K., Agogino, A.M.: Rolling locomotion of cable-driven soft spherical tensegrity robots. Soft Rob. **7**(3), 346–361 (2020)
11. Morinaga, A., Svinin, M., Yamamoto, M.: A motion planning strategy for a spherical rolling robot driven by two internal rotors. IEEE Trans. Robot. **30**(4), 993–1002 (2014)
12. Haghshenas-Jaryani, M.: Dynamic modeling and trajectory control of a soft cylindrical rolling robot with shape morphing-based steering mechanism. In: 2023 IEEE International Conference on Robotics and Biomimetics (ROBIO), pp. 1–6. IEEE (2023)

13. Yan, W., Li, S., Deguchi, M., Zheng, Z., Rus, D., Mehta, A.: Origami-based integration of robots that sense, decide, and respond. Nat. Commun. **14**(1), 1553 (2023)
14. Comoretto, A., Schomaker, H.A., Overvelde, J.T.: Physical synchronization of soft self-oscillating limbs for fast and autonomous locomotion. Science. **388**(6747), 610–615 (2025)
15. Kamp, L.M., Zanaty, M., Zareei, A., Gorissen, B., Wood, R.J., Bertoldi, K.: Reprogrammable sequencing for physically intelligent underactuated robots. Proc. Natl. Acad. Sci. **122**(38), e2508310122 (2025)
16. Denavit, J., Hartenberg, R.S.: A kinematic notation for lower-pair mechanisms based on matrices. J. Appl. Mech. **77**, 215–221 (1955)

Actuation Along a Single Linear Axis: The Dynamics of the Single-Rail Tripteron

Paolo Boscariol[1(✉)] and Iacopo Tamellin[2]

[1] Dipartimento di Tecnica e Gestione dei sistemi industriali, Università di Padova, Vicenza, Italy
paolo.boscariol@unipd.it

[2] Department of Engineering for Innovation Medicine, University of Verona, Verona, Italy

Abstract. The aim of this work is to develop and test the formulation of an inverse dynamic model for a 3-DOF parallel mechanism that belongs to the family of the Tripteron robots. The variant analyzed here is the so-called 'single-rail' Tripteron, whose main feature is having all actuated prismatic joints with coincident axes. This variant is particularly interesting since it allows to actuate the robot, which can provide translations in the three dimension Cartesian space, by a single Permanent Magnet Linear Synchronous motor with three shuttles. The analytic development of the inverse dynamic model is based on Kane's method, resulting in a simple but very effective implementation. The model simulation, performed using Matlab, has been compared with the results from a multibody simulation performed in Simscape Multibody. The match between them provides a verification of the correctness of the proposed modeling method.

Keywords: single-rail Tripteron · dynamic model · Kane's method · Simscape Multibody · parallel robot

1 Introduction

The ever growing availability of high-speed manipulation devices based on Permanent Magnet Linear Synchronous Motors (PMLSM) is providing to researchers and robotics practitioners new possibilities and new challenges. In particular, multiple PLMSM can be arranged as tracks allowing to move a large number of carts independently from each other. Hence, they are often referred to as independent cart conveyor systems. This capability, together with the notable maximum available speed and efficiency [5,11], explain why they are replacing more traditional devices such as conveyor belts and why they are often used in packaging applications.

Supported by the University of Padova by the SID project "Development of high-speed manipulation devices with collinear actuation".

© The Author(s), under exclusive license to Springer Nature Switzerland AG 2026
A. Chaker et al. (Eds.): EFIMMS 2026, MMS 205, pp. 183–192, 2026.
https://doi.org/10.1007/978-3-032-22270-1_18

Machines based on PMLSMs are designed to provide translational motion, and when they are used to move carts, all the carts are forced to follow the same single-DOF motion. The parallel manipulator analyzed here is meant to overcome this limitation, by allowing to transform three individual parallel displacements into three Cartesian displacements. The manipulator proposed here is one the many variants of the Tripteron robot, whose first appearance was in the work [9]. Then, it has been studied by many eminent scientists (see e.g.[10]) in its popular implementation where three orthogonal axes are employed. Each one actuates the prismatic joint of a PRRR (or CRR) limb. The three limbs are identical. It should be noted that the three translational axes can be rearranged in several ways. In this work, we consider the axes to be coincident. Such architecture, to the best of the Authors' knowledge, appeared first in the RepRap project website [1] under the name of 'single-rail Tripteron' or 'monorail Tripteron'. The kinematics of the single-rail Tripteron has been presented in the Authors work [6]. Besides the already discussed mechanical design related advantages of the Tripteron it should be noted that this manipulator is also kinematically fascinating. Indeed, its Jacobian matrix is constant, therefore its forward and inverse kinematic analysis can be solved through simple linear equations. A prototype of the manipulator is shown in Fig. 1 together with its 3D representation developed in Matlab.

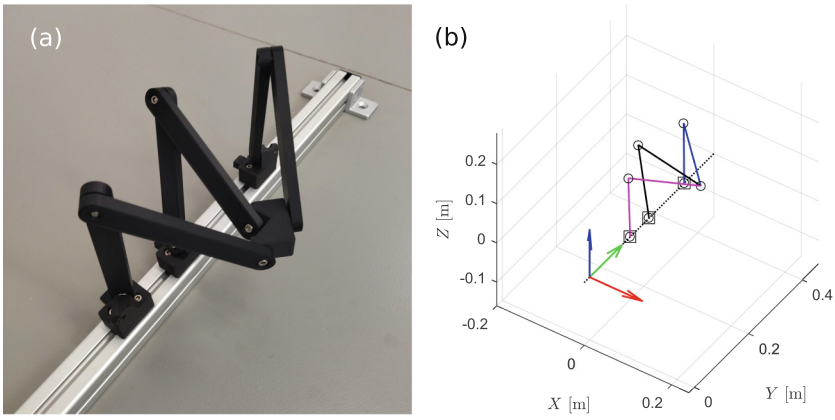

Fig. 1. (a) lab prototype of the monorail Tripteron (b) 3D representation of the monorail Tripteron.

In this work an inverse dynamic model for the single-rail Tripteron is proposed exploiting the Kane's method [7]. The proposed model is verified through the comparison of its results with those obtained through an ad-hoc developed Simscape Multibody simulator. The availability of an analytic formulation of the inverse dynamic problem can be very useful to the development of a fully working prototype of the manipulator, for example to re-evaluate the distribution of masses or the introduction of springs in the light of a proper gravity

balancing [2], or for enhancing the energy efficiency during the execution of a task exploiting natural motion [3] or the optimization of motion profiles [4].

2 Dynamic Model

The dynamics of the manipulator under consideration can be formulated according to the Kane's formula [7] as an equilibrium of generalized forces:

$$F_r^{act} + F_r^{in} = 0 \qquad (r = 1, 2, 3) \tag{1}$$

being F_r^{act} the rth generalized active force and F_r^{in} the rth generalized inertia force. The application of the Kane's equation is systematic and can be effectively applied to the monorail Tripteron, as the dynamic model can be formulated exploiting the results of the speed and acceleration analysis of the manipulator.

2.1 Position, Velocity and Acceleration Kinematics

A complete formulation of the kinematics of the 'single rail' Tripteron is developed here. The position kinematics is just briefly recalled, being it the subject of a previous work by the same Authors [6]. It is assumed that the single actuation line is parallel to the Y direction of a Cartesian space, according to the convention established in Fig. 2. The actuated prismatic joints are located in **A**, **C** and **F**, while the end-effector is positioned in point **E**.

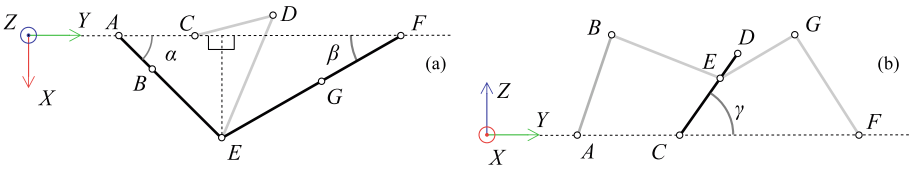

Fig. 2. (a) Projection on the $\{XY\}$ plane, (b) projection on the $\{YZ\}$ plane.

The kinematic constraint set by each of the three RRR limbs of the robot makes the three angles α, β and γ constant, so that the end-effector is characterized by just linear translations. Hence, as proved in [6], the formulation of the direct kinematic problem is simply:

$$\mathbf{E} = \begin{bmatrix} -\dfrac{t\alpha\, t\beta}{t\alpha + t\beta} & 0 & \dfrac{t\alpha\, t\beta}{t\alpha + t\beta} \\ \dfrac{t\alpha}{t\alpha + t\beta} & 0 & \dfrac{t\beta}{t\alpha + t\beta} \\ \dfrac{t\alpha\, t\gamma}{t\alpha + t\beta} & -t\gamma & \dfrac{t\beta\, t\gamma}{t\alpha + t\beta} \end{bmatrix} \mathbf{q} = \mathbf{J_E q} \tag{2}$$

Matrix $\mathbf{J_E}$ is the constant Jacobian matrix that relates the displacement of point **E** to the displacement of the actuated DOFs **q**. A similar notation is

carried throughout the whole manuscript, so that $\mathbf{J_P}$ relates the speed of the generic point $\mathbf{P}$ with the speed of the free coordinate vector $\mathbf{q}$.

Equation (2) serves the purpose of the velocity and acceleration analyses as well, again owing to the constant nature of the Jacobian matrix $\mathbf{J_E}$, so that the relationship between positions is shared by velocities and accelerations as well:

$$\dot{\mathbf{E}} = \mathbf{J_E}\dot{\mathbf{q}}; \qquad \ddot{\mathbf{E}} = \mathbf{J_E}\ddot{\mathbf{q}}; \tag{3}$$

The formulation of the dynamics, however, requires also the investigation of the kinematics of the individual RRR limbs, which is formulated in a straightforward manner when referring to a local reference frame in which the axis of rotation of the three revolute joint are parallel to one of the main axes. According to this, the local reference frame $\{X'Y'Z'\}$ can be centered on point $\mathbf{A}$ and the motion of the first RRR limb is restricted to the $\{Y'Z'\}$ plane (Fig. 3).

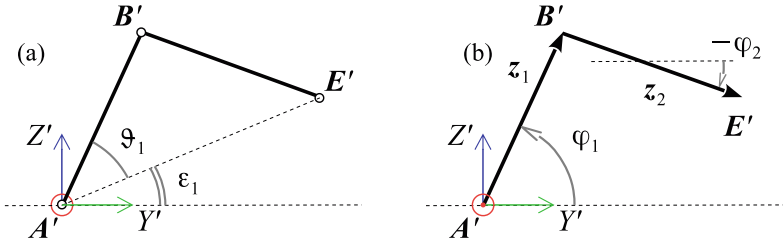

Fig. 3. (a) first RRR limb in the local reference frame $\{X'Y'Z'\}$ (b) position vectors $\mathbf{z}_1$ and $\mathbf{z}_2$ of the first limb.

The angular positions of the two vector $\mathbf{z}_1$ and $\mathbf{z}_2$ that describe the RRR limb are to be evaluated using vector $\mathbf{E}'$, defined by the rotation of vector $\mathbf{E}-\mathbf{A}$ as in:

$$\mathbf{E}' = \mathbf{R}_z\,(\alpha)\,(\mathbf{E}-\mathbf{A}) \tag{4}$$

i.e., by performing the rotation of the reference frame by α about the vertical axis centered in $\mathbf{A}$. In the local reference frame the angular position the two vectors $\mathbf{z}_1$ and $\mathbf{z}_2$ are:

$$\varphi_1 = \varepsilon_1 + \vartheta_1; \qquad \varphi_2 = \varepsilon_1 - \vartheta_2 \tag{5}$$

with:

$$\varepsilon_1 = \operatorname{atan2}\left(z_{\mathbf{E}'}, y_{\mathbf{E}'}\right); \qquad \vartheta_1 = \pm\left(\frac{\|\mathbf{E}-\mathbf{A}\|}{2\,L}\right) \tag{6}$$

which is written assuming identical link lengths L and for both elbow solutions. Point $\mathbf{B}'$ can be evaluated as:

$$\mathbf{B}' = \left[0,\, Lc_1,\, Ls_1\right]^T \tag{7}$$

which is written by using the common short-hand notation $c_1 = \cos\varphi_1$ and $s_1 = \sin\varphi_1$. Finally, the position of $\mathbf{B}$ measured in the global reference frame is found by applying another rotation about Z' as:

$$\mathbf{B} = \mathbf{R}_Z(-\alpha)\,\mathbf{B}' + \mathbf{A} \tag{8}$$

A similar analysis can then be repeated for the other two limbs: the formulation is left to the reader owing to the space constraints of this manuscript.

The velocity analysis of the first RRR limb can be developed starting from the loop closure equation:

$$\dot{\mathbf{z}}_1 + \dot{\mathbf{z}}_2 + \dot{\mathbf{A}}' - \dot{\mathbf{E}}' = 0 \tag{9}$$

which can be used to relate the angular velocities of the two links, $\dot{\varphi}_1$ and $\dot{\varphi}_2$ to the end-effector speed $\dot{\mathbf{E}}'$, the latter being evaluated as the time derivative of eq. (4). The projection of eq. (9) on axes Y' and Z' is:

$$\begin{cases} -Ls_1\dot{\varphi}_1 - Ls_2\dot{\varphi}_2 = \dot{y}_{\mathbf{E}'} \\ Lc_1\dot{\varphi}_2 + Lc_2\dot{\varphi}_2 = \dot{z}_{\mathbf{E}'} \end{cases} \tag{10}$$

The angular velocities are then to be computed as:

$$\begin{bmatrix} \dot{\varphi}_1 \\ \dot{\varphi}_2 \end{bmatrix} = \begin{bmatrix} -Ls_1 & -Ls_2 \\ Lc_1 & Lc_2 \end{bmatrix}^{-1} \begin{bmatrix} \dot{y}_{\mathbf{E}'} \\ \dot{z}_{\mathbf{E}'} \end{bmatrix} \tag{11}$$

The velocity of $\mathbf{B}'$ is therefore:

$$\dot{\mathbf{B}}' = \begin{bmatrix} 0, -Ls_1, Lc_1 \end{bmatrix}^T \dot{\varphi}_1 \tag{12}$$

Finally, the speed of $\mathbf{B}$ in the global reference frame and as a function of just the speed of the free coordinates can be computed as:

$$\dot{\mathbf{B}}(\mathbf{q}, \dot{\mathbf{q}}) = \mathbf{R}_Z(-\alpha) \begin{bmatrix} 0 \\ -Ls_1 \\ Lc_1 \end{bmatrix} \dot{\varphi}_1 + \mathbf{J}_{\mathbf{A}}\dot{\mathbf{q}} \tag{13}$$

$$\text{with: } \dot{\varphi}_1 = \begin{bmatrix} 0\,1\,0 \end{bmatrix} \begin{bmatrix} 1 & 0 & 0 \\ 0 & -Ls_1 & -Ls_2 \\ 0 & Lc_1 & Lc_2 \end{bmatrix}^{-1} \mathbf{R}_Z(\alpha)\,(\mathbf{J}_{\mathbf{E}} - \mathbf{J}_{\mathbf{A}})\,\dot{\mathbf{q}} \tag{14}$$

The acceleration analysis can be performed by the time derivation of eq. (13), which just requires the computation of the angular acceleration $\ddot{\varphi}_1$, as in:

$$\begin{bmatrix} \ddot{\varphi}_1 \\ \ddot{\varphi}_2 \end{bmatrix} = \begin{bmatrix} -Ls_1 & -Ls_2 \\ Lc_1 & Lc_2 \end{bmatrix}^{-1} \begin{bmatrix} \ddot{y}_{\mathbf{E}'} + z_1c_1\dot{\varphi}_1^2 + z_2c_2\dot{\varphi}_2^2 \\ \ddot{z}_{\mathbf{E}'} + z_1s_1\dot{\varphi}_1^2 + z_2s_2\dot{\varphi}_2^2 \end{bmatrix} \tag{15}$$

The expression of $\ddot{\varphi}_1$ from eq. (15), together with:

$$\ddot{\mathbf{E}}' = \mathbf{R}_z(\alpha)\left(\ddot{\mathbf{E}} - \ddot{\mathbf{A}}\right) = \mathbf{R}_z(\alpha)\,(\mathbf{J}_{\mathbf{E}} - \mathbf{J}_{\mathbf{A}})\,\ddot{\mathbf{q}} \tag{16}$$

can be then used in:

$$\ddot{\mathbf{B}}\left(\mathbf{q},\dot{\mathbf{q}},\ddot{\mathbf{q}}\right)=\mathbf{R}_Z\left(-\alpha\right)\ddot{\mathbf{B}}'+\mathbf{J_A}\ddot{\mathbf{q}} \tag{17}$$

with:

$$\ddot{\mathbf{B}}'=\begin{bmatrix}0\\-Ls_1\ddot{\varphi}_1-Lc_1\ddot{\varphi}_1^2\\Lc_1\ddot{\varphi}_1-Ls_1\ddot{\varphi}_1^2\end{bmatrix} \tag{18}$$

Similar calculations, which are omitted again due to the space constraints, apply to the determination of the speed and acceleration of any point relevant to the formulation of the inertial and active forces.

2.2 Forces Acting on Moving Parts and Dynamics Equations Formulation

Having completed the description of the kinematics of the manipulator, the focus can be set on the application of the Kane's equations. Equation (1) can be slightly reformulated to separate the contributions associated with the three generalized actuation forces, $\boldsymbol{\tau}$, from the remaining generalized active forces $\mathbf{F}_{act}$ and the generalized inertial forces $\mathbf{F}_{in}$, as in:

$$\tau_r=-F_r^{act}-F_r^{in}\qquad(r=1,2,3) \tag{19}$$

The concept of generalized forces in the context of Kane's equations rely on the concept of generalized speeds, which are any linear combination of the time derivatives of the generalized coordinates - in this case a linear combination of the speeds of the three actuated prismatic joints. The application of the Kane's method therefore is rooted in the solution of the speed kinematics of the system under consideration, and in particular in the determinations of the Jacobian matrix that relates the speed of any body with non-zero mass and/or subject to an active force to the speed of the vector of free coordinates $\dot{\mathbf{q}}$.

For an easier representation, the mass distribution of the prototype robot under investigation can be condensed in a set of point masses. The point masses represent the mass of the three actuated translating elements, and the mass of the end-effector. All three RRR limbs are represented by lumped masses concentrated at the extremal points of each link: this simplification does minimally affect the accuracy of the model, given that the robot links are very lightweight and the majority of their weight is constituted by the ball bearings that constitute the revolute pairs.

Given this assumption, all inertial and active forces are acting on point masses, hence the computation of the generalized forces requires just the evaluation of the acceleration and speed of the 7 point masses of the robot. In the light of a more uniform representation of the forces to be computed in the formulation of the Kane's equation, all active forces and inertia forces are condensed in a single contribution that relates to each mass. Therefore, for a given point P_i with mass m_i, the ith contribution to eq. (19) can be expressed as:

$$F_r^{P_i}=\mathbf{v}_r^{P_i}\cdot\left(-m_i\mathbf{a}^{P_i}+m_i\mathbf{g}+\mathbf{F}_{P_i}^{ext}\right)\qquad(r=1,2,3) \tag{20}$$

being $\mathbf{v}_r^{P_i}$ the rth partial velocity of point P_i with mass m_i, $\mathbf{a}^{P_i}$ its absolute acceleration, $\mathbf{g} = [0, 0, -9.81]^T$ the gravity acceleration vector and $\mathbf{F}_{P_i}^{ext}$ the external force acting on P_i.

Now, collecting active and inertial forces with actuation forces leads to:

$$\dot{q}_r \tau_r + \mathbf{v}_r^{P_i} \cdot \left(-m_i \mathbf{a}^{P_i} + m_i \mathbf{g} + \mathbf{F}_{P_i}^{ext} \right) = 0 \qquad (r = 1, 2, 3) \tag{21}$$

Equation (21) consists of three scalar equations, that can be however condensed in a single matrix equation by exploiting Jacobian matrix $\mathbf{J}_{P_i}$, which relates the speed $\mathbf{P}_i$ with the speed $\dot{\mathbf{q}}$ as in $\dot{\mathbf{P}}_i = \mathbf{J}_{P_i} \dot{\mathbf{q}}$, so that eq. (21) can be rewritten, after cancelling out $\dot{\mathbf{q}}$, as:

$$\boldsymbol{\tau} = -\sum_{i=1}^{7} \mathbf{J}_{P_i}^T \left(-m_i \mathbf{a}^{P_i} + m_i \mathbf{g} + \mathbf{F}_{P_i}^{ext} \right) \tag{22}$$

with the index i spanning all the point masses concentrated in points from **A** to **F**. The formulation used in (22) is particularly convenient since the Jacobian matrices for some points are of very straightforward computation, such as the Jacobian for point **E**, according to eq. (2). The Jacobians for points **A**, **C** and **F** are even simpler:

$$\mathbf{J_A} = \begin{bmatrix} 0 & 0 & 0 \\ 1 & 0 & 0 \\ 0 & 0 & 0 \end{bmatrix}; \qquad \mathbf{J_C} = \begin{bmatrix} 0 & 0 & 0 \\ 0 & 1 & 0 \\ 0 & 0 & 0 \end{bmatrix}; \qquad \mathbf{J_F} = \begin{bmatrix} 0 & 0 & 0 \\ 0 & 0 & 1 \\ 0 & 0 & 0 \end{bmatrix}; \tag{23}$$

The Jacobians for the intermediate points of the *RRR* limbs, such as those for points **B**, **C** and **G**, can be extracted from equations (13–14) or from the analogous ones developed for the other two limbs.

3 Results

The dynamic model of eq. (22) has been implemented in Matlab to evaluate its accuracy. The dynamics of the monorail Tripteron as per eq. (22) is expressed as an inverse dynamic model, hence it allows to evaluate the actuation forces, in this case the forces to be provided to the three sliding elements, to achieve the desired end-effector motion. The numerical validation of the results is provided by the comparison with the results provided by a multibody simulation performed using Simscape Multibody. Both models include also the effects of friction forces, modeled as a simple combination of Coulomb and viscous friction torques acting on the actuated prismatic joints, but more complex models [8] could be implemented as well without significant alterations to the simulators.

The task planned and executed by the manipulator is a pick & place task, whose path is designed by joining a lifting motion, an horizontal translational motion, and a lowering motion by circular arc segments. The speed profile of the end-effector is set to follow a trapezoidal speed profile. The actual End-Effector path (in this case the path followed by point **E**) is displayed in Fig. 4

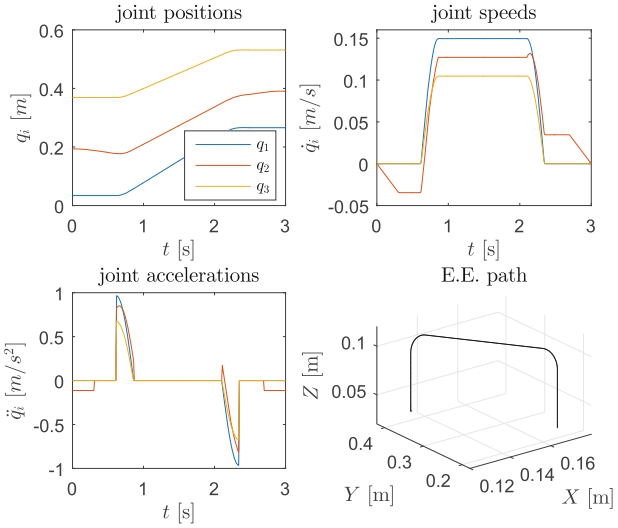

Fig. 4. Execution of the pick&place task: joint positions, speeds, acceleration and end-effector (EE) path.

in the fourth plot. The other three plots in the same figure refer to the motion of the joints in terms of positions, speeds and accelerations. This very same task is then executed by the two inverse dynamic simulators, and the resulting actuation force profiles are displayed in Fig. 5. The three graphs refer to the actuation force for each joint, the solid black line is used for the proposed model and the red dashed line is used to show the results obtained by the Simscape model.

Figure 5 highlights the almost perfect overlapping of the results, which proves the overall accuracy of the proposed formulation. The overlapping is however not perfect, as quantified by the coefficient of correlation R^2 that is reported in Fig. 5. The evaluated R^2 values are, however, so close to the unitary value that the discrepancies between the two models can be regarded as negligible. The small differences between the computed actuation forces are mainly due to the approximation brought by the used of condensed masses to represent the links mass distribution that is present in the proposed model and absent in the Simscape multibody model. The physical parameters used for the simulations are reported in table 1.

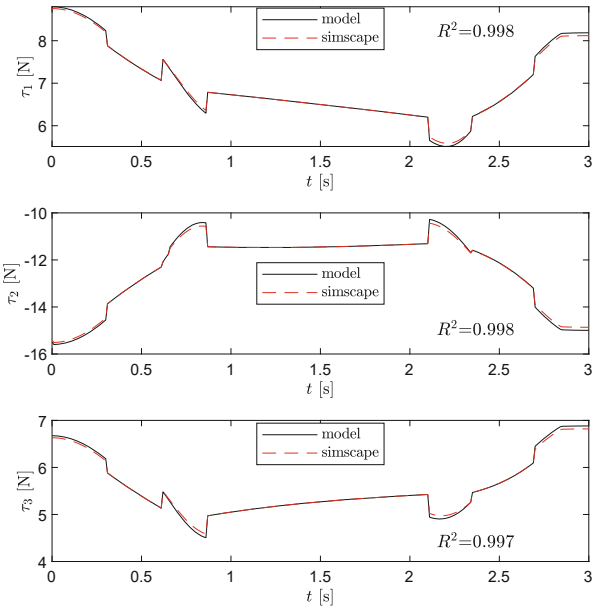

Fig. 5. Execution of the pick&place task: validation of the inverse dynamic model.

Table 1. Inertial, geometrical and friction parameters of the prototype

parameter	symbol	value	unit
cart mass	m_{cart}	0.1	kg
link mass	m_{link}	0.1	kg
end-effector mass	m_{EE}	0.15	kg
link length	L	0.15	m
Coulomb friction force	F_c	0.1	N
viscous friction coefficient	f_v	0.2	Ns/m

4 Conclusion

The dynamics of the monorail implementation of the Tripteron robot has been investigated in this paper. The proposed formulation, developed in the form of an inverse dynamic model, is based on Kane's method. The model has also been implemented in Matlab and has been validated numerically by comparing it to a state-of-the-art multibody simulator. The numerical validation has highlighted the virtually perfect reproduction of the results generated by the Simscape Multibody model when executing a pick & place task. The model can be adapted to several implementation of the Tripteron architectures, and can be used as the basis for tasks such as a mechanical re-design, for gravity balanc-

ing, for trajectory planning and for control design purposes, just to cite a few relevant areas of further developments to the monorail Tripteron manipulator.

References

1. Tripteron - RepRap.org website. https://reprap.org/wiki/Tripteron. Accessed 12 Jan 2024
2. Arakelian, V., Briot, S.: Balancing of Linkages and Robot Manipulators: Advanced Methods with Illustrative Examples, vol. 27. Springer, Cham (2015). https://doi.org/10.1007/978-3-319-12490-2
3. Bettega, J., Richiedei, D., Tamellin, I., Trevisani, A.: Reducing energy consumption and driving torque in an underactuated robotic arm through natural motion. In: Petuya, V., Quaglia, G., Parikyan, T., Carbone, G. (eds.) Proceedings of I4SDG Workshop 2023. I4SDG 2023. Mechanisms and Machine Science, LNCS, vol. 134, pp. 89–96. Springer, Cham (2023). https://doi.org/10.1007/978-3-031-32439-0_11
4. Boscariol, P., Richiedei, D.: Trajectory design for energy savings in redundant robotic cells. Robotics **8**(1), 15 (2019)
5. Boscariol, P., Richiedei, D., Tamellin, I., Trevisani, A.: Machine-learning based energy estimation on a high-speed transportation system. In: Petuya, V., Quaglia, G., Parikyan, T., Carbone, G. (eds.) Proceedings of I4SDG Workshop 2023. I4SDG 2023. Mechanisms and Machine Science, LNCS, vol. 134, pp. 290–297. Springer, Cham (2023). https://doi.org/10.1007/978-3-031-32439-0_33
6. Boscariol, P., Tamellin, I.: Actuation along a single linear axis: the kinematics of the single-rail Tripteron. In: Lovasz, E.C., Ceccarelli, M., Ciupe, V. (eds.) Mechanism Design for Robotics. MEDER 2024. Mechanisms and Machine Science, LNCS, vol 166, pp. 73–81. Springer, Cham (2024). https://doi.org/10.1007/978-3-031-67383-2_8
7. Buffinton, K.W.: Kane's method in robotics. In: Robotics and Automation Handbook, pp. 89–119. CRC Press (2018)
8. Fabris, G., Scalera, L., Gasparetto, A.: Online optimization of minimum-time and minimum-energy trajectories for a 1-DOF belt-driven robotic system. Robotica 1–16 (2025)
9. Hervé, J., Sparacino, F.: Structural synthesis of 'parallel' robots generating spatial translation. In: Fifth International Conference on Advanced Robotics' Robots in Unstructured Environments, pp. 808–813. IEEE (1991)
10. Kong, X., Gosselin, C.M.: Kinematics and singularity analysis of a novel type of 3-CRR 3-DOF translational parallel manipulator. Int. J. Robot. Res. **21**(9), 791–798 (2002)
11. Krämer, C., Kugi, A., Kemmetmüller, W.: Modeling of a permanent magnet linear synchronous motor using magnetic equivalent circuits. Mechatronics **76**, 102558 (2021)

Numerical Analysis of a Variable-Stiffness Actuator Intended for Exoskeleton Use

John E. Bermeo[1,2(✉)], Eduardo Castillo-Castañeda[1], Abdelbadiâ Chaker[2], and Med Amine Laribi[2]

[1] Instituto Politécnico Nacional, Centro de Investigación en Ciencia Aplicada y Tecnología Avanzada Unidad Querétaro, 76090 Querétaro, Mexico
jbermeoc2400@alumno.ipn.mx

[2] Department of GMSC, Pprime Institute CNRS, École Nationale Supérieure de Mécanique et d'Aérotechnique, University of Poitiers, 86000 Poitiers, France
med.amine.laribi@univ-poitiers.fr

Abstract. This work presents a finite element analysis of PneuNet-based soft actuators with different internal chamber geometries, aimed at identifying geometry-dependent trade-offs relevant for variable-stiffness actuator (VSA) applications in wearable exoskeletons. Using a Yeoh hyperelastic material model with explicit inter-chamber contact, quasi-static pressurization is simulated to evaluate bending angle, base reaction torque, stress and strain fields, total strain energy, and contact behavior. The results show that chamber geometry critically governs pressure-to-bending efficiency, load-bearing capability, and deformation energy accumulation. In particular, the rounded-rectangular geometry (P-RR) achieves the largest bending angles and highest strain energy, favoring motion amplification and stiffness modulation potential when coupled with a jamming interface. Stress and contact analyses further emphasize the role of geometric smoothing and wall orientation in controlling stress localization and inter-chamber interaction, which are key factors for durability and effective stiffness modulation. Overall, the results provide geometry-level design guidelines for selecting the soft backbone of jamming-based variable-stiffness actuators under application-specific requirements.

Keywords: Soft robotics · variable-stiffness actuator · finite element · exoskeleton

1 Introduction

Soft pneumatic actuators are widely used in soft robotics and wearable assistive devices due to their ability to produce large deformations while ensuring safe physical human–robot interaction [15]. Among them, PneuNet actuators—comprising arrays of inflatable chambers separated by elastomeric ribs—are a common solution for generating bending motions in finger-like actuators, grippers, and continuum manipulators [4,5,9].

© The Author(s), under exclusive license to Springer Nature Switzerland AG 2026
A. Chaker et al. (Eds.): EFIMMS 2026, MMS 205, pp. 193–206, 2026.
https://doi.org/10.1007/978-3-032-22270-1_19

PneuNets are soft actuators composed of arrays of internal inflatable chambers embedded in an elastomeric structure. When internal air pressure is applied, the chambers expand asymmetrically—typically due to geometry and differential wall thickness—resulting in controlled bending motion. This mechanism allows smooth, continuous deformation without the need for rigid joints, making PneuNets particularly attractive for applications such as soft grippers, robotic fingers, and wearable systems where compliant actuation is essential [5].

Their strongly nonlinear behavior, driven by hyperelasticity, large deformations, and inter-chamber self-contact, has established finite element (FE) modeling as a standard approach for performance prediction and design, with prior studies highlighting the critical role of geometric parameters on bending efficiency and load-bearing capability.

In parallel, variable-stiffness actuators (VSAs) have become increasingly relevant for soft robotics and exoskeletons, as they enable switching between compliant and stiff states according to task demands [2,3,6,12,16]. Jamming-based mechanisms are particularly attractive due to their large stiffness modulation capability, which strongly depends on contact pressure and contact area at interfaces [2,12,16]. This has motivated hybrid architectures combining pneumatic bending modules with jamming layers for wearable applications such as hand exoskeletons and soft gloves [1,7,11,14,17].

In this context, the elbow joint represents a strategic target for actuation, especially in load-lifting tasks where significant torque is required during forearm flexion. Integrating soft actuators into wearable modules positioned along the anterior side of the arm can reduce muscle fatigue by generating assistive torque. This work explores a soft actuator architecture suitable for such applications, with the potential to combine bending motion and variable stiffness to support lifting activities in industrial or rehabilitation settings.

The paper is structured as follows: Sect. 2 describes the concept of the actuator, its geometry, and the material modeling used in finite element analysis. Section 3 presents the numerical results, including deformation behavior, pressure–bending response, stress distribution, strain energy, reaction torque, and inter-chamber contact characteristics. Section 4 discusses the main findings, highlighting the trade-offs between bending efficiency, torque generation, and stiffness modulation. Section 5 concludes the study by summarizing the implications of chamber geometry on the design of variable-stiffness actuators for wearable exoskeletons.

2 Numerical Model

2.1 Actuator Concept

The target application is a wearable exoskeleton in which each joint is actuated by a variable-stiffness element. The actuator consists of a soft PneuNet bending module responsible for motion generation under positive pressure, intended to be coupled in future work with an external jamming layer. In this study, only the

soft backbone is modeled to isolate the effect of chamber geometry on stiffness-relevant variables [2,3,10,11].

2.2 Geometry and Material Model

All actuator variants share identical external dimensions (length L, width W, height H, number of chambers N_c, and wall and rib thicknesses. The chamber length and rib configuration used for volume calculations are depicted in Fig. 1. The only design variable is the internal chamber cross-sectional shape (Fig. 2), which is defined as rectangular (P-R), rounded-rectangular (P-RR), trapezoidal (P-T), or ellipsoidal (P-E). The rounded, trapezoidal, and ellipsoidal geometries are introduced to reduce stress concentrations and promote smoother stress distributions compared to the conventional rectangular design [4,5,9,11]. Chamber dimensions are adjusted so that the internal volume per chamber remains comparable across all configurations, isolating the effect of geometry.

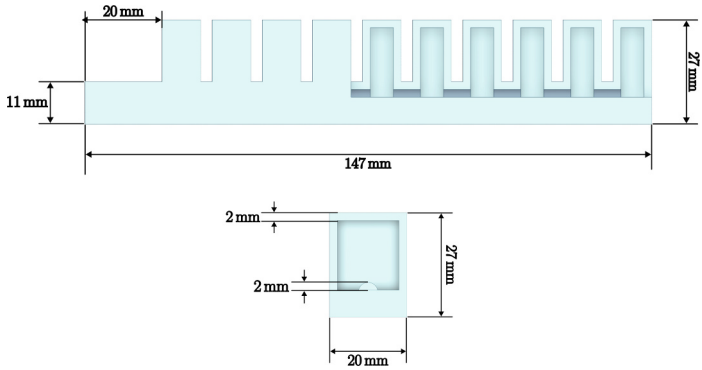

Fig. 1. Longitudinal section of the actuator showing internal chamber dimensions and rib spacing.

The actuator body is assumed to be fabricated from Mold Star 15 Slow, a platinum-cure silicone elastomer widely used in soft robotic systems. The material is modeled as an isotropic, nearly incompressible hyperelastic solid using a second-order Yeoh formulation. The strain energy density function W of the Yeoh model is defined in terms of the first invariant I_1 of the modified right Cauchy–Green deformation tensor as:

$$W = C_{10}(I_1 - 3) + C_{20}(I_1 - 3)^2 \tag{1}$$

Here, the material constants are set to $C_{10} = 0.0667$ MPa and $C_{10} = 7.99 \times 10^{-3}$ MPa used in the Yeoh model were experimentally identified through uniaxial tensile testing of Mold Star 15 Slow, following ASTM D412 guidelines. Curve fitting was performed using a second-order Yeoh formulation, as detailed

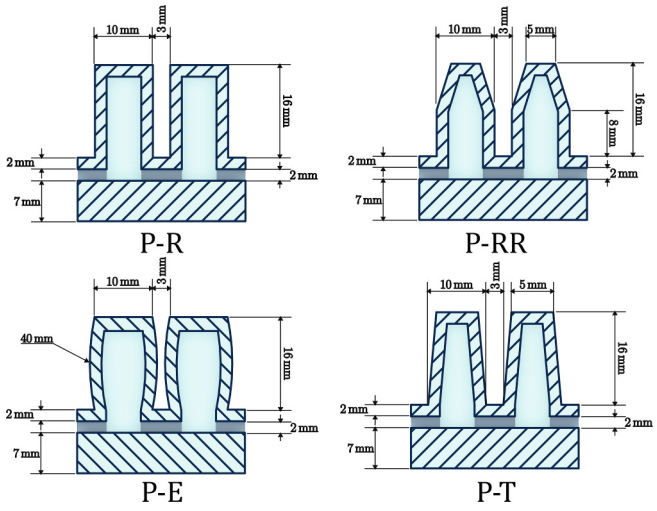

Fig. 2. Cross-sectional CAD of the four chamber geometries, with main dimensions and wall thicknesses.

in [11], while the density is defined as $\rho = 1.18\ \mathrm{g \cdot cm^{-3}}$. To approximate the nearly incompressible behavior of the elastomer, the volumetric penalty parameter was set to $D_1 = 1 \times 10^{-5}\ \mathrm{MPa^{-1}}$, which corresponds to a Poisson's ratio close to 0.499. This avoids the numerical instability associated with perfect incompressibility [10,11,13,15].

2.3 Finite Element Model, Loading, and Output Variables

Finite element simulations were performed in ANSYS Workbench using a static structural solver with large-deformation effects enabled. The actuator was modeled with 3D solid elements, with mesh refinement at chamber walls and ribs. A mesh sensitivity analysis was conducted to ensure numerical accuracy. The actuator was meshed with linear tetrahedral elements using the Patch Conforming algorithm. The final mesh included approximately 234.560 elements and 53,142 nodes. Mesh convergence was confirmed by monitoring bending angle and strain energy across different mesh densities. Results varied less than 5% beyond ∼200.000 elements, indicating sufficient mesh resolution (see Fig. 3).

The base was fully clamped to represent attachment to an exoskeleton frame. The internal pressure range (10–40 kPa) was selected to reflect typical operating conditions for soft pneumatic actuators in wearable applications. These pressure levels are sufficient to induce significant deformation in the Mold Star 15 elastomer, while ensuring user safety and compatibility with portable air sources. Similar ranges have been reported in previous studies on PneuNet actuators [4,5,9,11]. Inter-chamber self-contact was modeled via surface-to-surface interactions with hard normal behavior and tangential friction coefficient

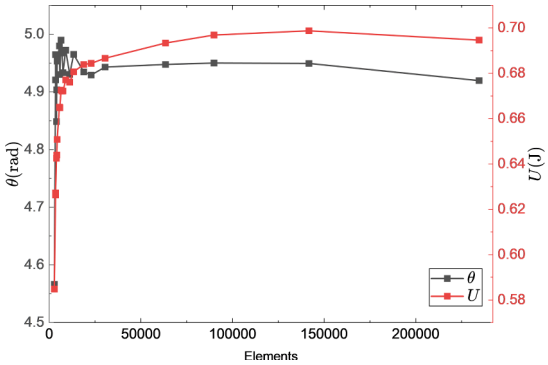

Fig. 3. Mesh convergence results showing the variation in bending angle (black) and strain energy (red) as a function of element count.

$\mu = 1.0$, implemented via the Augmented Lagrange formulation. This high-friction value reflects a conservative scenario to promote strong inter-chamber locking during deformation, which is beneficial for jamming-based stiffness modulation. Small sliding and contact detection were controlled automatically by ANSYS. For each geometry and pressure level, the extracted outputs (Fig. 4) include bending angle and tip displacement, stress and strain fields (von Mises and maximum principal stress), total strain energy, inter-chamber contact area and pressure, and the base reaction moment representing the available actuation torque.

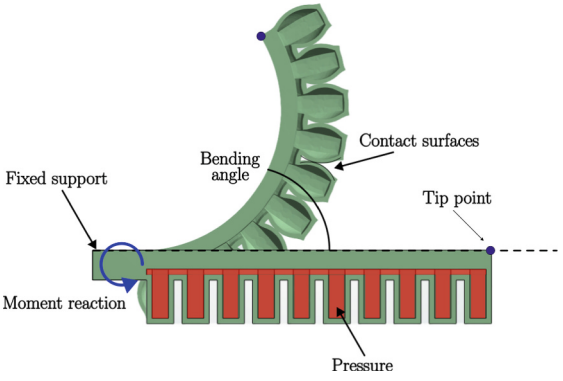

Fig. 4. Post-processing scheme of the PneuNet actuator illustrating the definition of bending angle θ, tip reference point and displacement, base reaction moment M_{base}, applied internal pressure, and inter-chamber contact regions.

3 Numerical Results

This section presents the numerical results obtained from the finite element simulations, focusing on the influence of the internal chamber geometry on the bending response of the actuator. All geometries are evaluated under identical material properties, boundary conditions, and pressure levels in order to isolate geometry-driven effects.

3.1 Qualitative Deformation and Stress Distribution

Fig. 5 shows the deformed configurations and stress contours of four PneuNet chamber geometries under identical pressure, highlighting differences in bending, expansion, and contact. Smoother contours result in more uniform deformation and less stress, while sharper profiles cause localized stress and earlier chamber interaction. This initial visual comparison helps understand the impact of chamber geometry for subsequent analyses.

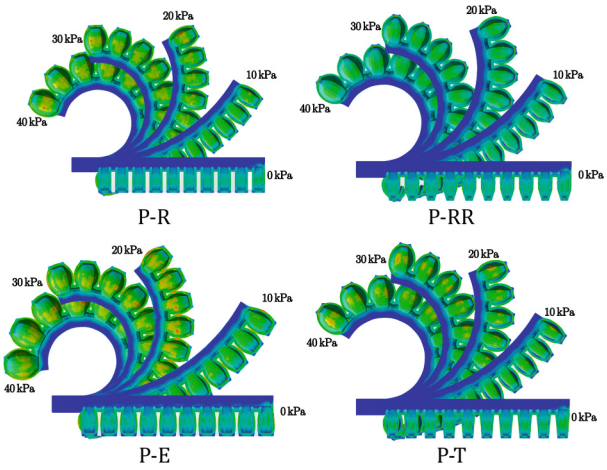

Fig. 5. Deformed configurations and stress contours of the four PneuNet chamber geometries under identical internal pressure, illustrating differences in bending curvature, chamber expansion, and inter-chamber contact behavior.

3.2 Pressure–Bending Angle Response

The quantitative influence of chamber geometry on actuator bending is reported in Fig. 6, which presents the pressure–bending angle relationships $\theta(P)$ for the four designs. For all geometries, the bending angle increases monotonically with the applied pressure and follows a nearly linear trend over the investigated range. A consistent separation between the curves is observed, indicating a strong and

systematic effect of chamber geometry on bending efficiency. P-E achieves the largest bending angles for a given pressure, reaching 4.94 rad at 40 kPa, followed by P-R (4.62 rad). The P-RR and P-T geometries exhibit lower angular responses (4.29 rad and 4.22 rad, respectively). The preserved ordering across all pressure levels suggests that chamber shape directly governs the pressure-to-bending conversion of the actuator, rather than introducing pressure-dependent effects.

These differences indicate that P-E favor larger bending angles for a given input pressure, while P-T and P-RR geometries reduce bending efficiency. The preserved ordering across pressures confirms that chamber shape governs the pressure-to-bending gain of the actuator.

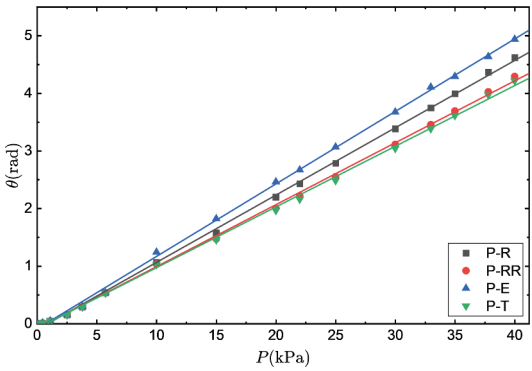

Fig. 6. Pressure–bending angle curves $\theta(p)$ Pressure–bending angle curves.

3.3 Stress and Strain Distribution

Figure 7 shows von Mises stress distributions at maximum pressure for four chamber geometries, using a common color scale for comparison. Clear differences in magnitude and distribution are observed.

The P-R has localized stress at sharp corners, with a peak of 395.4 kPa and a minimum of 1.6 kPa. The P-RR redistributes stress along the curved walls but exhibits the highest peak stress at 456.1 kPa, with a base value of 2.7 kPa. The P-E shows a more uniform stress distribution with reduced concentrations (max 408.0 kPa, min 2.3 kPa), while the P-T presents stress localization near the transition between the wider base and narrower top (max 428.2 kPa, min 2.4 kPa) where wall inclination changes. These results confirm chamber geometry influences stress patterns, consistent with previous findings [4,8–10,13].

Interestingly, P-RR yields the highest peak stress despite its rounded corners, suggesting that curvature alone does not ensure stress relief. In contrast, P-E and P-T distribute stress more uniformly, which may benefit durability and fatigue performance in repeated use scenarios.

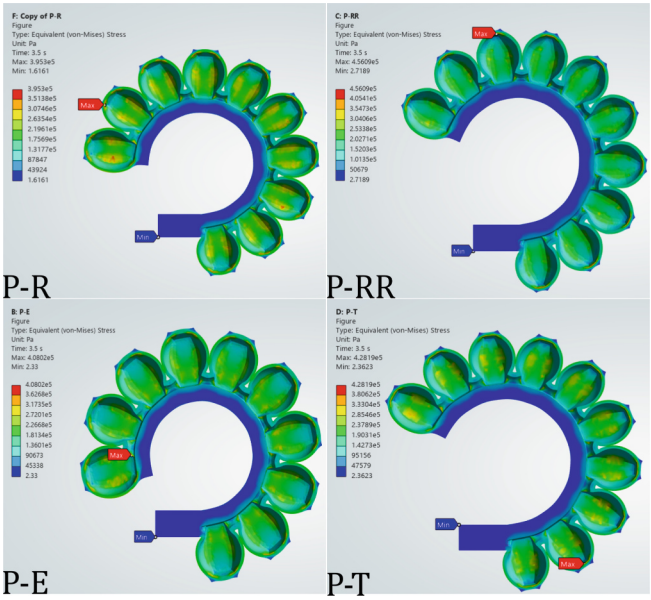

Fig. 7. Von Mises stress fields at maximum internal pressure for the four chamber geometries (P-R, P-RR, P-E, and P-T).

3.4 Strain Energy and Stiffness Potential

Figure 8 shows the evolution of strain energy U as a function of internal pressure for four chamber geometries. Strain energy increases monotonically with pressure across all designs, with a nonlinear rise at higher levels. Notable differences are observed throughout the loading range. In contrast to the bending trends, P-E stores the largest strain energy, reaching 0.656 J at 40 kPa, followed closely by P-R at 0.646 J. P-T displays intermediate values (0.563 J at 40 kPa), while P-RR accumulates the least (0.548 J). The preserved ordering across pressures indicates that chamber geometry affects how deformation energy is stored within the elastomeric structure. Designs that store more strain energy may benefit variable-stiffness strategies, as this energy can be locked upon activation of a jamming interface, leading to higher apparent stiffness [2,3,10,11]. Conversely, geometries with lower strain-energy accumulation may offer energetic advantages for actuation efficiency and pneumatic power usage.

These results highlight a trade-off: P-E and P-T favor energy storage and stiffness modulation, whereas P-RR and P-R prioritize bending and torque output. Depending on the desired actuation mode, designers may choose between energy efficiency or enhanced stiffness-locking potential.

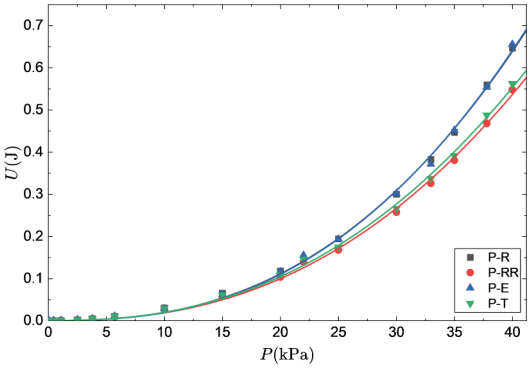

Fig. 8. Total strain energy U as a function of internal pressure p for the four chamber geometries.

3.5 Base Reaction Torque and Exoskeleton Requirements

Figure 9 presents the base reaction moment M_{base} as a function of internal pressure for the four chamber geometries. For all configurations, the base torque increases monotonically with pressure, exhibiting an approximately linear trend over the investigated range. However, significant differences in torque magnitude are observed among the geometries.

The P-R and P-E geometries generate the highest and closely matched torque levels, reaching 51.4 N · mm and 51.0 N · mm at 40 kPa, respectively. The P-T design produces slightly lower base moments (47.2 N·mm at 40 kPa), while P-RR yields the lowest torque across the full pressure range (41.9 N · mm at 40 kPa). This behavior indicates a reduced torque-per-angle efficiency for P-RR, likely associated with its more compliant deformation mode. Taken together, P-R and P-E provide the highest pressure-to-torque efficiency, which is advantageous for joint rotation. In contrast, P-RR offers lower torque output due to its more compliant deformation, which may limit its effectiveness in high-load tasks.

3.6 Inter-chamber Contact and Implications for Jamming

Figure 10 shows that the evolution of inter-chamber contact pressure with increasing internal pressure is strongly geometry dependent, influencing the location, onset, and magnitude of contact. P-E chambers initiate contact at very low pressures (∼3.8 kPa) and maintain a broad, gradual pressure distribution, peaking at 63.3 kPa. P-R initiates contact near 15 kPa, with a relatively uniform

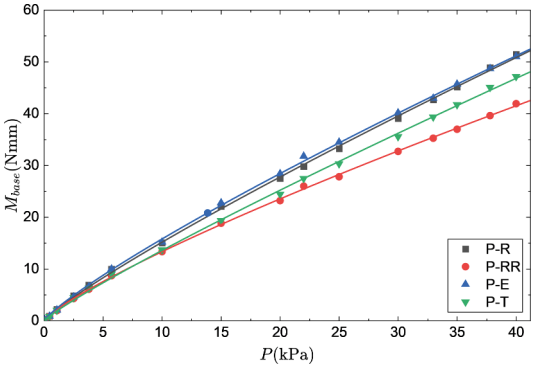

Fig. 9. Base reaction moment M_{base} versus pressure P for the four geometries.

contact band stabilizing around 56.3 kPa. The P-RR design shows a delayed but steep increase, starting near 20 kPa and reaching the highest contact pressure at 88.6 kPa, consistent with concentrated inter-chamber compression. In contrast, P-T exhibits minimal contact below 22 kPa, followed by a moderate rise to only 35.9 kPa, suggesting localized and non-uniform contact patterns.

These distinct contact behaviors are crucial for jamming-based variable-stiffness actuators, where both the contact pressure and area govern frictional locking efficiency. Geometries like P-E and P-RR that promote broad and uniform contact may support more predictable stiffness modulation, while designs like P-T may introduce spatial variation in stiffness due to their asymmetric contact development. The relative timing and magnitude of contact pressure suggest that P-RR and P-E may improve frictional locking behavior during jamming. In contrast, P-T may produce spatially heterogeneous stiffness due to delayed and localized contact development.

3.7 Global Comparison of Geometric Trade-Offs (radar Analysis)

Figure 11 presents a normalized radar chart comparing the performance of the four chamber geometries across five key metrics: bending angle, base reaction moment, strain energy, stress robustness, and inter-chamber contact behavior. Rather than identifying a universally superior design, the plot highlights trade-offs between different performance criteria

To enable fair comparison among metrics with differing units and scales, all values were normalized to the range to a common scale from 0 to 1. For each metric j, the normalized value for geometry i was calculated using the expression:

$$x_{i,j}^{norm} = \frac{x_{i,j} - \min(x_j)}{\max(x_j) - \min(x_j)} \tag{2}$$

where $x_{i,j}$ is the raw performance value, and $\min(x_j)$, $\max(x_j)$ represent the minimum and maximum values of metric j across all geometries. Lower values

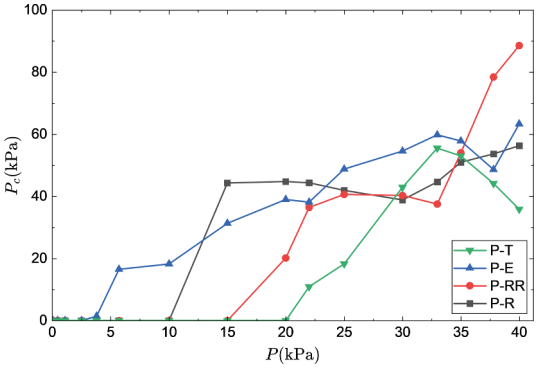

Fig. 10. Inter-chamber contact evolution and contact-pressure distribution as a function of pressure for the four chamber geometries.

indicate better performance (e.g., peak von Mises stress), an inverse normalization was applied prior to scaling. This ensures that higher normalized values always represent better performance. The resulting radar plot provides an intuitive, dimensionless comparison that makes geometry-dependent trade-offs visually interpretable.

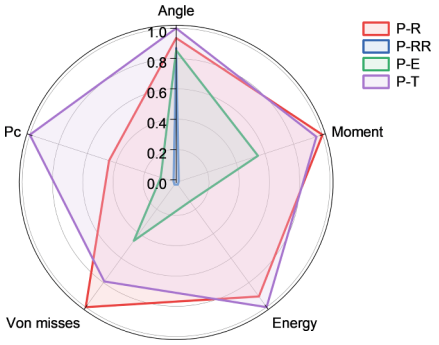

Fig. 11. Radar diagram of normalized performance metrics for the four PneuNet chamber geometries.

Among the designs, P-RR shows outstanding bending efficiency and maximum energy storage, making it well-suited for tasks requiring motion amplification or variable stiffness, though its base torque is lower due to increased compliance. In contrast, P-R achieves the highest base moment, offering greater load-handling capability, but also exhibits higher stress concentrations. P-E delivers the most balanced response, combining moderate bending, torque, smooth stress distribution, and broad inter-chamber contact. The P-T design yields interme-

diate performance across most categories, with no single dominant strength but no major weaknesses either.

Overall, the radar-based analysis confirms that geometry selection involves inherent trade-offs between motion range, load capacity, material stress, and contact behavior. Therefore, the optimal chamber design is application-specific, and should be chosen based on the relative importance of these competing factors in a given variable-stiffness actuator system.

4 Discussion

Internal chamber geometry is a key design variable in PneuNet-based soft actuators, governing bending behavior, torque generation, stress distribution, energy storage, and inter-chamber contact, and inherently defining a multi-objective design space. A central trade-off emerges between bending efficiency and torque output: rounded-rectangular geometry (P-RR) maximizes bending and strain energy, favoring motion amplification and stiffness modulation when coupled with jamming, but delivers limited torque, whereas the rectangular geometry (P-R) achieves the highest torque at the cost of increased stress concentration and reduced bending efficiency. The trapezoidal (P-T) and ellipsoidal (P-E) geometries provide intermediate or more balanced compromises between motion range and load capacity.

Stress and contact analyses further indicate that geometric smoothing and wall orientation strongly influence durability and stiffness modulation. While sharp corners in P-R lead to localized stress peaks, ellipsoidal geometry exhibits the most uniform stress and contact distribution, supporting a more consistent jamming-based stiffness modulation. Overall, no single geometry is universally optimal; chamber selection must balance motion range, torque demand, stress robustness, and stiffness tunability according to application-specific exoskeleton requirements. Future work will integrate explicit jamming models and experimental validation to further assess stiffness modulation and load-bearing performance. Although not modeled here, cyclic loading and fatigue testing will be part of future work to assess durability under repeated actuation.

While this study is computational, future work will include experimental validation of the actuator prototypes under pressurization and stiffness modulation tests, to confirm the simulated performance trends.

5 Conclusions

This work presents a finite element study of PneuNet-based soft actuators, isolating the effect of internal chamber geometry on bending behavior, stress distribution, inter-chamber contact, strain energy storage, and base reaction torque under exoskeleton-relevant conditions.

The results show that the geometry of the chamber defines fundamental trade-offs between motion efficiency, load capacity, and energy accumulation. Rounded-rectangular chambers favor large bending and high strain energy,

enabling greater stiffness modulation potential but limited torque output, while rectangular chambers maximize torque at the expense of higher stress concentration. Trapezoidal and ellipsoidal geometries offer more balanced performance depending on the application priorities.

In general, no single geometry is universally optimal; geometry selection must balance motion range, torque demand, stress robustness, and stiffness tunability according to application-specific requirements. The results provide geometry-level design guidelines for the soft backbone of jamming-based variable-stiffness actuators for wearable exoskeletons, while future work will address explicit jamming modeling, dynamic effects, and experimental validation.

References

1. Bermeo, J.E., Castillo-Castañeda, E., Laribi, M.A.: A soft variable stiffness actuator with a chain mail structure as a particle jamming interface. Actuators **14**(5), 247 (2025). https://doi.org/10.3390/act14050247
2. Caro, F., Carmichael, M.G.: A review of mechanisms to vary the stiffness of laminar jamming structures and their applications in robotics. Actuators **13**(2), 64 (2024). https://doi.org/10.3390/act13020064
3. Fitzgerald, S.G., Delaney, G.W., Howard, D.: A review of jamming actuation in soft robotics. Actuators **9**(4), 104 (2020). https://doi.org/10.3390/act9040104
4. Gariya, N., Kumar, P.: A comparison of plane, slow pneu-net, and fast pneu-net designs of soft pneumatic actuators based on bending behavior. Mater. Today: Proc. **65**, 3799–3805 (2022). https://doi.org/10.1016/j.matpr.2022.06.576
5. Hu, W., Mutlu, R., Li, W., Alici, G.: A structural optimisation method for a soft pneumatic actuator. Robotics **7**(2), 24 (2018). https://doi.org/10.3390/robotics7020024
6. Lalegani Dezaki, M., Bodaghi, M., Serjouei, A., Afazov, S., Zolfagharian, A.: Soft pneumatic actuators with controllable stiffness by bio-inspired lattice chambers and fused deposition modeling 3D printing. Adv. Eng. Mater. **25**(6) (2023). https://doi.org/10.1002/adem.202200797
7. Li, K., Zhang, D., Chu, Y., Zhao, X., Ren, S., Hou, X.: A pneumatic soft exoskeleton system based on segmented composite proprioceptive bending actuators for hand rehabilitation. Biomimetics **9**(10), 638 (2024). https://doi.org/10.3390/biomimetics9100638
8. Liu, Z., Xu, L., Liang, X., Liu, J.: Design of under-actuated soft adhesion actuators for climbing robots. Sensors **22**(15), 5639 (2022). https://doi.org/10.3390/s22155639
9. Moutousi, M., Polygerinos, P.: Omnidirectional soft pneumatic actuators: a design and optimization framework. Front. Robot. AI **11** (2024). https://doi.org/10.3389/frobt.2024.1418484, https://www.frontiersin.org/articles/10.3389/frobt.2024.1418484/full
10. Palacios-Lazo, J.S., Galván-Guerra, R., Niño-Suarez, P.A., Velázquez-Velázquez, J.E.: Stress analysis and operational limits of an SLA-printed soft antagonistic actuator using a yeoh-calibrated finite element model. Actuators **14**(11), 540 (2025). https://doi.org/10.3390/act14110540
11. Sandoval-Castro, X.Y., Cortes-Gonzalez, J.G., Ruiz-Torres, M.F., Castillo-Castaneda, E., Laribi, M.A.: Enhancing dexterity: soft pneumatic actuation utilizing granular jamming for a human finger flexo-extension. Wearable Technol. **6**, e15 (2025). https://doi.org/10.1017/wtc.2024.29

12. Singh, K., Gupta, S.: Discrete stiffness control of soft actuators using laminar jammers made of abrasive materials. Materials Today: Proceedings (2023). https://doi.org/10.1016/j.matpr.2023.02.109
13. Slim, M., Rokbani, N., Terres, M.A., Watelain, E., Ben Khelifa, M.M.: Optimization of soft actuator geometry and material modeling using metaheuristic algorithms. Actuators **14**(11), 520 (2025). https://doi.org/10.3390/act14110520
14. Tang, D., Bi, H., Lv, X., Tang, X.: Design and experiment of soft exoskeleton gloves for hand rehabilitation. Proc. Inst. Mech. Eng. Part C: J. Mech. Eng. Sci. **239**(20), 8373–8388 (2025). https://doi.org/10.1177/09544062251352701
15. Xavier, M.S., Fleming, A.J., Yong, Y.K.: Finite element modeling of soft fluidic actuators: overview and recent developments. Adv. Intell. Syst. **3**(2) (2021). https://doi.org/10.1002/aisy.202000187
16. Yang, Y., Zhang, Y., Kan, Z., Zeng, J., Wang, M.Y.: Hybrid jamming for bioinspired soft robotic fingers. Soft Robotics **7**(3), 292–308 (2020). https://doi.org/10.1089/soro.2019.0093
17. Yap, H.K., Jeong Hoon Lim, Nasrallah, F., Goh, J.C.H., Yeow, R.C.H.: A soft exoskeleton for hand assistive and rehabilitation application using pneumatic actuators with variable stiffness. In: 2015 IEEE International Conference on Robotics and Automation (ICRA), pp. 4967–4972. IEEE (2015). https://doi.org/10.1109/ICRA.2015.7139889

Capability Mapping of a Tendon-Driven Continuum Robot Using Task-Space Sampling and PSO-Based IK

Mohammad Jabari[1,2(✉)], Carmen Visconte[2], Giuseppe Quaglia[2], Abdelbadia Chaker[3], and Med Amine Laribi[3]

[1] Department of Informatics, Bioengineering, Robotics and Systems Engineering (DIBRIS), University di Genova, Genoa, Italy

[2] Department of Mechanical and Aerospace Engineering, Politecnico di Torino, Corso Duca degli Abruzzi 24, 10129 Torino, Italy
{mohammad.jabari,carmen.visconte,giuseppe.quaglia}@polito.it

[3] Department of GMSC, Pprime Institute, University of Poitiers, CNRS, ISEA-ENSMA, UPR, 3346 Poitiers, France
{abdelbadia.chaker,med.amine.laribi}@univ-poitiers.fr

Abstract. Tendon-driven continuum robots (TDCRs) are increasingly used in minimally invasive settings due to their compliance and dexterity, yet quantifying their effective workspace remains challenging because inverse kinematics is computationally expensive and sensitive to pose constraints. This paper presents a voxel-based capability mapping framework for a custom-built, two-segment TDCR with antagonistic tendon actuation and a non-interference routing sleeve around the pulley region. The method samples task-space targets within a discretized volume and enforces a downward tip-orientation constraint to reflect surgical operation requirements. For each sampled target pose, a particle swarm optimization (PSO) based inverse kinematics solver estimates a feasible configuration, and the resulting position and orientation errors are evaluated against predefined tolerances. Capability is then summarized per voxel as a success ratio over multiple randomized trials, producing a compact map that highlights regions with higher reliability for task execution. The resulting capability map provides practical insight for target selection and procedure planning while avoiding repeated online inverse-kinematics calls.

Keywords: Capability Map · Tendon-Driven Continuum Robot · Task-Space Sampling · Particle Swarm Optimization · Inverse Kinematics

1 Introduction

Tendon-driven continuum robots (TDCRs) are promising for minimally invasive procedures because their compliant bodies can navigate constrained anatomical pathways while maintaining a slender form factor [1]. In such scenarios, selecting feasible target regions is not only a matter of geometric reach, but also of whether the robot can realize

© The Author(s), under exclusive license to Springer Nature Switzerland AG 2026
A. Chaker et al. (Eds.): EFIMMS 2026, MMS 205, pp. 207–214, 2026.
https://doi.org/10.1007/978-3-032-22270-1_20

desired task-space poses with sufficient accuracy under task constraints [2]. A practical way to address this need is through capability maps, which discretize task space and assign a capability value to each region, thereby providing an interpretable representation that can be queried during planning and design studies [3, 4]. Classical capability-map literature often relies on dexterity metrics such as manipulability to quantify local kinematic performance [5, 6], and it has been used to support task planning, robot placement, and design decisions by shifting heavy computations to an offline stage [3, 4].

For continuum and surgical continuum robots, reachability and dexterity considerations are central not only for execution but also for early-stage design and evaluation [7]. However, dense task-space characterization can be computationally demanding when it is based on repeated inverse kinematics (IK) computations, and this burden becomes more pronounced for nonlinear and redundant continuum kinematics. Recent work continues to emphasize the relevance of dexterity evaluation for continuum robots and the practical cost of IK-centric assessment [7, 8]. In parallel, learning-based directions have been explored to accelerate capability-map generation by predicting capability values directly in task space, for example using neural fields trained on synthetic data [9]. Despite these advances, for a new custom TDCR design, an explicit offline capability map remains a direct and transparent tool to (i) guide prototype design choices, (ii) define meaningful test regions and target distributions, and (iii) establish quantitative success criteria before extensive experimental campaigns.

This paper reports the first stage of our overall study on a custom two-segment TDCR intended for surgical-like operation. Specifically, we develop a voxel-based capability mapping framework that evaluates task-space feasibility under a downward tip-orientation constraint, reflecting a typical operating convention for tool deployment. The method discretizes a region of interest into voxels, samples multiple targets pose per voxel with downward-oriented directions, and evaluates each target using a particle swarm optimization (PSO) based numerical IK solver. Each trial is labelled as success or failure according to predefined position and orientation error tolerances, and capability is summarized per voxel as a success ratio, yielding a compact 3D voxel capability map. The resulting map highlights task-relevant regions where the robot is expected to achieve reliable pose tracking, and it provides actionable guidance for subsequent prototype testing and experimental validation.

Alongside the mapping pipeline, we describe the key design intent of the two-segment TDCR and the practical tendon-routing considerations that motivated our mechanical layout, including antagonistic tendon actuation and a non-interference routing feature near the pulley region. A full experimental characterization and extended results are planned as follow-up work and will be reported in a journal version.

2 Two-Segment TDCR Modeling and Prototype

The continuum robot considered in this paper is a custom-built, two-segment tendon-driven continuum robot (TDCR) developed as an experimental platform for evaluating task-space capability mapping. The robot comprises two serial continuum sections with identical structural layout, each formed by a compliant backbone and a stack of vertebrae that guide bending over two degrees of freedom while preserving a slender profile. The

overall setup and the fabricated prototype are shown in Fig. 1(a), while the corresponding CAD model is reported in Fig. 1(b). Each segment has an active length of 132.63 mm, resulting in a total continuum length of 265.26 mm (Fig. 1(b)).

Each segment is actuated by four tendons routed through the vertebrae and arranged symmetrically around the backbone (Fig. 1(e)). The tendons are equally spaced at 45° intervals and placed at a different radial distance from the vertebra center. Tendons are arranged in antagonistic pairs to reduce the number of required actuators for steering. Each motor-driven pulley controls an opposing tendon pair, so bidirectional bending can be produced with fewer actuated channels reducing the number from eight to four motors.

Tendon length variations are generated by a pulley-driven four axis actuation unit housed in the motor box (Fig. 1(c)). The prototype employs two dual axis Dynamixel® 2XL430-W250-T servomotors to drive the tendon pairs through the pulleys, where pulley rotation directly defines the commanded tendon displacement. During repeated bidirectional motions, antagonistic tendons can overlap or cross near the pulley exit, which may lead to interference and, in the worst case, tendon locking. To prevent this behavior, a dedicated pulley guard (anti-interference tendon guide) is integrated at the pulley region to keep antagonistic tendon paths separated and ensure consistent routing during cyclic actuation (Fig. 1(c)).

The compliant joint design enabling smooth inter-vertebral bending is highlighted in Fig. 1(d). The continuum body is fabricated as a monolithic structure using PA12 Nylon® via selective laser sintering (SLS), providing a lightweight and robust platform for the subsequent capability mapping study.

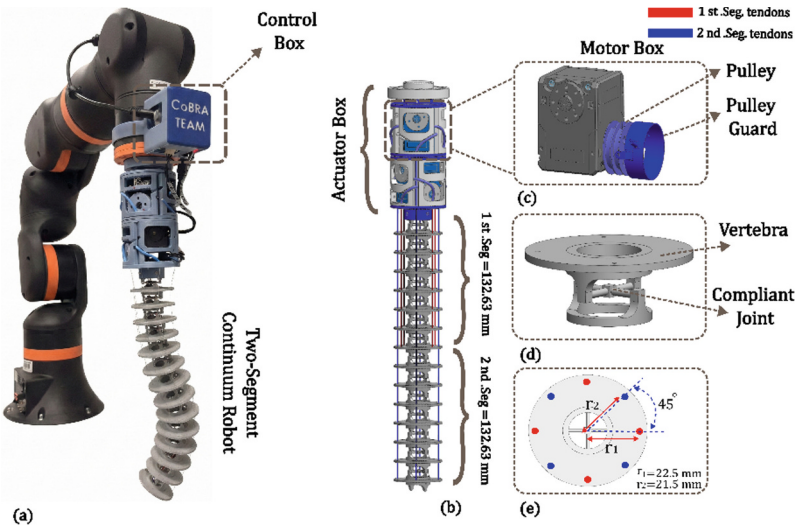

Fig. 1. Two-segment TDCR prototype and main components. (a) Experimental setup. (b) CAD model. (c) Actuation module with pulley and pulley guard. (d) Compliant joint. (e) Eight-tendon layout (45° spacing) for both segments.

2.1 Kinematic Modelling (Disk-Wise Discretization)

To generate the capability map, the backbone is represented as a chain of N vertebrae aligned with the robot. This is more flexible than the standard PCC model that represents each segment with a single constant-curvature arc. Here, the bending direction and the axial twist are allowed to change along the robot length, which gives a closer approximation of the actual shape while keeping the computation manageable.

Each vertebra i is described by three parameters: curvature k_i, bending-plane angle φ_i, and twist τ_i over its length l_i leading to a homogeneous transform $T_i(k_i, \varphi_i, \tau_i)$. The overall tip pose is computed by chaining the transformations of all vertebrae, as defined in Eq. (1).

$$\boldsymbol{T_{tip}} = \boldsymbol{T_0} \prod_{i=1}^{N} \boldsymbol{T_i}(k_i, \varphi_i, \tau_i) \tag{1}$$

where T_0 is the base pose. This formulation directly associates the robot shape with vertebrae-level parameters and captures variations along the backbone more effectively than single-arc PCC models [1, 2].

3 Capability Map Generation Method

The task-space workspace of the two-segment TDCR is defined here as the set of end-effector tip positions that can be produced by feasible robot configurations under the adopted kinematic model and actuation limits. To obtain a practical representation of this workspace, a finite set of robot configurations is sampled and mapped to the corresponding tip positions through forward kinematics. Figure 2(a) visualizes these reachable tip positions as a point cloud (orange), together with a semi-transparent volume (blue) that indicates the workspace boundary inferred from the samples. This visualization is intended to provide an indicative workspace boundary and guide the selection of the distal region used for capability mapping, rather than claiming an exhaustive workspace reconstruction.

3.1 Task-Space Voxelization

Capability mapping is performed over a bounded region of interest (ROI) located in the distal portion of the sampled workspace, where the tool tip is expected to operate, Fig. 2(b). The ROI is discretized into a 3D voxel grid, in which each voxel represents a small cubic region in task space and is identified by its center point. In this implementation, the grid is defined such that a total of 180 voxels are evaluated inside the ROI, with the voxel edge length determined by the chosen grid spacing. This discretization converts the continuous task space into a finite set of query locations that can be evaluated offline and later accessed efficiently. Figure 2(c) shows a zoomed view of the voxel lattice; for visualization clarity, voxels are depicted as touching spheres while preserving the underlying grid spacing.

3.2 Downward-Hemisphere Orientation Sampling

To reflect the intended tool-tip convention, orientation sampling is restricted to the downward hemisphere. For each voxel center, a set of target tool-axis directions is generated by sampling unit vectors whose global z-component is negative, as illustrated in Fig. 2(d). Each sampled direction is converted into a right-handed rotation matrix such that the tool axis aligns with the sampled downward direction, ensuring that all evaluated targets satisfy the imposed z-down constraint. To balance angular coverage and computational cost, 300 downward directions are evaluated per voxel, yielding a dense set of orientation queries within each voxel for the subsequent feasibility assessment.

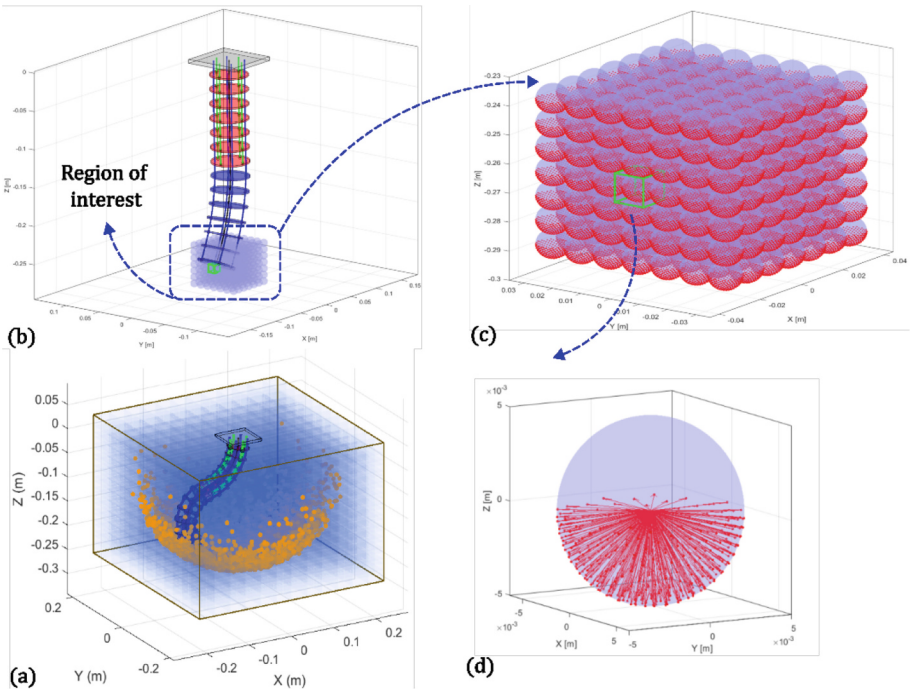

Fig. 2. Capability-map sampling pipeline. (a) Sampled reachable tip positions and an approximate workspace envelope. (b) Distal ROI. (c) Distal ROI discretized into a voxel grid (shown as touching spheres). (d) Downward-hemisphere orientation sampling enforcing the z-down constraint.

3.3 Orientation Sampling PSO-Based Inverse Kinematics Evaluation

The capability map is constructed by discretizing a bounded portion of the robot task space and evaluating, for each discrete region, how reliably the robot can achieve target poses that satisfy a downward tip-direction convention. First, a task-space region of interest (ROI) is selected in the distal workspace and discretized into a 3D voxel grid. Each voxel is represented by its center position $p_v \in \mathbb{R}^3$, which serves as the target

position for all trials associated with that voxel. This converts the continuous workspace into a finite set of task-space locations that can be evaluated offline and later queried efficiently.

For each voxel center p_v, orientations are sampled only from the downward hemisphere to enforce the z-down convention. Specifically, a set of unit direction vectors with negative global z-component is generated and converted into right-handed rotation matrices $R_{v,j} \in SO(3)$ by constructing an orthonormal frame whose tool axis aligns with the sampled direction. Each trial thus defines a target pose $(p_v, R_{v,j})$ at the voxel center with a downward-pointing tool axis. The IK feasibility of each target pose is then assessed using particle swarm optimization (PSO). PSO is adopted to handle the nonconvexity and redundancy of the tendon-driven continuum robot without requiring gradient information. The decision variables parameterize the robot configuration using a disk-wise representation, where curvature magnitude, bending-plane angle, and axial twist are allowed to vary along the backbone.

For each target $(p_v, R_{v,j})$, PSO searches for a configuration x that minimizes a pose-matching objective combining position and orientation errors. This optimization problem is defined in Eq. (2).

$$x^* = \underset{x}{\operatorname{argmin}} \big(p(x) - p_{v2} + \lambda d_R\big(R(x), R_{v,j}\big)\big) \quad s.t. x \in \big[\underline{x}, \overline{x}\big] \tag{2}$$

where $p(x)$ and $R(x)$ are the tip position and orientation returned by forward kinematics, $d_R(.,.)$ denotes an angular distance between rotations, λ is an orientation weight, and $\big[\underline{x}, \overline{x}\big]$ are element-wise bounds on the disk-wise parameters. After convergence, the candidate solution is validated via forward kinematics and labeled as successful if both the position and orientation errors are below predefined tolerances; otherwise, it is labeled as failure. The capability value assigned to voxel v is then defined in Eq. (3).

$$C_v(\%) = 100 \times \frac{n_{success(v)}}{n_{trails\ (v)}} \tag{3}$$

yielding an interpretable scalar score in [0, 100] that quantifies how reliably task-consistent poses can be achieved within that region.

4 Results

Figure 3 summarizes the capability-map results obtained within the selected region of interest (ROI). For each voxel center, a set of downward-oriented target poses was evaluated by the PSO-based inverse kinematics routine. Each trial was classified as successful if the final forward-kinematics pose satisfied both the position and orientation tolerances. The voxel capability score was then computed as the success ratio, i.e., the fraction of successful trials over the total number of evaluated targets in that voxel.

The 3D voxel rendering in Fig. 3(a) reveals a consistent spatial pattern in the ROI. Voxels with higher success ratios are mainly concentrated in the inner portion of the ROI, whereas the capability decreases toward the outer boundaries. This trend indicates

that simultaneously satisfying the target position and the enforced z-down orientation becomes more demanding as the voxel centers move away from the central region. To provide a clearer interpretation of this distribution, Fig. 3(b) reports 2D cross-sections of the capability map at three representative z-levels. These slices show that the success ratio is not uniform across the ROI and varies both laterally (x–y) and along depth (z). In particular, the middle layer exhibits a broader area of moderate-to-high capability compared to the deeper layer, where the success ratio becomes more localized.

Overall, the proposed voxel capability map offers a compact and interpretable representation of task-consistent feasibility in 3D. Once computed offline, the map can be queried to identify regions where downward-oriented poses are achieved reliably, reducing the need for repeated online IK attempts during planning.

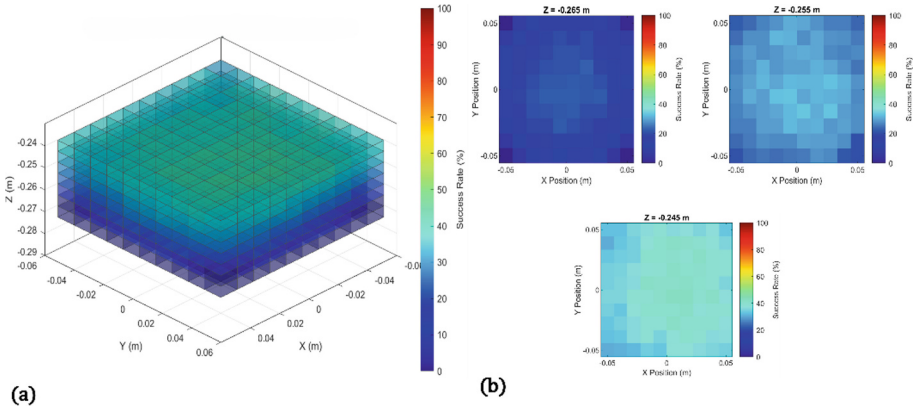

Fig. 3. Capability-map results in the ROI: **(a)** 3D voxel visualization of success rate (%) across the ROI. **(b)** 2D x–y cross-sections of voxel success rate at three z-levels.

5 Conclusion

This paper presented an offline capability mapping pipeline for a custom two-segment tendon-driven continuum robot, focusing on task-consistent feasibility rather than position-only reachability. By discretizing a distal region of interest into voxels and evaluating downward-oriented target poses through a PSO-based inverse kinematics solver, we generated a 3D voxel capability map where each voxel is assigned an interpretable success ratio. The resulting map highlights regions where the robot can reliably achieve downward-oriented poses within the selected tolerances and regions where feasibility degrades as kinematic demands increase, providing a practical tool for target selection without repeated online IK calls.

For future work, we will test the robot in the regions that the capability map predicts as feasible, confirming whether the prototype can consistently achieve the corresponding poses during real operation. This step will help validate the offline analysis and refine the limits of the robot's effective workspace.

In addition, we plan to use the generated dataset to train a deep learning model that can provide fast inverse-kinematics estimates. The aim is to create a lightweight predictor that supports real-time use while keeping the clarity and interpretability of the voxel-based capability map.

Acknowledgments. This publication is part of the project PNRR-NGEU which has received funding from the MUR – DM 351/2022.

References

1. Jabari, M., Visconte, C., Quaglia, G., Laribi, M.A.: Feasible static workspace optimization of tendon driven continuum robot based on Euclidean norm. In: Laribi, M.A., Carbone, G., Pisla, D., Zeghloul, S. (eds.) New Trends in Medical and Service Robotics. MESROB 2025. Mechanisms and Machine Science, vol. 186. Springer, Cham (2025). https://doi.org/10.1007/978-3-031-96081-9_49
2. Jabari, M., Botta, A., Tagliavini, L., Visconte, C., Quaglia, G.: A safe, high-precision reinforcement learning-based optimal control of surgical continuum robots: a monotone tube boundary approach with prescribed-time control capability. Robot. Auton. Syst. **190**, 104992 (2025). https://doi.org/10.1016/j.robot.2025.104992
3. Zacharias, F., Borst, C., Hirzinger, G.: Capturing robot workspace structure: representing robot capabilities. In: Proceeding of the IEEE/RSJ IROS, pp. 3229–3236 (2007)
4. Porges, O., Stouraitis, T., Borst, C., Roa, M.A.: Reachability and capability analysis for manipulation tasks. In: ROBOT2013, AISC, vol. 253, pp. 703–718. Springer (2014)
5. Yoshikawa, T.: Manipulability and redundancy control of robotic mechanisms. In: Proceedings of the IEEE ICRA, pp. 1004–1009 (1985)
6. Vahrenkamp, N., Asfour, T., Metta, G., Sandini, G., Dillmann, R.: Manipulability analysis. In: Proceedings of the IEEE-RAS Humanoids, pp. 568–573 (2012)
7. Leibrandt, K., da Cruz, L., Bergeles, C.: Designing robots for reachability and dexterity: continuum surgical robots as a pretext application. IEEE Trans. Robotics. **39**(4), 2989–3007 (2023)
8. Du, F., et al.: Continuum robots: developing dexterity evaluation algorithm based on inverse kinematics (DEAIK). Measurement. **223**, 113580 (2023)
9. Chen, X., Külz, J., Althoff, M.: Generating Robot Capability Maps with Neural Fields. (2024)

About the Design and Development of the Omnidirectional Electric Powered Wheelchair MoviWE.Q

Luigi Tagliavini(✉), Andrea Botta, Giovanni Colucci, Lorenzo Baglieri, Simone Duretto, Francesco Amodio, Lorenzo Toccaceli, and Giuseppe Quaglia

DIMEAS: Department of Mechanical and Aerospace Engineering, Politecnico di Torino, Turin, Italy
luigi.tagliavini@polito.it

Abstract. This paper presents the design and development of the electric-powered wheelchair (EPW) MoviWE.Q. The main characteristic of this EPW is its ability to perform omnidirectional motions thanks to its locomotion system based on two swerve-drive units. MoviWE.Q is designed to be driven by the user with a three-axis joystick and by caregivers using a custom-made force-sensitive interface named SensHB.Q, mounted on the backrest. This paper presents the entire mechatronic system, from the locomotion system kinematics to the developed prototype and some experimental tests with the force-sensitive drive interface SensHB.Q.

Keywords: electric powered wheelchair · omnidirectional mobility · swerve-drive locomotion · force-sensitive drive interface

1 Introduction

Population aging has become a major global issue, driven by low birth rates and increasing life expectancy [8,16]. By 2050, the number of people over 65 is expected to double, reaching about 16% of the global population. International organizations including the United Nations, World Health Organization (WHO), and the European Commission identify this trend as one of the most significant social transformations of the twenty-first century, affecting sectors such as family structures, healthcare, housing, and transportation [12]. On this context, the WHO estimates that around 80 million people are likely to require a wheelchair [14], yet accessibility remains limited: only about 70% of transit stations are wheelchair-accessible worldwide and 33% of public toilets are not accessible in developed countries [1]. In Italy, ISTAT (Italian Institute of Statistics) data show that many older adults experience severe mobility limitations, with 2.833 million people over 65 struggling to walk or climb stairs without assistance [5]. Accessibility issues also affect younger populations, as only 32% of Italian schools are fully accessible [4].

© The Author(s), under exclusive license to Springer Nature Switzerland AG 2026
A. Chaker et al. (Eds.): EFIMMS 2026, MMS 205, pp. 215–224, 2026.
https://doi.org/10.1007/978-3-032-22270-1_21

Electric-powered wheelchairs (EPWs) help users with mobility limitations but tend to be bulky, reducing maneuverability in tight indoor environments. As differential-drive platforms, they cannot move laterally, often requiring multiple maneuvers in narrow spaces (Fig. 1).

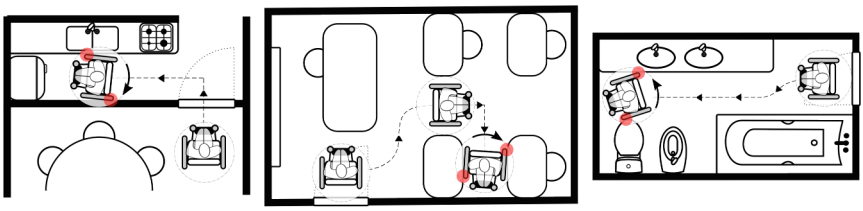

(**a**) (**b**) (**c**)

Fig. 1. Critical situations of conventional wheelchair navigation in indoor environments: (a) moving in narrow corridors, (b) approach maneuver to school desks, (c) approach maneuver to sanitary facilities.

To overcome these constraints, omnidirectional wheelchairs have been proposed. Designs using mecanum or omni wheels [7,11] are mechanically simple but limited by small passive rollers that reduce load capacity and comfort. Spherical-wheel systems [20] improve comfort and ground adaptation but are mechanically complex and difficult to control.

Many studies have examined user control interfaces for EPWs [3], including joysticks, sip-and-puff devices [13], tongue-operated systems [6], head movements [2], and eye-tracking approaches [15]. Caregiver-oriented interfaces have received less attention. Existing solutions are either position-based or force-based, such as the ASBGo handlebar [9], the approach by Trujillo et al. [19], and SensHB.Q [18]. Position-based systems are inexpensive but not always intuitive, especially for omnidirectional motion, while force-based interfaces are more natural but often limited to two degrees of freedom [10] or rely on costly six-axis sensors [19].

In this context, the present paper introduces the electric-powered wheelchair MoviWE.Q, extending the conceptual design previously presented in [17] and providing the prototype description and its experimental validation.

2 Locomotion System Kinematics

To overcome the limitations of both differential-drive locomotion and systems that rely on specially engineered wheels (e.g., mecanum, omni, or spherical wheels), the authors developed the omnidirectional swerve-drive electric-powered wheelchair MoviWE.Q. As illustrated in Fig. 2 (a), the system consists of a seat with removable armrests, a footrest mechanism, an omnidirectional mobile base

equipped with swerve-drive locomotion, and the control interfaces used to operate the device. Two primary control interfaces are provided: a 3-axis joystick for the seated user and the force-sensitive SensHB.Q interface, designed to allow a caregiver to control the EPW.

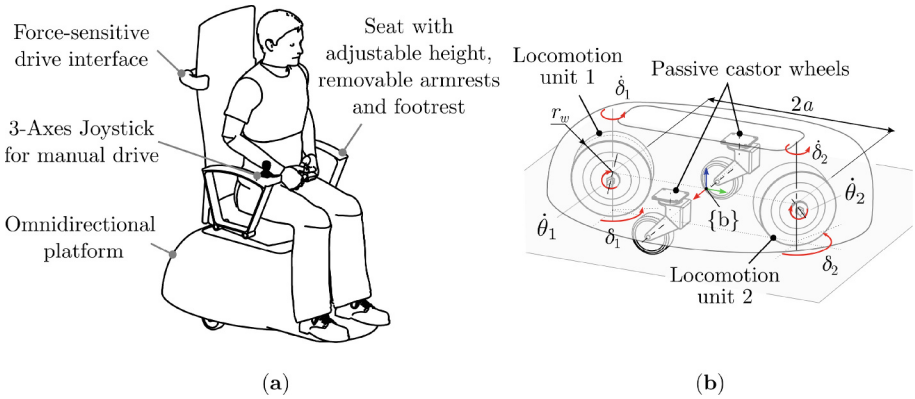

Fig. 2. (a) MoviWE.Q concept, (b) locomotion system functional scheme.

To enable omnidirectional movement, the wheelchair's drive system is composed of two locomotion units. Each unit features a motorized wheel mounted on a steering mechanism with a vertical axis. According to the nomenclature shown in Fig. 2(b), each locomotion unit provides two degrees of freedom: the wheel's rotation θ_i about its own axis and its rotation δ_i about the vertical steering axis. By regulating these four actuated degrees of freedom, namely the two steering angles δ_1 and δ_2 and the two wheel angular velocities $\dot{\theta}_1$ and $\dot{\theta}_2$, the system can control both the linear and angular velocities of the wheelchair, thereby achieving omnidirectional planar motion. To ensure stability without relying on complex self-balancing mechanisms, two passive caster wheels with an integrated suspension system are mounted on the non-axially-symmetric footprint of MoviWE.Q. A non-axially-symmetric footprint is preferred over a symmetric one when navigating cluttered or narrow environments, as its reduced dimension can be oriented to maneuver through confined spaces.

With this locomotion architecture and under the assumptions of planar motion and pure rolling, Eq. (1) defines the forward kinematic model that maps the four actuated variables to the 2D velocity twist of the wheelchair. Conversely, Eq. (2) provides the corresponding inverse kinematic transformation.

$$\begin{bmatrix} {}^b\dot{\gamma}_b \\ {}^b\dot{x}_b \\ {}^b\dot{y}_b \end{bmatrix} = \frac{r_w}{2} \begin{bmatrix} (\dot{\theta}_1 c_{\delta_1} - \dot{\theta}_2 c_{\delta_2})/a \\ \dot{\theta}_1 c_{\delta_1} + \dot{\theta}_2 c_{\delta_2} \\ \dot{\theta}_2 s_{\delta_1} + \dot{\theta}_2 s_{\delta_2} \end{bmatrix} \tag{1}$$

$$\begin{bmatrix}\dot{\theta}_1\\ \dot{\theta}_2\end{bmatrix} = \frac{1}{r_w}\begin{bmatrix}\pm\sqrt{\left({}^b\dot{x}_b + a\,{}^b\dot{\gamma}_b\right)^2 + \left({}^b\dot{y}_b\right)^2}\\ \pm\sqrt{\left({}^b\dot{x}_b - a\,{}^b\dot{\gamma}_b\right)^2 + \left({}^b\dot{y}_b\right)^2}\end{bmatrix};$$
$$\begin{bmatrix}\delta_1\\ \delta_2\end{bmatrix} = \begin{bmatrix}\text{atan2}\left(\frac{{}^b\dot{y}_b}{r_w\dot{\theta}_1}, \frac{{}^b\dot{x}_b + a\,{}^b\dot{\gamma}_b}{r_w\dot{\theta}_1}\right)\\ \text{atan2}\left(\frac{{}^b\dot{y}_b}{r_w\dot{\theta}_2}, \frac{{}^b\dot{x}_b - a\,{}^b\dot{\gamma}_b}{r_w\dot{\theta}_2}\right)\end{bmatrix} \tag{2}$$

where $c_\beta = \cos\beta$, $s_\beta = \sin\beta$, ${}^b\dot{x}_b$, ${}^b\dot{y}_b$ are the wheelchair linear velocity components expressed with respect to the local frame $\{b\}$ and ${}^b\dot{\gamma}_b$ is the wheelchair angular velocity (yaw angular velocity). The inverse kinematic problem yields two possible values for each of $\dot{\theta}_1$ and $\dot{\theta}_2$, leading to two corresponding solutions for both δ_1 and δ_2. As a result, four total inverse kinematic solutions are obtained. To determine the actuation variables required for a commanded motion, the wheelchair's control system takes the 2D velocity twist produced by the control interface and computes all four inverse-kinematic solutions, selecting the one that minimizes variations in the steering angles. Because the actuation set is redundant, a kinematic relationship must hold among the variables $\dot{\theta}_1$, $\dot{\theta}_2$, δ_1, and δ_2 (Eq. (3)).

$$\dot{\theta}_1 s_{\delta_1} = \dot{\theta}_2 s_{\delta_2} \tag{3}$$

3 Executive Design and Prototype

This section presents the executive design of MoviWE.Q base platform. From a mechanical design perspective, the locomotion units represent the most complex subsystems. Since no commercially available solutions exist at this size scale, a fully custom design was developed. In each locomotion unit, the motorwheel[1] is mounted on an aluminum fork supported by a commercial slewing-ring bearing, as shown in Fig. 3.

The bearing is attached to the main flange, which is fixed to the tubular frame of the wheelchair by four clamps. The bearing's rotating ring is connected on one side to the fork and on the other to a worm gear that engages with a worm driven by a stepper motor[2]. Dedicated supports are included for the worm-gear shaft to eliminate radial and axial loads on the motor mounts. To ensure unrestricted steering rotation, an electrical slip ring is used to transmit power and control signals to the motorwheel. Steering angle measurement is performed using an absolute optical encoder coupled through a spur-gear transmission. The final prototype and the main dimensions are shown in Fig. 4.

[1] A commercial brushless motorwheel with a diameter of 202 mm, rated voltage +24 VDC, maximum speed 200 rpm, rated torque 20 Nm, and peak torque 40 Nm, and Hall-effect sensors for measuring wheel angular velocity.

[2] A commercial stepper motor NEMA 23, rated voltage of +24 VDC, holding torque 3.3 Nm, and 1.8° step angle.

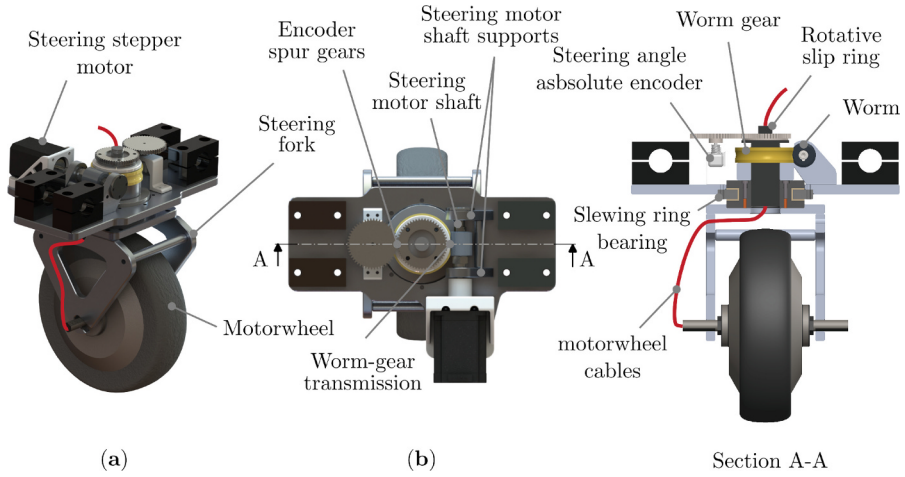

Fig. 3. Locomotion unit executive design: (a) 3D render view, (b) top view, (c) section $A - A$.

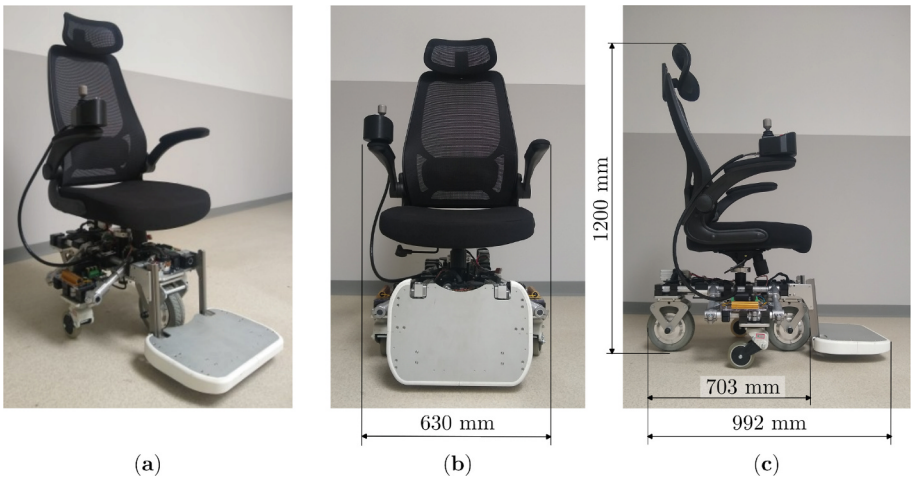

Fig. 4. MoviWE.Q prototype: (a) 3D view, (b) front view, (c) side view.

4 Force-Sensitive Interface for Caregivers

In [18], the authors presented the first prototype of the force–torque-sensitive handlebar, SensHB.Q. This human–machine interface measures the three main components of the driver's applied wrench, enabling the control of omnidirectional motorized systems. The device relies on a six-bar linkage ($A_0 - A - B - C - D - D_0$ in Fig. 5 (a)) constrained by three uniaxial load cells (LC1, LC2, LC3), which greatly lowers costs compared to interfaces using expensive six-axis force–torque sensors. Indeed, the three uniaxial cells in SensHB.Q cost about

167€, whereas typical six-axis sensors range from 5000€ to 12000€. A patent application for the SensHB.Q concept is currently pending (Title: Sensorized Handlebar for Motorized System, Authors: Giuseppe Quaglia, Luigi Tagliavini, Priority Date: 27/02/2024, Priority Number: 102024000004177).

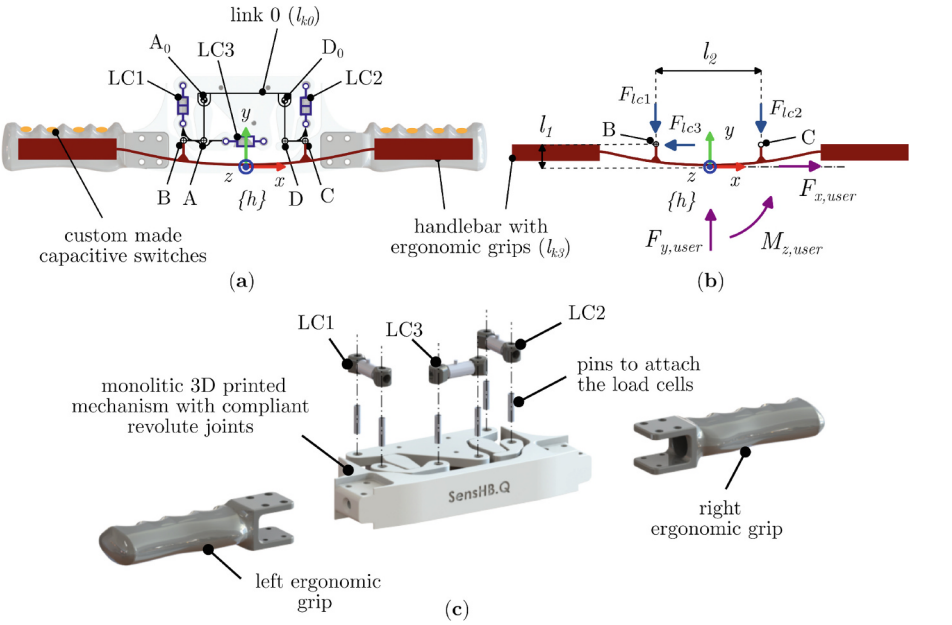

Fig. 5. SensHB.Q design: (a) functional scheme, (b) free-body diagram.

Figure 5 shows the functional design of the interface with the render of the CAD in transparency. Link 0 (l_{k0}) is fixed behind the backrest, while the caregiver grips the two ergonomic handles connected to link 3 (l_{k3}). The caregiver applies the forces $F_{x,user}$ and $F_{y,user}$ and the torque $M_{z,user}$ and the system measures the three load cells reactions F_{lci}, where $i = 1, 2, 3$. All the other components of the applied wrench are supported by the six-bar linkage. Given the free-body diagram and the geometrical parameters l_1 and l_2 illustrated in Fig. 5 (b), the equilibrium of forces and torques of the handlebar (l_{k3}), the relation between the forces measured by the uniaxial load cells F_{lci} ($i = 1, 2, 3$), defined positive under traction, and the components of the user wrench is described by Eq. (4).

$$
{}^{h}\begin{bmatrix} M_z \\ F_x \\ F_y \end{bmatrix}_{user} = -\begin{bmatrix} \frac{l_2}{2}(F_{lc1} - F_{lc2}) - l_1 F_{lc3} \\ F_{lc3} \\ F_{lc1} + F_{lc2} \end{bmatrix} = -\begin{bmatrix} \frac{l_2}{2} & -\frac{l_2}{2} & -l_1 \\ 0 & 0 & 1 \\ 1 & 1 & 0 \end{bmatrix} \begin{bmatrix} F_{lc1} \\ F_{lc2} \\ F_{lc3} \end{bmatrix} \tag{4}
$$

Figure 6 depicts SensHB.Q prototype. In Fig. 6 (c) the interface is mounted on MoviWE.Q and the reference frames of the two systems are defined. Once

the wrench components $F_{x,user}$, $F_{y,user}$, and $M_{z,user}$ are measured within the reference frame $\{h\}$, they are can be transposed into the wheelchair base reference frame $\{b\}$ and used as inputs to a simplified dynamic model, and the resulting velocity twist is used as the velocity twist reference for MoviWE.Q. In this case, the wheelchair is modeled as an empty trolley sliding on the ground plane with Coulomb dry-friction: center of mass in $\{b\}$, mass of the trolley 20 kg, moment of inertia around z-axis of $\{b\}$ 0.3 kgm^2, and static friction coefficient 0.042. In this case, the parameters have been tuned manually according to the driver preferences over initial tests with the system. Future works will focus on automatic tuning procedures.

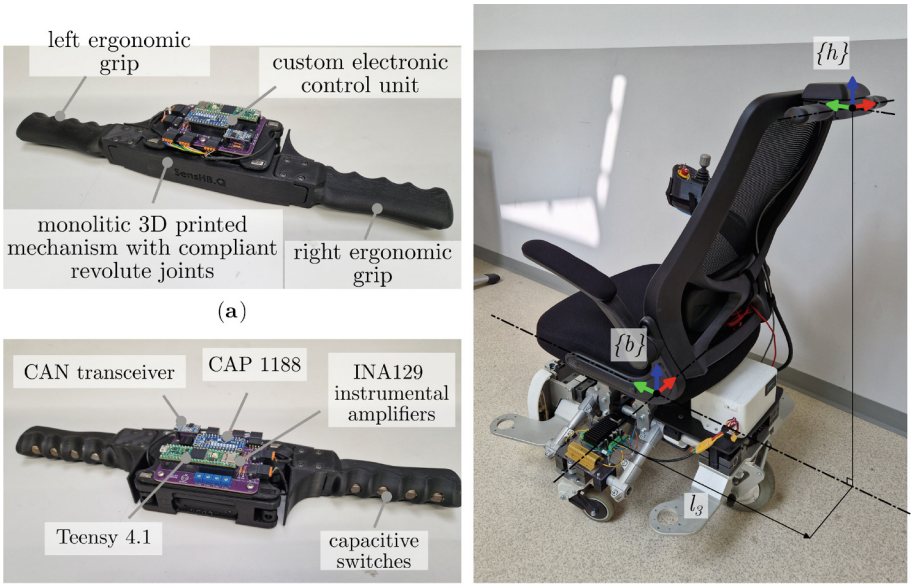

Fig. 6. SensHB.Q prototype: (a) front view, (b) back view, (c) SensHB.Q mounted on MoviWE.Q.

5 Experimental Tests

Experimental tests were carried out on the developed prototypes. The purpose of this preliminary assessment was to demonstrate that MoviWE.Q can effectively navigate indoor environments with obstacles, even when controlled by a caregiver using the force-sensitive SensHB.Q handlebar. To evaluate both aspects, six members of the research group (four men and two women, aged 25 to 61) were asked to drive MoviWE.Q with the force-sensitive interface inside the laboratories of Politecnico di Torino. The test setup is shown in Fig. 7 (a) and (b).

Various objects were placed along the route to act as obstacles and assess the system's ability to pass through narrow spaces. In the first segment of the trajectory, each driver was instructed to maintain a steady wheelchair orientation to test the pure translational driving mode.

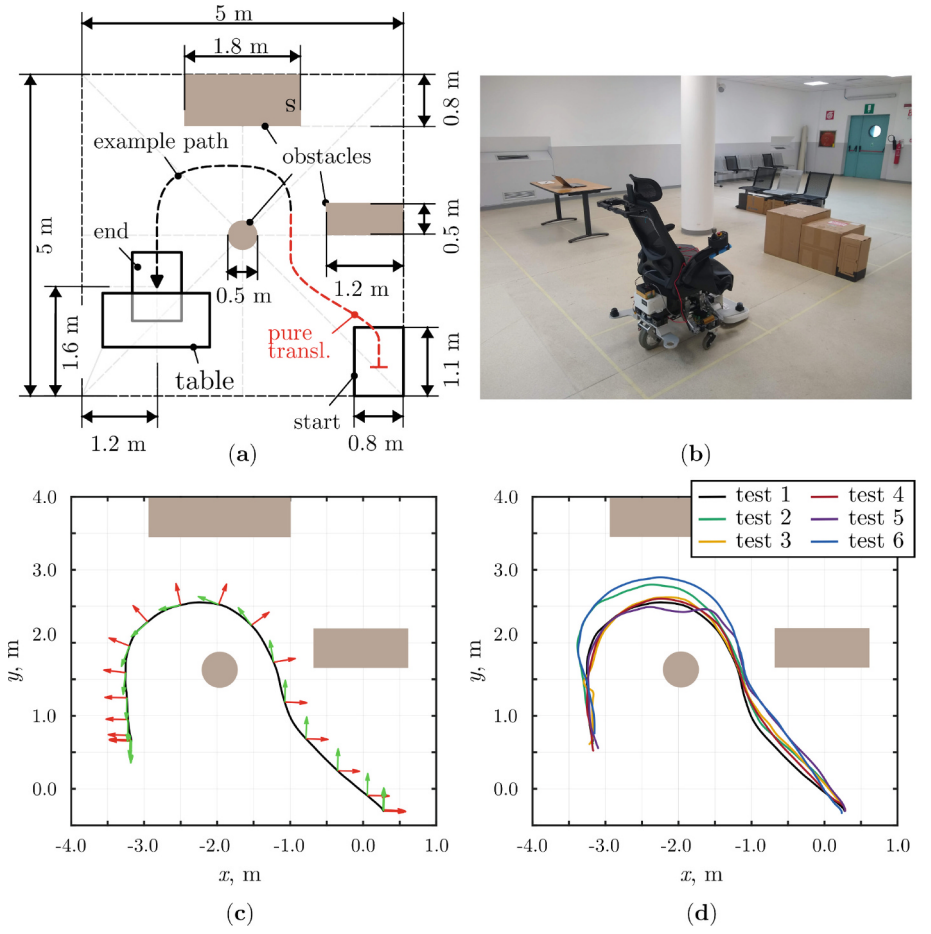

Fig. 7. Experimental test setup and results: (a) test track top view scheme with dimensions, (b) photo of the test track, (c) trajectory of the wheelchair base during test 1 with $\{b\}$ frame orientation, (d) trajectories of the wheelchair base during all tests.

Figure 7 (c) and (d) illustrates the trajectories followed by the wheelchair base during the trials conducted by the six volunteers. The data show that all participants successfully completed the task, positioning the wheelchair under the table as instructed. Consistently with the test requirements, the drivers kept the wheelchair's orientation stable during the initial segment of the path.

On average, the task was completed in 31.13 s over a track of approximately 7 m. The individual completion times were: 28.38 s (test 1), 35.34 s (test 2), 38.81 s (test 3), 27.81 s (test 4), 25.07 s (test 5), and 31.37 s (test 6). For comparison, the same task was performed five times with a person seated in the wheelchair and driving via MoviWE.Q's 3-axis joystick, yielding an average time of 29.23 s. The similarity between the two average times indicates that users were able to complete the task efficiently using the sensorized handlebar.

6 Conclusions

This work presented the design, development, and preliminary validation of the omnidirectional electric-powered wheelchair MoviWE.Q and its force–torque-sensitive caregiver interface, SensHB.Q. The proposed swerve-drive locomotion architecture enables full planar omnidirectional mobility without relying on specialized wheel technologies such as mecanum and omni wheels. The SensHB.Q interface offers an intuitive and low-cost solution for caregiver control, measuring the three components of the applied wrench on the plane of motion through three uniaxial load cells that constraints a six-bar linkage.

Preliminary experimental tests confirmed that caregivers can effectively maneuver MoviWE.Q in indoor environments with obstacles and narrow passages. Task time completion with the force-sensitive interface was comparable to that obtained with a standard 3-axis joystick, indicating that the system can be operated efficiently even by untrained users. These results are promising in demonstrating the feasibility and potential of the proposed platform for improving indoor accessibility.

Future work will focus on expanding experimental validation with end users, refining control strategies, and integrating advanced sensing and autonomy features to further enhance safety and usability.

References

1. Affairs, U.N.D.o.E.a.S.: Disability and Development Report 2024: Accelerating the Realization of the Sustainable Development Goals by, for and with Persons with Disabilities. United Nations (2025). https://doi.org/10.18356/9789210024891, https://www.un-ilibrary.org/content/books/9789210024891
2. Baglieri, L., Matsuura, D., Kobayashi, T., Quaglia, G.: Motion tracking hands-free HMI of electric wheelchair. In: Carbone, G., Quaglia, G. (eds.) Proceedings of I4SDG Workshop 2025 - IFToMM for Sustainable Development Goals. I4SDG 2025. Mechanisms and Machine Science, LNCS, vol. 179, pp. 181–189. Springer, Cham (2025). https://doi.org/10.1007/978-3-031-91151-4_20
3. Ghorbel, A., Amor, N.B., Jallouli, M.: A survey on different human-machine interactions used for controlling an electric wheelchair. Procedia Comput. Sci. **159**, 398–407 (2019)
4. ISTAT: Alunni con disabilità - Anno scolastico 2020–2021. https://www.istat.it/comunicato-stampa/linclusione-scolastica-degli-alunni-con-disabilita-anno-scolastico-2020-2021/

5. ISTAT: Salute degli anziani. https://www.istat.it/comunicato-stampa/le-condizioni-di-salute-della-popolazione-anziana-in-italia-anno-2019/
6. Kim, J., et al.: The tongue enables computer and wheelchair control for people with spinal cord injury. Sci. Transl. Med. **5**(213), 213ra166–213ra166 (2013)
7. Kundu, A.S., Mazumder, O., Lenka, P.K., Bhaumik, S.: Omnidirectional assistive wheelchair: design and control with isometric myoelectric based intention classification. Procedia Comput. Sci. **105**, 68–74 (2017)
8. Lutz, W., Sanderson, W., Scherbov, S.: The coming acceleration of global population ageing. Nature **451**(7179), 716–719 (2008). https://www.nature.com/articles/nature06516, publisher: Nature Publishing Group UK London
9. Martins, M., Santos, C., Seabra, E., Frizera, A., Ceres, R.: Design, implementation and testing of a new user interface for a smart walker. In: 2014 IEEE International Conference on Autonomous Robot Systems and Competitions (ICARSC), pp. 217–222. IEEE (2014). https://ieeexplore.ieee.org/abstract/document/6849789/
10. Martins, M.M., Frizera-Neto, A., Santos, C.P., Ruíz, R.C.: Smart walker control through the inference of the user's command intentions. In: ICINCO (1), pp. 458–463 (2012)
11. Matsuo, K., Barolli, L.: Design and implementation of an omnidirectional wheelchair: control system and its applications. In: 2014 Ninth International Conference on Broadband and Wireless Computing, Communication and Applications, pp. 532–535. IEEE (2014)
12. McNicoll, G.: World population ageing 1950–2050. Popul. Dev. Rev. **28**(4), 814–816 (2002). publisher: John Wiley & Sons, Inc
13. Mougharbel, I., El-Hajj, R., Ghamlouch, H., Monacelli, E.: Comparative study on different adaptation approaches concerning a sip and puff controller for a powered wheelchair. In: 2013 Science and Information Conference, pp. 597–603. IEEE (2013)
14. Organization, W.H.: Wheelchair services. https://www.who.int/teams/health-product-policy-and-standards/assistive-and-medical-technology/assistive-technology/wheelchair-services
15. Plesnick, S., Repice, D., Loughnane, P.: Eye-controlled wheelchair. In: 2014 IEEE Canada International Humanitarian Technology Conference-(IHTC), pp. 1–4. IEEE (2014)
16. Sander, M., et al.: The challenges of human population ageing. Age Ageing **44**(2), 185–187 (2015). https://academic.oup.com/ageing/article-abstract/44/2/185/93994, publisher: Oxford University Press
17. Tagliavini, L., Quaglia, G.: On the design of moviwe. q: an omnidirectional electric-powered wheelchair for indoor mobility. In: Okada, M. (eds.) Advances in Mechanism and Machine Science. IFToMM WC 2023. Mechanisms and Machine Science, LNCS, vol 148, pp. 311–321. Springer, Cham (2023). https://doi.org/10.1007/978-3-031-45770-8_31
18. Tagliavini, L., Quaglia, G.: SensHB.Q: a cost-effective force-sensitive handlebar to control omnidirectional robots and wheelchairs. J. Field Robot. (2025). https://doi.org/10.1002/rob.70104, https://onlinelibrary.wiley.com/doi/abs/10.1002/rob.70104
19. Trujillo-León, A., Bachta, W., Castellanos-Ramos, J., Vidal-Verdú, F.: Assistive handlebar based on tactile sensors: control inputs and human factors. Sensors **18**(8), 2471 (2018). https://www.mdpi.com/1424-8220/18/8/2471, publisher: MDPI
20. Wada, M., Asada, H.H.: Design and control of a variable footprint mechanism for holonomic omnidirectional vehicles and its application to wheelchairs. IEEE Trans. Robot. Autom. **15**(6), 978–989 (1999)

Underactuated Gravity-Assisted Cable Robot for Microphone Transportation

Mykhailo Riabtsev[1](✉), Med Amine Laribi[2], and Victor Petuya[1]

[1] University of the Basque Country UPV/EHU, Plaza Torres Quevedo 1, Bilbao 48013, Spain
mykhailo.riabtsev@univ-poitiers.fr
[2] Department GMSC, Pprime Institute, CNRS - University of Poitiers – ENSMA, UPR 3346, Poitiers 86073, France

Abstract. This paper investigates the feasibility of using a gravity-assisted underactuated cable-driven robot to transport a handheld microphone across a conference hall. The proposed system employs four ceiling-mounted winch actuators connected to a lightweight platform, enabling three-dimensional motion within the hall while keeping all actuators and moving parts away from the audience. To assess whether such a system can support safe and practical microphone delivery, we develop a simplified kinematic and dynamic model that includes inverse kinematics for cable direction computation, a minimum-norm static tension formulation, and a dynamic tension model based on platform acceleration along a predefined trajectory. The end-effector is modeled as a point mass and only translational motion is considered, while orientation is assumed to be passively stabilized by gravity. A representative conference-hall geometry is considered, including both flat and inclined seating configurations. A smoothed point-to-point path is generated to reflect realistic microphone delivery motions, and the resulting cable tensions are evaluated through numerical simulation in MATLAB. The simulation allows identification of regions where the cable configuration becomes sensitive to motion-induced forces or where individual cables approach zero tension. These findings illustrate the key challenges of operating an underactuated cable-driven system in a collaborative, human-centered environment and provide a foundation for future work involving trajectory optimization, active tension control, and experimental validation.

Keywords: Cable Robot · Collaborative Robot · Transportation System · Dynamic Analysis

1 Introduction

In many conference venues and large meeting halls, the handover of handheld microphones is still performed manually. Operators often need to traverse long distances or climb stepped seating structures, which introduces safety risks, disrupts audience flow, and becomes increasingly impractical in large auditoriums. Automating this process using wheeled service robots is difficult because many halls include tiered seating, narrow aisles, and densely packed chair rows, severely restricting ground-robot mobility.

© The Author(s), under exclusive license to Springer Nature Switzerland AG 2026
A. Chaker et al. (Eds.): EFIMMS 2026, MMS 205, pp. 225–235, 2026.
https://doi.org/10.1007/978-3-032-22270-1_22

Aerial robots (drones) are also unsuitable due to noise, the need for relatively large payload-capable platforms, safety concerns associated with operating near people, and documented psychological discomfort among occupants when drones fly in confined indoor spaces [1, 2].

Overhead cable-suspended systems provide an alternative means of covering large workspaces. In professional broadcasting, multi-winch "sky-cam" platforms such as Spidercam and Robycam enable full 3D camera motion above stadiums [3–5]. In conference-room audio, ceiling-mounted microphone arrays (e.g., Sennheiser TeamConnect Ceiling, Shure ceiling arrays) offer wide-area coverage without floor-level hardware, but cannot physically reposition a handheld microphone [6, 7]. Ceiling-mounted microphone winches such as the igus® microphone lift [8] allow vertical repositioning only and do not provide lateral transport.

The system proposed in this work extends these ideas by employing a lightweight cable-suspended mechanism capable of moving a handheld microphone along arbitrary paths within a conference hall. The microphone is carried on a small platform connected to four overhead anchor points, forming an underactuated cable-driven configuration. Prior research shows that such systems can still achieve meaningful workspaces and feasible tension distributions even when cable count is lower than the number of controlled degrees of freedom [9].

Although the platform is physically a rigid body with six degrees of freedom, the task considered in this paper is defined only by the translational motion of the center of mass. The orientation of the microphone is not actively controlled and is assumed to remain passively stabilized by gravity and cable geometry. From a task perspective, the system is therefore underactuated with respect to the full rigid-body motion, while only a reduced translational task is addressed. Gravity assistance plays a dual role by providing static equilibrium and by contributing to passive orientation stabilization.

The objective of this study is to evaluate the tension feasibility of a prescribed microphone trajectory using a minimal yet representative dynamic model. Cable directions are obtained from a simple inverse-kinematic step; static tensions are computed to characterize gravity load distribution; and dynamic tensions are evaluated to assess whether the desired motion remains physically realizable. This approach highlights both the potential and the limitations of gravity-assisted underactuated cable-suspended systems in human-centered environments.

This article has the following structure. Section 2 describes the system architecture and key safety considerations. Section 3 introduces the inverse kinematic model and the computation of cable direction vectors. Section 4 formulates the static tension distribution. Section 5 presents the reduced dynamic model. Section 6 outlines the simulation procedure, and Sect. 7 discusses the static and dynamic results. Section 8 concludes the paper and identifies directions for future work.

2 System Description and Constraints

We propose a gravity-assisted underactuated cable-driven robot for transporting a handheld microphone within a conference hall. The system consists of four motorized winch actuators mounted at the hall's upper corners, labeled A, B, C, and D. Each actuator

controls a cable routed to one of the four corners of the suspended transport platform, denoted E, F, G, and H (see Fig. 1a). The platform itself carries a standard handheld wireless microphone with an approximate mass of 0.3 kg, shown in Fig. 1b. This overhead configuration provides a large and unobstructed workspace while keeping all actuators and moving parts safely away from the audience. Since the robot operates in close proximity to people and may interact with users in its stationary state, safety remains a primary design requirement throughout the development of the system.

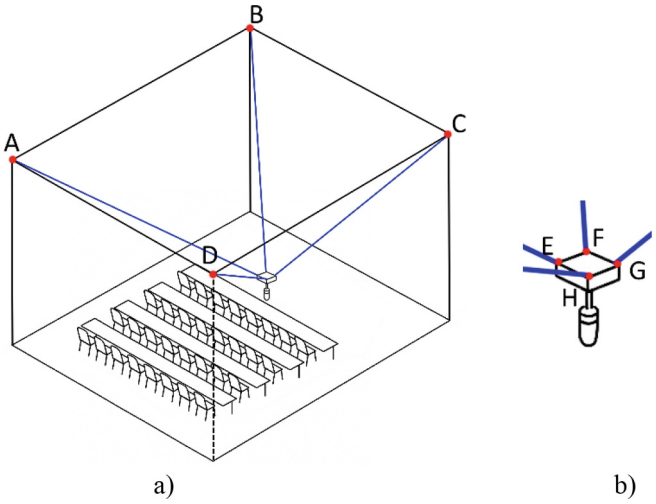

Fig. 1. Proposed system: a) general view; b) microphone platform.

To ensure safe operation, both passive and active safety measures are incorporated. Passive safety relies on the physical design of the platform, which is padded with compliant foam to reduce impact forces in case of accidental contact. Active safety focuses on reducing the likelihood and potential severity of collisions. The former is addressed by constraining the robot's planned motion to regions of the hall where the probability of intersecting with people is minimal, while the latter is addressed by limiting the maximum platform speed to 2 m/s. This bound corresponds to a kinetic energy of approximately 0.6 J, following the guidelines of the EN-71 toy safety standard [10], and is low enough to avoid injury in typical accidental contact scenarios. Additionally, the system is intended to be handled only when fully stopped, ensuring predictable and safe interaction for participants and session chairs.

The robot is supposed to be controlled via a tablet interface that displays a live overhead camera feed augmented with a grid overlay representing seating locations. The operator can select a seating cell, prompting the robot to deliver the microphone to the corresponding audience member. The interface also provides essential functions such as home-position return and emergency stop. Given that the system is designed to operate in a collaborative human environment, future functional prototypes are expected to include intent recognition, automatic seat detection, and obstacle awareness.

2.1 Motion Strategy and Safety-Aware Height Planning

Safety is a primary concern in applications involving humans. The proposed system benefits from a low payload mass and limited kinetic energy. Even in the presence of temporary cable unloading, the gravity-assisted configuration and conservative motion parameters reduce potential hazards. In practical implementations, additional safety measures such as redundant cables, tension monitoring, and emergency stop mechanisms would be employed.

To further reduce the risk of unintended contact, the robot follows predefined height layers depending on the region of the hall. These heights represent conservative safety-oriented estimates chosen to minimize both collision probability and the energy a falling microphone could accumulate.

- Over main aisles, the microphone travels at approximately 2.5 m above the floor, ensuring clearance above virtually all attendees.
- On stage, the path follows the table edge at ~1.5 m, allowing a session chair to retrieve the microphone if needed while maintaining cable clearance above head level; however, the chair is expected to use a separate microphone under normal circumstances.
- Above conference tables, the robot maintains a height of roughly 1.0 m, avoiding interference with seated participants and their belongings.
- When reaching a selected participant, the platform descends to about 0.7 m above the table surface, enabling the user to take the microphone while keeping the cables sufficiently high to avoid entanglement or accidental pulling.

Although these values are not strict limits, they serve as practical safety guidelines for initial system deployment and can be fine-tuned as part of future optimization or experimental evaluation. Additional safety can be achieved through computer-vision modules capable of detecting people or objects along the intended path, allowing the robot to adjust its trajectory to avoid obstacles. Vision-based attention or gesture recognition could also support the operator by automatically highlighting participants wishing to ask questions, reducing cognitive load during interactive sessions.

3 Inverse Kinematic Model and Cable Directions

In this section, we introduce the inverse kinematic model of our cable-driven microphone transport system and compute the corresponding cable direction vectors. This formulation is essential because the geometric relationship between the platform and the fixed anchor points directly determines the feasible tension distributions used later in the static and dynamic analyses. We do not address the full forward-kinematic problem because in underactuated cable-driven systems the forward kinematics is often non-unique, numerically ill-posed, or computationally expensive to solve, especially when the platform is suspended by fewer cables than degrees of freedom. Since our study operates with a predefined trajectory and thus a known platform position at each time step, only the inverse kinematic model is required. This approach follows common practice in cable-driven robot research, where the inverse problem is favored for its analytical simplicity and reliable force estimates [11].

The inverse kinematic model of the proposed system is straightforward, since the platform position is prescribed and the cable anchor coordinates are fixed. Each cable forms a vector between one platform attachment point (E, F, G, H) and the corresponding ceiling-mounted anchor point (A, B, C, D) as shown in Fig. 2. Because the anchor coordinates are known and the position of the platform center (point M) is provided at each time step, the coordinates of the platform vertices can be obtained by applying constant geometric offsets.

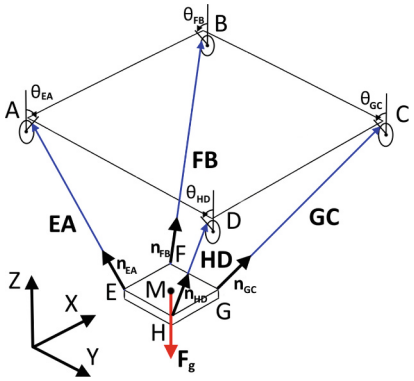

Fig. 2. Vectorial representation of the proposed manipulator.

Once all point coordinates are known, the cable vectors are computed as:

$$\mathbf{EA} = A - E, \mathbf{FB} = B - F, \mathbf{GC} = C - G, \mathbf{HD} = D - H \tag{1}$$

The instantaneous cable lengths are

$$L_{\mathbf{EA}} = |\mathbf{EA}|, L_{\mathbf{FB}} = |\mathbf{FB}|, L_{\mathbf{GC}} = |\mathbf{GC}|, L_{\mathbf{HD}} = |\mathbf{HD}| \tag{2}$$

Since each cable is wound onto a motorized winch, the cable length directly determines the angular rotation of the actuator drum. Assuming a cylindrical spool of radius r, the required actuator angle θ for each cable can be computed as:

$$L_{\mathbf{EA}} = \frac{L_{\mathbf{EA}} - L^0_{\mathbf{EA}}}{r}, L_{\mathbf{FB}} = \frac{L_{\mathbf{FB}} - L^0_{\mathbf{FB}}}{r}, L_{\mathbf{GC}} = \frac{L_{\mathbf{GC}} - L^0_{\mathbf{GC}}}{r}, L_{\mathbf{HD}} = \frac{L_{\mathbf{HD}} - L^0_{\mathbf{HD}}}{r} \tag{3}$$

where L^0 is the cable length corresponding to the actuator's zero-angle reference.

The unit cable direction vectors, which define the direction of tension forces, follow from normalization:

$$\mathbf{n_{EA}} = \frac{\mathbf{EA}}{|\mathbf{EA}|}, \mathbf{n_{FB}} = \frac{\mathbf{FB}}{|\mathbf{FB}|}, \mathbf{n_{GC}} = \frac{\mathbf{GC}}{|\mathbf{GC}|}, \mathbf{n_{HD}} = \frac{\mathbf{HD}}{|\mathbf{HD}|} \tag{4}$$

4 Static Tension Distribution

In this static analysis, the end-effector is modeled as a point mass located at its center of mass. Rotational equilibrium is not considered, since the orientation of the platform is not actively controlled and is assumed to be passively stabilized by gravity and symmetric cable attachment. The purpose of this section is to evaluate force feasibility along the prescribed translational task.

In the absence of motion, the only external force acting on the system is gravity,

$$\mathbf{F_g} = m\mathbf{g} \tag{5}$$

where m is the total mass of the microphone and the platform, and $\mathbf{g} = [0\ 0\ -9.81]^T$ m/s^2.

Using the Eq. (4) the direction matrix can be formed as,

$$\mathrm{U} = \left[\, \mathbf{n_{EA}}\ \mathbf{n_{FB}}\ \mathbf{n_{GC}}\ \mathbf{n_{HD}} \,\right] \tag{6}$$

Under static conditions, the sum of the cable tension forces must balance the gravitational load:

$$\mathrm{U}\mathbf{T_{st}} + \mathbf{F_g} = 0 \tag{7}$$

Because there are four cables and only three equilibrium equations, the system is statically redundant. A standard technique widely used in the modelling of cable-driven parallel robots [12] is to compute the minimum-norm solution of the equilibrium equation using the Moore–Penrose pseudoinverse of U. The resulting tension vector is,

$$\mathbf{T_{st}} = \mathrm{U}^{\mathrm{T}}\left(\mathrm{U}\mathrm{U}^{\mathrm{T}}\right)^{-1}\left(-\mathbf{F_g}\right) \tag{8}$$

The resulting vector $\mathbf{T_{st}}$ provides the unique tension distribution with the smallest Euclidean norm that counterbalances gravity. While pseudoinverse-based solutions may become ill-conditioned or produce small negative values near singular cable configurations within the considered workspace all tensions remained positive, and thus the solution is physically consistent.

5 Dynamic Model and Required Cable Forces

The dynamic behavior of the system must account not only for gravity but also for the inertial forces resulting from the prescribed motion of the platform. As in the static case, only translational dynamics are considered, while rotational dynamics are neglected. Let the trajectory provide the platform position $\mathbf{x}(t)$, from which velocity $\dot{\mathbf{x}}(t)$ and acceleration $\ddot{\mathbf{x}}(t)$ are obtained numerically.

Using matrix U, obtained in Eq. (6), the force balance on the moving platform is expressed as

$$\mathrm{U}\mathbf{T_{dyn}} + \mathbf{F_g} = m\ddot{\mathbf{x}}(t) \tag{9}$$

The term on the right-hand side represents the total force required to generate the desired platform acceleration. Rearranging gives the cable force that must be generated:

$$\mathbf{F_{req}}(t) = m\ddot{\mathbf{x}}(t) - \mathbf{F_g} \tag{10}$$

Similar to the Eq. (8) the minimum-norm dynamic tension distribution using the Moore–Penrose pseudoinverse is computed as,

$$\mathbf{T_{dyn}} = \mathrm{U}^{\mathrm{T}}\left(\mathrm{U}\mathrm{U}^{\mathrm{T}}\right)^{-1}\mathbf{F}_{req}(t) \tag{11}$$

6 Simulation Procedure

The simulation was carried out using a simplified geometric and dynamic model of the proposed cable-driven system and the conference hall. The hall dimensions were set to 10 m in length (X), 15 m in width (Y), and 5 m in height (Z). A 2-m-deep stage occupied the region from X = 8 m to X = 10 m. To reflect typical conference-room configurations, two floor types were considered: a flat floor and an inclined floor descending toward the stage with a 20° slope, representing auditorium-style seating. The trajectory was pre-computed and parameterized in MS Excel, while all subsequent geometric, kinematic, and dynamic computations were performed in MATLAB R2022a.

The transported payload consisted of a standard handheld wireless microphone (0.3 kg) mounted on a lightweight platform (0.2 kg), resulting in a total mass of approximately 0.5 kg. The maximum simulated platform speed was limited to 2 m/s, and additional simulations were performed at reduced speeds, such as 1 m/s, to observe how the velocity influences the resulting cable tensions. The previously mentioned 0.6 J value refers only to the mass of the microphone itself, representing the worst-case scenario of accidental detachment; all dynamic simulations use the full payload mass of 0.5 kg (Fig. 3).

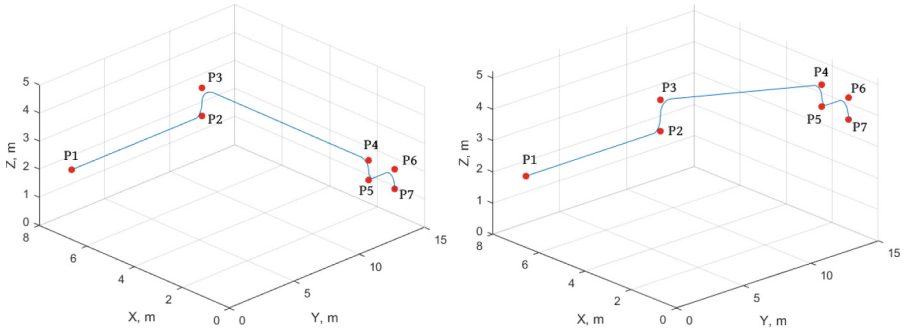

Fig. 3. 3D trajectories of the end-effector center of mass used in simulations: a) flat floor simulation; b) inclined floor simulation.

The reference trajectory (see Fig. 5) guided the platform between the points $P_1(8\ 2.5\ 1.5)$, $P_2(8\ 12.5\ 1.5)$, $P_3(8\ 12.5\ 2.5)$, $P_4(1\ 12.5\ 2.5)$, $P_5(1\ 12.5\ 1.8)$, $P_6(1\ 14.5\ 1.8)$, and $P_7(1\ 14.5\ 1.1)$. The coordinates of these points are defined relative to the floor level.

Point P_1 corresponds to a location on the stage where the microphone is initially placed by the session chair, while P_7 represents a position near an audience member at the far end of the hall. Although these points define the intended route, the robot does not move along straight segments between them; abrupt direction changes would produce discontinuities in cable forces. To avoid this, the trajectory was smoothed using circular fillets with radii between 0.25 m and 0.71 m, ensuring continuous curvature and preventing tension spikes. The effects of cable mass and elasticity, drum friction, actuator limits, and delays were omitted in the current simulation because their magnitudes are small compared to the dominant geometric and inertial factors identified in this study, and a detailed sensitivity analysis is planned as future work.

During the simulation, the platform position at each time step was read from the Excel dataset. Velocities and accelerations were computed numerically using central finite differences. Cable unit direction vectors were obtained from the known positions of the anchor points and the moving platform. Static tensions were computed for reference, and dynamic tensions were obtained using the same minimum-norm pseudoinverse formulation introduced in Sect. 5. Plots of the computed quantities are presented in the following section.

7 Simulation Results and Discussion

This section summarizes the essential outcomes of the static and dynamic tension analysis performed along the prescribed trajectory.

7.1 Static Tensions Along the Trajectory

Static tensions $\mathbf{T_{st}}$ were computed at each point of the smoothed path. The resulting profiles are smooth across the entire trajectory, and none of the cables approaches zero tension. A comparison between the flat-floor and inclined-floor configurations shows that the static tension curves are practically identical, with only minor numerical differences. For this reason, only the plot corresponding to the inclined-floor configuration is presented here (see Fig. 4). This confirms that the trajectory is statically feasible and that any undesired effects observed in the dynamic analysis arise from motion-induced forces rather than geometric constraints.

7.2 Dynamic Tension Profiles

Dynamic tensions were first evaluated for the flat-floor configuration. The corresponding profiles are shown in Fig. 5. In Fig. 5a (2 m/s), the EA cable reaches zero tension during the turn into the aisle ($\approx$0.25 s). When entering the target row, both EA and HD drop to zero, while BF approaches near-zero tension during the final descent. Tension peaks

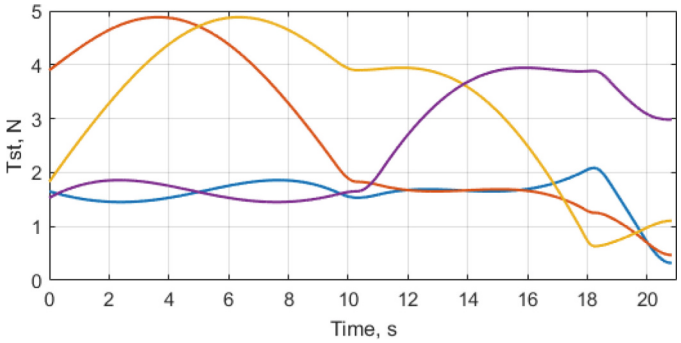

Fig. 4. Static tension profiles along the trajectory for the inclined-floor simulation.

of up to approximately 11 N appear in the final segment, where the curvature radius is smallest.

In contrast, Fig. 5b (1 m/s) shows substantially smoother behavior: only EA reaches zero tension, and only during the aisle turn. No other cable drops to zero during row entry or the final descent, and peak tensions are noticeably reduced.

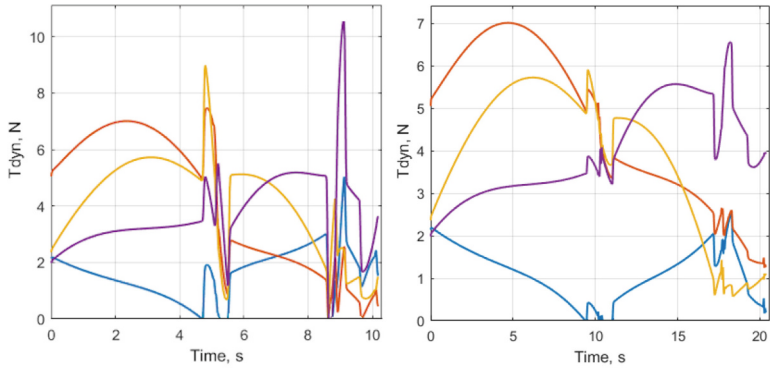

Fig. 5. Dynamic tension profiles for flat-floor scenario at: a) 2 m/s; b) 1 m/s. Cable color coding: EA – blue, BF – red, CG – yellow, HD – purple.

The same trajectory was simulated in the inclined-floor configuration (20°), with results shown in Fig. 6.

In Fig. 6a (2 m/s), the tension distribution is practically identical to the one in Fig. 5a with only minor numerical differences. In Fig. 6b, the overall behavior is noticeably smoother. EA again drops to zero during the aisle turn, and a brief additional zero occurs at the trajectory endpoint. The GC cable touches zero momentarily when entering the seating row but rapidly recovers. No other cables reach zero tension at this speed.

The peak dynamic cable tension obtained in the simulations does not exceed 11 N. Assuming a pulley diameter of 40 mm, this corresponds to a maximum actuator torque

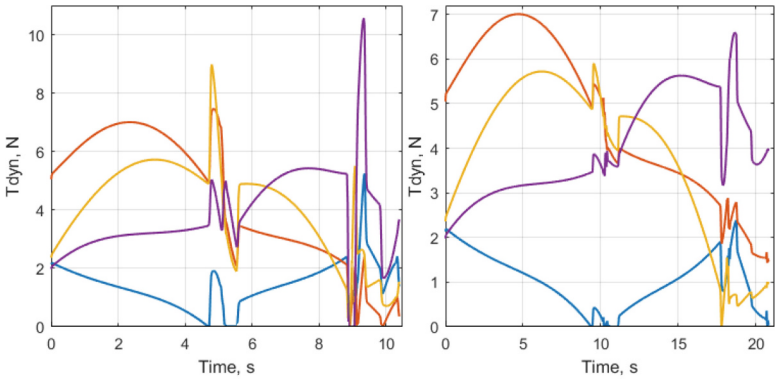

Fig. 6. Dynamic tension profiles for inclined-floor scenario at: a) 2 m/s; b) 1 m/s. Cable color coding: EA – blue, BF – red, CG – yellow, HD – purple.

of approximately 0.44 N·m. Such torque levels are modest and can be readily achieved by compact commercial winch motors.

7.3 Discussion

The simulation results reveal several important insights. First, the trajectory itself is structurally feasible, as demonstrated by the static analysis. Second, high-speed execution amplifies inertial effects, which in turn produces tension peaks and short intervals of near-zero tension. Although these behaviors do not pose immediate mechanical risks, they underscore the sensitivity of underactuated cable-driven systems to trajectory curvature and motion speed. Third, reducing speed significantly improves tension regularity, suggesting that a well-chosen velocity profile could eliminate most undesirable effects without major modifications to the geometric layout.

Overall, the findings indicate that practical implementation will require coordinated trajectory design, balancing safety, execution time, and tension feasibility. Smoothing radii and velocity limits appear to be effective tuning parameters for avoiding sudden tension changes. These observations point toward future work in trajectory optimization, real-time speed adaptation, and potentially predictive tension management, enabling more robust and reliable operation in human-centered environments.

8 Conclusions

This study examined the feasibility of using a gravity-assisted underactuated cable-driven robot to transport a handheld microphone within a conference hall. A simplified kinematic and dynamic model was developed, including inverse kinematics for cable direction computation and minimum-norm formulations for static and dynamic tension evaluation. The prescribed trajectory was shown to be statically feasible, while dynamic simulations highlighted the sensitivity of tension distribution to platform speed and

trajectory curvature. High-speed motion introduced transient tension drops and sharp peaks, whereas reduced speeds significantly improved tension smoothness. These findings indicate that safe and reliable operation is achievable with appropriate trajectory shaping and velocity selection. Future work will focus on optimizing motion profiles, incorporating active tension regulation, and validating the approach through physical prototyping.

Acknowledgements. The authors wish to acknowledge the financial support received from the Programa Posdoctoral de Perfeccionamiento de Personal Investigador Doctor and the Project IT1480-22 provided by the Regional Basque Government. Also, the funding received from the Spanish Government through the Ministerio de Ciencia e Innovación (Project PID2020-116176GB-I00) financed by MCIN/AEI/ 10.13039/501100011033.

References

1. Yaacoub, J.P., Noura, H.N.: Security analysis of drones systems: attacks, limitations, and recommendations. Sensors. **20**(18), 1–33 (2020)
2. Vogel, O., Caspar, K., Sporer, T.: What is buzzing around me? Assessing the influence of indoor drones on human perception and acceptance. Cognit. Res.: Princ. Implic. **10**, 12 (2025)
3. Spidercam GmbH. Spidercam systems overview. https://www.spidercam.tv/. Last accessed 01 Feb 2025
4. Movicom. Robycam 3D cable-suspended camera system. https://www.movicom.tv/en/products/robycam/robycam-3d/. Last accessed 01 Feb 2025
5. Skycam LLC. Skycam system description. https://skycam.tv/. Last accessed 01 Feb 2025
6. Sennheiser. TeamConnect Ceiling Solutions. https://www.sennheiser.com/teamconnect-ceiling-solutions. Last accessed 01 Feb 2025
7. Shure. MXA Series Ceiling Microphone Arrays. https://www.shure.com/en-US/products/microphones/mxa910. Last accessed 01 Feb 2025
8. Igus GmbH. Automated microphone winch system. https://www.igus.eu/info/microphone-lift. Last accessed 2025/02/01.
9. Carricato, M., Idà, E., Berti, A., Bruckmann, T.: Static workspace computation for underactuated cable-driven parallel robots. Mech. Mach. Theory. **199**, 105086 (2024)
10. European Committee for Standardization (CEN). EN 71 — Safety of toys. https://standards.cen.eu/dyn/www/f?p=204:110:0::::FSP_PROJECT:18625&cs=1D6F1F4D0F8D0F4C0ACF91D23E6694F09. Last accessed 01 Feb 2025
11. Pott, A., Schmidt, V.: On the forward kinematics of cable-driven parallel robots. In: 2015 IEEE/RSJ International Conference on Intelligent Robots and Systems (IROS), pp. 3182–3187. Hamburg, Germany (2015). https://doi.org/10.1109/IROS.2015.7353818
12. Pott, A.: Cable-Driven Parallel Robots: Theory and Application (2018). https://doi.org/10.1007/978-3-319-76138-1

AI-Augmented Adaptive Control of Lower-Limb Exoskeletons Considering Human Parametric Variations

Zaven Khanamiryan(✉) and Azatuhi Ulikyan

National Polytechnic University of Armenia (NPUA), Yerevan, Armenia
zavenkhanamiryan@polytechnic.am

Abstract. This paper addresses the challenge of robust and adaptive control for lower-limb exoskeletons operating under nonlinear dynamics and user-dependent parametric uncertainties. Human variability in parameters such as body mass, joint stiffness, and gait characteristics significantly degrades the performance of fixed-parameter controllers, often requiring costly re-tuning for each user.

To address these limitations, a hybrid AI-augmented adaptive control framework integrating Model Reference Adaptive Control (MRAC) with Deep Deterministic Policy Gradient (DDPG) is proposed. The resulting DDPG-Augmented MRAC (DAM) controller combines the stability guarantees of MRAC with the learning and generalization capabilities of reinforcement learning, enabling improved robustness and inter-subject adaptability.

The proposed controller compensates for parametric variations across different users without requiring system redesign or full retraining. Simulation results demonstrate enhanced trajectory tracking accuracy and robustness under varying biomechanical conditions, indicating the potential of the proposed approach for intelligent and personalized control of wearable robotic systems.

Keywords: Reinforcement Learning · Lower Limb Exoskeletons · Adaptive Control · Wearable Robotics · Model Reference Adaptive Control · DAM

1 Introduction

Wearable assistive devices represent a rapidly developing field at the intersection of robotics, biomechanics and medical engineering. Among them, lower-limb exoskeletons play a central role in supporting, restoring, or enhancing human locomotion across rehabilitation, industrial and military applications. Their effectiveness critically depends on the control system, which must handle strong human-robot interaction, nonlinear dynamics and substantial inter-subject variability in parameters such as mass, inertia and joint stiffness.

Early exoskeleton controllers relied on PID and computed-torque control, but these methods show limited robustness to modeling uncertainties and user variability. Impedance and admittance control improved interaction comfort but require careful tuning and assume stable user parameters. Model Reference Adaptive Control (MRAC)

© The Author(s), under exclusive license to Springer Nature Switzerland AG 2026
A. Chaker et al. (Eds.): EFIMMS 2026, MMS 205, pp. 236–246, 2026.
https://doi.org/10.1007/978-3-032-22270-1_23

addresses parameter uncertainty and has been applied to improve robustness; however, its performance remains sensitive to unmodeled dynamics and human variability. More recently, learning-based approaches such as neural networks and reinforcement learning (RL) have been explored, though they often demand large datasets and raise stability and safety concerns in human-in-the-loop applications. These limitations have motivated hybrid adaptive-learning controllers that combine the stability of model-based methods with the generalization capability of AI techniques, though their application to inter-subject adaptability in lower-limb exoskeletons remains limited [1].

Recent developments in exoskeleton control have explored advanced adaptive and model-based strategies to improve robustness during gait. Variants of MRAC, adaptive impedance control, and disturbance-observer-based controllers have been proposed to compensate for user-specific variations, but these approaches still rely on simplified models and may struggle with rapid parametric changes or unmodeled effects such as joint misalignment and soft-tissue compliance. Robust and sliding-mode controllers offer improved stability under uncertainty but may introduce discontinuous control signals that are undesirable for safe human-robot interaction. In parallel, reinforcement learning has been used to optimize assistance profiles, yet fully end-to-end RL methods face challenges related to safety, training time, and limited cross-subject generalization. Hybrid frameworks integrating adaptive control with learning components have shown promise, but existing work mostly focuses on single-user adaptation or constrained environments and does not explicitly target inter-subject adaptability, which is crucial for practical rehabilitation and assistive deployment [2].

In this work, we propose an AI-augmented adaptive control framework that integrates reinforcement learning with MRAC to improve robustness across different users, rather than performing real-time adaptation within a single gait cycle. Here, adaptability refers to maintaining accurate joint tracking under varying anthropometric and dynamic parameters without manual re-tuning. The controller is designed to tolerate modeling simplifications and unmodeled dynamics, and its performance is evaluated through simulations using multiple user parameter sets.

2 Mathematical Modeling of the Lower-Limb Exoskeleton System

The mathematical model includes the kinematic structure of the exoskeleton, the dynamic behavior of its actuated joints, and the simplified representation of the human-exoskeleton interaction. To keep the focus on evaluating the proposed control strategy, several simplifications are introduced. Motion is restricted to the sagittal plane, as flexion-extension dynamics dominate lower-limb movement during gait and sagittal-plane models are widely used in preliminary control studies due to their ability to capture the main locomotor behavior with reduced complexity. All joints are modeled as ideal revolute joints, representing the primary motion of the hip and knee. Although these interactions influence real gait, their effects are implicitly addressed through the robustness of the adaptive controller.

The simulation model was implemented in MATLAB, and a Simulink Multibody model was used to visually represent the exoskeleton's kinematic structure and joint movements. This visualization allows clearer insight into the motion behavior and supports the interpretation of the simulation results.

2.1 Kinematic Modeling of the Lower-Limb Exoskeleton

The rehabilitation lower-limb exoskeleton (R-LLE) consists of six rotational joints and four actuators located at the hip and knee joints, while the ankle joint is passive and mechanically supported through a pneumatic damper. Due to the passive ankle, each leg is modeled with two active degrees of freedom. Based on the structure shown in Fig. 1(a), a kinematic scheme was developed and the corresponding equations were derived. Figure 1(b) illustrates the full kinematic layout of the R-LLE, including both legs. Joint coordinate frames and rotational axes were assigned following the Denavit-Hartenberg (D-H) convention. During locomotion, it is assumed that one leg remains in contact with the ground to provide support while the other performs the swing phase. This assumption is incorporated into the kinematic formulation.

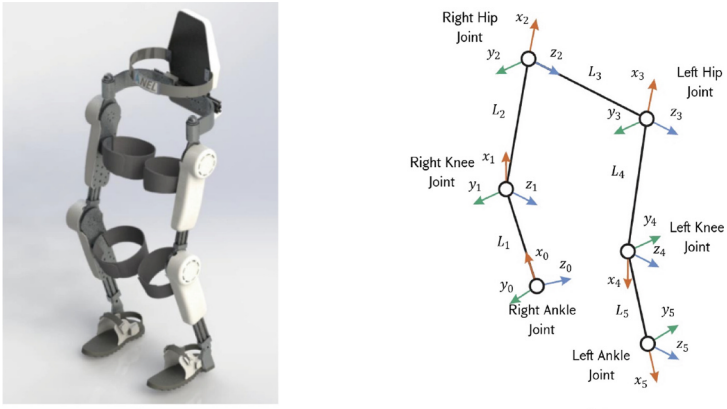

Fig. 1. (a) 3D model of R-LLE (b) Kinematic structure of the R-LLE

Using the Denavit-Hartenberg parameters, homogeneous transformation matrices were constructed to describe the motion of each joint and the transformation between adjacent coordinate frames [3]. The general form of a transformation matrix for joint i, with rotation angle θ_i and link parameters a_i, d_i, and α_i, is given as:

$$T_i(q_i) = \begin{bmatrix} \cos(q_i) & -\sin(q_i), & 0 & a_i \\ \cos(\alpha_i) \bullet \sin(q_i) & \cos(\alpha_i) \bullet \cos(q_i) & -\sin(\alpha_i) & 0 \\ \sin(\alpha_i) \bullet \sin(q_i) & \cos(q_i) \bullet \sin(\alpha_i) & \cos(a_i) & d_i \\ 0 & 0 & 0 & 1 \end{bmatrix} \quad (1)$$

The multiplication of the homogeneous transformation matrices from the base joint to the end-effector yields the complete transformation matrix of the rehabilitation lower-limb exoskeleton. This final matrix represents both the orientation and the position of the end-effector in Cartesian space.

$$T_0^6 = T_0^1 \bullet T_1^2 \bullet T_2^3 \bullet T_3^4 \bullet T_4^5 \bullet T_5^6 = \begin{bmatrix} n_x & o_x & a_x & p_x \\ n_y & o_y & a_y & p_y \\ n_z & o_z & a_z & p_z \\ 0 & 0 & 0 & 1 \end{bmatrix}, \tag{2}$$

where:

$$\begin{cases} n_x = \cos(\theta_1 + \theta_2 + \theta_3) \\ n_y = \sin(\theta_1 + \theta_2 + \theta_3) \\ n_z = 0 \\ o_x = \sin(\theta_1 + \theta_2 + \theta_3) \\ o_y = \cos(\theta_1 + \theta_2 + \theta_3) \\ o_z = 0 \\ a_x = 0 \\ a_y = 0 \\ a_z = 1 \\ p_x = L_3 + L_5\cos(\theta_1 + \theta_2) + L_4\cos\theta_1 \\ p_y = L_1 - L_5\sin(\theta_1 + \theta_2) - L_4\sin\theta_1 \\ p_z = -L_2 \end{cases}. \tag{3}$$

Here, θ_i denotes the joint angles, and L_i represents the geometric lengths of the corresponding limb segments. The obtained kinematic relationships describe the forward kinematics of the lower-limb exoskeleton and form the theoretical basis for further dynamic modeling, gait planning, and control system development.

2.2 Dynamic Modeling of the Lower-Limb Exoskeleton

To derive the dynamic equations of motion for the lower-limb exoskeleton, the Euler-Lagrange formulation was applied. Every mechanical system can be characterized by a specific function called the Lagrangian, defined as the difference between the system's kinetic and potential energy. The general form of the Euler-Lagrange equation is expressed as:

$$\frac{d}{dt}\frac{\partial L}{\partial \dot{q}_i} - \frac{\partial L}{\partial q_i} = F_i, \quad i = 1, 2, 3 \ldots n, \tag{4}$$

where $L = T - P$ is the Lagrangian of the system; T and P denote the kinetic and potential energies, respectively. The variables q_i represent the generalized coordinates, while F_i are the generalized forces, which, in the case of rotational motion, correspond to torques applied to the joints.

The kinetic energy of the system is determined using the following relationship:

$$\begin{aligned} T &= \tfrac{1}{2}m_1 v_1^2 + \tfrac{1}{2}m_2 v_2^2 \\ &= \tfrac{1}{2}m_1 L_1^2\dot{\theta}_1^2 + \tfrac{1}{2}m_2\left(L_1^2\dot{\theta}_1^2 + L_2^2\dot{\theta}_2^2 + 2L_1L_2\dot{\theta}_1\dot{\theta}_2\cos(\theta_2-\theta_1)\right) \\ &= \tfrac{1}{2}(m_1+m_2)L_1^2\dot{\theta}_1^2 + \tfrac{1}{2}m_2L_2^2\dot{\theta}_2^2 + m_2L_1L_2\dot{\theta}_1\dot{\theta}_2\cos(\theta_2-\theta_1), \end{aligned} \tag{5}$$

where m_1 is the mass of the thigh segment and m_2 is the mass of the shank segment. The potential energy of the system due to gravity is given by:

$$\begin{aligned} P &= -m_1gy_1 - m_2gy_2 \\ &= -m_1gL_1\cos(\theta_1) - m_2g(L_1\cos(\theta_1) + L_2\cos(\theta_2)) \\ &= -(m_1+m_2)gL_1\cos(\theta_1) - m_2gL_2\cos(\theta_2). \end{aligned} \tag{6}$$

Using the derived expressions for kinetic and potential energies, the generalized dynamic model of the lower-limb exoskeleton can be formulated. Neglecting friction and ground reaction forces, the dynamic equation takes the following form:

$$M(q)\ddot{q} + V(q,\dot{q})\dot{q} + G(q) = \tau, \text{ where } q = [\theta_1, \theta_1]^T. \tag{7}$$

Here, $M(q)$ is the inertia matrix, $V(q,\dot{q})$ represents the Coriolis and centrifugal terms, $G(q)$ is the gravity vector, and τ is the control torque vector applied to the joints. These terms have the following expressions:

$$M(q) = \begin{bmatrix} (m_1+m_2)L_1^2 & m_2L_1L_2\cos(\theta_2-\theta_1) \\ m_2L_1L_2\cos(\theta_2-\theta_1) & m_2L_2^2 \end{bmatrix}, \tag{8}$$

$$V(q,\dot{q}) = \begin{bmatrix} m_2L_1L_2\dot{\theta}_2^2\left(\dot{\theta}_2-\dot{\theta}_1\right)\sin(\theta_2-\theta_1) \\ -m_2L_1L_2\dot{\theta}_1^2\sin(\theta_2-\theta_1) \end{bmatrix}, \tag{9}$$

$$G(q) = \begin{bmatrix} (m_1+m_2)gL_1\sin(\theta_1) \\ m_2gL_2\sin(\theta_2) \end{bmatrix}. \tag{10}$$

This comprehensive model enables accurate simulation and serves as the foundation for designing the reinforcement learning controller [4, 5].

2.3 Human-Exoskeleton Interaction Modeling

The human-exoskeleton interaction is modeled as two parallel kinematic chains, each represented as a two-DoF manipulator. Assuming a rigid attachment between the human limb and the exoskeleton simplifies the formulation by making their joint angles and angular velocities identical, resulting in fully synchronized motion. Under this assumption, the combined Lagrangian of the system is expressed as:

$$L(q,\dot{q},t) = T_h(q,\dot{q}) + T_e(q,\dot{q}) - P_h(q) - P_e(q), \tag{11}$$

where T_h and T_e are the kinetic energies of the human and exoskeleton, and P_h and P_e are their potential energies. The corresponding motion equation becomes:

$$\frac{d}{dt}\frac{\partial L}{\partial \dot{q}_i} - \frac{\partial L}{\partial q_i} = \tau_{hi} + \tau_{ei} - B_i\dot{q}_i,\ i = (1,2,\ldots,n), \tag{12}$$

where B_i represents the resisting torque between the human and exoskeleton at joint i. In the case of flexible attachment, an interaction torque appears between the systems, expressed as:

$$\tau_{int} = K(q_h - q_e) + D(\dot{q}_h - \dot{q}_e), \tag{13}$$

where K and D are the stiffness and damping coefficients. Thus, the generalized dynamic equations describing both subsystems become:

$$\begin{cases} M_h(q_h)\ddot{q}_h + V_h(q_h, \dot{q}_h)\dot{q}_h + G_h(q_h) = \tau_h - \tau_{int} \\ M_e(q_e)\ddot{q}_e + V_e(q_e, \dot{q}_e)\dot{q}_e + G_e(q_e) = \tau_e + \tau_{int} \end{cases}. \tag{14}$$

These equations fully describe the coupled dynamic behavior of the human-exoskeleton system, capturing both kinematic constraints and the interaction forces acting between them.

3 Classical DDPG Controller Design Using RL

The control strategy for the R-LLE was initially developed using the Deep Deterministic Policy Gradient (DDPG) algorithm, a model-free, off-policy actor-critic reinforcement learning method well suited for systems with continuous action spaces. DDPG enables learning nonlinear control policies directly from interaction data without requiring an accurate dynamic model, making it attractive for complex human-robot systems.

3.1 Controller Architecture and NN Structures

The controller uses two neural networks: an actor that generates continuous torque commands for the motors, and a critic that evaluates the expected return (Q-value) for state-action pairs. The state vector includes the angles for each joint, their errors, and integrals, while the action vector consists of motor torque commands. The actor network receives the state vector, passes it through two fully connected hidden layers with 50 neurons and ReLU activation, and outputs two normalized torque commands using a *tanh* activation to constrain actions within $[-1, 1]$. The critic network has two input streams: states and actions. The state input passes through two hidden layers (50 and 25 neurons), while the action input passes through a 25-neuron layer. The merged outputs are refined through a shared hidden layer and produce a scalar Q-value. ReLU activation is used in all hidden layers. This architecture enables efficient policy learning and accurate value estimation for nonlinear continuous control.

3.2 Reward Function

The reward function was designed to encourage accurate tracking of the desired angles while penalizing deviations. It is mathematically expressed as:

$$R = 2^{-|q_r^\theta - q^\theta|} - 1, \tag{15}$$

where q_r^θ represents the desired angles for exoskeleton joints, and q^θ is the actual measured angles. This function produces high rewards for small errors and rapidly decreases as the deviation grows. The reward calculation was implemented as a Simulink subsystem based on simple blocks.

3.3 DDPG Training Process and Results

The neural controller was trained in the MATLAB/Simulink Simscape environment using a gait-tracking task under nominal user load. The training was performed using the following parameters: sampling time of 0.05 s, discount factor of 0.99, mini-batch size of 128, replay buffer length of 10^6, and a maximum of 10,000 training episodes. During training, experience replay was used to decorrelate samples, and separate target networks were employed for both the actor and critic to enhance stability. The networks were updated using mini-batch gradient descent following the standard DDPG learning procedure.

No variations in load were introduced during training. To evaluate the controller's performance across different users, the load was systematically increased by up to + 70% relative to the nominal value while the controller remained unchanged. As shown in Fig. 2, the controller follows the reference gait cycle under nominal conditions, but its performance deteriorates significantly as the load increases. The tracking error grows, and clear delays, amplitude reductions, and distortions in hip and knee trajectories are observed across three consecutive gait cycles. This demonstrates that a neural controller trained under fixed conditions lacks robustness and does not generalize well to users with different physical characteristics.

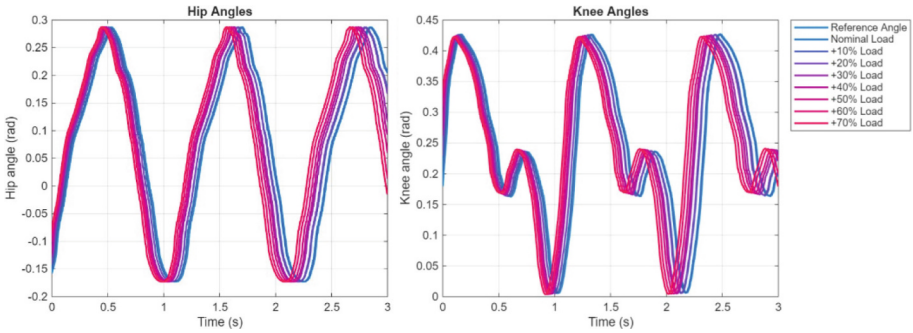

Fig. 2. Response of the neural controller under different user physical parameters

One possible solution to improve robustness is to retrain the agent while randomly varying user parameters, such as mass or joint lengths, during training. However, this approach greatly increases computational complexity and training duration. For example, fixed-parameter training requires approximately 4 h, whereas introducing even a single time-varying parameter substantially prolongs the training process due to the need to accumulate experience across multiple dynamic scenarios.

4 DDPG-Augmented MRAC (DAM Controller) Design for R-LLE

To address the poor robustness and limited generalization of a standalone DDPG controller under human parameter variability, this work introduces a hybrid intelligent control strategy for R-LLE. The proposed DDPG-Augmented Model Reference Adaptive

Control (DAM) controller combines the learning capability of DDPG with the real-time adaptation and stability of MRAC. By merging these strengths, the DAM controller adapts to changing user dynamics while preserving stability and ensuring reliable gait tracking across different users [6].

By combining these methods, the controller can adjust its behavior online using adaptation laws (MIT rule), while preserving the policy learned during training. This enables stable and accurate gait trajectory tracking even when user-specific physical parameters such as mass, joint lengths, or movement patterns vary significantly. Unlike classical RL-based control designs, the DAM controller does not require full retraining when system parameters change, making it more efficient and practical for real-world exoskeleton applications. The proposed architecture for the R-LLE gait control system is shown in Fig. 3. In this architecture, T_p represents the trajectory planner that generates the human gait reference signal μ_r, based on the selected operating mode S_r. The inverse kinematics matrix K_B transforms gait trajectories into desired joint angles q_r^θ. The joint angle controller C compares the desired and measured joint angles to generate control inputs. W_m models the motor dynamics, while E represents the exoskeleton dynamics, and H represents the human limb dynamics. The reference model W_{ref} provides the desired joint response characteristics, and the adaptive mechanism (AM) updates the control parameters in real time using MRAC. The neural network block (NN) represents the DDPG agent, which supplies the baseline control policy learned during training.

By leveraging both model-based adaptation and data-driven policy learning, the proposed DAM controller improves robustness, generalization, and adaptability for human-exoskeleton interaction control. This allows the system to maintain precise gait tracking across different users and varying movement conditions.

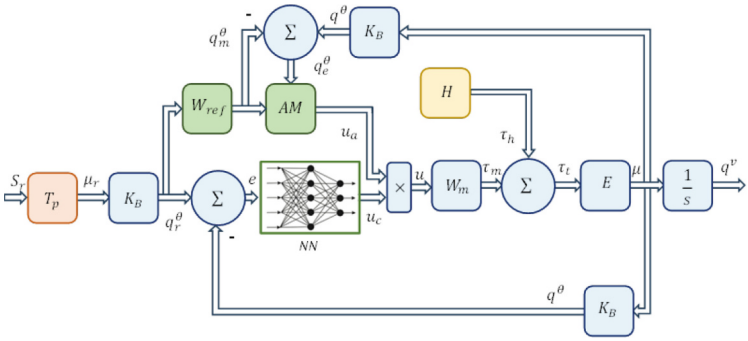

Fig. 3. Architecture of the proposed DDPG-Augmented MRAC (DAM Controller).

In this structure, the DDPG agent generates nominal control action u_c based on the observed state of the system, while an MRAC-based adaptive law generates an additional corrective signal u_a to compensate for any mismatch between the system dynamics and the reference model. The final control input u applied to the R-LLE motors is thus:

$$u = u_c \bullet u_a. \tag{16}$$

The control input in Eq. (16) uses a multiplicative combination of the RL-based policy and the MRAC adaptive signal. Unlike an additive structure, this formulation treats the adaptive term as a gain modulation of the learned control action, preserving the RL policy while compensating for modeling uncertainties and inter-subject variations. The multiplicative design also helps maintain bounded control actions, since the adaptive term adjusts the control effort proportionally rather than adding large corrective torques. Similar gain-modulation concepts are common in adaptive and robust control when integrating learning-based and model-based methods. In the proposed approach, the DDPG controller provides the main control policy, while the MRAC component modulates it to improve robustness across different users.

The MRAC component aims to minimize the tracking error $q_e^\theta = q_m^\theta - q^\theta$, where q^θ is the system state and q_m^θ is the reference model states. The adaptation law for the adaptive signal u_a is derived based on the MIT rule [7]. According to the MIT rule, the adaptation is driven by minimizing a cost function of the form:

$$J = \tfrac{1}{2}\left(q_e^\theta\right)^2, \tag{17}$$

leading to the adaptive law:

$$\dot{k} = -\gamma q_e^\theta \frac{\partial q_e^\theta}{\partial K}, \tag{18}$$

where: K is the adaptive gain vector, $\gamma > 0$ is the adaptation rate, and $\partial q_e^\theta / \partial K$ is the sensitivity derivative of the error with respect to the parameter K.

To evaluate the performance of the proposed DAM controller, three consecutive gait cycles were simulated for the nominal load and progressively increased user loads up to $+70\%$. The tracking behavior was compared against the standalone DDPG controller, as illustrated in Fig. 4, which shows the joint responses of the DAM controller under different user physical parameters. For each load condition, the root-mean-square error (RMSE) between the reference trajectory and the actual hip and knee joint angles was computed. The combined results are presented in Table 1, containing RMSE values for both joints.

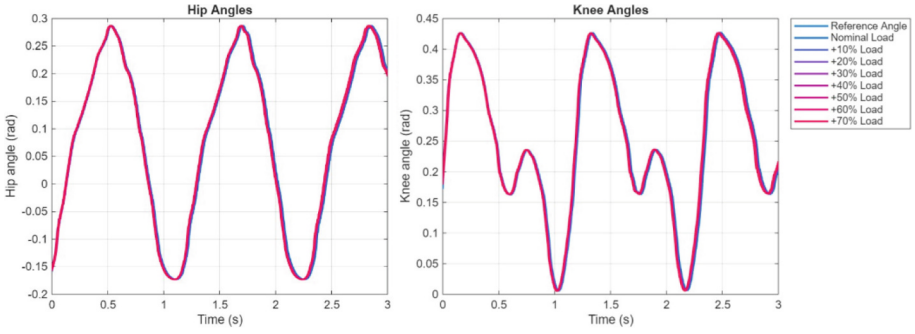

Fig. 4. Response of the DAM controller under different user physical parameters.

Table 1. Tracking Performance Under Inter-Subject Load Variations: DDPG vs. DAM

Load (%)	Hip Joint			Knee Joint		
	RMSE		Improvement (%)	RMSE		Improvement (%)
	DDPG	DAM		DDPG	DAM	
+10%	0.0382	0.0074	+80.6%	0.0316	0.0058	+81.6%
+20%	0.0420	0.0032	+92.4%	0.0355	0.0026	+92.7%
+30%	0.0670	0.0047	+93.0%	0.0579	0.0035	+93.9%
+40%	0.0789	0.0058	+92.7%	0.0693	0.0045	+93.5%
+50%	0.0919	0.0035	+96.2%	0.0821	0.0027	+96.7%
+60%	0.1069	0.0075	+92.9%	0.0985	0.0055	+94.4%
+70%	0.1183	0.0071	+94.0%	0.1120	0.0060	+94.6%

The standalone DDPG controller exhibits a clear decline in performance as load increases, showing growing delays, overshoot, undershoot, and distorted cycle shapes. In contrast, the DAM controller maintains stable and accurate tracking across all load variations. As shown in Table 1, the DAM controller reduces RMSE by approximately 80–97% for both hip and knee joints under all tested conditions, demonstrating substantially improved robustness and inter-subject adaptability. These results confirm that the adaptive MRAC component effectively compensates for user-dependent parameter changes, eliminating the need for retraining when switching between users.

5 Conclusion

This work presented an intelligent control system for rehabilitation lower-limb exoskeletons, supported by modeling and a high-fidelity simulation environment. While the DDPG controller performed well under nominal conditions, it showed sensitivity to changes in human physical parameters. To overcome this, a hybrid DDPG-Augmented MRAC (DAM) controller was proposed. Simulation results demonstrated that the DAM controller maintains stable and accurate gait tracking across all load variations without retraining. Quantitatively, the DAM controller reduced joint-tracking RMSE by 80–97% compared to the pure DDPG controller for both hip and knee joints under load increases of up to $+70\%$, confirming its superior robustness and inter-subject adaptability. Future work will incorporate joint misalignment, friction, and ground-contact dynamics, followed by experimental validation under strict safety constraints and medical device compliance.

References

1. Chauhan, A., Sangwan, P., Kumar, V., Cerqueira, J., Arya, R.K., Kumar, R.: A comprehensive review on lower-limb exoskeletons for rehabilitation and assistance. Robot. Auton. Syst. **167**, 104495 (2023)

2. Moosavi, M., Arami, A., Faraji, S., Kasaei, H.: Control strategies for lower-limb exoskeleton systems: a review. IEEE Trans. Neural Syst. Rehabil. Eng. **31**(1), 45–59 (2023)
3. Wang, W., Li, Z., Huang, Y., Wang, Y.: Kinematic modeling of lower-limb exoskeleton based on DH method and human motion analysis. IEEE Access. **9**, 78941–78954 (2021)
4. Mkhitaryan, A.L., Ulikyan, A.T., Khanamiryan, Z.G.: Design of non-linear exoskeleton foot system by gain scheduling method. Sci. Herit. Budapest. **88**, 74–81 (2022). https://doi.org/10.5281/zenodo.6532724
5. Mkhitaryan, A.L., Ulikyan, A.T., Muradyan, S.T., Khanamiryan, Z.G.: Design of two-linked robot manipulator adaptive control system by gain scheduling method. Proc. NPUA: Inf. Technol. Electron. Radio Eng. **1**, 64–75 (2022). https://doi.org/10.53297/18293336-2022.1-64
6. Khanamiryan, Z., Sargsyan, L.: Design of a DDPG-augmented MRAC (DAM Controller) for a differential drive mobile robot. In: (MES 2025) Mechanisms and Machine Science, vol. 191. Springer (2025). https://doi.org/10.1007/978-3-032-02352-0_30
7. Ioannou, P.A., Sun, J.: Robust Adaptive Control. Prentice Hall, Upper Saddle River (1996)

Gait Trajectory Planning for Biped Robots via LIPM and LPM Models

Refka Ajili[1(✉)], Badreddine Kribi[1,2], and Ajmi Houidi[1,2]

[1] University of Sousse, Mechanics Laboratory of Sousse, National Engineering School of Sousse, Sousse 4023, Tunisia
Refka.Ajili@eniso.u-sousse.tn, {badreddine.kribi, ajmi.houidi}@issatso.u-sousse.tn

[2] High Institute of Applied Sciences and Technology of Sousse, Sousse 4003, Tunisia

Abstract. This paper presents a mathematical framework for generating stable and smooth gait trajectories for bipedal robots. Traditional approaches using the Linear Inverted Pendulum Model (LIPM) often neglect the double-support phase, resulting in discontinuities in acceleration and impulsive forces during foot transitions. To address this, we propose a hybrid planning method that integrates the LIPM for the Single Support Phase (SSP) with a Linear Pendulum Model (LPM) for the Double Support Phase (DSP). This paper details the analytical formulation of both models, the geometric and dynamic boundary conditions required to ensure continuity, and the periodicity constraints necessary for stable cyclic locomotion. The resulting framework provides a computationally efficient method for generating Center of Mass (CoM) trajectories with continuous acceleration profiles.

Keywords: Trajectory Planning · Bipedal Locomotion · Hybrid Dynamics · LIPM · LPM · Gait Generation

1 Introduction

Humanoid robots represent a pivotal frontier in robotics, offering unparalleled potential for seamless operation within complex, unstructured environments designed for humans. Their anthropomorphic design enables advanced mobility capabilities, such as traversing stairs, stepping over obstacles, and navigating cluttered spaces, which remain challenging for wheeled or tracked systems [1]. However, realizing these potential hinges on overcoming the fundamental challenge of bipedal locomotion: generating stable motion for a high-dimensional, naturally unstable, and underactuated system [2].

A central difficulty lies in maintaining dynamic stability during motion. Stability is universally assessed using the Zero-Moment Point (ZMP) criterion, first proposed by Vukobratović [3]. For stable locomotion, the ZMP must strictly remain within the support polygon formed by the feet. Consequently, viable gait generation algorithms must produce Center of Mass (CoM) trajectories that satisfy this constraint.

Gait planning methods generally fall into two categories: trajectory optimization and model-based planning. Full-body trajectory optimization can produce highly dynamic

© The Author(s), under exclusive license to Springer Nature Switzerland AG 2026
A. Chaker et al. (Eds.): EFIMMS 2026, MMS 205, pp. 247–255, 2026.
https://doi.org/10.1007/978-3-032-22270-1_24

and natural motions by minimizing energy cost functions [4]. However, the computational complexity of high degree of freedom (DOF) optimization often precludes real-time adaptation. To enable real-time control, researchers predominantly rely on simplified models that reduce robot dynamics to a lower-dimensional space. The most widely adopted approach is the Linear Inverted Pendulum Model (LIPM), introduced by Kajita et al. [5]. By constraining the CoM to a constant height, the LIPM linearizes the dynamics, allowing for analytical solutions and efficient Model Predictive Control (MPC) implementation [6].

Despite its popularity, the standard LIPM formulation has a significant kinematic limitation: it assumes an instantaneous transfer of support from one foot to the other. In physical reality, stable walking requires a finite Double Support Phase (DSP) to transfer weight smoothly. Neglecting the DSP results in discontinuities in CoM acceleration at the moment of leg exchange. Physically, these discontinuities manifest as infinite jerk and impulsive Ground Reaction Forces (GRFs), which can cause foot slippage, mechanical stress, and instability [7].

Various methods have been proposed to smooth these transitions, such as using polynomial interpolation or spline-based trajectories during the DSP [8]. However, these kinematic fixes often lack dynamic consistency with the underlying physics of the robot. A more robust solution is to explicitly model the dynamics of the double-support phase.

This paper presents a unified trajectory planning framework that integrates the LIPM with a Linear Pendulum Model (LPM), as proposed in recent hybrid frameworks [9]. By stitching the "falling" dynamics of the LIPM (during single support) with the stable "swinging" dynamics of the LPM (during double support), we derive a unified mathematical framework.

2 Robot Kinematic Modeling

To validate the proposed planning framework, we model a 12-degree-of-freedom (DOF) bipedal robot (Fig. 1). This section details the kinematic structure and physical parameters used in the study.

2.1 Kinematic Structure

The bipedal robot is modeled with a central torso acting as a floating base and two identical 6-degree-of-freedom (DOF) legs. To provide a more intuitive understanding of the robot's motion and to align the model with human biomechanics, the joint configuration of each leg is expressed using standard anatomical terms. From the hip to the foot, the joint sequence consists of hip internal/external rotation, hip abduction/adduction, and hip flexion/extension. These are followed by knee flexion/extension, ankle dorsiflexion/plantarflexion, and finally ankle inversion/eversion. This anatomical mapping ensures that the generated trajectories are biologically inspired and facilitates the visualization of the robot's gait patterns in relation to human locomotion. Forward kinematics are derived using the Denavit-Hartenberg (DH) convention (Table 1). The homogeneous transformation matrices allow us to compute the precise position and orientation of the foot relative to the hip, which is essential for the Inverse Kinematics solver.

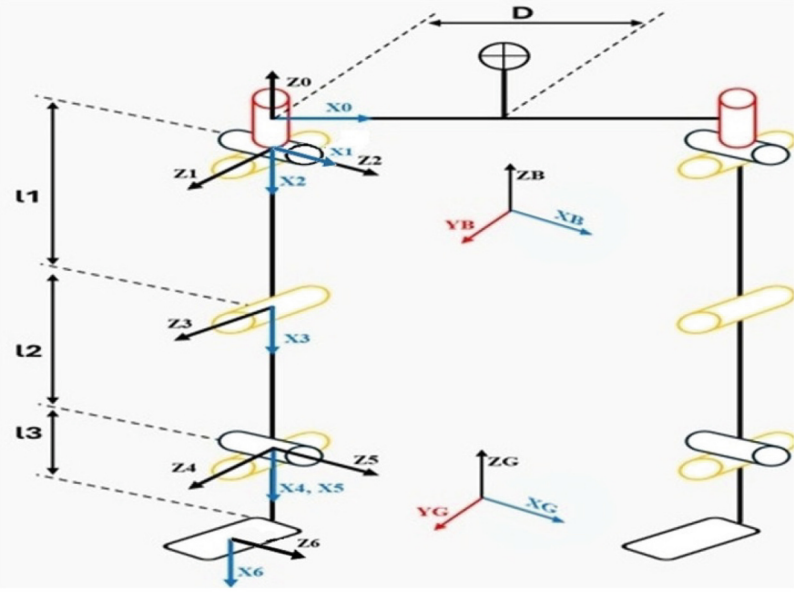

Fig. 1. Kinematic diagram of the robot with joint axes.

Table 1. The Denavit-Hartenberg (DH) parameters for a bipedal robot

Articulation i	a_i	α_i	d_i	θ_i
1	0	$\frac{\pi}{2}$	0	q_1
2	0	$-\frac{\pi}{2}$	0	$q_2 - \frac{\pi}{2}$
3	l_1	$\frac{\pi}{2}$	0	q_3
4	l_2	0	0	q_4
5	0	$-\frac{\pi}{2}$	0	q_5
6	l_3	0	0	q_6

3 Hybrid Trajectory Planning Methodology

3.1 Modeling Assumptions

To derive analytical solutions for the trajectory, we decouple the sagittal (forward) and lateral (sideways) motions and apply the following assumptions:

- The robot is modeled as a point mass concentrated at the CoM.
- The CoM moves at a constant height h_s during the single-support phase.
- The equations of motion for the sagittal (x) and lateral (y) planes are independent.

3.2 Single Support Phase (LIPM)

During the Single Support Phase (SSP), denoted as the path from A_k to B_k in Fig. 2, the robot pivots over the stance leg (O_k). The dynamics are governed by the LIPM equation, describing an unstable equilibrium:

$$\ddot{x} = \frac{g}{h_s}x(t) = \frac{1}{T_s^2}x(t) \tag{1}$$

where:

- $x(t)$ is the horizontal position of the CoM relative to the stance ankle (the pivot point).
- $\ddot{x}$ (t) is the horizontal acceleration of the CoM.
- g is the acceleration due to gravity.
- h_s is the constant height of the CoM above the ground.
- $T_s = \sqrt{\frac{h_s}{g}}$ is the time constant of the inverted pendulum.

The general solution to this equation is given by:

$$x(t) = x(0)\cosh\left(\frac{t}{T_s}\right) + T_S\dot{x}(0)\sinh\left(\frac{t}{T_s}\right) \tag{2}$$

This phase represents the natural "falling" motion of the robot and is active for the duration $0 \leq t \leq T_{SSP}$.

3.3 Double Support Phase (LPM)

To bridge the gap between steps (path B_k to A_{k+1}), the Double Support Phase (DSP) is modeled using the Linear Pendulum Model (LPM). Here, the CoM is treated as if suspended from a Virtual Suspension Point (S_k) located at height h_d above the CoM. The equation of motion becomes:

$$\ddot{x} = -\frac{g}{h_d}x(t) = -\frac{1}{T_d^2}x(t), \;\; T_d = \sqrt{\frac{h_d}{g}} \tag{3}$$

where $x(t)$ is the horizontal position of the CoM, S_k is horizontal position of the CoM relative to the virtual suspension point which is located midway between the two support feet, h_d is the effective height of the virtual suspension point and T_d is the time constant of the linear pendulum.

The solution describes stable oscillatory motion:

$$x(t) = x(0)\cos\left(\frac{t}{T_d}\right) + T_d\dot{x}(0)\sin\left(\frac{t}{T_d}\right) \tag{4}$$

where $x(0)$ and $\dot{x}(0)$ are the initial state at the beginning of the DSP.

Crucially, the acceleration here opposes the displacement, acting to decelerate the CoM from the previous step and redirect it toward the next support foot (O_{k+1}).

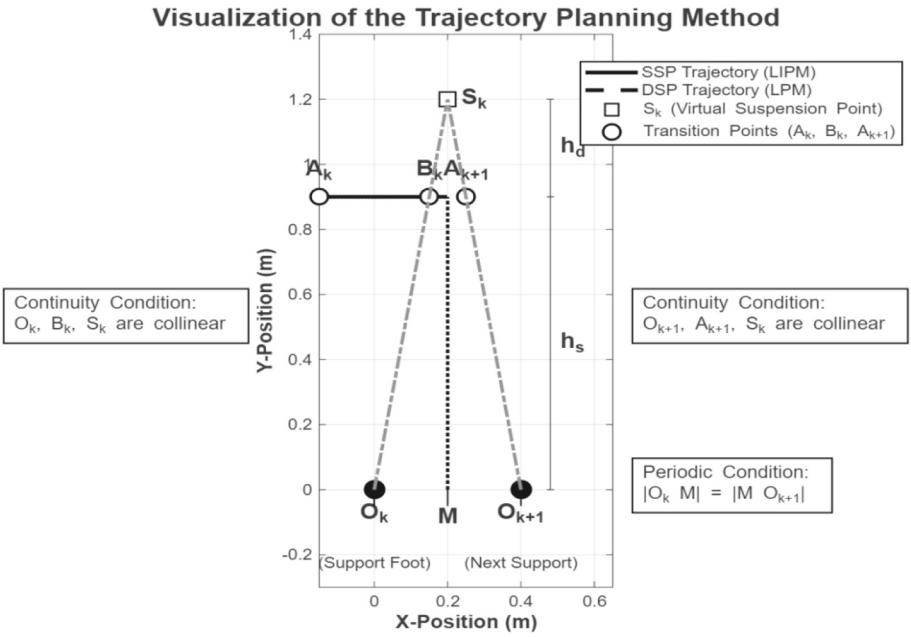

Fig. 2. Visualization of the LIPM-LPM trajectory planning method

3.4 Geometric and Dynamic Continuity

The core contribution of this method is the seamless stitching of these equations. As illustrated in (Fig. 2), mathematical continuity (C^1) implies specific geometric conditions:

- **State Continuity:** The kinematic state at the transition point B_k must be identical for both models:

$$x_{LIPM}(T_{SSP}) = x_{LPM}(0) \tag{5}$$

$$\dot{x}_{LIPM}(T_{SSP}) = \dot{x}_{LPM}(0) \tag{6}$$

- **Collinearity Condition:** For the transition to be dynamically smooth (continuous acceleration), the Ground Reaction Force vector must not change direction instantaneously. This requires that the support foot O_k, the transition point B_k, and the virtual suspension point S_k must be **collinear** at the switching moment. Similarly, at the end of the DSP ($A_k + 1$), the points $O_k + 1$, $A_k + 1$, and S_k must also align.

3.5 Periodicity and Analytical Initialization

For stable, steady-state walking, the gait must be periodic. We enforce Geometric Symmetry, as shown by point M in (Fig. 2). The virtual suspension point S_k s placed exactly

vertically aligned with the midpoint M between the two feet ($|O_kM| = |MO_{k+1}|$).To initialize the planner, we define a target Apex Velocity (v_{apex}), which is the desired speed of the CoM when it passes directly over the stance foot. We analytically derive the required initial state (x_{A0}, v_{A0}) for the SSP to guarantee this apex velocity:

$$v_{A0} = v_{apex} \cosh\left(\frac{T_{SSP}}{2T_s}\right) \tag{7}$$

$$x_{A0} = -T_s v_{A0} \tanh\left(\frac{T_{SSP}}{2T_s}\right) \tag{8}$$

This analytical initialization ensures the robot naturally enters a stable limit cycle from the very first step, following the symmetric path visualized in Fig. 2.

4 3D Extension and Foot Trajectory

To achieve practical 3D locomotion, the planar planning is extended to the lateral plane and combined with swing foot generation.

4.1 Swing Foot Trajectory

The swing foot trajectory is generated kinematically to move from the previous stance position to the next.

- **Horizontal (x):** A cubic polynomial interpolates the position, ensuring zero velocity at lift-off and touch-down to minimize impact.
- **Vertical (z):** A cycloidal profile is used for clearance:

$$z_{swing} = R(1 - \cos(2\pi\tau)) \tag{9}$$

where R: The foot clearance parameter R = 0.05 m results in a maximum foot lift of 2R = 10 cm, which is a practical and realistic height to clear small, unmodeled obstacles on a flat floor while minimizing energy expenditure.

This shape guarantees smooth lift and landing phases with zero vertical impact velocity (Fig. 3).

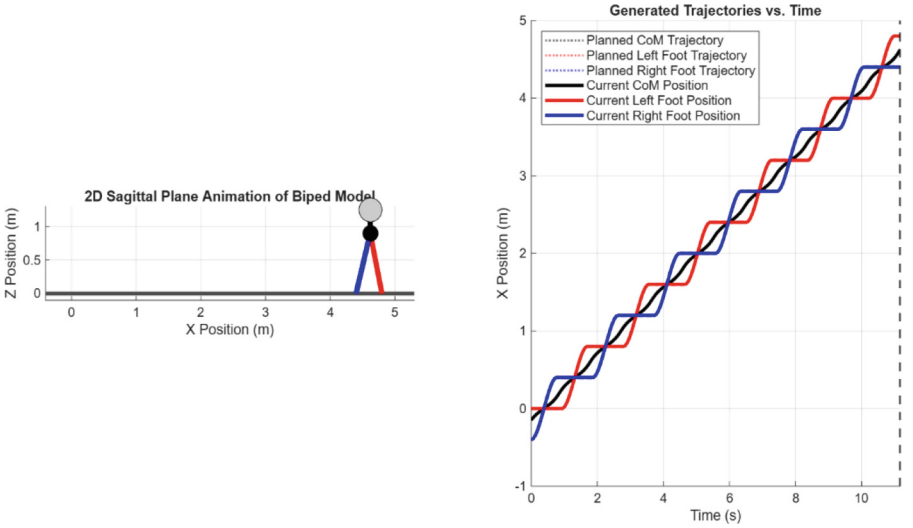

Fig. 3. COM and foot position in X, Z-directions

4.2 Lateral CoM Motion

This shape guarantees smooth lift and landing phases with zero vertical impact velocity. The lateral motion $y(t)$ prevents the robot from tipping sideways. It is modeled as a harmonic oscillator synchronized with the step period T_{step}:

$$y_{com}(t) = D_{hip}\cos(\omega t + \phi) \tag{10}$$

Where D_{hip} is the lateral amplitude determined by the hip width, $\omega = 2\pi/T_{step}$ is the frequency, and ϕ is a phase shift ensuring the CoM is fully shifted over the stance foot during single support phase.

4.3 Gait Parameters and Simulation

The framework was validated in MATLAB (Fig. 4) using the following gait generation parameters (Table 2):

Table 2. Gait parameters.

Parameter	Value	Description
Step Length (L)	0.4 m	Distance between footsteps
LIPM Height (h_s)	0.9 m	Height during single support
LPM Height (h_d)	0.3 m	Virtual height during double support
Apex Velocity	0.5 m/s	Target speed

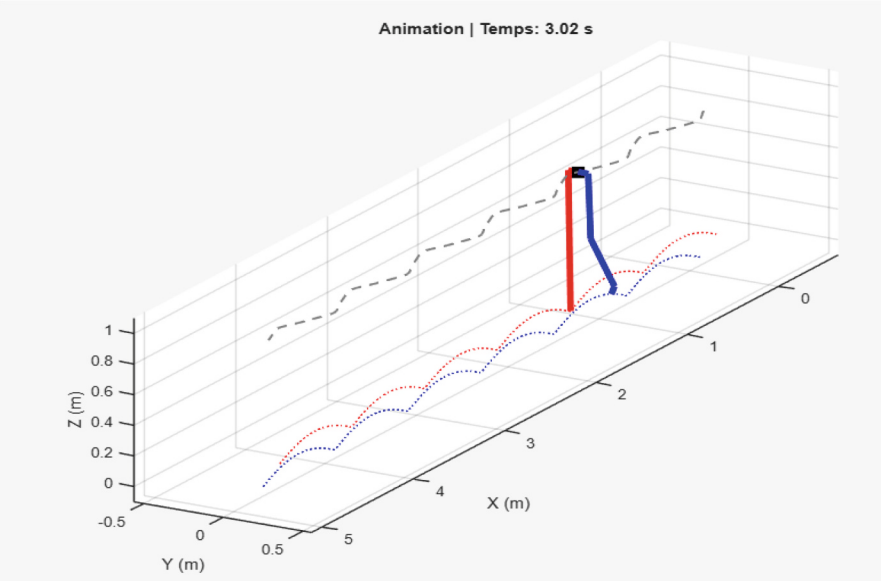

Fig. 4. Snapshots of the simulated bipedal walking gait, showing the transition from left leg support to right leg support. The dashed gray line indicates the CoM trajectory.

5 Conclusion

This study presented a unified mathematical framework for bipedal gait trajectory planning. By integrating the Linear Inverted Pendulum Model (LIPM) and the Linear Pendulum Model (LPM), we successfully addressed the acceleration discontinuity problem inherent in standard gait planners. The explicit modeling of the Double Support Phase results in smooth load transfers. The analytical formulation allows for real-time generation of trajectories that are symmetric, periodic, and dynamically stable.

References

1. Hirai, K., Hirose, M., Haikawa, Y., Takenaka, T.: The development of Honda humanoid robot. In: Proceedings 1998 IEEE International Conference on Robotics and Automation, vol. 2, pp. 1321–1326, Leuven, Belgium (1998)
2. Grizzle, J.W., Chevallereau, C., Sinnet, R.W., Ames, A.D.: Models, feedback control, and open problems of 3D bipedal robotic walking. Automatica. **50**(8), 1955–1988 (2014)
3. Vukobratović, M., Borovac, B.: Zero-moment point—proper interpretation and new applications. Int. J. Humanoid Rob. **1**(01), 157–173 (2004)
4. Kuindersma, S., et al.: Optimization-based locomotion planning, estimation, and control design for the atlas humanoid robot. Auton. Robot. **40**(3), 429–455 (2016)
5. Kajita, S., Kanehiro, F., Kaneko, K., Yokoi, K., Hirukawa, H.: The 3D linear inverted pendulum mode: a simple modeling for a biped walking pattern generation. In: Proceedings 2001 IEEE/RSJ International Conference on Intelligent Robots and Systems, pp. 239–246, Maui, HI, USA (2001)

6. Wieber, P.B.: Trajectory free linear model predictive control for stable walking in the presence of strong perturbations. In: 2006 6th IEEE-RAS International Conference on Humanoid Robots, pp. 137–142, Genova, Italy (2006)
7. Kajita, S. et al.: Biped walking pattern generation by using preview control of zero-moment point. In: IEEE International Conference on Robotics and Automation (ICRA 2003), pp. 1620–1626. IEEE, Taipei (2003)
8. Park, J.H., Kim, K.D.: Biped robot walking using gravity-compensated inverted pendulum mode and computed torque control. In: IEEE International Conference on Robotics and Automation (ICRA), pp. 3528–3533. IEEE, Pasadena (1998)
9. Li, L., Xie, Z., Luo, X., Li, J.: Trajectory planning of flexible walking for biped robots using linear inverted pendulum model and linear pendulum model. Sensors. **21**(4), 1082 (2021)

Automated GPU Code Generation for Rigid-Body Simulations Using SYMKIN Symbolic Optimizer

Louis Guigon[1(✉)], Benjamin Boudon[2], Youcef Mezouar[2], Chedli Bouzgarrou[2], and Andrés Kecskeméthy[1]

[1] Chair of Mechanics and Robotics, University Duisburg-Essen, Lotharstr. 1, 47057 Duisburg, Germany
{louis.guigon,andres.kecskemethy}@uni-due.de
[2] Institut Pascal, CNRS, University Clermont Auvergne, Clermont Auvergne INP, 63000 Clermont-Ferrand, France
{benjamin.boudon,youcef.mezouar,belhassen-chedli.bouzgarrou}@sigma-clermont.fr

Abstract. With the increasing need of simulators to compute the dynamics of complex mechanisms, parallel processors are investigated to boost the code execution and respect real-time constraints. However, the programming and code optimization of parallel processors is non-trivial and requires the consideration of several parameters. On Graphic Processing Units (GPU), rules, implementation strategies and considerations are case dependent and have to be considered by programmers. This overload of considerations is discussed in the presented work and a symbolic code generator SYMKIN GPU is proposed to help mechanical engineers to simulate rigid-body dynamics in real-time leveraging GPU parallelization without spending time to optimize the GPU code. The generation process is detailed with the specific case of 2D serial chains parallelized on GPU using NVIDIA CUDA API. Presented as a base foundation for later developments, attention is ported to modularity in order to handle other cases in later contributions such as tree forms and loops. Various options are programmed to satisfy a large range of applications, such as code generation for prototyping or real-time applications with portability of the code to other computers or devices.

Keywords: Real time simulation · GPU parallelization · Kinematics and Dynamics compiler · lenient computations

1 Parallelization Constraints

Coding habits for serial processors has been associated to the necessity of minimizing the number of instructions that compose a program. Parallel processors disrupt these programming habits, bringing new parameters that need to be taken into account such as the number of available processors, the memory size and bandwidth. In the reference paper for parallel computing in multibody system dynamics [1], the conclusion details that parallel software design is not trivial as the structures are not organized as the problem logic anymore, but rather

© The Author(s), under exclusive license to Springer Nature Switzerland AG 2026
A. Chaker et al. (Eds.): EFIMMS 2026, MMS 205, pp. 256–263, 2026.
https://doi.org/10.1007/978-3-032-22270-1_25

in a way that benefits to the parallel performance. This reformulation blurs the mechanical logic of the code for something more digital that complicates the programming session. A major constraint in programming on GPUs is the amount of parameters to take into account when optimizing a code. For instance, to parallelize some threads in a GPU function, called kernel, programmers have to define how the parallel threads will be handled by internal schedulers. To do so, the threads are grouped into blocks, but it is the work of the programmer to determine if the GPU should deal with one block of N threads, N blocks of one thread or something in between. Even if NVIDIA released occupancy tables to help on this choice, the optimal code is obtained from experiments while tracking processing time for each possibility. This example handles the choice of one of several other parameters which complicates the programming phase as described in details in [2]. In the scope of the work, a compiler is designed using the SYMKIN (SYMbolical KINematics) Mathematica Package to find the optimal code for the simulation of rigid body mechanisms for their GPU execution while asking only a description to the user [3,4]. This algorithm has been designed to ease the coding and optimization process, which was done by hand until then. The optimization framework combines mechanical modeling and implementation strategies to produce GPU-accelerated simulations. It incorporates a method referred to as lenient computation, which relaxes strict sequential dependencies by introducing controlled estimation errors [5,6]. This approach enables significantly higher parallel throughput while maintaining numerical accuracy, with errors remaining negligible relative to traditional schemes such as explicit Euler integration.

An overview of the code generation is shown on Fig. 1 and described in the following sections.

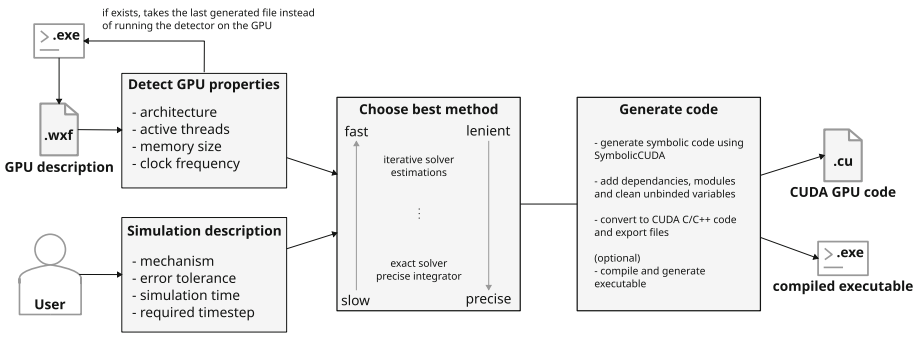

Fig. 1. Overview of the SYMKIN GPU compiler

2 Simulation Description in SYMKIN

Originally designed for serial processing optimizations, SYMKIN development have introduced automatic code generation for simulators and pipelining opti-

mizations on CORDIC boards [7] using Mathematica's benefits of symbol manipulation. In the context of the paper, a package has been designed, following its predecessors, to generate CUDA GPU code.

The SYMKIN core is first used to sort mechanisms on their topology: it detects serial chains, tree forms with branching joint locations and loop systems with the number of loops and connecting joint locations. This sorting tasks is required to extract maximum parallelism out of the topology. The original method used by SYMKIN to analyze the mechanism is to read its description in a *frame connectivity matrix*. As presented on Fig. 2, the matrix ease the process of detecting the topology and the dimension in which the mechanism is represented. The matrix should be read as the line i corresponds to frame $\mathcal{K}_i$ and the column j corresponds to frame $\mathcal{K}_j$. then, the element $FDM(i,j)$ is the connection between frame $\mathcal{K}_i$ and $\mathcal{K}_j$ described by 0 if they are not connected, and the transformation A_{ij} otherwise. While the current state of the parallelization handles only serial chains, the compiler is thought to facilitate the later addition of tree forms and loops.

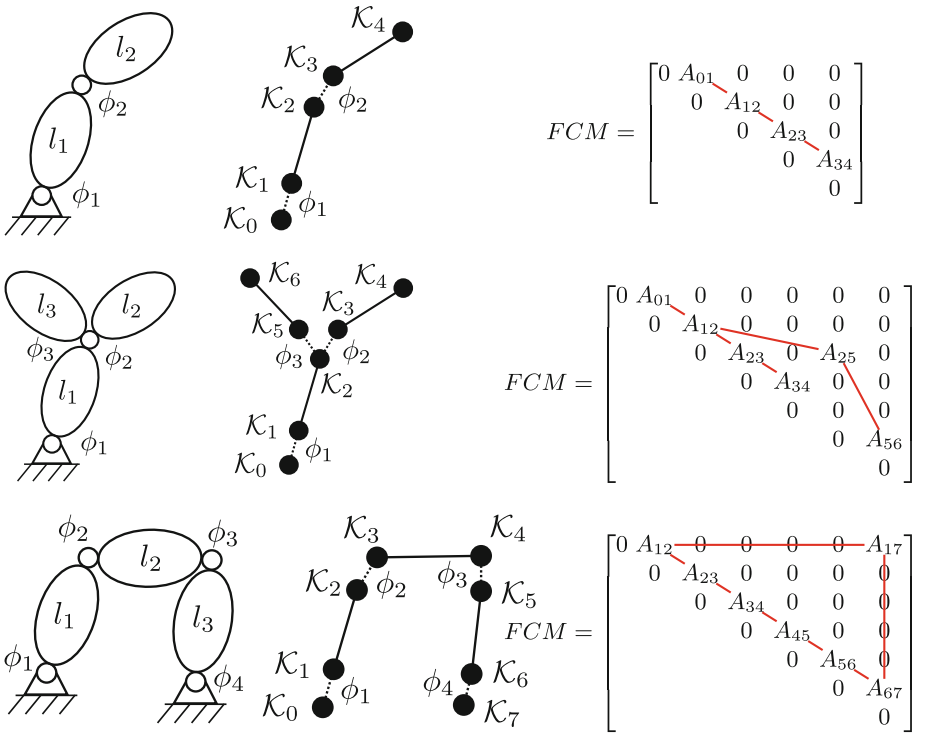

Fig. 2. Frame connectivity matrices patterns for topology detection

3 GPU Device Properties

The optimization process requires a description of the GPU on which the simulation will be held. This description contains for instance the number of physical processors, available memory on different layers such as the global VRAM or the amount of shared memory per block. Each of these parameters affect the programming strategy and thus the final performance. While the code generation is currently designed for only one NVIDIA GPU using CUDA tools [8], the detection program gets the information from all available GPUs and let the user select one for the simulation. Later implementations can consider optimizing for more than one GPU.

This task is performed using a report file generated using a portable program given by SYMKIN. This task is programmed in two ways: either fully-automated for which SYMKIN generates, compiles and runs the detection program on its own, or in portable version. The benefit of a portable program is to run it on external computers like, for instance, an embedded NVIDIA Jetson board on a mobile robot.

4 Selection of Methods

4.1 Selection Criteria

The final purpose of the discussed algorithm is to make the decision regarding the optimal parameters that guarantee optimal code. While programming rules are implemented as for the choice of blocks and threads discussed in the introduction, pending work on leniency rules and accuracy is still under research and requires the current version of SYMKIN to accelerate the experimental validation.

4.2 Optimization Modes

The design of dynamics algorithms is generally meant for two purposes: real-time control and simulations, where the code must be fast and optimized, or research purposes where the code is opened for add-ons and modifications.

real-time mode this mode generates a hard-coded and lightweight code which is the best choice to process the dynamics of a specific mechanism. It removes dynamic allocations for modifiable user inputs, profiling options and minimizes CPU-GPU exchanges. While this version is meant to fast processing and on-line control of robots, any change in the code will require to compile again.

research mode this mode is used for an off-line computation of the dynamics. This is a dynamic allocation version which permits the modification of initial conditions, chain length and other parameters. This flexible code is meant for simulation and analysis but is in general slower than the real-time mode as it contains additional add-ons such as time measurement, data export and debbuging options. This case is helpful for SYMKIN further developments and for testing or prototyping.

5 GPU Code Generation and Optimization

Once the parameters are analyzed and the optimal options are found, the code generation begins. A symbolic version of the code is first generated using SymbolicCUDA, a code generation package designed for the current application and extending the philosophy of Mathematica's SymbolicC package [9]. SymbolicCUDA offers a better handling of symbols and objects in different contexts and takes into account the CUDA C/C++ programming routines, including CPU and GPU code distribution.

The symbolic representation of the code is efficient to manipulate pieces of code and arrange them. As shown on Fig. 3, encapsulation of Mathematica symbols gives the possibility to arrange code locally. For instance in the figure, the time profiling of two variable declaration and a kernel is done using `cuGetTime[]`. When converting symbols to CUDA code, the generator understands the order and adds all the required elements to perform the time measurement. Conversely, the generator is capable to detect and remove useless commands, such as the declaration of `var2` which has been initialized but not used. Finally, general routines

```
(* Mathematica code to ask the time measurement of "myKernel" *)
cuGetTime[
    cuAssign[cuDeclare[double, var1],0];
    cuAssign[cuDeclare[int   , var2],1];
    cuKernelCall["myKernel",{var1},...];
] // AssembleCUDACode

/* resulting CUDA code automatically generated by SymbolicCUDA */
#include <cuda.h>
#include <stdio.h>

cudaEvent_t start, end;
float ms = 0.0f;

cudaEventCreate(&start);
cudaEventCreate(&stop);

cudaEventRecord(start);
    double var1 = 0;
    myKernel<<<...>>>(var1);
cudaEventRecord(stop);

cudaEventSynchronize(stop);

cudaEventElapsedTime(&ms, start, stop);
printf("%0.6f",ms);

cudaEventDestroy(start);
cudaEventDestroy(stop);
```

Fig. 3. Comparison of the Mathematica input and the generated CUDA code output

are automated, such as adding the includes. These automated process works as a list which is updated when calling specific symbols. For instance, `cuGetTime[]` calls `cuPrint[]` internally which will add the `printf` function but also adds `<stdio.h>` to the include list if not yet inside. Later, the code assembler will generate the `#include` commands for each member of the list.

Other customization options are available such as data export in `.csv` files or live visualization using OpenGL GPU graphics rendering.

6 Output

Currently, the generator can output the CUDA code folder with dependancies if the user wants to read or modify kernels but can also compile automatically using the NVIDIA CUDA "nvcc" compiler. Another portable alternative is the addition of a command script like a `.bash` file on Linux systems to compile the code on external computers.

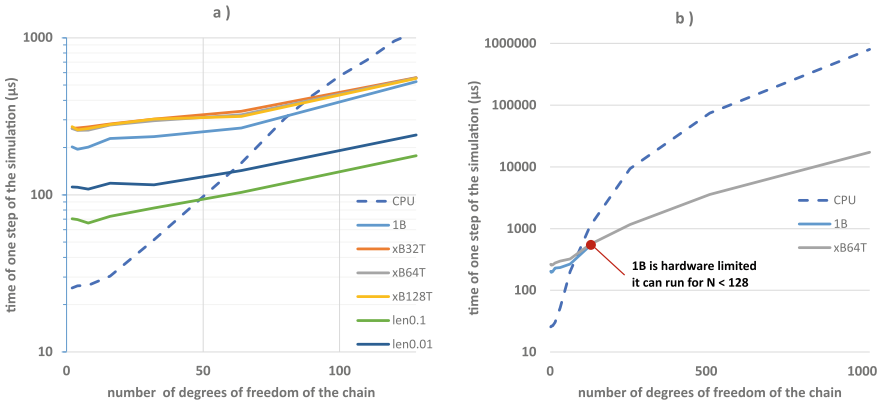

Fig. 4. Time efficiency of generated codes for different input parameters

7 Conclusion and Results

The SYMKIN GPU package is designed to help on the choice of algorithms required for efficient simulations. The theory behind GPU optimization for dynamics simulation has been discussed in [5,6] and further investigated in upcoming papers for complex topologies. The SYMKIN GPU package is a helper which automates the decision process to get an efficient algorithm for GPU processing of a rigid-body dynamics application.

Figure 4 shows the performance of available algorithms for the simulation of 2D serial chains given user defined initial conditions on a NVIDIA RTX 4060

Ti GPU. Figure 4.a shows the time comparison between GPU codes identified as $1B$ for the exact simulation with one block of threads, $xByT$ for multiple-blocks where y stands for the number of threads allocated in a block. Then, *len* stands for the lenient simulation where the following number corresponds to the maximum percentage of error induced compared to the error generated by an explicit Euler integration to a Runge Kutta 4. The last curve CPU is the serial implementation of the method. The current state of the program is not able to deal with accuracy when asking for lenient computations, but further research is in progress to take rules into account for error tolerance. Once implemented, the package will be able to propose faster GPU codes depending on the user defined error tolerance on the result.

On Fig. 4.b, larger chains are shown to highlight the necessity of switching methods: while $1B$ performs well until 128 joints in the chain, the way it is programmed prevents it to run for larger chains. The generator will then switch for xB methods after 128 joints and another switch is required for 8192 joints. These limitations are related to shared memory and maximum limits imposed for blocks and threads which are indicated in the GPU property file.

The presented work is the foundation of the targeted code generator, where SymbolicCUDA and symbol handling functions have been designed to satisfy the 2D serial chain case, but they are flexible to ease the development of other topologies.

Acknowledgments. This work was supported by the International Research Center "Innovation Transportation and Production Systems" of the I-SITE CAP 20-25.

References

1. Negrut, D., Serban, R., Mazhar, H., Heyn, T.: Parallel computing in multibody system dynamics: why, when, and how. J. Comput. Nonlinear Dyn. **9**(4), 041007 (2014)
2. Klöckner, A., Pinto, N., Lee, Y., Catanzaro, B., Ivanov, P., Fasih, A.: PyCUDA and PyOpenCL: a scripting-based approach to GPU run-time code generation. Parallel Comput. **38**(3), 157–174 (2012)
3. Kecskemethy, I.A., Krupp, T.: Application of Symbolical Kinematics to Real-Time Vehicle Dynamics (No. FG169502). (1995)
4. Kecskemethy, A., Krupp, T., Hiller, M.: Symbolic processing of multiloop mechanism dynamics using closed-form kinematics solutions. Multibody Sys. Dyn. **1**(1), 23–45 (1997)
5. Guigon, L., Rosaz, P., Boudon, B., Mezouar, Y., Bouzgarrou, C., Kecskeméthy, A.: A case study on parallelization of multibody dynamic equations for graphic processing units (GPUs) in real-time simulations- the planar nR serial chain. In: Proceedings of the 7^{th} International Conference on Multibody System Dynamics. Madison, WI, USA (2024)
6. Guigon, L., Boudon, B., Mezouar, Y., Bouzgarrou, C., Kecskeméthy, A.: Boosting GPU parallelization for Real-Time Multibody simulations using leniency: case study of forward dynamics of a planar serial chain. In: Proceedings of the 12^{th} ECCOMAS Thematic Conference on Multibody Dynamics. Innsbruck, Austria (2025)

7. Krieger, C., Hosticka, B., Krupp, T., Hiller, M., Kecskeméthy, A.: A combined hardware/software approach for fast kinematic processing. Microprocess. Microsyst. **22**(5), 263–275 (1998)
8. NVIDIA Corporation. NVIDIA: CUDA Toolkit Documentation. (2025)
9. Papegay, Y. Industrial C code generation, SymbolicC : a C wrapper. In Wolfram Technology Conference, Champaign, Illinois, USA (2006)

Motion Simulation for the Anatomical Reconstruction of Facial Muscles and Skulls with a Spherical 3D Printer

Lucian-Mihai Micle[1(✉)], Elida Tulcan[1], Carmen Sticlaru[1], Alexandru Oarcea[1], and Erwin-Christian Lovasz[1,2]

[1] Politehnica University of Timisoara, Bvd. Mihai Viteazu 1, Timisoara 300222, Romania
{lucian.micle,alexandru.oarcea}@student.upt.ro, {elida.tulcan, carmen.sticlaru,erwin.lovasz}@upt.ro
[2] Technical Sciences Academy of Romania, 26 Dacia Blvd, Bucharest 030167, Romania

Abstract. Advances in 3D printing have enabled new interdisciplinary applications in archaeology and forensic sciences. This paper presents the design and kinematic formulation of a customized spherical 3D printer developed for reproducing human skulls and facial muscles based on digital facial reconstruction. The complete forward and inverse kinematic models are derived using Denavit–Hartenberg parameters to define the positional configuration of the printer head.

A key contribution of this work is the slicer software generation of toolhead trajectories for printing reconstructed facial muscles with complex curvature. The trajectory of the spherical printer head is dynamically adapted to the anatomical surface geometry, ensuring accurate material deposition on concave and convex regions. The printer also features a modified spherical hotbed optimized for skull and muscle reconstruction. The proposed system supports more efficient and anatomically faithful fabrication, contributing to improved visualization and preservation of human remains in archaeological and forensic contexts.

Keywords: 3D printing · facial reconstruction · additive manufacturing · kinematic positional analysis · motion simulation

1 Introduction

3D printing has become an important tool in archaeology and forensic science, where it is increasingly used to replicate fragile artifacts, skeletal remains, and reconstructed human skulls for research, preservation, and public presentation. In facial reconstruction, additive manufacturing enables the physical realization of digital skull and soft-tissue models, supporting both scientific analysis and cultural interpretation. However, when printing highly curved anatomical structures with conventional planar-layer 3D printers, large amounts of material are wasted due to extensive support structures and fully filled layers that poorly follow organic geometries.

Recent reviews of additive manufacturing (AM) [1–3] document rapid advances in materials, hardware, and software, allowing AM to expand beyond prototyping into fields

© The Author(s), under exclusive license to Springer Nature Switzerland AG 2026
A. Chaker et al. (Eds.): EFIMMS 2026, MMS 205, pp. 264–273, 2026.
https://doi.org/10.1007/978-3-032-22270-1_26

such as aerospace, healthcare [4], and archaeology. Contemporary 3D printers employ a wide range of architectures, including Cartesian, SCARA, Delta, cylindrical, spherical, cable-driven, and multi-axis systems. Cartesian FDM printers remain dominant due to their simplicity and ease of calibration, with ongoing architectural improvements such as the CoreH-bot design proposed by Idà et al. [5] and speed-oriented developments described by Consalvi [6]. Alternative architectures—including SCARA [7], Delta [8], cylindrical [9], spherical [10, 11], cable-driven [12], and multi-axis systems [13]—address limitations related to workspace, speed, accessibility, and support requirements.

Despite these advances, general-purpose 3D printers are often ill-suited for anatomical reconstruction tasks. Printing skulls and facial structures demands high geometric fidelity, efficient handling of complex meshes, and material deposition strategies that conform to curved surfaces without excessive waste. Planar slicing approaches inherently struggle with such requirements, motivating the exploration of non-Cartesian architectures and geometry-aware toolpaths.

Facial reconstruction itself has a long history, dating back to 19th-century anatomical studies by researchers such as Hermann Welcker, who compared skulls with portraits and death masks to assess morphological correspondence. Modern reconstruction methods are commonly categorized into 2D and 3D approaches and include established manual techniques such as the anatomical (Russian), anthropometric (American), and Manchester (British) methods [14–16], now largely supported by digital modeling tools.

Within this context, the present paper introduces a specialized spherical-coordinate 3D printer designed for fabricating reconstructed skulls and facial muscle structures derived from digital facial reconstruction and scanning of human remains. By aligning printer kinematics and trajectory generation with the natural geometry of anatomical forms, the proposed system aims to reduce material waste, improve deposition on curved surfaces, and enhance the physical accuracy of archaeological and forensic reconstructions.

2 Kinematic-Positional Analysis of the Spherical 3D Printer

For facial reconstruction printing, it is advantageous to replace the conventional planar hotbed with a half-spherical build surface. To support this requirement, we propose a spherical 3D printer architecture in which the build platform provides two rotational degrees of freedom for orientation, while the printing head combines a translational axis with an additional rotational motion in the vertical plane [23]. This configuration enables the extruder to reach complex anatomical regions and to deposit material accurately across curved geometries.

The resulting system is a purpose-built 3D printer engineered specifically for high-detail anatomical fabrication, designed from the ground up for reliability and precision. Its mechanical architecture prioritizes accurate motion control, material flexibility, and structural stability, all optimized for printing directly onto spherical or sphere-like surfaces. This section presents an overview of the primary mechanical components that enable these capabilities.

The overall architecture of the printer can be described as comprising two main sections: a lower body, consisting of two components (labeled 1 and 2 in Fig. 1), and an

upper body, consisting of two additional components (labeled 3 and 4 in Fig. 1). Both sections are supported by a common frame, identified as element 0.

Element 1 is connected to frame 0 and actuated by the first motor, enabling a roll rotation about the Y_0 axis, designated as θ_1. Element 2 is mounted onto element 1 and driven by the second motor, providing a pitch rotation about the X_0 axis, denoted as θ_2.

Above the lower assembly, element 3 is attached to element 0 and is actuated by the third motor. This element moves along a diameter defined by radius r_3 and performs a roll rotation around the Y_0 axis, with a maximum deflection of $\pm 30°$ from the Z_0 axis; this motion is marked as θ_3. The rotational movement is accomplished through a gear mechanism consisting of a pinion engaging with an internal spur gear characterized by pitch radii r_3, r_0 and module m.

Element 4 is connected to element 3 and provides translational motion along the vertical Z_0 axis. This movement, indicated as s_4, is driven by the fourth motor and guided by a rod in combination with a pinion–rack transmission. The terminal point of element 4 corresponds to point M, which represents the position of the extruder nozzle.

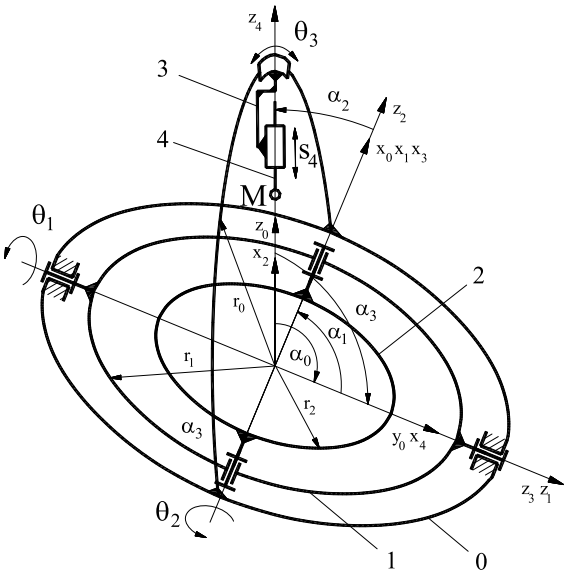

Fig. 1. Kinematic scheme of the 3D printer (in press) [23]

The kinematic positional analysis for the spherical 3D printer was developed with the Denavit-Hartenberg (DH) method, using the following parameters (Table 1):

The position of point M is described in two ways. One through the orientation spherical table and the second through the printing head.

Table. 1. Spherical 3D printer DH parameters, in press [23]

Range	Angle offset	Elements offset	Translation	Rotation
0–1	$\alpha_0 = 90°$	$a_0 = 0.0000$	$d_0 = 0.0000$	0
1–2	$\alpha_1 = 90°$	$a_1 = 0.0000$	$d_1 = 0.0000$	θ_1
2–4	$\alpha_2 = 90°$	$a_2 = 0.0000$	$d_2 = 0.0000$	θ_2
0–3	$\alpha_3 = -90°$	$a_3 = 0.0000$	$d_3 = 0.0000$	θ_3
3–4	$\alpha_4 = 180°$	$a_4 = 0.0000$	s_4	0

The pose equation matrix of the orientation spherical hot table is given as: [23]

$$\begin{bmatrix} {}^0x_M \\ {}^0y_M \\ {}^0z_M \\ 1 \end{bmatrix} = {}^0T_1 \bullet {}^1T_2 \bullet {}^2T_4 \begin{bmatrix} {}^2x_{Mt} \\ {}^2y_{Mt} \\ {}^2z_{Mt} \\ 1 \end{bmatrix} = \begin{bmatrix} c_{\theta 1}c_{\theta 2} & s_{\theta 1} & s_{\theta 2}c_{\theta 1} & 0 \\ -s_{\theta 2} & 0 & c_{\theta 2} & 0 \\ s_{\theta 1}c_{\theta 2} & -c_{\theta 1} & s_{\theta 1}s_{\theta 2} & 0 \\ 0 & 0 & 0 & 1 \end{bmatrix} \bullet \begin{bmatrix} {}^2x_{Mt} \\ {}^2y_{Mt} \\ {}^2z_{Mt} \\ 1 \end{bmatrix} \quad (1)$$

with:

$${}^0T_1 = Rot(x, \alpha_0), {}^1T_2 = Rot(z, \theta_1) \bullet Rot(x, \alpha_1), {}^2T_4 = Rot(z, \theta_2) \bullet Rot(x, \alpha_2) \quad (2)$$

The pose equation matrix of the 3D spherical printer head becomes: [23]

$$\begin{bmatrix} {}^0x_M \\ {}^0y_M \\ {}^0z_M \\ 1 \end{bmatrix} = {}^0T_3 \bullet {}^3T_4 \bullet \begin{bmatrix} {}^4x_{Mh} \\ {}^4y_{Mh} \\ {}^4z_{Mh} \\ 1 \end{bmatrix} = \begin{bmatrix} c_{\theta 3} & 0 & -s_{\theta 3} & -(r_4 - s_4) \bullet s_{\theta 3} \\ 0 & -1 & 0 & 0 \\ -s_{\theta 3} & 0 & -c_{\theta 3} & -(r_4 - s_4) \bullet c_{\theta 3} \\ 0 & 0 & 0 & 1 \end{bmatrix} \bullet \begin{bmatrix} {}^4x_{Mh} \\ {}^4y_{Mh} \\ {}^4z_{Mh} \\ 1 \end{bmatrix} \quad (3)$$

with:

$${}^0T_3 = Rot(x, -\alpha_3) \quad (4)$$

$${}^3T_4 = Rot(z, \theta_3) \bullet Rot(x, \alpha_3) \bullet Tr(z, r_4 - s_4) \quad (5)$$

The relationships (1) and (3) describe the forward kinematical analysis of the proposed spherical 3D printer.

For the inverse kinematic positional analysis relations (1) and (3) are used in a scalar form. By multiplying the transformation matrix with the position of the characteristic point in the mobile system of the spherical plate ${}^0T_1$.

The matrix Eq. (1) of the orientation plate becomes: [23]

$$\begin{bmatrix} {}^0x_M \\ {}^0y_M \\ {}^0z_M \\ 1 \end{bmatrix} = \begin{bmatrix} c_{\theta 1}c_{\theta 2}{}^4x_{Mt} + s_{\theta 1}{}^4y_{Mt} + s_{\theta 2}c_{\theta 1}{}^4z_{Mt} \\ s_{\theta 2}{}^4x_{Mt} - c_{\theta 2}{}^4z_{Mt} \\ -s_{\theta 1}c_{\theta 2}{}^4x_{Mt} + c_{\theta 1}{}^4y_{Mt} - s_{\theta 1}s_{\theta 2}{}^4z_{Mt} \\ 1 \end{bmatrix} \quad (6)$$

From the second line of the matrix Eq. (6) results: [23]

$$ {}^{4}z_{Mp}\cos(\theta_2) - {}^{4}x_{Mp}\sin(\theta_2) + {}^{0}y_M = 0 \tag{7} $$

with the solution:

$$ \theta_2 = 2 \bullet atan\frac{-{}^{4}x_{Mt} \mp \sqrt{\left({}^{4}z_{Mt}\right)^2 + \left(-{}^{4}x_{Mt}\right)^2 - \left({}^{0}y_M\right)^2}}{{}^{4}z_{Mt} - {}^{0}y_M} \tag{8} $$

From the next 2 equations resulted from matrix Eq. (8) after the substitutions is obtained the equation: [23]

$$ {}^{0}z_M\cos(\theta_1) + {}^{0}x_M\sin(\theta_1) - {}^{4}y_{Mt} = 0 \tag{9} $$

with the solution:

$$ \theta_1 = 2 \bullet atan\frac{-{}^{0}x_M \mp \sqrt{\left({}^{0}z_M\right)^2 + \left(-{}^{0}x_M\right)^2 - \left({}^{4}y_{Mt}\right)^2}}{{}^{0}z_M - {}^{4}y_{Mt}} \tag{10} $$

The matrix equation ${}^{1}T_2$ of the 3D printer head becomes: [23]

$$ \begin{bmatrix} {}^{0}x_M \\ {}^{0}y_M \\ {}^{0}z_M \\ 1 \end{bmatrix} = \begin{bmatrix} c_{\theta 3}{}^{4}x_{Mh} - s_{\theta 3}{}^{4}z_{Mh} - (r_4 - s_4) \bullet s_{\theta 3} \\ {}^{4}y_{Mh} \\ -s_{\theta 3}{}^{4}x_{Mh} - c_{\theta 3}{}^{4}z_{Mh} - (r_4 - s_4) \bullet c_{\theta 3} \\ 1 \end{bmatrix} \tag{11} $$

From the first and third line of the matrix Eq. (11) results: [23]

$$ {}^{0}x_{Mh}\cos(\theta_3) - {}^{0}z_{Mh}\sin(\theta_3) - {}^{4}x_M = 0 \tag{12} $$

with the solution:

$$ \theta_3 = 2 \bullet atan\frac{-{}^{0}z_{Mh} - \sqrt{\left({}^{0}x_{Mh}\right)^2 + \left(-{}^{0}z_{Mh}\right)^2 - \left(-{}^{4}x_M\right)^2}}{{}^{0}x_{Mh} + {}^{4}x_M} \tag{13} $$

Than from first line equation results:

$$ s_4 = r_4 - \sqrt{\left({}^{4}x_{Mh}\right)^2 - \left({}^{4}z_{Mh}\right)^2} \tag{14} $$

3 CAD of the Analyzed 3D Spherical Printer

In order to replicate the form of a skull, we chose a spherical surface for the hot-bed's shape rather than the more common flat surface. The goal of this study is to determine the most efficient method for printing a subject's face muscles following facial restoration while minimizing material waste. Therefore, printing an object intended for placement on a nearly spherical surface on a spherical surface would accomplish this. The second reason is that the existing semi-spherical hotbed may eventually be replaced with a frame that allows an already printed skull to be positioned and the reconstructed muscles to be printed on top of it, resulting in a completely formed face at the conclusion of the printing process.

Figures 2 and 3 show the CAD of the analyzed 3D spherical printer, designed entirely using PTC Creo.

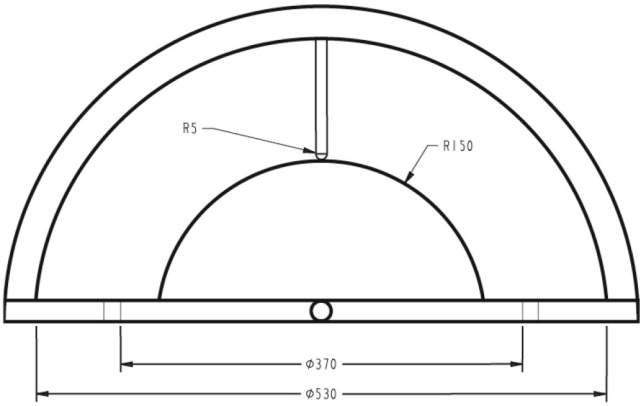

Fig. 2. CAD of the analyzed 3D Spherical Printer and parameters – front view

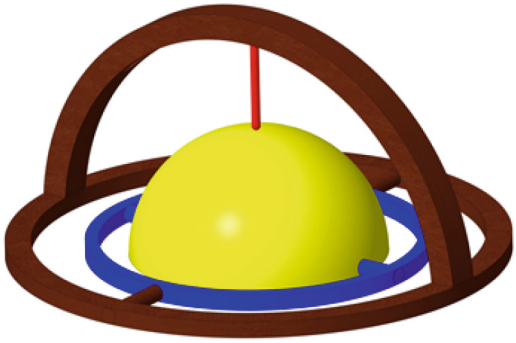

Fig. 3. CAD of the analyzed 3D Spherical Printer – isometric view and elements highlighted

4 Trajectory of the Printing Toolhead

A printing toolhead's trajectory is the route it takes to deposit material for a 3D print, which is determined by slicer software. This path, which consists of "travel" portions where the tool moves between sites without extruding and printing segments that follow the geometry of the model, is tuned to be accurate and efficient. The toolhead moves in a regulated acceleration and deceleration rather than instantly, and factors like jerk (maximum instantaneous velocity change) affect how smooth turns are [17].

According to different studies [18–22], when the layering accuracy is constant, the single-layer printing time must be decreased to increase printing efficiency. Among these, if the hardware circumstances remain constant, optimizing the single-layer printing path is an efficient way to increase the efficiency of single-layer printing.

Figure 4 illustrates the trajectory of the printing toolhead of the 3D spherical printer, while performing the outer contour of the first layer. The shape corresponds to a Temporalis muscle.

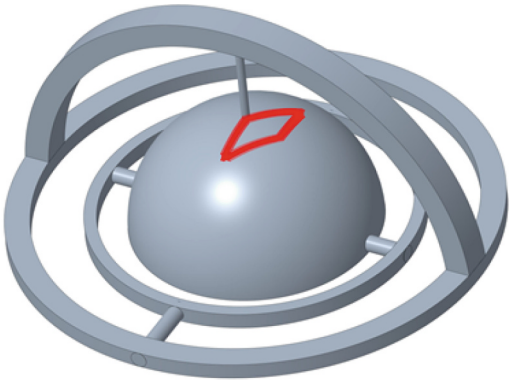

Fig. 4. Trajectory of the printing toolhead

In order to obtain the trajectory of the printing toolhead of the 3D spherical printer, presented in Fig. 3, the inputs were the rotational angles θ_1 and θ_2, given as a first attempt to replicate the shape of a Temporalis muscle, by imposing linear law of motions. Figures 5 and 6 present the variation of the rotational angles θ_1 and θ_2 in time. The values can be further optimized by imposing different other types of laws of motion.

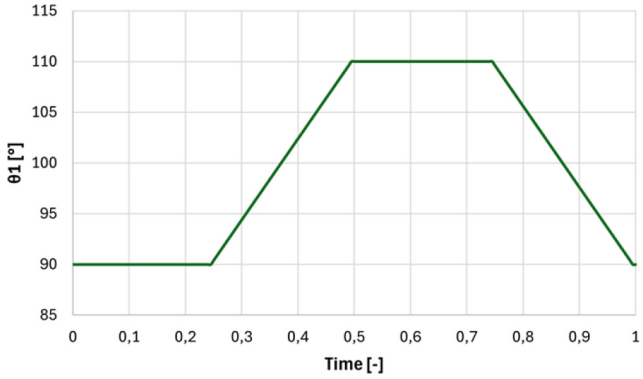

Fig. 5. Variation of rotational angle θ_1 in time

Moreover, the obtained trajectory can be interpolated in MATLAB, using Curve Fitter Toolbox, in order to estimate the entire first layer surface. The result is presented in Fig. 7.

Nevertheless, the polynomial function that is the best fit for the (x,y) data can also be obtained using MATLAB. The resulting polynomial function, which is presented in Fig. 8 for the total time t ∈ [0,1], consists of six different polynomial functions, one for each of the different sectors of the trajectory, as follows:

$x_1(t) = -118.45 \bullet t$, $y_1(t) = 0$ when t ∈ [0; 0.245]
$x_2(t) = -29.02$, $y_2(t) = -88.8 \bullet (t - 0.25)$ when t ∈ [0.25; 0.275]

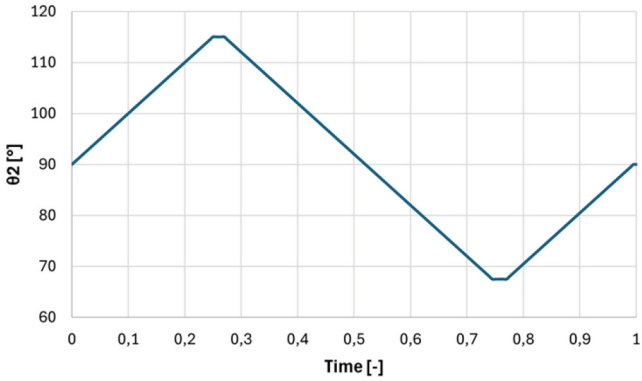

Fig. 6. Variation of rotational angle θ_2 in time

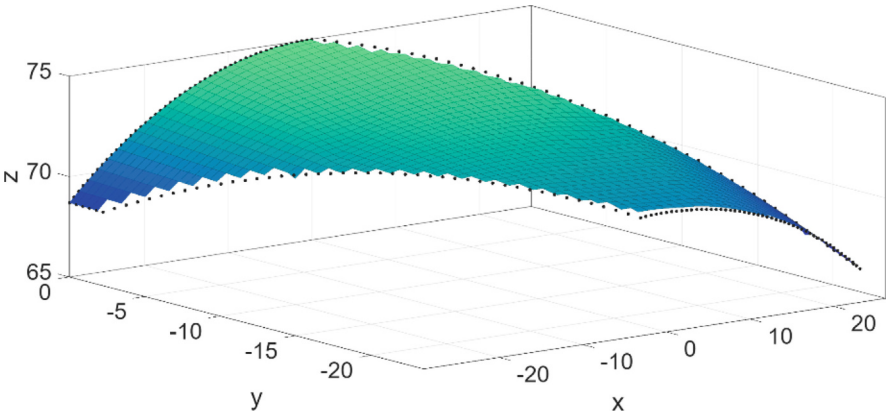

Fig. 7. The resulting trajectory, interpolated using Curve Fitter Toolbox from MATLAB

$$
\begin{aligned}
&x_3(t) = -29.02 + 123.67 \bullet (t - 0.28),\\
&y_3(t) = 0.0001 \bullet t^3 + 0.0046 \bullet t^2 - 0.7411 \bullet t - 25.7610 \quad \text{when t} \in [0.28; 0.49]\\
&x_4(t) = -3.05 + 121.95 \bullet (t - 0.495),\\
&y_4(t) = 0.0023 \bullet t^2 - 0.0002 \bullet t - 23.4811 \quad \text{when t} \in [0.495; 0.735]\\
&x_5(\text{t}) = 26.22,\\
&y_5(t) = -21.77 + 86 \bullet (t - 0.74) \quad \text{when t} \in [0.74; 0.765]\\
&x_6(\text{t}) = 26.22 - 114 \bullet (t - 0.77),\\
&y_6(t) = 0.0001 \bullet t^3 + 0.0002 \bullet t^2 - 0.7986 \bullet t - 0.0018 \quad \text{when t} \in [0.77; 1]
\end{aligned}
$$

It can be observed that the first sector of the trajectory corresponding to the printing toolhead of the 3D spherical printer is a horizontal line, while the sectors 2 and 5 are a vertical line. For the remaining sectors of the trajectory, the best fit for the (x,y) data was identified as a second-degree polynomial function.

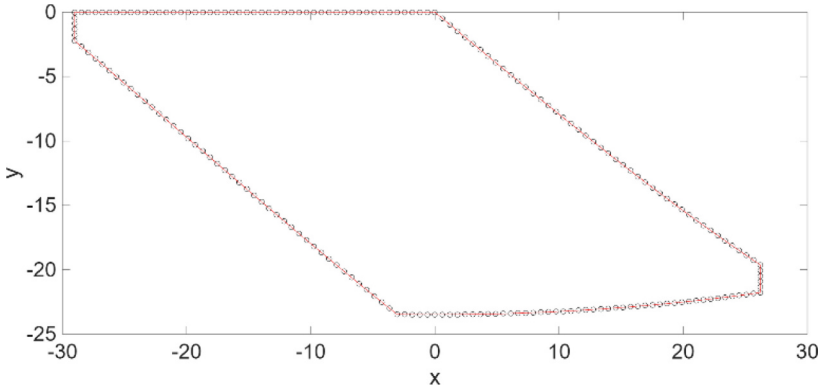

Fig. 8. Representation of the trajectory and the corresponding polynomial functions

5 Conclusions

This paper proposes a spherical 3D printer with three rotational and one translational degree of freedom for printing reconstructed skulls and facial muscles using a spherical coordinate system better suited to organic geometries. The proposed design offers reduced material waste, improved nozzle reach at difficult angles, stable operation within a 90° rotation range, and a cost-effective, user-friendly structure that is easy to assemble.

Using FDM technology, the spherical deposition strategy enables an estimated 30–40% material savings by forming shell-based structures instead of fully filled layers. Although this reduces internal stiffness, the increased material thickness in sensitive facial regions compensates for this effect, while small reconstructed muscle structures remain unaffected due to their limited volume and relatively flat shape.

Future work will focus on refining the inverse kinematic-based trajectory generation, developing an experimental prototype to evaluate print quality, fabrication time, and material savings, and performing analytical and CAD-based simulations of the printer mechanism.

References

1. Ngo, T., Kashani, A., Imbalzano, G., Nguyen, K., Hui, D.: Additive manufacturing (3D printing): a review of materials, methods, applications and challenges. Compos. Part B: Eng. **143**, 172–196 (2018)
2. Chattopadhyay, S., Mahapatra, S.D., Mandal, N.K.: Advancements and challenges in additive manufacturing: a comprehensive review. Eng. Res. Express. **6**, 012505 (2024)
3. Zhou, L. et al.: Additive manufacturing: a comprehensive review. Sensors. **24**(9), 2668 (2024)
4. Munaz, A., Vadivelu, R., St. John, J., Barton, M., Kamble, H., Nguyen, N.T.: Three-dimensional printing of biological matters. J. Sci.: Adv. Mater. Devices. **1**(1), 1–17 (2016)
5. Idà, E., Nanetti, F., Mottola, G.: An alternative parallel mechanism for horizontal positioning of a nozzle in an FDM 3D printer. Machines. **10**(7), 542 (2022)
6. Consalvi, J.: High-speed FDM 3D printer with closed-loop CoreXY motion. (US 11370164; international classification B29C 64/118, 20170101). JUSTIA patents. (2022)

7. Pan, J. et al.: Design and development of a dual-extruder SCARA food 3D printer. J. Food Eng. **370**, 11973 (2024)
8. Rozsos, R.S., Buna, Z.L., Bodi, Ş., Comes, R., Tompa, V.: Design and development of a linear delta 3D printer. Acta Techn. Napoc. Appl. Math. Mech. Eng. Series. **63**(2), 185–190 (2020)
9. Huang, B., Xie, W.: High-performance computing of 3D printing processing accuracy considering cylindrical coordinate slicing algorithm. In: Muzammal, Z. (ed.) Mobile Information System Issue: Mobile Internet of Things (IoT) Multi-Sensor Data Fusion. Wiley (2022)
10. Demjen, T., Lovasz, E.-C., Sticlaru, C., Teuşdea, D., Cărăbaş, I.: Development of a novel 3D spherical printer. Robot. Manag. **24**(2), 16–18 (2019)
11. Şencan, İ., Alaçam, S., Şener, S.-M.: Designing printers that print onto spherical geometries: a lo-fi prototyping case. In: XXV International Conference of the Iberoamerican Society of Digital Graphics, pp. 559–570. Blucher, São Paulo (2021)
12. Qian, S., Li, C., Zhao, Z., Zi, B.: Modeling and experimental validation of a cable-driven robot for three-dimensional printing construction. J. Mech. Robot. **17**(6), 061002 (2025)
13. Kainz, M.: Development of a five-axis printer for the fabrication of hybrid 3D scaffolds: from soft to hard phases and planar to curved surfaces. Int. J. Bioprint. **10**(3), 3189 (2024)
14. Gerasimov, M.M.: The Reconstruction of the Face from the Basic Structure of the Skull, Russia (1955) [s.n.]. https://scholar.google.com/scholar_lookup?title=The+Reconstruction+of+the+Face+from+the+Basic+Structure+of+the+Skull&author=MM+Gerasimov&publication_year=1955&. Last accessed 16 Aug 2025
15. Micle, L.-M., Lovasz, E.-C.: Facial reconstruction from an archeological starting point. In: 17th International Conference on Engineering of Modern Electric Systems (EMES), pp. 1–4. IEEE, Oradea (Romania) (2023)
16. Lee, W.-J., Wilkinson, C., Hwang, H.-S.: An accuracy assessment of forensic computerized facial reconstruction employing cone-beam computed tomography from live subjects. J. Forensic Sci. **57**(2), 318–327 (2011)
17. Beneventi, D., Graziano, A., Furia, G., Charpin, L., Jean-Louis, M.: Optimization of trajectory processing algorithms to print 3D circuit boards using piezo ink jet and 6-axis robots. J. Manuf. Process. **101**, 1497–1507 (2023)
18. Hu, K., Li, H., Xi, K.: A toolpath optimization algorithm for layered 3D printings based on solving the TSP. J. Phys. Conf. Ser. **2456**, 012039 (2023)
19. Chao, Y.: Research on 3D Printing Path Planning Technology Based on FDM Technology. Changchun University of Technology, Changchun (2016)
20. Peng, A., Zhang, J.: Research on scanning path planning based on plane contour convex decomposition. J. Comput. Aided Des. Comput. Graph. **23**(5), 62–64 (2007)
21. Li, W.: (2012) Research on Tool Path Planning Algorithm of Complex Surface Machining Based on Hilbert Curve in Fractal. Nanjing University of Aeronautics and Astronautics, Nanjing (2012)
22. He, X., Pan, X.: Scanning path algorithm and optimization based on feature partition in FDM process. Mech. Electr. Eng. Mag. **17**(1), 24–26 (2014)
23. Micle, L.M., Scurt, A.M., Lovasz, E.C.: Spherical 3D printer for facial reconstruction of skulls. In: Proceedings of the 14th IFToMM International Symposium on Science of Mechanisms and Machines (SYROM 2025) Springer Book Series: Mechanism and Machine Science, Advances in Mechanism and Machine Science, vol. 198, (2025)

Latency and Safety Assessment of Low-Cost Distance Sensor Integration into ROS2 for Human–Robot Collaboration

Sophie Charlotte Keunecke[1(✉)], Marcel Ochsendorf[2], Mathias Hüsing[1], and Burkhard Corves[1]

[1] Institute of Mechanism Theory, Machine Dynamics and Robotics, RWTH Aachen University, Aachen, Germany
{keunecke,Huesing,Corves}@igmr.rwth-aachen.de
[2] Fraunhofer Institute for Digital Medicine MEVIS, Bremen, Germany
ochsendorf@mevis.fraunhofer.de

Abstract. Collaborative robots (Cobots) are increasingly being used as assistance systems to relieve humans in private and commercial environments. Current systems are designed to stop in the event of a collision, which means that robots only stop after unwanted contact. For completely safe physical collaboration, collisions should be avoided as far as practicable, and distance measurement should take place instead. The internal sensors of Cobots typically do not provide exteroceptive distance measurement, which is why additional sensors must be added. To ensure safe collision avoidance, low-latency systems are required to monitor the work area and avoid collisions. This work investigates how different integration methods for distance-sensors in ROS2 affect end-to-end latency when running on a resource-constrained microcontroller. A Raspberry Pi Pico is used to connect two low-cost sensors that are representative of typical HRC cells: an ultrasonic-sensor and a time-of-flight-sensor. Both sensors use different communication standards. Two integration strategies are compared. In the standard ROS2 integration, the sensor firmware runs on the microcontroller, which streams the data via a serial connection to a ROS2 node. In the micro-ROS-based integration, the firmware and ROS2 publisher are combined in a single application. For each sensor, the latency between measurement acquisition and publication in a ROS2 topic is quantified over multiple trials. The results show that micro-ROS reduces average latency and suppresses extreme outliers, although the overall update rate remains limited by the sensor's intrinsic sampling frequency. The study derives practical design guidelines for latency-aware integration in ROS2 on low-cost microcontrollers and discusses their implications for safe HRC.

Keywords: HRC · Distance sensing · ROS2 · micro-ROS · Embedded systems · Latency analysis

© The Author(s), under exclusive license to Springer Nature Switzerland AG 2026
A. Chaker et al. (Eds.): EFIMMS 2026, MMS 205, pp. 274–284, 2026.
https://doi.org/10.1007/978-3-032-22270-1_27

1 Introduction

1.1 Speed of Measurement for Safe HRC

Collaborative robots (Cobots) are increasingly used in manufacturing and assembly because they enable safe human–robot collaboration (HRC) as defined in standards such as DIN EN ISO 10218 [2]. Unlike conventional industrial robots, they share a workspace with humans and are intended to support and extend capabilities rather than replace human labour, in line with the human centred vision of Industry 5.0 [3].

Close interaction requires the robot to react predictably and with low latency to human motion and other obstacles. This assumes that the entire perception chain from sensing to motion adjustment is reliable and time bounded. Besides internal proprioceptive sensors, external sensing is often used, for example distance measurement for speed and separation monitoring or vision-based tracking [4, 5]. Such systems usually require multiple viewpoints, extensive processing and frequent reconfiguration when the layout changes.

An alternative is to monitor the workspace from the robot's perspective directly by mounting small low-cost distance sensors on the arm. These sensors can provide a simple basis for collision avoidance, provided that their data reach the robot control software with low delay and jitter [6]. In this work, only the communication time is evaluated; internal sensor evaluation times are not considered.

Many modular systems use embedded microcontrollers for low level communication. ROS2 offers a flexible middleware for such systems, and there are two main integration strategies. Either a micro-ROS client runs directly on the microcontroller [7], or user defined messages are sent via USB and converted to ROS2 topics on the host. Both are functionally equivalent but differ in latency and complexity. This paper experimentally compares these strategies for two low-cost distance sensors on a Raspberry Pi Pico, focusing on the latency from data transmission on the microcontroller to availability in ROS2 topics on the host.

1.2 Objectives and Contributions

Based on the implementation and measurements, the goal is to provide a systematic, quantitative comparison of latency-aware integration strategies in ROS2. The main contributions are:

(1) A unified architecture that connects two distance sensors via two alternative integration paths (serial bridge or Micro-ROS) with identical functionality but different communication stacks and processing to a Pico and a ROS2-based control system.
(2) A measurement methodology for quantifying end-to-end latency from sensor measurement to ROS2 topic publication for each strategy and sensor, including a precise latency definition, experimental procedure, and data analysis pipeline.
(3) Design guidelines for selecting appropriate sensors, microcontroller configurations, and integration strategies in latency-critical HRC scenarios, highlighting the trade-offs between achievable latency and robustness of the communication chain.

The paper is structured as follows. Section 2 reviews related work. Section 3 describes the system and integration strategies. Section 4 details the experimental methodology. Section 5 presents results. Section 6 discusses implications and limitations. Section 7 concludes and outlines future work.

2 Background and Related Work

2.1 Inclusive HRC and Distance Sensing

Inclusive human–robot collaboration (HRC) targets work systems that remain safe, intuitive, and adaptable for heterogeneous user groups and changing tasks. In inclusive production settings, additional emphasis is placed on low setup overhead and transparent safety behavior, because assistive workstations must be deployable by non-experts and remain maintainable over long operating periods. In industrial practice, Cobots support human decision-making and quality assurance while taking over repetitive or ergonomically demanding subtasks; safety functions therefore need to remain robust under frequent workstation reconfiguration [8].

Beyond post-collision concepts such as force and power limitation, many collaborative scenarios rely on pre-collision measures (e.g., speed and separation monitoring) that require continuous perception of humans and obstacles [8–11]. While external camera or LiDAR systems can provide such perception, on-robot sensing is attractive for modular, low-cost deployments. However, protective actions depend on bounded end-to-end reaction time, which makes the latency and jitter of the sensing and communication chain a central design variable, especially in inclusive workplaces where predictable behavior is critical for user acceptance [12, 13].

2.2 Distance Sensing Technologies for Collaborative Workspaces

Workspace monitoring has been implemented with various active modalities, and recent work increasingly considers distributed or on-robot sensor arrays to shape a configurable protective volume around the manipulator [4, 14]. This study focuses on two representative low-cost options with minimal infrastructure requirements: ultrasonic ranging and multi-zone optical Time-of-Flight (ToF).

Ultrasonic sensors provide single-beam ranges with simple GPIO-level interfaces but are sensitive to target geometry and acoustic reflections. Multi-zone ToF sensors measure the propagation delay of modulated infrared light and output coarse depth images that can cover a larger volume from a compact package [15]. In contrast, camera-based approaches typically require heavier post-processing and are therefore not considered here. When sensors are mounted on moving links, limited beam angles and occlusions interact with update rates and communication delays, so both spatial coverage and timing must be considered jointly. For both modalities, system usability in HRC is determined not only by range or field of view, but also by whether measurements arrive in the robot software with sufficiently low and predictable delay.

2.3 ROS2 and Micro-ROS on Resource Constrained Hardware

ROS2 is widely used to integrate perception, planning, and control via a publisher–subscriber model and configurable quality-of-service settings, including deadlines and reliability [7]. In modular cells, sensors are frequently interfaced through microcontrollers that forward measurements to a ROS2 host. In such setups, host-side scheduling, buffering, and serialization overhead can dominate the timing behavior, even when the sensor sampling itself is stable.

Two integration patterns are common: custom serial streaming with host-side parsing and ROS2 publication or running a micro-ROS client on the microcontroller that communicates with a micro-ROS agent on the host [7]. micro-ROS can reduce protocol translations and intermediate buffering by encapsulating sensor data as ROS2 messages at the source, but it increases firmware complexity and resource demands. A quantitative comparison of the resulting latency behavior on low-cost hardware motivates the evaluation in this paper.

2.4 Related Work on Sensor Integration Latency and Real Time

In safety-relevant applications, the timeliness of sensor information is as important as its correctness. Real-time capability, as defined in DIN 44300, requires that system responses meet specified time constraints; therefore, communication latency and jitter must be treated as first-class performance metrics [16]. In practice, both average delay and occasional interruptions of the sensor update stream can affect proximity-based reactions. For this reason, the following evaluation reports mean latency, variability (standard deviation), and observed outlier events.

Prior HRC studies demonstrate that compact ToF proximity sensing can support human detection and workspace monitoring around collaborative manipulators [18, 19]. However, most contributions emphasize spatial coverage and detection performance rather than the microcontroller-to-middleware communication path. Quantitative analyses of latency distributions and outlier behavior for alternative ROS2 integration strategies on low-cost microcontrollers are still limited; this gap is addressed by the measurements reported here.

3 System Architecture and Integration Methods

3.1 Use Case Scenario and Design Requirements

The target scenario is a collaborative workstation in which a robot arm shares workspace with a human worker. On-robot distance sensors should enable timely slowing or stopping when thresholds are reached. Therefore, the sensor-to-ROS2 communication latency must be low and predictable, while the solution should remain low-cost and modular.

3.2 Hardware Platform and Latency

A Raspberry Pi Pico (RP2040; dual-core ARM Cortex-M0+ at 133 MHz; 264 kB SRAM) serves as the microcontroller interface for the distance sensors and streams timestamped data to a Linux host running ROS2 Humble.

Two representative low-cost distance sensors are evaluated: an HC-SR04 ultrasonic module and a VL53L5CX multi-zone Time-of-Flight sensor (8×8). Table 1 summarizes key sensor specifications relevant for the latency evaluation.

Table 1. Technical specifications of evaluated distance sensors (datasheet [20, 21] values and configuration used in this study).

Parameter	HC-SR04 (Ultrasonic)	VL53L5CX (ToF, 8×8)
Measurement principle	Ultrasonic time-of-flight	Direct Time-of-Flight (SPAD array)
Output	Single distance value	Multi-zone distance image (up to 8×8)
Interface to MCU	Digital signal, TRIG/ECHO (Input timing)	I^2C, up to 1 MHz (Fast Mode Plus)
Typical field of view	Approx. 15° measuring angle (module spec.)	45° × 45° (side), 65° diagonal
Operating range	2 cm to 4 m (module spec.)	2 cm to 4 m
Update rate (stable operation)	Configured sampling rate used in this study: 40 Hz	Configured sampling rate used in this study: 15 Hz (8×8)

The HC-SR04 is triggered by a digital pulse and the echo time is measured with hardware timers. The VL53L5CX is accessed via I^2C and returns a distance image frame.

The analysis focuses on the communication latency between the microcontroller and ROS2 topics on the host. Internal sensor measurement latency and downstream robot reaction time are outside the scope.

Depending on the integration strategy, the host either runs a dedicated serial-bridge node that parses microcontroller messages or a micro-ROS agent that bridges micro-ROS traffic into the ROS2 network

As illustrated in Fig. 1, the total latency is the time required to transmit the data from the microcontroller to the ROS2 host PC. This depends on the chosen communication system, micro-ROS or a serial USB connection. More precisely, on the host side, the arrival time of the corresponding ROS2 message is measured using the system clock. The end-to-end latency is then calculated as the difference between the host side reception time and the original microcontroller timestamp, considering any necessary synchronization or offset correction.

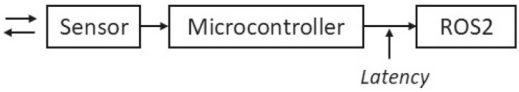

Fig. 1. Latency measurement

3.3 Standard ROS2 Serial Integration

In the first integration strategy, referred to as standard integration, the Pico firmware is limited to low-level sensor communication and formatting measurements into custom serial messages. For each sensor, the Pico transmits compact frames over a virtual serial port to the host at a configured baud rate. On the host, a ROS2 node reads the stream, parses it into structured sensor data, and publishes the corresponding ROS2 messages on dedicated topics. This keeps the firmware comparatively simple, since it contains no ROS2-specific code, and allows the bridge node to be developed and debugged with standard ROS2 tools. The serial layer introduces additional latency and jitter sources, including driver buffering and scheduling, parsing overhead, and mismatches between sensor sampling and host-side readout. The standard integration is illustrated in the upper half of Fig. 2.

3.4 Micro-ROS Based Integration on the Pico

The second integration strategy uses micro-ROS and shifts ROS2 message publication from the host to the microcontroller. The Pico firmware integrates the sensor drivers and the micro-ROS client library in a single application, initializes a micro-ROS node, creates publishers for each sensor topic, and uses timer callbacks to periodically read the sensors and publish the corresponding ROS2 messages. A micro-ROS agent on the host translates the messages into native ROS2 and injects them into the ROS2 network. To other ROS2 nodes, the Pico appears as a regular ROS2 node publishing, for example, a one-dimensional range message for the ultrasonic sensor and a multidimensional range or point cloud for the ToF sensor. Compared to the standard integration, this removes the serial parsing node and reduces copying and reformatting. Latency from sensor readout to message publication is mainly determined by the timer configuration and Pico–agent communication. Firmware complexity increases, since scheduling, memory management, and error handling must respect micro-ROS client constraints. The micro-ROS integration is illustrated in the lower half of Fig. 2.

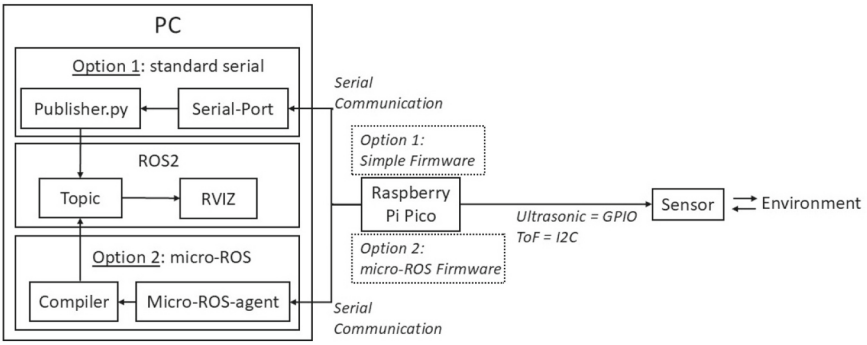

Fig. 2. Architecture and Communication flow; the upper third implements the Standard ROS2 serial integration and the lower third the micro-ROS integration. Sensor communication and topic evaluation are the same for both.

4 Experimental Setup and Measurement Methodology

4.1 Latency Instrumentation and Data Logging

To measure the communication latency, each sensor message on the Pico is stamped with a local timestamp and a sequence number the moment when the processed measurement becomes available to the firmware. In the standard integration, these fields are embedded in the custom serial message. On the host, the bridge node reconstructs the sensor data and records the host system time immediately before publishing the corresponding ROS2 message. The latency is obtained as the difference between the host publication time and the embedded microcontroller timestamp. In the micro-ROS integration, the Pico constructs ROS2 messages directly and places timestamp and sequence number in the message header. A subscriber on the host records the reception time of each message, and latency is again computed as the difference to the microcontroller timestamp. Only the communication time from the Pico to the host ROS2 topic is considered; internal sensor evaluation times are not analysed.

4.2 Evaluation Metrics and Data Analysis

For each configuration, the logged timestamps are processed offline to obtain latency time series. From these, the mean latency and standard deviation are computed. In addition, the maximum observed latency and time-series plots are used to identify interruptions due to buffering or scheduling. The effective update rate is determined from the number of received messages over the run duration in order to verify that the integration strategy keeps up with the sensor output.

5 Results

5.1 Ultrasonic Sensor HC SR04

For the HC SR04, the 40 hertz sampling rate corresponds to an update interval of 25 000 µs. With micro-ROS integration, the mean communication latency from the Pico timestamp to the host side ROS2 topic is close to this value and shows a narrow spread;

no missing sequence numbers were observed in the recorded sample set. The standard integration yields a higher mean latency of 48,574 µs and shows outliers up to about 1.46 s caused by serial buffering effects. Thus, micro-ROS keeps the latency close to the sampling period and avoids long interruptions in distance updates.

5.2 Time of Flight Sensor VL53L5CX

For the VL53L5CX, the 15 hertz frame rate implies an update interval of about 66,666 µs. Both integration strategies achieve the expected number of frames, but their latency differs. The standard integration shows a mean latency of 132,958 µs with considerable spread. Micro-ROS reduces the mean to 66,179 µs, very close to the nominal interval, with all values confined to a relatively narrow band. This yields lower and more stable communication latency for the VL53L5CX.

5.3 Comparison

The latency dataset consists of 100 samples per integration strategy (200 observations in total), recorded under identical conditions for each sensor (same baud rate and measurement frequency within the respective run). The figure shows the latency time series with mean and mean ± one standard deviation (left) and the corresponding box plots (right).

In the time-series plot, the Standard-ROS curve lies consistently above the micro-ROS curve, indicating systematically longer times and higher jitter; the larger spread around its mean confirms this. The box plots support these observations: Standard-ROS exhibits a higher median and mean and a wider interquartile range with more outliers, whereas micro-ROS appears lower and more compact. Overall, the micro-ROS integration yields shorter and more stable communication times than the Standard-ROS setup (Fig. 3).

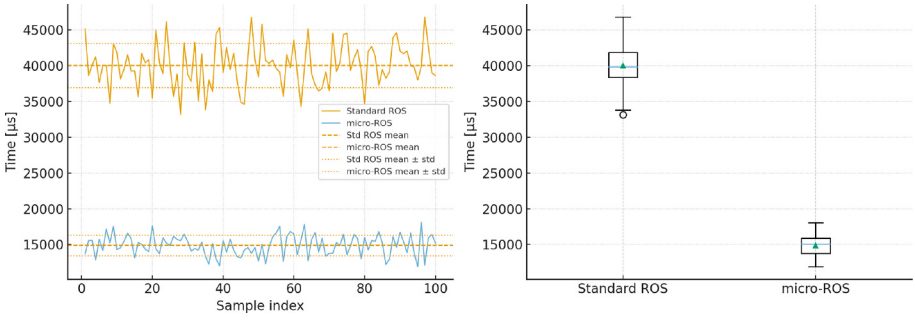

Fig. 3. Latency Analysis over 100 Samples: Standard serial vs. micro-ROS

6 Discussion

This section interprets the experimental findings for safe HRC and inclusive workplaces and derives concise design guidelines for latency aware sensor integration in ROS2 on low-cost microcontrollers.

6.1 Implications for Safe HRC

The experiments show that the integration strategy has a strong influence on the communication latency between a low-cost microcontroller and a ROS2 host. For the HC SR04 ultrasonic sensor, the standard serial bridge introduces second-scale outliers (up to about 1.46 s), so that the robot would occasionally operate on very outdated distance information. Such behaviour is clearly unacceptable for speed and separation monitoring. The micro-ROS integration removes these outliers and keeps the latency close to the update interval imposed by the sampling frequency. For the VL53L5CX time of flight sensor, both strategies keep latencies within the scale of a few sampling periods, but the standard integration roughly doubles the average delay. micro-ROS reduces the mean latency and variability to near the theoretical frame interval. In inclusive workplaces, where some workers require larger safety margins or slower robot motions, stable and predictable sensor update timing is particularly important.

6.2 Design Guidelines for Latency-Aware Integration and Limitations

Several practical guidelines for latency aware sensor integration follow from these findings. Whenever microcontroller resources permit it, micro-ROS should be preferred over custom serial bridges, because it reduces protocol translations and buffering between the microcontroller and ROS2 and therefore reduces latency and jitter. Sensor sampling and publication frequencies should be aligned carefully, for example by synchronising timer callbacks with sensor frame generation, to avoid systematic variability. Measurement and logging of microcontroller and host timestamps should be treated as part of the system design so that latency distributions can be analysed and unexpected effects can be diagnosed early.

The study has limitations. It is based on a single microcontroller type and two distance sensors, and it considers only the communication path from the Pico to ROS2 topics on a Linux host. Additional delays in motion planning and robot controllers are not quantified and would have to be included for a complete safety assessment. The experiments were conducted under laboratory conditions with stable targets and minimal disturbances. Future work will therefore extend the evaluation to additional sensor types, including low-cost radar, and to full control loops in realistic inclusive workstations and mobile demonstrators.

7 Conclusion and Outlook

This paper investigated how two integration strategies for low-cost distance sensors affect the communication latency from a Raspberry Pi Pico microcontroller to ROS2 topics on a host PC in a collaborative robotics context. An ultrasonic sensor (HC-SR04)

and a ToF-sensor (VL53L5CX) were integrated using either a standard serial bridge with a ROS2 parsing node on the host or a micro-ROS client on the Pico with an agent on the host. The measurements show that micro-ROS consistently yields lower and more predictable latency than the serial bridge. For the ultrasonic, micro-ROS removes second-scale outliers (up to about 1.46 s) caused by serial buffering and keeps the latency close to the update interval. For the ToF, micro-ROS reduces the latency to a narrow band around the frame period; the standard integration roughly doubles the delay.

The results support a clear design recommendation for latency critical HRC applications on low-cost microcontrollers. Whenever resources permit it, sensor data should be published as ROS2 messages directly from the microcontroller using micro-ROS, and latency distributions should be measured explicitly during development. In future work, the evaluation will be extended to additional sensor modalities such as low-cost radar and to complete control loops in realistic inclusive workstations and mobile demonstrators, in order to quantify the total reaction time from distance measurement to commanded robot stop

Acknowledgments. This work is part of the IIDEA [1] project on the safe inclusion of physically impaired people in the primary labour market through Cobots.

References

1. Project IIDEA.: Inclusion and Integration with Cobots in the Primary Labour Market. Funded by the Equalisation Fund of the German Federal Ministry of Labour and Social Affairs. www.iidea.rwth-aachen.de. Last accessed 30 Nov 2025
2. DIN EN ISO 10218-2:2012.: Robots and robotic devices – Safety requirements for industrial robots – Part 2 (ISO 10218-2:2012)
3. Hasani, N., Dantas, C., Margherita, A., Ruggiero, A., Rosa, P.: Outlook on human-centred design in industry 5.0. Int. J. Prod. Res. (2025). https://doi.org/10.1080/19397038.2025.2486343
4. Saleem, Z., Gustafsson, F., Furey, E., McAfee, M., Huq, S.: A review of external sensors for human detection in a human–robot collaborative environment. J. Intell. Manuf. **36**(4), 2255–2279 (2025). https://doi.org/10.1007/s10845-024-02341-2
5. Halme, R.J., Lanz, M., Kämäräinen, J., Pieters, R., Latokartano, J., Hietanen, A.: Review of vision-based safety systems for human–robot collaboration. Procedia CIRP. **72**, 111–116 (2018). https://doi.org/10.1016/j.procir.2018.03.043
6. Moon, S.J., Yim, H., Kang, H., Shim, J., Jung, D., Choi, H.R.: Safety-critical reactive motion using constrained variable admittance control with dual-type proximity sensors. IEEE Rob. Autom. Lett. **10**(9), 8890–8897 (2025). https://doi.org/10.1109/LRA.2025.3589826
7. Belsare, K., Cuadros Rodriguez, A., Garrido Sánchez, P.: Micro-ROS. In: Koubaa, A. (ed.) Robot Operating System (ROS): The Complete Reference, vol. 7, pp. 3–55. Springer, Cham (2023). https://doi.org/10.1007/978-3-031-09062-2_2
8. Li, W., Hu, Y., Zhou, Y., Pham, D.T.: Safe human–robot collaboration for industrial settings: a survey. J. Intell. Manuf. **35**(5), 2235–2261 (2024). https://doi.org/10.1007/s10845-023-02159-4
9. Scholz, C., Cao, H.-L., Imrith, E., Roshandel, N., Firouzipouyaei, H., Burkiewicz, A.: Sensor-enabled safety systems for HRC: a review. IEEE Sensors J. **25**(1), 65–88 (2025). https://doi.org/10.1109/JSEN.2024.3496905

10. Angleraud, A., Ekrekli, A., Samarawickrama, K., Sharma, G., Pieters, R.: Sensor-based HRC for industrial tasks. Robot. Comput. Integr. Manuf. **86**, 102663 (2024). https://doi.org/10.1016/j.rcim.2023.102663
11. Amaya-Mejía, S., Blanc, C., Haddadin, S.: Vision-based safety system for barrierless HRC. In: 2022 IEEE/RSJ International Conference on Intelligent Robots and Systems (IROS), pp. 7331–7336 (2022). https://doi.org/10.1109/IROS47612.2022.9981689
12. Hüsing, E., Weidemann, C., Lorenz, M., Corves, B., Hüsing, M.: Determining robotic assistance for inclusive workplaces for people with disabilities. Robotics. **10**(1), 44 (2021). https://doi.org/10.3390/robotics10010044
13. Mandischer, N. et al.: Toward adaptive HRC for the inclusion of people with disabilities in manual labor tasks. Electronics. **12**(5), 1118 (2023). https://doi.org/10.3390/electronics12051118
14. Avanzini, G.B.: Safety control of industrial robots based on a distributed distance sensor. IEEE Trans. Control Syst. Technol. **22**(6), 2127–2140 (2014). https://doi.org/10.1109/TCST.2014.2300696
15. Sifferman, C., Gupta, M., Gleicher, M.: Efficient detection of objects near a robot manipulator via miniature time-of-flight sensors. IEEE Rob. Autom. Lett. **10**(2), 1–8 (2025). https://doi.org/10.48550/arXiv.2509.16122
16. DIN 44300-1:1985-04.: Information processing – Terminology – Basic terms (Informationsverarbeitung – Begriffe – Grundbegriffe). (DIN 44300-1:1985)
17. Scholz, P.: Softwareentwicklung eingebetteter Systeme: Grundlagen, Modellierung, Qualitätssicherung. Springer, Berlin/Heidelberg (2005) ISBN 978-3-540-27522-0
18. Adamides, O.A., Modur, A.S., Kumar, S., Sahin, F.: A time-of-flight on-robot proximity sensing system to achieve human detection for collaborative robots. In: 2019 IEEE 15th International Conference on Automation Science and Engineering (CASE), Vancouver, Canada, pp. 1230–1236 (2019). https://doi.org/10.1109/COASE.2019.8842875
19. Kumar, S., Sahin, F.: Sensing volume coverage of robot workspace using on-robot time-of-flight sensor arrays for safe human–robot interaction. In: 2019 IEEE International Conference on Systems, Man and Cybernetics (SMC), Bari, Italy, pp. 378–384 (2019). https://doi.org/10.1109/SMC.2019.8914418
20. VL53L5CX.: Time-of-Flight 8x8 multizone ranging sensor with wide field of view, DS13754 - Rev 13, STMicroelectronics (2024). https://www.st.com/resource/en/datasheet/vl53l5cx.pdf. Accessed 3 Jan 2026
21. HC-SR04.: Ultrasonic Sonar Distance Sensor, Product ID: 3942, Mouser Electronics Inc. (2021). https://www.mouser.com/pdfDocs/Product-Overview-Adafruit-3942.pdf. Accessed 3 Jan 2026

Optimization of PID-Controlled Semi-active Suspensions Using Metaheuristic Algorithms for Improved Railway Vehicle Passenger Comfort

Helmi Mahmoudi[1(✉)] and Ajmi Houidi[1,2(✉)]

[1] Laboratory of mechanics of Sousse (LMS), National School of Engineering of Sousse, University of Sousse, Sousse, Tunisia
helmi.mahmoudi@issatso.u-sousse.tn, ajmi.houidi@issatso.rnu.tn
[2] Higher Institute of Applied Sciences and Technology of Sousse, University of Sousse, Sousse, Tunisia

Abstract. Passenger comfort in railway vehicles is strongly influenced by the dynamic behavior of the suspension system. This study investigates the optimization of PID-controlled semi-active suspensions using metaheuristic algorithms, including Genetic Algorithm (GA), Particle Swarm Optimization (PSO), Water Flow Optimization (WFO), and Starfish optimization algorithm (SFOA). A quarter-vehicle model (QVM) with primary and secondary suspensions were developed using MATLAB/Simulink. The system dynamics were modeled using Newton's second law, and results were validated through Simscape Multibody simulations. The performance of the semi-active suspension system was evaluated based on the root mean square (RMS) of vertical accelerations and rail vertical offsets. Metaheuristic algorithms were applied to optimize PID gains, aiming to minimize RMS accelerations while satisfying system constraints. Results demonstrate that all algorithms significantly improve ride comfort compared to passive suspensions, with SFOA achieving the lowest RMS accelerations and best suppression of vertical offsets. This study highlights the effectiveness of metaheuristic-based PID optimization in enhancing passenger comfort and provides guidance for the design and implementation of advanced semi-active suspension systems in railway vehicles.

Keywords: PID Control · Railway Vehicle · Semi-active Suspension · Metaheuristic Optimization · Passenger Comfort

1 Introduction

Passenger comfort is a critical aspect of railway vehicle design, strongly influenced by the dynamic behavior of the suspension system. Traditional passive suspensions, while simple and reliable, often fail to adequately isolate passengers from track irregularities, leading to discomfort during travel. To address this issue, semi-active suspension systems have been developed, capable of adjusting forces in real-time to reduce vibrations and improve ride quality.

© The Author(s), under exclusive license to Springer Nature Switzerland AG 2026
A. Chaker et al. (Eds.): EFIMMS 2026, MMS 205, pp. 285–294, 2026.
https://doi.org/10.1007/978-3-032-22270-1_28

Optimization algorithms are widely used to tune PID controllers for semi-active suspension systems. Various metaheuristic algorithms have been applied in the literature to improve ride comfort and vehicle stability. For instance, Nui [1] employed a Genetic Algorithm (GA) to optimize PID parameters for a quarter-car active suspension, achieving enhanced dynamic performance and stability. Metered [2] used Particle Swarm Optimization (PSO) to tune PID gains for a semi-active quarter-car model, resulting in improved vibration suppression.

This study investigates the optimization of PID-controlled active suspensions for railway vehicles using metaheuristic algorithms. A detailed quarter-vehicle model with primary and secondary suspensions is developed in MATLAB/Simulink, incorporating track irregularities. A broad overview of the dynamic modeling of rail vehicles is presented in Sect. 1. In Sect. 2, the PID-based active suspension controller design and its optimization using metaheuristic algorithms (GA [3], PSO [4], SFOA [5], and WFO [6]) are described, focusing on minimizing RMS vertical accelerations and rail vertical offsets. Section 3 presents a comparative analysis of the simulation results, highlighting the effectiveness of each optimization method. Finally, Sect. 4 concludes the study, providing insights into the design and implementation of advanced active suspension systems for improved passenger comfort.

2 Dynamic Modeling of a Rail Vehicle

For vertical dynamic analysis of railway vehicles, it is standard practice to use a quarter-vehicle model, as noted in [7–9]. This simplified representation is widely adopted because it provides an efficient framework for studying dynamic behavior and optimizing structural parameters without excessive complexity. In this study, all computed results are referenced to the centers of mass of the respective rigid bodies. Figure 1 illustrates the used quarter railway vehicle model.

The system dynamics can be governed by the following equations that can be derived using Newton's laws:

$$M_C\ddot{Z}_C + K_s(X_C - X_B) + C_s\left(\dot{Z}_C - \dot{Z}_B\right) = Fa \tag{1}$$

$$M_B\ddot{Z}_B + K_p(Z_B - Z_r) + C_p\left(\dot{Z}_B - \dot{Z}_r\right) - K_C(Z_C - Z_B) - C_C\left(\dot{Z}_C - \dot{Z}_B\right) = -Fa \tag{2}$$

The QRV dynamic model's differential equations were solved using the Runge-Kutta method. The QRV dynamic model was built and solved using MATLAB, followed by validation using MATLAB Simscape simulations. Figure 2 shows the evolution of the car body center of mass, when the system input Z_r is a step function, reflecting a more severe disruption than a standard leveling defect. Table 1 shows the parameters used in these simulations.

2.1 Rail Design

The Table 2 illustrates three rail irregularity profiles considered in the simulations: a step discontinuity, a rail upward offset, and a rail downward offset. These irregularities

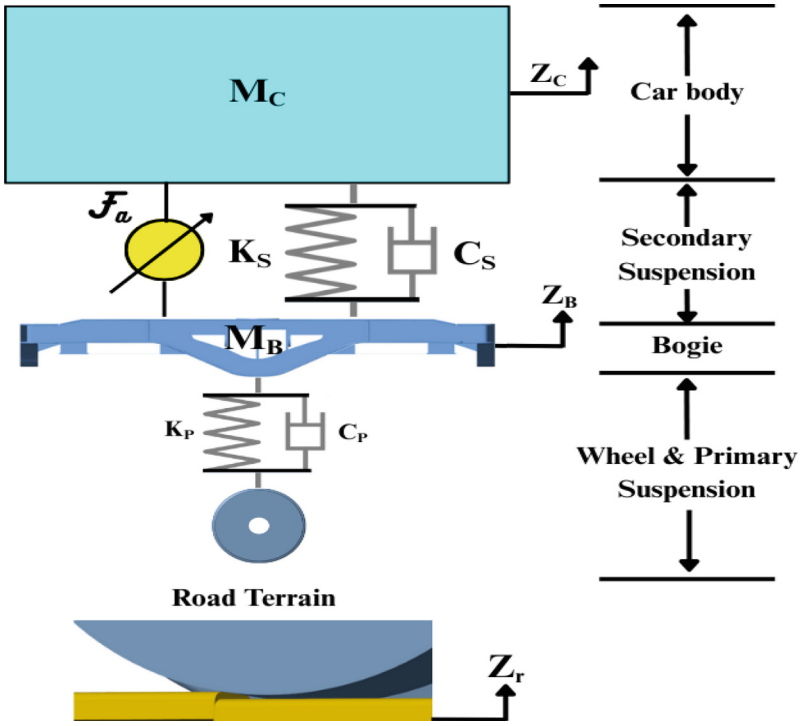

Fig. 1. Quarter railway vehicle (QRV) model.

Table 1. The RV design parameters [10].

Property	Unit	Symbol	Value
Mass of Car body	kg	M_C	24740
Mass of Bogie	*kg*	M_B	3200
Stiffness of Secondary Suspension	*N/m*	K_S	600000
Stiffness of Primary Suspension	*N/m*	K_P	4360000
Damping of Secondary Suspension	*Ns/m*	C_S	40000
Damping of Primary Suspension	*Ns/m*	C_P	0

are modeled using the equations shown, with a train speed of V = 130 km/h 33.11 m/s and an offset height of H = 0.03 m Such configurations are essential for analysing the dynamic response of the vehicle under realistic track conditions.

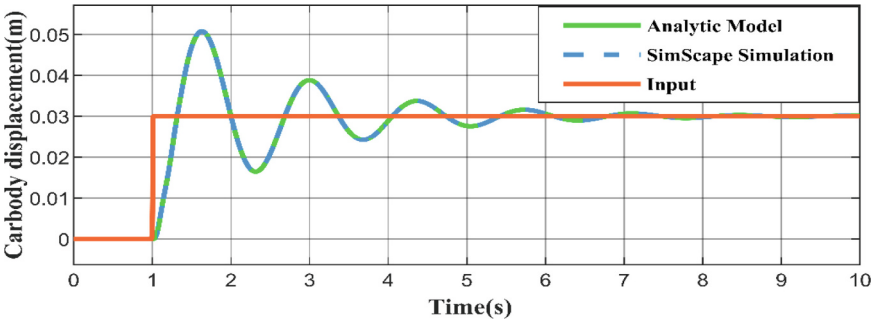

Fig. 2. Validation of the analytical QVM model using Simscape.

Table 2. Types of Rails Irregularities.

Rail discontinuity default	
	$Z_r(t) = \begin{cases} 0 & \text{if } 0 \le t \le 1 \\ H & \text{Otherwise} \end{cases}$ (3)
Rail Upward Offset.	
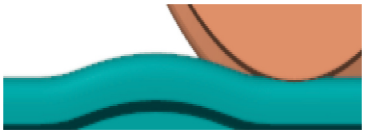	$Z_r(t) = \begin{cases} -\frac{H}{2}\left[1 - \cos\left(2\pi \frac{V}{D} t\right)\right] & \text{if } 0 \le t \le \frac{D}{V} \\ 0 & \text{Otherwise} \end{cases}$ (4)
Rail Downward Offset	
	$Z_r(t) = \begin{cases} \frac{H}{2}\left[1 - \cos\left(2\pi \frac{V}{D} t\right)\right] & \text{if } 0 \le t \le \frac{D}{V} \\ 0 & \text{Otherwise} \end{cases}$ (5)

3 Controller Design and Optimization Technique

The proposed control architecture integrates a PID controller with metaheuristic optimization algorithms to minimize RMS acceleration of the car body, thereby improving passenger comfort. Initial parameters for the PID gains (K_p, K_i, K_d) are generated randomly and optimized using algorithms such as PSO, WFO, GA, and SFOA. The

optimization process uses RMS acceleration as the objective function, ensuring effective vibration mitigation. The railway vehicle model is implemented in Simscape Multibody, where the semi-active suspension applies a control force F_c between the car body and bogie in parallel with secondary suspension elements (K_s, C_s), as illustrated in Fig. 3.

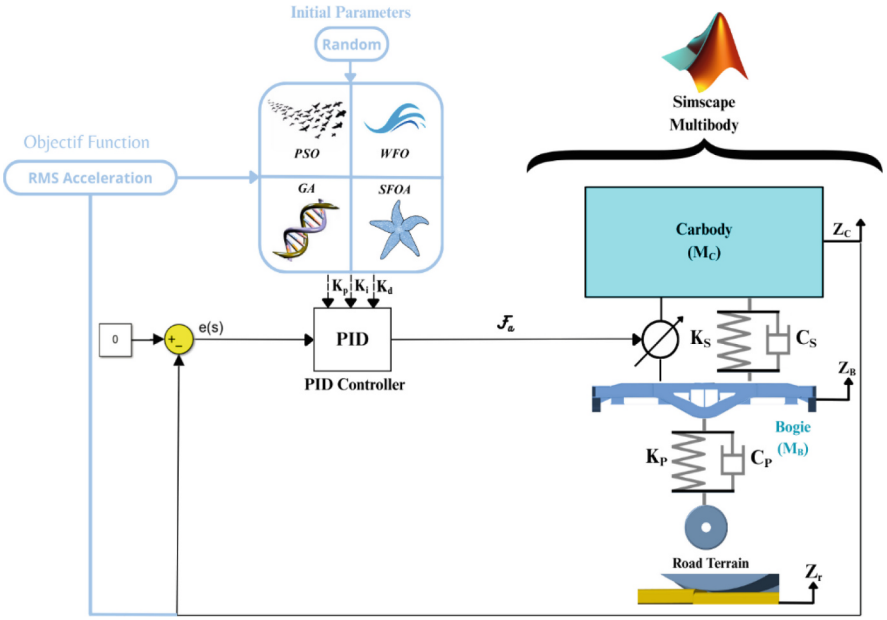

Fig. 3. PID Controller Architecture with Metaheuristic Optimization for Railway Vehicle Comfort.

3.1 Genetic Algorithm (GA)

The Genetic Algorithm [3] is an extensively used optimization method based on the process that mimics natural selection and genetics. In this study, GA Global Optimization Toolbox which is a one of the built-in method in MATLAB Global Optimization Toolbox [11] is used. The parameters of GA are given in Table 3.

3.2 Particle Swarm Optimization (PSO)

PSO algorithm [10] is inspired by social behavior of bird flocking or fish schooling. It is one of the most popular optimization algorithms which have been developed in 1995 by Kennedy and Eberhart. The parameters of PSO are given in Table 3.

3.3 Water Flow Optimizer

Water Flow Optimizer is physics-inspired approaches, simulate fluid dynamics to guide search processes [11]. The parameters of WFO are given in Table 3.

3.4 Starfish Optimization Algorithm (SFOA)

SFOA algorithm [5] is a new meta-heuristic algorithm which is introduced in 2024 by Changting Zhong, The pseudo-code of the SFOA can be found in [5], which describes the main procedure in detail.

Table 3. Metaheuristic Algorithms Parameters.

Algorithm	Parameters	Values
PSO [13]	Population of Particle (NoP) Maximum Iteration Inertia Weight (w) Individual Confidence Factor (c1) Swarm Confidence Factor (c2)	30 100 0.53514 1.1312 2.0149
GA [14]	Population Size Generations Elite Count Crossover Fraction	30 100 5 0.8
WFO [6]	Population Size Maximum Iteration Laminar probability Eddying probability	30 100 0.3 0.7
SFOA [10]	Population Size Maximum Iteration Exploration probability (Gp)	30 100 0.5

We applied the successive approximation method (SAM) to tune the PID controller parameters for an initial state. The obtained values are [KP, KI, KD] = [30000 200000 5000]. Based on these results, we defined the search space for the optimization as follows: PID Control: KP $\in$ [20000,50000], KI $\in$ [150000,250000], KD $\in$ [0,10000]

4 Results and Discussions

The optimization results indicate that the SFOA algorithm achieves the fastest convergence and the lowest fitness value, demonstrating superior performance in minimizing RMS acceleration under rail discontinuity conditions. WFO and PSO also show competitive results, converging to near-optimal solutions but at a slower rate compared to SFOA. In contrast, GA exhibits the weakest performance, with higher final fitness values and slower convergence throughout the iterations. These findings highlight SFOA as the most effective approach for improving ride comfort in railway systems (Figs. 4 and 7).

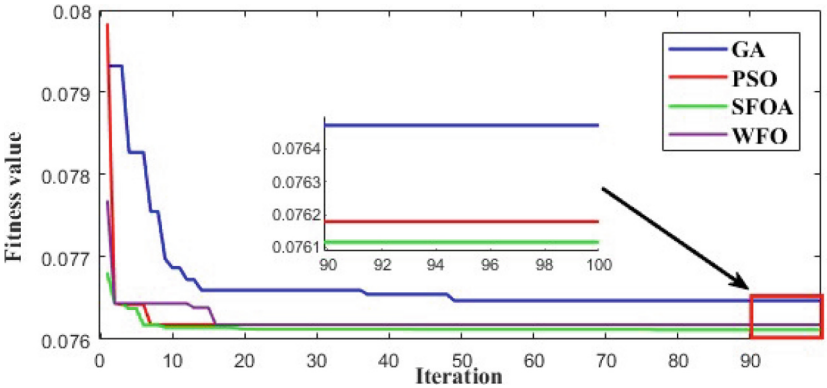

Fig. 4. Performance of GA, PSO, WFO, and SFOA in Minimizing Fitness Value.

The passive suspension shows the highest acceleration and displacement under rail discontinuity, indicating poor vibration control. All PID-based controllers improve performance, with SFOA achieving the lowest overshoot and fastest stabilization. SAM provides moderate improvement but is less effective than WFO, PSO, and especially SFOA. Overall, SFOA demonstrates superior relative performance, making it the most suitable method for enhancing ride comfort and dynamic stability.

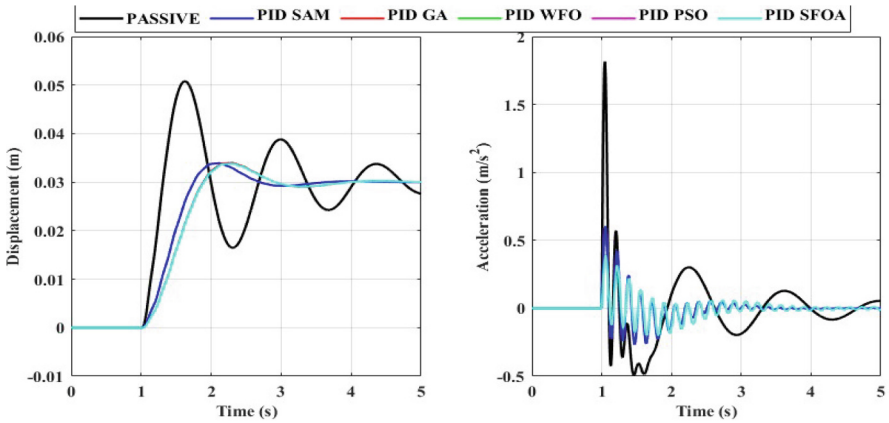

Fig. 5. Dynamic Response of Semi-Active Suspension for rail discontinuity default.

The optimized PID parameters obtained using SFOA and PSO will now be applied to additional simulations to evaluate the dynamic response of the system under different rail irregularity scenarios. These results suggest that the optimized parameters are suitable and robust for the different types of rail defects tested.

The results confirm that SFOA and PSO are the most effective optimization methods for PID tuning under rail irregularities, consistently achieving the lowest RMS acceleration values across all scenarios. According to the comparative analysis, SFOA

maintains superior performance with RMS values around 0.0761 for rail discontinuity and approximately 0.0540 for vertical offsets, while PSO follows closely with slightly higher but still very low values. This indicates that both methods significantly enhance ride comfort and dynamic stability compared to other approaches such as GA and SAM. Similarly, the system demonstrates excellent comfort levels, keeping RMS acceleration below 0.2 m/s^2 (Figs. 5 and 6), which ensures passenger comfort remains within a very comfortable range, as defined by the vibration exposure limits in ISO 2631 [15].

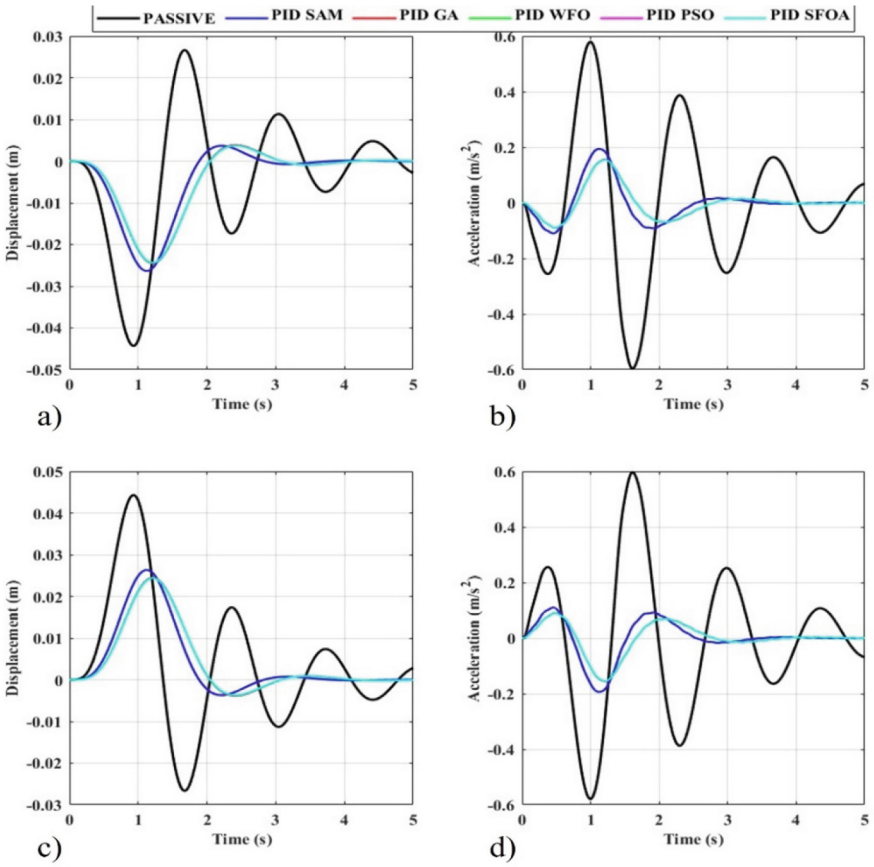

Fig. 6. Dynamic Response of Active Suspension Quarter Vehicle Model (a, b) Rail Downward Offset (c, d) Rail Upward Offset.

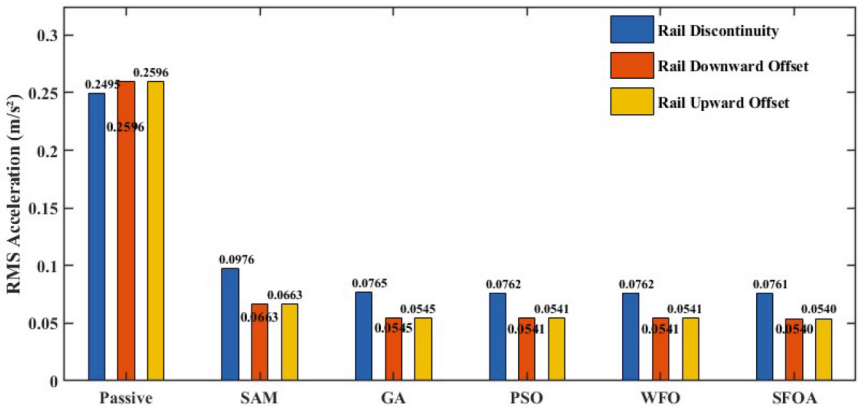

Fig. 7. Performance Comparison of PID Controllers Tuned by Metaheuristic Algorithms (Passive, SAM, GA, PSO, WFO, SFOA)

5 Conclusion

In this work, we have presented an optimization approach for PID-controlled semi-active suspensions using metaheuristic algorithms to enhance passenger comfort in railway vehicles. Comparative analysis under different track irregularities—rail discontinuity, downward vertical offset, and upward vertical offset—demonstrates that all optimized controllers outperform passive suspension systems significantly. Among the tested algorithms, SFOA consistently achieves the lowest RMS acceleration values, followed closely by PSO, confirming their robustness and efficiency in vibration mitigation. These findings highlight the potential of metaheuristic-based PID tuning, particularly SFOA, as a practical solution for improving ride comfort and dynamic stability in modern railway systems.

References

1. Niu, X.J.: The optimization for PID controller parameters based on genetic algorithm. Appl. Mech. Mater. **513–517**, 4102–4105 (2014)
2. Metered, H.: Vibration control of MR-damped vehicle suspension system using PID controller tuned by particle swarm optimization. SAE Int. J. Passeng. Cars Mech. Syst. **8**, 426–435 (2015)
3. Bramlette M.F.: Initialization, Mutation and Selection Methods in Genetic Algorithms for Function Optimization. (1991).
4. Kennedy, J.: Particle swarm optimization. Encyclopedia of Machine Learning, pp. 760–766. Springer, New York (2011)
5. Zhong, C., Li, G., Meng, Z., et al.: Starfish optimization algorithm (SFOA): a bio-inspired metaheuristic algorithm for global optimization compared with 100 optimizers. Neural Comput. Applic. **37**(5), 3641–3683 (2025)
6. Luo, K.: Water flow optimizer: a nature-inspired evolutionary algorithm for global optimization. IEEE Trans. Cybern. **52**(8), 7753–7764 (2021)

7. Nagarkar, M., Bhalerao, Y., Patil, G.V., Patil, R.Z.: Multi-objective optimization of nonlinear quarter car suspension system – PID and LQR control. Procedia Manuf. **20**, 420–427 (2018)
8. Abood, K., Khan, R.: Railway carriage model to study the influence of vertical secondary stiffness on ride comfort of railway carbody running on curved tracks. Mod. Appl. Sci. **5**, 11 (2011)
9. Foo, E., Goodall, R.: Active suspension control of flexible-bodied railway vehicles using electro-hydraulic and electro-magnetic actuators. Control Eng. Pract. **8**, 507–518 (2000)
10. Vincent, J., Jézéquel, L.: Laboratoire de mécanique des solides. Etude du concept de suspensions actives: Applications aux voitures ferroviaires (1999)
11. Global Optimization Toolbox Documentation.
12. Water Flow Optimizer.: A Nature-Inspired Evolutionary Algorithm for Global Optimization | Request PDF
13. Lopez-Franco, C., Diaz, D., Hernandez-Barragan, J., Arana-Daniel, N., Lopez-Franco, M.: A metaheuristic optimization approach for trajectory tracking of robot manipulators. Mathematics. **10**(7), 1051 (2022)
14. Şen, M.A., Kalyoncu, M.: Optimal tuning of PID controller using Grey wolf optimizer algorithm for quadruped robot. Balkan J. Electr. Comput. Eng. **6**, 29–35 (2018)
15. ISO 2631-4:2001. ISO

LQR Trajectory Tracking Control for Connected and Automated Vehicles in Unsignalized Intersections

Fernando Viadero-Monasterio[1(✉)], Miguel Meléndez-Useros[1], Nianhua Zhang[2], Beatriz López Boada[1], and María Jesús López Boada[1]

[1] Department of Mechanical Engineering, Vehicle Dynamics and Mechatronic Systems (VEDYMEC), Universidad Carlos III de Madrid, 28911 Leganés, Spain
fviadero@ing.uc3m.es

[2] School of Transportation Science and Engineering, Beihang University, Beijing, China

Abstract. Driving automation systems have received significant attention over the past few years due to their potential to revolutionize road transport. Modern intelligent vehicles integrate a variety of sensors that enable accurate localization and environment perception, supporting autonomous tasks such as lane keeping and collision avoidance. Moreover, vehicles can share information and cooperate to achieve common objectives. This paper investigates the use of such collective intelligence at an unsignalized intersection, assuming predetermined routes for all vehicles. An LQR controller is designed to ensure trajectory tracking for each vehicle. The multi-agent simulation setup is built in Simulink. Simulation results demonstrate the benefits of cooperative driving and validate the proposed approach.

Keywords: Vehicle safety · Intelligent Transportation Systems · Intelligent vehicles · Trajectory Tracking

1 Introduction

Over the past decades, series-production vehicles have increasingly integrated advanced technologies that enable them to interact with their surroundings [1]. With appropriate processing of lidar, radar and camera data, numerous driving automation features, such as lane-keeping assistance [2] and collision avoidance [3], have been successfully implemented, significantly enhancing driving safety and comfort. Moreover, advances in telecommunications now allow vehicles to communicate with one another and with the surrounding infrastructure. Such capabilities are particularly valuable in complex scenarios, including highway merging, vehicle platooning, intersection management, etc. [4–7].

Once all vehicles in a scenario are accurately positioned and their trajectories are carefully planned [8], the final step is to ensure that each vehicle can follow its assigned path without large deviations [9,10]. This step is crucial, as large tracking errors could lead to collisions or trigger traffic congestion [11]. Furthermore,

© The Author(s), under exclusive license to Springer Nature Switzerland AG 2026
A. Chaker et al. (Eds.): EFIMMS 2026, MMS 205, pp. 295–304, 2026.
https://doi.org/10.1007/978-3-032-22270-1_29

two different tracking approaches must be distinguished: path tracking and trajectory tracking. Path tracking involves following a predefined route without a specific timing requirement [12], whereas trajectory tracking requires the vehicle to reach each point at a precise time [13]. Path-tracking methods are generally applicable in static environments where other agents do not change their positions over time. Given the inherently dynamic nature of real-world traffic, trajectory tracking is therefore the more appropriate choice [14,15].

To control a vehicle, the inputs that generate the steering angle and throttle/brake commands must be carefully designed [16]. The choice of control approach depends on the complexity of the driving maneuvers and the vehicle's speed range. At low speeds, vehicle behavior can typically be analyzed using kinematic models [17], whereas high-speed driving requires dynamic models that account for tireâĂŞroad interactions [18,19]. Vehicles are also inherently multiple-input, multiple-output (MIMO) systems [20,21], which motivates the use of modern control methods capable of handling multiple system states and underactuated dynamics. Since energy efficiency is an important factor in road transport, the control strategy should also minimize input usage whenever it does not compromise vehicle safety [22,23].

Given the reasons outlined above, this paper presents a framework for cooperative driving at unsignalized intersections by implementing an LQR-based trajectory tracking controller on each vehicle.

2 Unsignalized Intersection Driving

This section briefly describes the intersection considered in this work (see Fig. 1). Each lane is assumed to have identical geometry, and a total of 12 possible maneuvers are defined. The path for each maneuver is fixed and generated using spline interpolation. A centralized intersection manager determines the crossing order and assigns the trajectory for each vehicle, defined as follows:

$$\left[T_r \; X_r \; Y_r \; \Phi_r \; V_r\right] \tag{1}$$

where T_r is a vector of successive reference time instants, X_r and Y_r denote the reference path, Φ_r denotes the desired orientation of the vehicle, and V_r is the reference longitudinal velocity. It is assumed that the trajectories generated by the intersection manager are safe and that vehicles will not collide unless they deviate excessively from their desired routes.

Remark 1. As the intersection manager was not the main contribution of this work, some details were omitted. However, these can be found in [24].

3 Vehicle Model

The trajectory tracking vehicle model (see Fig. 2) is based on the well-known single-track vehicle model. The list of the model parameters is presented in Table 1. The reference trajectory is given by a centralized intersection coordi-

nator. For a given time, the instantaneous reference trajectory is given by the tuple $\left[x_r\ y_r\ \varphi_r\ v_r\right]$. The lateral deviation error e_y, yaw error e_ϕ and longitudinal velocity error e_v are defined as [25]

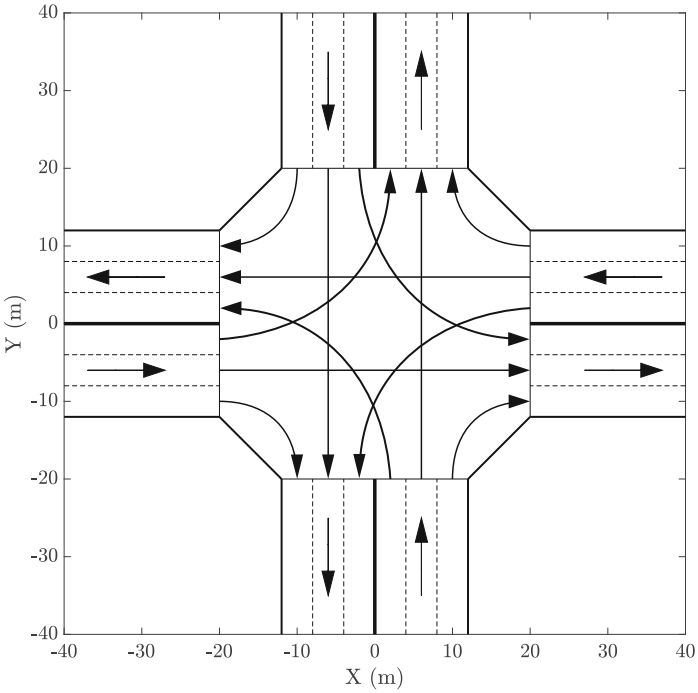

Fig. 1. The unsignalized intersection subject of study.

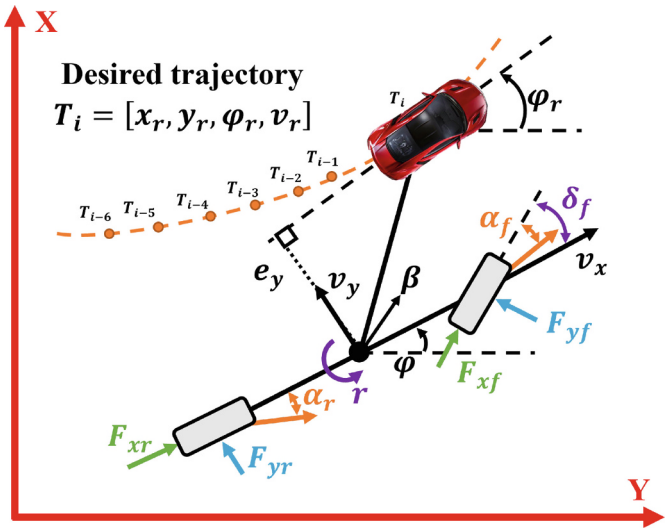

Fig. 2. Trajectory tracking model.

Table 1. Trajectory tracking model parameters

Parameters	Unit	Description
x, y	m	Coordinates of the vehicle center of gravity (CoG)
φ	rad	Yaw angle of the vehicle
r	rad/s	Yaw rate of the vehicle
v_x, v_y	m/s	Longitudinal and lateral velocity of the vehicle
e_y	m	Lateral tracking error
e_φ	rad	Yaw error
e_v	m/s	Longitudinal velocity error
m	kg	Vehicle mass
I_z	kgm^2	Yaw moment of inertia of the vehicle
l_f, l_r	m	Distance from CoG to the front/rear axle
F_{xf}, F_{xr}	N	Front/rear longitudinal tire force
F_{yf}, F_{yr}	N	Front/rear lateral tire force
C_f, C_r	N/rad	Front/rear cornering stiffness
α_f, α_r	rad	Front/rear wheel slip angle
F_x	N	Total longitudinal force
δ_f	rad	Steering angle of the front wheels
C_R	m^{-1}	Road curvature

$$\begin{aligned} e_y &= (x - x_r)\sin(\varphi_r) - (y - y_r)\cos(\varphi_r) \\ e_\varphi &= \varphi - \varphi_r \\ e_v &= v_x - v_r \end{aligned} \tag{2}$$

The reference yaw rate evolves as a function of the road curvature C_R

$$\dot{\varphi}_r = v_x C_R \tag{3}$$

Vehicle movement is described by

$$\begin{aligned} \dot{x} &= v_x\cos(\varphi) - v_y\sin(\varphi) \\ \dot{y} &= v_x\sin(\varphi) + v_y\cos(\varphi) \end{aligned} \tag{4}$$

The combination of (2–4) yields

$$\begin{aligned} \dot{e}_y &= \dot{x}\sin(\varphi_r) - \dot{y}\cos(\varphi_r) = v_x\sin(e_\varphi) + v_y\cos(e_\varphi) \\ \dot{e}_\varphi &= r - v_x C_R \\ \dot{e}_v &= \dot{v}_x - \dot{v}_r \end{aligned} \tag{5}$$

Now, following the Newton's laws,

$$\begin{aligned} m(\dot{v}_x - r v_y) &= F_{xf}\cos(\delta_f) + F_{xr} = F_x \\ m(\dot{v}_y + v_x r) &= F_{yf} + F_{yr} \\ I_z \dot{r} &= l_f F_{yf} - l_r F_{yr} \end{aligned} \tag{6}$$

with F_x denoting the traction/braking input force, and δ_f is the steering angle. Assuming small angles, lateral forces are expressed as [26]

$$F_{yf} = C_f \alpha_f, \quad F_{yr} = C_r \alpha_r \tag{7}$$

with α_f and α_r denoting the front and rear wheel slip angles, respectively [27]

$$\alpha_f = \delta_f - \frac{l_f r + v_y}{v_x}, \quad \alpha_r = \frac{l_r r - v_y}{v_x} \tag{8}$$

Putting together (6–8) returns

$$\begin{aligned} \dot{v}_y &= -\frac{C_f + C_r}{m v_x} v_y + \left(-v_x - \frac{l_f C_f - l_r C_r}{m v_x} \right) r + \frac{C_f}{m} \delta_f \\ \dot{r} &= -\frac{l_f C_f - l_r C_r}{I_z v_x} v_y - \frac{l_f^2 C_f + l_r^2 C_r}{I_z v_x} r + \frac{l_f C_f}{I_z} \delta_f \\ \dot{e}_y &= v_x \sin(e_\varphi) + v_y \cos(e_\varphi) \\ \dot{e}_\varphi &= r - C_R (e_v + v_r) \\ \dot{e}_v &= r v_y - \dot{v}_r + \frac{1}{m} F_x \end{aligned} \tag{9}$$

Under the assumption that e_ϕ is small, system (9) can be presented as a linear state-space model

$$\dot{x}(t) = \mathcal{A}(t) x(t) + \mathcal{B}(t) u(t) + \mathcal{B}_\omega \omega(t) \tag{10}$$

with the state-space matrices

$$\mathcal{A}(t) = \begin{bmatrix} a_{11} & a_{12} & 0 & 0 & 0 & 0 & 0 \\ a_{21} & a_{22} & 0 & 0 & 0 & 0 & 0 \\ 1 & 0 & 0 & v_x & 0 & 0 & 0 \\ 0 & 1 & 0 & 0 & -C_R & 0 & 0 \\ r & 0 & 0 & 0 & 0 & 0 & 0 \\ 0 & 0 & 1 & 0 & 0 & 0 & 0 \\ 0 & 0 & 0 & 0 & 1 & 0 & 0 \end{bmatrix}, \quad \mathcal{B}(t) = \begin{bmatrix} 0 & b_1 \\ 0 & b_2 \\ 0 & 0 \\ 0 & 0 \\ 1/m & 0 \\ 0 & 0 \\ 0 & 0 \end{bmatrix}, \quad \mathcal{B}_\omega = \begin{bmatrix} 0 & 0 \\ 0 & 0 \\ 0 & 0 \\ -1 & 0 \\ 0 & -1 \\ 0 & 0 \\ 0 & 0 \end{bmatrix}$$

$$\begin{aligned} a_{11} &= -\frac{(C_f + C_r)}{m v_x}, & a_{12} &= -v_x - \frac{(l_f C_f - l_r C_r)}{m v_x}, & b_1 &= \frac{C_f}{m} \\ a_{21} &= -\frac{l_f C_f - l_r C_r}{I_z v_x}, & a_{22} &= -\frac{(l_f^2 C_f + l_r^2 C_r)}{I_z v_x}, & b_2 &= \frac{l_f C_f}{I_z} \end{aligned}$$

The system state is $x = [v_y, r, e_y, e_\varphi, e_v, \int e_y, \int e_v]^\top$. The control input is $u = [F_x, \delta]^\top$. External disturbances are $\omega = [C_R v_x, \dot{v}_r]^\top$. The integral states $\int e_y$ and $\int e_v$ allow eliminating the steady-state lateral and longitudinal tracking errors.

4 Controller Design

Discrete-time trajectory tracking control is employed to facilitate real-time implementation. Following the Euler's discretization [28]

$$\dot{x}(t) \simeq \frac{x(k+1) - x(k)}{T_d}, \quad \forall k \in \mathbb{Z}_+ \tag{11}$$

the system (10) is transformed into its discrete-time counterpart

$$x(k+1) = A(k)x(k) + B(k)u(k) + B_\omega \omega(k) \tag{12}$$

with the discrete-time system matrices

$$A = I + T_d\mathcal{A},\ B = T_d\mathcal{B},\ B_\omega = T_d\mathcal{B}_\omega,\ T_d = 0.01\ s$$

Since v_x can be measured, the state space matrices $A(k)$ and $B(k)$ are known for any time instant k. Ignoring the effect of the external disturbance, the purpose of the linear quadratic regulator (LQR) is to minimize the cost [29]:

$$J = \sum_{k}^{\infty} \left(x(k)^\top Q x(k) + u(k)^\top R u(k) \right) \tag{13}$$

where Q and R are the state and control cost matrices, respectively. These have been defined heuristically following the Bryson's rule [30]:

$$Q = \text{diag}(2, 0.5, 1, 0.43, 1, 2, 2)^{-2}, \quad R = \text{diag}(10000, 0.52)^{-2} \tag{14}$$

Using the Matlab function *lqr*, the control gain matrix K can be obtained. The control input is generated as the state-feedback law

$$u(k) = Kx(k) \tag{15}$$

5 Simulation Results

The proposed trajectory tracking controller is validated through a series of simulations conducted in Simulink. The vehicle specifications are provided in Table 2. In the simulation, 12 vehicles approach the intersection. The intersection manager decides which vehicle should go first based on the sequence of vehicles reaching the control zone and their maneuvers. The manager also provides the trajectory and velocity profiles that each vehicle must follow.

Simulation results are presented through Fig. 3. The evolution of the vehicles' planar coordinates throughout the simulation indicates that the proposed trajectory-tracking scheme achieves robust and stable behaviour, yielding a continuously smooth path. Furthermore, the mechanical limits imposed on the control inputs, particularly the traction force and the steering angle, are consistently adhered to. In order to further mitigate the risk of secondary conflict events, it is essential that the lateral deviation of each vehicle from its reference path be minimized as much as possible. The maximum lateral separation error remains below 0.5 m, indicating a safe trajectory tracking operation as new potential crossing conflicts are unlikely to occur.

Table 2. Vehicle specifications

$m\ (kg)$	$I_z\ (kg \cdot m^2)$	$l_f\ (m)$	$l_r\ (m)$	$C_f,\ C_r\ (kN/rad)$
1750	2500	1.24	1.46	$60 \pm 10\%$
$v_x\ (m/s)$	$r\ (rad/s)$	$C_R\ (m^{-1})$	$F_x\ (N)$	$\delta_f\ (^\circ)$
3–15	± 0.75	± 0.02	± 8750	± 30

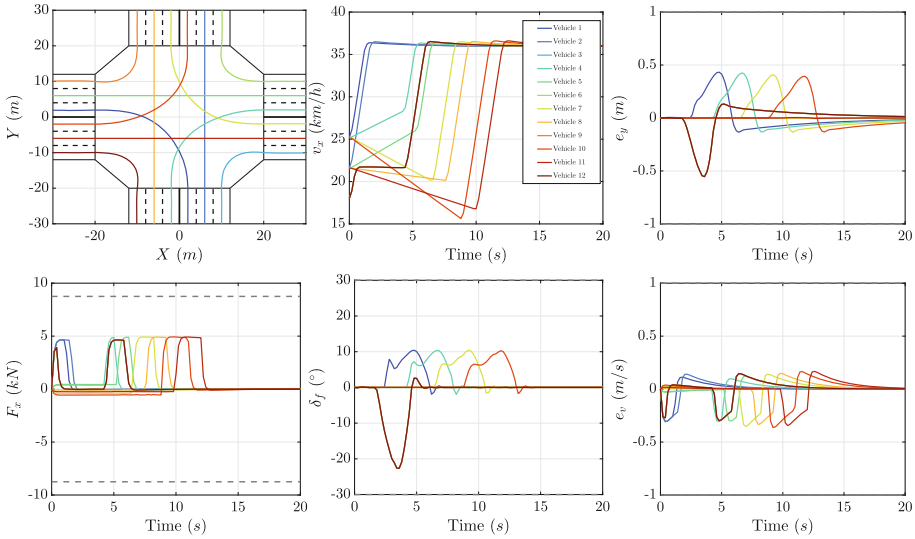

Fig. 3. Simulation results for the proposed controller.

6 Conclusion

This work has presented a LQR trajectory tracking controller for connected and automated vehicles in unsignalized intersections. A centralized intersection manager is assumed to determine the crossing sequence and trajectory (X-Y route and velocity profile) that each vehicle must follow. The Q and R matrices of the LQR controller are designed following the Bryson's rule.

A simulation environment was developed in Simulink to evaluate the effectiveness of the proposed approach. The results show that the controller enables vehicles to cooperatively navigate unsignalized intersections without collision risk. Each vehicle closely follows its assigned reference trajectory, exhibiting only minimal tracking deviations. Consequently, no potential conflict points emerge, demonstrating the precision and robustness of the trajectory tracking strategy.

Future works will explore energy efficient trajectory planning [31,32]. Different cooperative scenarios will be studied, such as highway merging or lane changing [33,34]. Finally, the impact of accurate trajectory tracking on autonomous mobility on demand will be explored [35].

Acknowledgments. The work was supported in part by the grant [PID2022-136468OB-I00] funded by MCIN/AEI/10.13039/501100011033, by "ERDF A way of making Europe", and by UC3M's grants for young doctors (Grant No.2024/00741/001).

References

1. Viadero-Monasterio, F., Meléndez-Useros, M., Jiménez-Salas, M., López Boada, B., Jesus Lopez Boada, M. Key influencing factors in vehicle platoons: a systematic study and review. Evolving Syst. **16**(4), 1–13 (2025)
2. Glida, H.E., Oudainia, M.R., Sentouh, C., Popieul, J.-C.: A new model-free shared control for lane-keeping assist system: theory and experimental validation. IEEE Trans. Intell. Veh., 1–11 (2024). https://doi.org/10.1109/TIV.2024.3445176
3. Liu, P., Liu, T., Chen, T., Liu, M., Piao, C., Huang, H.: Path optimization-based online data-driven obstacle avoidance trajectory planning for intelligent vehicles. IEEE Trans. Intell. Veh., 1–13 (2024). https://doi.org/10.1109/TIV.2024.3449131
4. Meng, Y., Liao, S., Wang, P., Jin, Y., Yang, P.: Optimal sequential merging strategy based on adaptive threshold for ramp traffic involving platoons. IEEE Trans. Intell. Transp. Syst. **26**(4), 4661–4675 (2025). https://doi.org/10.1109/TITS.2025.3534717
5. Viadero-Monasterio, F., Meléndez-Useros, M., Zhang, H., Boada, B.L., Boada, M.J.L.: Signalized traffic management optimizing energy efficiency under driver preferences for vehicles with heterogeneous powertrains. IEEE Trans. Consum. Electron. **71**(2), 3454–3464 (2025). https://doi.org/10.1109/TCE.2025.3569967
6. Viadero-Monasterio, F., Meléndez-Useros, M., Jiménez-Salas, M., Boada, B.L.: Robust adaptive control of heterogeneous vehicle platoons in the presence of network disconnections with a novel string stability guarantee. IEEE Trans. Intell. Veh. **11**(1), 63–75 (2026). https://doi.org/10.1109/TIV.2025.3578936
7. Viadero-Monasterio, F., Meléndez-Useros, M., Jiménez-Salas, M., Boada, B.L.: Robust adaptive heterogeneous vehicle platoon control based on disturbances estimation and compensation. IEEE Access **12**, 96924–96935 (2024). https://doi.org/10.1109/ACCESS.2024.3428341
8. Viana, I.B., Kanchwala, H., Ahiska, K., Aouf, N.: A comparison of trajectory planning and control frameworks for cooperative autonomous driving. J. Dyn. Syst., Measur., Control **143**(7), 071002 (2021)
9. Frison, G., Tota, A., Dimauro, L., Velardocchia, M.: Path planning and tracking algorithms for autonomous off-road vehicles. In: The International Conference of IFToMM ITALY, pp. 281–289. Springer (2024)
10. Nguyen, A.-T., Rath, J., Guerra, T.-M., Palhares, R., Zhang, H.: Robust set-invariance based fuzzy output tracking control for vehicle autonomous driving under uncertain lateral forces and steering constraints. IEEE Trans. Intell. Transp. Syst. **22**(9), 5849–5860 (2021). https://doi.org/10.1109/TITS.2020.3021292
11. Wang, L., Law, K.L.E., Lam, C.-T., Ng, B., Ke, W., Im, M.: Automatic lane discovery and traffic congestion detection in a real-time multi-vehicle tracking systems. IEEE Access **12**, 161468–161479 (2024). https://doi.org/10.1109/ACCESS.2024.3483439
12. Viadero-Monasterio, F., Nguyen, A.-T., Lauber, J., Boada, M.J.L., Boada, B.L.: Event-triggered robust path tracking control considering roll stability under network-induced delays for autonomous vehicles. IEEE Trans. Intell. Transp. Syst. **24**(12), 14743–14756 (2023). https://doi.org/10.1109/TITS.2023.3321415

13. Alcalá, E., Puig, V., Quevedo, J.: LPV-MP planning for autonomous racing vehicles considering obstacles. Robot. Auton. Syst. **124**, 103392 (2020)
14. Hu, J., Yi, S., Zhu, P., Sun, Z.: Obstacle avoidance decision and trajectory tracking control of intelligent vehicle considering surrounding vehicles. Proc. Inst. Mech. Eng., Part D: J. Automob. Eng. **239**(1), 276–290 (2025)
15. Kim, C., Yoon, Y., Kim, S., Yoo, M.J., Yi, K.: Trajectory planning and control of autonomous vehicles for static vehicle avoidance in dynamic traffic environments. IEEE Access **11**, 5772–5788 (2023). https://doi.org/10.1109/ACCESS.2023.3236816
16. Moreno-Gonzalez, M., Artuñedo, A., Villagra, J.: Model-free speed tracking control for automated cars. IEEE Open J. Intell. Transp. Syst. **7**, 1–15 (2026). https://doi.org/10.1109/OJITS.2025.3640943
17. Alcala, E., Puig, V., Quevedo, J., Escobet, T., Comasolivas, R.: Autonomous vehicle control using a kinematic Lyapunov-based technique with LQR-LMI tuning. Control. Eng. Pract. **73**, 1–12 (2018)
18. Alcalá, E., Puig, V., Quevedo, J.: LPV-MPC control for autonomous vehicles. IFAC-PapersOnLine **52**(28), 106–113 (2019)
19. Alcalá, E., et al.: Comparison of two non-linear model-based control strategies for autonomous vehicles. In: 2016 24th Mediterranean Conference on Control and Automation (MED), pp. 846–851 (2016). https://doi.org/10.1109/MED.2016.7535921
20. Meléndez-Useros, M., Viadero-Monasterio, F., Jiménez-Salas, M., López-Boada, M.J.: Static output-feedback path-tracking controller tolerant to steering actuator faults for distributed driven electric vehicles. World Electr. Veh. J. **16**(1), 40 (2025)
21. Viadero-Monasterio, F., Gutiérrez-Moizant, R., Meléndez-Useros, M., López Boada, M.J.: Static output feedback control for vehicle platoons with robustness to mass uncertainty. Electronics **14**(1), 139 (2024)
22. Galvagno, E., Rolando, L., Pulvirenti, L., Zerbato, L., Tresca, L.: Hybrid electric vehicle platoon control and optimal energy management system for fuel economy, safety, and dynamic performance. In: IFToMM World Congress on Mechanism and Machine Science, pp. 980–991, Springer (2023)
23. Hu, D., Tian, C., Nguyen, A.-T., Huang, C.: Uncertainty-driven active reinforcement learning for energy management strategy in electrified vehicles. IEEE Trans. Transp. Electrification, 1–1 (2025). https://doi.org/10.1109/TTE.2025.3614254
24. Viadero-Monasterio, F., Meléndez-Useros, M., Zhang, N., Zhang, H., Boada, B.L., Boada, M.J.L.: Motion planning and robust output-feedback trajectory tracking control for multiple intelligent and connected vehicles in unsignalized intersections. IEEE Trans. Veh. Technol., 1–13 (2025). https://doi.org/10.1109/TVT.2025.3586769
25. Yang, K., Tang, X., Qin, Y., Huang, Y., Wang, H., Pu, H.: Comparative study of trajectory tracking control for automated vehicles via model predictive control and robust H-infinity state feedback control. Chin. J. Mech. Eng. **34**(1), 74 (2021)
26. Viadero-Monasterio, F., García, J., Meléndez-Useros, M., Jiménez-Salas, M., Boada, B.L., López Boada, M.J.: Simultaneous estimation of vehicle sideslip and roll angles using an event-triggered-based IoT architecture. Machines **12**(1), 53 (2024)
27. Viadero-Monasterio, F., Meléndez-Useros, M., Lenzo, B., Boada, B.L.: Interval observer for vehicle sideslip angle estimation using extended Kalman filters. Machines **13**(8), 707 (2025)

28. Viadero-Monasterio, F., Meléndez-Useros, M., Jiménez-Salas, M., Boada, M.J.L.: Fault-tolerant robust output-feedback control of a vehicle platoon considering measurement noise and road disturbances. IET Intel. Transport Syst. **19**(1), e70007 (2025)
29. Lenzo, B., Goel, T., Christian Gerdes, J.: Autonomous drifting using torque vectoring: innovating active safety. IEEE Trans. Intell. Transp. Syst. **25**(11), 17931–17939 (2024). https://doi.org/10.1109/TITS.2024.3437177
30. Okyere, E., Bousbaine, A., Poyi, G.T., Joseph, A.K., Andrade, J.M.: LQR controller design for quad-rotor helicopters. J. Eng. **2019**(17), 4003–4007 (2019)
31. Wang, X., Li, F., Tang, Y., Peng, X., Ni, J.: A deep reinforcement learning approach for optimized speed planning of connected and autonomous vehicles. IEEE Trans. Intell. Veh. **10**(8), 4242–4254 (2025). https://doi.org/10.1109/TIV.2024.3477940
32. Wu, D.-M., et al.: Fast velocity trajectory planning and control algorithm of intelligent 4wd electric vehicle for energy saving using time-based mpc. IET Intel. Transport Syst. **13**(1), 153–159 (2019)
33. Kamal, M.A.S., Bakibillah, A., Hayakawa, T., Yamada, K., Imura, J.-I.: Cooperative look-ahead lane change system for improving driving intelligence of automated vehicles in critical scenarios. IEEE Trans. Intell. Veh. **9**(9), 5876–5888 (2024). https://doi.org/10.1109/TIV.2024.3357983
34. Yin, Y., Gao, Z., Long, K., Fei, Y.: A cooperative lane change control strategy for cooperative adaptive cruise control platoons with insufficient headway gaps. XXPhys. A **655**, 130175 (2024)
35. Viadero-Monasterio, F., Meléndez-Useros, M., Zhang, H., Boada, B.L., Boada, M.J.L.: Low-cost vehicle rebalancing control for an autonomous mobility on demand system. J. Franklin Inst., 108333 (2025)

Experimental Evaluation of Position-Based Visual Servoing Using AprilTag for Mobile Robot Docking

Houssein Lamine[1(✉)], Hassen Makki[2], and Lotfi Romdhane[1,3]

[1] Mechanical Laboratory of Sousse (LMS), National School of Engineers of Sousse, University of Sousse, Sousse, Tunisia
houssein.lamine@eniso.u-souse.tn, lromdhane@aus.edu

[2] Networked Objects, Control, and Communication Systems (NOCCS), National School of Engineers of Sousse, University of Sousse, Sousse, Tunisia
hassen.mekki@eniso.u-sousse.tn

[3] College of Engineering, American University of Sharjah, PO Box 26666, Sharjah, United Arab Emirates

Abstract. Docking a mobile robot to a charging station is a critical capability for long-term autonomy, enabling continuous operation without human intervention. This paper investigates a Position-based visual servoing as a local alignment strategy for a docking a mobile robot to a charging station. In the first stage, the robot employs autonomous navigation using ROS2 NAV2 to reach an initial approach pose in front of the charging station. Once reached, a camera system detects fiducial tags placed on the station in aim to compute the relative pose. A PI controller is used to align the robot toward a precise staging pose. However, as the robot advances closer to the dock, the camera's field of view becomes occluded, rendering visual feedback unavailable. To address this limitation, wheel odometry is integrated to maintain trajectory and ensure accurate completion of the docking maneuver. The proposed method thus leverages a hybrid sensing approach: global navigation for coarse positioning, visual tag detection for fine alignment, and odometry for blind final approach. Experimental trials demonstrate that this layered strategy achieves acceptable docking performance under realistic conditions.

Keywords: Differential Mobile Robots · AprilTag · Docking · Position-based Visual Servoing · RGB Camera

1 Introduction

Autonomous docking of mobile robots to charging stations is a fundamental capability for ensuring long-term operation in service, industrial, and research environments [1]. Without reliable docking, robots require manual intervention, which limits scalability and autonomy [2]. Recent advances in navigation frameworks such as ROS2 Navigation (Nav2) have enabled robots to reach coarse target positions with high reliability, but the final docking manoeuvre demands greater precision than standard path planning can provide [3].

© The Author(s), under exclusive license to Springer Nature Switzerland AG 2026
A. Chaker et al. (Eds.): EFIMMS 2026, MMS 205, pp. 305–312, 2026.
https://doi.org/10.1007/978-3-032-22270-1_30

To address this challenge, vision-based methods have been widely explored. Fiducial markers such as AprilTags or ArUco tags provide robust, low-cost localization cues that allow robots to estimate their relative pose with respect to docking stations [4]. These markers are particularly effective in structured environments, where visual features can be deliberately placed to guide docking [5]. Several studies have demonstrated that monocular cameras combined with fiducial detection can achieve centimeter-level accuracy in docking tasks [6].

However, vision systems face inherent limitations. As the robot approaches the dock, the camera's field of view narrows and may become occluded, rendering visual feedback unavailable [7]. To overcome this, researchers have proposed hybrid approaches that combine vision with odometry or other proprioceptive sensors [8]. Wheel odometry, despite being prone to drift, provides short-range reliability that can sustain the robot's trajectory during the blind final approach. This layered sensing strategy—global navigation for coarse positioning, vision for fine alignment, and odometry for blind completion—has been shown to improve docking robustness [9, 10].

In this paper, we investigate such a hybrid docking method. First, the robot navigates autonomously to an initial approach pose in front of the charging station using ROS2 Nav2. Then, a camera detects an AprilTag placed on the dock, and a PI controller aligns the robot to a staging pose. Finally, when the camera becomes blind, wheel odometry guides the robot to complete docking.

This paper is structured into two primary sections: Materials and Methods, which describes the docking setup and control equations, and Results and Discussion, which reports the experimental tests.

2 Materials and Methods

2.1 Materials

The experimental setup is illustrated in Fig. 1(a). It is composed of a mobile differential robot, referred to as "EduBot". An Intel RealSense RGB-D camera D435 is installed at front. The robot navigates toward a battery charging station, which is localized using an AprilTag marker, as shown in Fig. 1(b). EduBot is controlled through the linear velocity v (m/s) along the x_{mr} axis and the angular velocity ω (rad/s) around the z_{mr} axis. Since docking is the primary target application, the robot velocities are constrained to 0.4 m/s and 0.5 rad/s. The camera operates at 30 Hz with a resolution 640 × 480, and only RGB data is processed. Camera intrinsic parameters are: FocalLength = [fx = 586.0671, fy = 587.8830] and PrincipalPoint = [ppx = 323.9769, ppy = 234.9307].

The employed tag is an AprilTag 36 h11 with a size of 120 mm. The AprilTag frame R_{ap} origin is placed at its center. The planar pose of the EduBot is defined as the pose of the mobile robot frame R_{mr} in relation to R_{ap}: $q = (x, z, \theta)^T$ [m, m, deg.(°)]; x along x_{ap}, y along y_{ap} and θ is rotation about z_{ap}.

2.2 Methods

The developed control law is a Position-Based Visual Servoing. The tracked AprilTag pose in the captured images is used as the controller feedback.

Figure 2 explains the docking task strategy as following:

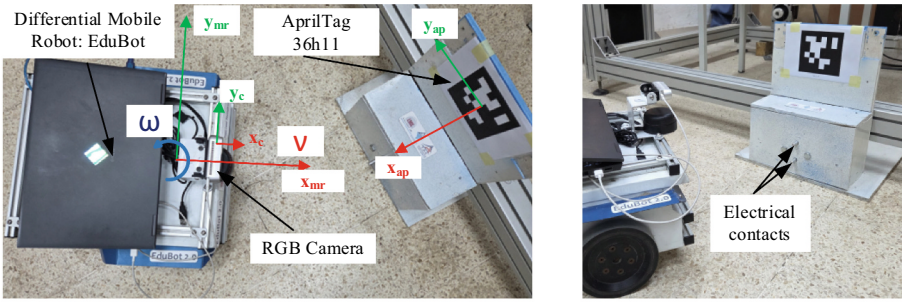

(a): Notations **(b): Charging Station**

Fig. 1. Experimental setup: EduBot + charging station

- the robot employs autonomous navigation using ROS2 NAV2 to reach an initial approach pose $P_{initial}$ in front of the charging station at an approximate distance of 1.2 m (xy_tolerance = 0.2 m and yaw_tolerance = 0.2 rad = 11,5°).
- Once P_{ini} is reached, the camera system detects the Apriltag placed on the charging station, thereby, the relative pose of the robot is computed cyclically (dt = 33 ms).
- A proportional–integral (PI) controller is used to adjust the robot's velocity, guiding it toward $P_{heading}$, and then, $P_{staging}$.
- Due to sensor blindness, based on wheel odometry, the robot is guided to the final pose P_{final}.

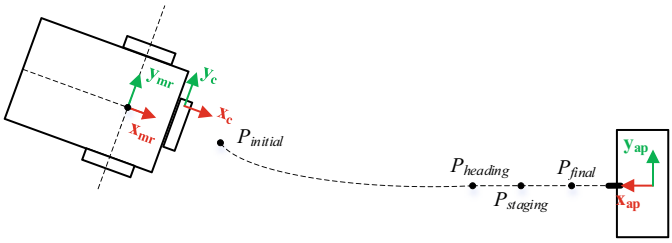

Fig. 2. Docking strategy

In the sequel, a comprehensive description of the docking task steps is given.

The AprilTag pose is detected and estimated in the Camera frame R_c (see Fig. 1(a)) and must be transformed into the Robot Frame (R_{mr}). The camera is mounted with a longitudinal offset $d_x = 0.15813\ m$ and a lateral offset $d_y = 0.0325\ m$. the final pose is $q = (x, y, \theta)^T$ obtained from ${}^{mr}T_{ap}$ such that:

$$ {}^{mr}T_{ap} = {}^{mr}T_c \cdot {}^{c}T_{ap} $$

$$ {}^{mr}T_c = \begin{bmatrix} 1 & 0 & 0 & d_x \\ 0 & 1 & 0 & d_y \\ 0 & 0 & 1 & 0 \\ 0 & 0 & 0 & 1 \end{bmatrix}; {}^{c}T_{ap} = \begin{bmatrix} \cos(\theta) & -\sin(\theta) & 0 & x_c \\ \sin(\theta) & \cos(\theta) & 0 & y_c \\ 0 & 0 & 1 & 0 \\ 0 & 0 & 0 & 1 \end{bmatrix} \quad (1) $$

The control system calculates the error between the current robot pose q and the desired docking pose $P_{staging}$ as show in Eq.(2).Then, a linear (distance) error and an angular error are deducted for mapping to robot velocity $\mathrm{v} = (\mathrm{v}, \omega)^T$. $P_{heading}$ is employed in order to reduce e_y and align the robot heading e_θ before reaching $P_{staging}$.

$$\begin{aligned} e_y &= y_{staging} - y \\ e_x &= x_{staging} - x \\ e_\theta &= \theta_{staging} - \theta \\ e_{lin} &= \sqrt{e_x^2 + e_y^2} + x_{heading}; x_{heading} = 0.2\ m \\ e_{ang} &= \mathrm{atan2}\left(e_y, e_x\right) - e_\theta \end{aligned} \tag{2}$$

The robot is controlled via a Proportional-Integral (PI) controller in order to reduce the steady state error Eq. (3):

$$\begin{aligned} I_{lin} &= I_{lin} + e_{lin} \cdot dt \\ I_{ang} &= I_{ang} + e_{ang} \cdot dt \\ I_{lin} &= \max\left(\min\left(I_{lin}, I_{lin_\max}\right), I_{lin_\min}\right); \\ I_{ang} &= \max\left(\min\left(I_{ang}, I_{ang_\max}\right), I_{ang_\min}\right); \\ v &= K_{Plin} \cdot e_{lin} + K_{Ilin} \cdot I_{lin} \\ \omega &= K_{Pang} \cdot e_{ang} + K_{Iang} \cdot I_{ang} \end{aligned} \tag{3}$$

Where, I_{lin} and I_{ang} are integral terms computed using a sampling period dt = 33 ms, which is limited to the camera 30 fps. To prevent overshoot, the integral terms are clamped using minimal and maximal values of -1 and 1, respectively. Finally $\mathrm{v} = (\mathrm{v}, \omega)^T$ are obtained using 4 gains: (k_{Plin}, k_{Pang}, k_{Ilin}, and k_{Iang}) in aim to tune the controller for both linear and angular velocity.

Ultimately docking task and actuator constraints are taken into account, i.e., velocity saturation and deadzone (Minimum) Velocity Eq. (4):

$$\begin{aligned} v_{final} &= \begin{cases} \mathrm{sgn}(v) \cdot v_{min} & \text{if } 0 <\mid v \mid < v_{min} \\ v & \text{if } v_{min} <\mid v \mid < v_{sat} \\ v_{sat} & \text{otherwise} \end{cases} \\ \omega_{final} &= \begin{cases} \mathrm{sgn}(\omega) \cdot \omega_{min} & \text{if } 0 <\mid \omega \mid < \omega_{min} \\ \omega & \text{if } \omega_{min} <\mid \omega \mid < \omega_{sat} \\ \omega_{sat} & \text{otherwise} \end{cases} \end{aligned} \tag{4}$$

Where v_{sat}, ω_{sat} are maximum velocity, and v_{min}, ω_{min} are minimum velocity to move the robot. $\mathrm{v}_{\mathrm{final}} = (\mathrm{v}_{final}, \omega_{final})^T$ is the mobile robot's control input.

3 Results and Discussion

A series of experiments was conducted to analyze the behavior of the control systems applied to EduBot. In the initial setup, the robot was positioned approximately 1.2 m from the AprilTag, with variations introduced in its lateral position and orientation. The first tests employed a proportional (P) controller, starting from a quasi-straight

posture facing the charging station (Fig. 3(a)), which enabled the tuning of the K_P gains. Subsequently, a proportional–integral (PI) controller was implemented to regulate the straight-line trajectory. In the second set of trials, the robot was placed laterally with a certain inclination (Fig. 3(b)), where the objective was to generate a curved trajectory

Observation of the Edubot's behavior was conducted using the pose error in [m, m, °] and the robot velocity $v_{\text{final}} = (v_{final}, \omega_{final})^T$.

(a): Quasi-straight initial posture **(b):** Inclined initial posture

Fig. 3. Experimental trials initial postures

3.1 Quasi-Linear Motion

In this stage, EduBot was positioned in front of the charging station at an approximate distance of 1.2 m, with the initial orientation constrained to less than 10°. Several trial-and-error tests were first conducted to tune the gains using only a proportional (P) controller, based on the robot's output behavior and final pose error. When both $K_{Plin} = K_{Pang} = 0.4$, EduBot exhibited oscillations along its longitudinal axis while approaching the target. To mitigate this, K_{Pang} was reduced to 0.05, and the resulting pose errors are illustrated in Fig. 4. The docking operation was successful, yielding a lateral error of 20 mm and an orientation error of −2.8°. It should be noted that, since mobile robots are typically stopped by a dedicated sensor, residual error along the x_{ap} axis can be considered acceptable.

Subsequently, a proportional–integral (PI) controller was applied to regulate straight-line motion. The corresponding pose-error curves are presented in Fig. 5. The results demonstrate improved performance, yielding a lateral error of 0.007 m and an orientation error of −0.7°

3.2 Curve Motion

Hereafter, non-straight trials were conducted in which EduBot was oriented between 10° and 20°. The resulting pose errors and robot velocities are presented in Figs. 6 and 7, respectively. The controller is PI using gains: $K_{Plin} = 0.4$, $K_{Pang} = 0.05$, $K_{Ilin} = 0.05$, $K_{Iang} = 0.01$.

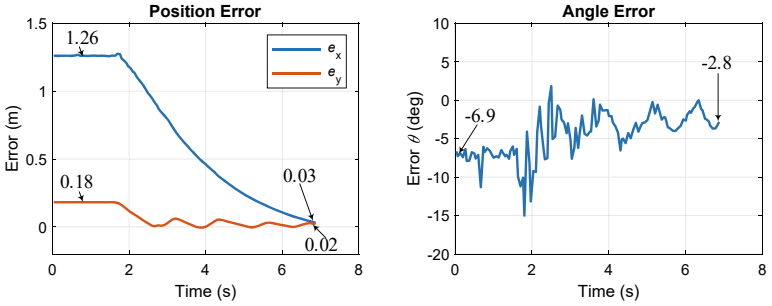

Fig. 4. Pose error vs. time for linear motion (P Controller: $K_{Plin} = 0.4$, $K_{Pang} = 0.05$)

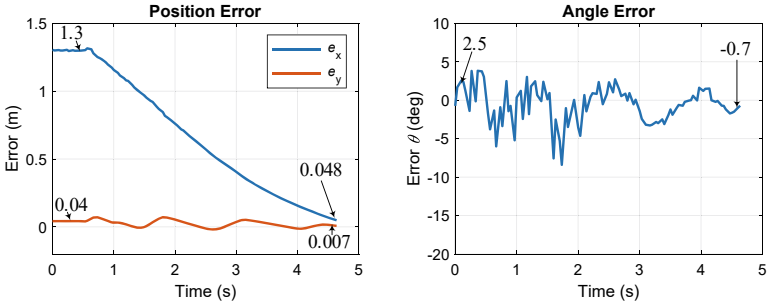

Fig. 5. Pose error vs. time for linear motion (PI Controller: $K_{Plin} = 0.4$, $K_{Pang} = 0.05$, $K_{Ilin} = 0.05$, $K_{Iang} = 0.01$)

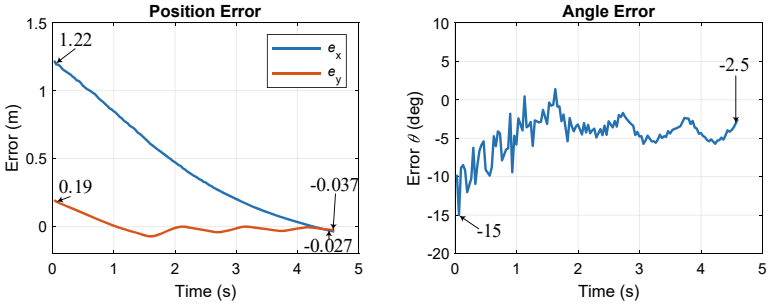

Fig. 6. Pose error vs. time for curve motion

The obtained pose error is q = (−0.037, −0.027, −2.5), that allowed to obtain a successful docking. It was observed that linear velocity was saturated due to integral term. In the opposite, angular velocity was in operational range. Finally, Fig. 8 plots the planar robot motion. Some oscillations can be observed and has to be investigated.

During the experimental trials, extensive tuning was required to characterize the behavior of the control law. The observed limitations of the controller were as follows:

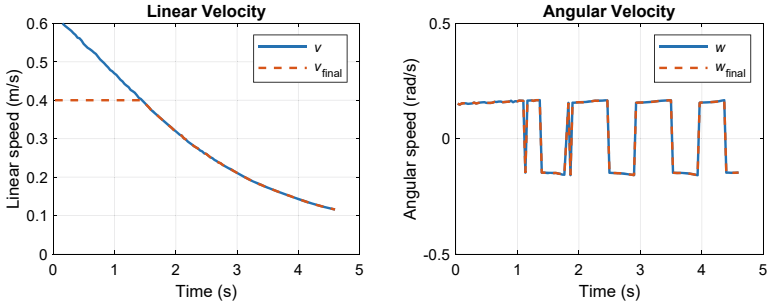

Fig. 7. Robot velocity vs. time for curve motion

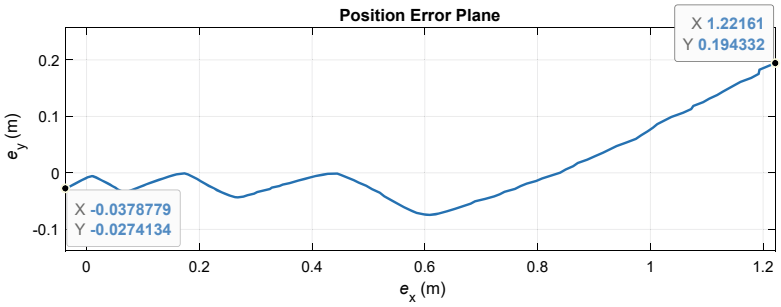

Fig. 8. Movement of the EduBot in plane xy

- Low rate of the control loop, which leads to noisy orientation trajectories,
- Saturation of control velocity,
- Minimum velocity is often reached,
- Robot velocity should be corrected, e.g. slowing down if robot not aligned.

4 Conclusion

This work presented the implementation and experimental evaluation of a position-based visual servoing strategy for autonomous docking of a mobile robot to a charging station. By combining ROS2 Nav2 for coarse navigation, AprilTag pose estimation for fine alignment, and wheel odometry for the blind final approach, the proposed method achieved reliable docking performance.

Using position-based visual servoing, proportional–integral (PI) control laws were implemented to guide the mobile robot toward its target station. The docking task and actuator constraints were explicitly considered. Experiments were conducted under different scenarios, with gain tuning performed to achieve improved results. For both quasi-linear and curve motion, acceptable results were obtained: accuracy from 7 to 20 mm laterally and from 0.7 to 2.8° for yaw orientation.

Despite these promising results, several limitations were identified, including the low control loop rate constrained by camera frame acquisition, velocity saturation effects, and oscillations in certain trajectories.

Ongoing work focuses on enhancing the robot controller through controlled velocity, sensor fusion, and path-planning techniques, with the objective of achieving smoother trajectories

Acknowledgments. We gratefully acknowledge the support of DIGINOVC for supplying the necessary hardware, including the EduBot mobile robot, which enabled the execution of our experimental tests.

References

1. Oh, J.S., Kim, M.Y.: Regression-based docking system for autonomous mobile robots using a monocular camera and ArUco markers. Sensors. **25**(12), 3742 (2025)
2. Roy, H., Héry, E., Kubo, R.: Docking control and priority scheduling for single battery charging station with multiple mobile robots. In: Mecatronics & AISM (Asia International Symposium on Mechatronics) (2023)
3. Michel, A., Paul, A.: Robot docking and charging techniques in real time deep learning model. J. Robot. Spectr. (2024)
4. Bian, X., Chen, W., Ran, D., Liang, Z., Mei, X.: FiMa-reader: a cost-effective fiducial marker reader system for autonomous mobile robot docking. Appl. Sci. **13**(24), 13079 (2023)
5. Alam, M.S., Gullu, A.I., Gunes, A.: Fiducial markers and particle filter based localization and navigation framework. SN Comput. Sci. **5**, 748 (2024)
6. Chatterjee, A.: Autonomous Docking for mobile Robots Using Fiducial Markers. GitHub Project: (2023). https://github.com/ArghyaChatterjee/autonomous-docking-for-mobile-robots
7. Automatic Addison.: Autonomous Docking with AprilTags Using Nav2 – ROS2 Jazzy: (2025). https://automaticaddison.com/autonomous-docking-with-apriltags-using-nav2-ros-2-jazzy/
8. Nav2 Documentation.: Using Docking Server. Nav2 Tutorials: (2025). https://docs.nav2.org/tutorials/docs/using_docking.html
9. Poon, J.N.: Automatic docking and charging station for a mobile robot. GitHub Project: (2019). https://github.com/JNPoon/FYP18-19_AutomaticDocking
10. Park, Jong Jin. Graceful Navigation for Mobile Robots in Dynamic and Uncertain Environments. Dissertation (2016)

Vibration and Materials

Hybrid Actuator and Sensor Fault Diagnosis for Active Steering Systems

Miguel Meléndez-Useros(✉), Fernando Viadero-Monasterio, María Jesús López Boada, and Beatriz López Boada

Departamento de Ingeniería Mecánica, Universidad Carlos III de Madrid, Madrid, Spain
{mmelende,fviadero,mjboada,bboada}@ing.uc3m.es

Abstract. The reliability and safety of active steering systems are fundamental to the successful operation of modern automated vehicles, since these systems directly control vehicle dynamics and trajectory. However, the increasing complexity of these systems increases the likelihood of faults occurring in the actuators, which can severely impact performance and compromise vehicle safety. Therefore, it is essential to accurately detect and identify these faults in order to enable effective fault-tolerant control strategies. Furthermore, sensor anomalies pose a significant threat, as unreliable sensor data can lead to incorrect estimations of actuator faults and compromise diagnostic integrity. This paper presents a novel, integrated fault diagnosis architecture that addresses these two challenges. The framework's primary objective is robust actuator fault estimation using a dual-observer structure that combines state and fault estimation. This is synthesised using linear matrix inequalities. To prevent misdiagnosis caused by sensor errors, the framework incorporates a long short-term memory neural network dedicated to real-time sensor fault detection. When an anomaly is detected, the neural network output activates a configuration switch in the main observer, effectively isolating the unreliable sensor data. This integrated approach ensures that the diagnostic system remains highly accurate and robust. The efficacy of this complex methodology has been confirmed through extensive hardware-in-the-loop validation using CarSim, which is high-fidelity vehicle dynamics simulation software.

Keywords: active steering system · fault detection · fault estimation · fault diagnosis

1 Introduction

The rapid development of modern automated vehicles fundamentally relies on the integration of highly sophisticated components, such as advanced sensors and actuators, in order to perform complex functions such as trajectory control and autonomous manoeuvring [1–3]. One critical consequence of this complexity

© The Author(s), under exclusive license to Springer Nature Switzerland AG 2026
A. Chaker et al. (Eds.): EFIMMS 2026, MMS 205, pp. 315–325, 2026.
https://doi.org/10.1007/978-3-032-22270-1_31

is the potential for faults in these components. Ensuring the operational reliability of automated vehicles and the safety of their occupants demands the immediate and accurate identification of these issues [4]. Therefore, implementing reliable Fault Detection and Isolation (FDI) techniques for key vehicular systems is essential to prevent catastrophic faults, minimise maintenance costs, and extend the lifespan of these systems.

The move towards automated driving has intensified the focus on advanced lateral control systems, particularly Active Steering Systems (ASS) and Steer-By-Wire (SBW) technology. Steer-by-wire (SBW) replaces mechanical linkages with sensors and actuators to control vehicle direction. Because a sensor or motor failure can cause a catastrophic loss of control, there is a critical need for advanced Fault Diagnosis and Isolation (FDI) and fault-tolerant systems to maintain safety. [5–8]. Some common approaches rely on hardware redundancy, consisting of duplicate components, but this increases the cost and reduces the available space. For this reason, research focuses more on analytical redundancy methods based on system dynamics. In, [9], a robust method based on $\mathscr{H}_\infty$ is used to estimated the fault while in [10], method based on residual generation are used to detect actuator faults. On the other hand, data-driven approaches have gained interest in recent years. In [11], a support vector machines was used to classify different types of actuator faults while in [12], a long-short term memory (LSTM) neural network was used for fault detection.

However, none of the previous approaches has addressed faults in both the sensor and the actuator due to the complexity of designing a single observer that considers both kind of faults [13]. We propose a novel hybrid fault diagnosis methodology for active steering systems that addresses the issue of potential sensor and actuator faults in active steering systems. Unlike traditional, single-component observers, this approach overcomes limitations by integrating two distinct yet cooperative elements: a switched robust Luenberger observer for precise actuator fault estimation and a LSTM neural network for real-time sensor fault detection. The core innovation lies in the adaptive interaction between these components. The LSTM network acts as a safety mechanism; when it detects a sensor anomaly, it instantly triggers a configuration switch within the Luenberger observer to prevent false detections.

2 Vehicle Modelling

2.1 Lateral Dynamics

For the design of the Luenberger observer, we need to account for the vehicle lateral dynamics. For this purpose, we employ the bicycle model [8], depicted in Fig. 1, whose dynamics are represented in Eq. 1:

$$\begin{aligned} m(\dot{v}_y + r v_x) &= F_{y,f} cos(\delta) + F_{y,r} \\ I_z \dot{r} &= l_f F_{y,f} - l_r F_{y,r} \end{aligned} \tag{1}$$

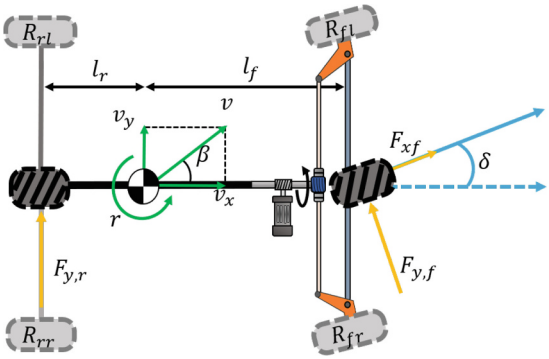

Fig. 1. Bicycle model representation.

The parameters and variables are described in Table 1. $F_{y,f}$ and $F_{y,r}$ represent for the lateral force of the front and rear axle, respectively. These forces are strongly related to the tire slip angles, defined as $\alpha_f = \delta - \frac{v_y + r l_f}{v_x}$ for the front axle and $\alpha_r = \frac{r l_r - v_y}{v_x}$, for the rear axle. However, they also depend on other factors such as the vertical tire load or tire-road adhesion coefficient. Although there are many tire models that consider these nonlinearities [14,15], they are particularly challenging to consider within the observer design. For that reason, the following tire model has been considered [16]:

$$\begin{aligned} F_{y,f} &= C_f \alpha_f = (C_{f0} \pm \Delta C_f)\alpha_f \\ F_{y,r} &= C_r \alpha_r = (C_{r0} \pm \Delta C_r)\alpha_r \end{aligned} \tag{2}$$

where C_f and C_r stand for the front and rear tire stiffnesses, respectively. These parameters are variable, they are modeled in this study as a bounded uncertainty:

$$\begin{aligned} C_{i0} &= \frac{max(C_i) + min(C_i)}{2} \\ \Delta C_i &= \frac{max(C_i) - min(C_i)}{2}, \\ &\text{for } i \in f, r \end{aligned} \tag{3}$$

By defining the sideslip angle β (see Fig. 1) as:

$$\beta = \arctan\left(\frac{v_y}{v_x}\right) \tag{4}$$

and considering low values for both β and δ, the lateral dynamics of the vehicle can be expressed obtained by combining Eqs. 1 and 2:

$$\begin{aligned} \dot{\beta} &= -\frac{2(C_f + C_r)}{m v_x}\beta - r + \frac{2(l_r C_r - l_f C_f)}{m v_x^2} r + \frac{2C_f}{m v_x}\delta \\ \dot{r} &= \frac{2(l_r C_r - l_f C_f)}{I_z}\beta - \frac{2(l_r^2 C_r + l_f^2 C_f)}{I_z v_x} r + \frac{2 l_f C_f}{I_z}\delta \end{aligned} \tag{5}$$

Table 1. Nomenclature of the vehicle model.

Parameter	Description	Value
v_x	Longitudinal velocity	5–20 m/s
v_r	Lateral velocity	m/s
r	Yaw rate	rad/s
δ	Longitudinal velocity	rad
l_f	C.o.g to front axle distance	1.08 m
l_r	C.o.g to front axle distance	1.50 m
m	Mass of the vehicle	1504 kg
C_f	Front tires stiffness	60000 N/rad
C_r	Rear tires stiffness	60000 N/rad
ΔC_f	Rear tires stiffness uncertainty	6000 N/rad
ΔC_r	Rear tires stiffness uncertainty	6000 N/rad
J_s	Steering column inertia	2413 kgm^2
c_s	Steering column damping coefficient	0.05 Ns/m^2
K	Gear ratio of the steering column	18.9
N	Motor reducer ratio	15
t_t	Tire contact patch length	40 mm

2.2 Steering Dynamics

The dynamics of the steering system are typically modeled as a second-order linear system:

$$J_s\ddot{\delta}_s = -c_s\dot{\delta}_s + M_{sa} + NT_m \tag{6}$$

being the steering column angle:

$$\delta_s = K\delta \tag{7}$$

The self-aligning torque can be obtained as [17]:

$$M_{sa} = t_t F_y = t_t C_f \left(\beta + \frac{rl_f}{v_x} - \delta\right) \tag{8}$$

where t_t is the tire length contact. By combining Eqs. 9 and 7 we obtain:

$$\ddot{\delta} = \frac{C_f t_t \beta}{J_s R_s^2} + \frac{C_f l_f r t_t}{J_s R_s^2 v_x} - \frac{C_f t_t \delta}{J_s R_s^2} - \frac{c_s\dot{\delta}}{J_s} + \frac{NT_m}{J_s R_s} \tag{9}$$

When the steering motor presents fault the real control action is not the same as the commanded control input [18,19]:

$$u_f(t) = k_{gain}u(t) + k_{bias} \tag{10}$$

where $u(t)$ is the commanded control action, $u_f(t)$ is the actual control action and k_{gain} and k_{bias} determine the kind of faults: $k_{gain} = 1$; $k_{bias} \neq 0$ is a bias fault, $0 < k_{gain} < 1$; $k_{bias} = 0$ is a gain fault and $k_{gain} = 0$; $k_{bias} \neq 0$ is an stuck fault. Note that $k_{gain} = 1$; $k_{bias} = 0$ corresponds to a healthy actuator.

2.3 Combined Lateral-Steering Dynamics

By integrating the lateral vehicle dynamics, Eq. 5, with the steering system dynamics, Eq. 9, and including the effects of actuator faults, we obtain the complete combined dynamics model. When expressed in the standard state-space form, this integrated model is given by:

$$\dot{x}(t) = (A(\mu) + \Delta A(\mu))x(t) + Bu_f(t) + B_d d(t) \tag{11}$$

with $x = [\beta \quad r \quad \delta \quad \dot{\delta}]^\top$ is the state-space vector, $u = T_m$ is the steering motor torque [17] and d is the system noise and

$$A(\mu) = \begin{bmatrix} \frac{-C_1}{mv_x} & -(1 + \frac{C_2}{mv_x^2}) & \frac{C_f}{mv_x} & 0 \\ -\frac{C_2}{I_z} & \frac{-C_3}{I_z vx} & \frac{l_f C_f}{I_z} & 0 \\ 0 & 0 & 0 & 1 \\ \frac{t_t C_f}{J_s R_s^2} & \frac{t_t l_f C_f}{J_s R_s^2 v_x} & -\frac{-t_t C_f}{J_s R_s^2} & \frac{-c_s}{J_s} \end{bmatrix},$$

$$\Delta A(\mu) = \begin{bmatrix} \frac{\Delta C_1}{mv_x} & -(1 + \frac{\Delta C_2}{mv_x^2}) & \frac{\Delta C_f}{mv_x} & 0 \\ -\frac{\Delta C_2}{I_z} & \frac{-\Delta C_3}{I_z vx} & \frac{l_f \Delta C_f}{I_z} & 0 \\ 0 & 0 & 0 & 0 \\ \frac{t_t C_f}{J_s R_s^2} & \frac{t_t l_f \Delta C_f}{J_s R_s^2 v_x} & -\frac{-t_t \Delta C_f}{J_s R_s^2} & 0 \end{bmatrix}, \quad B = \begin{bmatrix} 0 \\ 0 \\ 0 \\ \frac{N}{J_s R_s} \end{bmatrix}, \quad B_d = I$$

where $C_1 = C_f + C_r$, $\Delta C_1 = \Delta C_f + \Delta C_r$, $C_2 = l_f C_f - l_r C_r$, $\Delta C_2 = l_f \Delta C_f - l_r \Delta C_r$, $C_3 = l_f^2 C_f + l_r^2 C_r$ and $\Delta C_3 = l_f^2 \Delta C_f + l_r^2 \Delta C_r$. Matrix $\Delta A(\mu)$ in Eq. (11) is an uncertain matrix, defined by the upper and lower bounds $-A_{max}(\mu)$ and $A_{max}(\mu)$, respectively.

As matrices A and ΔA depend on velocity related parameters through $\mu = \left[1/v_x, \quad 1/v_x^2\right]$, we can make a change of variable of the from:

$$\frac{1}{v_x} = \frac{1}{v_1} + \frac{1}{v_2}\xi \tag{12}$$

where $-1 \leq \xi \leq 1$ is a parameter that depends on the vehicle speed defined in a certain range $\underline{v}_x \leq v_x \leq \overline{v}_x$. Using Taylor, we can approximate terms v_x and $1/v_x^2$ linearly. From this approximation, we can write the system in Eq. 11 as weighted sum of linear systems, corresponding each one to a limit on the velocity range:

$$\dot{x}(t) = \sum_{i=1}^{2} \alpha_i [(A_i + \Delta A_i)x(t) + Bu(t) + B_d d(t)] \tag{13}$$

where the weights are $\alpha_1 = \frac{\overline{v}_x - v_x}{\overline{v}_x + \underline{v}_x}$ and $\alpha_2 = \frac{v_x - \underline{v}_x}{\overline{v}_x + \underline{v}_x}$ and satisfy $\sum_{i=1}^{2} \alpha_i = 1$.

The system's observable outputs are strictly limited to sensors typically available on production vehicles:

$$y(t) = Cx(t) + r(t) \tag{14}$$

where $C = \begin{bmatrix} 0\,1\,0\,0 \\ 0\,0\,1\,0 \\ 0\,0\,0\,1 \end{bmatrix}$ and $r(t)$ stands for the measurement noise. Regarding the system output, the available measurements are limited to the steering angle, the steering angle rate and the yaw rate, which can be obtained easily using standard on-board sensors. The sideslip angle is excluded from the set of measurable variables due to the high cost and specialized nature of the equipment required for its direct measurement in production vehicles.

3 Proposed Robust Fault Diagnosis Framework

3.1 Sensor Fault Detection

In order to provide sensor fault information to the observer, an LSTM neural network has been used. This network gets information from the available measurements and precesses to provide a indicator flag of the fault sensor by using a softmax final layer. The network is feed using time windowed data of $n \times w$ size being n the number of inputs (3 measurements, velocity and control input) and a time dimension of 20 steps and outputs a boolean variable indicating which of the three considered sensors (Eq. 14) is faulty. To avoid false negative detection given by the network, an EMA algorithm is used to process the network's outputs:

$$\mathrm{E}_{j,k} = \mathit{flag}_{j,k}\pi_j + \mathrm{E}_{j,k-1}(1 - \pi_j), \text{for } j = f_r, f_\delta, f_{\dot{\delta}} \tag{15}$$

where $\mathrm{E}_{j,k-1}$ is the EMA output, $\mathit{flag}_{j,k}$ is the network's output at instant k for signal j and π_j is the weighting factor for signal j.

3.2 Design of the Combined State and Actuator Fault Observer

We propose the following Luenberger observer to estimate the vehicle states from Eq. 11:

$$\begin{aligned} \dot{\hat{x}}(t) &= \sum_{i=1}^{2} \alpha_i \left[A_i \hat{x}(t) + Bu(t) + L_i(\tilde{y}(t) - \hat{y}(t)) + B\hat{f}_a(t)\nu \right] \\ \hat{y}(t) &= C\hat{x}(t) \end{aligned} \tag{16}$$

where $\hat{x}$ represents the estimated states and $\hat{f}_a$ denotes the actuator fault estimation provided by the unknown input (UI) estimator and L_i stands for the observer gain to find and ν is a boolean variable that indicates if there is a fault in any sensor. The actuator fault, as defined in Eq. (10) is estimated using an unknown input estimator, which is a standard method for estimating input perturbations [20]. The resulting estimations of the unknown input, $\hat{f}_a$, can be obtained as follows:

$$\dot{\hat{f}}_a(t) = \frac{1}{T_f} B^{\dagger} L(\mu)(\tilde{y}(t) - \hat{y}(t)) \tag{17}$$

where T_f is the cut-off frecuency of the estimator and $B^{\dagger}$ is the Penrose inverse of matrix B.

By defining the estimation error as the difference between the true state and its estimate, $e = x - \hat{x}$, and the fault estimation error as $f_a - \hat{f}_a$, we can derive the error dynamics by substituting Eqs. (13) and (16):

$$\dot{e}(t) = \sum_{i=1}^{2} \alpha_i [(A_i - L_i C)e(t) + \Delta A_i x(t) + B e_f(t) + B_d d(t) - L_i r(t)] \tag{18}$$

If we define an extended space-state that includes both the the vehicle states x and the estimation error e, the dynamics of this extended space-state is:

$$\dot{\rho}(t) = \sum_{i=1}^{2} \alpha_i [(A_{1,i} + \Delta A_{1,i})\rho(t) + B_{\zeta}\zeta(t)] \tag{19}$$

where $\rho = [e^{\top} \quad x^{\top}]^{\top}$ and $\zeta = [u^{\top} \quad d^{\top} \quad e_f^{\top} \quad r^{\top}]^{\top}$ and

$$A_{1,i} = \begin{bmatrix} A_i - L_i C & 0 \\ 0 & A_i \end{bmatrix}, \quad \Delta A_{1,i} = \begin{bmatrix} 0 & \Delta A_i \\ 0 & \Delta A_i \end{bmatrix}, \quad B_{\zeta} = \begin{bmatrix} 0 & B_d & \nu B & -L_i \\ B & B_d & B & 0 \end{bmatrix}$$

To derive the Luenberger observer defined by the matrices L_i while obtaining an $\mathscr{H}_{\infty}$ performance attenuation from disturbances γ to the estimation error e, matrices $P_{1,i} \succ 0$, $P_{2,i} \succ 0$ and Q_i must be obtained such that the following LMI conditions hold:

$$\begin{aligned} &\Xi_{ii,\nu} \prec 0, \text{ for } 1 \leq i \leq 2, \text{ and for } \nu \in \{0,1\} \\ &\Xi_{ij,\nu} + \Xi_{ji} \prec 0, \text{ for } 1 \leq i \leq j \leq 2, \text{ and for } \nu \in \{0,1\} \end{aligned} \tag{20}$$

where

$$\Xi_{ij,\nu} = \begin{bmatrix} \mathrm{He}(P_{1,j}A_i - Q_j C) & 0 & 0 & P_{1,j}B_d & \nu P_{1,j}B_i & -Q_j & I & P_{1,j}\mathcal{A}_i & 0 \\ \star & \mathrm{He}(P_{2,j}A_i) & P_{2,j}B & P_{2,j}B_d & P_{2,j}B_i & 0 & 0 & P_{1,j}\mathcal{A}_i & F^{\top} \\ \star & \star & \star & \star & \star & -\gamma^2 I & 0 & 0 & 0 \\ \star & \star & \star & \star & \star & \star & -\gamma^2 I & 0 & 0 \\ \star & \star & \star & \star & \star & \star & \star & -\epsilon I & 0 \\ \star & \star & \star & \star & \star & \star & \star & \star & -\epsilon I \end{bmatrix} \prec 0$$

4 Results

The proposed methodology was validated through simulation utilizing Simulink-CarSim co-simulation. The gains of the observer are obtained by finding matrices $P_{1,j}$, $P_{2,j}$ and Q_j while minimizing γ and satisfying Eq. 20 using the parameters from Table 1.

To test the performance of the system, several sensor and actuator faults, including bias, gain and stuck, are introduced to the system while the vehicle is performing a manuevre. The results of the sensor fault detection are shown in Fig. 2, where it can be appreciated that the detection algorithm based on LSTM algorithm is able to detect faults precisely, reaching a good balance between detectability and speed. The estimation of the actuator faults is shown in Fig. 3. The RMS errors of estimation for the actuator fault is 2.44 Nm. It can be seen that we information about faults is available, the observer do not produce actuator fault estimation (blue line) and prevents false negative (red line).

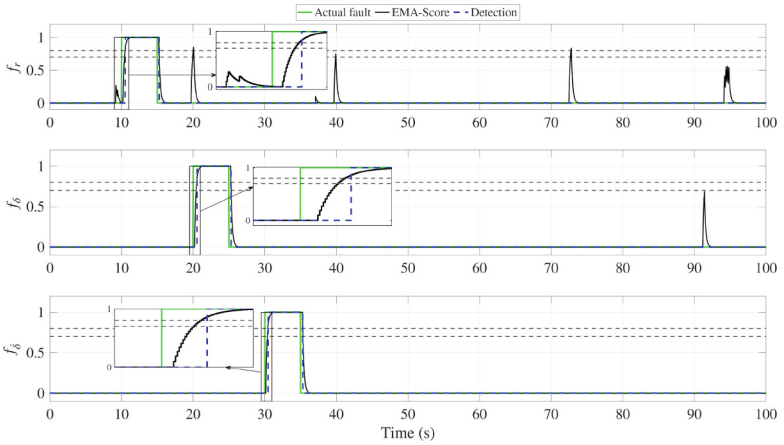

Fig. 2. Sensor fault detection.

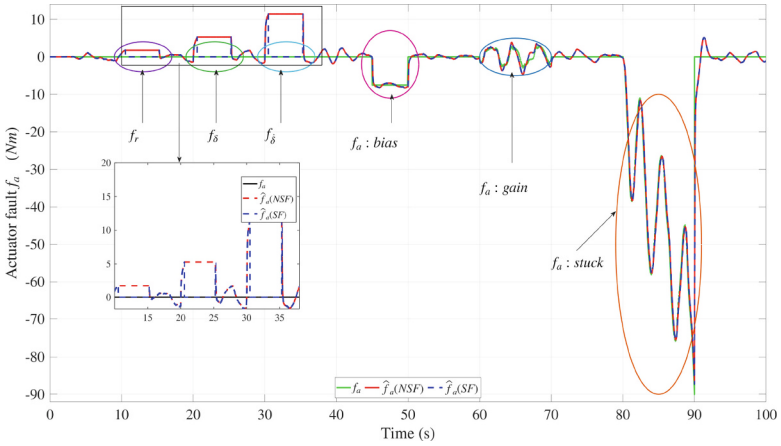

Fig. 3. Estimation of the actuator faults. NSF does not consider sensor faults. SF considers sensor faults.

5 Conclusions

This work presents a robust, integrated fault diagnosis framework designed to address actuator and sensor faults in active steering systems in automated vehicles concurrently. The proposed architecture successfully overcomes challenges arising from model uncertainties and unmeasured states. Actuator fault estimation is achieved using a Luenberger observer and a decoupled unknown input observer for robust tracking.

Furthermore, a LSTM neural network is integrated to detect sensor faults in real time and trigger a configuration switch to prevent misdiagnosis. Validation using a Hardware-in-the-Loop (HIL) setup with CarSim demonstrated the system's ability to provide precise estimation of different types of actuator fault.

Acknowledgements. Grant [PID2022-136468OB-I00] funded by MCIN/AEI/10.13039/501100011033 and, by "ERDF A way of making Europe".

References

1. Viadero-Monasterio, F., Meléndez-Useros, M., Zhang, N., Zhang, H., Boada, B.L., Boada, M.J.L.: Motion planning and robust output-feedback trajectory tracking control for multiple intelligent and connected vehicles in unsignalized intersections. IEEE Trans. Veh. Technol. (2025)
2. Viadero-Monasterio, F., Meléndez-Useros, M., Zhang, H., Boada, B.L., Boada, M.J.L.: Signalized traffic management optimizing energy efficiency under driver preferences for vehicles with heterogeneous powertrains. IEEE Trans. Consum. Electron. (2025)

3. Conceicao, A.G., Santos, T.L., Ribeiro, T.T.: Soft trajectory tracking control for wheeled unmanned ground vehicles under uncertain slippage conditions. J. Franklin Inst. 107706 (2025)
4. Melendez-Useros, M., Jimenez-Salas, M., Viadero-Monasterio, F., Lopez-Boada, M.J.: Novel methodology for integrated actuator and sensors fault detection and estimation in an active suspension system. IEEE Trans. Reliab. **74**(1), 2171–2184 (2024)
5. Viadero-Monasterio, F., Boada, B., Boada, M., Díaz, V.: H_∞ dynamic output feedback control for a networked control active suspension system under actuator faults. Mech. Syst. Sig. Process. **162**, 108050 (2022)
6. Zhou, Z., Chen, M., Zhang, G., Shen, W., Yang, R.: Research on active fault tolerant control strategy for distributed drive electric vehicles based on multi-actuator failure. Eng. Lett. **33**(2) (2025)
7. Viadero-Monasterio, F., Boada, B.L., Zhang, H., Boada, M.J.L.: Integral-based event triggering actuator fault-tolerant control for an active suspension system under a networked communication scheme. IEEE Trans. Veh. Technol. **72**(11), 13848–13860 (2023)
8. Meléndez-Useros, M., Viadero-Monasterio, F., Jiménez-Salas, M., López-Boada, M.J.: Static output-feedback path-tracking controller tolerant to steering actuator faults for distributed driven electric vehicles. World Electric Veh. J. **16**(1), 40 (2025)
9. Su, X., Xiao, B.: Actuator-integrated fault estimation and fault tolerant control for electric power steering system of forklift. Appl. Sci. **11**(16), 7236 (2021)
10. Pan, J., Nguyen, A.-T., Guerra, T.-M., Sentouh, C., Wang, S., Popieul, J.-C.: Vehicle actuator fault detection with finite-frequency specifications via takagi-sugeno fuzzy observers: theory and experiments. IEEE Trans. Veh. Technol. **72**(1), 407–417 (2023)
11. Shi, Q., Zhang, H.: Fault diagnosis of an autonomous vehicle with an improved SVM algorithm subject to unbalanced datasets. IEEE Trans. Industr. Electron. **68**(7), 6248–6256 (2021)
12. Zhang, S., Liang, W., Zhao, W., Luan, Z., Wang, C., Xu, K.: Electro-hydraulic SBW fault diagnosis method based on novel 1DCNN-LSTM with attention mechanisms and transfer learning. Mech. Syst. Signal Process. **220**, 111644 (2024)
13. Dimassi, H.: A novel fault reconstruction and estimation approach for a class of systems subject to actuator and sensor faults under relaxed assumptions. ISA Trans. **111**, 192–210 (2021)
14. Meléndez-Useros, M., Jiménez-Salas, M., Viadero-Monasterio, F., Boada, B.L.: Tire slip H_∞ control for optimal braking depending on road condition. Sensors **23**(3), 1417 (2023)
15. Huang, S., Zhou, C., Yang, L., Qin, Y., Huang, X., Hu, B.: Transient fault tolerant control for vehicle brake-by-wire systems. Reliab. Eng. Syst. Saf. **149**, 148–163 (2016)
16. Meléndez-Useros, M., Viadero-Monasterio, F., Jiménez-Salas, M., Boada, M.J.L.: Active steering fault diagnosis via integrated LSTM-based sensor detection and robust actuator fault estimation. Reliab. Eng. Syst. Saf. 111573 (2025)
17. Zou, S., Zhao, W., Liang, W., Wang, C., Chen, F.: Fault diagnosis and fault-tolerant compensation strategy for wheel angle sensor of steer-by-wire vehicle via extended Kalman filter. IEEE Sens. J. **22**(2), 1756–1766 (2022)
18. Wang, Y., et al.: Sensor fault detection of vehicle suspension systems based on transmissibility operators and Neyman-Pearson test. Reliab. Eng. Syst. Saf. **232**, 109067 (2023)

19. Fang, Y., et al.: Anomaly diagnosis of connected autonomous vehicles: a survey. Inf. Fusion **105**, 102223 (2024)
20. Nguyen, A.T., Guerra, T.M., Sentouh, C., Zhang, H.: Unknown input observers for simultaneous estimation of vehicle dynamics and driver torque: theoretical design and hardware experiments. IEEE/ASME Trans. Mechatron. **24**(6), 2508–2518 (2019)

Anisotropic Polyurethane Foams: Evolution of Mechanical Properties Under Cyclic Compression

Dorra Ben Abdeljelil[1(✉)], Sami Chatti[1], and Raja Ouled Ahmed Ben Ali[2]

[1] Mechanical Laboratory of Sousse - Higher Institute of Applied Sciences and Technology of Sousse, Sousse University, Sousse, Tunisia
dora.ben.abdeljelil@gmail.com

[2] Mechanical Laboratory of Sousse - Higher Institute of Applied Sciences and Technology of Kaiouan, Kaiouan University, Kaiouan, Tunisia

Abstract. Polyurethane foams are widely used in applications requiring efficient energy absorption and damping, especially in components subjected to repeated mechanical loading. This study investigates the cyclic compressive behavior of an anisotropic polyurethane foam to understand how its mechanical response evolves under successive loading cycles. Microscale analysis was first conducted to characterize the foam's directional properties, revealing a cellular microstructure with a predominant orientation that underpins its anisotropic behavior. The foam was then subjected to cyclic compression along different principal directions to evaluate the influence of loading orientation on mechanical performance. Experimental results indicate a progressive decline in stiffness and overall mechanical response with increasing cycles, demonstrating pronounced cyclic softening. Furthermore, the degree of softening is strongly dependent on the direction of applied load, highlighting the significant role of anisotropy in governing the foam's behavior under repeated deformation. These findings provide insights into the directional evolution of mechanical properties under cyclic loading with direct implications for their application in energy-dissipating systems.

Keywords: Polyurethane foam · anisotropic behavior · cellular microstructure · cyclic softening

1 Introduction

Cellular anisotropic materials, such as polymeric foams, are used in several applications ranging from energy absorption to thermal and acoustic insulation and lightweight design (Koohbor et al. 2020), (Liu et al. 2005), (Sun and Li 2018), (Ousji et al. 2017). In fact, these materials have a complex microscopic structure of cellular ribs that provides a range of highly interesting mechanical and thermal properties (He et al. 2021), (Atiqah et al. 2019), (Kairyté et al. 2019), (Zhu and ai Xu 2019), (Kim et al. 2021), (Wang et al. 2013). The mechanical behavior of foams has been the subject of several previous studies. Typically, polymeric foams exhibit a complex behavior (Koohbor et al. 2020).

© The Author(s), under exclusive license to Springer Nature Switzerland AG 2026
A. Chaker et al. (Eds.): EFIMMS 2026, MMS 205, pp. 326–334, 2026.
https://doi.org/10.1007/978-3-032-22270-1_32

In particular, under compression testing, the stress-strain curve shows a primary elastic response, manifested by high resistance to deformation, followed by a plateau where the material undergoes continuous deformation without significant resistance. Finally, a densification zone appears, where stress increases exponentially (Koohbor et al. 2020). The work of (Garrido and Correia 2018) was devoted to the characterization of a polyethylene terephthalate foam used as the core of an industrial sandwich panel. Quasi-static tensile, compression and shear tests were carried out. Similarly, the static response of the foam to shear creep was evaluated considering different load levels. The results obtained contributed to the study of the flexural response of the sandwich structure. The cyclic behavior of an isotropic polyurethane foam was investigated by (Demirel and Ergun Tuna 2019). They proved that the foam density controls the indentation force deflection and the foam firmness significantly. (Linul et al. 2017) studied the variation of the compressive maximal stress and the energy absorption capacity of a polyurethane foam as a function of its density via dynamic compression tests. The experimental results proved that these mechanical properties would increase with the density. One of the first works to consider an anisotropic polyurethane foam was presented by (Huber and Gibson 1988). The microstructure of the foam was visualized using scanning electron micrographs. It was shown that the foam exhibits a cellular structure with cells oriented in the direction of foam rise. In addition, this work presents the macroscopic mechanical properties of the foam in the rising direction and along two perpendicular directions. (Lee and Lee 2014) studied the mechanical behavior of an anisotropic polyurethane foam using uniaxial tensile and compression tests in different directions. They also proposed an anisotropic elasto-visco-plastic model in order to predict the foam's damage-coupled behavior. Meanwhile, (Marvi-Mashhadi et al. 2018) carried out compression tests on an anisotropic closed-cell polyurethane foam in both the foaming and perpendicular directions. They reported that buckling controlled deformation in the rising direction, while deformation perpendicular to the upward direction was controlled by bending of the cell edges. In a more interesting approach, (Li et al. 2018) carried out quasi-static and dynamic compression tests on polyurethane samples cut at a set of angles to the rising direction. They found that the stiffness, yield strength and energy absorption capacity of the foam decreased with increasing cutting angle.

Recent studies have further emphasized the importance of understanding the mechanical response of polyurethane foams under complex loading conditions, particularly for applications involving energy absorption and durability under repeated loading. Chung et al. (2024) investigated shape memory polyurethane foams with tunable mechanical properties, highlighting the strong influence of microstructure on mechanical performance and energy dissipation, especially in biomedical and protective applications. Their results confirm that the deformation mechanisms and energy absorption capabilities of polyurethane foams are highly sensitive to material architecture. In parallel, Boumdouha et al. (2022) conducted an experimental investigation on the dynamic behavior of polyurethane foams, focusing on the relationship between microstructural features and macroscopic mechanical response under impact loading. Their findings underline the critical role of foam morphology in governing stiffness degradation and energy absorption, which are key aspects also observed under cyclic compression conditions. More recently, Yao et al. (2025) proposed a dynamic constitutive model for

polyurethane foams subjected to different strain rates, demonstrating that both loading history and material anisotropy significantly affect stress evolution and energy dissipation mechanisms. These recent contributions clearly indicate that, despite growing interest in polyurethane foams under dynamic and cyclic loading, the combined effect of microscopic anisotropy and cyclic compression remains insufficiently explored.

In this context, the present study aims to experimentally investigate the cyclic compressive behavior of an anisotropic polyurethane foam, with particular emphasis on the evolution of maximum stress and absorbed energy as a function of loading direction and number of cycles.

The aim of this work is to evaluate the cyclic response of a polyurethane foam, considering microscopic anisotropy. First, the cellular microstructure of the foam is presented. Then, cyclic compression tests at different directions are experimentally analyzed. The effect of the number of cycles on the foam cyclic response is discussed and the variations of the maximum stress and the energy absorption ability are discussed.

2 Preparation of Foam Samples

The foam under study is an open-cell polyurethane foam (PUF) with a density of 40 Kg/m^3. Standardized specimens have a cross-section of 50 $\times$ 50 mm^2 and a thickness of 25 mm. The samples were extracted from an industrialized sandwich panel, then cut into rectangular prisms in three directions. One is the direction of foam expansion (D1) and the two others are perpendicular to (D1). Justified by the panel manufacturing process, as shown in Fig. 1, it can be assumed that the two directions (D2) and (D3) have almost the same mechanical properties. In fact, the foam is free to expand in the privileged direction (D1), while the expansion of the foam is blocked in the other two perpendicular directions (D2) and (D3).

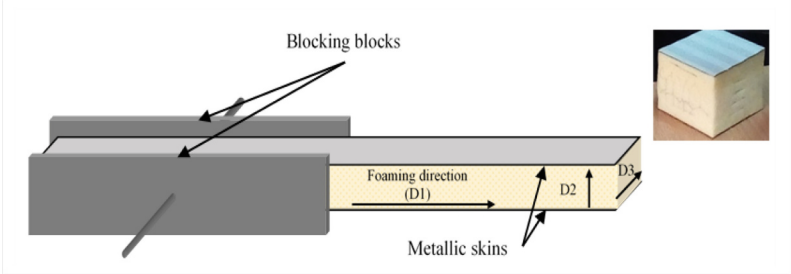

Fig. 1. Schematic presentation of the manufacturing process of foamed-core sandwich panels.

3 Microscopic Observations

A transmitted light microscope (Fig. 2) has been used to observe the microstructure of a section (D1, D2) of the polyurethane foam. The sample is thinned to a transparent body and then placed under different magnifications to study the foam's anisotropy and

determine approximate cell sizes and the degree of geometric anisotropy, which is the ratio of cell dimensions in the two directions (D1) and (D2).

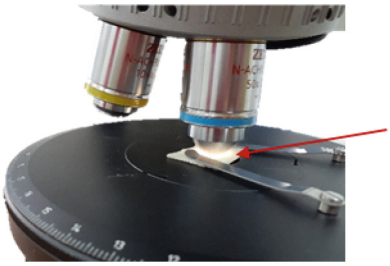

Fig. 2. Thinned polyurethane foam sample observed by transmitted light microscope.

Figure 3 presents microscopic observations of the investigated polyurethane foam. The graph shows that the foam has a cellular microstructure with a pore size of the order of a few hundred microns. In addition, the foam cells are mainly oriented in the direction of foaming or expansion (D1). This figure further shows that the foam is anisotropic and highly polydisperse. Moreover, the geometric Degree of Anisotropy, DA, which is the ratio between cell sizes along (D1) and (D2), is on average of 2.35.

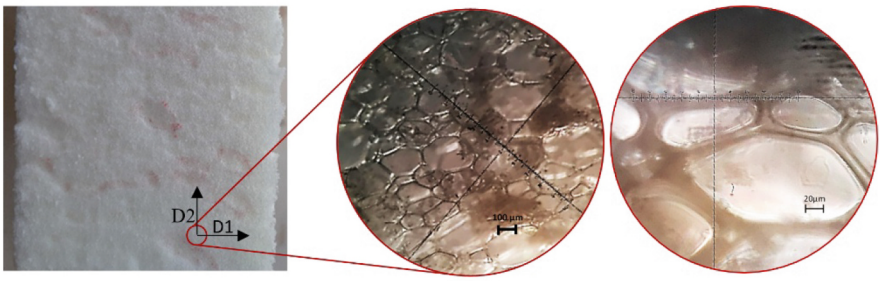

Fig. 3. Microscopic observation of polyurethane foam

4 Cyclic Compression Tests

Experimental tests have been carried out in accordance with ASTM D1621 for compression properties of rigid cellular plastics. In order to study the cyclic behavior of the anisotropic PUF, 20 cycles of loading – unloading compression tests have been applied for a displacement rate of 50 mm/min. All tests have been performed using a universal tensile testing machine shown in Fig. 4. Samples have been placed between two perfectly parallel platens of the machine. The directions (D1) and (D2) have been considered when applying the charge. Finally, to ensure repeatability, three specimens have been tested for each loading direction.

Fig. 4. Compression tests using a universal tensile machine.

4.1 Cyclic Stress-Strain Curves

The graphs shown in the left columns of Figs. 5 and 6 illustrate the foam response for the first five loading-unloading cycles of compression. Subsequent foam responses are shown by the stress-strain curves in the right columns of the same figures.

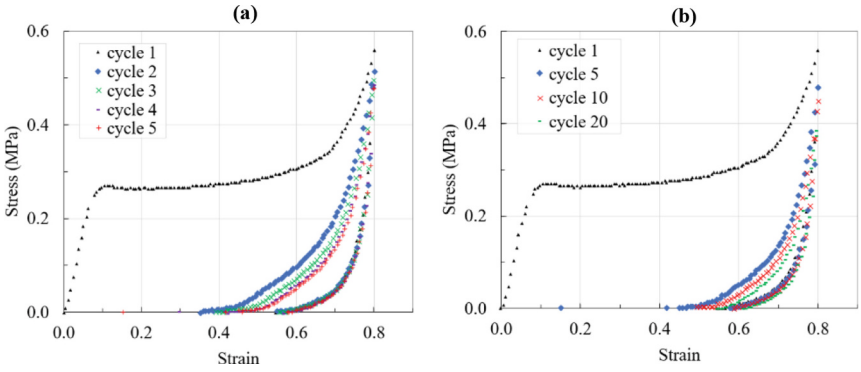

Fig. 5. Cyclic compression curves for polyurethane foam in direction (D1): (a) cycle 1 to cycle 5; (b) cycle 5 to cycle 20.

These figures clearly show the significant difference between the foam response in directions (D1) and (D2). When considering the very first compression, the curve for (D1) shows a primary linear zone followed by a plateau, then a densification zone where stresses increase rapidly. However, the same curve for (D2) does not show a plateau, since stresses continue to increase after the linear trend until they reach the densification zone. This result is to be expected since the foam cells are oriented in the foaming direction. In fact, the buckling of the cell edges, generating the linear zone (Ben

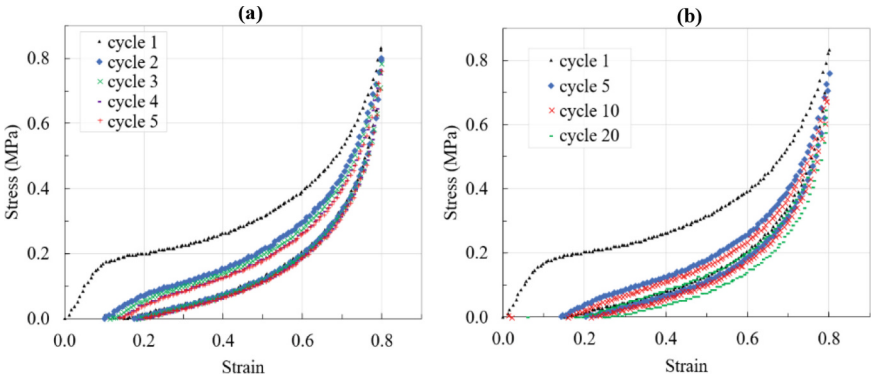

Fig. 6. Cyclic compression curves for polyurethane foam in direction (D2): (a) cycle 1 to cycle 5; (b) cycle 5 to cycle 20.

Abdeljelil et al. 2022), controls the deformation following (D1). Then, since buckling is unstable, the cells begin to collapse, and the stresses remain almost constant. By the time the cells are completely crushed, their opposite edges come into contact and stresses rise sharply, graphically creating the densification zone. In addition, the bending of the cell edges controls deformation in other spatial directions. Edge bending resistance is initially linear elastic, then stress continues to rise until the total crush of the cells (Ben Abdeljelil et al. 2022).

Furthermore, whatever the loading direction, the polyurethane foam loses its mechanical properties from one cycle to another. This behavior is well explained by the Mullin effect, which generally characterizes polymeric materials (Taherkhani et al. 2016). This cyclic softening is more pronounced during first loading-unloading cycles, in particular from the first to the second cycle. In the following, the evolution of the maximum stress and the absorbed energy will be described as a function of the number of cycles.

4.2 Evolution of the Maximum Stress as a Function of the Number of Cycles

Variations in the maximum stress as a function of the number of cycles in the (D1) and (D2) directions are shown in Fig. 7. This graph shows that, independently of the loading direction, the polyurethane foam is increasingly damaged within 20 loading – unloading cycles. Moreover, the curves show that the reduction in stress over the cycles in the (D1) direction, corresponding to 31%, is more pronounced than the one in (D2), equal to 28%, meaning that the PUF cells are more damaged within 20 cycles when loading in (D1) than in (D2).

4.3 Evolution of the Absorbed Energy as a Function of the Number of Cycles

Figure 8 shows the variation in absorbed strain energy density, defined as the energy absorbed per unit volume (kPa $\equiv$ kJ/m^3), as a function of the number of cycles in the (D1) and (D2) directions. It was found that the foam was able to absorb more energy in the direction (D2) than in direction (D1) during the very first few cycles. Moreover, the

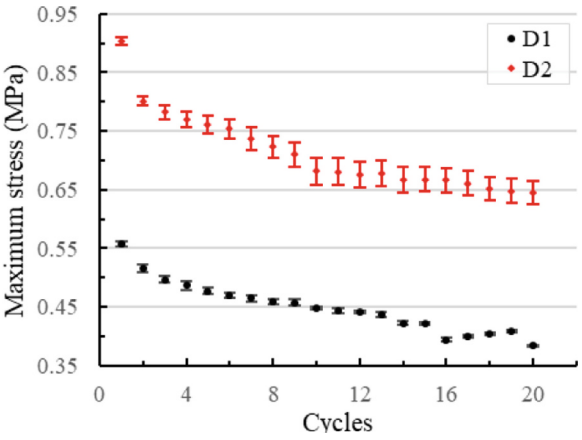

Fig. 7 Maximum stress vs. number of cycles in directions (D1) and (D2).

reduction in energy as a function of the number of cycles is greater in the first direction (93%) than in the second one (78%).

This pronounced directional difference can be directly attributed to the high degree of microstructural anisotropy of the foam (DA ≈ 2.35), which governs the evolution of both maximum stress and energy absorption under cyclic compression.

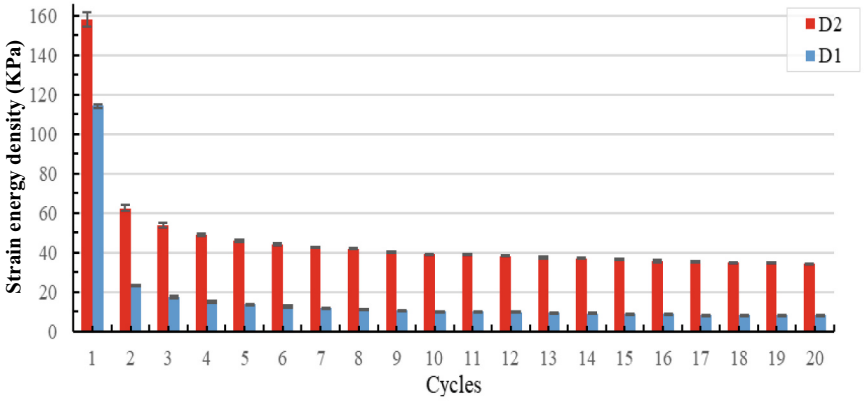

Fig. 8. Variation in the energy absorbed by the foam as a function of the number of cycles in the (D1) and (D2) directions.

5 Conclusions

The cyclic softening behavior of an anisotropic polyurethane foam was investigated. The results reveal that the foam has microscopic anisotropy that affects its overall mechanical response. Furthermore, there is a clear degradation of the foam's mechanical performance

with increasing the number of cycles, strongly influenced by the material's microscopic anisotropy. The maximum stress exhibits a pronounced reduction, decreasing by approximately 28% in direction D2 and by about 31% in direction D1 after 20 cycles. Similarly, the absorbed energy shows a sharp decline during the first cycles followed by a gradual stabilization. A total reduction of nearly 78% is observed in D2, while D1 exhibits a more severe decrease of about 93%. These results clearly demonstrate that cyclic softening and energy dissipation loss are strongly direction-dependent, highlighting the critical role of anisotropy in the durability of polyurethane foams under repeated loading.

These findings provide valuable guidelines for the design of anisotropic polyurethane foams intended for energy-absorbing components subjected to repeated mechanical loading.

The present study could be further expanded to an analytic modeling of foam's softening behavior in order to develop a relationship between the cycle's number and the evolution of the investigated mechanical properties along directions (D1) and (D2).

References

Koohbor, B., Singh, N.K., Kidane, A.: Radial and axial inertia stresses in high strain rate deformation of polymer foams. Int. J. Mech. Sci. **181**, 105–679 (2020). https://doi.org/10.1016/j.ijmecsci.2020.105679

Liu, Q., Subhash, G., Gao, X.L.: A parametric study on crushability of open-cell structural polymeric foams. J. Porous. Mater. **12**, 233–248 (2005). https://doi.org/10.1007/s10934-005-1652-1

Sun, Y., Li, Q.M.: Dynamic compressive behavior of cellular materials: a review of phenomenon, mechanism and modelling. Int. J. Impact Eng. **112**, 74–115 (2018). https://doi.org/10.1016/j.ijimpeng.2017.10.006

Ousji, H., et al.: Air-blast response of sacrificial cladding using low density foams: experimental and analytical approach. Int. J. Mech. Sci. **128**, 459–474 (2017). https://doi.org/10.1016/j.ijmecsci.2017.05.024

He, Y., Wu, J., Qiu, D., Yu, Z.: Construction of 3-D realistic representative volume element failure prediction model of high-density rigid polyurethane foam treated under complex thermal-vibration conditions. Int. J. Mech. Sci. **193**, 106–164 (2021). https://doi.org/10.1016/j.ijmecsci.2020.106164

Atiqah, Jawaid, M., Sapuan, S.M., Ishak, M.R., Ansari, M.N.M., Ilyas, R.A.: Physical and thermal properties of treated sugar palm/glass fibre reinforced thermoplastic polyurethane hybrid composites. J. Mater. Res. Technol. **8**(5), 3726–3732 (2019). https://doi.org/10.1016/j.jmrt.2019.06.032

Kairytė, S., Vaitkus, A., Kremensas, I., Pundienė, S., Członka, Strzelec, K.: Moisture-mechanical performance improvement of thermal insulating polyurethane using paper production waste particles grafted with different coupling agents. Constr. Build. Mater. **208**, 525–534 (2019). https://doi.org/10.1016/j.conbuildmat.2019.03.048

Zhu, H., ai Xu, S.: Synthesis and properties of rigid polyurethane foams synthesized from modified urea-formaldehyde resin. Constr. Build. Mater. **202**, 718–726 (2019). https://doi.org/10.1016/j.conbuildmat.2019.01.035

Kim, M.S., Kim, J.D., Kim, J.H., Lee, J.M.: Mechanical performance degradation of glass fiber-reinforced polyurethane foam subjected to repetitive low-energy impact. Int. J. Mech. Sci. **194**, 106–188 (2021). https://doi.org/10.1016/j.ijmecsci.2020.106188

Wang, Y.C., Ko, C.C., Huang, Y.H.: Viscoelastic properties of foam under hydrostatic pressure and uniaxial compression. Procedia Eng. **67**, 397–403 (2013). https://doi.org/10.1016/j.proeng.2013.12.039

Garrido, M., Correia, J.R.: Elastic and viscoelastic behavior of sandwich panels with glass-fibre reinforced polymer faces and polyethylene terephthalate foam core. J. Sandw. Struct. Mater. **20**(4), 399–424 (2018). https://doi.org/10.1177/1099636216657388

Demirel, S., Ergun Tuna, B.: Evaluation of the cyclic fatigue performance of polyurethane foam in different density and category. Polym. Test. **76**, 146–153 (2019). https://doi.org/10.1016/j.polymertesting.2019.03.019

Linul, E., Şerban, D.A., Marsavina, L., Sadowski, T.: Assessment of collapse diagrams of rigid polyurethane foams under dynamic loading conditions. Arch. Civ. Mech. Eng. **17**(3), 457–466 (2017). https://doi.org/10.1016/j.acme.2016.12.009

Taherkhani, M., Sadighi, A.S., Vanini, Mahmoudabadi, M.Z.: An experimental study of high-velocity impact on elastic-plastic crushable polyurethane foams. Aerosp. Sci. Technol. **50**, 245–255 (2016). https://doi.org/10.1016/j.ast.2015.11.013

Li, P., Guo, Y.B., Zhou, M.W., Shim, V.P.W.: Response of anisotropic polyurethane foam to compression at different loading angles and strain rates. Int. J. Impact Eng. **127**, 154–168 (2018). https://doi.org/10.1016/j.ijimpeng.2018.12.009

Lee, S., Lee, J.M.: Failure analysis of reinforced polyurethane foam-based LNG insulation structure using damage-coupled finite element analysis. Compos. Struct. **107**(1), 231–245 (2014). https://doi.org/10.1016/j.compstruct.2013.07.044

Huber, T., Gibson, L.J.: Anisotropy of foams. J. Mater. Sci. **23**(8), 3031–3040 (1988). https://doi.org/10.1007/BF00547486

Marvi-Mashhadi, M., Lopes, C.S., LLorca, J.: Effect of anisotropy on the me-chanical properties of polyurethane foams: an experimental and numerical study. Mech. Mater. **124**, 143–154 (2018). https://doi.org/10.1016/j.mechmat.2018.06.006

Ben Abdeljelil, S., Chatti, S., Ali, R.O.A.B.: Effect of strain rate and load orientation on cyclic response of anisotropic polyurethane foam. Cell. Poly. **41**(4), 147–162 (2022). https://doi.org/10.1177/02624893221084895

Chung, K., Zhao, Y., Boyle, A.J., Boyle, A.J.: Shape memory polyurethane foams with tunable mechanical properties and radiation tolerance for breast repair and reconstruction. J. Biomed. Mater. Res. Part A. **113**(1) (2024). https://doi.org/10.1002/jbm.a.37821

Boumdouha, N., Safidine, Z., Boudiaf, A., Duchet-Rumeau, J., Gérard, J.-F.: Experimental study of the dynamic behaviour of loaded polyurethane foam: free fall investigation and evaluation of microstructure. Int. J. Adv. Manuf. Technol. **120**, 3365–3381 (2022). https://doi.org/10.1007/s00170-022-08963-1

Yao, H., Pang, Y., Jiang, L., Li, Y., Qu, J.: Mechanical properties and dynamic constitutive model of polyurethane foam under different strain rates. Appl. Compos. Mater. **32**(1), 257–279 (2025). https://doi.org/10.1007/s10443-024-10277-2

Experimental Study of the Axial Crushing Mechanics of Yoshimura Tubes

Daniel Lavayen(✉), Johan Barrueta, Ludwing Gonzales, Jesus Monge, Mario Quispe, Erick Requena, and Estefania Hermoza

Applied Mechanics, Machines and Mechanisms Group, Department of Engineering, Pontificia Universidad Católica del Perú, Universitaria Ave. 1801, 15088 Lima, Peru
dlavayen@pucp.edu.pe

Abstract. Origami has inspired a wide range of engineering applications, from deployable systems to structures with enhanced mechanical performance. In this context, Yoshimura patterns, commonly observed during the axial crushing of circular thin-walled tubes, offer a promising basis for designing energy-absorbing components. This paper presents an experimental investigation into how the geometric parameters of a Yoshimura cylindrical tube influence its axial crushing response. The parameters examined include the in-plane panel angle and the number of sides around the circumference. The results indicate that these geometric features significantly affect both the peak load and the energy absorbed during collapse. Higher in-plane angles lead to increased peak loads and stiffness within the tested range, while tubes with fewer sides, particularly three, exhibit a more gradual post-peak load reduction. Conversely, tubes with a larger number of sides show a sharper drop in load after the peak. These findings demonstrate that the crushing mechanics of Yoshimura tubes can be tailored to specific energy-absorption requirements through appropriate geometric design.

Keywords: origami · axial crushing · yoshimura · axial collapse · buckling

1 Introduction

Origami, understood as the transformation of a flat thin-walled surface into a complex three-dimensional configuration, has inspired a wide range of engineering applications [6,9,10]. Beyond its traditional artistic use, the geometric principles underlying Origami enable the design of periodic and symmetric structures based on well-defined crease patterns. Several of these patterns, such as Miura, Yoshimura, Kresling, and the waterbomb pattern, have been studied extensively due to their capacity to generate deployable, load-bearing, or morphing structures. Owing to their periodicity, many of these crease patterns can also be wrapped into axisymmetric configurations, leading to origami-inspired cylindrical tubes.

© The Author(s), under exclusive license to Springer Nature Switzerland AG 2026
A. Chaker et al. (Eds.): EFIMMS 2026, MMS 205, pp. 335–344, 2026.
https://doi.org/10.1007/978-3-032-22270-1_33

Depending on the selected crease pattern, complete rigid foldability may or may not be achievable. A rigidly foldable pattern permits deformation through rotations along crease lines without producing stretching in the panels [1]. Fully foldable origami cylinders can serve as deployable or reconfigurable structures [11]. In contrast, when a crease pattern does not allow isometric folding, the resulting structure behaves as a mechanically stable body that resists deformation unless elastic or plastic strains develop in the panels or crease lines. This latter case is of particular interest for structural applications, as it can yield stiff or energy-absorbing components.

A classical example illustrating this phenomenon is the Yoshimura buckling pattern observed in thin-walled circular cylinders subjected to axial compression. As described by Miura and Tachi [8], the corrugated diamond-shaped configuration that emerges during the crushing of a soda can closely resembles the Yoshimura crease pattern. Once this pattern forms, further change in the cylinder's axial length is only possible through elastic or plastic deformation of the panels or crease lines. Consequently, the Yoshimura pattern is not suitable for use as a rigidly foldable origami cylinder. Nevertheless, this same geometric constraint makes Yoshimura-type tubes promising candidates for energy absorption, where structural stability and sustained load-carrying capacity beyond the initial collapse are essential.

Energy-absorbing devices must operate not only in the elastic regime but also under significant plastic deformation, as the collapse process itself is responsible for dissipating mechanical energy. Under axial loading, the absorbed energy corresponds to the area under the force–displacement curve $F(\delta)$. As shown in Fig. 1, thin-walled metallic cylinders commonly exhibit a sharp load drop after the peak load is reached, followed by oscillations around a mean crushing force [2]. These fluctuations imply variations in instantaneous energy absorption and periodic losses in stiffness. An ideal energy absorber would, in contrast, approach a perfectly plastic response with minimal post-peak load reduction. In this sense, it is desired that the load does not drop suddenly after the collapse.

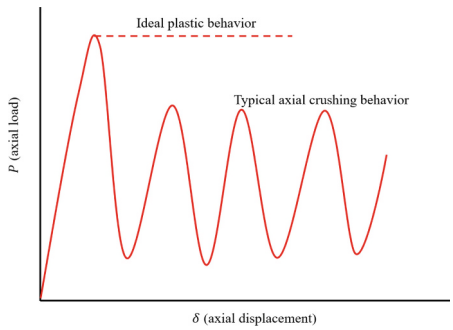

Fig. 1. Typical crushing behavior of cylindrical tubes and comparison with the perfect plastic behavior (dashed line).

Recent studies of origami-inspired and corrugated tubes have demonstrated that pre-folded patterns can improve stability and energy absorption during collapse [4,7,13]. Furthermore, recent work on Yoshimura-derived tubular mechanisms expands the design space and highlights their potential for structural applications [5,12]. These findings motivate a systematic investigation into how the geometric parameters of Yoshimura-type tubes influence their crushing behavior.

The aim of the present study is to experimentally evaluate the influence of geometric parameters, specifically the number of sides or patterns around the circumference and the corresponding in-plane face angles, on the axial crushing response and collapse kinematics of an origami-inspired cylindrical tube. Due to the large number of planned tests and the manufacturing complexity associated with folding metal sheets into precise crease patterns, cardboard paper was selected as the experimental material. Accordingly, the interpretation of collapse behavior is qualitative, while quantitative comparisons are made among the cardboard specimens themselves rather than against sheet-metal tubes.

2 Materials and Methods

To address the axial stiffness, peak crushing load and, most importantly, collapse behavior of the cylindrical origami and the influence of the angles and number of sides along the circumference, axial load tests are carried out on several Yoshimura tubes made out of cardboard.

2.1 Specimens

The specimens were fabricated using cardboard sheets due to their ease of folding, low thickness, and higher in-plane stiffness compared to standard paper. The crease patterns were printed on A4 cardboard sheets and subsequently folded into the desired configuration. To close each tube, an additional half-pattern was included so that the flat sheet could be wrapped and overlapped into a cylindrical form.

It is important to acknowledge several limitations associated with the use of cardboard:

- The quality of the folds may vary across the pattern, particularly in specimens with a large number of folds or very short fold lines. This limitation can be mitigated by increasing the number of tests and averaging the results.
- Manual handling during folding may cause tearing and introduce moisture into the cardboard, degrading fold quality over time. Reducing direct manipulation and using a straight edge such as a ruler during folding help improve uniformity. Printing the crease lines directly onto the cardboard further enhances consistency.
- The collapse loads are significantly lower than those obtained from metal sheets, owing to the difference in elastic moduli. As a consequence, direct scaling of the results to metallic materials is not straightforward. However, the collapse modes remain similar.

The specimens were designed to explore the influence of two geometric parameters: the number of sides around the circumference, n_p, and the in-plane angle of each panel with respect to the horizontal, α, as illustrated in Fig. 2.

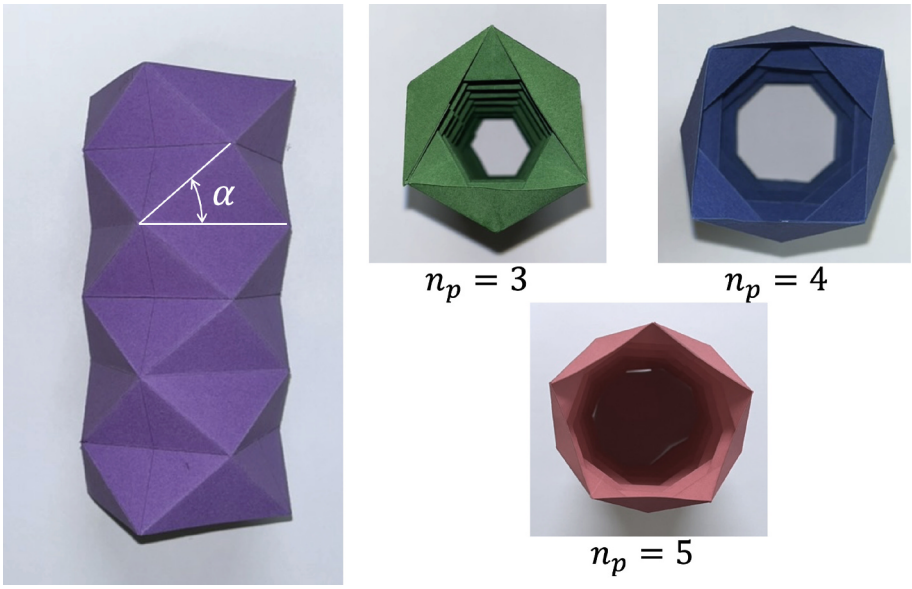

Fig. 2. Parameters of the Yoshimura cylinders.

Several combinations of (n_p, α) were examined. The angle α was varied from 30° to 60° in increments of 5°, while the number of sides ranged from 3 to 9. Not all combinations are suitable for experimental evaluation. Certain configurations result in apparently fully foldable tubes (very low axial stiffness), whereas others produce patterns that cannot be folded or compressed due to geometric incompatibilities, extreme difficulty to fold, or requiring different overlaps to form the tube. To the authors knowledge, there is no mathematical expressions yet to infer the stiffness and incompatibilities from n_p and α. The viable combinations used in this study are presented in Table 1.

Tubes with $\alpha = 60°$ were selected to study the influence of n_p. Additional values of α were tested with smaller values of n_p. It should be noted that combinations involving low values of α (close to 30°) together with high values of n_p (greater than 6) result in patterns that are extremely difficult to fold, due to the large number of required creases. The folding process for these cases often leads to premature wear or tearing off of the cardboard.

2.2 Testing

Axial crushing tests are carried out on a Zwick Roell testing machine Z0.5, with a load cell rated at 500 N. The Yoshimura tubes are placed in between two flat

Table 1. Values for pattern variables.

ID	Angle α [°]	No. sides n_p	ID	Angle α [°]	No. sides n_p
60-9	60	9	50-5	50	5
60-8	60	8	50-4	50	4
60-7	60	7	50-3	50	3
60-6	60	6	45-6	45	6
60-5	60	5	45-5	45	5
60-4	60	4	45-4	45	4
60-3	60	3	45-3	45	3
55-6	55	6	40-5	40	5
55-5	55	5	40-4	40	4
55-4	55	4	35-5	35	5
55-3	55	3	30-4	30	4

steel plates, with the bottom plate fixed in position and the top plate fixed to the crosshead applying the load, as seen in Fig. 3. The chosen displacement rate is 30 mm/min to simulate a quasi-static load. This load rate is consistent with previous research [3].

The load is continuously applied until either a maximum crosshead displacement of 80 mm is obtained. This chosen limit is half the average length of the tubes.

3 Results

In Figs. 4a–4e, the measured force–displacement ($f - \delta$) responses are grouped according to the number of sides n_p. The corresponding absorbed energies over the full crushing stroke are reported in Fig. 4f. These results allow several observations regarding the influence of geometric parameters on stiffness, strength, and collapse behavior.

An increase in the panel angle α generally results in higher initial stiffness and higher peak load. Nevertheless, variations in α do not appear to significantly modify the fundamental collapse mechanism. In contrast, the number of sides n_p has a pronounced influence on the collapse response, as evidenced by the distinct shapes of the force–displacement curves for different configurations, particularly in the case of the $\alpha = 60°$ specimens shown in Fig. 4e.

During crushing, the tubes exhibit a progressive, level-by-level collapse mode, as illustrated in Fig. 5. This sequential folding process accounts for the pronounced load oscillations observed in the experimental curves. Smaller load fluctuations are typically associated with local events such as crease inversion from valley to crest or relative sliding between the specimen and the compression platens.

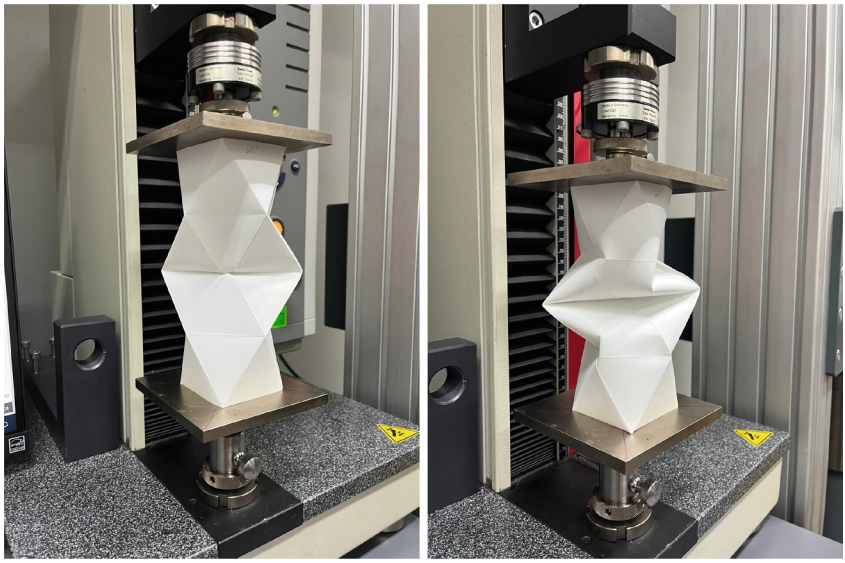

Fig. 3. Experimental setup during a test, showing the progressive collapse of a 60-4 tube along the middle.

Tubes with three sides (Fig. 4a) display a markedly different response. In these specimens, the load does not drop abruptly after reaching the first peak. Since the area under the $F - \delta$ curve represents the absorbed energy (Fig. 1), a gradual post-peak load decay is preferable, as it enables sustained energy dissipation over a larger deformation range. Consistent with this observation, three-sided tubes exhibit higher absorbed energy than the other configurations, as shown in Fig. 4f.

Four-sided tubes (Fig. 4b) exhibit a sharp load peak immediately following the elastic regime, followed by a sudden strength reduction. This first peak corresponds to the collapse of the initial folding level (e.g., the top level in Fig. 5a). Once this region can no longer sustain the applied load and folds onto itself (Fig. 5b), the force drops abruptly. Subsequent deformation leads to the formation of a new load peak (Fig. 5c), followed by the collapse of the next level and an associated sharp load reduction (Fig. 5d).

Among the tested configurations, four-sided tubes exhibit the most consistent and repeatable collapse behavior, particularly when compared with specimens having five or six sides (Figs. 4c and 4d). This repeatability coincides with their comparatively low energy absorption (Fig. 4f). The amplitude of load oscillations can be reduced by decreasing the panel angle. More generally, tubes with more than four sides tend to evolve toward a four-sided configuration during crushing. This tendency renders the initiation of collapse less predictable in higher $n - p$ specimens and does not guarantee the formation of subsequent load peaks. A larger number of patterns (eight or nine sides) increases the likelihood of

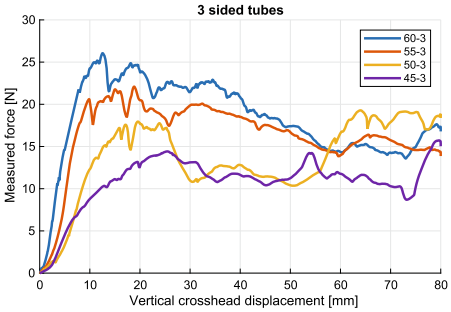

(a) Results for 3-sided tubes.

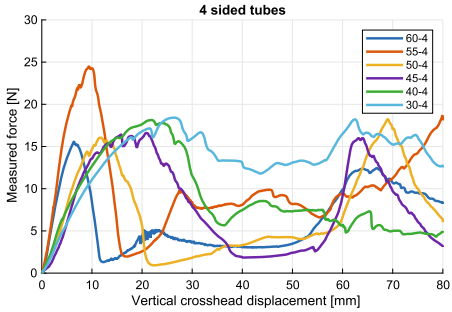

(b) Results for 4-sided tubes.

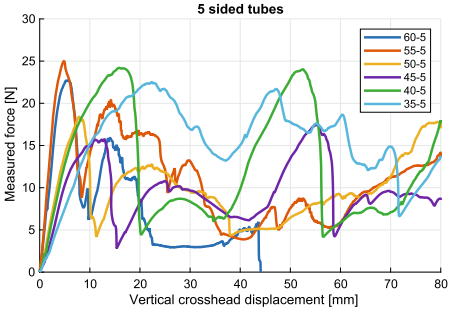

(c) Results for 5-sided tubes.

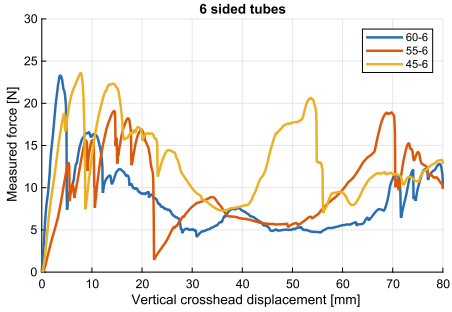

(d) Results for 6-sided tubes.

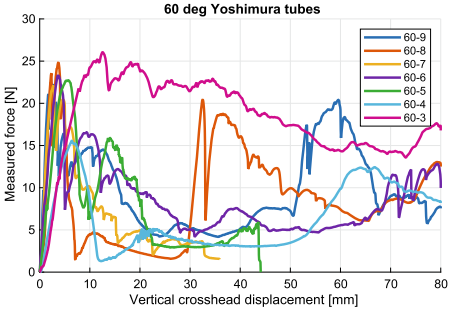

(e) Results for 60° tubes.

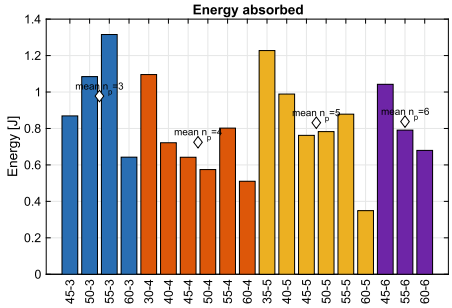

(f) Energy absorbed grouped by n_p.

Fig. 4. $F - \delta$ curves for different tube configurations.

additional peak loads, as observed in Fig. 4e. However, the precise location of these peaks remains difficult to anticipate, as an increasing number of sides also amplifies the sensitivity of the crushing response to geometric imperfections introduced during fabrication.

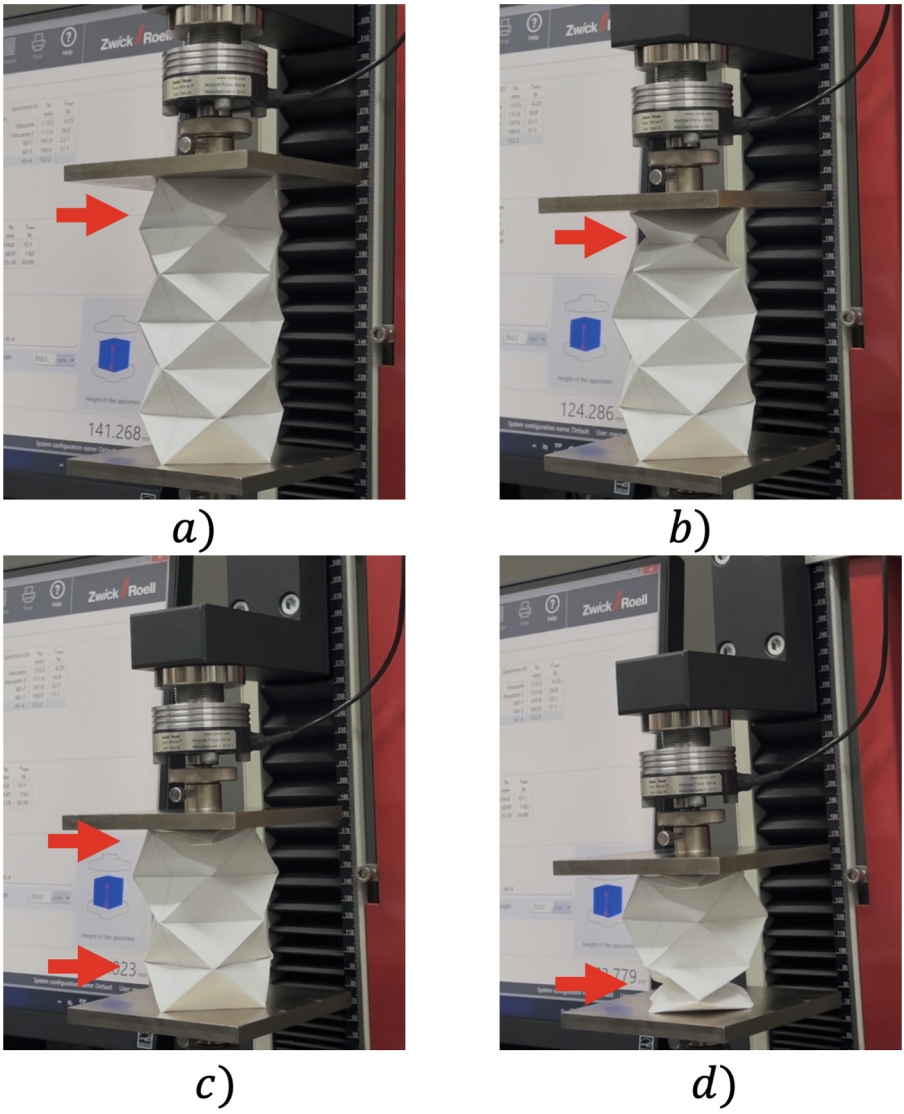

Fig. 5. Progression of the collapse. a) Collapse may begin in any "level", in this case, it began at the top. b) As it buckles, the load typically decreases drastically as it acts as a mechanism. c) Once this level is fully compressed, the tube regains part of its strength and stiffness until a new collapse occurs, in this case, at the bottom. d) The process repeats itself until all levels are collapsed.

4 Conclusions

This study presents a preliminary experimental investigation of the axial crushing behavior of Yoshimura cylindrical tubes, with particular emphasis on the

influence of geometric parameters on stiffness, peak load, and collapse mechanisms. The results indicate that the number of sides governs the global deformation mode, whereas the panel angle primarily modulates stiffness and load-carrying capacity without fundamentally altering the collapse sequence. Observations such as level-by-level folding, the tendency of specimens to evolve toward four-sided configurations during crushing, and the pronounced sensitivity to geometric imperfections underscore the complex mechanical response of these origami-inspired structures.

A noteworthy outcome of this work is the distinct response exhibited by three-sided tubes. In contrast to configurations with four or more sides, these specimens do not transition toward the characteristic four-sided collapse mode. Consequently, their force–displacement curves do not exhibit the abrupt post-peak load drop typically observed in other geometries. This comparatively stable post-peak response suggests that three-sided configurations may be advantageous for energy-absorption applications, as they sustain load over a longer crushing stroke and promote more progressive energy dissipation.

Given the exploratory nature of the present study, the reported findings should be regarded as an initial step toward a comprehensive understanding of the crushing behavior of Yoshimura tubes. All experiments were conducted using a single material system, which necessarily limits the generality of the conclusions. Extending the investigation to alternative materials—particularly those exhibiting higher ductility, increased stiffness, or anisotropic behavior—will be essential to evaluate the robustness of the identified trends and to assess their relevance for practical structural and energy-absorption applications. Future work should also incorporate improved fabrication techniques and complementary numerical modeling in order to more accurately capture the roles of imperfections, crease mechanics, and material nonlinearities in governing the crushing response.

Acknowledgments. This work was elaborated with the support of Estudios Generales Ciencias of the Pontificia Universidad Católica del Perú.

Disclosure of Interests. The authors have no competing interests to declare that are relevant to the content of this article.

References

1. Bös, F., Wardetzky, M., Vouga, E., Gottesman, O.: On the incompressibility of cylindrical origami patterns. J. Mech. Design **139** (2017). https://doi.org/10.1115/1.4034970
2. Chen, D.: Crush Mechanics of Thin-Walled Tubes. CRC Press (2016). https://doi.org/10.1201/b19257
3. Filipov, E.T., Tachi, T., Paulino, G.H., Weitz, D.A.: Origami tubes assembled into stiff, yet reconfigurable structures and metamaterials. Proc. Natl. Acad. Sci. U.S.A. **112**, 12321–12326 (2015). https://doi.org/10.1073/pnas.1509465112

4. He, J., Wen, G., Zhao, S., Liu, J., Kitipornchai, S., Yang, J.: Energy absorption of graded thin-walled origami tubes. Int. J. Mech. Sci. **282** (2024). https://doi.org/10.1016/j.ijmecsci.2024.109609
5. Jiang, B., Gao, W., Xie, Z., Pasini, D., Tan, H.: Thin-walled tubular structures integrating origami patterns and tension-dominated bulkheads for enhanced energy absorption. Thin-Walled Struct. **215** (2025). https://doi.org/10.1016/j.tws.2025.113433
6. Lang, R.J.: Twists, Tilings, and Tessellations. A K Peters/CRC Press (2017). https://doi.org/10.1201/9781315157030
7. Ma, J., Dai, H., Shi, M., Yuan, L., Chen, Y., You, Z.: Quasi-static axial crushing of hexagonal origami crash boxes as energy absorption devices. Mech. Sci. **10**, 133–143 (2019). https://doi.org/10.5194/ms-10-133-2019
8. Miura, K., Tachi, T.: Synthesis of rigid-foldable cylindrical polyhedra. Symmetry: Art Sci. (2010). www.tsg.ne.jp/TT/
9. Pujada-Gamarra, E., Lavayen-Farfán, D., Olivera-Oliva, D., Rodríguez-Hernández, J.: Origami-inspired photovoltaic modules—development of ecofriendly solutions for naval and mining operations. In: CITIIC 2023, p. 26. MDPI (2025). https://doi.org/10.3390/engproc2025083026, https://www.mdpi.com/2673-4591/83/1/26
10. Pujada-Gamarra, E., Zentner, L., Lavayen-Farfán, D., Rodriguez-Hernandez, J.A.: Analysis of the relative displacements in a thick origami with double-hinge technique for thickness accommodation. Mech. Mach. Theory **210** (2025). https://doi.org/10.1016/j.mechmachtheory.2025.106000
11. Qin, B., Lyu, S., Liu, S., Ding, X.: Design and optimization of origami-inspired inflatable deployable tubular structures. Chin. J. Aeronaut. **38** (2025). https://doi.org/10.1016/j.cja.2024.04.029
12. Wang, C., Xu, D., Song, S., Zhao, Y., Zhang, J.: Design and analysis of Yoshimura tubular origami mechanisms. Appl. Sci. (Switz.) **14** (2024). https://doi.org/10.3390/app142412048
13. Yang, K., Xu, S., Shen, J., Zhou, S., Xie, Y.M.: Energy absorption of thin-walled tubes with pre-folded origami patterns: numerical simulation and experimental verification. Thin-Walled Struct. **103**, 33–44 (2016). https://doi.org/10.1016/j.tws.2016.02.007

Evaluation of Equivalent Residual Stress Under Variable Loads for Fatigue Crack Propagation

Brahim Bouaziz(✉), Maher Eltaief, and Chokri Bouraoui

Mechanical Laboratory of Sousse, National Engineering School of Sousse, University of Sousse, BP 264, Erriadh, Sousse 4023, Tunisia
bouaziz_ibrahim@yahoo.fr

Abstract. Fatigue crack propagation can significantly reduce component lifespan and potentially lead to failure. The objective is to establish an equivalence relationship between variable and constant loading, thus avoiding complex cycle-by-cycle calculations, in order to determine, by means of finite element modelling, the residual stress field σ_r formed in front of the crack tip under an equivalent loading scheme and to compare it with that produced by real variable-amplitude loading.

The analysis is conducted within a two-parameter fatigue model in which crack propagation is governed by both the maximum total stress intensity factor $K_{\max_tot}$ and the stress intensity factor range ΔK_{tot}. Initially, the interaction effects of the plastic zone are neglected. The Willenborg model is then used to determine the equivalent stress that ensures a comparable crack growth rate.

Keywords: Residual stress · variable load · equivalent load

1 Introduction

In the automotive and aerospace sectors, cracks and geometric discontinuities are inevitable, and cyclic loading with variable amplitudes complicates fatigue life estimation. The objective is to estimate this life by replacing the variable loading with an equivalent constant-load problem, taking into account random loading sequences [1, 2], and subsequently forecasting the distribution of equivalent residual stresses at the crack tip using finite element analysis, and on the other hand, the distribution of these stresses under variable loading. The framework relies on a two-parameter fatigue model combining $K_{\max_tot}$. First ΔK_{tot}, plastic interactions are neglected to establish a variable-constant equivalence via a driving force framework. The Willenborg model [3], and its generalizations, is used to determine the equivalent stress $\Delta\sigma_{eq}$ that reproduces a comparable crack propagation rate under constant load.

© The Author(s), under exclusive license to Springer Nature Switzerland AG 2026
A. Chaker et al. (Eds.): EFIMMS 2026, MMS 205, pp. 345–352, 2026.
https://doi.org/10.1007/978-3-032-22270-1_34

2 Equivalent Stress Without Crack Closure Effect

The driving force model with two parameters estimates fatigue growth by taking into account $K_{\max_tot}$ and ΔK_{tot} [4], and the crack propagation speed is described by the equation associated with this frame.

$$\frac{da}{dN} = CK_{max}^{p}\Delta K^{q} \tag{1}$$

In the case of linear damage, the evolution of the crack length Δa on a cyclic spectrum of N_i variable amplitudes $\Delta\sigma_i$ can be calculated from the corresponding crack growth rates [5].

$$\Delta a = \left(\frac{da}{dN}\right)_1 .N_1 + \left(\frac{da}{dN}\right)_2 .N_2 + \cdots + \left(\frac{da}{dN}\right)_n .N_n \tag{2}$$

Combining two equations allows us to find:

$$\Delta a = C\left(K_{1\max}^{p}\Delta K_1^{q}N_1 + K_{2\max}^{p}\Delta K_2^{q}N_2 + \cdots + K_{nmax}^{p}\Delta K_n^{q}N_n\right) \tag{3}$$

Where

$$K_{max} = \frac{\Delta K}{1-R} \tag{4}$$

And

$$\Delta K = Y\Delta\sigma\sqrt{\pi a} \tag{5}$$

Where Y represents a geometric correction factor.
Thus, the total crack length can be rewritten as:

$$\Delta a = C.Y^{p+q}(\pi a)^{(p+q)/2}.\left(\frac{\Delta\sigma_1^{p+q}}{(1-R_1)^p}N_1 + \frac{\Delta\sigma_2^{p+q}}{(1-R_2)^p}N_2 + \cdots + \frac{\Delta\sigma_n^{p+q}}{(1-R_n)^p}N_n\right) \tag{6}$$

From Eq. (6), it is possible to calculate the growth of the equivalent crack from a constant amplitude loading:

$$\Delta a = C.Y^{p+q}(\pi a)^{(p+q)/2}.\left(\frac{\Delta\sigma_{eq}^{p+q}}{\left(1-R_{eq}\right)^p}N_{total}\right) \tag{7}$$

Equality between Eqs. (6) and (7) allows us to calculate $\Delta\sigma_{eq}$ [6]:

$$\Delta\sigma_{eq} = \left(\sum_{i=1}^{n}\frac{N_i}{N_{total}}\frac{\Delta\sigma_i^{p+q}}{(1-R_i)^p}\right)^{1/(p+q)} \tag{8}$$

3 Equivalent Stress with Crack Closure Effect

By combining The Willenborg model and the two-parameter modeling approach, the crack propagation speed can be described by:

$$\frac{da}{dN} = CK_{max}^{p}\Delta K_{eff}^{q} = \frac{C}{(1-R)^{p}}\Delta K_{eff}^{p+q} = C_T\Delta K_{eff}^{p+q} \tag{9}$$

With R the stress ratio and p, q the calibration parameters.

Studies on aluminium alloys often indicate p = 2 [3, 7], and the unknowns to be determined in Eq. (4) are C_T and q, from the curves $\frac{da}{dN}$ as a function of ΔK constant load.

4 Results and Discussion

4.1 A Plate with a Central Crack

The analysis was performed on a sample 2024-T3 aluminum alloy with a mid-plane crack of initial size (2a) equal to 12.7 mm, a specimen of 61 cm in length and 22,9 cm in width and a thickness t of 4.1 mm.

4.2 Calculation of Parameters *p* and *q*

To determine the equivalent load according to Eq. (3), the unknown q (with p = 2) [3, 6] must be known. This step is carried out using Eq. (4), which has two unknowns, C_T and q, determined using the experimental results of the curve $\frac{da}{dN}$ depending on the amplitude ΔK under constant load.

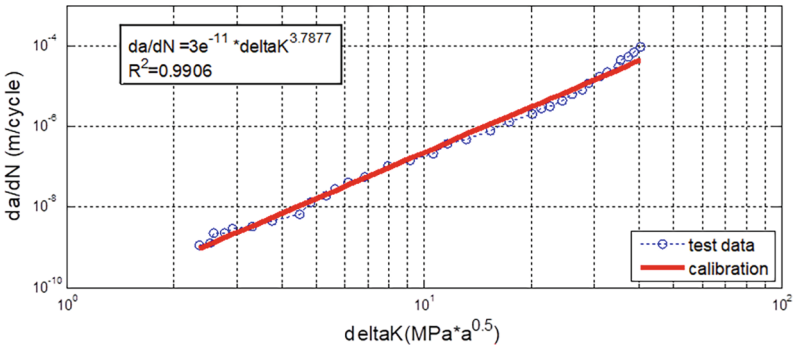

Fig. 1. $\frac{da}{dN} - \Delta K$ aluminium alloys $2024 - T3$ for $R = 0, 4$ [8].

The following Fig. 1 illustrates the variation of $\frac{da}{dN}$ with ΔK and is used to adjust the parameters and C_T.

For an aluminum alloy, we take p = 2, which allow us to determine: $q = 1.7877$.

4.3 Calculation of Residual Stress σ_r

Residual stresses formed ahead of the crack tip, extracted after the unloading phase, are assessed via finite element analysis based on the Chaboche model [9]. This model describes cyclic plasticity with high accuracy by taking into consideration the Bauschinger effect, mean stress relaxation, and cyclic hardening during the simulations. In our study, the nonlinear kinematic hardening model is integrated into ABAQUS [10] to evaluate the influence of variable amplitude loading on the cyclic plastic behavior upstream of the crack in the Al 2024- T3 alloy.

To correctly predict the kinematic effect, several parameters are introduced, including C_i and γ_i represent the characteristic parameters of each material.

This distribution of residual stresses remains unchanged under constant amplitude loading. The mechanical and cyclic fatigue properties of the Al 2024-T3 alloy are summarized in Table 1, where C_i and γ_i represent the Chaboche kinematic hardening parameters.

Table 1. Summary of properties mechanics and the cyclic fatigue resistance of the Al 2024-T3 alloy [11].

E(MPa)	ν	σ_y(MPa)	C_1(MPa)	C_2(MPa)	C_3(MPa)	γ_1	γ_2	γ_3
73000	0.33	289	2169.7	7471.9	65.761	11.74	90.05	555.09

Where $\boldsymbol{E}$ refers to the elastic modulus of the material, $\boldsymbol{\nu}$ denotes Poisson's ratio, $\boldsymbol{\sigma_y}$ denotes the yield stress, $\boldsymbol{C_1}, \boldsymbol{C_2}$ and $\boldsymbol{C_3}$ are the kinematic stress parameters for the inverse stress and $\boldsymbol{\gamma_1}$, $\boldsymbol{\gamma_2}$ and $\boldsymbol{\gamma_3}$ are the corresponding kinematic saturation velocity parameters.

Figures 2 and 3 below illustrate the finite element model, as well as the boundary conditions and the type of mesh used:

To improve the accuracy of the results and better predict the crack tip response to plastic deformation in the FE analysis, a highly refined mesh was applied around the CPS4R crack region, with an element size of 0.05 [12, 13].

We use then two block of loading in accordance with references [6, 14].

According to Eq. (8), the equivalent load associated with each loading sequence is expressed in the following form:

$$\Delta\sigma_{eq} = \left(\sum_{i=1}^{3} \frac{N_i}{N_{total}} \frac{\Delta\sigma_i^{p+q}}{(1-R_i)^p} \right)^{1/(p+q)} \tag{10}$$

This FE analysis resulted in a residual stress distribution, as illustrated in Fig. 4.

Finite element analysis is employed to estimate the residual stress based on the S_{22} stress distribution. It is observed that the compressive stress increases in absolute magnitude near the crack tip, which is confirmed by the results of several researchers [15].

In order to incorporate loading sequence effects, residual stresses are first computed for two loading histories illustrated in Fig. 4 and then contrasted with those obtained from the equivalent load.

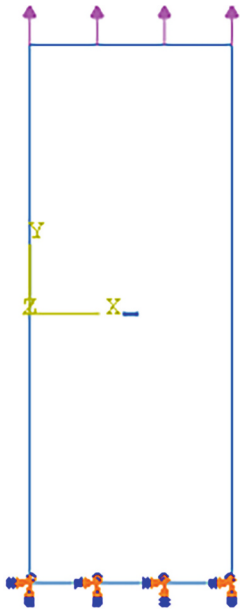

Fig. 2. Boundary conditions used in the simulation.

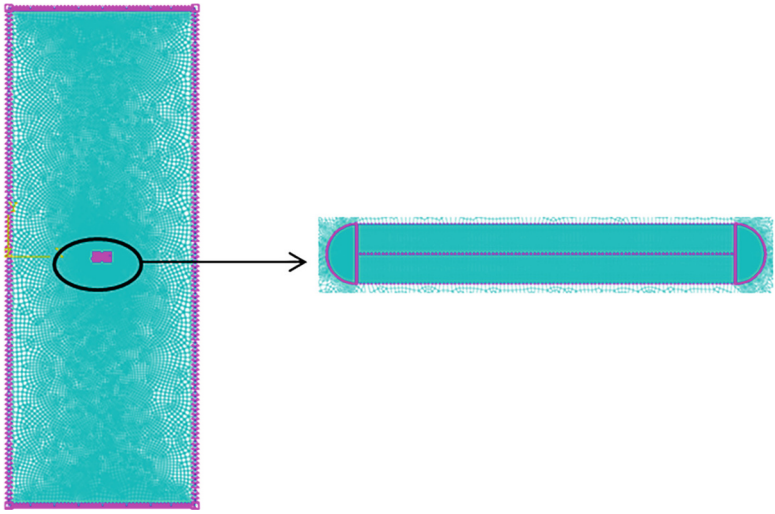

Fig. 3. Type of finite element mesh.

Each block of variable load is transformed into a constant load, and the variation of the residual stress is deduced.

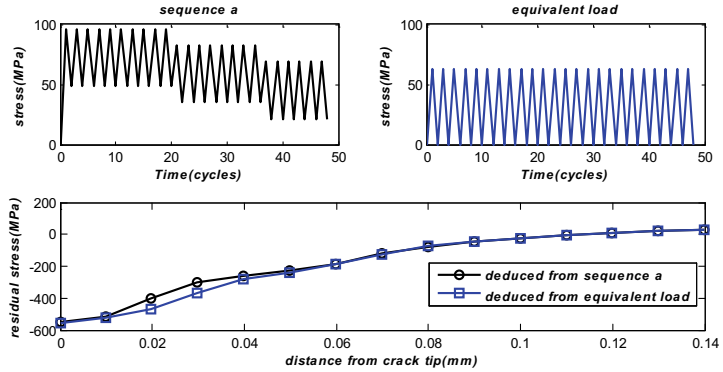

(a)

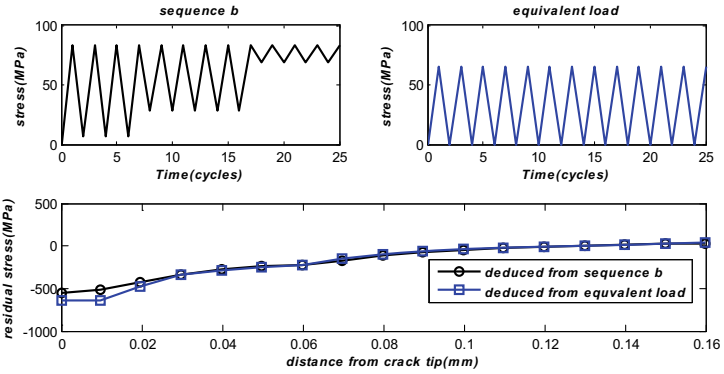

(b)

Fig. 4. (a, b) Residual stress distribution.

4.4 Comparison Between Equivalent and Variable Loading (Fig. 5)

L'erreur relative sera calculée comme suit:

$$e(\%) = \frac{\left|\sigma_{r\ seq} - \sigma_{r\ eq}\right|}{\left|\sigma_{r\ seq}\right|} * 100 \tag{11}$$

The figure shows the evolution of the relative error e(%) as a function of distance from the crack tip. Two distinct trends can be observed.

First, in the immediate vicinity of the crack tip, the relative error is non-zero and reaches its maximum values. The curve for 4.a shows an error peak of approximately 5%, while the curve for 4.b remains below 2%. This difference indicates that the discrepancies between the two methods for calculating residual stresses are more pronounced in the area strongly influenced by the local effects of the crack tip, where the stress gradients are high but close.

Second, as the distance from the crack tip increases, the relative error decreases rapidly. From a distance of approximately 0.05, the error becomes practically zero for

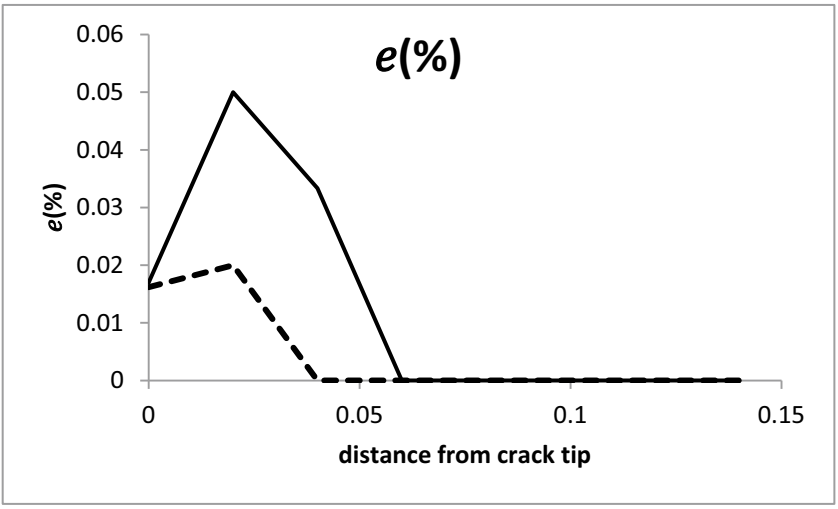

Fig. 5. Percentage difference between distribution of residual stress.

both curves. This suggests that, far from the crack tip, the residual stresses deduced from the different approaches become very close, or even equivalent.

5 Conclusion

The residual stresses σ_r generated upstream of the crack tip are a crucial component for assessing the reliability of structures subjected to variable cyclic loading. Our approach allows us, firstly, to replace a variable load with a constant-load equivalent and, secondly, to calibrate the parameters of the two-parameter frame from the da/ dN curves as a function of ΔK, in order to robustly estimate σ_r using finite element (FE) analysis. The results demonstrate that integrating random loading sequences and the plastic effect improves the representativeness of the σr under real-world conditions, compared to that obtained with the equivalent load alone. In particular, the equivalent residual stress tends to increase in absolute value near the crack tip, while remaining consistent with the residual stress estimated from real-world loads, highlighting the relevance of the approach for accurately predicting crack propagation and enhancing component safety.

References

1. Sérgio, E.R., Antunes, F.V., Neto, D.M.: Improving the fatigue crack growth prediction by accurate calibration of the constitutive material parameters. Theor. Appl. Fract. Mech. **138**, 104957 (2025)
2. AH Noroozi, Glinka, G., Lambert, S.: A study of the stress ratio effects on fatigue crack growth using the unified two-parameter fatigue crack growth driving force. Int. J. Fatigue. **29**, 1616–1633 (2007)

3. Willenborg, J., Engle, RM., Wood, HA., Air Force Flight Dynamics Lab Wright Patterson AFB OH.: A crack growth retardation model using an effective stress concept, Technical Report AFFDL-TM-71-1-FBR, Wright Patterson Air Force Lab, Wright-Patterson AFB, OH, USA, Jan. 1971
4. Glinka, G., Buczynski, A.: Experimental and numerical analysis of elastic-plastic strains and stresses ahead of a growing fatigue crack. In: Susmel, L., et al. (eds.) Workshop on Characterisation of Crack Tip Stress Fields, GruppoItalianaFrattura, Forni di Sopra, Italy, pp. 7–9 (2011)
5. Anderson, T.L.: Fatigue crack propagation. In: Fracture Mechanics: Fundamental and application, 3rd edn, pp. 451–507 (2005)
6. Bouaziz, B., Eltaief, M., Bouraoui, C.: An engineering methodology for predicting crack growth of 2024-T3 aluminium alloys under variable amplitude loading. Comptes Rendus. Mécanique. ***353***(G1), 1385–1404 (2025)
7. Meggiolaro, M.A., Castro, J.T.P.: Comparison of load interaction models in fatigue crack propagation. In: Proceedings of COBEM, pp. 247–256 (2001)
8. Lu, Z., Liu, Y.: A comparative study between a small time scale model and the two driving force models for fatigue analysis. Int. J. Fatigue. **42**, 57–70 (2012)
9. Hu, Q., Meng, W., Hu, F., Shen, Z., Zhan, Sun, L.: A continuum damage mechanics approach coupled with an improved pit evolution model for the corrosion fatigue of aluminum alloy. Corros. Sci. flight. **113**, 78–90 (2016). https://doi.org/10.1016/j.corsci.2016.10.006
10. Dassault Systèmes Simulia, Inc. (DS Simulia Corp.).: ABAQUS/Standard User's Manual (Version 6.14). Dassault Systèmes Simulia, Inc. (DS Simulia Corp.) (2014/2015)
11. Kebir, T., Mohamed, B., Abdelkader, M.: Simulation of the cyclic hardening behavior of aluminum alloys simulation of the cyclic hardening behavior of aluminum alloys. Mech. Eng. **79**, 240–250 (2017)
12. Remadi, A., Bahloul, A., Bouraoui, C.: Prediction of fatigue crack growth life under variable-amplitude loading using finite element analysis. CR Mecanique. **347**(8), 576–587 (2019)
13. Remadi, A., Bahloul, A., Bouraoui, C.H.: Fatigue crack growth behavior of AA2024T3 under mixed mode loading within the framework of EPFM. J. Mech. Sci. Technol. **37**(4), 1761–1771 (2023)
14. Mikheevskiy, S., Glinka, G.: Elastic-plastic fatigue crack growth analysis under variable amplitude loading spectra. Int. J. Fatigue. **31**(11–12), 1828–1836 (2009). https://doi.org/10.1016/j.ijfatigue.2009.02.035
15. Bahloul, A., Bouraoui, C.H.: The overload effect on the crack tip cyclic plastic deformation response in SA333 Gr 6 C- Mn steel. Theor. Appl. Fract. Mech. **99**, 27–35 (2018)

Numerical Study of the Effects of Thickness and Bracing on Lute Acoustics

Atef Dhokkar(✉), Mohamed Ali Rezgui, and Ali Trabelsi

Laboratory of Mechanics, Production and Energy (LR18ES01), University of Tunis, Higher National Engineering School of Tunis, Tunis, Tunisia
aldhokkar.atef@gmail.com, mohamedali.rezgui@esstt.rnu.tn, ali.trabelsi@ensit.rnu.tn

Abstract. In this study, we examine the influence of the soundboard thickness profile and bracing pattern on the vibrational and acoustic behavior of the Lute using finite element simulations. A fully parametric model of the instrument body was developed and combined with a full factorial design (2×3^2) to systematically explore the effects of these parameters. Numerical modeling is employed to evaluate the acoustic performance of the Lute in terms of sound pressure level and sound balance. Although several studies have investigated the acoustics of string instruments such as guitars and violins, the Lute remains insufficiently studied from a structural–acoustic interaction perspective. According to the literature, no previous work has integrated a full factorial design with harmonic acoustic simulations and multi-objective optimization to simultaneously evaluate sound pressure level and sound balance. This methodological framework and its findings represent the principal contribution of the present work.

Keywords: Lute · Finite Element Analysis · Design of Experiments · Modal Analysis · Harmonic · Acoustic

1 Introduction

Instrument acoustics is a field that concerns the musical technologies, the manufacture of instruments, the study of the process of sound formation, and the performance of vibration and sound analyses [1, 2]. Although the history of research in this field has been reserved for Western instruments like guitar, violin or piano. Thanks to the versatility that this field needs such as mechanics, physics, and musicology to interpret the phenomena that are created in musical instruments by generating different sounds. This paper focus on the objective of optimizing the sound formation characteristics of a Lute (stringed musical instrument) an oriental instrument that dates back more than 3000 years [3], while using the design of experiments method [4], In order to know what is the influence of certain factors on the sound pressure level we chose from the literature [5] the thickness of the upper plate of the Lute, the type of reinforcing bracing under the soundboard and their thicknesses, the choice of these last two factors led us to reflect on the mechanical behavior of the Lute which must absolutely have a robust structure resistive to the tension of the strings and the vibrations which propagate throughout this system taking into account the natural modes and the resonant frequencies [6].

© The Author(s), under exclusive license to Springer Nature Switzerland AG 2026
A. Chaker et al. (Eds.): EFIMMS 2026, MMS 205, pp. 353–367, 2026.
https://doi.org/10.1007/978-3-032-22270-1_35

2 Methodology

The soundboard is the most important component [7] that affects the sound pressure level of the guitar according to Richardson et al. [8]. Therefore, we chose the soundboard as a material for our study which is the upper plate of the Lute. For the shape of the soundboard we chose the Lute by luthier George Nahat from 1932 which is exhibited in the Paris Philharmonie and shown in Fig. 1.

Fig. 1. Nahat Lute

We used Solidworks design software to be able to model this Lute with the same geometric dimensions. Since we have chosen 3 factors to vary them which are the thickness of the soundboard, the type of bracing and the thickness of the bars. Concerning the second factor, we preferred to adopt a classic Lute bracing which is often used by luthiers [9] and bracing inspired by the guitar [10] which is crossed unlike the classic parallel bracing (Figs. 2, 3, 7, 8, 9, 11, 13, 14 and 15).

The length of the bars is the same for both types and equal to 2420 mm with different arrangements. For the thickness of the soundboard and the thickness of the bars we chose 3 levels for each. Therefore, the factorial design requires of 18 experiments (3*3*2) which are presented in the Appendix. The factors and their levels are presented in Table 1.

NB: type of bracing 1: parallel type; 2: crossed type

Once we have designed the 18 soundboards we will evaluate their behavior using the finite element software. In harmonic acoustics, analysis focuses on the response of a structure and the surrounding fluid medium to loads that vary sinusoidally (harmonically) with time. This type of analysis is crucial for understanding and optimizing the behavior of systems subjected to acoustic pressures. In a harmonic acoustics simulation,

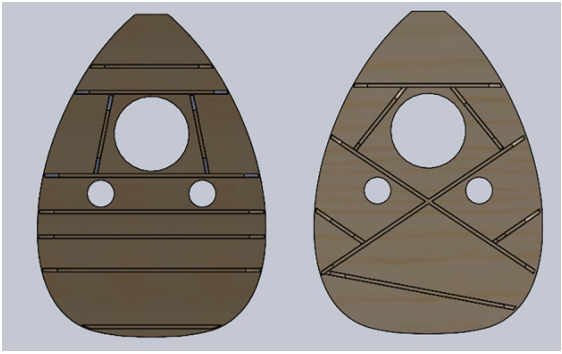

Fig. 2. Parallel bracing and crossed bracing

Table 1. The factors and their levels

Factor	Unity	Level 1	Level 2	Level 3
Thickness of the soundboard	mm	1	1.5	2
Thickness of bars	mm	6	7	8
Type of bracing	_	1	2	_

ANSYS calculates acoustic pressure and velocity fields [11], as well as displacement and structural stresses, in response to these oscillating loads. The following equation is resolved for pure acoustic problems:

$$\left(w^2[M_a] + jw[C_a] + [K_a]\right)\{p\} = \{f_F\} \tag{1}$$

Where $\{p\}$ is the acoustic pressure vector, $\{f_F\}$ is the acoustic force vector, $[M_a]$ is the acoustic mass matrix, $[C_a]$ is the acoustic damping matrix, $[K_a]$ is the acoustic stiffness matrix, is the angular frequency and j is the imaginary unit. For fluid-structure interaction problems, the acoustic and structural matrices are coupled using the following equation:

$$\left(-\omega^2\begin{bmatrix} M_s & 0 \\ \rho_0 R^T & M_f \end{bmatrix} + j\omega\begin{bmatrix} C_s & 0 \\ 0 & C_f \end{bmatrix} + \begin{bmatrix} K_s & -R \\ 0 & K_f \end{bmatrix}\right)\begin{Bmatrix} u \\ p \end{Bmatrix} = \begin{Bmatrix} f_s \\ f_F \end{Bmatrix} \tag{2}$$

ANSYS is able to do a complete simulation of how acoustic loads affect both the surrounding fluid and the structure itself. The system has two coupled degrees of freedom: the displacement of the structure $\{u\}$ and the pressure of the fluid $\{p\}$, where the matrices $[M_s]$, $[C_s]$, $[K_s]$ represent the mass, damping and stiffness of the structure, respectively, and the matrices $[M_f]$, $[C_f]$, $[K_f]$ represent the mass, damping and stiffness of the fluid, respectively. The vectors $\{f_s\}$ and $\{f_F\}$ are the external forces applied to the structure and the fluid, while $[R]$ is the coupling matrix between the structure and the fluid. The acoustic study of the Lute essentially involves modal analysis which gives the

natural modes of the structures which present the frequencies for which we will have the phenomenon of resonance [12]. In modal analysis, we do not need to apply any external load but instead introduce the characteristics of existing materials into the system. In our case the soundboard is made of spruce, the bridge is made of mahogany and the bars are made of fir. The material properties are presented in Table 2 [13]

Table 2. Wood physics' criteria, measured according to standard NF B51016

Wood	*E* (GPa)	Density (kg/m^3)	E/density (MPa.m^3/kg)
Spruce	11.123	432	26
Mahogany	10.790	600	18
Fir	10.522	463	23

As we know, the tonal quality of the soundboard [14] is affected by the underlying bracing system. The luthier Martin developed an X-shaped bracing for the acoustic guitar [15] in the 1850s [16], the radial layout in which the braces are placed around the bridge with radial orientation unlike parallel braces. So to know the influence of these geometric parameters (type of bracing), we focused in our study on the soundboard, which was simulated detached from the rest of the instrument [17], but the bracing was included.

3 Results and Discussion

Knowing the resonant frequencies of the soundboard constitute an essential step in understanding its vibrational and acoustic behavior by identifying the most influential modes in sound production, particularly those linked to acoustic tone.

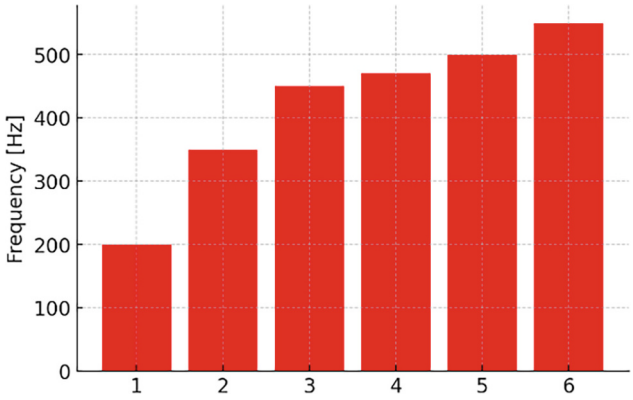

Fig. 3. The bar graph shows the specific frequency of each calculated mode

In the figure above the frequencies of the first 6 natural modes of the lute having the parameters of the 13th execution. Chladni figures [18] are shown in Fig. 4 for the first and second mode. This kind of shapes are discovered by Ernst Chladni in the 18th century and used to visualize the distribution of vibrations in plates as well as musical instruments (violins, guitars, Lutes) in acoustic research and obtain sound balance. Once we have completed this step the results will illuminate the part of the harmonic response knowing that it requires a dynamic loading of type (pressure or force) in our case we will apply a pressure on our soundboard of amplitude 10^5 Pa.

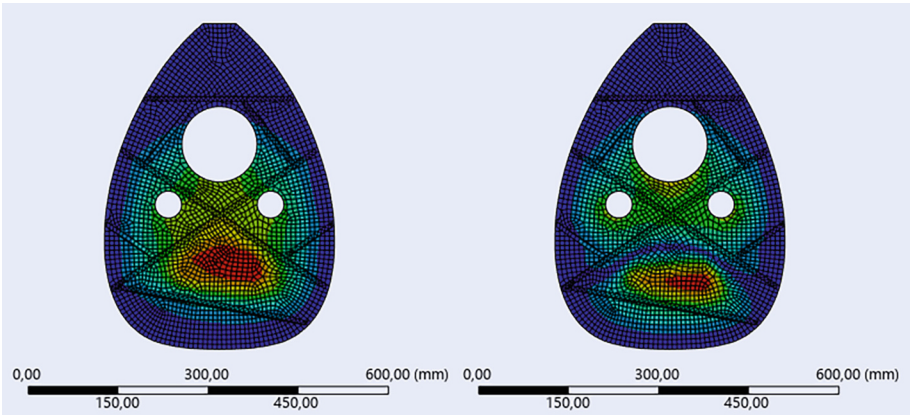

Fig. 4. The chladni figures of two first modes of the 13th Lute

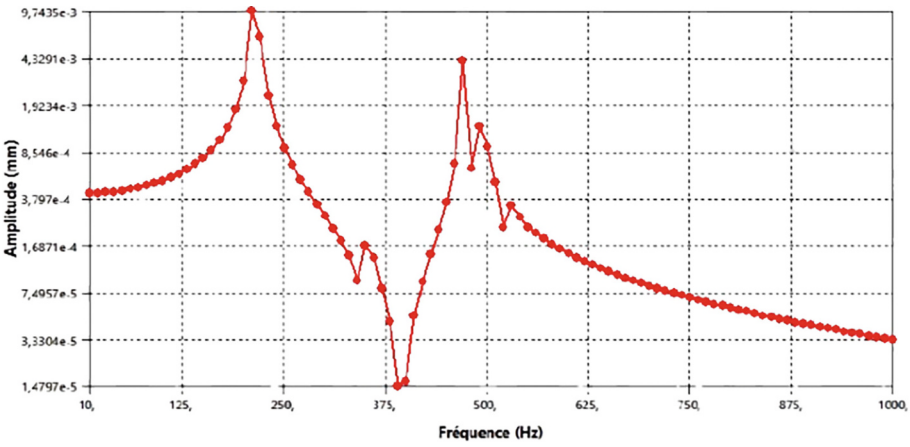

Fig. 5. The magnitude of a normal displacement of the soundboard into a range of frequency 10 to 1000 Hz

Figure 5 represents the magnitude of a normal displacement of the soundboard into a range of frequency 10 to 1000 Hz, and we notice that the maximum of magnitude

across with the resonant frequencies. This harmonic analysis will be used later for the part of harmonic acoustics, but at this level we are obliged to define an environment which includes the Lute knowing that this environment is full of air since sound waves only propagate in material.

The air domain is defined as a sphere around the Lute model. This sphere is assimilated to an open space by excluding the effect of reflection of the wave emitted by the Lute so that we will have no overlap. The load applied to the soundboard causes the structure to vibrate and as it propagates it will vibrate the atoms in the air to create sound waves which are measured by the Sound Pressure Level (SPL) [19] and its unit is the decibel (dB). According to the modal analysis we found that the first mode of resonance gives us an amplitude of displacement normal to the soundboard at the level of the bridge. This is why we measured the sound pressure level in this area using a plane orthogonal to the soundboard passing through the bridge as in the following figure.

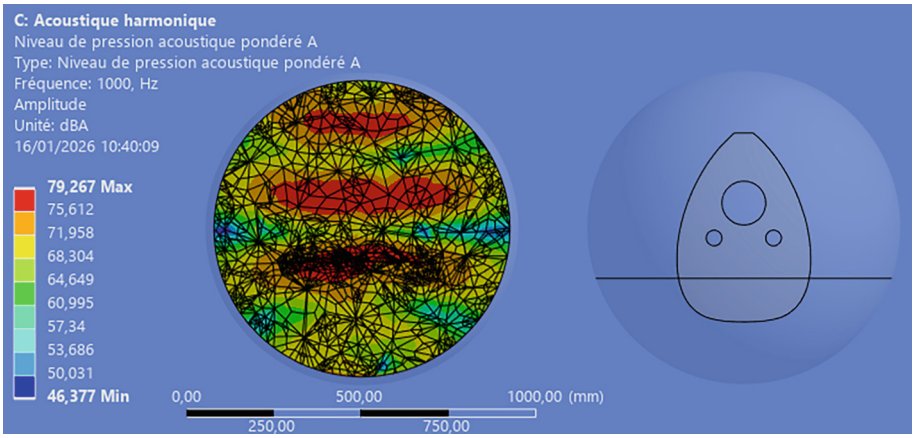

Fig. 6. Sound pressure level at bridge level

According to the acoustic simulations, a maximum sound pressure level (SPL) was obtained for the 18 lutes at the bridge as shown in Fig. 6.

The first execution of the DOE has the maximum SPL equal to 97.14 dB

This response of our system is important to know the influence of the control factors on the sound rendering but it lacks other criteria to properly judge the system and satisfy Lute users. We can add another response which characterizes the sound balance (SB) of the Lute by sweeping the bass frequencies up to the treble frequencies [20]. This criterion is crucial for musicians because sometimes Lutes have a good resonance in the high frequencies and an attenuation in the bass frequencies and vice versa. Table 2 presents how the Lute should be tunned (Tables 3, 4 and 5).

So on the bridge going from the first string to the sixth we pass through the high frequencies towards the low frequencies, so in the second bracing we chose to mount an inclined bar under the bridge making a small distance gap near the high frequency zone and a large distance gap near the frequency zone which probably leaves the low frequencies with long wavelengths to vibrate the bridge freely while the high frequencies

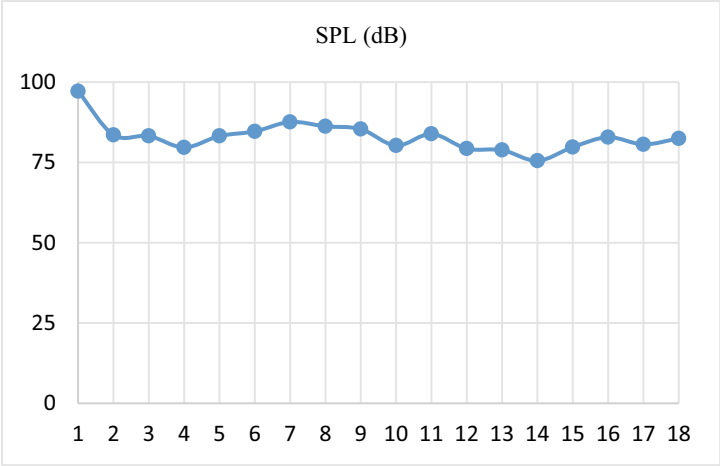

Fig. 7. Maximum Lute SPL of the design of experiments

Table 3. Summary of strings with their frequencies

String number	6	5	4	3	2	1
String note	Do	Sol	La	Ré	Sol	Do
Frequency (Hz)	*65*	97	110	146	194	261

have small wavelengths to propagate [7]. In order to find the acoustic balance of the Lute we took a path which is the edge of the bridge on which we fix the strings to measure the amplitude of normal movement along the bridge following loading on the soundboard.

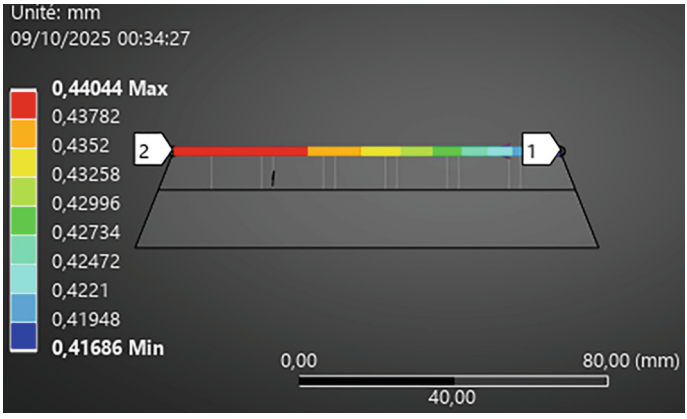

Fig. 8. Corresponds to the 2nd bracing

We note for the bridge of the 12th execution of the Lute had a maximum amplitude of normal displacement in the bass frequency zone but also the amplitude of displacement is progressive from right to left like the progression of the frequencies from the first string towards the sixth string.

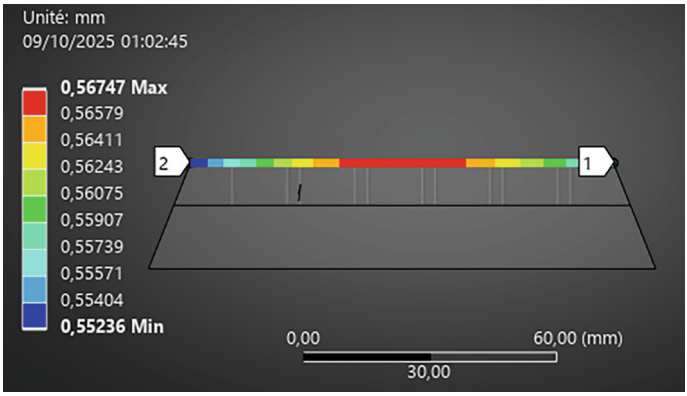

Fig. 9. Corresponds to the first bracing

Based on Fig. 10 it is clear that the behavior of the amplitudes along the bridge is symmetrical with low values in the ends which means highs and lows of close amplitudes therefore no balance [21].

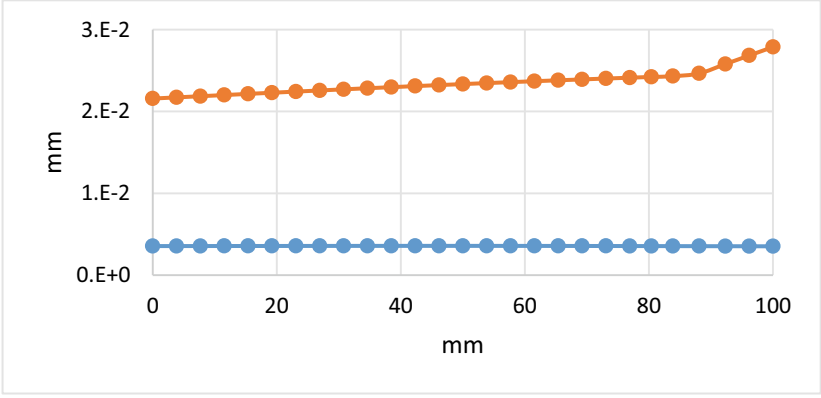

Fig. 10. Displacement amplitudes along the bridge for the two types of bracing

Figure 10 shows the normal displacement amplitude curves along the bridge for executions number 1 and 10 knowing that the latter have the same input factors except the bracing type factor and we have arrived at an observation that the type of crossed bracing is characterized by a progressive behavior from the high frequency zone towards the bass frequency zone. In order to be able to quantify the sound balance, we proposed to

calculate the difference between the maximum and minimum displacement amplitude, this response is to be maximized, the greater this difference, the more balanced the system is.

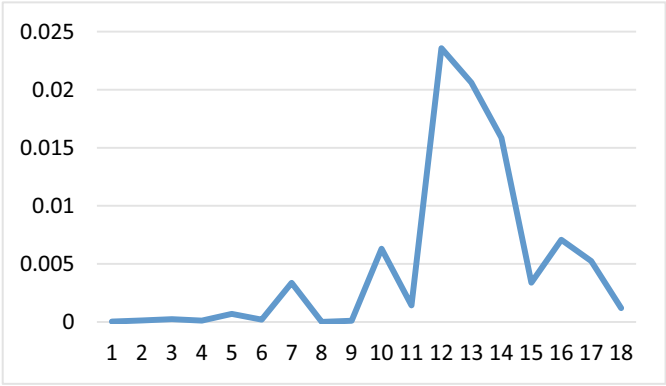

Fig. 11. The sound balance for the 18 lutes

This curve confirms that the cross-bracing is more balanced, which corresponds to executions from 10th to 18th (bracing type number 2).

A multi-objective problem approach is used via Grey Method (Grey Relational Analysis), which evaluate the following two outputs for the Lute: the sound level pressure (SPL) and the sound balance (SB) to identify the execution for which we find the best combination between the two outputs [22].

This method requires 5 important steps: firstly, the outputs must be normalized on the same scale (often between 0 and 1) depending on the type of objective, whether maximization, nominalization or minimization; secondly, we calculate the difference between the value of each test and the best value which is 1; thirdly, we measure the proximity between each test and the best condition.

$$\xi_i(k) = \frac{\Delta_{\min} + \zeta \Delta_{\max}}{\Delta_i(k) + \zeta \Delta_{\max}} \tag{3}$$

$\Delta_{\min}$ = smallest deviation observed
$\Delta_{\max}$ = largest deviation observed
ζ = coefficient of distinction (often = 0.5)

The next step is only the calculation of the average (or weighting) of the relationship coefficients for each test:

$$\gamma_i = \frac{1}{n} \sum_{k=1}^{n} \xi_i(k) \tag{4}$$

with

$i = 1,\ldots,18$

k = 1 or 2

And finally the classification of levels or combinations according to the value of γ (from the largest to the smallest) knowing that the greater γ, the closer the combination of parameters is to optimal performance. We used an Excel sheet to obtain the following ranking.

Table 4. Grey Relational Grade for the 18 executions

Run	Grey Relational Grade	Rank
1	0.3334	2
2	0.1944	13
3	0.1932	15
4	0.1791	18
5	0.1942	14
6	0.1997	9
7	0.2247	5
8	0.2078	7
9	0.2031	8
10	0.1989	11
11	0.1991	10
12	**0.3443**	**1**
13	0.2926	3
14	0.2344	4
15	0.1880	17
16	0.2118	6
17	0.1967	12
18	0.1922	16

So according to Fig. 12 results the 12th execution is the best design in terms of SPL and SB, the significance of the input design factors in relation to the two evaluated outputs for the Lute performance is studied. Starting with the first output which is the SPL, an analysis of variance is done to find out the contribution of each input factor to the result [23].

Source	DF	SomCar	CM	F-Value	P-value
Thickness of the soundboard	2	17.40	8.702	0.67	0.528
Thickness of bars	2	67.50	33.749	2.61	0.114
Type of bracing	1	123.85	123.853	9.58	**0.009**

(*continued*)

(*continued*)

Source	DF	SomCar	CM	F-Value	P-value
Error	12	155.15	12.929		
Total	17	363.91			

Based on ANOVA, the P-value indicates that the bracing type is significant, for other factors they have less influence on the SPL. For the R square of this experiment is 57.37% so the model lacks other factors to properly express the problem. And to visualize the contribution of each factor we use the signal-to-noise index of the Taguchi method [24].

The figure above shows that Type 1 gives a higher signal to noise level than Type 2. Therefore, Type 1 produces a better and more robust sound pressure level. Going to the Bracing thickness factor there is a strong drop at the central level. This shows that the 7 mm thickness of the bracing gives the lowest performance, while 6 and 8 mm give better results. The behavior is non-linear.

And finally for the Soundboard thickness factor it seems that the thinnest board (1 mm) gives a better result than the thicker ones. But the difference is not huge and this is due to the limitation of the thickness level intervals [25]. We repeat the same analysis for the second response which is the sound balance, starting with the ANOVA then the calculation of the signal to noise ratio and we see from the table below

Source	DL	SomCar	CM	F-Value	P-value
Thickness of the soundboard	2	0.000017	0.000008	0.18	0.835
Thickness of bars	2	0.000053	0.000026	0.58	0.567
Type of bracing	1	0.000356	0.000356	7.78	0.016
Error	12	0.000549	0.000046		
Total	17	0.000974			

Similar to the analysis of variance of the first design of experiments we have the type factor as the most significant factor, with a total variability level of the model R^2 which is worth 46.76%.

According to this graph of the main effects of signal to noise ratio we see the importance of the difference from level 1 to level 2 of the type factor this means that type 2 gives a much higher S/N ratio [26] This is the most influential factor on the robustness of the sound balance (SB). For the other factors the values of signal to noise levels are very close. With a remark that the thinnest board gives a better result so it is valid for both experiments. In order to decide between the levels of factors and have an overall combination giving the best results between a good sound pressure and a desirable sound balance we will carry out an analysis of variance on the basis of the results of the gray method since the type factor at the first level favors obtaining a maximum sound pressure level while the second level favors a better sound balance therefore ANOVA can help to solve this problem.

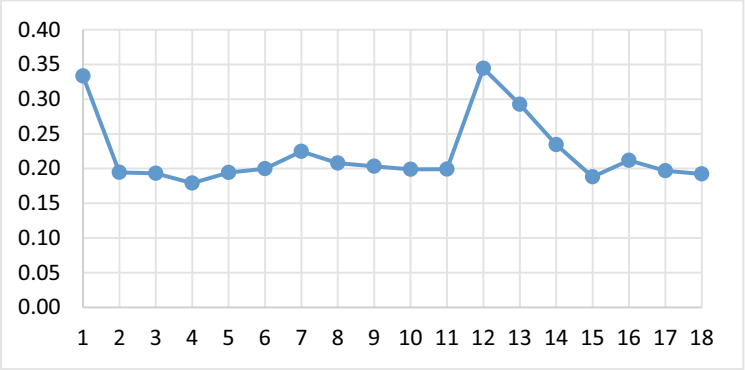

Fig. 12. Grey Relational Grade for 18 execussions

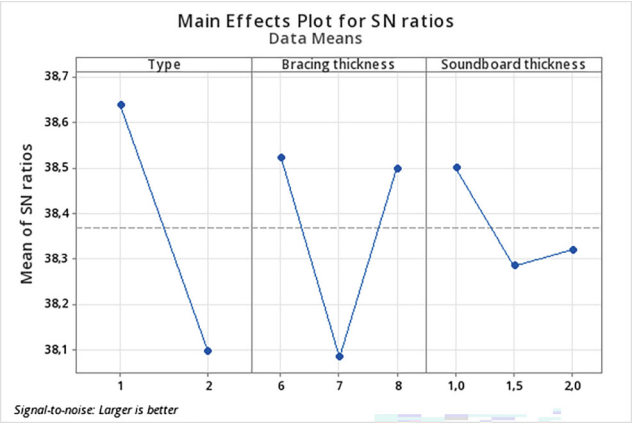

Fig. 13. Main Effects plot for SN ratios

Source	DL	SomCar	CM	F-Value	P-value
Thickness of the soundboard	2	0,003828	0,001914	0,71	0,509
Thickness of bars	2	0,004713	0,002356	0,88	0,440
Type of bracing	1	0,000914	0,000914	0,34	0,570
Error	12	0,032139	0,002678		
Total	17	0,041594			

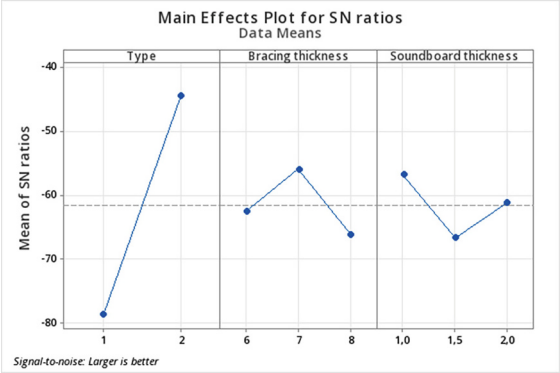

Fig. 14. Main Effects plot for SN ratios

Looking at the P-value of the factors which are all insignificant with a total level of variability which is 22.73%, therefore multi-objective problem serves necessitates the introduction of other factors to increase the accuracy of the model. At least the ANOVA can offer the rank of the contributions of the factors based on their P-value where the Bracing thickness seems the most important then the thickness of the soundboard and finally the type.

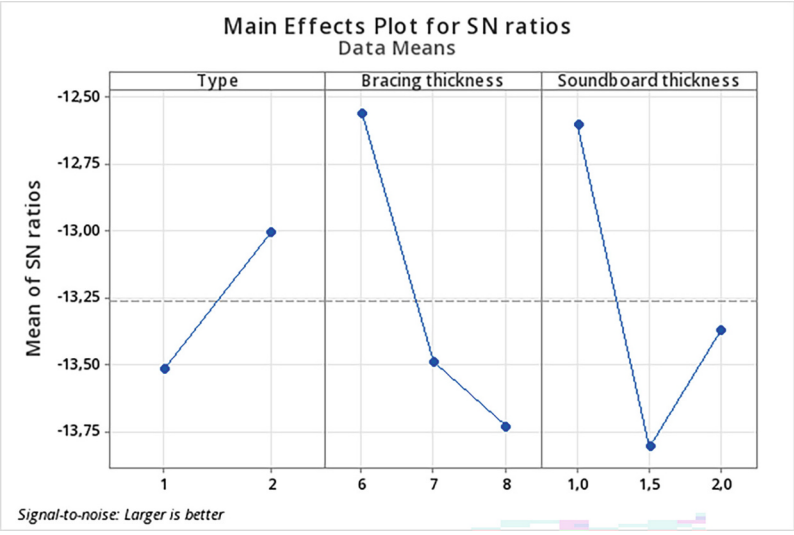

Fig. 15. Main Effects plot for SN ratios

We can see from this figure that the second type gives a better result for both responses with a confirmation that the thinnest soundboard is the best and the same for the bars thickness with this time obtaining a quasi-linear behavior.

4 Conclusion

This study made it possible to analyze the influence of the geometry of the soundboard and the bracing system on the vibrational and acoustic properties of the Lute using the finite element method combined with the Design of Experiments.

Numerical simulations showed that the parameters of bracing type, table thickness and bar thickness have an impact on the sound pressure level (SPL) of the instrument and its sound balance (SB). The analysis of variance revealed that the type of bracing is the most influential factor on the two responses studied.

The results of the design of experiments and the Gray Relational Analysis method yield the following optimal combination of design parameters for the 12th execution: table thickness = 1 mm, bracing thickness = 6 mm, and the type of bracing (type 2), this configuration offers the best compromise between power and sound balance. Finally, to strengthen and extend this research, future studies will incorporate additional factors — such as wood anisotropy, humidity conditions, boundary constraints, and rib spacing — in order to further improve model accuracy and deepen the understanding of structural–acoustic interactions in the Lute.

Appendix

Table 5. Design of experiments

Run	Thickness of the soundboard	Thickness of bars	Type of bracing
1	1	6	1
2	1.5	6	1
3	2	6	1
4	1	7	1
5	1.5	7	1
6	2	7	1
7	1	8	1
8	1.5	8	1
9	2	8	1
10	1	6	2
11	1.5	6	2
12	2	6	2
13	1	7	2
14	1.5	7	2
15	2	7	2
16	1	8	2
17	1.5	8	2
18	2	8	2

References

1. Benade, A.H.: Fundamentals of Musical Acoustics. Oxford University Press (1973)
2. Cremer, L.: The Physics of the Violin. MIT Press (1984)
3. Dumbrill, R.J.: The Archaeomusicology of the Ancient Near East. Trafford Publishing (2005)
4. Box, G.E.P., Hunter, J.S., Hunter, W.G.: Statistics for Experimenters. Wiley (2005)
5. Fletcher, N.H., Rossing, T.D.: The Physics of Musical Instruments. Springer (1998)
6. Richardson, B.E., Roberts, G.W.: The adjustment of mode frequencies in guitars: a study by means of holographic interferometry and finite element analysis. In: Proceedings of the Stockholm Music Acoustics Conference, pp. 285–302 (1985)
7. Christensen, O., Vistisen, B.B.: Simple model for low-frequency guitar function. J. Acoust. Soc. Am. **68**(3), 758–766 (1980)
8. Al Faruqi, L.I.: Music, Musicians and Muslim Law. Asian Music. **17**(1), 3–36 (1985)
9. Shiloah, A.: Music in the World of Islam. Wayne State University Press (1995)
10. Reddy, J.N.: An Introduction to the Finite Element Method. McGraw-Hill (2005)
11. Rao, S.S.: Mechanical Vibrations. Pearson Education (2019)
12. Bodig, J., Jayne, B.A.: Mechanics of Wood and Wood Composites. Van Nostrand Reinhold (1982)
13. NF B51-016.: Wood - Determination of modulus of elasticity in static bending (1985)
14. Schelleng, J.C.: The violin as a circuit. J. Acoust. Soc. Am. **35**(3), 326–338 (1963)
15. Siminoff, R.H.: The Luthier's Handbook. Hal Leonard (2002)
16. Dick, B.: The Martin Guitar: An Illustrated History of America's Premier Guitarmaker. Running Press (2002)
17. Gough, C.: The violin bridge: how does it work? J. Acoust. Soc. Am. **138**(3), 1753–1763 (2015)
18. Kinsler, L.E., Frey, A.R., Coppens, A.B., Sanders, J.V.: Fundamentals of Acoustics. Wiley (1999)
19. Beranek, L.L., Vér, I.L.: Noise and Vibration Control Engineering. Wiley (1992)
20. Gabrielsson, A., Sjögren, H.: Perceived sound quality of sound-reproducing systems. J. Acoust. Soc. Am. **65**, 1019–1033 (1979)
21. Bissinger, G.: Structural acoustics of good and bad violins. J. Acoust. Soc. Am. **124**(3), 1764–1773 (2008)
22. Deng, J.: Introduction to grey system theory. J. Grey Syst. **1**(1), 1–24 (1989)
23. Neter, J., Kutner, M. H., Nachtsheim, C. J., Wasserman, W.: Applied Linear Statistical (1996)
24. Ross, P.J.: Taguchi Techniques for Quality Engineering. McGraw-Hill (1996)
25. Anderson, M. J., & Whitcomb, P. J. (2015). DOE Simplified: Practical Tools for Effective
26. Lunani, M., Nair, V.N., Wasserman, G.S.: Graphical methods for robust design with dynamic characteristics. J. Qual. Technol. **29**(3), 327–338 (1997)

Estimation of Remaining Useful Life in Bearings Using Fusion of Machine Vision Features and Vibration Analysis

Tania Elizabeth Sandoval-Valencia(✉), Jose Emiliano Lopez-Ramirez, Eric Leonardo Huerta-Manzanilla, Gerardo Hurtado-Hurtado, and Juan Carlos Jauregui-Correa

Faculty of Engineering, Autonomous University of Queretaro, Santiago de Queretaro 76010, Mexico

{tania.sandoval,jc.jauregui}@uaq.mx

Abstract. This study develops a methodology to predict the Remaining Useful Life (RUL) of railway wheels in a 1:20 scale railway system. Unlike traditional unimodal analyses, quantitative microscopic image correlation and vibration analysis are performed. The central innovation lies in cross-validation between modalities, where surface wear quantified through digital image processing demonstrated a correlation greater than 79.0% with vibration energy characteristics, particularly with the mean energy 94.0%. This correlation physically validates the dynamic signals and allows for the creation of an enriched feature set for modeling. The Fully Connected Neural Network (FCNN) trained with these data showed stable convergence (epoch 91), a mean absolute error of less than 5.0%, and random residuals, confirming its robustness and generalizability. The resulting model allows for accurate RUL estimates, facilitating the optimization of predictive maintenance strategies in railway systems.

Keywords: Wear · Railway Wheels · Regression · Vibration · Remaining Service Life

1 Introduction

Predicting the Remaining Useful Life (RUL) of railway components, especially wheels, is crucial for ensuring safety and operational efficiency. Traditionally, single-mode techniques, such as vibration analysis or visual inspection, have been widely used to estimate the RUL of railway wheels. However, they have significant limitations in accuracy, robustness, and early detection capabilities, particularly in the face of complex defects or variable operating conditions [1–3]. Furthermore, they often rely on subjective thresholds and may not accurately reflect the actual failure, compromising safety [4].

Recent studies demonstrate that integrating vibration data with computer vision techniques significantly improves the accuracy and robustness of the diagnosis, thus overcoming the limitations inherent in unimodal methods [5, 6]. These non-invasive,

© The Author(s), under exclusive license to Springer Nature Switzerland AG 2026
A. Chaker et al. (Eds.): EFIMMS 2026, MMS 205, pp. 368–377, 2026.
https://doi.org/10.1007/978-3-032-22270-1_36

automated techniques, based on computer vision and in-depth analysis, enable remote, automated inspections, reducing operational downtime and significantly improving efficiency [7]. On the other hand, combining data from multiple sensors (such as impact, vision, and geometry sensors) with advanced machine learning techniques, particularly deep neural networks (CNNs, LSTMs), optimizes the prediction of Remaining Useful Life (RUL). This approach is particularly effective in complex scenarios involving the processing of large volumes of data [8, 9].

Despite these advancements in multimodal systems, there is still a critical need for methodologies that can directly correlate and physically validate the relationship between quantitative microscopic surface degradation and dynamic vibration signatures in a controlled experimental environment. Most existing models lack a standardized "ground truth" for wear that is captured simultaneously with vibration data, which limits their predictive reliability.

To address these specific deficiencies, this study proposes an integrated methodology that combines quantitative microscopic image analysis with vibration signal processing to predict the RUL of railway wheels in a scaled-down system. The innovation lies in the synergistic fusion, enabling a correlation that enriches the feature set for predictive modeling. Through a machine vision algorithm, surface wear is quantified with high repeatability, establishing a reliable ground truth. Simultaneously, statistical characteristics are extracted from the vibration signal, reflecting the evolution of the damage. This multimodal data feeds a Fully Connected Neural Network (FCNN), designed to model the nonlinear relationship between vibrations and progressive wear.

2 Methodology

This section describes the scale model railway system and the instrumentation used to acquire dynamic and image data. It then describes the data-processing techniques for quantifying wear and the signal-analysis methods for extracting vibration features. Finally, it outlines the training architecture for the artificial intelligence-based predictive model.

2.1 Railway System

The study was conducted using a 1:20 scale railway system, specifically designed for controlled braking tests (Fig. 1). The system features a track mounted on a 2.36 m × 5.68 m plywood structure with 5 mm diameter steel rails. The track has a total length of 13.524 m, configured as a closed circuit that combines a 3.37 m straight section (used for braking tests) with curves of 1.94 m radius, ensuring operational stability. It also includes a railcar incorporating an autonomous control and data acquisition system. A Pololu® 37D DC motor powers the railcar. A SPARTAN® Field-Programmable Gate Array (FPGA) board controls movement and signal processing. A LiPo battery powers the system. The wheels under study were manufactured from 7075 aluminum with a hardness of 345 MPa. The operating speed during all tests was kept constant at 1.2 m/s.

Scale Justification and Implications: The selection of a 1:20 scale was determined by the need for a highly controlled laboratory environment in which the full degradation

cycle of the wheels could be monitored within a practical timeframe. While scaling introduces differences in Hertzian contact pressures and dynamic frequencies compared to full-scale systems, the fundamental physical mechanisms of surface wear and their coupling with vibration energy remain consistent. This study focuses on the relative progression of damage and the validation of a multimodal fusion framework, rather than absolute operational values. By using 7075 aluminum wheels, which are softer than steel, the experimental setup effectively accelerates wear while maintaining the kinematic similarity required to validate the predictive capacity of the FCNN model. This approach provides a robust proof-of-concept that can be scaled to real-world settings through recalibration of the feature-extraction thresholds.

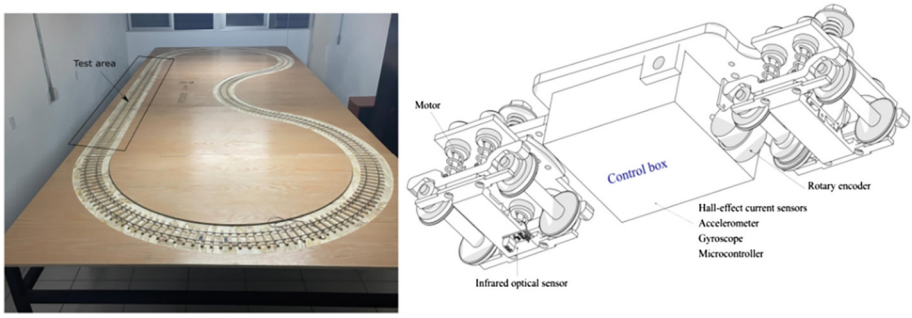

Fig. 1. Railway system at 1:20 scale.

Instrumentation for Data Acquisition

The vehicle instrumentation includes a rotary encoder with a resolution of 600 pulses per revolution for wheel speed measurement, a TCRT5000 infrared optical sensor for detecting track markings to calculate translational speed, and a triaxial LSM6DS3 Field Programmable Gate Array (FPGA)-based MEMS accelerometer-gyroscope for vibration monitoring. Specifically, the longitudinal acceleration component, AceX-Tre_SisFebLab, serves as the primary variable for wear prediction, with signal acquisition performed at 1 kHz using a DUA-III card with an FPGA to ensure high temporal fidelity.

Image Acquisition System

For model validation, surface wear was quantified using a CARYWON® Digital Optical Microscope. An automated acquisition system was implemented to ensure measurement repeatability by maintaining controlled conditions for height, wheel position, illumination level, and the number of images captured per sampling. As shown in Fig. 2, the system allowed for complete standardization of the capture process, eliminating variations in measurement conditions. A total of 240 images were captured (60 for each experimental wear state). These high-resolution images served as the "ground truth," allowing quantification of the percentage of worn area using image-processing algorithms and serving as the dependent (target) variable for training the predictive model.

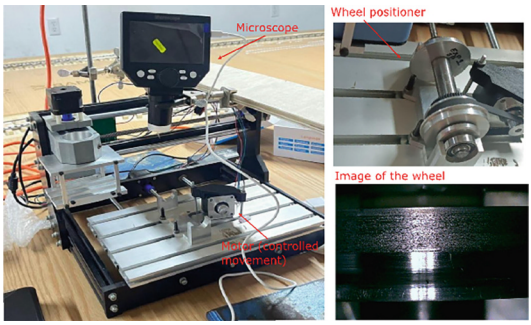

Fig. 2. Image acquisition system.

2.2 Data Processing

The proposed methodology integrates two parallel processes: the quantification of surface wear through microscopic image analysis to define the ground truth, and the extraction of predictive features from vibration signals. These processes were executed across different experimental stages to simulate progressive degradation on the 7075 aluminum specimen. The experimental progression, including the specific braking cycles and cumulative travel distances for each stage, is summarized in Table 1.

Table 1. Experimental structure and parameters.

Experiment ID	Braking cycles	Cumulative distance (m)	Measurement type
A1_B0	820	13.52	Initial state / Initial wear
A-1_B0	1,640	27.05	Intermediate degradation
A1_B1	2,460	40.57	Final state / Maximum wear

Quantitative Wear Measurement

The image processing methodology follows a structured sequence starting with the extraction of the contact patch tread as a predefined fixed Region of Interest (ROI). This spatial filtering ensures that the analysis focuses exclusively on the wheel-rail contact area, eliminating background noise and non-relevant surface sections. To reduce noise, the original color images are converted to grayscale, and a 5x5 Gaussian smoothing filter is applied. Subsequently, surface defects are segmented using a parallel approach that combines adaptive thresholding to identify material detachment with Canny edge detection to isolate fine contours. These binary masks are integrated via a bitwise OR operation, followed by a 3x3 kernel morphological opening and closing to refine the damage boundaries. Finally, the wear level is quantified using Eq. 1:

$$WornArea(\%) = \left(\frac{\sum Pixels_{Segmented}}{Pixels_{TotalROI}} \right) \tag{1}$$

Where $Pixels_{Segmented}$ represents the total count of pixels identified as damage in the binary mask, and $Pixel_{TotalROI}$ is the total number of pixels within the extracted region9. This metric provides a consistent numerical value to characterize the progression of surface degradation across all experimental stages.

Vibration Signal Processing and Feature Extraction

The longitudinal acceleration signal was characterized by extracting 12 time-domain statistical descriptors, including the Root Mean Square (RMS), maximum and minimum peak values, peak-to-peak value, kurtosis, skewness, crest factor, standard deviation, dynamic range, mean value, signal energy, and the square root of mean amplitude. These features were then averaged across experimental trials to form the input matrix for the predictive model.

Definition of Remaining Useful Life (RUL)

In this study, the RUL is defined as the number of braking cycles remaining before the wheel reaches its maximum degradation state. This final state was established at 2,460 cycles, as detailed in Table 1. Mathematically, the RUL for any given observation i is calculated using the following linear degradation model:

where C_{total} is the total life cycles (2,460) and $C_{current,\,i}$ represents the cumulative cycles at the moment of the measurement. By defining RUL in this manner, the FCNN can be trained to map the relationship between the component's multimodal features (vibration and wear percentage) and its remaining operational life.

Predictive Model Development and Training

The predictive model utilizes a Fully Connected Neural Network (FCNN) architecture comprising an input layer with 12 neurons, three sequential hidden layers, and a single-neuron output layer with a linear activation function. The hidden layers employ ReLU activation and incorporate regularization: the first layer contains 64 neurons with Batch Normalization and 30.0% Dropout, the second has 32 neurons with Batch Normalization and 20.0% Dropout, and the third consists of 16 neurons.

The dataset was divided into an 80.0% training and 20.0% validation split to ensure sufficient data for learning while maintaining a robust set for monitoring generalization. An Adam optimizer with a learning rate of 0.001 was selected based on standard empirical practices for regression tasks to achieve stable convergence. Input characteristics were normalized using the Z-score standardization shown in Eq. 2:

$$z = \frac{x - \mu}{\sigma} \tag{2}$$

where z is the standardized value, x is the original feature, μ represents the mean, and σ denotes the standard deviation.

Justification of Parameters and Constants

The selection of hyperparameters and experimental constants was based on empirical optimization and established academic standards in predictive maintenance and deep learning. Specifically, the 80/20 split for training and validation was chosen to ensure the model had a sufficiently large and diverse dataset to learn complex wear patterns while

maintaining a robust independent set to monitor and verify generalization performance. This ratio is a widely accepted standard for datasets of this scale to prevent overfitting.

For the optimization process, a learning rate of 0.001 was used with the Adam optimizer. This value provides an ideal balance between convergence speed and stability; a higher rate could cause the model to overshoot the global minimum, while a lower rate would unnecessarily increase computational time without significant accuracy gains. Furthermore, Early Stopping with a patience of 15 epochs was used as a regularization strategy to terminate training once the validation loss stabilized, further safeguarding against overfitting.

Other architectural and processing constants were defined based on the physical and experimental constraints of the study:

- Dropout rates (30.0% and 20.0%): These were integrated into the hidden layers to enhance the network's robustness by preventing neuron co-adaptation.
- ROI coordinates and dimensions: The fixed region (x = 30.0%, y = 28.0%, width 40.0%, height 20.0%) was determined by the geometry of the scaled wheel and the focus on the contact patch where wear is most prominent.
- Gaussian Filter (5x5) and Morphological Kernels (3x3): These sizes were selected to effectively suppress high-frequency noise from the microscopic capture while preserving the integrity of the micro-crack boundaries and pitting features.

Hyperparameter Optimization and Data Quality

The selection of hyperparameters was conducted through a manual tuning process (grid search) aimed at balancing convergence speed and model stability. The learning rate of 0.001 was chosen as the optimal starting point for the Adam optimizer, as it allowed for a steady decrease in the Loss Function without the oscillations associated with higher rates or the slow convergence of lower values. To ensure data quality and prevent features with larger scales from dominating the model, Z-score normalization was applied to all vibration features, centering the distribution at a mean of 0 and a unit variance. The 80/20 split for training and testing was adopted to provide a sufficiently large training set for the FCNN to learn the degradation patterns while maintaining a representative test set to evaluate generalization. Furthermore, Dropout (0.2) and Early Stopping were implemented as regularization techniques to prevent overfitting, ensuring that the final model parameters represent a generalized solution rather than memorizing the training noise.

2.3 Dataset Description and Limitations

The dataset generated for this study is multimodal, comprising 240 high-resolution images (60 per experimental state) and synchronized vibration signals sampled at 1 kHz. The images serve as ground truth for surface wear percentage, while the 12 statistical features extracted from longitudinal acceleration form the input vector for the FCNN.

Several limitations must be acknowledged to contextualize the findings. First, the dataset was collected under controlled laboratory conditions, which do not account for external variables such as varying track geometry, ambient humidity, or rail contaminants found in real-world environments. Second, the use of 7075 aluminum wheels, while

effective for accelerating wear for research purposes, exhibits a different wear rate and hardness than industrial-grade steel wheels. Finally, the dataset's size and the specific 1:20 scale limit the direct extrapolation of absolute RUL values to full-scale systems. These constraints imply that the results should be interpreted as a proof-of-concept validating the multimodal fusion methodology rather than a definitive predictive tool for operational railway networks. Consequently, conclusions regarding model accuracy are specific to the scaled experimental setup and would require recalibration for diverse operational contexts.

3 Results Analysis

Figure 3 shows the complete machine vision methodology for determining the percentage of wear across three operating states. The first column, Original + ROI, demonstrates that the fixed ROI cutout (yellow box) remained unchanged for all measurements, isolating the tire tread. The middle column, ROI Extracted Area of Analysis, shows the specific portion of the processed image. The third column, Wear mask, validates phase 2 (combined segmentation). The algorithm, which merges Adaptive Thresholding with Canny Edge Detection (followed by morphological operations), isolates surface defects (white pixels) from the base material (black background).

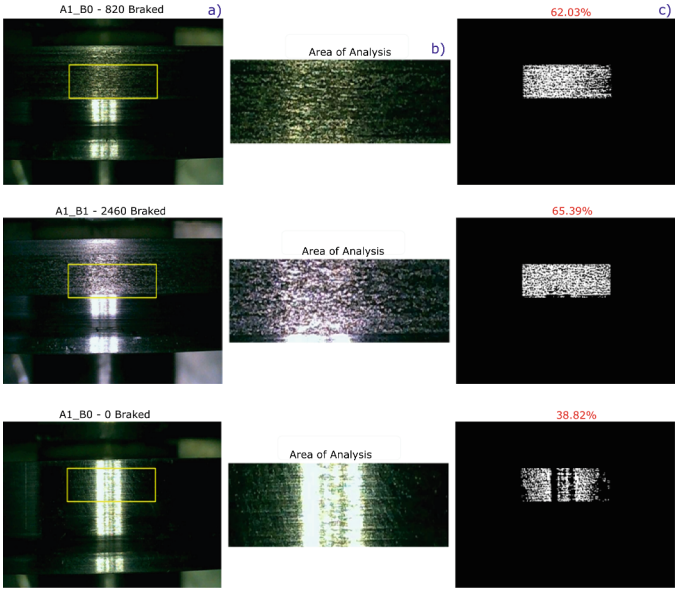

Fig. 3. Segmentation and quantification process of surface wear using the artificial vision algorithm: a) Original + ROI, b) ROI Extracted and, c) Wear mask.

In state 0 Braked (third row), the Extracted ROI shows a more polished, shiny surface, reflecting only the inherent manufacturing defects and the initial polishing.

In the braked states (820 and 2460 Braked), the surface appears rougher, with evidence of pitting and microcracks. The resulting mask is significantly denser, capturing the accumulated damage. The quantification of the wear percentage (text in red) confirms the monotonically increasing trend of the damage. The difference between the percentages validates that the algorithm is sensitive to the evolution of wear over operating time, providing the precise dependent variable for training the artificial intelligence model.

The correlation analysis between vibration characteristics and remaining useful life (RUL) revealed significant patterns that validate the effectiveness of the experimental methodology (Fig. 4). Mean vibration energy proved to be the most reliable indicator of progressive wear, with a correlation coefficient of 94.0%, followed by standard deviation (87.0%) and RMS value (83.0%). The 79.0% correlation between wear measured by imaging and RUL is particularly valuable, as it validates the reliability of the visual quantification method.

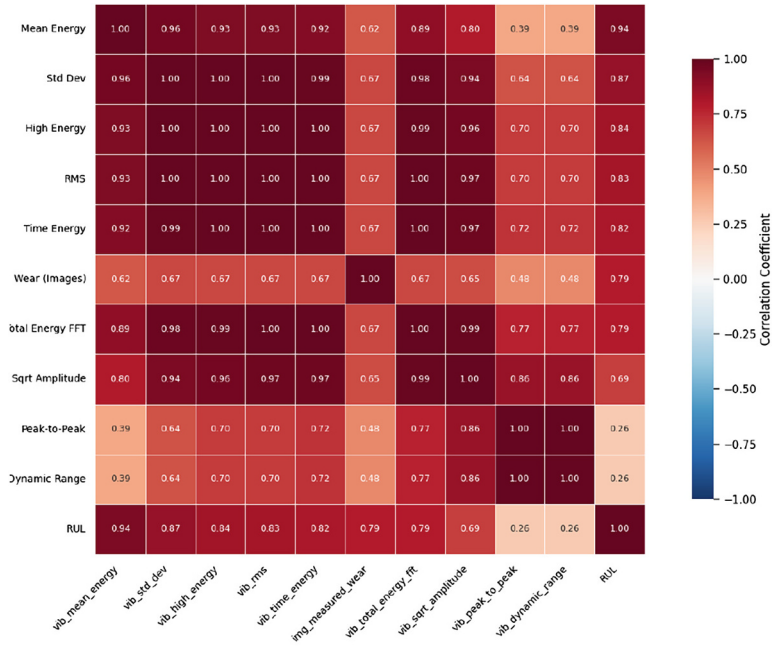

Fig. 4. Correlation Heatmap: 12 extracted vibration characteristics and remaining useful life (RUL).

The correlation analysis of the 12 vibration characteristics revealed strong linear dependence among most of them, with values exceeding 96.0%. This behavior indicates that the information contained in these variables is redundant, justifying the selection of a reduced subset of characteristics for the predictive model. This optimizes computational efficiency without affecting the accuracy of the estimates.

On the other hand, the amplitude characteristics, such as peak-to-peak value and dynamic range, showed the opposite behavior. Their correlation with the RUL was weak

($r = 0.26$), suggesting they are unreliable indicators of the wear status of individual wheels. These results reinforce the usefulness of the vibration energy components, which demonstrated greater sensitivity to the evolution of surface damage.

Figure 5 illustrates the performance and generalizability of the neural network developed to predict railway wheel wear. The integrated analysis of these graphs confirms the robustness of the model, not only because of its learning capacity, but also because of its predictive stability when faced with data not used during the training phase.

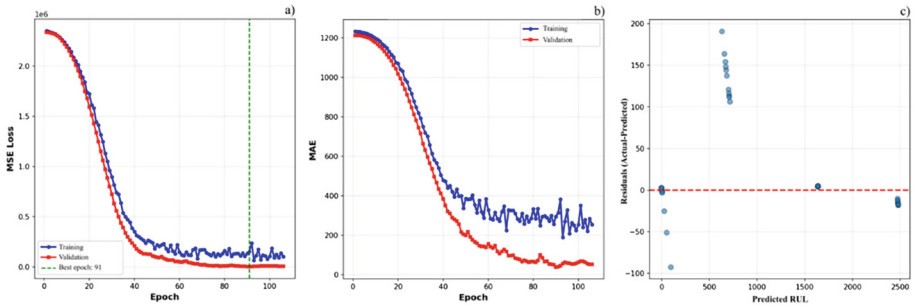

Fig. 5. Behavior of the wear predictive model: (a) Evolution of the loss during training, (b) Mean absolute error per epoch, (c) Distribution of prediction residuals.

Figure 5a describes the evolution of the loss function during model training. Both the training and validation losses decrease continuously until stabilizing around epoch 91. This behavior reflects that the model efficiently learned the wear patterns without overfitting the training data. The close relationship between the two curves throughout the process also confirms robust generalization to unseen data.

Figure 5b shows the progressive reduction of the mean absolute error (MAE) as the epochs progress. The model achieves MAE values below 5.0% in wear estimation, indicating high predictive accuracy. The stabilization of the error in the later stages suggests that a suitable balance between bias and variance was achieved, maintaining a consistent error level in both the training and validation sets.

Finally, Fig. 5c shows the distribution of residuals between the actual and model-predicted values. The random dispersion of the residuals around zero, without following any systematic patterns, confirms that there are no significant biases in the predictions. This validates that the model adequately captures the relationship between vibration characteristics and surface wear evolution.

4 Conclusions

This study has demonstrated the feasibility of a multimodal methodology for estimating the Remaining Useful Life (RUL) of railway wheels, combining digital image processing with vibration analysis. The objective quantification of surface wear using a standardized computer vision algorithm allowed for the establishment of a reliable ground truth, with a significant correlation of 79.0%.

The correlation analysis revealed that the energetic characteristics of the vibration signal, particularly the mean energy (correlation of 94.0%), are robust indicators of progressive wear, far surpassing traditional amplitude descriptors.

The Fully Connected Neural Network (FCNN) trained with these data showed good performance, with stable convergence from epoch 91 onwards, a mean absolute error of less than 5.0%, and random residuals, confirming the absence of predictive bias and a high capacity for generalization. The proximity of the training and validation loss curves indicates that the model does not overfit.

In conclusion, the fusion of machine vision and vibration analysis not only physically validates dynamic signals but also allows the development of accurate and reliable predictive models for RUL estimation.

Future research will incorporate advanced deep learning architectures, such as Convolutional Neural Networks (CNNs) for automated feature extraction from raw images and Long Short-Term Memory (LSTM) networks to better capture the temporal dependencies of vibration signals. In addition, acoustic emission and temperature sensors will be explored to improve the robustness of the fusion model. Finally, real-time RUL estimation is planned to facilitate immediate maintenance decisions in industrial applications.

References

1. Iliopoulos, I.A., Sakellariou, J.S.: Remaining useful life estimation of hollow worn railway vehicle wheels via on-board random vibration-based wheel tread depth estimation. Sensors. **24**(2), 375 (2024). https://doi.org/10.3390/s24020375
2. Li, Q., Zhou, J., Jiang, Z., E, M., Ma, J.: Train wheel degradation modeling and remaining useful life prediction based on mixed effect model considering dependent measurement errors. IEEE Access. **7**, 159058–159068 (2019). https://doi.org/10.1109/ACCESS.2019.2950696
3. Gómez, M.J., Castejón, C., Corral, E., García-Prada, J.C.: Railway axle condition monitoring technique based on wavelet packet transform features and support vector machines. Sensors. **20**(12), 3575 (2020). https://doi.org/10.3390/s20123575
4. Ni, Y.-Q., Zhang, Q.-H.: A Bayesian machine learning approach for online detection of railway wheel defects using track-side monitoring. Struct. Health Monit. **20**(4), 1536–1550 (2021). https://doi.org/10.1177/1475921720921772
5. Al-Qudah, S., Bai, X., Yang, M., Gao, Z.: Deep learning-based structural health monitoring through the infusion of optical photos and vibration data. Adv. Struct. Eng. **28**(3), 532–552 (2025). https://doi.org/10.1177/13694332241289173
6. Shen, Y., Zhong, Q., Zheng, S., Li, L., Peng, L.: A multi-modal approach to rail surface condition analysis: the MFDF-net. IEEE Access. **12**, 132480–132494 (2024). https://doi.org/10.1109/ACCESS.2024.3427347
7. Luo, K., Kong, X., Zhang, J., Hu, J., Li, J., Tang, H.: Computer vision-based bridge inspection and monitoring: a review. Sensors. **23**(18), 7863 (2023). https://doi.org/10.3390/s23187863
8. Hu, L., Dai, G.: Estimate remaining useful life for predictive railways maintenance based on LSTM autoencoder. Neural Comput. Applic. **37**(27), 22967–22978 (2025). https://doi.org/10.1007/s00521-021-06051-1
9. Lin, T., Song, L., Cui, L., Wang, H.: Advancing RUL prediction in mechanical systems: a hybrid deep learning approach utilizing non-full lifecycle data. Adv. Eng. Inform. **61**, 102524 (2024). https://doi.org/10.1016/j.aei.2024.102524

Application of Support Vector Machines and Principal Component Analysis for Wheel Wear Progression Diagnosis in a Scaled Railway Vehicle

Gerardo Hurtado-Hurtado(✉), Tania Elizabeth Sandoval Valencia, Luis Morales-Velázquez, and Juan Carlos Jáuregui Correa

Faculty of Engineering, Autonomous University of Queretaro, Santiago de Queretaro 76010, Mexico
{gerardo.hurtado,jc.jauregui}@uaq.mx

Abstract. Railway wheel wear is a critical safety and maintenance issue, which is why condition monitoring is essential to prevent accidents and unnecessary delays. This work proposes a method, based on Support Vector Machines and Principal Component Analysis, to detect and classify the progression of wheel wear using mechanical vibrations. Experiments were conducted on a scaled vehicle instrumented with accelerometers and gyroscopes, which was subjected to accelerated wear tests through start and brake cycles. From the acquired signals, time and frequency domain features are extracted to obtain the dataset used to train the machine learning classification model. A support vector machine (SVM) classifier is used to identify the level of wheel wear. A hybrid SVM-principal component analysis (PCA) model is also evaluated, which is a more simplified and faster version, although with lower accuracy. Both models are evaluated and discussed. It is demonstrated that the SVM is capable of classifying different wear levels with high accuracy. The use of PCA significantly reduces the computational cost with a slight decrease in accuracy, showing a clear trade-off balance.

Keywords: Railway Wheel Wear · Vibration Data · Principal Component Analysis

1 Introduction

The wear of railway wheels is a constant problem in the industry that every year costs tens of millions of dollars, in North America alone, in maintenance and work stoppage [1]. In addition, a wheel with uneven circumference can induce additional loads that can damage components such as the suspension, rails, and sleepers, which further increases maintenance costs. In real-world conditions, the lifespan of railway wheels can vary depending on the load, braking and acceleration cycles, but generally, wheels require inspection or replacement after several million cycles, which correspond to hundreds of thousands of kilometers traveled. This problem is unavoidable, due to constant interaction with the rails. However, the early diagnosis of this type of failure helps to better schedule maintenance routines, thus avoiding additional expenses due to downtime.

© The Author(s), under exclusive license to Springer Nature Switzerland AG 2026
A. Chaker et al. (Eds.): EFIMMS 2026, MMS 205, pp. 378–387, 2026.
https://doi.org/10.1007/978-3-032-22270-1_37

Current techniques allow the detection of several types of wear on railway wheels, mainly related to wheel-rail contact. Among the most common are polygonal wear, which generates periodic vibrations and affects the safety and comfort of the journey, and hollow wear on the wheel tread, caused by plastic deformation due to high temperatures during braking [2–5]. Lateral wear is also detected, such as flange wear and trackside wear, which affects the stability and guidance of the train. In addition, problems of uneven longitudinal wear are identified, such as rail corrugation, which influences the dynamic wheel-rail interaction [2]. Other types include rolling contact fatigue (RCF) wear and competitive wear between RCF and surface wear, which affect the integrity of the wheel material [6]. These detections are performed using vibration analysis, physical models, machine learning, and advanced spectral techniques that allow identifying the degree and distribution of wear under different operating conditions [3, 7, 8].

Techniques such as Principal Component Analysis (PCA) have been used to reduce data complexity and synthesize variables related to railway wheel wear, facilitating the identification of key characteristics in wear progression, such as the relationship between wheel flange thickness and slope. SVM has been used to identify suspension component failures in railway vehicles [9], as well as to monitor wheel condition [10].

SVM excels with small datasets, offering good accuracy and lower overfitting risk due to margin maximization, leading to better generalization [11, 12]. Its ability to model non-linear relationships using kernels, with relatively low computational complexity, makes it suitable for resource-limited systems [13].

In this work, a methodology is proposed for the diagnosis of wheel wear progression in railway wheels by analyzing mechanical vibrations in a test bench with a 1:20 scale vehicle. Two SVM-based classification strategies are implemented and compared: a hybrid model that incorporates dimensionality reduction using PCA to facilitate the physical interpretation of the critical frequency bands, and a robust model trained with a complete vector of statistical features in the time and frequency domains. The balance between computational efficiency and accuracy in the wear level is also evaluated. It is demonstrated that with the use of PCA analysis and the SVM algorithm, the wear severity levels in the wheels can be easily separated with very high accuracy.

2 Methodology

2.1 The Scaled Railway Vehicle

The 1:20 scale, single-car test railway vehicle is supported by two bogies, with the rear one providing traction via a servomotor and belt drive. It can reach a maximum speed of 1.5 m/s in 2 s on clean rails. The body is mounted on the bogies using a rigid secondary suspension of 8 springs. Control circuits, motor, sensors, and data storage are located in the middle. Figure 1 shows the vehicle on the test bench rails. The 1:20 scaling factor for the experimental setup was selected to optimize a balance between experimental practicality and the preservation of dynamic similarity with a full-scale prototype.

2.2 Data Acquisition System

The vehicle monitoring and control system includes an FPGA board, sensors, and a servomotor. The FPGA board receives instructions and configurations from a Bluetooth

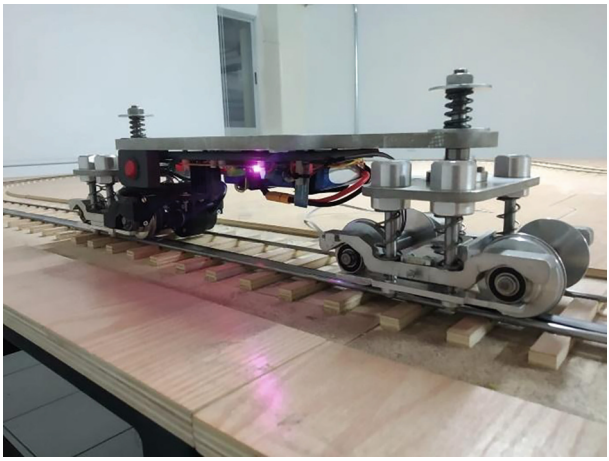

Fig. 1. The test vehicle used in the experiments.

module to control the vehicle's speed and store data on a micro-SD card. These modules are located in the control box, in the middle part of the test vehicle. The control box also contains accelerometers for monitoring vehicle vibrations. The speed of the traction wheel is measured by an incremental rotary encoder with 600 pulses per revolution, installed on the traction bogie, while an optical sensor mounted on the other (trailed) bogie measures the vehicle speed using an infrared optical sensor.

2.3 The Railway Track

The test track is a steel-structured Table (2.36 x 5.68 x 0.92 m) built from four plywood sheets with integrated sleepers (Fig. 2). Steel rods (5 mm diameter) affixed with epoxy resin serve as the rails.

2.4 The Experiment

The experiments involve operating the test vehicle on the straight section of the track up to its maximum velocity, followed by applying the brakes to induce slippage. This cycle is repeated up to 2460 times. This cycle of accelerating and braking causes the wheel to slide on the rail and accelerates wear.

2.5 Data Analysis

The data acquisition for the accelerometers (ax, ay, and az) and gyroscopes (gx, gy, and gz) was conducted at a sampling rate of 1 kHz. 1000 samples (1 s) were taken and saved in individual files. The samples were acquired from various points within the experiment and subsequently classified into four distinct categories:

- New wheels: from 0 to 100 cycles.
- First round: from 720 to 820 cycles.

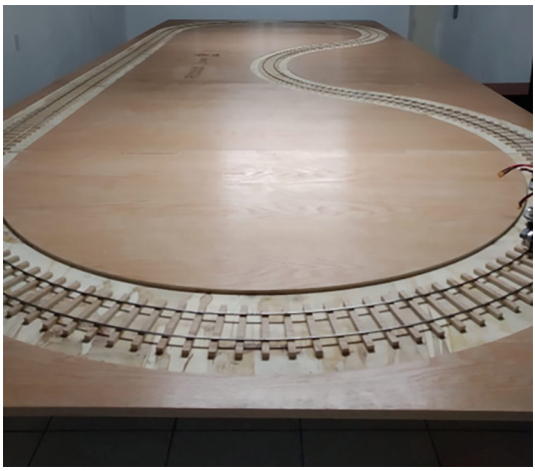

Fig. 2. Panoramic view of the test track

- Second round: from 1540 to 1640 cycles.
- Third round: from 2360 to 2460 cycles.

In this way, the machine learning algorithm can classify the different levels of wear.

2.6 Feature Engineering

Before training the machine learning models, Feature Engineering of all the data is necessary. A vector of 60 statistical features is calculated for each sample. In total, 10 features were obtained from each sensor.

Time Domain Analysis. The most basic features were processed, such as the arithmetic mean, peak-to-peak amplitude, standard deviation, and RMS value, to see how much energy is in the signal, up to the most advanced ones, such as skewness and kurtosis to see if the signal has a strange shape or unusual peaks, which is typical when something starts to fail. The crest factor was also computed during this preprocessing, which is defined as:

$$CF = \frac{|x|_{peak}}{x_{RMS}} \tag{1}$$

The crest factor is a classic feature for detecting sudden impacts. This feature indicates small wheel defects significantly sooner than any other feature, even the total vibration energy. This value is very sensitive to impacts between the wheel and the rail.

Frequency Domain Analysis. As wear alters the wheel surface, the vibratory signature is correspondingly modified. Consequently, the fast fourier Transform (FFT) is also employed to accommodate the resulting frequency shifts. The spectrum is therefore segmented into three distinct bands to facilitate a more comprehensive analysis of the underlying phenomena:

- Low Frequency (0–100 Hz). This zone shows the general movement of the train, such as suspension bounces.
- Medium Frequency (100–200 Hz). This is a transition zone where bogie and rotation vibrations begin to appear.
- High Frequency (200–500 Hz): This zone highlights the fine contact between the wheel and the rail. If there is more energy here, it is usually due to friction and the roughness of the metals in contact.

2.7 Principal Component Analysis

PCA was implemented to project the high-dimensional feature space onto a lower-dimensional orthogonal subspace by maximizing the preserved variance. This means that PCA summarizes the information in a smaller space. Prior to calculating the covariance matrix, all features were standardized (Z-score normalization) to ensure that variables with larger numerical magnitudes do not unduly influence the principal components:

$$z = \frac{x - \mu}{\sigma} \tag{2}$$

The initial three principal components (PC1, PC2, and PC3) were chosen, as their cumulative explained variance demonstrated that they captured the most significant dynamics of the system. It is important to note that PCA, as an unsupervised technique, prioritizes the directions of maximum variance within the data rather than class separability. Consequently, while the reduced feature set (PC1-PC3) simplifies the model, it may exclude subtle information critical for distinguishing between overlapping wear states.

2.8 Support Vector Machine

The Support Vector Machine (SVM) algorithm was employed for the classification of wear states, chosen for its mathematical robustness in high-dimensional spaces and its ability to generalize with limited datasets. This algorithm was used in two scenarios:

- SVM trained using only the projection of the data onto the first three principal components obtained with PCA (SVM-PCA Model). This design yields a more efficient model and reduces statistical noise or non-informative variance.
- SVM trained using the complete vector of 60 extracted features, allowing the algorithm to capture subtle non-linear relationships that might have been lost in the dimensionality reduction.

To ensure the statistical validity of the results and avoid overfitting, a 5-fold stratified cross-validation was employed, ensuring that the class proportion remained constant in each iteration. The optimization of the SVM hyperparameters (C, γ and kernel type) was performed using an exhaustive grid search. The search space included:

- A linear kernel was compared against a radial basis function (RBF) kernel, the latter being ideal for complex non-linear decision boundaries.

- Regularization parameter (C): {0.1, 1, 10, 100}, controlling the trade-off between maximizing the separation margin and minimizing the classification error on the training data.
- Kernel coefficient (, γ): {1, 0.1, 0.01, 0.001}, determining the radius of influence of each support vector in the formation of the decision boundary.

The final performance of the models was evaluated comprehensively using confusion matrices, which are important tools for analyzing error patterns and quantifying false positives between adjacent wear states.

3 Results

3.1 PCA Results

Following the application of PCA, heatmaps for accelerometers and gyroscopes are presented in Figs. 3 and 4, respectively. In the acceleration results (Fig. 3), it is observed how PC1 in the standard deviation of lateral acceleration (Accel_ay_std) has a considerable value (0.18) with respect to the others. The standard deviation of vertical acceleration (Accel_az_std) and its RMS versions also stand out as having very high and uniform loadings. Also, in the frequency bands, PC1 loads heavily in 0-100 Hz for both ax and ay. PC1 detects the increase in energy and the rigid body motion (suspension) that occurs simply because the wheel is rougher. It is the background noise that rises with wear.

The PC3 column is dominated by intense red color in the kurtosis of vertical acceleration (Accel_az_kurtosis), the kurtosis of lateral acceleration (Accel_ay_kurtosis), and the crest factor of lateral acceleration (Accel_ay_crest_factor). In this context, PC3 ignores average energy (RMS) and focuses exclusively on the shape of the wave. It detects sharp peaks (impacts). Physically, this component is locating the transient impacts that indicate localized surface defects. Furthermore, PC2 is characterized by high values in Accel_az_rms and Accel_ax_rms, and zero lateral acceleration. This suggests that PC2 is indicative of vertical (bounce) or longitudinal (traction) problems, as it isolates the effect of any lateral movement.

The heatmap in Fig. 4 is the result of the signals measured by the gyroscope. Observation of this graph reveals that PC2 demonstrates a significant loading of 0.27 in the 100-to-200 Hz frequency band, as indicated by the measurement of yaw rotation (Gyro_Gz_rms_100_200Hz). It is the highest value in the entire analysis. It is followed by Gyro_Gz_std (0.25) and Gyro_Gz_rms (0.24). In this case, PC2 almost completely ignores the roll (Gx) and pitch (Gy) to focus precisely on the yaw oscillation. This confirms that the 100–200 Hz band on the Z-axis is the critical spectral signature of advanced wheel wear. Conversely, PC1 is primarily characterized by the roll and pitch movements, specifically Gyro_Gx and Gyro_Gy, respectively. Therefore, PC1 shows how the test vehicle oscillates laterally due to the irregularity of the wheel wear. PC3, on the other hand, exhibits significant values on Gyro_Gx_kurtosis, Gyro_Gx_skew, and Gyro_Gy_rms_200_500Hz. This component detects structural noise or rattling, which implies that it does not measure the stability of the gait, but rather the “quality of the assembly” or the excitation of the structural modes of the bogie chassis.

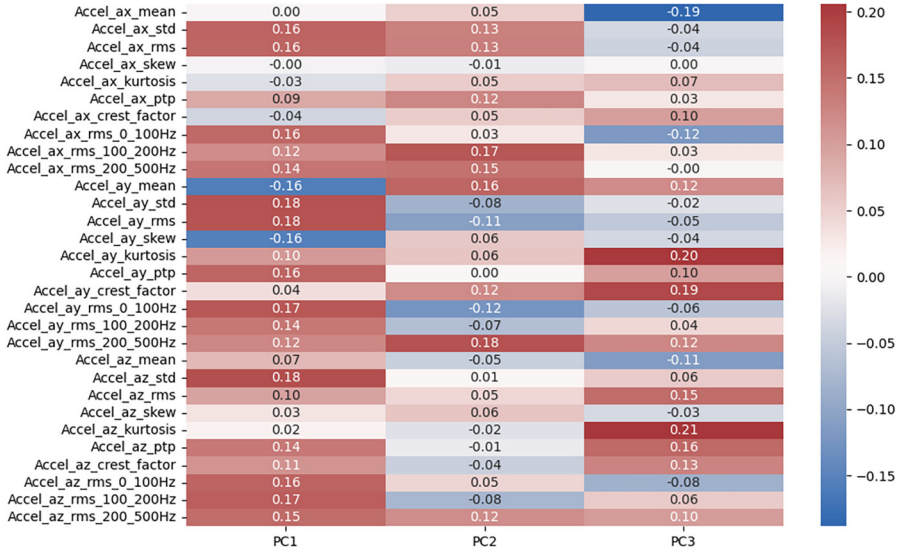

Fig. 3. Heatmap showing the results of the PCA applied to the acceleration signals.

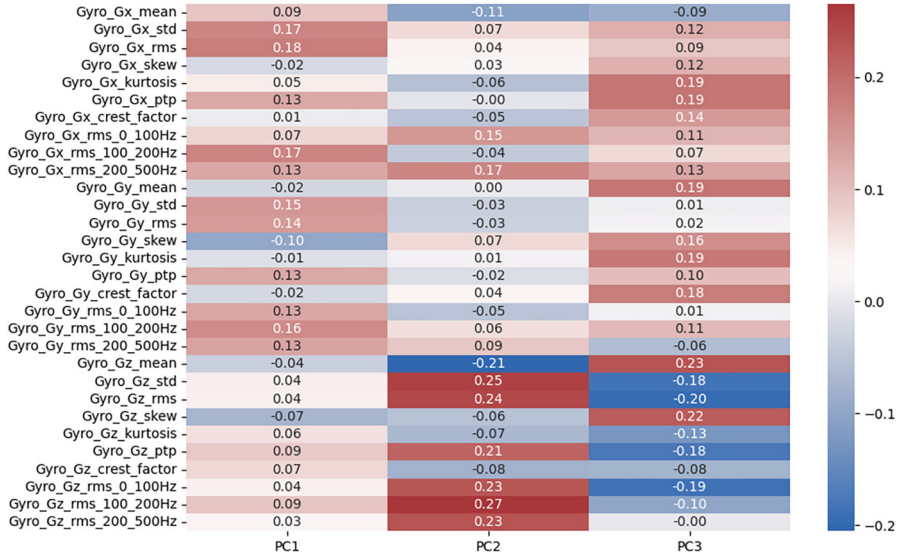

Fig. 4. Heatmap showing the results of the PCA applied to the rotation signals.

3.2 SVM Results

The results of the SVM analysis are presented below. Figure 5 illustrates the confusion matrix for the SVM, utilizing the first three principal components derived from the PCA analysis. These results yielded an accuracy of 84%, which is considered satisfactory for this classification task. The matrix indicates that the model's misclassifications primarily

occur between adjacent classes, which is an acceptable outcome, despite one instance where the model confused the vibrations of the first round with those of the third round. Nevertheless, the reduction to only three dimensions inherently sacrifices crucial information. By compressing 60 variables into three, the SVM was not afforded sufficient degrees of freedom to effectively separate the data overlap.

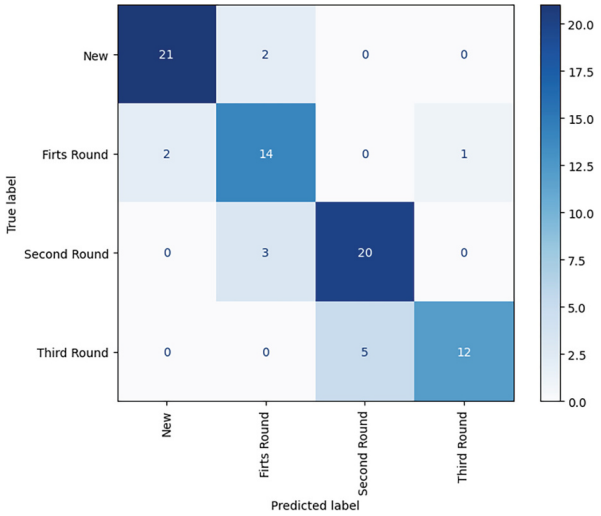

Fig. 5. Confusion matrix of the SVM results using the first 3 principal components.

Figure 6 shows the confusion matrix of the SVM model using all the features. The result is highly accurate within the tested conditions, achieving 100% accuracy. By feeding the SVM with all 60 features, the algorithm found a hyperplane that separates the classes with 100% accuracy on the test set. This observation corroborates that the acceleration and gyroscope sensors reliably capture the wear fingerprint. The clear separation of the classes in the controlled laboratory environment is confirmed. When all variables are utilized, the system demonstrates infallibility.

As the results clearly illustrate, the diagnostic model relying exclusively on Principal Component Analysis (PCA) demonstrated significant limitations and was deemed inadequate for providing a reliable, critical diagnosis. This failure suggests that simply reducing dimensionality did not preserve the essential information required for accurate classification in this specific context.

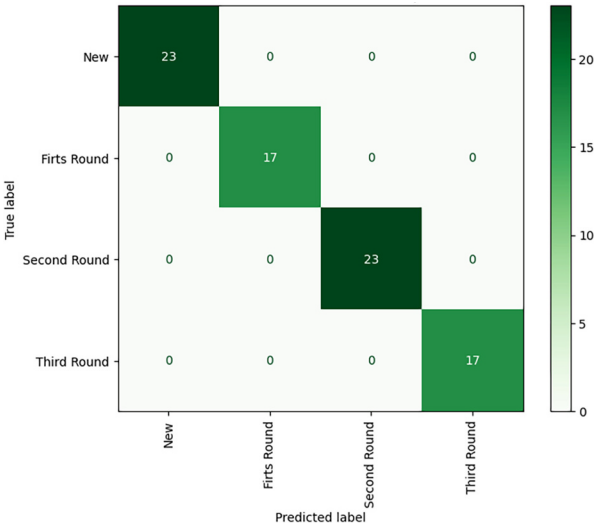

Fig. 6. Confusion matrix of the SVM results using all features.

4 Conclusions

The present study demonstrated the viability of diagnosing wheel wear progression in railway vehicles using an instrumented 1:20 scale vehicle, applying machine learning techniques to vibration signals. Based on the experimental results and the analysis of the classifiers, the following conclusions are derived:

1. Feature analysis (validated by PCA) identified the angular yaw velocity (100–200 Hz) as a critical indicator of wear severity.
2. The hybrid SVM-PCA model, although lighter, lost crucial information, limiting the accuracy to 84%. The SVM model with the complete 60-feature vector achieved 100% accuracy, concluding that aggressive dimensional reduction is counterproductive for reliability in this application.
3. The perfect classification is attributed to the controlled testing environment and the high quality of the extracted features. The scaled vehicle is validated as a robust platform for preliminary training of predictive maintenance algorithms, although transfer to real trains will require considering stochastic noise and environmental variables. The 100% accuracy achieved by the full-feature SVM model is representative of the controlled laboratory conditions and may be subject to overfitting.

References

1. Sapronova, S., Tkachenko, V., Braikovska, N., Zub, Y.: Scientific approach to the methods of increasing the life cycle of wheels of railway vehicles. Collect. Sci. Works State Univ. Infrastruct. Technol. Ser. Transp. Syst. Technol. **38**, 161–115 (2021)
2. Zhai, W., Jin, X., Wen, Z., Zhao, X.: Wear problems of high-speed wheel/rail systems: observations, causes, and countermeasures in China. Appl. Mech. Rev. **72**(6), 060801 (2020)

3. Sun, Q., Chen, C., Kemp, A., Brooks, P.: An on-board detection framework for polygon wear of railway wheel based on vibration acceleration of axle-box. Mech. Syst. Signal Process. **153**, 107540 (2021)
4. Kaliorakis, N., Sakellariou, J., Fassois, S.: On-board random vibration-based robust detection of railway hollow worn wheels under varying traveling speeds. Machines. **11**, 933 (2023)
5. Handa, K., Ikeuchi, K., Morimoto, F.: Temperature-dependent wear of tread-braked railway wheels. Wear. **452**, 203265 (2020)
6. Luo, K., Liu, X., Yang, Y., Cong, T., Zhang, F., Wang, W.: Modeling the competitive relationship between wear and rolling contact fatigue of railway wheel steel. Wear. **560–561**, 205615 (2024)
7. Wang, Q., Xiao, Z., Gong, Z., Zhang, Z., Wang, T.: An on-board detection method for polygonal wear of railway wheel based on modern spectral estimation. In: Civil-Comp Conferences (2023)
8. Shebani, A., Iwnicki, S.: Prediction of wheel and rail wear under different contact conditions using artificial neural networks. Wear. **406-407**, 173–184 (2018)
9. Liu, F., Guo, H., Zhang, X., Chen, W., Gu, F.: Condition monitoring of railway vehicle suspension system based on PCA-SVM method. In: International Conference on the Efficiency and Performance Engineering Network, pp. 254–261. Springer Nature, Switzerland, Cham (2024)
10. Lee, J.H. et al.: A study on wheel member condition recognition using machine learning (support vector machine). Sensors. **23**(20), 8455 (2023)
11. Cheng, Y., Gai, X., Jin, Y., Guan, R., Lu, M., Ding, Y.: A new method based on a WOA-optimized support vector machine to predict the tool wear. Int. J. Adv. Manuf. Technol. **121**, 6439–6452 (2022)
12. Wang, J., Xiang, Z., Cheng, X., Zhou, J., Li, W.: Tool wear state identification based on SVM optimized by the improved northern goshawk optimization. Sensors. **23**, 8591 (2023)
13. Sharma, P., Thulasi, H., Mishra, S., Ramkumar, J.: Identification of parameter-dependent machine learning models for tool flank wear prediction in dry titanium machining. Proc. Inst. Mech. Eng. Part E J. Process Mech. Eng. (2024)

Residual Vibration Suppression for Arbitrary Move Times Using a Novel Fourier-Based Profile Tuning

Mehmet Erkan Kütük(✉) and Sadettin Kapucu

Gaziantep University, Gaziantep 27310, Türkiye
mekutuk@gantep.edu.tr

Abstract. This study presents a novel profile tuning methodology for suppressing Residual Vibration (RV) in mechanical systems by integrating ramp functions with odd Fourier series harmonics. The suggested method offers superior control over vibration characteristics, in contrast to traditional methods that depend on even-harmonic profiles. The ramp-plus-Fourier harmonics motion tuning technique enables unrestricted motion time for a prescribed lift, making it suitable for systems with flexible actuator inputs. Modified conventional profiles are designed to reduce high-order harmonics and resonance effects, which makes RV suppression better at different speeds. When compared to standard approaches, adjusted Freudenstein and Gutman cam profiles with odd harmonics show significantly better performance. Simulations show that the proposed profiles work better than classical designs and Zero Vibration (ZV) input shaping techniques. They also show that they can greatly reduce RV for user-defined travel times. This method offers an adaptable approach to achieve RV-free mobility in mechanical systems that require precise control.

Keywords: Command Shaping · Odd Fourier Series · Profile Tuning · Residual Vibration Suppression · Feedforward Motion Control

1 Introduction

High-precision point-to-point motion control is essential in many mechanical systems, including robots, CNC machines, and precision positioning devices. In such systems, the objective is not only to reach the desired position but to do so within a specified time while minimizing RV. RVs degrade positioning accuracy, increase settling time, reduce productivity, and accelerate mechanical wear. Therefore, suppressing RV is a key objective in high-performance motion control.

Cam-follower systems have traditionally served as a basis for motion profile design, as cam profiles mathematically define follower motion in a feedforward manner. However, these profiles are fixed, tailored to specific motion durations and system dynamics, and therefore cannot be easily adapted to changing operating conditions in systems such as robots or CNC machines. This lack of flexibility limits their applicability in variable-motion environments.

© The Author(s), under exclusive license to Springer Nature Switzerland AG 2026
A. Chaker et al. (Eds.): EFIMMS 2026, MMS 205, pp. 388–397, 2026.
https://doi.org/10.1007/978-3-032-22270-1_38

To address this limitation, this study proposes a modification of conventional motion profiles by integrating tuned odd harmonic components. Unlike traditional even-harmonic profiles, the proposed approach provides greater control over vibration behavior while allowing arbitrary motion durations, subject only to actuator limits. The method combines a ramp function with Fourier harmonics, whose parameters are selected based on the system dynamics to suppress residual vibrations.

The primary contribution of this study is the creation of an innovative and extremely versatile Fourier Series Profile Tuning methodology that significantly enhances the functionalities of traditional cam-based motion design. Unlike fixed-structure profiles (e.g., Gutman, Freudenstein) which are optimal only for a specific natural frequency, our method introduces a tunable parameter, l_2, derived from the system dynamics and user-defined motion time. This allows for the first time, to the best of our knowledge, the generation of motion profiles that can eliminate RV for any arbitrarily specified travel time, τ_r, even for durations shorter than half the system's natural period—a significant limitation of traditional input shaping ZV techniques. This method combines a ramp function with odd Fourier harmonics in a smart way and gives an analytical solution for the tuning parameter. This makes it a useful and powerful tool for precise motion control that lets dynamic systems run without RV without adding extra sensors or cutting down on motion time.

2 Literature Survey

Cam motion profiles are widely used for vibration suppression in flexible systems by limiting induced vibrations and reducing residual vibrations (RV). Srinivasan and Ge enhanced the conventional Polydyne approach to formulate dynamically compensated cam profiles, while Gupta and Wiederrich examined the effects of modifier functions on cam profile shaping [1, 2]. Kwakernaak and Smit proposed cam profiles that limit follower velocity, acceleration, and jerk while minimizing RV over a range of cam speeds [3]. Kapucu et al. introduced a blended cam profile by superimposing three functions, referred to as ramp-plus-ramped cycloid-plus-ramped versine [4]. Liang and Huang focused on vibration reduction through command smoothing techniques [5], and Jiang and Iwai developed a dynamically tuned B-spline cam design method [6]. Pridgen and Singhose compared polynomial profiles and input shaping and showed the superiority of input shaping in RV suppression [7]. Meckl and Arestides proposed rapid S-curve point-to-point motions optimized for vibration reduction [8], while Chen and Polvanich analyzed the dynamics of high-speed cam-driven systems under various profiles [9]. Borboni et al. investigated profile interpolation effects to reduce vibration and improve smoothness [10]. Meckl and Seering introduced ramped sinusoidal series inputs with coefficients tuned to minimize spectral magnitude near resonance and thereby reduce RV [11, 12]. Wiederrich and Roth proposed finite trigonometric series cam profiles with improved dynamic performance and accuracy [13]. Aspinwall selected Fourier series coefficients to reduce response near system frequencies [14], Masoud and Alhazza applied multimode sine series for command shaping [15], and Silvestri introduced a flexible harmonic removal framework extending Gutman and Freudenstein methods [16].

Smith introduced a technique that splits the command signal into two half-period components and is widely recognized as the first study on command shaping. This approach led to the concept of self-canceling impulses convolved with a baseline reference, now known as input shaping [17]. Andresen and Singhose emphasized vibration reduction through command smoothing in cam-follower systems [18], while Singhose and Vaughan evaluated digital filtering and input shaping for vibration suppression [19]. Zhou and Misawa proposed motion profiles with both acceleration and velocity constraints [20]. Collectively, these studies highlight the effectiveness of motion profile modification for vibration mitigation across a wide range of systems.

The review of the existing studies highlights these technical shortcomings; i) when the travel time does not match the system's natural period or any of its integer multiples, traditional motion profiles tend to cause RVs, ii) in a different context, the standard ZV input shaping method works worse when the motion time is less than half of the natural period. The aim of the authors is to propose a new solution for the reduction of RV using feedforward motion control methods when modifying cam profiles based on system dynamics that overcome the technical shortcomings previously explained.

3 Proposed Approach for Modifying Motion Profiles Using Odd Fourier Series

For cam mechanisms with periodic motion, the cam follower's displacement is represented by a periodic function, $y(t)$. This function can then be expressed as

$$y(t) = \frac{a_0}{2} + \sum_{k=1}^{\infty} (a_k \cos(kRt) + b_k \sin(kRt)) \tag{1}$$

where a_k and b_k are sine and cosine coefficients. $R = 2\pi/\tau_r$ is the excitation frequency and τ_r is the period.

Since Eq. (1) contains an infinite range of frequencies, a Fourier series with a limited number of terms (N) is used to approximate the cam's displacement. This procedure makes sure that the motion is accurate and stops high-frequency components from causing resonance. Therefore, the cam's displacement transfer function, derived from this Fourier series, can be defined as:

$$y(t) = \frac{a_0}{2} + \sum_{k=1}^{N} (a_k \cos(kRt) + b_k \sin(kRt)) \tag{2}$$

Freudenstein showed that minimizing the dynamic acceleration factor requires symmetry in the cam acceleration curve [21]. Accordingly, the follower acceleration can be represented by a Fourier sine series containing only odd harmonics.

$$y(t) = \frac{a_0}{2} + \sum_{k=1}^{n} b_k \sin((2k-1)Rt) \tag{3}$$

where n is the number of odd Fourier harmonics.

Integrating tuned odd harmonic components into the motion profile enables more precise control of vibration characteristics and facilitates RV suppression. Once identified, these harmonics are incorporated into conventional cam profiles to adapt the motion to the system dynamics.

The method builds on the Freudenstein and Gutman profiles. Parabolic profiles minimize peak acceleration but contain rich harmonics, whereas cycloidal profiles reduce harmonic content at the expense of higher acceleration. Cam design therefore involves a trade-off between harmonic content and acceleration, and the Fourier representation must include only odd harmonics to ensure polar symmetry [22]. Based on these considerations, suitable harmonic profiles are developed below.

(a) Gutman 1-3 harmonic [22]

$$y(t) = \frac{L\theta}{\beta} - \frac{L}{2\pi}\left(\frac{15}{16}\sin\frac{2\pi\theta}{\beta} + \frac{1}{48}\sin\frac{6\pi\theta}{\beta}\right) \tag{4}$$

(b) Freudenstein 1-3 [21, 22]

$$y(t) = \frac{L\theta}{\beta} - \frac{L}{2\pi}\left(\frac{27}{28}\sin\frac{2\pi\theta}{\beta} + \frac{1}{84}\sin\frac{6\pi\theta}{\beta}\right) \tag{5}$$

(c) Freudenstein 1-3-5 [21, 22]

$$y(t) = \frac{L\theta}{\beta} - \frac{Lm}{2\pi}\left(\sin\frac{2\pi\theta}{\beta} + \frac{1}{54}\sin\frac{6\pi\theta}{\beta} + \frac{1}{1250}\sin\frac{10\pi\theta}{\beta}\right) \tag{6}$$

where $m = 1125/1192$.

The Fourier coefficients, denoted as, a_0 and b_k, are determined with the objective of achieving null RVs subsequent to the motion segment of length . It is important to notice that retuning of the aforementioned cam profile is necessary when selecting arbitrary time durations, τ_r.

4 Integration of Ramp Plus Trigonometric Excursion Tuning Method into the Motion Profile Modification Process

The odd-harmonic cam profiles consist of a ramp and a trigonometric component, and the proposed strategy tunes the prescribed motion profile accordingly. Unlike conventional approaches, this method does not impose a fixed time constraint on the prescribed lift L, provided that the actuators can supply the required input. This flexibility enables improved control of vibration behavior. The odd-harmonic Fourier series can be expressed as the superposition of a ramp and a trigonometric function, as in Eq. (7), where the ramp amplitude L and the trigonometric excursion l_2 must be properly selected.

$$y(t) = \frac{l_1 Rt}{2\pi} + \frac{l_2}{2\pi}[Rt - b_1\sin(Rt) - b_2\sin(3Rt) - \cdots - b_n\sin((2n-1)Rt)] \tag{7}$$

where l_1 is the ramp distance, l_2 is the odd parts distance at the end of user specified time τ_r. The total lift L to traverse from the start to the end of a motion within a designated time frame equals the sum of l_1 and l_2. By changing the partial-lift distance of each function, it is possible to get rid of any RV while still keeping the move time and total lift L. Eq. (7) is alternatively as follows:

$$y(t) = \frac{LRt}{2\pi} - \frac{l_2}{2\pi}[b_1\sin(Rt) + b_2\sin(3Rt) + \cdots + b_n\sin((2n-1)Rt)] \tag{8}$$

Then, Eqs. (4), (5), and (6) yields, respectively:

$$y(t) = \frac{LRt}{2\pi} - \frac{l_2}{2\pi}[b_1 \sin(Rt) + b_2 \sin(3Rt)] \tag{9}$$

where $b_1 = 15/16$, $b_2 = 1/48$.

$$y(t) = \frac{LRt}{2\pi} - \frac{l_2}{2\pi}[b_1 \sin(Rt) + b_2 \sin(3Rt)] \tag{10}$$

where $b_1 = 27/28$, $b_2 = 1/84$.

$$y(t) = \frac{LRt}{2\pi} - \frac{l_2}{2\pi}[b_1 \sin(Rt) + b_2 \sin(3Rt) + b_3 \sin(5Rt)] \tag{11}$$

where $b_1 = 1125/1192$, $b_2 = 125/7152$, $b_3 = 9/11920$.

5 Description of the Mathematical Formulations and Algorithms Utilized in the Methodology

This study utilizes a mathematical model of an equivalent or analogous spring-mass system. Mechanical system modeling is commonly based on constructing approximate lumped-parameter models governed by ordinary differential equations [23]. Accordingly, this study employs an equivalent spring–mass model to represent the system dynamics. It is given in Fig. 1, consisting of an equivalent mass (m_e) moving along the input *y(t)* and an equivalent stiffness (k_e).

$$\ddot{x}(t) + \omega_n^2 x(t) = \omega_n^2 y(t) \tag{12}$$

where $\omega_n = (k_e/m_e)^{0.5}$, is the circular natural frequency.

The objective is to design a reference input $y(t)$ that transfers the flexible system between two states in minimum time while ensuring zero residual vibration at the end of the motion.

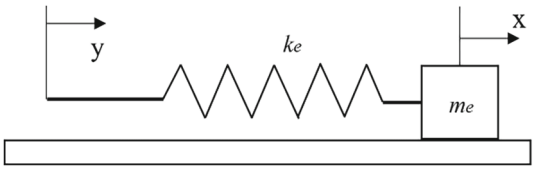

Fig. 1. Mathematical model for an equivalent physical system

Assuming the system starts from rest, its response is obtained using cam profiles composed only of odd harmonics, as given in Eq. (8). The resulting transient and steady-state vibrations at the final position after the prescribed motion time τ_r are then evaluated.

$$x(t) = C_3 \sin(\omega_n(t - \tau_r)) + C_4 \cos(\omega_n(t - \tau_r)) + L \tag{13}$$

where

$$C_3 = \left[L - l_2 \sum_{i=1}^{n} b_i \left(\frac{\omega_n^2}{\omega_n^2 - R^2} \right) \right] (\cos(\omega_n \tau_r) - 1) \tag{14}$$

$$C_4 = \left[L - l_2 \sum_{i=1}^{n} b_i \left(\frac{\omega_n^2}{\omega_n^2 - R^2} \right) \right] \sin(\omega_n \tau_r) \tag{15}$$

C_3 and C_4 are set to zero to have zero vibration after τ_r. It is clear from the Eqs. (14) and (15), that zero RV condition can be satisfied if only if

$$L = l_2 \omega_n^2 \sum_{i=1}^{n} b_i \left(\frac{1}{\omega_n^2 - R^2} \right) \tag{16}$$

Substituting the natural period of the system τ_n, and τ_r into Eq. (16) and solving for l_2

$$l_2 = \frac{L \left(\prod_{j=1}^{n} \left(1 - Z_{2j-1}^2 \right) \right)}{\sum_{m=1}^{n} \left(b_m \prod_{\substack{j=1 \\ j \neq m}}^{n} \left(1 - Z_{2j-1}^2 \right) \right)} \tag{17}$$

where $m = 1, 2, \ldots, n, j = 1, 2, \ldots, n, Z_{(2j\text{-}1)} = \tau_n / ((2\,J\text{-}1)\,\tau_r)$ is the normalized time ratio of natural frequency period to raise period of the (2 J-1) harmonics.

After identifying these factors, they are included to the system, which makes it a tuned system that works best for suppressing RVs.

6 Simulation Results and Discussions

The proposed cam profile is validated through simulations and compared with conventional cam profiles and the ZV input shaping method introduced by Singer and Seering [24]. The ZV method suppresses residual vibrations by convolving the reference command with a sequence of impulses. Further details and applications can be found in [4, 7, 18, 24]. This section presents the simulation results.

Eq. (12) is solved numerically using the MATLAB® ode45 solver. The mass and stiffness are set to 1 kg and 100 N/m, respectively. A travel distance of $L = 0.5$ m and prescribed travel times of $0.25\tau_n$ (0.1571 s), $0.5\tau_n$ (0.3142 s), $0.75\tau_n$ (0.4712 s), and $1.5\tau_n$ (0.9425 s) are considered to compare the proposed odd-harmonic cam profile with traditional profiles and the ZV input shaping method. System's natural period is $\tau_n = 2\pi\,(m_e/k_e)^{0.5} = 0.6283$ s. When the user-specified excursion time is less than 50% of the system's period, the ZV input shaping method does not work. The excursion time is

Table 1. RV amplitudes comparison after τ_r

Method	Function	User-defined travelling time			
		$\tau_r = 0.25\tau_n$	$\tau_r = 0.5\tau_n$	$\tau_r = 0.75\tau_n$	$\tau_r = 1.5\tau_n$
No modified input, $l_2 = 0.5$ m is arbitrarily selected	Gutman 1-3	±478.488	±418.349	±331.543	±70.735
	Freudenstein 1-3	±479.208	±420.947	±232.059	±76.799
	Freudenstein 1-3-5	±482.144	±431.28	±355.059	±94.13
Modified input, l_2 is calculated	Gutman 1-3	±2.094	±1.21	±0.345	±0.877
	Freudenstein 1-3	±1.164	±0.373	±0.192	±0.484
	Freudenstein 1-3-5	±28.716	±20.059	±9.251	±5.525
ZV input shaping	Freudenstein 1-3	None	±0.398*	± 2.778**	±1.397 ***

Notes:
* Step function is convolved using two impulses
** Freudenstein 1-3 is modified with $l_2 = 0.5$ m between $0 < \tau_r < 0.25\tau_n$ then the signal is convolved using two impulse.
*** Freudenstein 1-3 is modified with $l_2 = 0.5$ m between $0 < \tau_r < \tau_n$ then the signal is convolved using two impulse.

not chosen as a single period because the RV approaches zero regardless of the curve's characteristic. When the command input $y(t)$, as indicated by Eqs. (9), (10), and (11) with arbitrary values (l_2) adjusted to 0.5 m, the system makes RV after the motion is finished. The equations of Gutman 1-3 and Freudenstein 1-3 given in Eq. (9) and (10) show almost the same results, as seen in Table 1. The values in Table 1 are in mm.

Consequently, only the outcomes related to Freudenstein 1-3-5 given in Eq. (11) for different user-defined travel times of $0.25\tau_n$, $0.5\tau_n$, $0.75\tau_n$, and $1.5\tau_n$ are depicted in Fig. 2 to assess references and responses (Table 1, no modified input). Motion time of the reference signals (Ref. (1 to 4)) are $0.25\tau_n$, $0.5\tau_n$, $0.75\tau_n$ and $1.5\tau_n$, successively. Reference signal is y in Fig. 1. Res. (1 to 4) are the responses of m_e. Response is x in Fig. 1. It is observed that an increase in the prescribed user time leads to a decrease in RV amplitude. The system's response to the command input $y(t)$, described by Eqs. (9, 10, and 11), with the computed values (l_2) derived from the proposed Eq. (17), is recorded and tabulated in Table 1. Notably, among the three methods, Freudenstein 1-3 yields superior results. The modified inputs and outputs from the three functions exhibit similar characteristics with slight distinctions. Figure 2 illustrates that when the travel time for point-to-point motion exceeds one period of the system, vibration amplitudes decrease but are not completely eliminated, or at least not reduced to near-zero levels.

The simulation results shown in Table 1 for Freudenstein 1-3 function (given in Eq. (10)) corresponding to the various user-specified travel times of $0.25\tau_n$, $0.5\tau_n$, $0.75\tau_n$, and $1.5\tau_n$ are depicted in Fig. 3 to visually represent reference inputs and responses. Calculated and used l_1 and l_2 values are given in Table 2.

To demonstrate the applicability and feasibility of the proposed method, it is compared with a well-known ZV input shaping method. The responses for various user specified travel times of $0.25\tau_n$, $0.5\tau_n$, $0.75\tau_n$, and $1.5\tau_n$ are presented in Fig. 4.

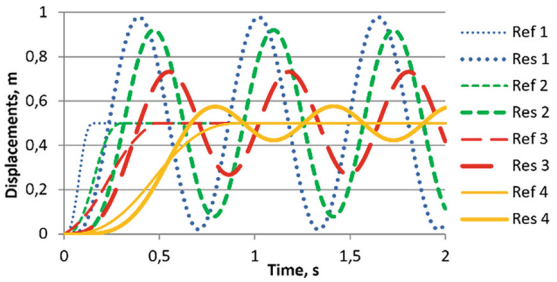

Fig. 2. References and responses of untuned Freudenstein 1–3-5 for various user-specified travel times (arbitrarily selected L = 0.5 m. and $l_2 = 0.5$ m.)

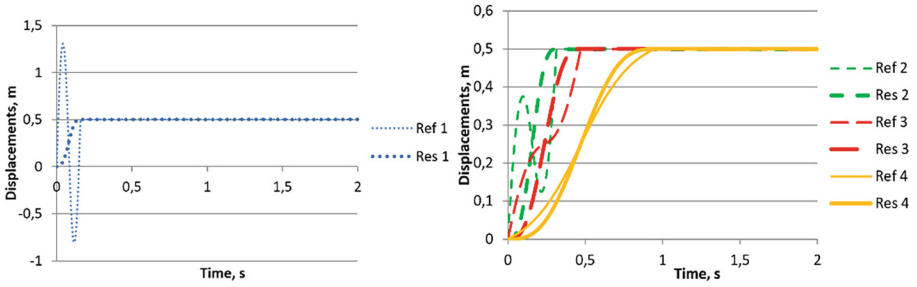

Fig. 3. Tuned Freudenstein 1-3 references for various user-specified travel times and their responses

Table 2. l_1 and l_2 parameters in tuned Freudenstein 1-3 with different τ_r

τ_r	l_1	l_2
0.1571	8.2677	−7.7677
0.3141	2.0539	−1.5539
0.4712	0.903	−0.403
0.9425	0.2113	0.2887

For travel times equal to 50% of the system period, a step function is convolved due to the time constraint of the method. When the travel time exceeds this threshold, arbitrary profiles can be shaped using two impulses. For consistency, when $\tau_r > 0.5\ \tau_n$, Freudenstein's 1–3 profile in Eq. (10) is modified with $L = l_2 = 0.5$ m, as noted below Table 1.

Simulation results indicate that the modified inputs neither restrict nor prolong the motion time to reduce vibrations in flexible systems. Through the proposed method, these functions can theoretically eliminate RVs at any user-defined duration. All travel times for all functions demonstrate vibration suppression after the motion of the input ceases.

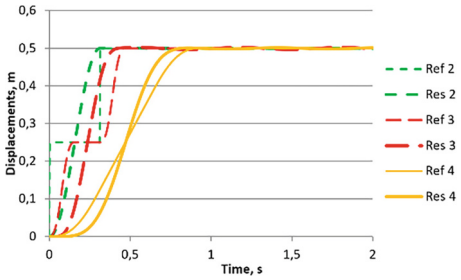

Fig. 4. Input shaping for various user-specified travel times and their responses

Among the modified functions, the modified Freudenstein 1-3 function exhibits superior results. The input shaping method also demonstrates favorable vibration suppression characteristics, as evident from Table 1, which shows comparatively better results than input shaping. For user-defined time durations less than 25% of the system natural period, the proposed method outperforms ZV input shaping. Modified functions lack smoothness and impose velocity shocks at the start and end of motion, aligning with the main principle of the proposed method to suppress vibrations.

7 Conclusions

This study proposes odd Fourier series cam profile modification technique for command shaping to effectively eliminate or minimize endpoint RVs of flexible systems during rapid point-to-point movements. The conventional cam profiles, formed by odd harmonics, consist of two parts: a ramp and a trigonometric component, each with different excursion displacements. The first part represents the destination displacement, while the second part represents the amplitude of the superimposed trigonometric part onto the ramp part. Results indicate the potential to reduce RV in undamped mechanical systems through the proposed Fourier Series cam motion profile modification strategy. Compared to ZV input shaping, this method significantly reduces RV in undamped mechanical systems. Simulation outcomes demonstrate that the proposed inputs neither restrict nor prolong motion time to reduce vibrations in flexible systems. However, a limitation of this method, similar to ZV input shaping, is its sensitivity to system parameter estimation error.

The proposed motion control method has potential applications in precision machinery utilizing high-speed, high-precision motion stages, including pick-and-place manipulators, industrial robots, and positioning systems.

References

1. Srinivasan, L.N., Ge, Q.J.: Designing dynamically compensated and robust cam profiles with Bernstein–Bézier harmonic curves. J. Mech. Des. **120**(1), 40–45 (1998)
2. Gupta, K.C., Wiederrich, J.L.: On the modification of cam-type profiles. Mech. Mach. Theory. **21**(5), 439–444 (1986)

3. Kwakernaak, H., Smit, J.: Minimum vibration cam profiles. J. Mech. Eng. Sci. **10**(3), 219–227 (1968)
4. Kapucu, S., Das, M.T., Kılıç, A.: Cam motion tuning of shedding mechanism for vibration reduction of heald frame. Gazi Univ. J. Sci. **23**(2), 227–232 (2010)
5. Liang, X., Huang, Y.: Design of high-speed cam profiles for vibration reduction using command smoothing technique. Proc. Inst. Mech. Eng. C J. Mech. Eng. Sci. **228**(18), 3322–3328 (2014)
6. Jiang, J.K., Iwai, Y.R.: Improving the B-spline method of dynamically-compensated cam design by minimizing or restricting vibrations in high-speed cam–follower systems. J. Mech. Des. **131**(4), 041003 (2009)
7. Pridgen, C., Singhose, W.: Comparison of polynomial cam profiles and input shaping for driving flexible systems. J. Mech. Des. **134**(12), 124505 (2012)
8. Meckl, P., Arestides, J.: Optimized s-curve motion profiles for minimum residual vibration. In: American Control Conference (ACC 1998), vol. 5, pp. 2627–2631. IEEE, Philadelphia (1998)
9. Chen, L., Polvanich, R.: Dynamics of high-speed cam-driven mechanisms—part 1: linear system models. ASME J. Eng. Ind. **97**(3), 769–775 (1975)
10. Borboni, A., Aggogeri, F., Elamvazuthi, I., Incerti, G., Magnani, P.L.: Effects of profile interpolation in cam mechanisms. Mech. Mach. Theory. **144**, 103664 (2020)
11. Meckl, P., Seering, W.: Reducing residual vibration in systems with time-varying resonances. In: IEEE International Conference on Robotics and Automation, pp. 1690–1695. IEEE, Raleigh (1987)
12. Meckl, P., Seering, W.: Reducing residual vibration in systems with uncertain resonances. IEEE Control. Syst. Mag. **8**(2), 73–76 (1988)
13. Wiederrich, G., Roth, B.: Dynamic synthesis of cams using finite trigonometric series. J. Eng. Ind. **97**(1), 287–293 (1975)
14. Aspinwall, D.: Acceleration profiles for minimizing residual response. J. Dyn. Syst. Meas. Control. **102**(1), 3–6 (1980)
15. Masoud, Z.N., Alhazza, K.A.: A smooth multimode waveform command shaping control with selectable command length. J. Sound Vib. **397**, 1–16 (2017)
16. Silvestri, M.: Motion law assisted design to reduce the vibrational effect of controlled axes in automated machines. Int. J. Recent Technol. Eng. **8**(2), 3778–3783 (2019)
17. Smith, M.: Posicast control of damped oscillatory systems. Proc. IRE. **45**(9), 1249–1255 (1957)
18. Andresen, P., Singhose, W.: A simple procedure for modifying high-speed cam profiles for vibration reduction. J. Mech. Des. **126**(6), 1105–1108 (2004)
19. Singhose, W., Vaughan, J.: Reducing vibration by digital filtering and input shaping. IEEE Trans. Control Syst. Technol. **19**(6), 1410–1420 (2011)
20. Zhou, Q., Misawa, E.: Vibration suppression control profile generation with both acceleration and velocity constraints. In: American Control Conference (ACC 2005), pp. 4736–4741. IEEE, Portland (2005)
21. Freudenstein, F.: On the dynamics of high-speed cam profiles. Int. J. Mech. Sci. **1**(4), 342–349 (1960)
22. Rothbart, H.: CAM Design Handbook. McGraw-Hill, New York (2004)
23. Kapucu, S., Alici, G., Bayseç, S.: Residual swing/vibration reduction using a hybrid input shaping method. Mech. Mach. Theory. **36**(3), 311–326 (2001)
24. Singer, N., Seering, W.: Preshaping command inputs to reduce system vibration. J. Dyn. Syst. Meas. Control. **112**(1), 76–82 (1990)

Development and Validation of a Load Equivalence Framework for Predicting Crack Growth in Al 2024-T3 Aluminum Alloy

Brahim Bouaziz(✉), Maher Eltaief, and Chokri Bouraoui

Mechanical Laboratory of Sousse, National Engineering School of Sousse, University of Sousse, BP 264, Erriadh, 4023 Sousse, Tunisia
bouaziz_ibrahim@yahoo.fr

Abstract. Fatigue crack propagation can significantly reduce component life and potentially lead to failure. This study aims to evaluate the fatigue life of the 2024-T3 aluminum alloy under variable loading by transforming it into an equivalent constant-load problem, thereby avoiding cycle-by-cycle calculations. The framework relies on a two-parameter fatigue model that accounts for both the maximum total stress intensity factor $K_{\max_tot}$ and the magnitude of the total stress intensity factor ΔK_{tot}. Initially, plastic-zone interaction effects are neglected to establish an equivalence between variable and constant loading via the driving-force model. The Willenborg model is then employed, generalized by Meggiolaro and Castro and subsequently Gallagher, to determine the equivalent stress $\Delta\sigma eq$ that yields a comparable crack-growth rate under constant loading.

The study outlines the transition from variable to equivalent constant loading, with the potential inclusion of crack-closure effects as needed. The calibrated parameters (C_T,p,q) are obtained from experimental da/dN versus ΔK data for 2024-T3. Preliminary validation shows encouraging agreement with experimental results for two loading sequences. In conclusion, the proposed methodology provides a robust estimate of fatigue life under variable loading, preserving the main propagation mechanisms while simplifying industrial-scale calculations.

Keywords: Fatigue crack length · variable load · equivalent load

1 Introduction

In structural components used in the automotive and aerospace sectors, the presence of cracks or geometric discontinuities is unavoidable. These parts are frequently subjected to cyclic loading of varying amplitudes, which complicates fatigue life estimation and increases the risk of failure. Given the safety challenges and the current economic climate, it is crucial to develop robust prediction methods to extend the service life of these structures.

Fatigue and crack growth (FCG) depend not only on the current loading but also on the loading history [1, 2], which can induce interaction effects in the plastic zone and sequence effects (order and magnitude of overloads and relaxations). These phenomena

© The Author(s), under exclusive license to Springer Nature Switzerland AG 2026
A. Chaker et al. (Eds.): EFIMMS 2026, MMS 205, pp. 398–406, 2026.
https://doi.org/10.1007/978-3-032-22270-1_39

can accelerate or decelerate propagation under real-world conditions and are not always captured by simple criteria based on ΔK.

Numerous studies have attempted to predict crack life under variable loading. Some focus on the size of the plastic zone and its effects on crack propagation delay, as summarized by Wheeler [3]. Others concentrate on the concept of crack closure (Elber) [4], and Noorozi and Glinka [5] proposed a two-parameter model based on the elastoplastic response at the crack tip. Predicting crack life under variable loading remains a major challenge for structures in real-world conditions.

This study aims to estimate fatigue life under variable loading by replacing this loading with an equivalent constant loading problem, while taking into account the effects of random loading sequences [6].

To achieve this, we propose an equivalent stress transformation approach, replacing the two-parameter crack growth model with a more tractable framework. This approach is physically justified: plastic interactions and residual stresses generated at the crack tip modulate the loading gradients and influence the driving force model that governs propagation.

In a first step, the interaction effects of the plastic zone are neglected in order to establish an equivalence relationship between variable and constant loading via the driving force model [5], which combines the total maximum intensity factor $K_{\max_tot}$ and the magnitude of the total intensity factor ΔK_{tot}. Then, the Willenborg model [7], generalized by Meggiolaro and Castro [8] and then Gallagher [9], is used to determine the equivalent stress $\Delta\sigma_{eq}$ that produces a comparable crack growth rate under constant loading.

2 Equivalent Stress Without Crack Closure Effect

The two-parameter driving force model is used to estimate fatigue growth, taking into account both $K_{\max_tot}$ and ΔK_{tot} . The crack propagation rate is described by the equation associated with this framework.

$$\frac{da}{dN} = CK_{max}^{p}\Delta K^{q} \tag{1}$$

In the case of linear damage, when a crack is subjected to a cyclic loading spectrum of variable amplitude $\Delta\sigma_i$ over N_i, the evolution of the crack length during this spectrum is Δa, which can be calculated from the crack growth rates such as.

$$\Delta a = \left(\frac{da}{dN}\right)_1 .N_1 + \left(\frac{da}{dN}\right)_2 .N_2 + \cdots + \left(\frac{da}{dN}\right)_n .N_n \tag{2}$$

Combining two equations allows us to find:

$$\Delta a = C\left(K_{1\max}^{p}\Delta K_1^{q}N_1 + K_{2\max}^{p}\Delta K_2^{q}N_2 + \cdots + K_{nmax}^{p}\Delta K_n^{q}N_n\right) \tag{3}$$

Where

$$K_{max} = \frac{\Delta K}{1-R} \tag{4}$$

And

$$\Delta K = Y \Delta\sigma \sqrt{\pi a} \tag{5}$$

Where Y represents a geometric correction factor.
Thus, the total crack length can be rewritten as:

$$\Delta a = C.Y^{p+q}(\pi a)^{(p+q)/2}.\left(\frac{\Delta\sigma_1^{p+q}}{(1-R_1)^p}N_1 + \frac{\Delta\sigma_2^{p+q}}{(1-R_2)^p}N_2 + \cdots + \frac{\Delta\sigma_n^{p+q}}{(1-R_n)^p}N_n\right) \tag{6}$$

From Eq. (6), it is possible to calculate the growth of the equivalent crack from a constant amplitude loading:

$$\Delta a = C.Y^{p+q}(\pi a)^{(p+q)/2}.\left(\frac{\Delta\sigma_{eq}^{p+q}}{(1-R_{eq})^p}N_{total}\right) \tag{7}$$

Equality between Eqs. (6) and (7) allows us to calculate $\Delta\sigma_{eq}$ [10]:

$$\Delta\sigma_{eq} = \left(\sum_{i=1}^{n}\frac{N_i}{N_{total}}\frac{\Delta\sigma_i^{p+q}}{(1-R_i)^p}\right)^{1/(p+q)} \tag{8}$$

Figure 1 illustrates the procedure for converting a variable load into a constant load equivalent to R = 0.

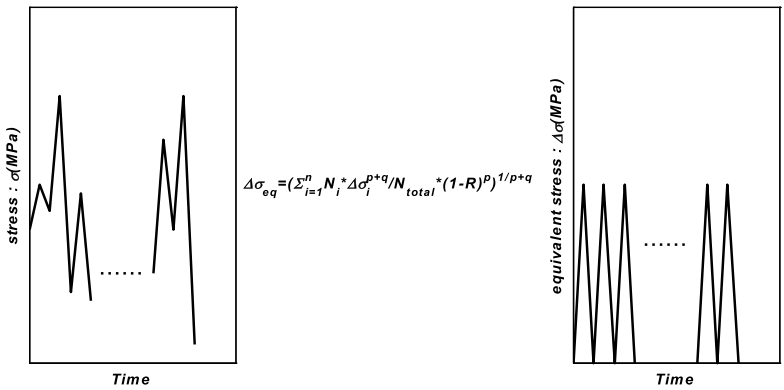

Fig. 1. Equivalent load.

3 Equivalent Stress with Crack Closure Effect

By combining the two-parameter model with the Willenborg model, the crack propagation rate can be described in this form [11]

$$\frac{da}{dN} = CK_{max}^{p}\Delta K_{eff}^{q} = \frac{C}{(1-R)^p}\Delta K_{eff}^{p+q} = C_T \Delta K_{eff}^{p+q} \tag{9}$$

Where R represents the stress ratio for a constant load, p and q are the calibration parameters of the fatigue crack propagation data. Several studies carried out on aluminium alloys show that p = 2 [12, 13].

In Eq. (4), we note the presence of two unknowns to be determined: the coefficient C_T and q, which will be deduced from the experimental data relating to the crack propagation speed $\frac{da}{dN}$ curve ΔK as a function of constant underload.

4 Results and Discussion

4.1 A Plate with a Central Crack

The analysis was carried out on a sample (Fig. 2) of 2024-T3 aluminum alloy with a central crack of initial size (2a) equal to 12.7 mm, a length L of 610 mm, a width w of 229 mm and a thickness t of 4.1 mm.

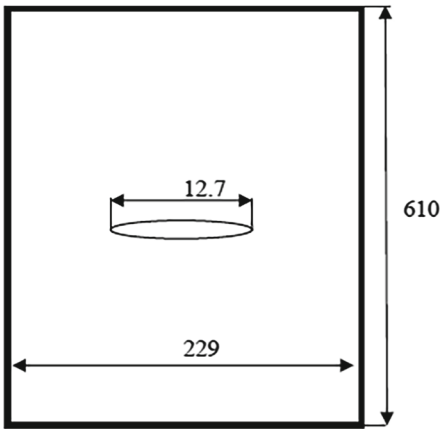

Fig. 2. Sample dimensions.

The mechanical properties of AL2024-T3 are summarized in Table 1:

Table 1. Mechanical properties of the Al 2024-T3 alloy [14].

$E(MPa)$	v	$\sigma_y(MPa)$
73000	0.33	289

4.2 Calculation of Calibration Parameters: C_T, p, q

To determine the equivalent load according to Eq. (3), it is necessary to determine the unknown q (p being equal to 2). This is done using Eq. (4), which has two unknowns

(C_T *and* q) . To determine these two parameters, experimental data from the crack propagation rate $\frac{da}{dN}$ curve as a function of the magnitude of the stress intensity factor ΔK under constant load are used.

The following curve (Fig. 3) represents the variation of the crack propagation speed $\frac{da}{dN}$ as a function of the amplitude of the stress intensity factor ΔK and is then used to adjust the parameters p, q and C_T.

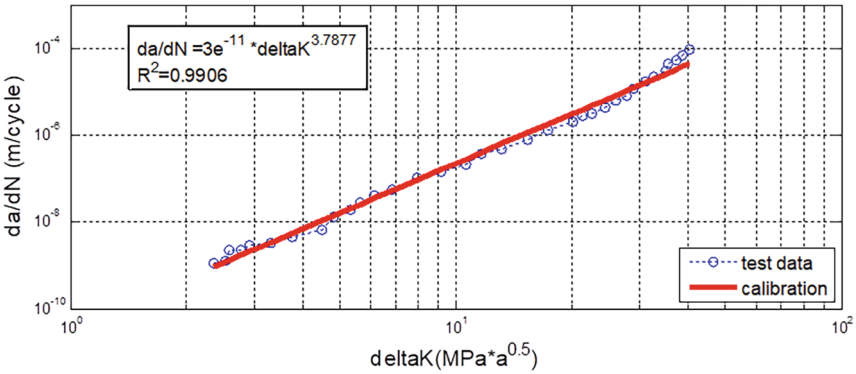

Fig. 3. $\frac{da}{dN} - \Delta K$ of $2024 - T3$ aluminium alloys for $R = 0, 4$ [15].

For an aluminum alloy, we take p = 2, which allows us to determine:

$$C_T = 1.2037 \times 10^{-11} \text{ and } q = 1.7877$$

4.3 Flowchart for Determining the Crack Propagation Increment

The following flowchart illustrates the method for determining the fatigue cycle growth increment relative to a fatigue crack growth increment (Fig. 4):

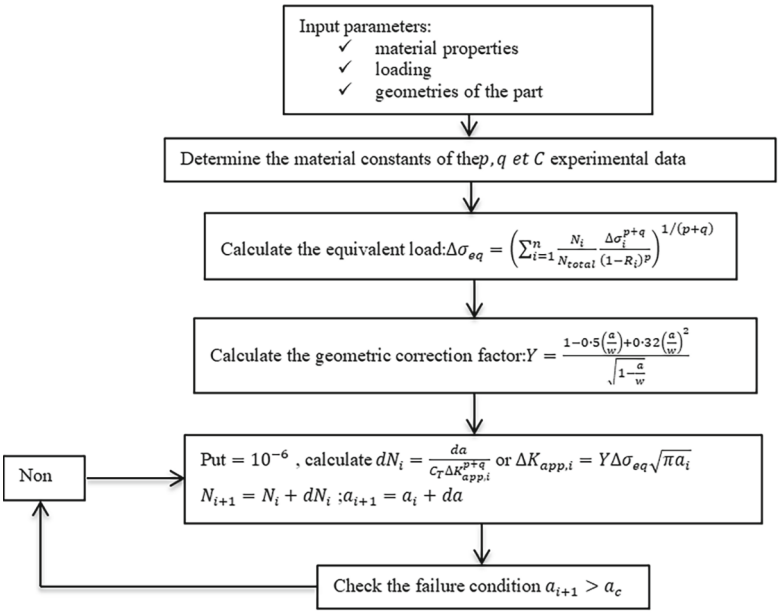

Fig. 4. Flowchart for determining the crack propagation increment.

4.4 Lifespan Prediction

To validate the calculation model, two loading sequences are studied [16, 17]. The first sequence presents a constant maximum load of 83 MPa, with a stress variation Δσ from 75 MPa to 55 MPa then 14 MPa, the second sequence goes from 96 MPa to 49 MPa then to 35 MPa and from 83 MPa to 35 MPa.

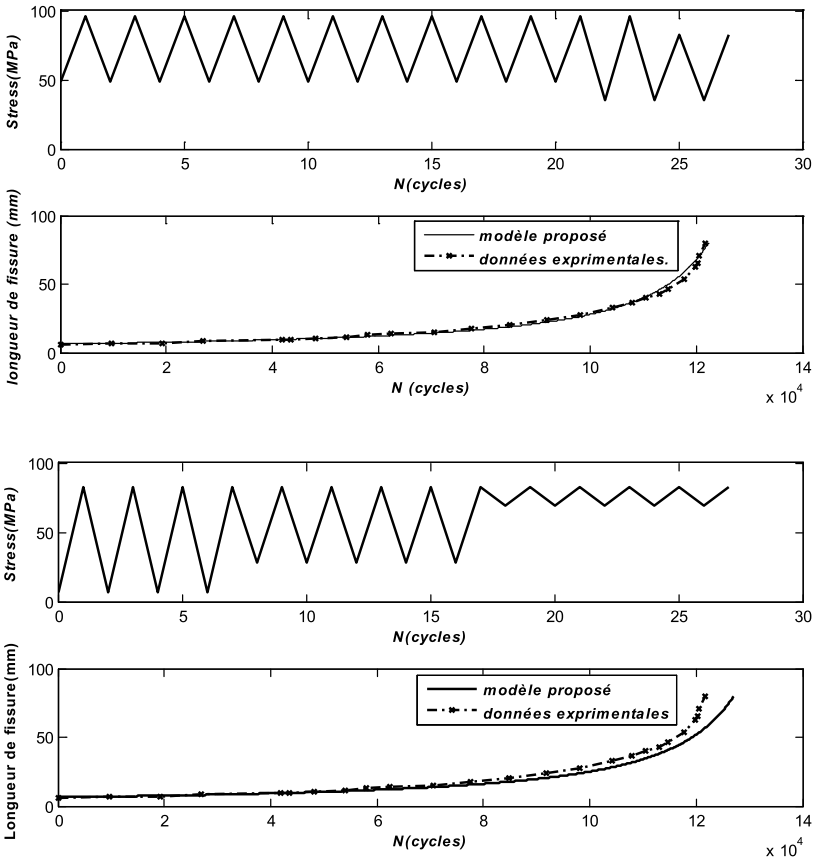

Fig. 5. Comparison of model results with experimental results for 2024-T3 aluminum

A comparison of the results presented in Fig. 5 indicates a good agreement between the experimental observations and the predictions obtained from the fatigue life model. The crack growth prediction curves are able, in most cases, to closely reproduce the experimental trends. This agreement is achieved while accounting for uncertainties associated with loading conditions, material properties, and in situ diagnostics, through an approach based on defining an equivalent constant-amplitude crack growth process that yields kinetics comparable to those observed under actual random loading conditions.

The estimation of the error as a function of the number of cycles is shown in the following graph (Fig. 6).

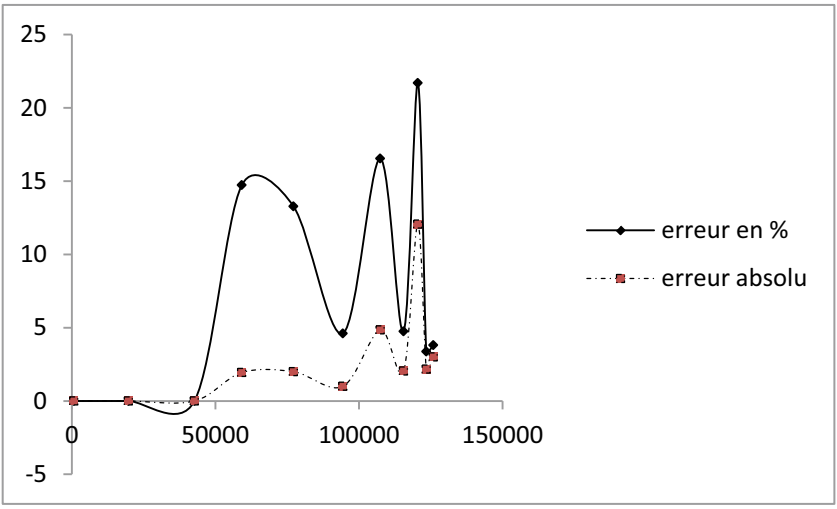

Fig. 6. variation of the error depending on the number of cycles

5 Conclusion

In summary, this study proposes a robust methodology for estimating fatigue life under variable loading by replacing the load with an equivalent constant-load problem. This approach preserves the dominant crack propagation mechanisms while reducing the complexity of cycle-by-cycle calculations. The results suggest that stress equivalence, combined with a two-parameter framework and, where necessary, a crack closure model, can provide reliable predictions for industrial applications.

References

1. Sérgio, E.R., Antunes, F.V., Neto, D.M.: Improving the fatigue crack growth prediction by accurate calibration of the constitutive material parameters. Theor. Appl. Fract. Mech. **138**, 104957 (2025)
2. Noroozi, A.H., Glinka, G., Lambert, S.: A study of the stress ratio effects on fatigue crack growth using the unified two-parameter fatigue crack growth driving force. Int. J. Fatigue. **29**, 1616–1633 (2007)
3. Wheeler, O.E.: Spectrum loading and crack growth. J. Basic Eng. **94**, 181–186 (1972)
4. Elber, W.: Fatigue crack closure under cyclic tension. Eng. Fract. Mech. **2**, 35–47 (1970)
5. Glinka, G., Buczynski, A.: Experimental and numerical analysis of elastic-plastic strains and stresses ahead of a growing fatigue crack. In: Susmel, L., et al. (eds.) Workshop on Characterization of Crack Tip Stress Fields, pp. 7–9. GruppoItalianaFrattura, Forni di Sopra, Italy (2011)
6. Wu, Q., Zhao, Y., Liu, X.: Fatigue life prediction of metal materials under random loads based on load spectrum extrapolation. Int. J. Fatigue. **187**, 108473 (2024)

7. Willenborg, J., Engle, R.M., Wood, H.A.: A crack growth retardation model using an effective stress concept. In: Air Force Flight Dynamics Lab Wright Patterson AFB OH. Wright Patterson Air Force Lab, Wright-Patterson AFB, OH, USA., Tech. Rep. AFFDL-TM-71-1-FBR (1971)
8. Meggiolaro, M.A., Castro, J.T.P.: Comparison of load interaction models in fatigue crack propagation. In: Proceedings of the COBEM, 2001, pp. 247–256
9. P. Gallagher,"A generalized development of yield zone models," Wright Patterson Air Force Lab, Wright-Patterson AFB, OH, USA., Tech.Rep.AFFDL-TM-74-28-FBR, 1974.
10. Bouaziz, B., Eltaief, M., Bouraoui, C.: An engineering methodology for predicting crack growth of 2024-T3 aluminium alloys under variable amplitude loading. Comptes Rendus. Mécanique. **353**(G1), 1385–1404 (2025)
11. Dowling, N.E.: Mechanical Behavior of Materials Engineering Methods for Deformation, Fracture, and Fatigue, 4th edn,
12. McEvily, A.J.: Phenomenological and microstructural aspects of fatigue. In: Proceedings of the Microstructure Design Alloys, pp. 204–225 (1973)
13. Lardner, R.W.: A dislocation model for fatigue crack growth in metals. Philos. Mag. **17**(145), 71–82 (1968)
14. Kebir, T., Mohamed, B., Abdelkader, M.: Simulation of the cyclic hardening behavior of aluminum alloys simulation of the cyclic hardening behavior of aluminum alloys. Mech. Eng. **79**, 240–250 (2017)
15. Lu, Z., Liu, Y.: A comparative study between a small time scale model and the two driving force model for fatigue analysis. Int. J. Fatigue. **42**, 57–70 (2012)
16. Mikheevskiy, S., Glinka, G.: Elastic-plastic fatigue crack growth analysis under variable amplitude loading spectra. Int. J. Fatigue. **31**(11–12), 1828–1836 (2009). https://doi.org/10.1016/j.ijfatigue.2009.02.035
17. Wang, W.J., Yim, M.-S.: A fatigue crack growth prediction model for cracked specimen under variable amplitude loading. Int. J. Fatigue. **168**, 107387 (2023)

Finite Element Analysis of a Novel Active Ankle-Foot Prosthesis for Improved Load Distribution

Akhmejanov Sayat[1], Zhetenbayev Nursultan[2,3](✉), Sultan Aidos[2,3], Bigaliyeva Zhanar[1], Shylmyrza Ussen[1], Nurgizat Yerkebulan[2,3], and Sergazin Gani[3]

[1] Satbayev University, Almaty, Kazakhstan
akhmejanov.s@stud.satbayev.university, {zh.bigaliyeva, u.shylmyrza}@satbayev.university
[2] Almaty University of Power Engineering and Telecommunications, Almaty, Kazakhstan
{n.zhetenbaev,a.sultan,y.nurgizat}@aues.kz
[3] ALT University named after Mukhamedzhan Tynyshpaev, Almaty, Kazakhstan
g.balbayev@alt.edu.kz

Abstract. This work presents a structural evaluation of an ankle-foot prosthesis developed from a high-resolution 3D laser scan of the human foot. The acquired geometry was used to create a detailed mechanical model in SolidWorks. An ABS prototype was manufactured exclusively for early-stage kinematic validation and verification of the actuation mechanism, whereas the structural performance of the final design was assessed through Finite Element Analysis (FEA) using AISI 304 stainless steel material properties. Three static load cases 800 N, 1000 N, and 1200 N were applied to represent the vertical forces acting on the foot during the midstance phase of walking. The Finite Element Method was employed to evaluate the distributions of Von Mises stress, total displacement, and equivalent strain within the structure.

The numerical results revealed a consistent response across all load cases, with stress and strain primarily concentrated in the mid-section transition zone of the foot plate, where geometric changes govern load transfer. For AISI 304, all computed values remained well within the elastic range. The maximum displacement did not exceed 0.15 mm, confirming sufficient structural stiffness, while strain levels increased proportionally with load without approaching plastic deformation.

Overall, the findings confirm that the proposed geometry and mechanical layout are structurally safe when evaluated with AISI 304 stainless steel, making it suitable for the final prosthesis design. The ABS prototype should be regarded solely as a laboratory test platform for kinematic and functional verification. The presented analysis provides a reliable basis for further refinement of anatomically accurate and mechanically robust ankle-foot prosthesis systems.

Keywords: Finite Element Method · Static Loading · Stress Distribution · Equivalent Strain · AISI 304 · 3D Laser Scanning

© The Author(s), under exclusive license to Springer Nature Switzerland AG 2026
A. Chaker et al. (Eds.): EFIMMS 2026, MMS 205, pp. 407–418, 2026.
https://doi.org/10.1007/978-3-032-22270-1_40

1 Introduction

Ankle-foot prostheses play a central role in restoring mobility for individuals who have undergone lower-limb amputation. Beyond enabling basic walking, these devices help users return to daily activities and regain social independence. How stable a prosthesis feels during gait, how it distributes body weight, and the degree of comfort it provides all depend heavily on its mechanical design. For this reason, evaluating the structural behavior of the foot section has become an essential part of modern rehabilitation engineering [1, 2].

Most commercially available ankle-foot prostheses still rely on passive components or limited elastic elements. While such designs perform adequately in simple, steady walking conditions, they often struggle to replicate the full complexity of natural biomechanics. Changes in gait phases, uneven terrain, or rapid maneuvers can reveal several shortcomings: stiffness that remains fixed regardless of load, limited energy return, and reduced fatigue resistance in long-term use. These factors can influence not only walking efficiency, but also the user's overall comfort and endurance throughout the day.

In recent years, researchers have shown increasing interest in integrating active or semi-active mechanisms into prosthetic systems. Devices equipped with controllable stiffness, phase-dependent responses, or energy-assisting elements have the potential to behave more like a biological foot. Such enhancements can improve energy storage and release, make the prosthesis more adaptable to varying ground conditions, and distribute loads more effectively across the structure.

Within this broader effort to refine prosthetic design, the Finite Element Method (FEM) has become one of the most valuable analytical tools. FEA enables engineers to investigate how stress, deformation, and displacement develop within complex geometries areas that are often difficult or impossible to assess through direct experimental measurements. In the context of ankle-foot prostheses, FEA is particularly useful for evaluating the structural response of the foot plate, which serves as the primary load-bearing element during walking. By focusing the numerical analysis on this critical component, informed decisions can be made regarding material selection, geometric refinement, and design comparison, while still supporting the overall ankle-foot system architecture. As a result, FEA has established itself as a reliable approach for reducing design uncertainties at early development stages and improving the structural safety of both prototype and final prosthetic models.

2 Literature Review

The development of ankle-foot prostheses has grown rapidly over the past several decades, and today a wide range of models exists to meet different activity levels and user needs [3]. Systematic scientific work in this area began around the middle of the twentieth century. One of the earliest foundational studies was conducted by [4], who provided a detailed description of the SACH foot and examined how its combination of a rigid keel and a cushioned heel influenced gait stability. Later experimental work compared the SACH design with alternatives such as the Seattle and Flex-Foot models, focusing on their effects on step length, ground reaction forces, and gait symmetry.

Gitter and colleagues, for example, demonstrated through direct measurements that the geometry and material properties of the prosthetic foot have a decisive influence on overall walking mechanics [5]. These early studies laid the groundwork for many of the engineering approaches used in modern prosthetic design.

As research progressed, efforts to improve traditional SACH-type feet intensified. Some studies aimed to adapt these designs for low-resource settings, testing affordable models made from natural rubber or other locally available materials. According to [6], an updated SACH foot retained the simplicity of the original design while showing better shock absorption and overall durability. In parallel, ESAR feet gained significant attention in clinical research. Findings in [7] indicated that although energy-storing-and-return designs can improve gait symmetry, they do not always lead to better metabolic efficiency. These results highlight that prosthetic design must account not only for biomechanical performance but also for the social and economic context in which the device will be used.

The contrast between passive and dynamic prosthetic feet remains a central topic in current studies. Passive feet are mechanically simple and operate solely through the elasticity of their materials and geometry. In contrast, active or semi-active feet can adjust stiffness during different phases of gait, supply additional power, or respond to load variations through electronically controlled components. Despite their higher cost, actively controlled systems can offer clear advantages on slopes, stairs, or when walking speed changes.

Within the engineering domain, the Finite Element Method (FEM) has become one of the most reliable tools for evaluating prosthetic foot structures. Earlier studies used FEM to map stress distributions in SACH and ESAR feet, assess how geometric modifications affect loading, and estimate fatigue resistance of various materials. Some authors modeled dynamic loading conditions corresponding to realistic gait phases and examined load transfer between the prosthesis and the residual limb. Comparisons between FEM predictions and clinical measurements have repeatedly confirmed the accuracy of these models. For these reasons, FEM is now viewed not just as an analytical aid but as a key method for assessing safety and performance in the early stages of prosthetic design.

3 Materials and Methods

In this work, the design and structural evaluation of the ankle-foot mechanism were carried out in several sequential stages. The overall methodology included acquiring the initial anatomical geometry, preparing a detailed CAD model, defining the material properties, and performing a static analysis using the Finite Element Method (FEM).

3.1 Geometry Acquisition via 3D Scanning

When developing the prosthetic mechanism, several baseline requirements were taken into account: anatomical accuracy, adequate structural stiffness, and the ability to adapt the design to the user's needs. To meet these criteria, the first essential step was to obtain a precise geometric representation of the ankle and foot region. For this purpose, a 3D

digital copy of the outer foot surface was captured using a Creality Raptor optical/laser scanner.

One of the main advantages of this scanner is its ability to record complex curved surfaces with high accuracy while preserving small anatomical details. Fine surface textures, edge contours, and transition zones are captured without losing contrast, which is particularly important when working with irregular biological shapes. In addition, the device tolerates minor movement during scanning; thus, even if the patient's foot does not remain completely still, the likelihood of motion-related artifacts remains low. This reduces the need for repeat scans and makes the overall data acquisition process more efficient (Fig. 1).

Fig. 1. Foot 3D Scanning Procedure Using a Handheld Structured-Light Scanner.

Based on the collected data, a continuous and metrically accurate 3D anatomical model of the foot was reconstructed. This model served as a reliable foundation for designing the ankle and foot sections of the prosthesis with proper anatomical conformity. It also played a crucial role in later engineering tasks, such as evaluating load distribution, optimizing the cross-sections of structural components, and determining key functional parameters.

Overall, the scanning stage ensured that the design started with geometrically accurate input, which is essential for meaningful mechanical simulations and for defining the final architectural layout of the prosthetic mechanism.

3.2 CAD Modeling

Using the foot geometry obtained from the 3D scan, a fully parametric model of the prosthetic assembly was developed in SolidWorks. During the modeling stage, every element of the foot plate and the active motion module was defined in detail, including their spatial arrangement, contact regions, and expected motion paths. The overall layout of the assembled mechanism is illustrated in Fig. 2.

The assembly consists of several main components:

- Upper Mount Bracket – the top structural mounting element;
- SFU1204 Washer Back – support washer for the leadscrew system;
- SFU1204-300 Leadscrew – a 300-mm ball-screw drive of the SFU1204 type;
- Nema 17 Stepper Motor – the actuator generating the linear motion;
- Motor Mount Bracket – bracket securing the motor in place;
- Hex Flange Bolt – fastener connecting the key joints;
- Base Mount Bracket – lower bracket attaching the foot section;
- Shank Linkage – linkage responsible for transmitting motion to the shank segment;
- Foot Base Plate – the primary structural platform of the foot.

While building the CAD model, all mechanical joints such as revolute, sliding, and rigid mates were defined with their actual parameters. The range of motion for each joint was adjusted to match realistic anatomical limits, and contact regions between components were identified specifically for the subsequent FEM analysis. These preparations ensured that later simulations of stress, strain, and deformation would reflect the behavior of the mechanism as accurately as possible.

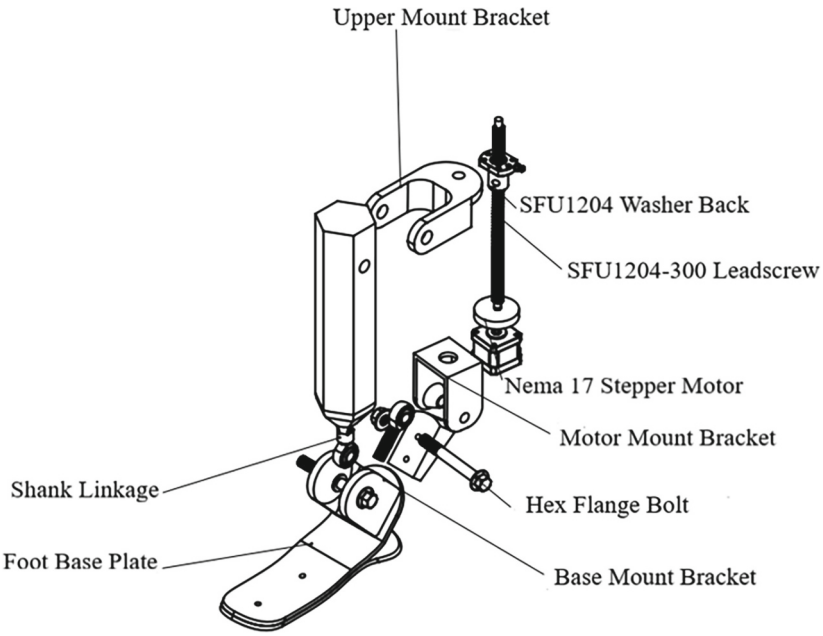

Fig. 2. Mechanical structure of the ankle–foot prosthetic test assembly with all major components labeled (Upper Mount Bracket, SFU1204 Leadscrew system, Nema 17 Stepper Motor, Shank Linkage, and Foot Base Plate).

3.3 Material Properties

At the initial stage of this study, an experimental prototype was fabricated using ABS plastic (Acrylonitrile Butadiene Styrene). ABS is widely used in rapid prototyping due to its affordability, ease of processing, and compatibility with 3D printing technologies. These characteristics made it a practical choice for early-stage development, allowing rapid verification of the prosthesis kinematic layout, joint motion limits, and the functional behavior of the actuation mechanism. Although ABS is not suitable for clinical application, it is well adapted for laboratory-based testing focused on motion and assembly validation.

The ABS material used for the prototype was characterized by the following mechanical properties:

- Young's Modulus (E): 1.8–2.2 GPa
- Poisson's Ratio (ν): 0.34–0.36
- Yield Strength: ~ 40 MPa
- Density: 1.03–1.05 g/cm^3 (Fig. 3)

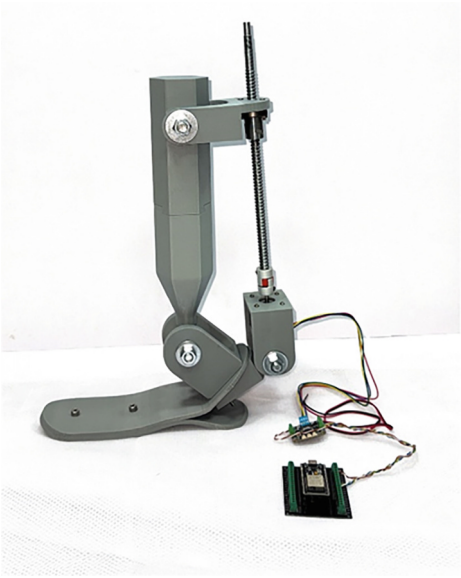

Fig. 3. Experimental prototype of the ankle–foot actuation module equipped with an SFU1204 leadscrew, Nema 17 stepper motor, and control electronics.

These material properties were implemented in SolidWorks Simulation to obtain a preliminary estimate of deformation behavior under static loading. However, the ABS-based simulations were used only for conceptual evaluation and internal consistency checks and are not reported as part of the structural safety assessment.

For the final prosthesis design, ABS does not satisfy the mechanical and fatigue-resistance requirements associated with long-term clinical use. Therefore, AISI 304

stainless steel was selected as the target material for the finite element analysis of the load-bearing structure. Owing to its high strength, good fatigue performance, and environmental stability, AISI 304 is suitable for sustaining repeated body-weight loads during daily activities.

Accordingly, the two materials served distinct roles within the scope of this study:

- ABS was used exclusively for experimental prototyping and validation of the kinematic and actuation architecture;
- AISI 304 stainless steel was used for evaluating the structural integrity and load-bearing performance of the final design.

This staged material strategy reduced development time and cost while enabling systematic refinement of the prosthetic mechanism prior to final structural validation.

3.4 FEA Simulation Setup

To evaluate how the prosthetic assembly responds under load, a static analysis based on the Finite Element Method (FEM) was carried out. The simulation conditions were designed to represent the midstance phase of the gait cycle, a moment when the ankle-foot structure typically experiences the highest vertical load and its stiffness characteristics become most apparent.

Loading Conditions. Three vertical load levels were examined to reflect different real-world scenarios:

- 800 N - representative of users with moderate body weight;
- 1000 N - a commonly reported value in clinical gait studies for normal walking;
- 1200 N - used to represent higher-intensity motion or to include a basic safety margin.

In all cases, the load was applied vertically to the upper surface of the Foot Base Plate, specifically at the central load-bearing region aligned with the shank linkage axis, to clearly represent the force transmission path from the residual limb through the ankle-foot structure during the midstance phase.

To verify that the selected Nema 17 stepper motor can drive the mechanism under peak loading, a simplified torque estimation was performed. For the maximum applied load of 1200 N and the SFU1204 leadscrew (lead = 4 mm), the required driving torque was estimated using standard screw mechanics. The resulting torque demand falls within the achievable range of a Nema 17 motor when appropriate efficiency and safety margins are considered, confirming that the actuation system is capable of moving the assembly during static loading conditions.

Boundary Conditions. To approximate realistic mechanical behavior, the following constraints were applied:

- the bottom surface of the Foot Base Plate was fully fixed, preventing any movement;
- joints between the Shank Linkage and Mount Bracket were assigned degrees of freedom similar to natural joint behavior, allowing controlled motion where appropriate;

– the leadscrew-motor assembly was restricted along its axis to avoid unwanted displacement and to reflect the actual mechanical configuration.

These boundary conditions ensured that the simulated behavior resembled the conditions the device would experience during use.

Mesh Parameters. Because mesh quality strongly influences FEM accuracy, the model was discretized using tetrahedral elements suitable for its complex geometry.

– Average element size: 3–5 mm
– Refined mesh regions: joint interfaces, mounting bolt areas, and the leadscrew thread zone.

These regions were meshed more densely due to their higher likelihood of stress concentration. Mesh convergence was checked to confirm that further refinement would not meaningfully change the results.

4 Results

Static FEM analysis was performed for three loading conditions 800 N, 1000 N, 1200 N to represent the vertical forces typically observed during the midstance phase of walking. All simulations used the material properties of AISI 304 stainless steel. Across the three scenarios, the Von Mises stress consistently accumulated in the central transition region of the foot plate, where geometric changes naturally lead to stress concentration. The maximum stress values increased proportionally with the applied load:

– 800 N: max $\approx 4.95 \times 10^7$ N/m^2 $\rightarrow$ 49.5 MPa
– 1000 N: max $\approx 5.34 \times 10^7$ N/m^2 $\rightarrow$ 53.4 MPa
– 1200 N: max $\approx 7.05 \times 10^7$ N/m^2 $\rightarrow$ 70.5 MPa

The overall stress pattern remained the same in each load case, indicating that the concentration zone is primarily driven by geometry rather than load magnitude. Since AISI 304 has relatively high strength, all obtained values were well below its allowable limits. This means that the structure operated entirely in the elastic region for loads between 800 and 1200 N, with no signs of fatigue or instability. In summary, the simulations confirm that both the geometry and overall stiffness of the design are appropriate, and that AISI 304 is a suitable material for the final prosthesis (Fig. 4).

Displacement under static loading was also evaluated, as it provides insight into the stiffness and general structural stability of the foot component. The same three load levels (800 N, 1000 N, and 1200 N) were simulated using AISI 304 parameters. Because the bottom surface of the foot plate was fully constrained as a fixed support, the minimum displacement was 0 mm in every case. The maximum deformation occurred near the upper portion of the structure, close to the leadscrew attachment area. As expected, displacement increased steadily with higher loads:

– 800 N: max $\approx 9.36 \times 10^{-2}$ mm $\rightarrow$ 9.36 MPa
– 1000 N: max $\approx 1.21 \times 10^{-1}$ mm $\rightarrow$ 1.21 MPa

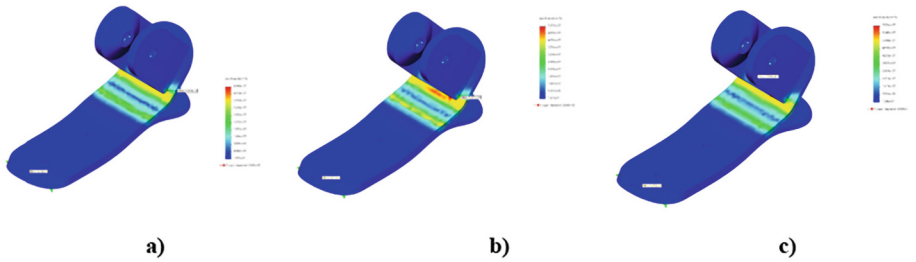

Fig. 4. Von Mises stress distribution at different loading conditions: a) 800 N, b) 1000 N, c) 1200 N.

– 1200 N: max $\approx 1.49 \times 10^{-1}$ mm $\rightarrow$ 1.49 MPa

All displacement values fell within the elastic range for AISI 304, with no indication of plastic deformation or structural instability. The deformation pattern remained consistent across all simulations, with the largest deflection appearing at the upper transition region near the ankle joint interface. This behavior suggests that the overall stiffness and load-bearing capacity of the design are sufficient for clinical and everyday loading conditions (Fig. 5).

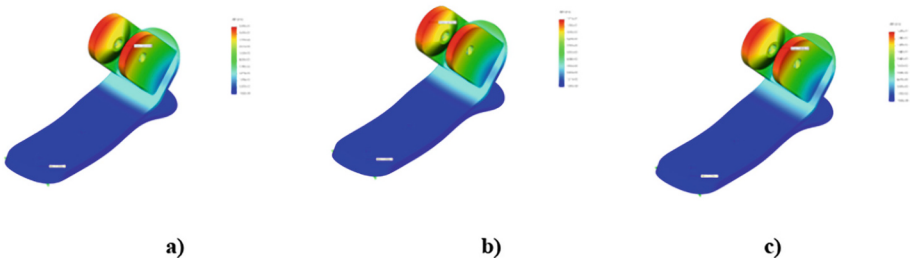

Fig. 5. Total displacement distribution of the ankle–foot assembly: a) 800 N, b) 1000 N, c) 1200 N.

Equivalent strain was assessed for the same three loading conditions. In all cases, the highest strain values occurred in the midsection of the foot plate the region where the cross-section transitions and where both stress and strain naturally tend to concentrate. The maximum strain values were:

– 800 N: max strain $\approx 1.05 \times 10^{-4} \rightarrow$ 1.05 MPa
– 1000 N: max strain $\approx 1.49 \times 10^{-4} \rightarrow$ 1.49 MPa
– 1200 N: max strain $\approx 1.55 \times 10^{-4} \rightarrow$ 1.55 MPa

Given the high elastic modulus of AISI 304 and its resistance to plastic deformation, all recorded strain values remained well within the material's elastic range. The strain maps for the three load cases displayed nearly identical patterns: peak strain in the central region and gradually diminishing values toward the outer sections. These results show that strain increases in a linear fashion with loading and confirm that AISI 304 can comfortably withstand the simulated forces without approaching critical deformation

levels. This indicates that the foot component has sufficient structural rigidity for long-term use (Fig. 6).

5 Discussion

In this study, the mechanical behavior of the ankle–foot prosthesis was evaluated under three static loading conditions 800 N, 1000 N, and 1200 N using finite element analysis (FEA). All numerical simulations were performed using the material properties of AISI 304 stainless steel, which represents the intended material for the final load-bearing design. The physical prototype, manufactured from ABS plastic, was used solely for experimental validation of kinematic behavior and assembly feasibility.

Across all load cases, the predicted stress, displacement, and equivalent strain values increased proportionally with the applied force while remaining well within the elastic range of AISI 304. The maximum Von Mises stress increased from approximately 49 MPa to 70 MPa, with stress consistently concentrated in the mid-section transition zone of the foot plate. This localization is primarily governed by geometric changes in cross-section and represents a predictable stress concentration rather than an indication of structural inadequacy. Nevertheless, this region may be considered for local geometric refinement or reinforcement in future design iterations.

The displacement results further indicate sufficient structural stiffness. Maximum deflections remained very small, ranging from approximately 0.093 mm to 0.149 mm, with the largest values observed near the upper region of the structure close to the actuation assembly. All deformations remained elastic for AISI 304, suggesting that the prosthesis geometry can safely accommodate the investigated loading conditions.

Equivalent strain values ($\approx 1.05 \times 10^{-4} - 1.55 \times 10^{-4}$) followed the same spatial distribution as the stress field and showed no indication of plastic behavior. The consistency between stress, displacement, and strain responses supports the validity of the numerical model and confirms that the simulated structural response is physically reasonable.

While the ABS prototype is not intended for structural load-bearing or long-term use, it served its purpose as a laboratory platform for verifying the kinematic layout, joint motion, and actuation concept. Conclusions regarding clinical performance and long-term durability are therefore drawn exclusively from the AISI 304 simulations. Overall, the results demonstrate that the proposed geometry and mechanical layout are

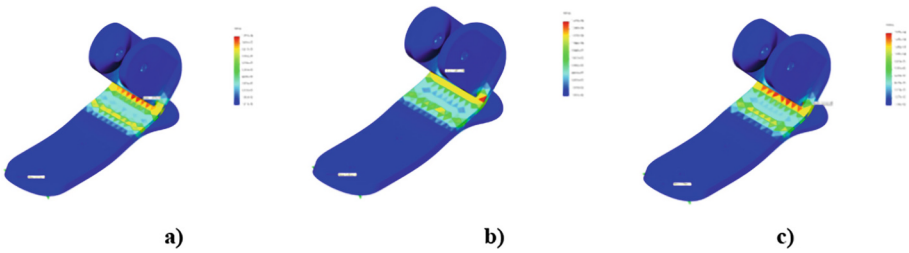

Fig. 6. Equivalent strain distribution for the simulated load cases: a) 800 N, b) 1000 N, c) 1200 N.

well suited for further development, provided that a high-strength material such as AISI 304 stainless steel or a carbon-based composite is employed in the final prosthesis design.

6 Conclusion

This study evaluated the mechanical behavior of an ankle-foot prosthesis design under static loads of 800 N, 1000 N, and 1200 N using finite element analysis (FEA). The simulations showed that the maximum Von Mises stress reached approximately 70.5 MPa under the highest load condition, with both stress and equivalent strain consistently concentrated in the mid-section transition zone of the foot plate. This confirms that the structural response is primarily governed by the geometric characteristics of the design.

When the results are interpreted with respect to material limitations, a clear distinction emerges between the experimental prototype and the intended final material. For the ABS prototype, the calculated stress levels exceed the typical yield strength of ABS ($\approx$ 40 MPa), indicating that structural safety cannot be ensured under the investigated loading conditions. Therefore, the ABS-based prototype should be considered suitable only for early-stage kinematic testing and verification of the mechanical layout, rather than for load-bearing or clinical use.

In contrast, when the same loading scenarios are evaluated using the material properties of AISI 304 stainless steel, all computed stress, displacement, and equivalent strain values remain well within the elastic range. This confirms that structural safety under the considered loads is validated exclusively for AISI 304, making it an appropriate candidate for the final prosthesis design.

Overall, the FEA results demonstrate that the proposed geometry and mechanical configuration are fundamentally sound, while also highlighting the necessity of employing a high-strength material for real-world application. Future work will focus on dynamic simulations over a full gait cycle and further optimization of material distribution to improve long-term durability and performance.

Acknowledgement. This research was funded by the Science Committee of the Ministry of Science and Higher Education of the Republic of Kazakhstan within the framework of the program BR24992820.

References

1. Akhmejanov, S., Zhetenbayev, N., Sultan, A., Nurgizat, Y., Sergazin, G., Ozhikenov, K.: Engineering an active ankle-foot prosthesis: conceptual design for enhanced walking dynamic. In: Carbone, G., Quaglia, G. (eds.) Proceedings of I4SDG Workshop 2025 - IFToMM for Sustainable Development Goals. I4SDG Mechanisms and Machine Science, vol. 180. Springer, Cham (2025). https://doi.org/10.1007/978-3-031-91179-8_19
2. Akhmejanov, S., et al.: Foot and ankle prosthetics using artificial intelligence: innovative developments and conceptual solutions. In: Laribi, M.A., Carbone, G., Pisla, D., Zeghloul, S. (eds.) New Trends in Medical and Service Robotics. MESROB Mechanisms and Machine Science, vol. 186. Springer, Cham (2025). https://doi.org/10.1007/978-3-031-96081-9_22

3. Sultan, A., Zhetenbayev, N., Nurgizat, Y., Ayazbay, A., Ozhikenov, K., Sergazin, G.: Analysis of the lower limb prosthesis market and a research of advanced prosthetic methods. In: Laribi, M.A., Carbone, G., Pisla, D., Zeghloul, S. (eds.) New Trends in Medical and Service Robotics. MESROB Mechanisms and Machine Science, vol. 186. Springer, Cham (2025). https://doi.org/10.1007/978-3-031-96081-9_19
4. Staros, A.: The sach (solid-ankle cushion-heel) foot. In: Orthotics and Prosthetics (1957)
5. Gitter, A., et al.: Biomechanical analysis of the influence of prosthetic feet on below-knee amputee gait. J. Rehabil. Res. Dev. **28**(4), 1–8 (1991)
6. Sasaki, K., et al.: The development and testing of a modified natural rubber solid ankle–cushion heel prosthetic foot for developing countries. J. Rehabil. Assist. Technol. Eng. **4**, 2055668317712978 (2017)
7. Houdijk, H., et al.: Energy storing and return prosthetic feet improve step length symmetry but not walking economy in people with transtibial amputation. J. Neuroeng. Rehabil. **15**, 76 (2018)

Anomaly Detection in Scale Model Trains Using LSTM Neural Networks

Jose Emiliano Lopez-Ramirez, Tania Elizabeth Sandoval-Valencia(✉), Hannia Rangel-Escobar, Eric Leonardo Huerta-Manzanilla, J. E. Basaldúa-Sánchez, and Juan Carlos Jauregui-Correa

Faculty of Engineering, Autonomous University of Queretaro, Santiago de Queretaro 76010, Mexico
tania.sandoval@uaq.mx

Abstract. This study presents an analysis for detecting anomalies in model trains using LSTM (Long Term Short Term Memory) neural networks. A database compiled in a laboratory at the Autonomous University of Querétaro was used, containing 6 blocks of 19 experimental runs, with a total of 114 tests, including accelerometer data, angular velocities, and motor current. Z-score normalization and automatic anomaly labeling were employed, using a threshold of 3.5 standard deviations from the baseline. The LSTM model used has two layers: one with 64 units and the other with 32. The model was trained with the Adam optimizer and stopped early using EarlyStopping. Data fragments from 100 samples were used to train the model to learn patterns, and class weights were adjusted to ensure that less frequent anomalies were not ignored. The model correctly identified most cases with an accuracy between 97.66% and 95.71%, detected almost all anomalies with a recovery rate between 98.00% and 96.00%, and achieved an overall F1 score between 0.90 and 0.77. The LSTM model was also compared with an Isolation Forest algorithm to assess their performance. Therefore, these results support the claim that the proposed neural network can be applied to the preventive monitoring of railway systems.

Keywords: Anomaly · LSTM · Scale Model Train · Neural Network · Automatic Detection · Isolation Forest

1 Introduction

Railway systems are a fundamental component of modern transport infrastructure, where safety and operational reliability are crucial to ensuring the efficient movement of passengers and goods [1]. Mechanical failures, excessive wear, or abnormal operating conditions can lead to service disruptions, infrastructure damage, and even accidents [2]. Therefore, the ability to detect anomalies in railway systems early is key to monitoring system health and planning predictive maintenance [3].

Traditional maintenance approaches in the railway sector typically rely on scheduled inspections. However, the traditional method has significant limitations, as it may fail to detect failure patterns, which in some cases lead to unnecessary maintenance, increased

© The Author(s), under exclusive license to Springer Nature Switzerland AG 2026
A. Chaker et al. (Eds.): EFIMMS 2026, MMS 205, pp. 419–430, 2026.
https://doi.org/10.1007/978-3-032-22270-1_41

operating costs, and system downtime. Consequently, data-driven and algorithm-based approaches have become increasingly relevant thanks to the widespread availability of sensors and advances in machine learning techniques [4]. Anomaly detection enables the identification of abnormal patterns by modeling the system's operation.

Deep learning techniques, a subset of machine learning, have proven to be an excellent tool for analyzing complex data and time series. Recurrent Neural Networks (RNNs), especially Long-Term Short-Term Memory Networks (LSTMs), have been used for time series analysis due to their ability to capture short- and long-term temporal dependencies [5]. These characteristics make LSTMs useful for condition monitoring and anomaly detection applications in dynamic systems.

Several studies have demonstrated the efficiency of LSTM-based models for detecting faults or anomalies in railway systems by analyzing signals such as vibrations, electrical current, or other relevant dynamic factors [6]. The main advantage of these models lies in their ability to learn automatically from the data, which reduces the need for manual intervention and allows for the detection of more complex patterns that might go unnoticed with traditional statistical methods.

Scale models of railway systems allow for controlled, reproducible, and safe experiments, facilitating the evaluation of different scenarios under varying conditions that would be very difficult and costly to implement in full-scale systems. These scale models are also very useful for validating data collection methods, preprocessing techniques, and machine learning models before their implementation in full-scale applications [7].

In this context, this work proposes the use of LSTM neural networks for the automatic detection of anomalies in a scale railway system installed in a laboratory at the Faculty of Engineering of the Autonomous University of Querétaro (UAQ), Mexico. Furthermore, the performance of the proposed method is compared with an Isolation Forest model, which detects unusual points and isolates them. Nowadays, it is an algorithm commonly used because of its speed and big data efficiency. Data collection utilizes multiple sensors integrated into a scale model railway vehicle, including an accelerometer, angular velocity sensors, and motor current measurements.

The proposed approach is based on the analysis of time series obtained during multiple experimental runs using one of the 19 collected datasets.

2 Methodology

This section describes the scale model railway system used in the study, along with the instrumentation employed for data collection.

Next, the data logging process is explained, encompassing multiple experiments in which accelerometer signals, angular velocity measurements, and motor current were recorded.

The preprocessing steps are also detailed, including normalization using z-scores, the selection of a reference dataset, and automatic anomaly labeling based on statistical thresholds. Furthermore, the construction of the time sequences used as input for the learning models is described.

Finally, the architecture of the LSTM neural network and the associated training strategy are presented. Key aspects such as class imbalance handling, the optimization

method, layer configuration, and the regularization techniques implemented for anomaly detection are discussed. In addition, an Isolation Forest model was implemented as a comparative baseline and evaluated under the same experimental conditions and dataset partitioning as the LSTM model. This comparative analysis was conducted to contrast detection performance and to confirm the superior capability of the LSTM architecture in capturing the temporal dynamics and complexity of the railway system data.

2.1 Scale Model Railway System

The study was conducted using a 1:20 scale model railway system designed to simulate the dynamic operating conditions of a train in a controlled manner. The scale model railway track is a closed, horizontal, "beta"-shaped circuit. The track is fixed to a structural base of plywood and is composed of 5 mm diameter steel rails, reaching a total length of 13.524 m (Fig. 1).

Fig. 1. Scale railway system.

Data acquisition was performed using a series of sensors integrated into the scale model railway vehicle (Fig. 2), specialized in monitoring different dynamic variables.

- Accelerometer and gyroscope: Located on a single chip in the central part of the vehicle, they measure accelerations (lateral, vertical, and longitudinal in g's) and angular velocities (°/s). This data is used for vibration analysis and to detect roll, pitch, and yaw movements.
- Current sensor (Hall effect): Measures the current (A) flowing to the motor. This information is correlated with the tangential forces and torque on the drive wheels.
- Infrared optical sensor: Together with a black-and-white variation strip installed on the track, it measures the vehicle's instantaneous position and velocity, generating pulses correlated with the time between variations.
- Rotary encoder: Measures the angular speed of the traction wheels, generating pulses (pulses/ms) that require post-processing for conversion.

During each of the 19 experimental repetitions, the sensors continuously recorded the dynamic parameters. The raw data were stored on the SD card in .mat format.

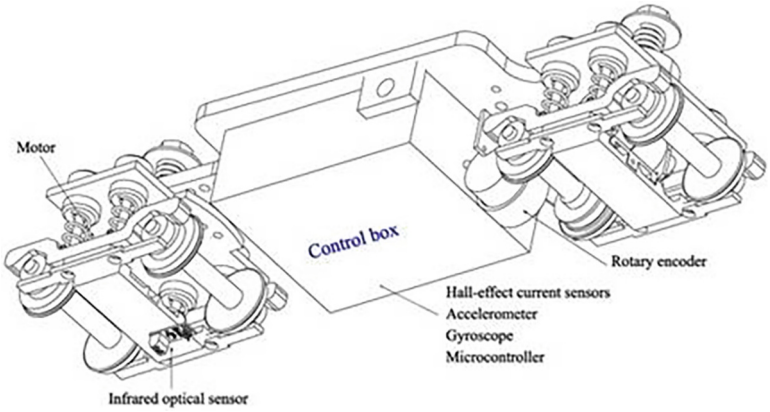

Fig. 2. Railway vehicle [8].

2.2 Experimental Configuration

The tests were conducted using a 2^k Full Factorial Experimental Design (Table 1). This indicates that tests were performed controlling two variables of interest, each with three levels (low, medium, and high). Factor A represents the speed of the rail vehicle, with low (−1, 0.75 m/s), medium (0, 1.4 m/s), and high (1, 1.4 m/s) levels. Factor B shows the starting and stopping areas of the experiment; in this case, −1 indicates that the test started on the straight section of the track and stopped at the first curve, and 1 indicates that the test started on the curved section of the track and stopped on the straight section.

Table 1. Experimental matrix.

Run	A	B
Exp1Rec_Cur	0	−1
Exp2Rec_Cur	−1	−1
Exp3Rec_Cur	1	-1
Exp4Cur_Rec	0	1
Exp5Cur_Rec	-1	1
Exp6Cur_Rec	1	1

The experimental matrix (Table 1) indicates that the first run was performed at a speed of 0.75 m/s, the second at 1.15 m/s, and finally at 1.4 m/s, all starting on the straight section of the track and braking at the beginning of the first curve. The second experimental stage shows that the first run was performed at a speed of 0.75 m/s, the second at 1.15 m/s, and finally at 1.4 m/s, all starting on the curved section of the track and braking on the straight section. In each experiment, 19 trials were conducted.

2.3 Statistical Normalization and Automatic Anomaly Labeling

Statistical normalization and automatic anomaly labeling were performed based on the anomaly detection code and methodology, using data obtained from multiple experimental runs. Eight features were used for the analysis: translational speed, angular velocities, and motor current: VelRueTra_SisFebLab, AceXTre_SisFebLab, AceYTre_SisFebLab, AceZTre_SisFebLab, VelXAngTre_SisFebLab, VelYAngTre_SisFebLab, VelZAngTre_SisFebLab, and CorrMot_SisFebLab.

The data were normalized using the Z-score, with the mean (μ) and standard deviation (σ) calculated from the baseline for runs 1 through 5 using the following expression.

$$Scaled\ data = \frac{Data - \mu}{\sigma} \tag{1}$$

The automatic labeling of anomalies was performed by identifying systematic deviations from the baseline, thus establishing a deviation of $K = 3.5$.

2.4 Generation of Time Sequences for the LSTM Model

Generating time sequences is crucial for preprocessing time series data for recurrent neural network (RNN) models such as LSTMs. Its purpose is to transform continuous tabular data into a three-dimensional format (samples, time step, features) that the model can interpret as a time-dependent sequence.

This process was carried out using the sliding window method. This method involves taking a fixed, sequential portion of input data (X) and associating it with a single output data point (Y).

In the window size, the length of the time sequence was set to 100, meaning that to predict whether a data point is not normally distributed, the model observes the 100 immediately preceding time points, including the current point.

Similarly, the "create_sequence" function was implemented to iterate over the preprocessed dataset, which consists of the Z-score scaling and labels. For each iteration, a window of 100 consecutive samples from the eight input features is extracted as the sequence of input. This feeds the LSTM layer with the time history of the kinematic and electrical variables.

Similarly, the sequence of labeling does not treat the sequence as a complete whole, but rather as the anomaly state of the last data point in that window. This approach transforms anomaly detection into a binary classification based on the history of the window.

Before starting the generation of the time sequences, the data were divided into training, validation, and test sets according to the experimental runs, which are presented in Table 2.

After applying the sliding window method (size 100), the final dimensions of the data tensors are presented below in Table 3.

Table 2. Experimental runs.

Dataset	Identifier	Included runs
Training	train_ids	1 to 14
Validation	val_ids	15 to 16
Test	test_ids	17 to 19

Table 3. Final dimensions.

Dataset	Shape (samples,time steps, features)	Included runs
Training (X_train, Y_train)	(162387,100,8)	Sequences used to train the model.
Validation (X_val, Y_val)	(24848,100,8)	Sequences used to monitor loss and trigger early stopping during training.
Test (X_test, Y_test)	(41774,100,8)	Independent sequences used for the final, unbiased evaluation of the model performance

2.5 Architecture and Training of the LSTM Neural Network

A Long Term Memory Recurrent Neural Network (LSTM) was used to classify whether a sequence of 100 points corresponded to a normal (0) or abnormal (1) sample.

The proposed architecture was implemented as a sequential Keras model, specifically designed to process sequential information from multivariate time-domain signals. A 64-unit LSTM was used as the input layer, configured with an input_shape of (100,8). This corresponds to the length of the time window (100 time steps) and the total number of features extracted at each time step. The return_sequences = true option was enabled to preserve the sequential nature of the information. This allowed the layer to produce a complete sequence of outputs and facilitated the chaining of multiple LSTM layers, which is essential for the hierarchical extraction of complex time patterns.

After that, a dropout layer with a 20% rate was incorporated, which acts as a regulatory mechanism by randomly deactivating a fraction of the neurons during training. This strategy makes the neural network learn more robustly and generally, avoiding excessive dependence on individual neurons, which helps significantly reduce the risk of overfitting, especially when the scenario involves very noisy data or limited training sets.

The latent representation of the sequence was obtained using a second LSTM layer with 32 units and return_sequences = False. This configuration allows the network to condense the information from the entire 100-step time sequence into a single feature

vector, which corresponds to the last hidden state. This vector acts as a dynamic summary of the signal's behavior and is used as input for the final classification stage.

The output layer consisted of a dense layer with a Sigmoid activation function and a single neuron, suitable for binary classification tasks. This function converts the model's output into a continuous value ranging from 0 to 1. This value can be understood as the probability that the evaluated sample is an anomaly. In total, the model has 31,127 trainable parameters, representing a suitable balance between modeling capacity and computational complexity.

The training process was conducted as a supervised classification problem, explicitly taking into account the marked class imbalance that characterizes anomaly detection systems. Adam was the optimization algorithm used. It is frequently used in deep learning applications because it has fast convergence performance and can dynamically modify the learning rate for each model parameter.

The binary_crossentropy loss function was chosen, as it is suitable for binary classification situations when a sigmoid activation function is used in the final layer. The accuracy metric was used to monitor the model's performance throughout the training, allowing for the evaluation of the proportion of correct classifications at each epoch.

Regarding the training parameters, a maximum of 50 epochs and a batch size of 64 were established. These values provided a suitable balance between gradient stability and computational efficiency. To address this class imbalance, a class weighting scheme was used, in which the minority class corresponding to anomalies received greater weight. This resulted in a heavier penalty for classification errors in this class and encouraged the model to learn to identify anomalous events effectively.

Finally, as the main regulatory mechanism during training, an EarlySropping callback with a patience of 5 epochs was incorporated. This method allows for monitoring of attrition in the validation set and automatically stops training when no improvement is observed for five consecutive epochs, restoring the model weights that achieved the best performance. This strategy not only reduces the risk of overfitting but also optimizes computation time and contributes to obtaining a model with better generalizability.

2.6 Comparative Anomaly Detection Using Isolation Forest

Isolation Forest is a non-supervised algorithm used to detect anomalies in data of scale model trains. Information is organized in temporal windows, which helps to analyze how the system behavior changes over time instead of evaluating individual values. To ensure consistency with the proposed LSTM-based approach, the same window-based data representation is used; however, due to the structural limitations of Isolation Forest, each temporal window is flattened into a single feature vector. This model is trained just with normal values and learns the pattern of normal operation of the system. Then it identifies as anomalies the values that deviate a lot in the pattern. Finally, the results are represented in statistical graphs over the original sign. It is easier to appreciate the moments where the system presents an anomaly.

2.7 Consistent Preprocessing and Window-Based Data Representation

To ensure a fair comparison between all anomaly detection models considered in this study, a consistent preprocessing strategy was applied to the experimental data. Measurements were obtained from multiple runs, which were uploaded to the model in an Excel file where they were combined into a single dataset, preserving their temporal order. This is a common structure in both models that helps to prevent significant differences in data preparation.

2.8 Comparative Evaluation Criteria and Performance Validation

Both models were tested using the same data representation and identical experiment conditions. They were mostly evaluated using basic and standard metrics such as accuracy, F1-score, recall, and confusion matrices. All these metrics were generated using synthetic anomaly labels for evaluation. In addition, qualitative validation was performed through a visual inspection of each model's ability to identify abnormal operating conditions at the scale of the railway system.

3 Results

The LSTM model achieved an accuracy of 97.35% in the test set, confirming its ability to distinguish between normal and anomalous behavior. The loss and accuracy curves reflect stable convergence during training: the loss decreased progressively until stabilizing around 0.13, while the validation accuracy remained in the 96–97% range. This behavior indicates that the model did not overfit, thanks in part to Early Stopping and Dropout regularization (Fig. 3).

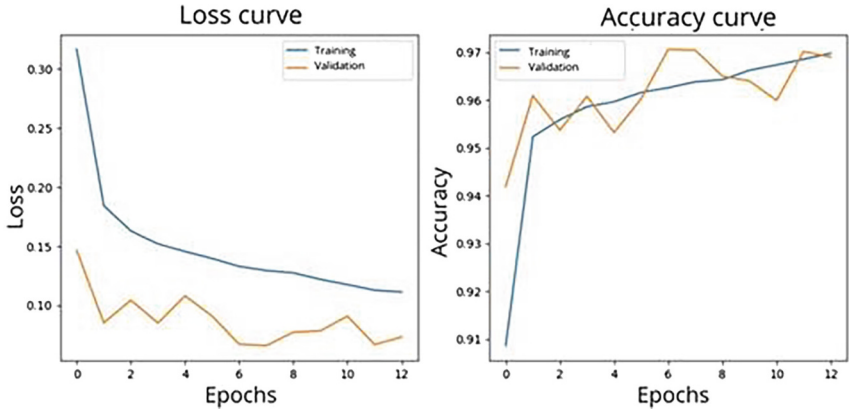

Fig. 3. The curves show a steady decrease in loss and a continuous increase in accuracy, indicating good learning and strong model generalization.

The loss curve shows a progressive decrease in both the training and validation data, indicating that the model is learning to minimize prediction error in a stable manner.

On the other hand, the accuracy curve shows a steady increase in the model's accuracy, with similar values between training and validation, suggesting good generalization capabilities without overfitting. Taken together, both curves reflect a successful training process, with continuous improvement in model performance (Fig. 4).

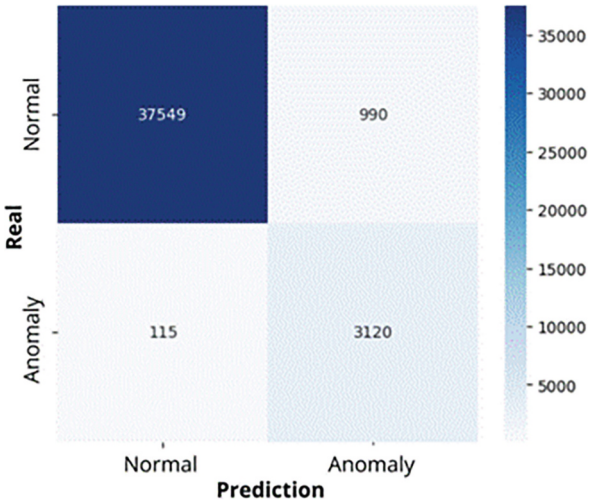

Fig. 4. The confusion matrix indicates that the algorithm performs well; thanks to this, we can see the high sensitivity for detecting anomalies and the low false negative rate.

The confusion matrix reveals that the model correctly classified 37,549 normal cases (true negatives) and 3,120 true anomalies (true positives). On the other hand, 990 false positives and 115 false negatives were recorded. These values reflect a high level of sensitivity (recall) in anomaly detection, as well as robust specificity. Table 4 details the metrics by class: for the normal class (0), a precision of 1.00, a recall of 0.97, and an F1-score of 0.99 were obtained; for the anomalous class (1), the values were 0.76, 0.96, and 0.85, respectively. The overall weighted F1-score was 0.97.

Table 4. The classification model obtained the following values per class.

Page	Precision	Recall	F1-score	Support
0	1.00	0.97	0.99	38539
1	0.76	0.96	0.85	3225
Accuracy			0.97	41774
Macro avg	0.88	0.97	0.92	41774
Weighted avg	0.985.0	0.97	0.97	41774

In the motor current time series (Fig. 5), the detected anomalies (red dots) coincide with extreme signal peaks, confirming that the model can identify significant deviations

from expected behavior. The concentration of anomalies in the initial segment of the series suggests that atypical events occurred during that phase, possibly associated with sudden starts or transients. This temporal localization capability is valuable for real-time monitoring and predictive maintenance applications.

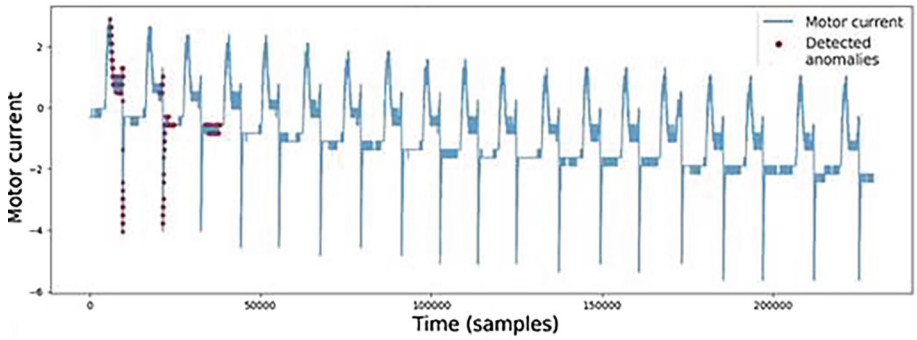

Fig. 5. Time series of the motor current detected anomalies (red dots) from a laboratory railway system dataset.

The graph shows the evolution of the motor current over time, where the red dots indicate anomalies detected by the LSTM model. These anomalies are concentrated in the initial part of the time series, suggesting that significant deviations from normal behavior occurred during that period. The model identifies these points as out of the ordinary, possibly due to abrupt spikes or sharp drops in the signal. This visualization allows for the precise location of critical moments in the system's operation.

The comparison of the six experimental blocks (Table 5), each with 19 runs, shows high consistency between the statistical descriptors and performance metrics, confirming the stability of the experimental process. This consistency supports the representativeness of each block and reinforces the robustness and generalizability of the proposed methodology.

Table 5. Performance Evaluation of the LSTM model.

Block	Accuracy
1	0.9729
2	0.9739
3	0.9766
4	0.9760
5	0.9631
6	0.9575

The results obtained with the Isolation Forest (Table 6) model reveal limitations in detecting anomalies within the analyzed dataset, especially in scenarios with high

dynamic variability. Although the model identifies general deviations, its performance is inferior to that of the LSTM-based approach.

Table 6. Performance Evaluation of the Isolation Forest Model.

1	0.896
2	0.886
3	0.876
4	0.897
5	0.895
6	0.883

Across the six experimental blocks, the LSTM model consistently achieved higher accuracy (0.963–0.977) than Isolation Forest (0.876–0.897), indicating greater stability and robustness. Although Isolation Forest identified general deviations, its lower performance confirmed its limitations in capturing complex temporal dynamics, underscoring the advantage of the LSTM-based approach.

4 Conclusions

A robust and advanced framework for anomaly detection in scale model railway systems was developed based on the sequential modeling capabilities of Long Short-Term Memory (LSTM) neural networks. The experimental validation confirmed not only the effectiveness of the proposed approach under controlled laboratory conditions but also its strong potential for implementation in real-world railway monitoring and Predictive Maintenance (PdM) strategies.

The success of the proposed methodology relies on a reproducible data processing pipeline and an appropriate network architecture. The use of a sliding window of 100 samples proved to be a key methodological element, enabling the model to capture temporal dependencies and precursor patterns associated with anomalous behavior. This temporal modeling capability provides a clear advantage over traditional approaches based on static thresholds or point-wise analysis.

From a performance perspective, the LSTM model demonstrated high reliability, achieving an accuracy of 97.35% on the test dataset and a recall of 96% for the anomalous class. This high sensitivity is particularly critical for railway safety applications, as it minimizes false negatives and ensures timely detection of abnormal operating conditions. Additionally, the model captured approximately 73% of the variability associated with anomalous events, reinforcing its usefulness for quantitative risk assessment.

A comparative analysis with the Isolation Forest algorithm further highlighted the advantages of the proposed LSTM-based approach. While Isolation Forest was able to detect general deviations, its performance was consistently lower across all experimental blocks and it showed limitations in capturing complex temporal dynamics. In contrast, the LSTM model exhibited greater stability, robustness, and superior detection accuracy, confirming its suitability for time-dependent railway system monitoring.

Overall, the results demonstrate that LSTM neural networks represent a more effective and reliable solution for anomaly detection in railway systems than non-sequential methods, particularly in scenarios characterized by dynamic and temporally correlated behavior.

Competing Interests. The author(s) has no competing interests to declare that are relevant to the content of this manuscript.

References

1. Sanz-Bobi, J., Martínez-Llop, P., Marcos, P., Jiménez, Á., Fernández, J.: Prediction of degraded infrastructure conditions for railway operation. Sensors (Basel, Switzerland). **24** (2024). https://doi.org/10.3390/s24082456
2. Fomin, O., Burlutskyi, O., Khara, M., Rybachenko, Y.: Cause and effect relationships of failures in the functioning of structural components of railway rolling stock. Вісник Східноукраїнського національного університету імені Володимира Даля. https://doi.org/10.33216/1998-7927-2025-290-4-83-89 (2025)
3. López Galdo, A., Gómez García, M.J., Martínez Olmos, P., Castejón Sisamón, C.: Monitorización de estado de ejes ferroviarios mediante procesamiento con redes neuronales convolucionales y temporales de señales vibratorias. Revista Iberoamericana de Ingeniería Mecánica. **27**(1), 3–12 (2023)
4. Chandola, V., Banerjee, A., Kumar, V.: Anomaly detection: a survey. ACM Comput. Surv. **41**(3), 1–58 (2009)
5. Hochreiter, S., Schmidhuber, J.: Long short-term memory. Neural Comput. **9**(8), 1735–1780 (1997)
6. Zhao, R., Wang, D., Yan, R., Mao, K.: Deep learning and its applications to machine health monitoring. Mech. Syst. Signal Process. **115**, 213–237 (2019)
7. Sandoval Valencia, T.E.: Information about a laboratory railway system: a dataset that integrates dynamic parameters and images of wheel wear. Mendeley Data. **V1** (2025). https://doi.org/10.17632/pz9s2ph94d.1
8. Sandoval-Valencia, T.E., Hurtado-Hurtado, G., Huerta-Manzanilla, E.L., Ruiz-Robles, D., Morales-Velázquez, L., Jáuregui-Correa, J.C.: Analysis of 3k experiments applied to railway braking: influence of contaminants and train speed. Vehicles. **6**(4), 1886–1901 (2024). https://doi.org/10.3390/vehicles6040092

A Review of Additively Manufactured Polymer and Steel Gears - Tribology and Modeling

Mahmood M. Mustafa[1(✉)], Mustafa A. Ali[1], Rania W. Abdula[1], Omar D. Mohammed[2], and Haitham M. Wadullah[1]

[1] Northern Technical University, Mosul, Iraq
mahmoodmahamd5@ntu.edu.iq
[2] School of Science and Technology, Örebro University, Örebro, Sweden

Abstract. Gears and sliding mechanical contacts are indispensable elements in power-transmission systems, where material selection, tribological behavior, thermal stability, and fault prediction govern functional life and reliability. The current article reviews three major research directions: (1) mechanical and tribological characteristics of additively manufactured polymers used in gear applications, (2) steel-on-steel tribological systems and the integration of artificial intelligence (AI) and physics-informed machine learning (PIML), and (3) advancements in gear dynamics of combined material gears, and fault detection methods. The additive manufacturing process, fused deposition modeling (FDM) especially, has facilitated fast production of complex-shaped gears using polymers; yet these gears lack the capability to handle loads owing to their anisotropic property, low stiffness, thermal sensitivity, and surface roughness**.** However, gears made of polymers offers light weight and self-lubrication. The steel gears offer far greater loading capability, stiffness, durability under fatigue loading, and thermal stability; yet their noise level, weight, and machinability can be prohibitive factors at times**.** Emerging combined material designs attempt to merge the benefits of both materials by improving heat dissipation and wear resistance. Meanwhile, tribological research—especially involving steel systems—has advanced through machine learning and physics-informed neural networks (PINN) architectures that enhance friction and wear prediction.

Conventional vibration analysis techniques for gear diagnosis have been expanded to artificial intelligence-based systems with the capability of identifying variances in worn-out mechanisms, simulating crack growth patterns, and solving equations for distributed damage models.

Keywords: Gears · Tribology · Additive manufacturing · Bio composites · Data driven · Dynamic modeling

1 Introduction

Power transmission systems in automobiles, aircraft, and robotic applications utilize the efficiency and reliability of gears to a large extent [1, 2]. Efficiency of gears cannot be dissociated with either material sciences or lubrication or accuracy of geometry. Conventional gears made of steel were preferred for high-speed and high-loading applications

© The Author(s), under exclusive license to Springer Nature Switzerland AG 2026
A. Chaker et al. (Eds.): EFIMMS 2026, MMS 205, pp. 431–439, 2026.
https://doi.org/10.1007/978-3-032-22270-1_42

because of their toughness and well-defined life under fatigue conditions. The new era of engineering requires efficiency and noise reduction and lightweight designs, leading to growing applications and research on gears made of polymers and engineered using additive manufacturing techniques [3]. At the same time, a paradigm shift can be observed in the field of Tribology. Conventional empirical models of wear and simulations using Finite Element (FE) analysis increasingly tend to be extended and completed by data-driven models [4, 5]. Physics-Informed Neural Networks (PINNs) were introduced with a goal to overcome black box models of artificial intelligence and provide a systematic framework that correctly incorporates physical knowledge with large amounts of data [6–8]. The objective of this particular review paper is to integrate knowledge related to mechanical properties of AM polymers, development of artificial intelligence in steel tribology studies, and state-of-the-art studies on combined material gear systems.

2 Additively Manufactured Polymers: Mechanical and Tribological Behavior

2.1 Material Composition and Processing

The commonly used polymers for gear systems can be either Polyamide (Nylon 6 or PA12), Acrylonitrile Butadiene Styrene (ABS), or Polycarbonate (PC) with carbon or glass fibers for added mechanical strength [1, 2]. Although these materials make it easy to achieve lightweight and noise-free operation, they show large temperature-dependent effects such as creep and viscoelasticity. FDM (Fused Deposition Modeling), which is the main AM technique to date, offers novel mechanical property challenges. In particular, parametric research was conducted by Zhang et al. [3] to emphasize how component fabrication with an FDM system promotes anisotropic properties of strength that are much greater in the direction of the filament rather than perpendicular to it. Apart from these factors, other manufacturing factors like nozzle temperature or even filament color were revealed to affect component tribological properties or microstructure [4–6].

2.2 Tribological Characteristics

The tribology of AM polymers fundamentally differs from those of metallic systems. The dominant failure mode is often adhesive wear, driven by low surface hardness and material transfer, research by Hanon et al. [7] and Stoimenov et al. [8] indicates that FDM components are uniquely susceptible to delamination wear and have distinct static and kinetic friction profiles compared to bulk polymers see Fig. 1. Environmental sensitivity is also a major factor; for instance, fiber-reinforced composites behave differently in varying environmental conditions [9], and surface modifications are often required to improve performance [10].

3 AI-Enhanced Predictive Modeling and Steel Tribology

3.1 Data-Driven vs. Classical Tribology

Steel gears are susceptible to failure modes like micro-pitting, scuffing, and rolling contact fatigue when operating under boundary to elastohydrodynamic lubrication (EHL) regimes. Recent research has shown that AI models are superior to classical models,

which rely on hardness and surface finish to predict wear [11, 12]. This paradigm shift is comprehensively outlined by Rosenkranz et al. [13], who position AI as a transformative tool across tribology, while Shah et al. [14] specifically documents its breakthroughs in wear prediction. Data-driven methods that use inputs like surface roughness and time-series signal data often outperform traditional regression when predicting wear volume and friction coefficients [15–17] with recent studies demonstrating successful applications in tool wear prediction using Bayesian-regularized neural networks [18].

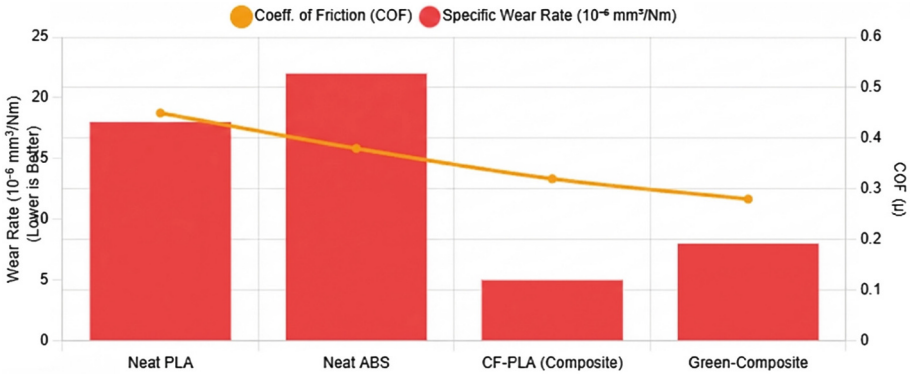

Fig. 1. Tribological performance of different polymeric printed materials

3.2 PIML and Advanced Classification

Convolutional Neural Networks (CNNs) have eliminated human subjectivity in the classification of wear mechanisms by differentiating between adhesive wear, fatigue spalling, and surface deformation [19, 20]. Furthermore, a major advancement is represented by Physics-Informed Machine Learning (PIML) [21]. The systematic review by Lawal et al. [22] traces the evolution of PINNs from their conceptual origins in 'hidden physics models' [23] to their current status as a mature framework. PINNs enable precise modeling of wear progression and friction transitions even with small datasets by integrating physical equations, such as partial differential equations (PDEs), into the learning process [24, 25]. The foundational work by Raissi et al. [25–27] on solving nonlinear PDEs using deep learning has paved the way for these applications in tribology, although their application in dry steel contacts remains an active area of research [28]. while concurrently, research by Sieberg et al. [29] demonstrates how AI has matured for complementary tasks like automated wear mechanism classification.

4 Gear Dynamics and Fault Detection

4.1 Time-Varying Mesh Stiffness (TVMS)

Dynamic analysis of gears centers on TVMS, which fluctuates based on tooth contact position, load, geometry and material properties. Variations in TVMS are critical indicators of fault evolution. Studies by Chaari et al. [30, 31] and Mohammed et al. [32, 33]

demonstrate that defects like spalling and root cracks cause local damage and cause a certain reduction in the tooth mesh stiffness, see Fig. 2. This has been investigated extensively for steel gears [29, 30, 31, 34, 36, 37]. However, polymer gears are not similarly covered.

4.2 Dynamic Modeling and Fault Detection

To capture realistic gear-mesh interactions, researchers studied different models from simple 1-DOF models to high-DOF models, e.g., 12 DOF that account for shaft dynamics, bearing stiffness, and gyroscopic effects [38]. These complex models feed into intelligent fault detection systems. Recent work by Bachar et al. [39] focuses on dynamic modeling of distributed wear-like faults, as shown in Fig. 3, building upon earlier statistical approaches to fault detection [40]. while Zhao et al. [41] have developed integrated explainable diagnosis systems. Furthermore, hybrid approaches combining dynamic modeling with deep learning and statistical features have shown high accuracy in detecting gear wear and tooth breakage [36, 42]. However, for polymer gears, detailed mesh stiffness and dynamic analyses are not covered yet by the researchers.

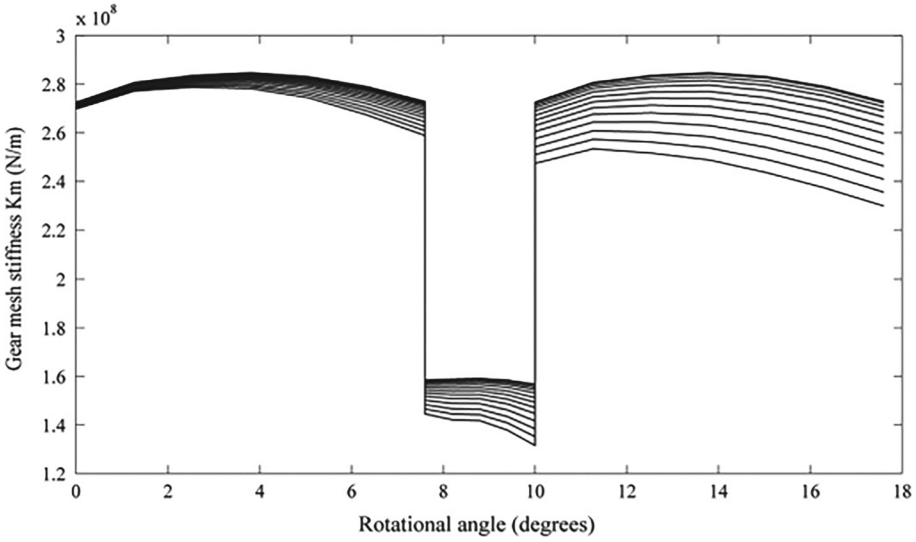

Fig. 2. Time-Varying Mesh Stiffness Analysis [32]

5 Steel vs. Polymer Comparative Study

There are specific trade-offs when choosing between steel and polymer gears.

- **Mechanical Properties:** Steel has an elastic modulus of about 200 GPa, while polymers have an elastic modulus of 1–5 GPa. Polymers offer low density and less noise, while steel has high stiffness and thermal conductivity.

- **Tribology and Thermal Behavior:** Steel gears are very resistant to wear, but they need to be lubricated. Polymer gears, on the other hand, can function with less friction but are constrained by low thermal conductivity, which causes heat buildup.
- **Failure Modes:** Pitting and other fatigue mechanisms are common ways for steel gears to fail. Polymer gears vary greatly; they are prone to melting at high RPMs and typically experience surface wear before root failure [8].

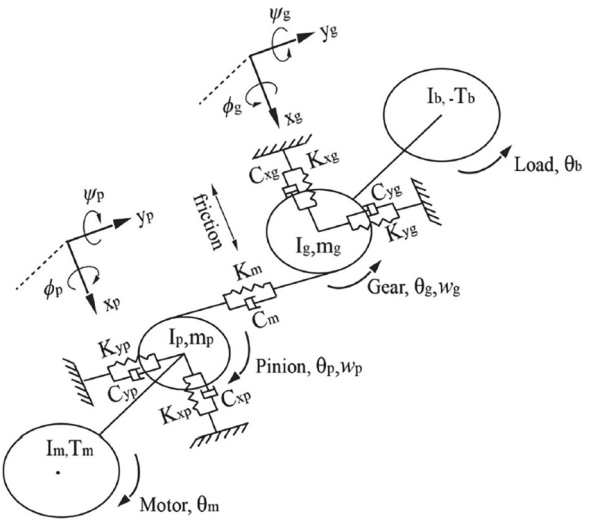

Fig. 3. 12 DOF gear dynamic modelling [42, 43]

6 Combined Material Gear Systems

To close the gap between these material classes, combined material gears with metal hubs and polymer teeth have been created. These designs improve wear resistance and heat dissipation while maintaining the lightweight benefits of polymers [44]. Recent experimental analysis by Šuljić et al. [45] provides critical data on the thermal behavior and wear of such FDM-produced hybrid gears, while modeling work by Chernets et al. [46, 47] offers calculated assessments of their load capacity and durability, helping to bridge the gap between traditional metal gear analysis and emerging polymer-composite systems. For example, Reitschuster et al. [48] verified the performance of high-performance polymer gears in EV powertrains, while Šuljić et al. [44] conducted experimental analyses on the wear and thermal behavior of combined material FDM gears shown in Fig. 4. However, potential delamination and stress concentrations at the material interface remain challenges [49, 50].

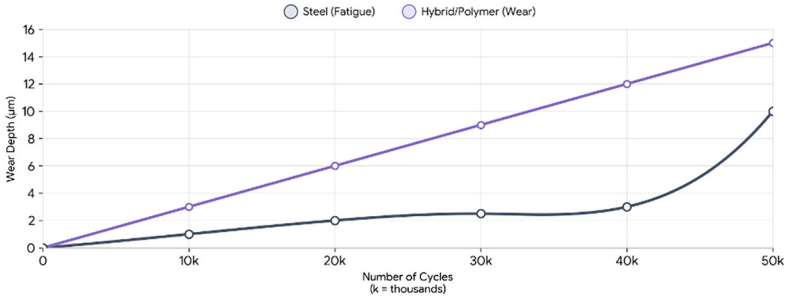

Fig. 4. Wear Rate Progression of steel and Combined Material Gear Systems

7 Conclusion

In conclusion, this review outlines the changing trends in gear materials, modeling tools, and testing methods, with special emphasis on the ever-increasing application scope of additively manufactured gears made from polymer materials and their hybrid combinations. Although steel gears continue to be highly useful for applications requiring high strength, polymer materials offer valuable advantages such as reduced weight, noise damping properties, robust corrosion resistance, etc., making their application in lightweight transmission systems gain further momentum.

The study emphasizes the importance of the dynamic model parameters, particularly the time-varying mesh stiffness, as accurate markers for the condition of the gears. The current literature shows that spalling or root crack defects will cause stiffness to decrease in the case of steel gears; however, studies regarding polymeric gears are relatively scarce. The reason for this is the lack of experiments taking into account the special characteristics regarding the viscoelastic behavior as well as the wear mechanisms concerning polymeric materials.

Furthermore, the confluence of advanced sensing technologies, data-driven techniques, and AI-enabled modeling of tribological and dynamical phenomena has opened up a promising area of research for the development of intelligent gear systems with the possibility of providing real-time monitoring, diagnosis, and prediction of remaining useful life.

Future research should be focused on the development of comprehensive dynamic models, which would be common to metal and polymeric gears. The validation of these models should be performed during experimental investigations. It is also proposed to extend the fault diagnosis databases related to polymeric and combined gears. The use of machine learning methods is recommended to develop predictive maintenance. All these activities would contribute to the development of next-generation gear systems with increased efficiency and smartness.

References

1. Stoimenov, N., Kandeva, M., Zagorski, M., Panev, P.: Static and kinetic friction of 3D printed polymers and composites. Tribol. Ind. **46**(1), 97–106 (2024)

2. Baran, E.H., Erbil, H.Y.: Surface modification of 3D printed PLA objects by fused deposition modeling: a review. Colloids Interfaces. **3**(2), 43 (2019)
3. Zhang, Y., Mao, K., Leigh, S., Shah, A., Chao, Z., Ma, G.: A parametric study of 3D printed polymer gears. Int. J. Adv. Manuf. Technol. **107**, 4481–4492 (2020)
4. Hanon, M.M., Zsidai, L.: Understanding the influence of process parameters and filament color on the structure and tribological properties of 3D printed PLA. J. Mater. Res. Technol. **15**, 647–660 (2021)
5. Portoacă, A.I., Ripeanu, R.G., Diniță, A., Tănase, M.: Optimization of 3D printing parameters for enhanced surface quality and wear resistance. Polymers. **15**(16), 3419 (2023)
6. Bachar, L., Sigonde, V.C., Cohen, R.: Dynamic modeling of distributed wear-like faults in spur gears. Proc. Eur. Conf. PHM Soc. **8**(1), 7 (2024)
7. Ali, M.H.: 3D printer selection for aircraft component manufacturing using a nonlinear FGM and dependency-considered fuzzy VIKOR approach. Mathematics. **11**, 4069 (2023)
8. Prusinowski, A., Kaczyński, R.: Tribological behaviour of additively manufactured fiber-reinforced thermoplastic composites in various environments. Polymers. **12**(7), 1548 (2020)
9. Ramadan, M.A., Sabour, H.A., EL-Shenawy, E.: Tribological properties of 3D printed polymers: PCL, ABS, PLA and co polyester. Tribol. Ind. **45**(1), 161–167 (2023)
10. Hanon, M.M., Kovács, M., Zsidai, L.: Tribology behaviour investigation of 3D printed polymers. Int. Rev. Appl. Sci. Eng. **10**(2), 173–181 (2019)
11. Marian, M., Tremmel, S.: Current trends and applications of machine learning in tribology—a review. Lubricants. **9**(9), 86 (2021)
12. Sose, A.T., Joshi, S.Y., Kunche, L.K., Wang, F., Deshmukh, S.A.: A review of recent advances and applications of machine learning in tribology. Phys. Chem. Chem. Phys. **25**, 4408–4443 (2023)
13. Rosenkranz, A., Marian, M., Profito, F.J., Aragon, N., Shah, R.: The use of artificial intelligence in tribology—a perspective. Lubricants. **9**(1), 2 (2021)
14. Shah, R. et al.: Machine learning in wear prediction. J. Tribol. **147**(4), 040801 (2025)
15. Perčić, M., Zelenika, S., Mezić, I.: Artificial-intelligence-based predictive model of nanoscale friction using experimental data. Friction. **9**(6), 1726–1748 (2021)
16. Deshpande, A.R., Kulkarni, A.P., Wasatkar, N., Gajalkar, V., Abdullah, M.: Prediction of wear rate of glass-filled PTFE composites based on machine learning approaches. Polymers. **16**, 2666 (2024)
17. Villanueva, E., Albizuri, J., Caballero, P., Guraya, T., Vicario, I.: Prediction of wear rate by a new direct method using the friction coefficient curve. J. Manuf. Mater. Process. **9**(1), 6 (2025)
18. Truong, T.T. et al.: Data-driven prediction of tool wear using Bayesian regularized artificial neural networks. Measurement. **238**, 115303 (2024)
19. Shao, T., Wang, S., Wang, Q., Wu, T., Huang, Z.: Comparison-embedded evidence-CNN model for fuzzy assessment of wear severity using multi-dimensional surface images. Friction. **12**(6), 1098–1118 (2024)
20. Zjavka, L., Pedrycz, W.: Constructing general partial differential equations using polynomial and neural networks. Neural Netw. **73**, 58–69 (2016)
21. Bustillo, A., Pimenov, D.Y., Matuszewski, M., Mikolajczyk, P.: Using artificial intelligence models for the prediction of surface wear based on surface isotropy levels. Robot. Comput. Integr. Manuf. **53**, 215–227 (2018)
22. Lawal, Z.K., Yassin, H., Lai, D.T.C., Che Idris, A.: Physics-informed neural network (PINN) evolution and beyond: a systematic literature review and bibliometric analysis. Big Data Cogn. Comput. **6**(4), 140 (2022)
23. Raissi, M., Karniadakis, G.E.: Hidden physics models: machine learning of nonlinear partial differential equations. J. Comput. Phys. **357**, 125–141 (2018)

24. Zjavka, L., Snášel, V.: Short-term power load forecasting with ordinary differential equation substitutions of polynomial networks. Electr. Power Syst. Res. **137**, 113–123 (2016)
25. Raissi, M., Perdikaris, P., Karniadakis, G.E.: Physics-informed neural networks: a deep learning framework for solving forward and inverse problems involving nonlinear partial differential equations. J. Comput. Phys. **378**, 686–707 (2019)
26. Raissi, M., Perdikaris, P., Karniadakis, G.E.: Physics-informed deep learning: Data-driven solutions of nonlinear partial differential equations. arXiv preprint, arXiv, 1711.10561 (2017)
27. Raissi, M.: Deep hidden physics models: deep learning of nonlinear partial differential equations. J. Mach. Learn. Res., 1–24 (2018)
28. Marian, M., Tremmel, S.: Physics-informed machine learning—an emerging trend in tribology. Lubricants. **11**(11), 463 (2023)
29. Sieberg, P.M., Kurtulan, D., Hanke, S.: Wear mechanism classification using artificial intelligence. Materials. **15**(7), 2358 (2022)
30. Chaari, F., Fakhfakh, T., Haddar, M.: Analytical modelling of spur gear tooth crack and influence on gearmesh stiffness. Eur. J. Mech. A Solids. **28**(3), 461–468 (2009)
31. Chakroun, A.E. et al.: Gear mesh stiffness of polymer-metal spur gear system using generalized Maxwell model. Mech. Mach. Theory. **175**, 104934 (2022)
32. Mohammed, A., Rantatalo, M.: Gear tooth crack detection using dynamic response analysis. Insight - Non-Destr. Test. Cond. Monit. **55**(8), 417–421 (2013)
33. Mohammed, A., Rantatalo, M., Aidanpää, J.: A method for calculating gear mesh stiffness for propagating cracks in tooth roots. In: Proceedings of the 26th International Congress on Condition Monitoring and Diagnostic Engineering Management (COMADEM), pp. 1–8, Helsinki, Finland (2013)
34. Eskezia, E., Abebaw, M.: Effect of gear materials on the surface contact strength of spur gears. Proc. Eng. Technol. Innov. **22**, 50–59 (2022)
35. Jaen-Cuellar, A.Y., Trejo-Hernández, M., Martínez-Ramírez, J.: Gear wear detection based on statistical features and heuristic scheme by using data fusion of current and vibration signals. Energies. **16**(2), 948 (2023)
36. Mohammed, A.: Dynamic modelling and fault diagnosis of a high contact ratio gear. In: Proceedings of the 5th International Conference on Structural Nonlinear Dynamics and Diagnosis (CSNDD), Marrakech, Morocco (2023)
37. Mohammed, A., Rantatalo, M.: Dynamic response and time-frequency analysis for gear tooth crack detection. In: Proceedings of the 29th Congress of the International Council of the Aeronautical Sciences (ICAS). Published in DiVA Portal, St. Petersburg, Russia (2014) (2016)
38. Reitschuster, S., Tobie, T., Stahl, K.: Experimental verification of high-performance polymer gears in an electric vehicle powertrain. Forsch. Ingenieurwes. **87**, 1–12 (2023)
39. Chaari, F., Baccar, W., Abbes, M.S., Haddar, M.: Effect of spalling or tooth breakage on gearmesh stiffness and dynamic response of a one-stage spur gear transmission. Eur. J. Mech. A Solids. **27**(4), 691–705 (2008)
40. Mohammed, A., Rantatalo, M., Aidanpää, J., et al.: Performance of statistical fault detection indicators for various crack propagation scenarios in gear tooth roots. In: Proceedings of the 26th International Congress on Condition Monitoring and Diagnostic Engineering Management (COMADEM), Helsinki, Finland (2013)
41. Mohammed, O.D.: Dynamic Modelling and Vibration Analysis for Gear Tooth Crack Detection. PhD thesis. Luleå University of Technology (2015)
42. Mohammed, A., Rantatalo, M., et al.: Dynamic modelling of a one-stage spur gear system and vibration-based tooth crack detection analysis. In: Proceedings of the 9th IFToMM International Conference on Rotor Dynamics. Springer, Cham (2015)
43. Mohammed, O.D.: Dynamic Modelling and Vibration Analysis for Gear Tooth Crack Detection. Luleå University of Technology (2015)

44. Vignesh, S., Johnney Mertens, A.: A deflection study of steel-polypropylene gear pair using finite element analysis. Mater. Today Proc. **90**, 36–42 (2023)
45. Šuljić, I., Tvrdić, V., Perkušić, M., Vrljičak, I.: Experimental analysis on hybrid polymer gears produced with fused deposition modeling method: thermal behavior and wear. Appl. Sci. **14**, 11509 (2024)
46. Chernets, M., Kornienko, A., Dukhota, A., Chernets, Y.: Modeling of load carrying capacity and durability of metal-polymer spur gears made of polyamide RA6 based compositions. FME Trans. **50**(1), 55–63 (2022)
47. Chernets, M., Shil'ko, S., Kornienko, A.: calculated assessment of contact strength, wear and resource of metal-polymer gears made of dispersion-reinforced composites. Appl. Eng. Lett. **6**(2), 54–62 (2021)
48. Rohrmoser, A., Bode, C., Schleich, B., Hagenah, H., Wartzack, S., Merklein, M.: Influence of metal gear tooth geometry on load and wear within metal-polymer gear pairs. Appl. Sci. **12**(1), 270 (2022)
49. Chernets, M.: Method of calculation of tribotechnical characteristics of the metal-polymer gear, reinforced with glass fiber, taking into account the correction of tooth. Eksploat. Niezawodn.– Maint. Reliab. **21**(4), 546–552 (2019)
50. Sainsot, P., Velex, P., Duverger, O.: Contribution of gear body to tooth deflections—a new bidimensional analytical formula. J. Mech. Des. **126**(4), 748–752 (2004)

Education and history of mechanisms

Implementing a Student-Centered Teaching Strategy in a Theory of Machines and Mechanisms Course

Paulo Flores(✉)

CMEMS-UMinho, Departamento de Engenharia Mecânica, Universidade do Minho, Campus de Azurém, 4804-533 Guimarães, Portugal
pflores@dem.uminho.pt

Abstract. In this work, a pedagogical activity that applies a student-centered approach to teaching the theory of machines and mechanisms is presented. To support this methodology, the Race Party project is utilized, in which student teams design and build a minicar able to run five meters on a horizontal plane as fast as possible. This project provides a coherent progression from fundamental principles to hands-on application and effectively covers the main topics related to the science of machines and mechanisms. Within the objectives of the Race Party, students explore key concepts such as types of motion, degrees of freedom, kinematic constraints, free-body diagrams, and equations of motion. Furthermore, students also develop computational models and apply appropriate manufacturing and assembly techniques, which are relevant to their technical growth. Additionally, the project fosters important soft skills, including creativity, teamwork, leadership, communication, and interaction with sponsors and partners. This structured workflow helps students link theoretical principles to practical engineering decision-making. The study focuses on the implementation of the Race Party project at the University of Minho, enabling an assessment of its impact on the teaching-learning process in an undergraduate course on dynamics of machinery. Overall, the collected outcomes show that the Race Party is an effective strategy for engaging students in the field of machine and mechanism science.

Keywords: Theory of Machines and Mechanisms · Student-Centered Approach · Race Party Challenge

1 Introduction

Teaching theory of machines and mechanism is very old topic that has been object of investigation and interest over the last decades. Satshi et al. [1] examined key visual aids for teaching analysis of mechanisms, and discussed challenges in using them, and presented examples of how they can enhance communication in lectures. Midha and co-authors [2] presented a collection of studies related to linkage design that have resulted from a mechanism synthesis course to promote the creativity in the classroom based on design projects. More recently, Canfield [3] presented a complete set of problems related to kinematics and dynamics of machinery course.

© The Author(s), under exclusive license to Springer Nature Switzerland AG 2026
A. Chaker et al. (Eds.): EFIMMS 2026, MMS 205, pp. 443–453, 2026.
https://doi.org/10.1007/978-3-032-22270-1_43

Mikesell and Yoder [4] used a project-based learning approach to teach dynamics through a design project. Overall, students reported learning more effectively with active tasks compared to a traditional lecture-based format. Gramoll [5] discussed the use of computer simulation programs to introduce design concepts to first-year engineering students and highlighted the advantages and disadvantages of incorporating commercial software into engineering education. Esche [6] conducted a comprehensive study on an innovative method for integrating project-based learning into a junior-level mechanical engineering course on the dynamics of machines and mechanisms, demonstrating improvements in students' understanding of machine dynamics. Similarly, Yang [7] presented an application of simulation tools in the theory of machines and mechanisms for engineering training. This work emphasized the use of software to help students grasp the abstract theoretical concepts commonly encountered in classical courses on kinematics and dynamics of machinery. In turn, Shen and his co-authors [8] introduced a methodology for teaching machines and mechanisms science by using MATLAB platform as a tool to address problems related to kinematics and dynamics of mechanical systems. Their findings showed that their approach effectively helped students gain a deeper understanding of the core topics associated with analysis and design of machinery. William II [9] presented different computational tools designed to support teaching and learning processes in mechanisms, robotics, and biomechanics, and discussed their integration into several courses at the Ohio University.

Faas and Gong [10] investigated whether varying design objectives in introductory mechanical engineering courses with a competitive component can enhance design novelty and quality. These authors examined robot designs from four different configurations used in a design-and-build activity, comparing one unchanged design prompt with three semesters of modified prompts. Robot evaluations considered performance, design type and quality, and the influence of the competition format. Their findings indicate that changing design objectives leads to a broader range of design solutions. Although average novelty did not increase, students were no longer constrained to a narrow set of design ideas. More recently, Flores and Lankarani [11] presented a study on the use of a ping-pong ball launcher challenge, a project-based learning activity for first-year students to teaching kinematics, dynamics, and mechanical system design. Its success relied on the strong commitment of students and instructors. According to students, the use of competitions improves the engagement and motivation compared to traditional lectures. This study demonstrates how innovative project-based learning approach can enhance engineering education and inspire future engineers.

This work discusses the implementation of a student-centered pedagogical strategy designed to help students engage with a dynamics of machinery course offered to first-year engineering students. The approach combines traditional lectures with a design project in which students, working in teams of five, are tasked with developing and building a mini-car capable of traveling five meters on a horizontal surface as quickly as possible. The key components of the project, named Race Party, include identifying the power source, creating the conceptual design, analyzing the mini-car's dynamics, and constructing a physical prototype. The pedagogical activity involves multiple deliverables, including oral presentations, written reports, individual exams, and other assessment tools intended to support and enhance the teaching and learning process.

2 Race Party Project: A Student-Centered Pedagogical Activity

The Race Party challenge consists of a minicar competition where the students, organized in groups of five, have to design, develop and build a minicar of dragster type powered by a standard helical spring to run five meters in a horizontal and smooth surface, as fast as possible [12]. For this purpose, each group of students receive a basic kit of components, as it is shown in Fig. 1a, which must be utilized in within the Race Party challenge. Figure 1b and c show, respectively, an example of a car without body part developed by a team of students, and a minicar in competition [13].

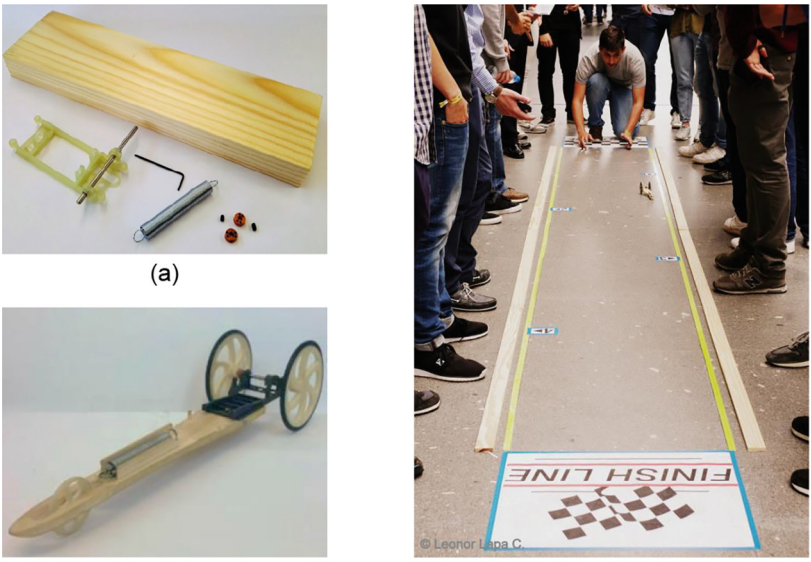

Fig. 1. **(a)** Basic kit of components provided to each team of students; **(b)** Example of a minicar developed by students; **(c)** Track used during the Race Party competition at the end of semester.

The central goal of the Race Party challenge is to design and build a dragster-style minicar powered by a tensioned helical spring, with a focus on maximizing its dynamic performance. The minicar's success is evaluated based on aesthetics, speed, reliability, repeatability of results, adaptability to different scenarios, cost, and safety. It should be noted that all design choices and decisions made by the teams throughout the project must be supported by technological and scientific principles of mechanics. To develop the minicar, each team must follow to a predefined set of requirements and specifications. The minicar begins its run from rest and travels along a smooth, horizontal surface without any form of directional guidance. The minicar is powered solely by the helical spring, which must be installed inside the vehicle. The minicar is driven by its rear wheels, whose diameter is twice that of the front wheels. Furthermore, the wheels must describe pure rolling motion [12].

The wheelbase must be within the range of 120 to 180 mm. The maximum allowable dimensions of the minicar are 100 mm in height and 60 mm in width. The helical spring may be deflected up to a maximum of 50 mm, and no pre-tension is permitted. In addition, the use of electronic or magnetic devices is strictly prohibited. Dry lubrication may be applied to the bearings supporting both the rear and front axles. The exterior of the car must feature high-quality finishing and paintwork, while the inclusion of bodywork is optional [12, 13].

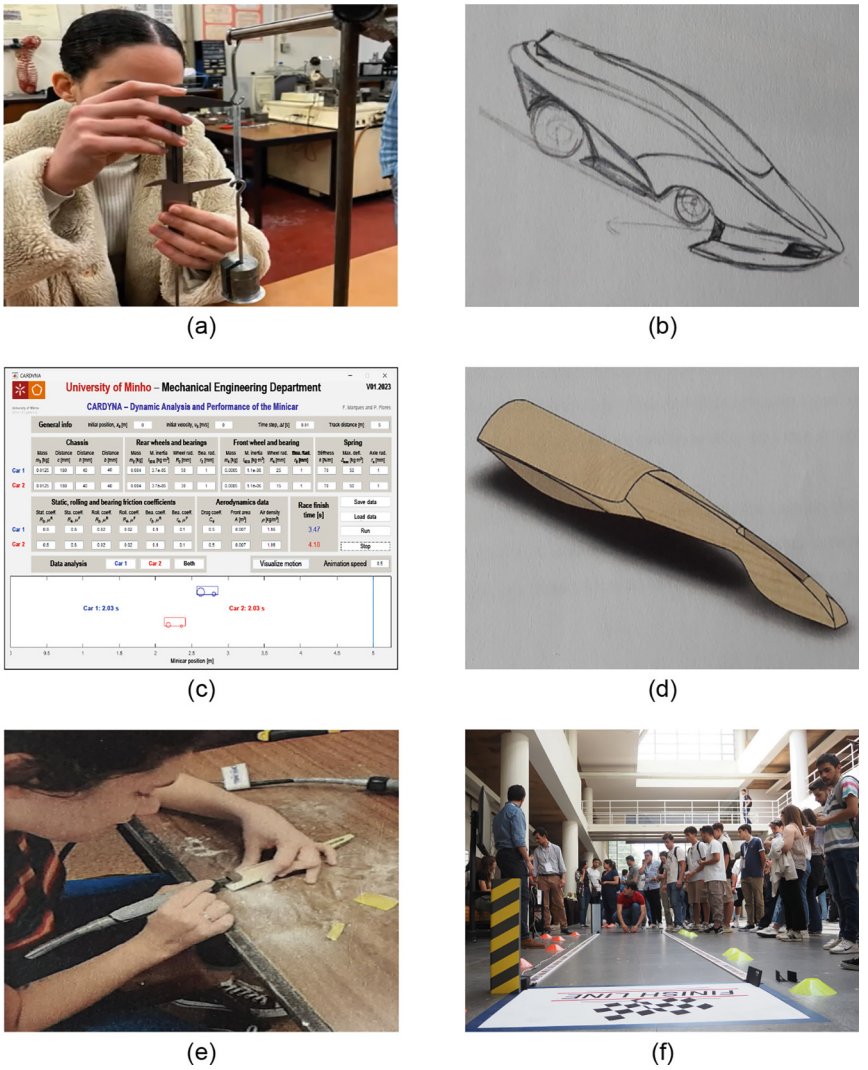

Fig. 2. key stages in the Race Party development process: **(a)** Evaluation of the spring stiffness; **(b)** Concept design of the minicar; **(c)** Minicar dynamic performance analysis; **(d)** Minicar bodywork model; **(e)** Minicar physical prototype; **(f)** End-of-semester Race Party competition.

The primary tasks for students, along with the scope and objectives of the Race Party project, are outlined as follows:

- Determining the stiffness of the tensioned helical spring through theoretical and experimental methods (see Fig. 2a),
- Designing and conceptualizing the minicar solution, including the number of wheels, bodywork aesthetics, and other design features (see Fig. 2b),
- Evaluating the dynamic performance of the designed minicar using a dedicated MATLAB code developed for this purpose (see Fig. 2c),
- Creating a CAD/CAE/CAM model of the final minicar for structural analysis and manufacturing (see Fig. 2d).
- Defining manufacturing and assembly procedures for the minicar to carry out preliminary testing (see Fig. 2e),
- Demonstrating the final version of the minicar during the Race Party competition at the end of the semester (see Fig. 2f).

At the completion of each task described above, each student team must submit one deliverable (a one-page report) summarizing the key aspects and conclusions. Further, each team must also give oral presentations detailing their work and results. These presentations encourage discussion of the project process and outcomes, helping to promptly identify and resolve any team challenges.

3 Race Party Project Implementation

This section describes the implementation of the Race Party pedagogical activity within a course devoted to theory of machines and mechanisms [14], offered in the second semester of the first year of the Bachelor's degree in Mechanical Engineering at the University of Minho. This course focuses on the kinematics and dynamics of mechanical systems. The course consists of three hours per week and includes various instructional activities, one of which is the Race Party project, representing 50% of the overall course grade. During the Race Party project, lectures feature traditional classroom presentations on topics such as dimensional metrology, laboratory safety rules, equations of motion, dynamics of mechanical systems, car performance, and product design and development. Students are expected to come to lectures prepared by reviewing relevant materials, including slides, textbooks, and educational videos. Students typically spend a significant amount of time developing and designing their mini car solutions and familiarizing themselves with the laboratories and machine shop.

Within the objectives of the Race Party project, students gain and develop technical skills related to the selection of kinematic and dynamic parameters of mechanical systems, the analysis and synthesis of mechanisms, the selection of mechanical transmissions, manufacturing processes, and mechanical design. As a result, product design and development serve as key areas for in-depth analysis and discussion throughout the activity. In addition to these technical competencies, students are also expected to develop soft skills such as teamwork, creativity, effective communication with a broad audience, and the ability to articulate and defend their viewpoints [15].

The main learning outcomes associated with the Race Party pedagogical project are summarized below. By the end of the semester, students should be able to accomplish the following outcomes, either individually or in a group setting:

- Identify the key variables that influence the dynamic response of a minicar,
- Conduct kinematic and dynamic analyses of mechanical systems,
- Design a mechanism or machine for a specific purpose,
- Develop computational and physical models of machines and mechanisms,
- Create CAD models and technical drawings suitable for use in a machine shop,
- Identify and select materials and mechanical components for building a machine,
- Construct, assemble, and test a mechanical system using standard components.

Beyond being a simple and practical activity, the Race Party challenge is a demanding project, involving multiple aspects of kinematics and dynamics of mechanical systems, along with numerous assessment requirements and specifications. It should be noted that this project places strong emphasis on an assessment-for-learning approach, which not only motivates students but also enhances their overall learning process [16]. The activities and progress of the teams, as well as individual students, in the Race Party project are monitored through their attendance at scheduled sessions. To facilitate this process, which is overseen by tutors and the course coordinator, each student group is required to present a portfolio. Additionally, students must deliver mid-semester and final oral presentations, prepare midterm and final reports, complete six deliverables, and take three individual mini-exams. This comprehensive approach not only enables continuous monitoring of the project's progress but also supports the assessment and grading of both teams and individual students. In doing so, students engage with a variety of learning techniques, which have been shown to enhance overall learning outcomes.

Table 1 shows the percentages assigned to each component of the students' assessment and grading [12, 13].

Table 1. Percentage of the assessment and grading components.

Component	Percentage
Deliverables (maximum 1 page per deliverable)	25
Mini-exams (15 min duration for each mini-exam)	15
Final exam (30 min duration for the final exam)	15
Mid-semester oral presentation (30 min duration including discussion)	10
Final oral presentation (30 min duration including discussion)	10
Midterm report (maximum 6 pages, excluding appendices)	10
Final report (maximum 12 pages, excluding appendices)	15

The Race Party project is assessed based on students' technical performance, which includes both the development process and the final product, as well as the quality

of their reports and presentations. In addition, peer and self-assessments are encouraged throughout the semester, offering students valuable feedback on their skills and confidence in performing the various tasks associated with the Race Party project [12].

4 Findings and Implications

This section presents results from a particular semester, based on students' feedback regarding the implementation of the Race Party. At the end of the semester, a competition is held to evaluate the minicars developed by each team (see Fig. 3). Table 2 presents the scores obtained by the top five teams in the 2023 edition of the Race Party.

(a) (b)

Fig. 3. Scenes from the Race Party competition: **(a)** beginning of the race; **(b)** end of the race.

Table 2. Top 5 scores achieved by teams in the 2023 Race Party.

Team	Time [s]	Difference [s]
# 35	1.609	–
# 36	1.870	0.261
# 24	1.946	0.076
# 31	2.176	0.230
# 22	2.229	0.053

Figure 4 shows a group photo of the students who participated in the 2023 edition of the Race Party at the end of the competition.

The goals of the study reported in this section are twofold: to analyze students' perceptions regarding the implementation of the Race Party project and to discuss the implications of those perceptions for improving the teaching-learning process, particularly the roles of instructors and students. A questionnaire containing both closed and open-ended questions was designed for this purpose and administered at the end of the

Fig. 4. Group photo from the 2023 Race Party competition held at the University of Minho.

semester. The questionnaire covered several dimensions, including: students' motivation for pursuing an engineering degree, teaching methods, assessment procedures, teacher performance, and classroom climate, just to mention a few. A total of 70 students completed the questionnaire. Participation in the study was voluntary, and the average age of respondents was 19.7 years.

From the data collected, it can be observed that for the vast majority of respondents (68.6%), this course was their first choice when applying to the university (see Fig. 5a). Additionally, most participants (90.7%) reported that the course met their expectations (see Fig. 5b).

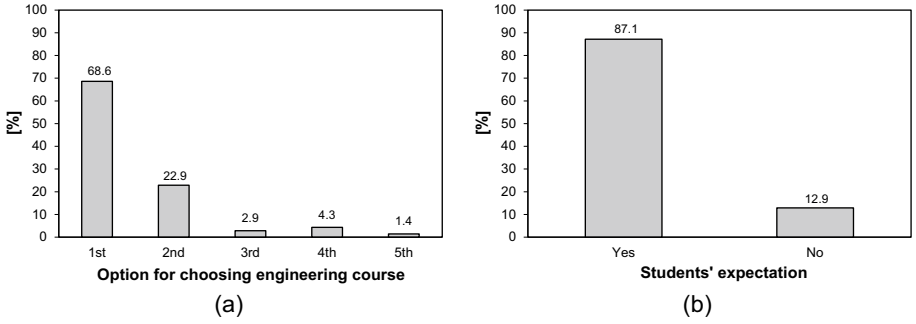

Fig. 5. **(a)** Option for choosing engineering course when entering at the university for the first time; **(b)** Does the engineering course correspond to the initial expectations?

In this study, respondents also highlighted several aspects of their experience with the Race Party activity, indicating varying levels of satisfaction. Regarding classroom engagement, 64.3% of students reported being very satisfied (see Fig. 6a). When asked whether they learned from the course, 65.7% indicated they were very satisfied (see Fig. 6b). Similarly, 61.4% of respondents expressed complete satisfaction with the teacher's commitment to class preparation and organization (see Fig. 6c). Finally, 61.4% of students reported that they understood the topics taught through the Race Party project (see Fig. 6d).

Year after year, new creative solutions emerge, reflecting many hours spent in the department's laboratories and machine shop. Students have the opportunity to review reports and watch videos of previous years' minicars, encouraging them to explore, improve upon. The Race Party has played a role in developing students' soft skills. This pedagogical activity promotes collaborative work toward a common goal and strengthens the ability to communicate ideas and results clearly and effectively. At the same time, students acquire technical competencies in dynamics and mechanical system design while learning to develop integrated solutions in mechanical engineering.

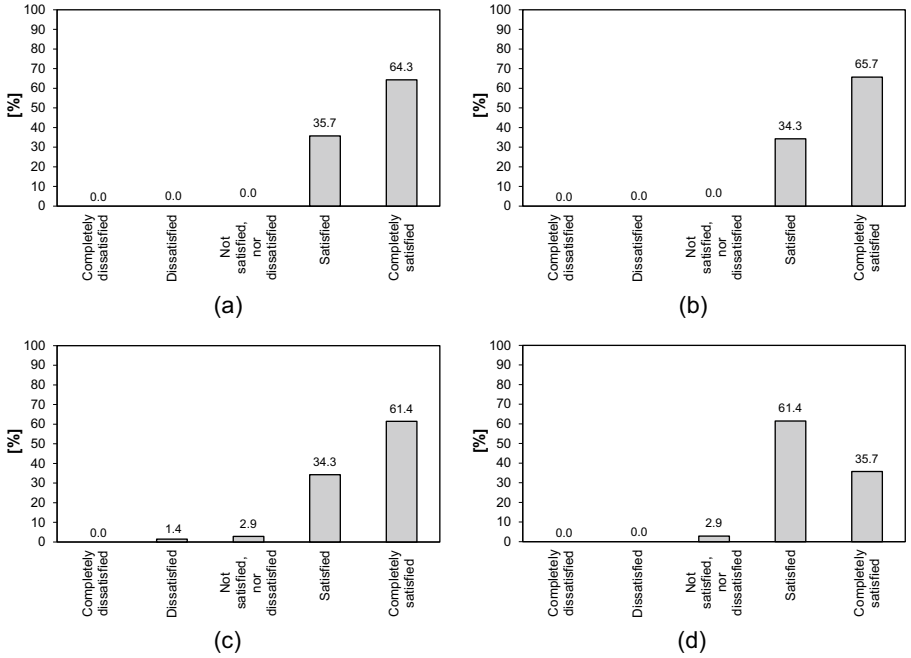

Fig. 6. **(a)** Were the classes intellectually stimulants? **(b)** Do I learn something important? **(c)** Did the teacher demonstrate pledge in the preparation and organization of the classes? **(d)** In general, I understood the subjects taught.

5 Concluding Remarks

This work presented the Race Party challenge to teach dynamics of machinery. The project offers a coherent progression from fundamental principles to hands-on application and covers the major topics within the field. Through the Race Party, students engage with essential concepts such as types of motion, degrees of freedom, kinematic constraints, free-body diagrams, and equations of motion. In addition to technical knowledge, the project helps students develop soft skills, including teamwork, leadership, communication, and collaboration with sponsors and partners. Overall, the results show

that the Race Party is an effective strategy for engaging students in the study of machine and mechanism science. The success of the Race Party is reflected in the strong performance of all minicar teams on the course and in the students' accomplishments. The continued success of the Race Party depends heavily on the enthusiasm and commitment of everyone involved, especially the students and instructors.

Acknowledgments. This work was supported by FCT - *Fundação para a Ciência e a Tecnologia* within the R&D units projects: UID/04436/2025 – *Centro de Microssistemas Eletromecânicos* of the University of Minho.

References

1. Satshi, B.A., Konstantinov, B.S., Eshkenazi, J.A., Zlatinov, I.P., Malinov, E.V.: Some visual aids for teaching mechanism analysis. Mech. Mach. Theory. **13**(5), 503–517 (1978)
2. Midha, A., Turcic, D.A., Bosnik, J.R.: Creativity in the classroom - a collection of case studies in linkage synthesis. Mech. Mach. Theory. **19**(1), 25–44 (1984)
3. Canfield, S.L., Hill, S., Hill, T., Zuccaro, S.: Creating a digital homework set for a kinematics and dynamics of machinery course. In: Proceedings of the ASME 2015 International Design Engineering Technical Conferences & Computers and Information in Engineering Conference IDETC/CIE 2015., Paper No: DETC2015–47558, p. 11 (2015)
4. Mikesell, D.R., Yoder, J.-D.S.: Teaching dynamics with a design project. In: American Society for Engineering Education, American Society for Engineering Education (2011)
5. Gramoll, K.: Using 'working model' to introduce design into a freshman engineering course. In: ASEE Conference Proceedings, Edmonton, Canada (1994)
6. Esche, S.K.: Project-based learning (PBL) in a course on mechanisms and machine dynamics. World Trans. Eng. Technol. Educ. **1**(2), 201–204 (2002)
7. Yang, G.: An application of simulation in theory of machines and mechanisms for excellent engineering training. World Trans. Eng. Technol. Educ. **12**(2), 209–2014 (2014)
8. Shen, Y., Yaun, M., Wang, M.: Teaching reform of course regarding theory and design of mechanisms based on MATLAB technology. High. Educ. Stud. **3**(6), 15–24 (2013)
9. William II, R.L.: Tools to assist teaching and learning of mechanisms, robotics and biomechanics. In: Proceedings of the ASME 2010 International Design Engineering Technical Conference & Computers and Information in Engineering Conference IDETC/CIE 2010, August 15–18, 2010. Montreal, Quebec, Canada., Paper DETC2010–28537 (2010)
10. Faas, D., Gond, S.: Improving novelty quality during introductory mechanical design competitions. In: Proceedings of the ASME 2016 International Design Engineering Technical Conferences and Computers and Information in Engineering Conference IEDTC/CIE 2016, August 21–24, 2016, Charlotte, Noth Carolina., Paper DETC2016–59251 (2016)
11. Flores, P., Lankarani, H.M.: Teaching kinematics and dynamics of machinery with a design project: the ping-pong ball launcher challenge. In: Proceedings of the ASME 2025 International Design Engineering Technical Conferences and Computers and Information in Engineering Conference IEDTC/CIE 2025, August 17–20, 2025, Anaheim, California., Paper DETC2025–167527 (2025)
12. Flores, P., Marques, F., Silva, M., Novais, F.: Projeto Integrador em Engenharia Mecânica, 1st edn. Engebook (2023)
13. Flores, P.: Race party: a project-based learning approach to teach dynamics and design of mechanical systems. Mech. Mach. Sci. **180**, 393–401 (2025)
14. Flores, P.: Ciência de Máquinas e Mecanismos, 1st edn. Engebook (2026)

15. Neto, D., Flores, P.: Introducing a project-based learning approach in a course on design of machine elements: a case study in two public universities in Portugal. Int. Symp. Proj. Approaches Eng. Educ. **15**, 8–16 (2025)
16. Pereira, D., Cadime, I., Brown, G., Flores, M.A.: How do undergraduates perceive the use of assessment? A study in higher education. Eur. J. High. Educ. **12**(1), 1–17 (2022)

A Seven-Step Procedure to Model and Simulate Dynamics of Machines and Mechanisms

Paulo Flores(✉)

CMEMS-UMinho, Departamento de Engenharia Mecânica, Universidade do Minho, Campus de Azurém, Guimarães 4804-533, Portugal
pflores@dem.uminho.pt

Abstract. It is widely recognized that teaching and learning the dynamics of machines and mechanisms is a challenging task for both students and instructors. In fact, dynamics is often perceived as a difficult and demanding subject because it draws on many areas, such as mechanics, physics, algebra, calculus, numerical methods, and computational techniques, to name a few. This challenge is particularly evident when working with first-year engineering students. In this context, the present work introduces a simple and straightforward technique for formulating and solving mechanism dynamics problems. To support this, a seven-step procedure is presented along with a demonstrative example involving a robotic arm. The proposed approach has been implemented in the "General Mechanics" course (3 h per week), which is part of the first-year curriculum of the bachelor's degree in mechanical engineering at the University of Minho. Preliminary results suggest that students responded positively to the dynamics module's activities and content. These findings provide a basis for discussing the main challenges and lessons learned from implementing this approach for teaching mechanism dynamics to freshman students.

Keywords: Dynamics of Machines and Mechanisms · Teaching and Learning Dynamics · Equations of Motion · Dynamics Problems

1 Introduction

It is well known that teaching and learning the dynamics of machines and mechanisms is a non-trivial task for both students and instructors. This difficulty arises from the broad range of concepts spanning multiple and different areas of mechanics and mathematics, including physics, algebra, calculus, numerical analysis, and computational methods [1–3]. Moreover, many of the fundamental concepts in dynamics that students have previously encountered are inherently non-intuitive [4]. It is also common for students' everyday beliefs to conflict with Newtonian mechanics, when they study motion of mechanical systems. As a result, many students enter the subject with a variety of misconceptions about dynamics, which can ultimately hinder their ability to understand more advanced principles and formulations [5].

In recent years, computer applications dedicated to the kinematic and dynamic analysis of machines and mechanisms have become an integral part of the global industrial

© The Author(s), under exclusive license to Springer Nature Switzerland AG 2026
A. Chaker et al. (Eds.): EFIMMS 2026, MMS 205, pp. 454–463, 2026.
https://doi.org/10.1007/978-3-032-22270-1_44

landscape, particularly in the metalworking and robotics sectors. These tools enable designers to create, evaluate, and visualize the motion of a mechanism without the need to build a physical prototype. The advantages of using such software are numerous: the ability to develop virtual models, observe component functionality and operability, process information quickly and flexibly, and significantly reduce material use, development time, and overall cost. In addition, these applications make it easier to assess the loads and forces involved in the mechanism's motion, which is essential for properly sizing and designing its components [6, 7].

It is unquestionable that teaching multibody systems methodologies is a demanding task—one that requires pedagogical strategies far beyond traditional lecture-based instruction. Conventional "chalk-and-talk" teaching does not effectively promote deep understanding of dynamics problems, and its effectiveness is generally limited to a relatively small number of students [8]. In contrast, project-based learning has been shown to yield better results, particularly in terms of comprehension and long-term retention across a wide range of learners. This approach has proven to be especially effective and appealing for teaching the dynamics of mechanical systems, as demonstrated in several recent studies [9, 10].

Traditionally, teaching and learning theory of machines and mechanisms is quite demanding and difficult course, for both students and instructors, since a good number of disciplines and non-intuitive aspects are involved. Thus, this work aims at presenting a simple, direct and intuitive approach for formulate any dynamics problem to freshman students. In fact, the proposed procedure allows students to understand both the physical and mathematical aspects when modeling and solving a problem related to dynamics of machines and mechanisms. For that purpose, the methodology described in this work is divided in seven logic and sequential steps, namely: *(i)* discretization of the system, *(ii)* selection of coordinates, *(iii)* drawing free-body diagrams, *(iv)* development of the equations of motion, *(v)* establishment of the kinematic constraints, *(vi)* assembly and resolution of the equations of motion and kinematic constraints, *(vii)* visualization of the outcomes. These dimensions associated with the proposed approach will be described in detail in following sections, together with applications examples.

The remaining of this work is organized and structured as follows. In Sect. 2, the fundamental aspects related to the proposed approach to formulate and solve dynamics of machines and mechanisms problems are presented. In the sequel of this process, a simple robotic arm is considered as example of application in order to better understand the main mathematical and physical aspects when solving a dynamics problem. Then, Sect. 3 deals with the description and discussion of a demonstrative example of application. For this purpose, the academic planar slider-crank mechanism is used, which include a number of constrained links that form a closed loop kinematic chain. Finally, the main concluding remarks are presented in the last section of this work, when the main conclusions are addressed.

2 The Seven-Step Proposed Approach

This section presents a comprehensive description of a general methodology to formulate and solve dynamics problems. In order to better understand the sequence of steps of the proposed approach, a 6-axis serial robot is considered (Fig. 1). For the sake of simplicity, this robotic arm is modeled as a two degrees-of-freedom system.

Fig. 1. Robotic arm utilized to support the description of the proposed approach to solve dynamics of machines and mechanisms, which is modeled as a two degrees-of-freedom system.

The proposed formulation to model and simulate dynamics of mechanisms presented in this work can be condensed in the following steps [2]:

(i) ***Discretization of the system***. The first step of the proposed approach consists of modeling the system under analysis, which should be conducted with an appropriate level of detail, bearing in mind the aim and purpose of the problem to be solved. The mathematical model should be as simple as possible without compromising the primary objectives of the analysis or the results to be obtained. For the robotic arm considered here, it is evident that the system can be modeled as a double pendulum, as it is illustrated in the schematic representation of Fig. 2a.

(ii) ***Selection of coordinates***. In this step, the type of coordinates utilized to define the position and orientation of the bodies that compose the system must be chosen. Among the various types of coordinates commonly used in dynamics of machines and mechanisms, absolute coordinates are selected for this study. Thus, the pose of each body of the robotic arm under analysis can be established by using the x and y coordinates of the corresponding center of mass, together with a rotational coordinate, θ, associated with the orientation of the body. These types of coordinates are represented in Fig. 2a. One of the key aspects when dealing with dynamics

problems is the establishment of the inertial frame of reference. The x-y Cartesian system of coordinates is a good choice for the inertial frame (Fig. 2a).

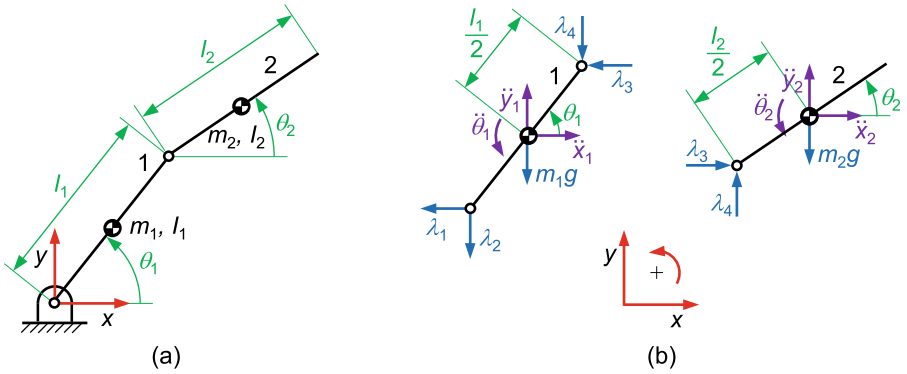

Fig. 2. **(a)** Model of the robotic arm as a double pendulum; **(b)** Free-body diagrams of the elements that compose the robot arm.

(iii) ***Drawing free-body diagrams***. The third step deals with the construction of the free-body diagrams of the parts that compose the system, which provide a simple and clear picture of the forces that act on each body of the mechanical system. Figure 2b shows the free-body diagrams of the arms 1 and 2 that constitute the robotic manipulator considered as a double pendulum in the present study. With the purpose of keeping the analysis simple, the gravitational force is the only external force that acts on the mechanical system. A separate free-body diagram is drawn for each body in the system.

(iv) ***Development of the equations of motion***. Based on the free-body diagrams constructed in the previous step, the Newton-Euler equations of motion must be written. For planar cases, Newton's second law states that the sum of the applied forces equals the mass times acceleration. In turn, Euler established that the sum of applied moments with respect to the center of mass equals the mass moment of inertia at the center of mass times the angular acceleration. Thus, with regard to Fig. 2b, the Newton-Euler equations of motion for arms 1 and 2 can be written as

$$m_1\ddot{x}_1 = -\lambda_1 - \lambda_3 \tag{1}$$

$$m_1\ddot{y}_1 = -\lambda_2 - \lambda_4 - m_1 g \tag{2}$$

$$I_1\ddot{\theta}_1 = -\lambda_1\frac{l_1}{2}\sin\theta_1 + \lambda_2\frac{l_1}{2}\cos\theta_1 + \lambda_3\frac{l_1}{2}\sin\theta_1 - \lambda_4\frac{l_1}{2}\cos\theta_1 \tag{3}$$

$$m_2\ddot{x}_2 = \lambda_3 \tag{4}$$

$$m_2\ddot{y}_2 = \lambda_4 - m_2 g \tag{5}$$

$$I_2\ddot{\theta}_2 = \lambda_3 \frac{l_2}{2}\sin\theta_2 - \lambda_4 \frac{l_2}{2}\cos\theta_2 \tag{6}$$

(v) ***Establishment of the kinematic constraints***. The equations of motion (1)–(6) represent a system of six equations with 10 unknowns, precisely six accelerations and four joint reaction forces. Thus, kinematic constraint equations associated with the system restrictions, namely the constraints imposed by the revolute joints, must be established. For this purpose, the position of the center of mass of each body, expressed in terms of the chosen coordinates, must be generated first. With regard to Fig. 2, the robotic arm can be constrained by four kinematic conditions expressed as

$$\Phi_1 = x_1 - \frac{l_1}{2}\cos\theta_1 = 0 \tag{7}$$

$$\Phi_2 = y_1 - \frac{l_1}{2}\sin\theta_1 = 0 \tag{8}$$

$$\Phi_3 = x_1 + \frac{l_1}{2}\cos\theta_1 - x_2 + \frac{l_2}{2}\cos\theta_2 = 0 \tag{9}$$

$$\Phi_4 = y_1 + \frac{l_1}{2}\sin\theta_1 - y_2 + \frac{l_2}{2}\sin\theta_2 = 0 \tag{10}$$

(vi) ***Assembly and resolution of the equations of motion and kinematic constraints***. In this step, the equations of motion and the kinematic constraint equations are combined and solved numerically. It should be noticed that Eqs. (7, 8, 9 and 10) are formulated at the position level and, therefore, they cannot be directly incorporated with Eqs. (1)–(6), since the last ones are expressed at the acceleration level. Thus, the constraint equations must be differentiated twice with respect to time. Finally, the combination of the equations of motion (1–6) and the constraint equations at the acceleration level leads to the set of differential-algebraic equations, written in matrix form as

$$\begin{bmatrix} \mathbf{M} & \mathbf{\Phi}_\mathbf{q}^{\mathrm{T}} \\ \mathbf{\Phi}_\mathbf{q} & \mathbf{0} \end{bmatrix} \begin{Bmatrix} \ddot{\mathbf{q}} \\ \boldsymbol{\lambda} \end{Bmatrix} = \begin{Bmatrix} \mathbf{g} \\ \boldsymbol{\gamma} \end{Bmatrix} \tag{11}$$

where $\mathbf{M}$ is the system's mass matrix, $\mathbf{\Phi}_\mathbf{q}$ represents the Jacobian matrix of the constraint equations, $\ddot{\mathbf{q}}$ denotes the vector containing the system accelerations, $\boldsymbol{\lambda}$ is the Lagrange multipliers vector that includes the joint reaction forces, $\mathbf{g}$ is the generalized vector of applied forces, and $\boldsymbol{\gamma}$ denotes the right-hand side vector of the acceleration equations. Equation (11) represents a differential-algebraic system of equations (DAE) of index-1 that is solved for the accelerations and Lagrange multipliers [6]. Then, the accelerations and velocities are integrated in time to determine the new velocities and positions. This numerical procedure is repeated until the final time of simulation is reached.

(vii) ***Visualization of the outcomes.*** The last step deals with the verification and visualization of the results produced, which can be presented in the form of tables, plots

and animations. This step is crucial to evaluate the accuracy and effectiveness of the developed model, as it allows for the physical interpretation of the obtained data in the analysis.

3 Example of Application: Planar Slider-Crank Mechanism

The slider-crank mechanism is utilized as a demonstrative example of the proposed approach. Figure 3 illustrates a generic configuration of the planar slider–crank system, which is composed of three rigid moving bodies: the crank (1), the connecting rod (2), and the slider (3). The ground serves as the fixed body and is labeled as body 0. The system includes three revolute joints and one translational joint, resulting in a total of eight kinematic constraints [11].

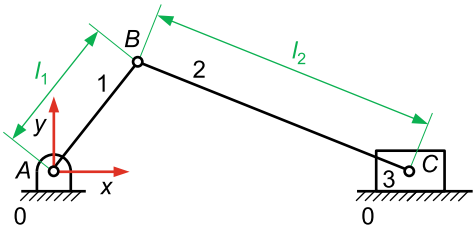

Fig. 3. Generic configuration of the planar slider-crank mechanism.

The coordinate vector that fully describes the configuration of the slider–crank mechanism is given b [6]

$$\mathbf{q} = \{x_1 \ y_1 \ \theta_1 \ x_2 \ y_2 \ \theta_2 \ x_3 \ y_3 \ \theta_3\}^{\mathrm{T}} \tag{12}$$

in which $\mathbf{q}$ is a 9×1 vector contains two Cartesian coordinates and one rotational angle per body, all defined with respect to a global reference frame. However, the nine absolute coordinates in Eq. (12) are not independent, since the slider-crank mechanism possesses only one degree of freedom.

With the purpose to construct the equations of motion for the slider–crank mechanism using the well-known Newton-Euler formulation, it is first necessary to draw the free-body diagrams for each component of the system, as shown in Fig. 4. For simplicity, the centers of mass of both the crank and the connecting rod are assumed to lie at the midpoints of their respective bodies, while the center of mass of the slider is taken to be located at revolute joint C. Newton's third law is applied in the free-body diagram representations, particularly with respect to the joint reaction forces.

Thus, with reference to Fig. 4, the seven reaction forces and the single reaction moment associated with the kinematic joints of the system can be assembled into an 8×1 vector of the form

$$\boldsymbol{\lambda} = \left\{ \lambda_1 \ \lambda_2 \ \lambda_3 \ \lambda_4 \ \lambda_5 \ \lambda_6 \ \lambda_7 \ \lambda_8 \right\}^{\mathrm{T}} \tag{13}$$

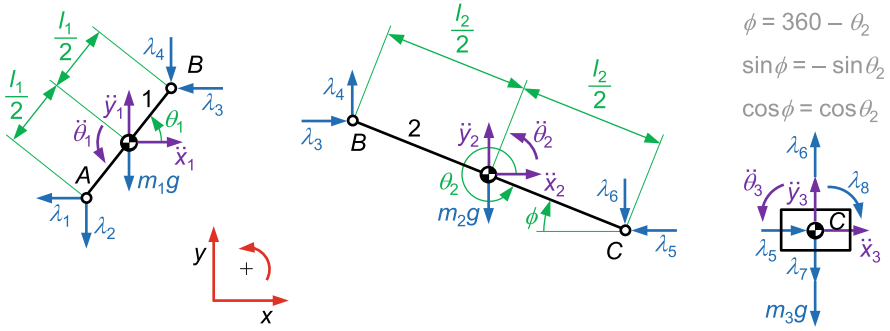

Fig. 4. Free-body diagrams of each body of the slider-crank mechanism.

The equations of motion for the slider–crank mechanism can be derived from the free-body diagrams shown in Fig. 4, yielding

$$m_1\ddot{x}_1 = -\lambda_1 - \lambda_3 \tag{14}$$

$$m_1\ddot{y}_1 = -\lambda_2 - \lambda_4 - m_1 g \tag{15}$$

$$I_1\ddot{\theta}_1 = -\lambda_1\frac{l_1}{2}\sin\theta_1 + \lambda_2\frac{l_1}{2}\cos\theta_1 + \lambda_3\frac{l_1}{2}\sin\theta_1 - \lambda_4\frac{l_1}{2}\cos\theta_1 \tag{16}$$

$$m_2\ddot{x}_2 = \lambda_3 - \lambda_5 \tag{17}$$

$$m_2\ddot{y}_2 = \lambda_4 - \lambda_6 - m_2 g \tag{18}$$

$$I_2\ddot{\theta}_2 = \lambda_3\frac{l_2}{2}\sin\theta_2 - \lambda_4\frac{l_2}{2}\cos\theta_2 + \lambda_5\frac{l_2}{2}\sin\theta_2 - \lambda_6\frac{l_2}{2}\cos\theta_2 \tag{19}$$

$$m_3\ddot{x}_3 = \lambda_5 \tag{20}$$

$$m_3\ddot{y}_3 = \lambda_6 - \lambda_7 - m_3 g \tag{21}$$

$$I_3\ddot{\theta}_3 = -\lambda_8 \tag{22}$$

his set of equations represents the translational and rotational motion equations of the slider-crank mechanism, forming a linear system of nine equations with 17 unknowns: nine accelerations and eight joint reaction forces. To obtain a unique and physically meaningful solution, it is necessary to incorporate eight additional equations derived from the kinematic constraints of the joints. Accordingly, with reference to Fig. 3, the eight algebraic constraint equations can be written as

$$\Phi_1 \equiv x_1 - \frac{l_1}{2}\cos\theta_1 = 0 \tag{23}$$

$$\Phi_2 \equiv y_1 - \frac{l_1}{2}\sin\theta_1 = 0 \tag{24}$$

$$\Phi_3 \equiv x_1 + \frac{l_1}{2}\cos\theta_1 - x_2 + \frac{l_2}{2}\cos\theta_2 = 0 \tag{25}$$

$$\Phi_4 \equiv y_1 + \frac{l_1}{2}\sin\theta_1 - y_2 + \frac{l_2}{2}\sin\theta_2 = 0 \tag{26}$$

$$\Phi_5 \equiv x_2 + \frac{l_2}{2}\cos\theta_2 - x_3 = 0 \tag{27}$$

$$\Phi_6 \equiv y_2 + \frac{l_2}{2}\sin\theta_2 - y_3 = 0 \tag{28}$$

$$\Phi_7 \equiv y_3 = 0 \tag{29}$$

$$\Phi_8 \equiv \theta_3 = 0 \tag{30}$$

The set of algebraic constraint Eqs. (23, 24, 25, 26, 27, 28, 29 and 30) can be represented in a general and compact form as [6]

$$\boldsymbol{\Phi} \equiv \boldsymbol{\Phi}(\mathbf{q}) = \mathbf{0} \tag{31}$$

The constraint equations in Eq. (31) are formulated at the position level and therefore cannot be directly incorporated into the equations of motion. Instead, the constraint equations must be expressed at the acceleration level. These acceleration-level constraint equations are obtained by differentiating Eq. (31) twice with respect to time, yielding

$$\ddot{\boldsymbol{\Phi}} \equiv \boldsymbol{\Phi}_{\mathbf{q}}\ddot{\mathbf{q}} = \boldsymbol{\gamma} \tag{32}$$

where $\boldsymbol{\gamma}$ is an 8×1 vector, commonly referred to as the right-hand side vector of the acceleration constraints, which includes the quadratic velocity terms in the equations of motion, specifically, the centrifugal terms. It is often called the quadratic velocity vector because it contains the velocity terms in quadratic form [6].

Thus, by combining the equations of motion with the acceleration-level constraint equations, a linear system of 17 equations with 17 unknowns can be obtained for the slider-crank mechanism. The resulting equations of motion for the slider-crank model can then be expressed as

$$\mathbf{M}\ddot{\mathbf{q}} + \boldsymbol{\Phi}_{\mathbf{q}}^{\mathrm{T}}\boldsymbol{\lambda} = \mathbf{g} \tag{33}$$

$$\boldsymbol{\Phi}_{\mathbf{q}}\ddot{\mathbf{q}} = \boldsymbol{\gamma} \tag{34}$$

or, alternatively, in a matrix structure [6]

$$\begin{bmatrix} \mathbf{M} & \boldsymbol{\Phi}_{\mathbf{q}}^{\mathrm{T}} \\ \boldsymbol{\Phi}_{\mathbf{q}} & \mathbf{0} \end{bmatrix} \begin{Bmatrix} \ddot{\mathbf{q}} \\ \boldsymbol{\lambda} \end{Bmatrix} = \begin{Bmatrix} \mathbf{g} \\ \boldsymbol{\gamma} \end{Bmatrix} \tag{35}$$

Equation (35) combines the differential equations of motion (31) with the kinematic algebraic equations at the acceleration level (32), and is commonly referred to as a mixed set of differential-algebraic equations (DAE). Specifically, Eq. (35) represents a linear index-1 DAE system in terms of the accelerations and the Lagrange multipliers [6].

The solution of the linear system in Eq. (35) constitutes an initial value problem, requiring the specification of the system state at a given instant in time. Since all linear and rotational components of positions and velocities can be readily determined from the characterization of the slider-crank model, the 17 equations in Eq. (35) can be solved for the nine linear and rotational accelerations, as well as the eight joint reaction forces and moments, $\boldsymbol{\lambda}$, using any standard numerical algorithm for linear systems. At each integration time step, the computed accelerations, together with the velocity vector, are integrated to update the system's velocities and positions for the next time step. This procedure is repeated until the final time of the dynamic analysis is reached [12].

It should be noted that solving the system of equations in Eq. (35) does not necessarily satisfy the position and velocity constraint equations, since these equations are not explicitly enforced during the dynamic analysis. As a result, for moderate or long simulation times, the initial constraints can be progressively violated due to numerical integration errors, particularly truncation errors. To eliminate, or at least minimize, such constraint violations during the numerical solution of the equations of motion, any of the established correction methods can be employed [13].

4 Concluding Remarks

This work presents a simple and systematic approach for addressing dynamics problems, which is taught to first-year students in the Dynamics of Machinery course. The proposed methodology consists of seven steps, illustrated through an application example, namely a planar robotic manipulator. This approach can be easily applied to analyze and discuss a wide range of mechanical systems, including mechanisms and linkages, Formula Student car models, and biomechanical human systems. Overall, the method has been recognized as effective by both students and instructors.

Acknowledgments. This work was supported by FCT - *Fundação para a Ciência e a Tecnologia* within the R&D units projects: UID/04436/2025 – *Centro de Microssistemas Eletromecânicos* of the University of Minho.

References

1. Dixon, J.C., Martin, J.K.: Three seconds in two days: a theoretical and practical model for teaching basic dynamics analysis. Proc. Inst. Mech. Engineers, Part K: J. Multi-Body Dyn. **214**(4), 195–208 (2000)
2. Novais, F., Silva, M.R., Gomes, I., Puga, H., Flores, P.: a simple and comprehensive approach to formulate and solve dynamics problems in a non-traditional engineering course. In MMT Symposium, pp. 1–2, Guimarães, Portugal (2024).

3. Flores, P., Lankarani, H.M.: Teaching kinematics and dynamics of machinery with a design project: The ping-pong ball launcher challenge. In: Proceedings of the ASME 2016 International Design Engineering Technical Conferences and Computers and Information in Engineering Conference IEDTC/CIE 2025, Anaheim, California., Paper DETC2025–167527 (2025)
4. Mikesell, D.R., Yoder, J.-D.S.: Teaching dynamics with a design project. In: American Society for Engineering Education (2011)
5. Prescott, A.E., Mitchelmore, M.: Student misconceptions about projectile motion. In: Clarkson, P., Gronn, A.D.D., Horne, M., McDonough, A., Pierce, R., Roche, A. (eds.) Building Connections: research, theory and practice, pp. 633–640, Sydney (2005)
6. Nikravesh, P.: Computer-Aided Analysis of Mechanical Systems. Prentice-Hall, New Jersey (1988)
7. Flores, P.: Ciência de Máquinas e Mecanismos, 1st edn. Engebook (2026)
8. Hadim, H., Esche, S.: Enhancing the Engineering Curriculum through Project-Based Learning. In Proc. Front. Educ., Boston (2002)
9. Flores, P.: Race party: a project-based learning approach to teach dynamics and Design of Mechanical Systems. Mechanisms and Machine Science. **180**, 393–401 (2025)
10. Neto, D., Flores, P.: Introducing a project-based learning approach in a course on design of machine elements: a case study in two public universities in Portugal. In: International Symposium on Project Approaches in Engineering Education, vol. 15, pp. 8–16 (2025)
11. Marques, F., Roupa, I., Silva, M.T., Flores, P., Lankarani, H.M.: Examination and comparison of different methods to model closed loop kinematic chains using Lagrangian formulation with cut joint, clearance joint constraint and elastic joint approaches. Mech. Mach. Theory. **160**, 104294 (2021)
12. Flores, P., Ambrósio, J., Lankarani, H.M.: Contact-impact events with friction in multibody dynamics: Back to basics. Mech. Mach. Theory. **184**, 105305 (2023)
13. Marques, F., Souto, A.P., Flores, P.: On the constraints violation in forward dynamics of multibody systems. Multibody Sys. Dyn. **39**(4), 385–419 (2017)

MECAPUCP: Interactive Teaching Tool for Mechanism Kinematics

Alonso Velis(✉), Mirko Flores, Tamie Tokuda, Daniel Lavayen, Estefania Hermoza, Enrique Carrillo, and Jorge Rodríguez

Applied Mechanics, Machines and Mechanisms Group, Department of Engineering, Pontificia Universidad Católica del Perú, Universitaria Ave. 1801, 15088 Lima, Peru
alonso.velis@pucp.edu.pe

Abstract. This paper presents *MECAPUCP*, an interactive desktop application developed in Python to support the teaching of planar kinematics as a foundational step for Engineering Dynamics, as well as Mechanism and Machine Theory. This tool combines a graphical user interface built with Tkinter, a numerical engine based on vectorized computations in NumPy and root-finding routines in SciPy, and real-time visualization of motion and kinematic variables using Matplotlib. *MECAPUCP* includes several classical mechanisms such as the slider-crank, four-bar linkage, Whitworth quick-return, to name a few, within a unified workflow for parameter definition, simulation, animation, and analysis. The contributions of this work are as follows: (i) It synthesizes a coherent theoretical framework for teaching kinematic analysis using a single software tool that is closely aligned with lecture content. (ii) It introduces a modular architecture that enables new mechanisms to be added with minimal modifications to the existing code. (iii) It demonstrates how the application can be used by students to verify manual calculations by comparing numerical results with hand-solved kinematic problems. (iv) It provides a practical evaluation tool for assessments or exams, allowing instructors to gauge students' conceptual understanding through simulation-based tasks.

Keywords: Linkage kinematics · engineering education · educational software · Interactive simulation

1 Introduction

The analysis and design of mechanisms is a fundamental component of engineering curricula, particularly in fields such as mechanical, mechatronics, and product-development engineering. Through classical systems such as the four-bar linkage and slider–crank mechanism, students learn to relate geometry and motion and to understand the behavior of real machines. However, the mathematical formulation of planar kinematics—based on nonlinear constraint

Supported by Pontificia Universidad Católica del Perú.

© The Author(s), under exclusive license to Springer Nature Switzerland AG 2026
A. Chaker et al. (Eds.): EFIMMS 2026, MMS 205, pp. 464–475, 2026.
https://doi.org/10.1007/978-3-032-22270-1_45

equations—often presents significant challenges for students encountering these concepts for the first time.

Traditional instruction typically combines: (i) hand derivations of constraint equations; (ii) problem sets limited to a few discrete configurations; and (iii) occasional demonstrations using commercial CAE or multibody software. While this approach helps to develop algebraic skills, it provides limited support for exploratory learning and rapid visualization of the effect of geometric and kinematic parameters.

While commercial tools are powerful, they tend to be used as "black boxes" offering limited opportunities for students to manipulate the underlying equations or experiment with geometric variations. Their high licensing cost and steep learning curves further restrict their use, especially in introductory courses [1]. By contrast, educational research on simulators and virtual laboratories shows that, when these tools are embedded in well-designed learning activities, they can significantly improve conceptual understanding, motivation, and academic performance. Positive effects have been reported in mathematics education using simulation environments such as PhET [2] and in chemistry courses during remote teaching conditions [3]. Similar benefits have been observed in digital systems and technology-related subjects in higher education [4] and in high school science and engineering contexts [5]. More broadly, a recent review highlights the role of simulation as a key resource for teaching and learning across disciplines, particularly during and after the COVID-19 pandemic [6]. In particular, interactive simulations allow students to explore the influence of variables in real time and to link symbolic representations with observable behavior.

Within engineering education, several works highlight the value of web-based resources and specialized software to support active learning and the development of spatial and investigative skills. Rodríguez Alba et al. [7] report that a dedicated web site for mechanical engineering students strengthens basic research abilities through structured digital resources, while Saeed Alqahtani et al. [8] survey techniques—including 3D graphics and virtual reality—aimed at improving spatial visualization in engineering graphics. In the specific field of Mechanism and Machine Theory (MMT), Macho et al. [9] describe the use of GIM software as a learning tool integrated into problem-based activities, and García-Prada and Castejón [10] compile a wide range of innovative educational practices that combine virtual simulations, prototypes, and active methodologies in mechanism science. These contributions motivate the development of domain-specific simulators that are aligned with course content and accessible to students.

Physical mechanism kits provide intuitive visualization, but they are costly, dimensionally fixed, and offer limited access outside the laboratory. Meanwhile, general-purpose engineering programs such as Autodesk Inventor or ANSYS, although available on campus, require substantial training before students can use them effectively.

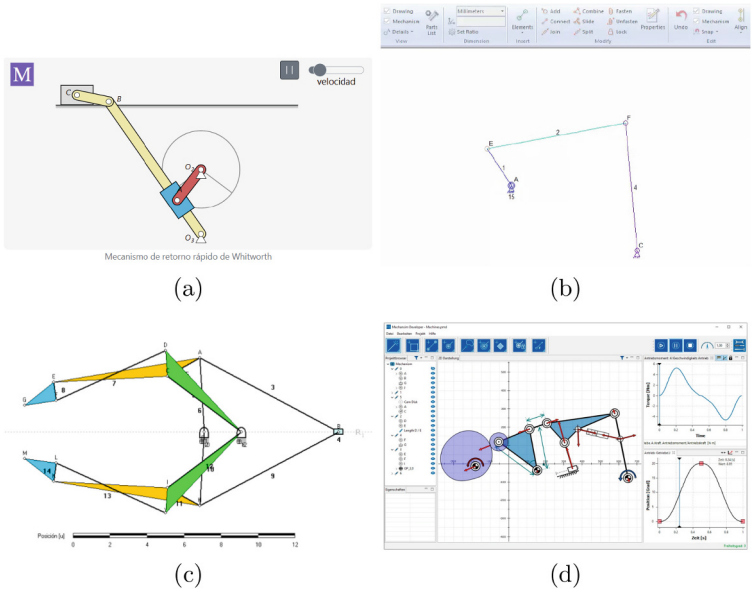

Fig. 1. Recent educational tools. (a) Whitworth quick-return mechanism in Mecapedia [11], (b) four-bar mechanism simulation in Linkage Mechanism Designer [12], (c) WinMecC interface [13], (d) MechDev interface [14].

In recent years, several educational tools have emerged that partially address these challenges; some interfaces of these tools can be seen in Fig. 1. Mecapedia [11] provides web-based animations of classical mechanisms with adjustable parameters. Linkage Mechanism Designer [12] enables quick sketching and animation of linkages but does not support advanced numerical analysis or code extensibility. WinMecC [13] offers kinematic simulation and basic force evaluation but requires commercial licensing. MechDev [14], developed at RWTH Aachen University, Germany, provides a comprehensive environment for mechanism design and analysis. Collectively, these tools highlight the value of interactive visualization but also reveal limitations related to accessibility, extensibility, and pedagogical integration. Table 1 shows a comparison of the educational tools mentioned for planar mechanism analysis.

At the same time, open-source scientific computing ecosystems—particularly Python and its libraries NumPy, SciPy, and Matplotlib—enable the development of lightweight, accessible tools that combine numerical analysis with intuitive visualization. These capabilities open new opportunities for inquiry-based teaching and for exposing students to the mathematical structure of kinematic problems in a controlled environment.

In this context, *MECAPUCP* is developed as an interactive Python-based "virtual laboratory" designed to support the teaching of planar mechanism kinematics at the Pontificia Universidad Católica del Perú (PUCP). The software

Table 1. Comparison of selected educational tools for planar mechanism analysis

Tool	Platform	Kinematic Analysis (pos., vel., acc.)	License/Availability
Mecapedia	Web-based (HTML5/JS)	Position only (no velocity/acceleration)	Free access online
Linkage Mechanism Designer	Windows desktop	Position-based animation only	Freeware
WinMecC	Windows desktop	Yes (positions, velocities, accelerations; basic forces)	Commercial license
MechDev	Windows/Linux	Yes (full kinematic and kinetostatic analysis)	Academic license (free for educational use)

aims to: (i) provide a unified workflow for parameter definition, simulation, animation, and plotting; (ii) lower the barrier to experimentation with mechanism geometry and input motion; (iii) remain lightweight, cross-platform, and free of commercial licensing restrictions; (iv) complement active-learning strategies in undergraduate courses; and (v) support students in design-oriented programs through intuitive motion visualization.

This paper presents the design and implementation of *MECAPUCP*. Section 2 summarizes the theoretical foundations of constraint-based kinematics. Section 3 describes the software architecture and development methodology. Section 4 reports classroom observations before and after incorporating *MECAPUCP*. Finally, Sect. 5 discusses conclusions based on the observed results and outlines future work.

2 Theoretical Background

2.1 Kinematic Problem Formulation

Kinematic analysis focuses on determining the motion of a mechanism independently of the forces involved. The configuration of the system is described by a vector of generalized coordinates $\mathbf{q} \in \mathbb{R}^n$, whose components may include Cartesian coordinates and orientation angles of the bodies.

In general, only g of these coordinates are *independent*, where g is the number of degrees of freedom (DOF) of the mechanism. The remaining coordinates are *dependent* and are related to the independent ones through a set of constraint equations. If $\boldsymbol{\phi}(\mathbf{q}) = \mathbf{0}$ denotes the vector of holonomic constraints, its dimension is $r = n - g$, where r is the number of constraint equations.

For numerical convenience the vector $\mathbf{q}$ is ordered as

$$\mathbf{q} = \begin{bmatrix} \mathbf{q}_d \\ \mathbf{q}_i \end{bmatrix} = \begin{bmatrix} q_1 \\ \vdots \\ q_r \\ q_{r+1} \\ \vdots \\ q_n \end{bmatrix},$$

where $\mathbf{q}_d \in \mathbb{R}^r$ collects the dependent coordinates and $\mathbf{q}_i \in \mathbb{R}^g$ the independent ones (coincident with the DOF of the system).

Although many references present the independent coordinates first, here we place the dependent coordinates first for numerical convenience. With this ordering, the Jacobian naturally partitions as $\boldsymbol{\Phi}_{\mathbf{q}} = [\, \boldsymbol{\Phi}_{\mathbf{q}_d} \; \boldsymbol{\Phi}_{\mathbf{q}_i} \,]$, so the unknown increments in $\mathbf{q}_d$ appear on the left-hand side of the linear systems used in the Newton step and in the velocity/acceleration solvers. The standard alternative ordering can be obtained by a simple permutation of the coordinate vector and the Jacobian columns.

2.2 Position Analysis

The constraint vector is written as

$$\boldsymbol{\phi}(\mathbf{q}) = \begin{bmatrix} \phi_1(\mathbf{q}) \\ \vdots \\ \phi_r(\mathbf{q}) \end{bmatrix} = \mathbf{0}, \tag{1}$$

where each scalar equation $\phi_j(\mathbf{q}) = 0$ enforces a geometric relation between bodies, and r is the number of constraints.

To solve for $\mathbf{q}$ such that $\boldsymbol{\phi}(\mathbf{q}) = \mathbf{0}$, a Newton–Raphson iterative method is employed at each time step. Let $\mathbf{q}^{(k)}$ denote the estimate of the generalized coordinates at the k-th iteration and $\boldsymbol{\Phi}_{\mathbf{q}}(\mathbf{q}) = \partial\boldsymbol{\phi}/\partial\mathbf{q}$ the Jacobian matrix of size $r \times n$. Linearizing $\boldsymbol{\phi}$ around $\mathbf{q}^{(k)}$ gives

$$\boldsymbol{\Phi}_{\mathbf{q}}(\mathbf{q}^{(k)})\big(\mathbf{q}^{(k+1)} - \mathbf{q}^{(k)}\big) = -\boldsymbol{\phi}(\mathbf{q}^{(k)}). \tag{2}$$

In (2), $\mathbf{q}^{(k+1)} - \mathbf{q}^{(k)} \in \mathbb{R}^n$ is the correction vector, $\boldsymbol{\phi}(\mathbf{q}^{(k)}) \in \mathbb{R}^r$, and $\boldsymbol{\Phi}_{\mathbf{q}}(\mathbf{q}^{(k)}) \in \mathbb{R}^{r\times n}$, so the equation is dimensionally consistent. The iterations proceed until the numerical error

$$e^{(k)} = \Big\| \boldsymbol{\phi}\big(\mathbf{q}^{(k)}\big) \Big\|_2 = \sqrt{\sum_{j=1}^{r} \phi_j\big(\mathbf{q}^{(k)}\big)^2} \tag{3}$$

falls below a prescribed tolerance, typically $e^{(k)} < 10^{-8}$.

2.3 Velocity Analysis

Differentiating the constraint equations (1) with respect to time yields

$$\sum_{i=1}^{n} \left.\frac{\partial \phi_j}{\partial q_i}\right|_{\mathbf{q}} \dot{q}_i = 0, \qquad j = 1, \ldots, r, \tag{4}$$

which in compact matrix form can be written as

$$\boldsymbol{\Phi}_{\mathbf{q}}(\mathbf{q})\, \dot{\mathbf{q}} = \mathbf{0}, \tag{5}$$

where $\dot{\mathbf{q}} \in \mathbb{R}^n$ is the vector of generalized velocities.

When a subset of velocities associated with the independent coordinates $\dot{\mathbf{q}}_i$ is prescribed (inputs or DOF), Eq. (5) is rearranged by partitioning the Jacobian as $\boldsymbol{\Phi}_{\mathbf{q}} = [\, \boldsymbol{\Phi}_{\mathbf{q}_d} \; \boldsymbol{\Phi}_{\mathbf{q}_i} \,]$, which leads to

$$\boldsymbol{\Phi}_{\mathbf{q}_d}\, \dot{\mathbf{q}}_d = -\boldsymbol{\Phi}_{\mathbf{q}_i}\, \dot{\mathbf{q}}_i. \tag{6}$$

This linear system is solved for the unknown dependent velocities $\dot{\mathbf{q}}_d$.

2.4 Acceleration Analysis

Acceleration equations are obtained by differentiating the velocity constraints with respect to time:

$$\sum_{i=1}^{n} \left.\frac{\partial^2 \phi_j}{\partial q_i \partial t}\right|_{\mathbf{q},\dot{\mathbf{q}}} \dot{q}_i + \sum_{i=1}^{n} \left.\frac{\partial \phi_j}{\partial q_i}\right|_{\mathbf{q}} \ddot{q}_i = 0, \qquad j = 1, \ldots, r. \tag{7}$$

Introducing the time derivative of the Jacobian, $\dot{\boldsymbol{\Phi}}_{\mathbf{q}} = d\boldsymbol{\Phi}_{\mathbf{q}}/dt$, and writing the result in matrix form, we obtain

$$\boldsymbol{\Phi}_{\mathbf{q}}(\mathbf{q})\, \ddot{\mathbf{q}} = -\dot{\boldsymbol{\Phi}}_{\mathbf{q}}(\mathbf{q}, \dot{\mathbf{q}})\, \dot{\mathbf{q}}. \tag{8}$$

Again, by partitioning the unknowns into dependent and independent coordinates, $\ddot{\mathbf{q}} = [\, \ddot{\mathbf{q}}_d^{\top} \quad \ddot{\mathbf{q}}_i^{\top} \,]^{\top}$, and separating the corresponding columns of $\boldsymbol{\Phi}_{\mathbf{q}}$, the linear system for the dependent accelerations $\ddot{\mathbf{q}}_d$ is obtained.

3 Methodology: Application Development

3.1 Software Architecture

MECAPUCP is implemented as a single Python application organized in several logical layers:

1. **Graphical User Interface (GUI) layer:** built with Tkinter, it manages windows, menus, tabs and input widgets (text boxes, sliders, combo boxes and buttons). This layer captures user actions and dispatches them to the simulation core.

2. **Simulation core:** a set of functions that perform the mechanism–independent tasks of time stepping, constraint solving and storage of kinematic variables. Mechanism–specific functions (for ϕ, $\mathbf{\Phi}_q$, etc.) are passed as arguments.
3. **Visualization layer:** a collection of Matplotlib plots embedded in Tkinter canvases. One figure is dedicated to the mechanism animation, while others show kinematic graphs (e.g. input angle versus time, slider position versus time).

This architecture decouples the user interface from the mathematical formulation and from the visualization details, facilitating maintenance and extension. The Home view can be seen in Fig. 2. Although the current GUI is shown in Spanish due to its use in a local course, an English interface is planned for future releases.

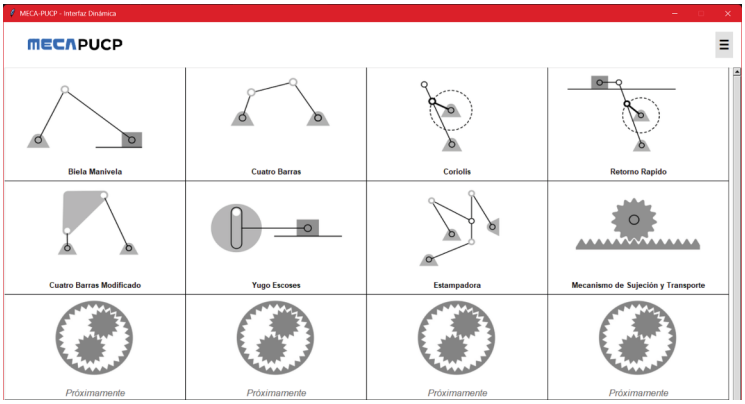

Fig. 2. *MECAPUCP*'s Home view

3.2 User Interaction Flow

The typical workflow for a student using *MECAPUCP* is:

1. **Mechanism selection:** choose a mechanism from a drop–down list.
2. **Parameter configuration:** adjust link lengths, input angular velocity, acceleration and simulation time step through text fields or spin boxes.
3. **Simulation:** start the simulation. The application iterates over time, solving the constraint equations at each time step and updating arrays of kinematic variables.
4. **Animation:** observe the mechanism motion in the main figure. Links, ground, sliders and joints are drawn with different colors and markers; the current configuration is highlighted.

5. **Analysis:** inspect the kinematic plots generated in separate tabs. Students can compare, for example, input angle versus time against slider displacement or velocity.

The interface also includes controls to pause, resume and reset the simulation, as well as to export plots if needed, as can be seen in Fig. 3 and 4 .

Fig. 3. *MECAPUCP*'s configuration panel

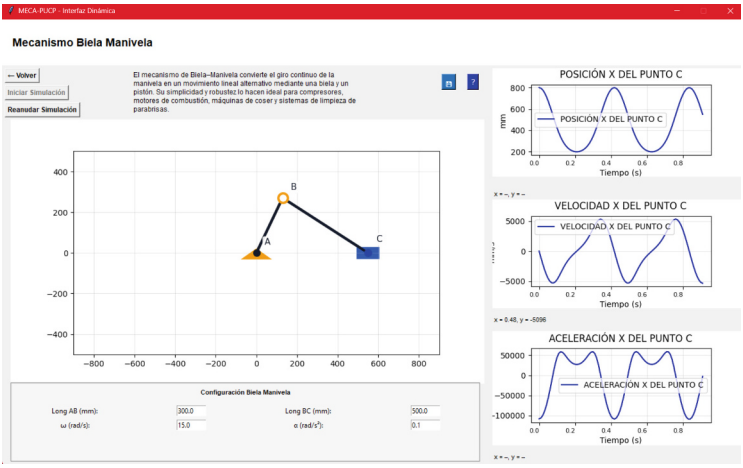

Fig. 4. Slider-crank mechanism simulation in *MECAPUCP*

4 Results and Discussion

Eight consecutive offerings of the undergraduate Engineering Dynamics lecture (2022–1 to 2025–2) were analyzed to evaluate longitudinal trends in student performance on the same graded practical assignment (Practical Assignment 5). The grading scale ranges from 0 to 20, with 11 as the minimum passing grade. This multi-year comparison enables measuring natural cohort variability as well as the impact of introducing *MECAPUCP* as a computational aid.

Across the 2022–1 to 2024–2 periods, when *MECAPUCP* had not yet been deployed, the mean scores exhibited substantial fluctuations, ranging from a low of 9.35 in 2023–1 to a high of 15.85 in 2022–2. Despite these variations, several semesters showed mean values near the passing threshold, indicating persistent student difficulties with kinematic synthesis and mechanism analysis using traditional methods. During 2024–2, the last semester before the introduction of the tool, the mean score was 10.81 with a standard deviation (SD) of 3.83, slightly below the passing cutoff. After deploying *MECAPUCP* in 2025–1, the mean increased to 16.01 (SD = 4.16), representing a substantial improvement relative to the preceding semester. This supports the hypothesis that providing an interactive visualization and computation environment can enhance conceptual understanding and problem-solving accuracy. It is worth noting, that the assignment included evaluation of new scenarios and take small design decisions, requiring students to engage with the software.

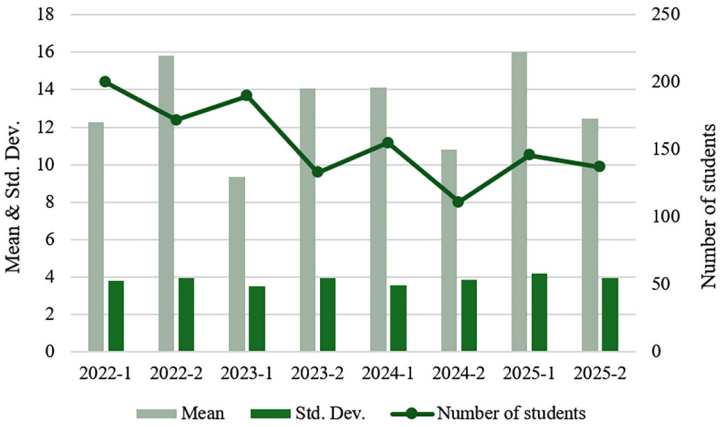

Fig. 5. Summary of the practical assignment results in Engineering Dynamics. This activity is related to rigid body motion and linkage analysis.

In 2025–2, the mean decreased to 12.46 (SD = 3.93). Conversations with the head teaching assistant confirmed that a considerable portion of students did not complete the *MECAPUCP*-related steps, leading to incomplete submissions. Thus, the lower performance appears to be linked not to the tool itself but to inconsistent usage among the group of students.

In addition to the mean and standard deviation, we report pass rates for Practical Assignment 5 (PA5) as a complementary performance metric. Table 2 summarizes, for each semester, the number of students with a recorded PA5 score (N), the number of students who passed (Pass, score ≥ 11 on a 0–20 scale), and the corresponding pass rate. Consistent with the trends observed in the mean scores, the highest pass rate is obtained in 2025–1 (92.1%), while 2025–2 shows a lower pass rate (73.8%), which is aligned with incomplete submissions reported by the teaching staff.

Table 2. Pass rates for Practical Assignment 5 (passing score ≥ 11 on a 0–20 scale). N denotes the number of students with a recorded PA5 score (withdrawn and missing entries excluded).

Semester	N	Approved students	Approval rate [%]
2022–1	153	108	70.6
2022–2	149	134	89.9
2023–1	169	63	37.3
2023–2	109	89	81.7
2024–1	142	121	85.2
2024–2	188	104	55.3
2025–1	139	128	92.1
2025–2	122	90	73.8

Because cohort sizes vary across semesters, the overall comparison between periods is computed using a weighted mean,

$$\bar{x}_w = \frac{\sum_s N_s \, \bar{x}_s}{\sum_s N_s}, \tag{9}$$

where N_s and $\bar{x}_s$ denote the sample size and mean PA5 score of semester s, respectively. Using the N_s values in Table 2, the weighted mean before *MECAPUCP* (2022–1 to 2024–2) is 12.72, while the post-*MECAPUCP* period (2025–1 to 2025–2) increases to 14.35. Overall, these statistics indicate that *MECAPUCP* can improve performance and approval rate when it is consistently integrated into the assignment workflow; therefore, future offerings will emphasize clearer scaffolding and structured usage to reduce incomplete submissions and stabilize gains across cohorts.

A bar plot summarizing mean and standard deviation across all semesters is shown in Fig. 5.

5 Conclusions and Future Work

This work presented *MECAPUCP*, an interactive Python-based application designed to support the teaching and learning of planar mechanism kinematics.

The multi-cycle evaluation shows promising evidence of pedagogical impact. In particular, the substantial increase in mean performance observed during the first deployment of the tool (2025–1 semester), with results well above the minimum passing grade of 11 on a 0–20 scale, suggests that students who actively engaged with *MECAPUCP* benefited from its interactive capabilities. The lower average observed in the following semester (2025–2) highlights the importance of providing clear guidance and structured integration to ensure consistent student engagement rather than reflecting limitations of the tool itself.

Overall, student feedback consistently emphasized the clarity gained from interactive simulations, real-time visualization of mechanism motion, and the ability to explore parametric variations. These findings underline both the educational value of *MECAPUCP* and the iterative nature of incorporating computational tools into engineering curricula.

Future work will focus on further enhancing usability and extensibility. Planned developments include (i) improving the graphical user interface, including clearer and more consistent visual notation and symbol usage, (ii) expanding documentation with guided tutorials and step-by-step examples, (iii) increasing the catalog of predefined mechanisms, (iv) enabling greater flexibility through user-defined mechanism configurations, and (v) adding an on-screen legend to standardize and explain the graphical notation used for joints, links, and ground constraints. Additionally, future studies will aim to conduct more controlled evaluations to quantitatively assess learning outcomes across different instructional settings. With these developments, *MECAPUCP* is expected to evolve into a robust and adaptable platform that can support mechanism kinematics education in a broader academic context.

Acknowledgements. This work was funded by the Pontifical Catholic University of Peru (PUCP), under the grant *Fondo Concursable para la Innovación en la Docencia Universitaria 2025* (Fund for Innovation in University Teaching 2025).

Data Availibility Statement. The MECAPUCP application, together with example files and supplementary teaching materials, is available in an online repository and can be accessed by clicking on the following link: MECAPUCP project.

Conflict of Interest. The authors have no competing interests to declare that are relevant to the content of this article.

References

1. Berselli, G., Bilancia, P., Luzi, L.: Project-based learning of advanced CAD/CAE tools in engineering education. Int. J. Interact. Des. Manuf. **14**, 1071–1083 (2020). https://doi.org/10.1007/s12008-020-00687-4
2. Díaz Pinzón, J.E.: Aprendizaje de las matemáticas con el uso de simulación. Sophia **14**(1), 22–30 (2018). https://doi.org/10.18634/sophiaj.14v.1i.519
3. Rosero-Mellizo, L.S., Rivera-Toro, K.A., Guerrero-Julio, M.L.: Simulaciones en PhET como estrategia en tiempos de COVID-19 para generar aprendizaje significativo. Panorama **16**(30) (2022). https://doi.org/10.15765/pnrm.v16i30.3135

4. Barradas-Arenas, U.D., Cocón-Juárez, J.F., Pérez-Cruz, D., Vázquez-Aragón, M.R.: El impacto de los simuladores en el aprendizaje de los sistemas digitales. Rev. Docentes 2.0 **16**(1), 67–76 (2023). https://doi.org/10.37843/rted.v16i1.350
5. Mendoza Hernández, L.E., Mendoza-Hernández, L.E., García-Contreras, J.M.: The use of simulators as a teaching-learning strategy in high school. UNO Sapiens, Boletín Científico de la Escuela Preparatoria No. 1 **6**(11), 12–15 (2023). https://doi.org/10.29057/prepa1.v6i11.10949
6. Castro-Maldonado, J.J., Bedoya-Perdomo, K., Pino-Martínez, A.A.: La simulación como aporte para la enseñanza y el aprendizaje en épocas de Covid-19. AiBi Rev. Invest. Adm. Ingeniería **8**(S1), 315–324 (2020). https://doi.org/10.15649/2346030X.2475
7. Rodríguez Alba, E., Bueno Montana, Y., Villavicencio Lozano, L., Mustelier Hechavarría, A.: Sitio web para el aprendizaje en la carrera de ingeniería mecánica. Rev. Ciencias Pedagógicas Innov. 41–46 (2016). https://doi.org/10.26423/rcpi.v4i2.134
8. Saeed Alqahtani, A., Daghestani, L.F., Ibrahim, L.F.: Techniques used to improve spatial visualization skills of students in engineering graphics course: a survey. Int. J. Adv. Comput. Sci. Appl. (IJACSA) **8**(3) (2017). https://doi.org/10.14569/IJACSA.2017.080315
9. Macho, E., Urízar, M., Petuya, V., Hernández, A.: Improving skills in mechanism and machine science using GIM software. Appl. Sci. **11**(17), 7850 (2021). https://doi.org/10.3390/app11177850
10. García-Prada, J.C., Castejón, C. (eds.): New Trends in Educational Activity in the Field of Mechanism and Machine Theory. Mechanisms and Machine Science, vol. 64. Springer (2014). https://doi.org/10.1007/978-3-319-01836-2
11. Iserte, J.: Mecapedia: interactive mechanism encyclopedia. Universitat Jaume I (2022). https://www.mecapedia.uji.es/Index.html
12. Rector, D.: Linkage mechanism designer and simulator (software) (2016). https://blog.rectorsquid.com/linkage-mechanism-designer-and-simulator/
13. Bataller, V., Romero, F.: WinMecC: kinematics and dynamics of mechanisms. Universidad de Málaga (2017). https://www.winmecc.com/
14. Müller, M., Mannheim, T., Hüsing, M., Corves, B. (2019). MechDev—a new software for developing planar mechanisms. In: Kecskeméthy, A., Geu Flores, F., Carrera, E., Elias, D. (eds.) Interdisciplinary Applications of Kinematics. Mechanisms and Machine Science, vol. 71. Springer, Cham. https://doi.org/10.1007/978-3-030-16423-2_15

The Italian Initiative for MMS Early Career Researchers: Lessons Learned and Historical Development

Giovanni Mottola[1(✉)], Matteo Russo[2], and Edoardo Ida[3]

[1] Department of Engineering, University of Messina, 98166 Messina, Italy
giovanni.mottola@unime.it
[2] Department of Industrial Engineering, University of Rome Tor Vergata, 00133 Rome, Italy
matteo.russo@uniroma2.it
[3] Department of Industrial Engineering, University of Bologna, 40136 Bologna, Italy
edoardo.ida2@unibo.it

Abstract. Many scientific associations active in fields relevant to Mechanism and Machine Science (MMS) have programs for young researchers, who may lack experience on scientific networking. The "International Federation for the Promotion of Mechanism and Machine Science" (IFToMM) launched its own initiative, called "Young Faculty Group" (YFG), in July 2023; it is structured as a "Cross Disciplinary Group" (CDG), designed to work across research areas. A concept similar in goals and scope has independently been launched in Italy in 2025 by a group of assistant professors, with the support of the "Gruppo di Meccanica Applicata" (GMA), the national association of professors and researchers working on MMS. The "Iniziativa Ricercatori Emergenti" (GMA-IRE) has already held surveys, promoted seminars, and started a newsletter. In this work, we report survey data, discuss how such groups can be effectively organized, and reflect on lessons learned and potential pitfalls. We also briefly report on the organization of Italian academia, to explain the constraints under which GMA-IRE operates. This work aims to support the development of YFG and promote the launch of similar groups in scientific organizations of interest for early-career researchers in MMS.

Keywords: Young researchers · Scientific societies · Career development · History of MMS · Education in MMS

1 Introduction

Mechanism and Machine Science (MMS) is a discipline within mechanical engineering with a rich history and an active research community. Several scientific organizations promote conferences and publish journals that are relevant to MMS researchers. Many of these organizations have launched programs to support the career development of young researchers. Indeed, scientific societies can support

© The Author(s), under exclusive license to Springer Nature Switzerland AG 2026
A. Chaker et al. (Eds.): EFIMMS 2026, MMS 205, pp. 476–486, 2026.
https://doi.org/10.1007/978-3-032-22270-1_46

people (especially from underrepresented groups) who are starting their academic careers in overcoming professional obstacles; more broadly, these societies aim to support mentorship opportunities and promote an inclusive environment for networking and discussion.

The *International Federation for the Promotion of Mechanism and Machine Science* (IFToMM), founded in 1969 (Zakopane, Poland), is historically organized [1] in 45 national *Member Organizations* (MOs), representing countries or territorial areas, and in 14 *Technical Committees* (TCs), organized [2] according to the main areas of interest for IFToMM (tribology, vibrations, transportation machinery and so on). Over time, a need emerged to introduce less formally organized *Cross Disciplinary Groups* (CDGs), independently of geographical location and research area. Currently, one CDG [3] is focused on applications of MMS research to the *Sustainable Development Goals* (defined by the *United Nations* in their *2030 Agenda*), while the other three represent women [4], graduate students [5] and young researchers [6] within IFToMM; the latter CDG is called *Young Faculty Group* (YFG). The CDG on sustainability organized its first scientific conference in 2021, while the YFG began with a symposium in 2024 [7].

Other international associations have launched similar initiatives for representing young scientists. Some of those closer to IFToMM in goals and research topic are *American Society of Mechanical Engineers (ASME) Young Professionals* [8], *Institute for Electrical and Electronics Engineers - Robotics and Automation Society (IEEE RAS) Young Professionals* [9], and the *European Community on Computational Methods in Applied Science (ECCOMAS) Young Investigators Committee* [10]; the *European Magnetism Association (EMA) Young Working Group* [11] and *European Physical Society (EPS) Young Minds* [12] are also worth citing.

A problem observed in the organization of such groups is the lack of guidelines and best practices for their effective management, also considering that younger members of the scientific community may not have the experience needed to lead effective groups.

In this work, we reflect on experiences and good practices for groups of interest to young researchers in MMS. As a case study, we consider the Italian *"Iniziativa Ricercatori Emergenti"* ("Early Career Researchers Initiative", or GMA-IRE), developed within the *"Gruppo di Meccanica Applicata"* (GMA) [13], the Italian association for MMS researchers. The GMA-IRE was launched in early 2025, and it has already organized several activities, including surveys, seminars, and a newsletter.

Considering this experiment at the national (rather than international) scale, we report the activities from the first year of the initiative and discuss the lessons learned, in the hope of supporting the development of IFToMM YFG and the birth of similar groups in other associations. We also present statistical data on the work and general interests of MMS researchers, reporting the results of surveys conducted by GMA-IRE and YFG.

The most immediate challenge is to define what "young faculty" means in this context and thus to identify the targets of such initiatives. GMA-IRE chose

to focus on Assistant professors, but is also open to PhD students and post-doctoral contract researchers (among whom the next generation of Assistant professors will be selected); Full and Associate professors may also participate in the activities. On the other hand, YFG has chosen a more open definition, letting any interested researcher in MMS join.

Another question we consider is what kind of activities can be successful (considering specific metrics that we identified) and interesting, thus worth organizing within similar groups; we consider both online and in-person events. Therefore, we describe the events organized by GMA-IRE so far and discuss the feedback from the participants.

The rest of this work is organized as follows. In Sect. 2, we describe the Italian academic context and the goals of GMA-IRE. In Sect. 3, we present surveys conducted among colleagues and report their results. In Sect. 4, we discuss the activities organized by GMA-IRE. Finally, in Sect. 5, we summarize our experience and discuss how it could be applied to promote similar initiatives in related scientific communities.

2 The GMA Framework

In creating GMA-IRE, it was necessary to consider the constraints and opportunities offered by the Italian academic context. Choosing to create such a group within GMA was a consequence of the role and visibility that GMA has in the national MMS community.

It is worth noting that GMA and *IFToMM Italy* (the national MO) are separate entities, albeit with a large membership overlap. This is due to historical reasons: GMA was created to ensure the relevance of MMS in Italian academia, and represents only MMS researchers, a constraint due to how research fields are divided under Italian law. GMA also has a formal role in academic policy, acting as a link with the *Ministry for University and Research* (MUR). On the other hand, IFToMM Italy (an affiliate group of GMA from 2003 to 2009, then an independent group) has a broader scope, and includes researchers in MMS-related fields, such as machine design. It publishes the *International Journal of Mechanics and Control* (JOMAC, since 2000) and organizes scientific conferences, for example the *International Conference of IFToMM Italy* (IFIT, since 2016).

2.1 The GMA

Italian academia has been organized since 1990 in academic fields, called *"Settori Scientifico Disciplinari"* (SSDs), which define specific fields of research and teaching [14]. Since 2024, each SSD is associated with a broader *"Gruppo Scientifico Disciplinare"* (GSD), which groups related SSDs. MMS research is mainly associated with the SSD/GSD *"IIND-02/A - Meccanica Applicata alle Macchine"* (Applied Mechanics).

The GMA, founded in Milan in 1986 [15], is governed by a board of four full professors and one president, elected by GMA members (∼300 professors and researchers at 40 Italian universities, all in IIND-02/A) every four years during the annual general assembly. GMA also defines the scope of teaching and research in MMS in a *"declaratoria"* (declaratory judgment), which is sent to the MUR and updated every few years.

2.2 The GMA-IRE

The idea for GMA-IRE started during IFIT 2024 [16] in Turin (Italy), when a group of assistant professors discussed the need for a group of early-career researchers with GMA board members, who approved and formally supported the project.

One of the first aims was to define for each University involved a contact person (ideally an Assistant professor, but postdoctoral researchers and Associate professors within 5 years of appointment were also considered for the position). This, however, was not possible in every case, because for example some smaller Universities did not have a person in such a role within the SSD. In total, 19 local representatives were selected. Assistant professors give the group a degree of stability over time, since they usually hold their position for several years before being promoted to Associate. Also, Assistant professors are one third of GMA members, and they are often involved in both research and teaching activities, with limited time and resources to devote to career development.

In addition, GMA-IRE organizers defined six main areas of interest in MMS; for each area, they sought to form a technical committee, by recruiting one chairperson among interested colleagues. These areas roughly correspond to IFToMM TCs, although some TCs are not represented and some were grouped together, as follows:

1. *Robotics and Mechatronics* (also includes automation and actuators);
2. *Transportation Machinery* (includes automotive and railway engineering);
3. *Biomechanical Engineering* (includes biomedical devices);
4. *Multi-body Dynamics* and *Computational Kinematics* (also mechanism optimization);
5. *Vibrations*, *Dynamics of Rotating Machines* and *Reliability*;
6. *Tribology.*

Each committee is responsible for organizing events and sharing news (conferences, collaboration opportunities, job openings, grants, awards and so on).

Before creating the project, specific goals and *Key Performance Indicators* (KPIs) were defined, to measure whether the activities were successful. These include counting:

- responses in surveys and participants in meetings organized by GMA-IRE;
- PhD theses co-supervised among members and grant applications submitted together;

– distinct topics (among the six areas defined above) covered in GMA-IRE events;
– joint journal publications (with co-authors from different Universities).

3 Survey

GMA-IRE and IFToMM YFG started their operations by conducting surveys (from November 2023 to November 2024 and from March 2025 to April 2025, respectively) among potential members, using mailing lists provided by GMA and IFToMM. One goal was to divide the population by research area, age range, general interests and so on; this allows representing members' needs and ideating events of broad interest. The YFG survey was anonymous, unlike the one by GMA-IRE, which aimed to profile the situation in each University (thus, the latter had no questions on respondents' personal situations).

3.1 Survey Design

The YFG survey (launched in 2023 at the *IFToMM World Congress* [17–19], Tokyo, Japan) had 78 questions, with sections on work-life balance and teaching styles; the one by GMA-IRE (36 questions) focused on research needs and opportunities. Both surveys took up to 15 min and included multiple-choice, Likert-scale, and open-ended questions.

The surveys also asked researchers about their perceived educational needs, e.g., on grant writing, modern teaching methods and soft skills. Finally, in GMA-IRE's survey, some questions gauged participants' willingness to contribute to the initiative.

3.2 Survey Results

The surveys had about the same number of responses (66 for YFG, 64 for GMA-IRE).

Most YFG respondents[1] are between 25 and 35 years old (Fig. 1, left); 68.2% of them are male. The most common academic roles are post-doc and Associate or Assistant professor (Fig. 1, right). 60.6% of respondents work in an institution different from the one where they completed their PhD, and 39.4% of them expect a promotion within two to five years. Respondents live and work in 19 different countries across the world (Fig. 2, left). Most of them publish one or two papers per year (Fig. 2, right).

Most GMA-IRE respondents are in at least one scientific society (Fig. 3, left).

Supervising a PhD student can be a fundamental career step, yet not all have this opportunity (Fig. 3, right). To share the responsibility and increase

[1] Due to restrictions, answers for the YFG survey on sections "Personal situation" and "Suggestions for next steps" were not available for respondents based in the People's Republic of China.

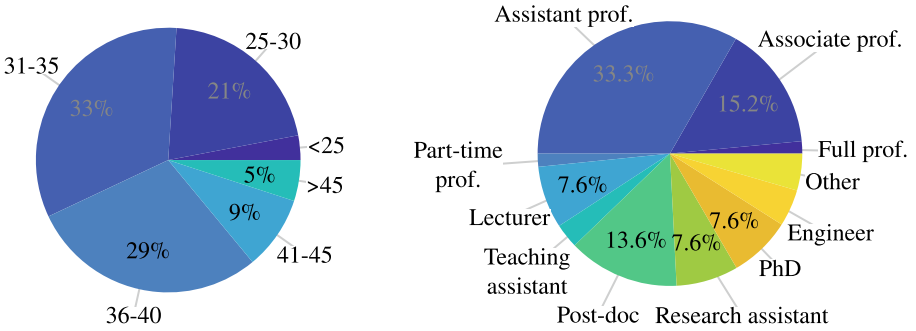

Fig. 1. YFG survey results. Left: age distribution (years), right: work position.

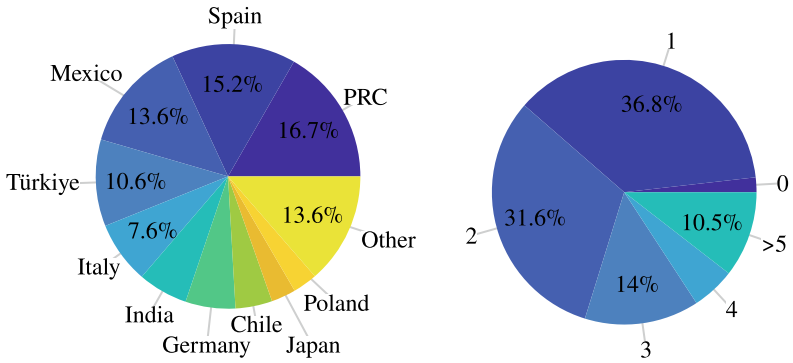

Fig. 2. Left: nationality, right: number of papers published per year (YFG respondents).

the offer of prospective students, 92% of GMA-IRE respondents are interested in co-supervising a student from another institution and 88% are willing to have their students co-supervised by colleagues.

YFG respondents prefer in-person events (44%, versus 16.7% online and 39.4% hybrid); despite this, the first YFG symposium was online due to travel cost constraints, which are more stringent for young researchers with limited funds. 18.75% of GMA-IRE respondents want exclusively in-person meetings, while the majority (75%) is open to all formats; preferences are split between two (51.5%) and four online events per year.

GMA-IRE asked a Likert-scale question (from 1 to 5) on the perceived need for educational events on various topics: the highest scores were for grant writing, EU funding opportunities and invited research talks, while the lowest were for social impact and teaching methods. Thus, GMA-IRE has focused on grant writing so far, also because many respondents have personal experience on it, 30% of them are willing to share what they learned, and most of them would feel confident in supervising a project (Fig. 4, left).

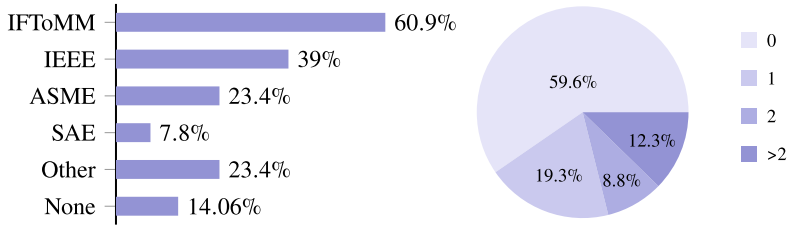

Fig. 3. Left: % of GMA-IRE respondents who are also registered in other scientific societies. Right: YFG respondents, number of PhD students supervised or co-supervised.

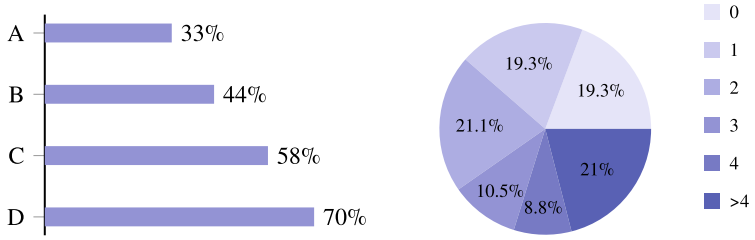

Fig. 4. Left: GMA-IRE respondents, % of positive answers (A = "I wrote a grant as coordinator", B = "I helped write a grant", C = "I believe I can supervise an entire grant project", D = "I can supervise a grant work package"). Right: YFG respondents, number of funded projects as coordinator.

YFG asked respondents what the group could offer them; the least selected options were sustainability, healthy science and teaching innovation. On the other hand, the most popular answers were international networking (88.3%), opportunities to present research (58.3%) and conferences (43.3%). Most respondents are or have been coordinators for at least one funded project (Fig. 4, right). Asked about what IFToMM could do to support them, 55% answer "by sharing information about funding"; other common options are organizing events for cross-disciplinary research (41.7%) and collaboration (35%), and launching new journals (31.7%) besides *Mechanism and Machine Theory*, which is the only one officially recommended by IFToMM at this time.

Some of the most popular research topics are robotics, multibody dynamics, kinematics, and vibrations (Fig. 5). For the YFG survey, we only report data for topics corresponding to a TC; other topics had lower response rates. Among YFG respondents, biomedical engineering is also popular: in a question on possible topics for the next YFG conference, "Robotics" and "Biomedical Engineering" are the first and third most popular answers, with a more generic "Mechanisms and Machines" being second.

Besides doing research, most YFG respondents (78.8%) also teach. 32.7% of them often use new techniques, but 5.8% have had negative experiences with them; 50% tend to use standard methods, and 25% are interested in conferences on teaching approaches.

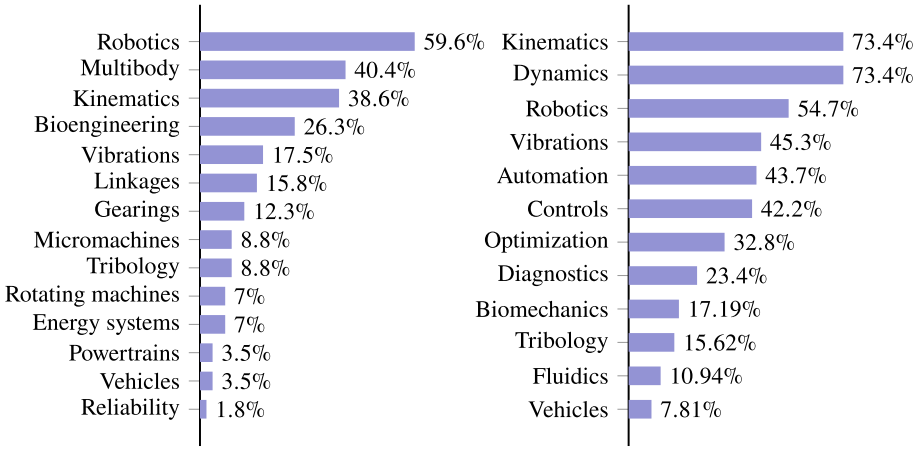

Fig. 5. % of respondents interested in MMS research topics (left: YFG, right: GMA-IRE).

Young researchers can face a heavy workload: 38.3% of YFG respondents report personal life pressure, yet at the same time most are happy about work-life balance (50% answer ≥ 7 in a Likert scale from 1 to 10). 65% have taken maternity or paternity leave.

4 Activities and Future Work

4.1 Activities

The main activity of YFG after the survey was completed was to organize an online symposium in November 2024, where the YFG survey results were presented [7].

The GMA-IRE survey results were presented during the GMA annual assembly (Desenzano del Garda, Italy, July 2025), in a brief meeting open to all GMA members.

The first events organized by GMA-IRE were online and recorded for maximum participation and visibility, also considering the results from the survey (Sect. 3). These events were focused on grant design; other options included modern teaching methods and soft skills, but these were met with less interest. After each workshop, to gauge its success, participants were asked to participate in a new survey (with both Likert-scale and open-ended questions); the degree of satisfaction is another KPI for the organizers.

The events include different types of education methods: a first phase with frontal presentations from experts, then a peer-to-peer discussion in a virtual round table.

The first event was about applying to *European Union* (EU) grants. It discussed the *Horizon Europe* funding schemes, explaining differences among the

three main pillars, and how to apply the *Logical Framework Approach*, a technique (first developed for Project Management in 1969) required by the EU in preparing applications; 49 participants joined. The vast majority reported high or very high satisfaction: the round table, which was the least popular part of the seminar, was still ranked at least 4 on a 5-point Likert scale by 76% of participants. Many appreciated the short format (1 h).

The second event was on success stories in grant writing: three young GMA members who won European grants (*ERC Starting Grant*, *MSCA* and *Pillar II*, on topics such as soft robotics, energy infrastructure design and dielectric elastomers) were invited. This online meeting had 33 participants and a round table session with the winners.

One goal of GMA-IRE is to promote collaborations among members. To this end, a monthly newsletter was started in October 2025; the idea and structure are inspired by the *euRobotics* mailing list [20] and *robotics-worldwide* [21], two moderated mailing lists for robotics researchers. The idea was also suggested by a lack of similar lists for other sectors of interest in MMS. The newsletter includes:

- calls for papers in journals and conferences and general event announcements;
- funding opportunities (including EU grants and national and regional calls);
- collaboration offers (e.g., supervision of Master's/PhD theses and research projects);
- job openings (for students and post-docs).

The newsletter is sent to all 70 GMA-IRE members and organized according to the six areas of interest (Sect. 2.2), to help readers find information that is relevant to them.

The KPIs set for the newsletter include the number of entries per month and of new results (such as collaborations or thesis supervisions) that started through it.

4.2 Future Work

The next goals for GMA-IRE include organizing an in-person meeting within one year since the start of the initiative. The focus will be on networking and starting new collaborations, with a hackaton-style event in which participants will split in groups, brainstorm and draft a project on a research topic, and present it to others, in a peer-to-peer learning environment. The event will be sponsored by GMA to be low-cost or free for participants, to ensure maximum participation, even for non-established researchers. Further online events will also be planned on topics suggested and voted by members.

The next steps for YFG are similar to the activities of IFToMM TCs and MOs, such as organizing conferences; the aim is to have a periodic in-person event organized by YFG and other CDGs, preferably in areas with limited IFToMM presence, to increase visibility and outreach. YFG also aims to create regular webinars on MMS topics and on complementary research skills, such as grant writing and project management.

Some common issues can be identified in the organization of both groups. Timing is a recurring problem, given how most young researchers have a significant workload due to teaching and exams; thus, events should be scheduled outside typical lesson periods.

The surveys show a general lack of interest in sustainability, teaching methods and healthy science practices. We hypothesize that, due to the pressure of career advancement, these topics seem of less immediate and practical concern for young researchers. Given their growing importance, stressing their role in shaping one's career is a worthy goal for young faculty groups, which however requires clear choices from the leadership.

In the surveys, many express interest in participating to conferences, but events targeted at young researchers can also be created by "regular" scientific communities (not organized by young members as a structured subgroup): see for instance the GIMC SIMAI Young [22] conferences in Italy, organized as joint events by the *"Gruppo Italiano di Meccanica Computazionale"* (a society of scholars in computational mechanics) and *"Società Italiana di Matematica Applicata e Industriale"* (for industrial and applied mathematics). Instead, young faculty groups should aim to make themselves irreplaceable, by ideating impactful and unique activities that could not be organized otherwise.

Keeping such groups active after an initial period of enthusiasm can be hard, especially after leadership changes (due to Assistant professors getting tenure, and also to ensure turnover). This also raises the question of how much democratic the internal procedures should be: elections can promote member engagement, but can also reduce stability.

Finally, both groups should maintain close contact with their parent organizations, to ensure alignment with broader goals and access to resources. To keep these links active, both GMA-IRE and YFG have defined one/two group leaders acting as contact persons.

5 Conclusions

In this work, we discuss experiences and results in organizing groups targeted for young researchers within larger (national or international) scientific communities. We discuss group organization, goals, activities and intended future work. We focus on the lessons learned and on how these could be transferred to similar groups, discussing strategies and potential pitfalls. We also report results from surveys proposed to our colleagues, also to support scientific communities in understanding the needs of their newer members.

Acknowledgments. The support of the GMA is gratefully acknowledged; we would like to thank in particular Vincenzo Niola, Riccardo Rubini, and Mauro Velardocchia for their constant support, encouragement, and enthusiasm for the GMA-IRE initiative. We also thank Pau Català Calderón, Francisco Geu Flores, Qizhi Meng, Jiang Ming, Saioa Herrero Villalibre and Claudio Nabil Villegas Ulloa for gathering and sharing the data from the YFG survey. Finally, we also thank all the colleagues who supported our initiatives and participated in the surveys and events organized by GMA-IRE and YFG.

References

1. IFToMM: IFToMM Member Organizations website. iftomm-world.org/members
2. IFToMM: IFToMM Technical Committees website. iftomm-world.org/technical-committees
3. IFToMM: Cross-Disciplinary "Securing our future environment" website. iftomm-world.org/cdg-1-securing-our-future-environent-air-water-energy
4. IFToMM: Cross-Disciplinary "Women's group" website. iftomm-world.org/cdg-1-securing-our-future-environent-air-water-energy
5. IFToMM: Cross-Disciplinary "Graduate student's" website. iftomm-world.org/cdg-4-iftomm-graduate-students-group
6. IFToMM: Cross-Disciplinary "Young Faculty Group" website. iftomm-world.org/cdg-2-iftomm-young-faculty-group
7. IFToMM: Proceedings of the 1st Young Faculty Group Symposium on Emerging Fields in Mechanism and Machine Science (2024). https://doi.org/10.17185/duepublico/82370
8. ASME: Young Professionals website. sections.asme.org/youngprofessionals
9. IEEE RAS: Young Professionals website. www.ieee-ras.org/membership/young-professionals
10. ECCOMAS: Young Investigators Committee (EYIC) website. eccomas.org/comittees/eyic/
11. EMA: Young EMA website. https://magnetism.eu/294-youngema.htm
12. EPS: Young Minds website. www.epsyoungminds.org/
13. GMA: Official website. meccanicaapplicata.it
14. MUR: DM 855/2015. Rideterminazione Settori Concorsuali ("Re-definition of scientific fields for public selections"), annex C (English version). www.mur.gov.it/sites/default/files/2024-05/DecretoMinisterialen.639del02-05-2024-AllegatoC.pdf
15. GMA: Archived historical website. wpage.unina.it/dellaval/GMA/
16. Quaglia, G., Boschetti, G., Carbone, G.: Advances in Italian mechanism science. In: Proceedings of the 5th International Conference of IFToMM, Italy (2024). https://doi.org/10.1007/978-3-031-64553-2
17. Okada, M.: Advances in mechanism and machine science. In: Proceedings of the 16th IFToMM World Congress, vol. 1 (2023). https://doi.org/10.1007/978-3-031-45705-0
18. Okada, M.: Advances in mechanism and machine science. In: Proceedings of the 16th IFToMM World Congress, vol. 2 (2023). https://doi.org/10.1007/978-3-031-45770-8
19. Okada, M.: Advances in mechanism and machine science. In: Proceedings of the 16th IFToMM World Congress, vol. 3 (2023). https://doi.org/10.1007/978-3-031-45709-8
20. euRobotics: eurobotics mailing list website. eu-robotics.net/mailing-list
21. Karlsruhe Institute of Technology: robotics-worldwide website. www.robotics-worldwide.org
22. GIMC, SIMAI: GIMC SIMAI Young 2024 website. https://sites.google.com/view/gsyw24/

Author Index

A
Abdeljelil, Dorra Ben 326
Abdula, Rania W. 431
Aidos, Sultan 407
Ajili, Refka 247
Alarcón-Gómez, Camila 107
Ali, Mustafa A. 431
Ali, Raja Ouled Ahmed Ben 326
Amodio, Francesco 215
Arıcı, Alperen 3

B
Baglieri, Lorenzo 215
Barrueta, Johan 335
Basaldúa-Sánchez, J. E. 419
Bermeo, John E. 193
Boada, Beatriz López 295
Boada, María Jesús López 295
Boscariol, Paolo 183
Botta, Andrea 215
Bouaziz, Brahim 345, 398
Boudon, Benjamin 256
Bouraoui, Chokri 345, 398
Bouzgarrou, Chedli 256
Bozdemir, İlkim Zahide 145

C
Carboni, Andrea Piga 126
Carrasco-Valenzuela, Diego 107
Carrillo, Enrique 464
Castillo-Castañeda, Eduardo 193
Català, P. 137
Çetin, Levent 145
Chaker, Abdelbadiâ 193
Chaker, Abdelbadia 47, 207
Chatti, Sami 326
Chen, Bai 87
Chen, Yan 171
Colucci, Giovanni 215
Correa, Juan Carlos Jáuregui 378
Corves, Burkhard 159, 274

D
Dana, Ünal 145
Delgado-Orias, Roberto 107
Dhokkar, Atef 353
Doudech, Imen 47
Duretto, Simone 215

E
Eltaief, Maher 345, 398
Essomba, Terence 25

F
Flores, Mirko 464
Flores, Paulo 443, 454
Fomin, Alexey 66

G
Gani, Sergazin 407
Gasparetto, Alessandro 56
Gezgin, Erkin 3, 35, 145
Gonzales, Ludwing 335
Guigon, Louis 256

H
Hermoza, Estefania 335, 464
Houidi, Ajmi 47, 247, 285
Huerta-Manzanilla, Eric Leonardo 368, 419
Hurtado-Hurtado, Gerardo 368, 378
Hüsing, Mathias 159, 274

I
Ida, Edoardo 476

J
Jabari, Mohammad 207
Jauregui-Correa, Juan Carlos 368, 419
Jordi, L. 137

K
Kapucu, Sadettin 388

© The Editor(s) (if applicable) and The Author(s), under exclusive license to Springer Nature Switzerland AG 2026
A. Chaker et al. (Eds.): EFIMMS 2026, MMS 205, pp. 487–489, 2026.
https://doi.org/10.1007/978-3-032-22270-1

Kecskeméthy, Andrés 76, 256
Kentel, Behzat Bahadir 116
Keunecke, Sophie Charlotte 274
Khanamiryan, Zaven 236
Koçak, Mertcan 35
Koçak, Mertcan 3
Kribi, Badreddine 247
Kütük, Mehmet Erkan 388

L
Lahdiri, Chaima 16
Lamine, Houssein 305
Laribi, Med Amine 47, 193, 207, 225
Laryushkin, Pavel 66
Lavayen, Daniel 335, 464
Li, Huanxiao 97
Li, Long 97
Ling, Jie 87
López Boada, Beatriz 315
López Boada, María Jesús 315
Lopez-Ramirez, Jose Emiliano 368, 419
Lovasz, Erwin-Christian 264
Lyu, Shengnan 97

M
Ma, Jiayao 171
Mahmoudi, Helmi 285
Makki, Hassen 305
Martins, Daniel 126
Meléndez-Useros, Miguel 295, 315
Meng, Qizhi 76
Mezouar, Youcef 256
Micle, Lucian-Mihai 264
Mlika, Abdelfattah 16, 47
Mohammed, Omar D. 431
Monge, Jesus 335
Morales-Velázquez, Luis 378
Mottola, Giovanni 476
Murai, Estevan Hideki 126
Mustafa, Mahmood M. 431

N
Novikov, Alexey 66
Nursultan, Zhetenbayev 407

O
Oarcea, Alexandru 264
Ochsendorf, Marcel 274
Öksüz, Mehmet 116

P
Petuya, Victor 225
Pierart-Vásquez, Fabian 107

Q
Quaglia, Giuseppe 207, 215
Quispe, Mario 335

R
Rangel-Escobar, Hannia 419
Requena, Erick 335
Rezgui, Mohamed Ali 353
Riabtsev, Mykhailo 225
Rodríguez, Jorge 464
Romdhane, Lotfi 305
Russo, Matteo 476

S
Saafi, Houssem 16
Sandoval-Valencia, Tania Elizabeth 368, 419
Sayat, Akhmejanov 407
Scalera, Lorenzo 56
Shen, Yayi 87
Souza, Gustavo Valdatti 126
Sticlaru, Carmen 264

T
Tagliavini, Luigi 215
Tamellin, Iacopo 183
Tao, Xinrui 171
Toccaceli, Lorenzo 215
Tokuda, Tamie 464
Trabelsi, Ali 353
Tulcan, Elida 264

U
Ulikyan, Azatuhi 236
Uslu, Tuğrul 35
Uslu, Tuğrul 3
Ussen, Shylmyrza 407

V
Valencia, Tania Elizabeth Sandoval 378
Veciana, J. M. 137
Velis, Alonso 464
Viadero-Monasterio, Fernando 295, 315

Vidoni, Renato 56
Villegas-Ulloa, Claudio 107
Visconte, Carmen 207

W
Wadullah, Haitham M. 431
Wang, Xin 87
Witte, Mark 159

X
Xu, Tianye 97

Y
Yang, Ziyun 159
Yazıcı, Mustafa Volkan 35
Yazıcı, Mustafa Volkan 3
Yerkebulan, Nurgizat 407

Z
Zhanar, Bigaliyeva 407
Zhang, Nianhua 295
Zhang, Tianwei 87